

#130928
(Letter)

O
NW

10th NAVY SYMPOSIUM on AEROBALLISTICS

LEVEL

AD 63355
354
353

VOLUME 3

15-16-17 JULY



DDC
APPROVED
JAN 17 1979
C

AD A O 6 3 3 5 5

DDC FILE COPY

SPONSORED BY THE

NAVY AEROBALLISTICS ADVISORY COMMITTEE

NAAC

HOSTED BY

NAVAL SURFACE WEAPONS CENTER
DAHLGREN LABORATORY, DAHLGREN, VA.

HELD AT THE

SHERATON MOTOR INN

FREDERICKSBURG, VA.

This document has been approved
for public release and sale; its
distribution is unlimited.

78 11 16 037

LEVEL III

12

D D C
RECEIVED
JAN 17 1979
RECEIVED

at c

6

PROCEEDINGS OF THE TENTH
NAVY SYMPOSIUM ON AEROBALLISTICS (109)

~~VOLUME 3~~

~~15-16-17 JULY 1975~~

HELD AT THE SHERATON MOTOR INN
FREDERICKSBURG, VIRGINIA

75-16-17 July 1975. Volume 3.

SPONSORED BY THE NAVY AEROBALLISTICS
ADVISORY COMMITTEE NAAC

11 17 Jul 75

12 554 p.

This document has been approved
for public release and sale; its
distribution is unlimited.

411 022

mt

FOREWORD

These *Proceedings*, published in four volumes, comprise the 45 papers presented at the Tenth Navy Symposium on Aeroballistics held at the Sheraton Motor Inn, Fredericksburg, Virginia, 15, 16 and 17 July 1975.

This symposium was the tenth in a series begun in 1950 under the sponsorship of the then Bureau of Ordnance Committee on Aeroballistics, and currently conducted by the Naval Aeroballistics Advisory Committee as sponsoring committee for the Naval Air Systems Command and the Naval Ordnance Systems Command. The continuing purpose of the symposiums has been to disseminate the results of aeroballistics research and to bring the research findings of industry, the universities, and government laboratories to bear upon the Navy's aeroballistic research and development programs.

Over 160 research scientists representing 56 organizations attended this tenth symposium. Session I covered the subjects of missile stability and performance; Session II was concerned with missile stability and performance/launch dynamics; Session III dealt with heat transfer; Session IV covered inlets and diffusers/gas dynamics; and Session V presented aero-elasticity and structures.

The papers in these *Proceedings* have been reproduced in facsimile. They appear in the order of presentation except that all classified papers have been taken out of sequence and grouped together as Volume 4, a confidential volume. Volumes 1 through 3 are unclassified. This is Volume 1.

Requests for or comments on individual papers should be addressed to the respective authors.

THOMAS A. CLARE
General Chairman
Symposium Committee

ACCESSION for	
NTIS	White Section <input checked="" type="checkbox"/>
DDC	Buff Section <input type="checkbox"/>
UNCLASSIFIED	<input type="checkbox"/>
BY <i>W. J. I.</i>	
DISTRICT/STATION/ACTIVITY CODES	
SPECIAL	
A	

CONTENTS

	Page
Author Index	xii
Greetings	xiv
Welcome	xv
Advisory Committee	xviii
NACC Panels and Panel Chairman for 1975	xviii
Past NACC Panel Chairman	xviii
U. S. Navy Symposium on Aeroballistics	xvi-xvii
Paper Selection Committee and Acknowledgements	xix
Attendees	xx through xxxi

Volume 1

1. Survey and Evaluation of Nonlinear Aeromechanics M. Michael Briggs <i>McDonnell Douglas Corporation</i> <i>Huntington Beach, California</i>	1
2. Aerodynamic Roll Characteristics of Canard Missiles Richard E. Meeker <i>Naval Weapons Center</i> <i>China Lake, California</i>	37
3. Roll Rate Stabilization of a Canard-Controlled Guided Missile Configuration at Subsonic and Supersonic Speed P. Daniels <i>Naval Surface Weapons Center, Dahlgren Laboratory,</i> <i>Dahlgren, Virginia</i>	63
4. Supersonic Lifting-Surface Program for Cruciform Missiles With Applications to Induced Roll M. F. E. Dillenius, J. N. Nielsen, and M. J. Hemsch <i>Nielsen Engineering and Research, Inc.</i> <i>Mountain View, California</i>	97
5. Prediction of Missile Aerodynamic Characteristics of Arbitrary Roll Orientation W. B. Brooks <i>Group Engineer</i> <i>McDonnell Douglas Astronautics Company</i> <i>Saint Louis, Missouri</i>	160
6. Wing Planform Studies for a Span-Constrained Missile L. S. Jernell and W. C. Sawyer <i>NASA Langley Research Center</i> <i>Hampton, Virginia</i>	197
	Paper Withdrawn
7. An Experimental Study of the Effects of Missile Configuration Variables on Pitch Linearity William A. Corlett and Roger H. Fournier <i>NASA Langley Research Center</i> <i>Hampton, Virginia</i>	198

CONTENTS (Continued)

Volume 1

	Page
9. Static and Dynamic Aerodynamics of Projectiles and Missiles Frankie G. Moore and Gil Y. Graff <i>Naval Surface Weapons Center Dahlgren Laboratory Dahlgren, Virginia</i>	216
10. A Review and Status of Wrap-Around Fin Aerodynamics C. Wayne Dahlke <i>U. S. Army Missile Command Redstone Arsenal, Alabama</i>	219
11. High Subsonic Aerodynamic Longitudinal Stability and Control Characteristics of Configurations Incorporating Wrap-Around Surfaces E. F. Lucero <i>Applied Physics Laboratory/The Johns Hopkins University Silver Spring, Maryland</i>	325
12. Transonic Flight Dynamics of Long Shell W. H. Mermagen and V. Oskay <i>U. S. Army Ballistic Research Laboratories Aberdeen, Maryland</i>	361

Volume 2

16. Store Separation State-of-the-Art Review A. R. Maddox J. R. Marshall <i>Naval Weapons Center China Lake, California</i> G. F. Cooper <i>Naval Missile Center Point Mugu, California</i> E. F. McCabe <i>Naval Research and Development Center Bethesda, Maryland</i>	1
17. An Estimate of the Effect of Multiple Ejection Rack Flexibility on Six-Degree-of-Freedom Store Ejection Conditions Leroy Devan <i>Naval Surface Weapons Center Dahlgren Laboratory Dahlgren, Virginia</i>	68
18. A Study of Variable Orifice Controlled Weapons Launching John Sun <i>Naval Surface Weapons Center Dahlgren Laboratory Dahlgren, Virginia</i>	106
19. The Aerodynamic Environment of Rockets Launched From Helicopters B. Z. Jenkins <i>U. S. Army Missile Command Redstone Arsenal, Alabama</i>	149

CONTENTS (Continued)

Volume 2

	Page
20. A Simple Method for Studying Some Aerodynamic Heating Problems Tse-Fou Zien <i>Naval Surface Weapons Center</i> <i>White Oak Laboratory</i> <i>Silver Spring, Maryland</i>	174
21. Structural Studies of Rough-Wall Boundary Layers Robert J. Moffat <i>Stanford University</i> <i>Stanford, California</i>	206
22. Heat Transfer From a Turbulent Boundary Layer on a Porous Hemisphere Robert H. Feldhuhn <i>Naval Surface Weapons Center</i> <i>White Oak Laboratory</i> <i>Silver Spring, Maryland</i>	239
23. Performance Characteristics of Transpiration Nose Tips At High Angles of Attack J. L. Nardacci, N. C. Campbell, and D. Quan <i>McDonnell Douglas Astronautics Company</i> <i>Huntington Beach, California</i>	273
24. Surface Temperature Measurements in Hypersonic Free Flight Daniel C. Reda, Robert A. Leverance and William G. Dorsey, Jr. <i>Naval Surface Weapons Center</i> <i>White Oak Laboratory</i> <i>Silver Spring, Maryland</i>	344
25. The Augmentation of Stagnation Point Heat Transfer By Particle-Flow Interactions W. J. Grabowski <i>Science Applications, Inc.</i> <i>El Segundo, California</i>	400
26. Heat Transfer to a Circumferential Gap On a Cone At Angle of Attack D. E. Nestler <i>General Electric Company</i> <i>Philadelphia, Pa.</i>	401
27. Experimental Investigation of a Fin-Cone Interference Flow Field at MACH 5 Joseph D. Gillerlain, Jr. <i>Naval Surface Weapons Center</i> <i>White Oak Laboratory</i> <i>Silver Spring, Maryland</i>	425
29. Aerodynamic Characteristics of a Missile Configuration Having a Forward Located Inlet M. Leroy Spearman and Clyde Hayes <i>NASA Langley Research Center</i> <i>Hampton, Virginia</i>	467
	Paper Withdrawn

10th Navy Symposium on Aeroballistics

Vol. 3

CONTENTS (Continued)

Volume 2

	Page
30. Analysis and Design of Ejector Diffuser for Optimum Thrust Tsze C. Tai <i>Naval Ship Research and Development Center Bethesda, Maryland</i>	468
31. Evaluation of a Coaxial Gas Flow Chamber R. E. Lee <i>Naval Surface Weapons Center White Oak Laboratory Silver Spring, Maryland</i> Paper Withdrawn	493

Volume 3

32. The Impact of Contemporary Fluid Mechanics Computational Techniques on Missile Design Technology Part I J. Xerikos <i>Chief, Aerodynamics Branch McDonnell Douglas Astronautics Company Huntington Beach, California</i> Part II Clark H. Lewis <i>Virginia Polytechnic Institute and State University Blacksburg, Virginia</i>	1 26
33. Survey of Three-Dimensional Flow Fields in the Presence of Wings at $M = 2.48$ George S. Pick and R. M. Hartley <i>Naval Ship Research and Development Center Bethesda, Maryland</i>	97
34. Two-Dimensional Analysis of Base Drag Reduction Using External Burning R. Cavalleri <i>Atlantic Research Corporation Alexandria, Virginia</i>	148
35. Wind-Tunnel Study of Projectile Base Drag Reduction Through Combustion of Solid, Fuel-Rich Propellants F. P. Baltakis <i>Naval Surface Weapons Center White Oak Laboratory Silver Spring, Maryland</i> J. R. Ward <i>Ballistic Research Laboratories Aberdeen Proving Ground, Maryland</i>	175

CONTENTS (Continued)

Volume 3

	Page
36. A Three-Dimensional Flow Field Computer Program for Maneuvering and Ballistic Re-entry Vehicle C. L. Kyriess and T. B. Harris <i>General Electric Company</i> <i>Philadelphia, Pennsylvania</i>	200
37. MACH 4.9 Turbulent Boundary-Layer Separation Induced by a Continuous Flow Compression Robert L. P. Voisinnet <i>Naval Surface Weapons Center</i> <i>White Oak Laboratory</i> <i>Silver Spring, Maryland</i>	240
38. Effects of Hypersonic Viscous Interaction on the Center of Pressure of Sharp and Blunt Cones as a Function of Angle of Attack A. G. Keel, Jr. and J. A. Darling <i>Naval Surface Weapons Center</i> <i>White Oak Laboratory</i> <i>Silver Spring, Maryland</i>	279
39. A State-of-the-Art Review of Methods in Aeroelasticity and Structural Analyses for Guided Weapons G. Dailey <i>Applied Physics Laboratory/The Johns</i> <i>Hopkins University</i> <i>Silver Spring, Maryland</i> R. Oedy <i>Hughes Missile Division</i> <i>Canoga Park, California</i> W. J. Werback <i>Naval Weapons Center</i> <i>China Lake, California</i>	294
40. Survey of Structural Materials Technology for Navy Tactical Missiles J. S. O'Connor and W. C. Caywood <i>Johns Hopkins University</i> <i>Applied Physics Laboratory</i> <i>Silver Spring, Maryland</i>	315
41. Nonlinear Hypersonic Aero-Thermo-Elastic Effects on Missile Lifting Surfaces B. Almroth, J. A. Bailie, and F. R. Brogon <i>Lockheed Missiles and Space Company, Inc.</i> <i>Sunnyvale, California</i>	337

10th Navy Symposium on Aeroballistics

Vol. 3

CONTENTS (Continued)

Volume 3

	Page
43. A Review of the Integral Theory of Impact Thomas B. McDonough <i>Aeronautical Research Associates of Princeton, Inc.</i> <i>Princeton, New Jersey</i>	403
44. Thermostructural Analysis of IR Seeker Domes W. R. Compton C. F. Markarian B. M. Ryan <i>Aerothermodynamics Branch</i> <i>Naval Weapons Center</i> <i>China Lake, California</i>	479
45. Effect of Multiple Impacts on Erosion Characteristics of Nose-Tip Materials N. W. Sheetz <i>Naval Surface Weapons Center</i> <i>White Oak Laboratory</i> <i>Silver Spring, Maryland</i>	508

**Volume 4
(Classified Papers)**

8. Aerodynamic Characteristics of a Missile Configuration in the Presence of an Exhaust Plume at Angles of Attack to 180° S. K. Carter <i>Naval Weapons Center</i> <i>China Lake, California</i> F. K. Shigeno M. M. Briggs <i>McDonnell Douglas Astronautics-West</i> <i>Huntington Beach, California</i>	1
13. Spinning Tubular Projectile Ronald S. Brunsvold C. A. Kalivretenos <i>Naval Surface Weapons Center</i> <i>White Oak Laboratory</i> <i>Silver Spring, Maryland</i>	52
14. Guided Projectile Aerodynamic Design Considerations H. Farley and F. Krens <i>Naval Surface Weapons Center</i> <i>Dahlgren Laboratory</i> <i>Dahlgren, Virginia</i>	83
15. The Aeroballistic Development of the Flat-Trajectory Projectile G. A. Kalivretenos <i>Naval Surface Weapons Center</i> <i>White Oak Laboratory</i> <i>Silver Spring, Maryland</i>	113

CONTENTS (Continued)

Volume 4
(Classified Papers)

	Page
28. Survey of Airbreathing Missile Inlet Development J. L. Keirsey and R. L. Rumpf <i>Applied Physics Laboratory/The Johns Hopkins University Silver Spring, Maryland</i>	159
42. Use of Rocket Sled Facilities in Missile Aeroelastic Investigations R. A. Deep and C. E. Brazzel <i>U. S. Army Missile Command Redstone Arsenal, Alabama</i>	216

AUTHORS

Page	Page
Almroth, B., Paper No. 41, Vol. 3 337	Kyriss, C. L., Paper No. 36, Vol. 3 200
Bailie, J. A., Paper No. 41, Vol. 3 337	Lee, R. E., Paper No. 31, Vol. 2 493
Baltakis, F. P., Paper No. 35, Vol. 3 175	Leverance, R. A., Paper No. 24, Vol. 2 344
Brazzel, C. E., Paper No. 42, Vol. 4 216	Lewis, C. H., Paper No. 32, Vol. 3 26
Briggs, M. M., Paper No. 1, Vol. 1 1	Lucero, E. F., Paper No. 11, Vol. 1 325
Paper No. 8, Vol. 4 1	
Brogon, F. R., Paper No. 41, Vol. 3 337	Maddox, A. R., Paper No. 16, Vol. 2 1
Brooks, W. B., Paper No. 5, Vol. 1 160	Markarian, C. F., Paper No. 44, Vol. 3 479
Brunsvold, R. S., Paper No. 13, Vol. 4 52	Marshall, J. R., Paper No. 16, Vol. 2 1
	McCabe, E. F., Paper No. 16, Vol. 2 1
Campbell, N. C., Paper No. 23, Vol. 2 273	McDonough, T. B., Paper No. 43, Vol. 3 403
Carter, S. K., Paper No. 8, Vol. 4 1	Mecker, R. E., Paper No. 2, Vol. 1 37
Cavalleri, R., Paper No. 34, Vol. 3 148	Mermagen, W. H., Paper No. 12, Vol. 1 361
Caywood, W. C., Paper No. 40, Vol. 3 315	Moffat, R. J., Paper No. 21, Vol. 2 206
Compton, W. R., Paper No. 44, Vol. 3 479	Moore, F. G., Paper No. 9, Vol. 1 216
Cooper, G. F., Paper No. 16, Vol. 2 1	
Corlett, W. A., Paper No. 7, Vol. 1 198	Nardacci, J. L., Paper No. 23, Vol. 2 273
	Nestler, D. E., Paper No. 26, Vol. 2 401
Dahlke, C. W., Paper No. 10, Vol. 1 279	Nielsen, J. N., Paper No. 4, Vol. 1 97
Dailey, G., Paper No. 39, Vol. 3 294	
Daniels, P., Paper No. 3, Vol. 1 63	O'Connor, J. S., Paper No. 40, Vol. 3 315
Darling, J. A., Paper No. 38, Vol. 3 279	Oedy, R., Paper No. 39, Vol. 3 294
Deep, R. A., Paper No. 42, Vol. 4 216	Oskay, V., Paper No. 12, Vol. 1 361
Devan, L., Paper No. 17, Vol. 2 68	
Dillenius, M. F. E., Paper No. 4, Vol. 1 97	Pick, G. S., Paper No. 33, Vol. 3 97
Dorsey, W. G., Jr., Paper No. 24, Vol. 2 344	
	Quan, D., Paper No. 23, Vol. 2 273
Farley, H., Paper No. 14, Vol. 4 83	Reda, D. C., Paper No. 24, Vol. 2 344
Feldhuhn, R. H., Paper No. 22, Vol. 2 239	Rumpf, R. L., Paper No. 28, Vol. 4 159
Fournier, R. H., Paper No. 7, Vol. 1 198	Ryan, B. M., Paper No. 44, Vol. 3 479
Gillerlain, J. D., Jr., Paper No. 27, Vol. 2 425	Sawyer, W. C., Paper No. 6, Vol. 1 197
Grabowski, W. J., Paper No. 25, Vol. 2 400	Sheetz, N. W., Paper No. 45, Vol. 3 508
Graff, G. Y., Paper No. 9, Vol. 1 216	Shigeno, F. K., Paper No. 8, Vol. 4 1
	Spearman, M. L., Paper No. 29, Vol. 2 467
Harris, T. B., Paper No. 36, Vol. 3 200	Sun, J., Paper No. 18, Vol. 2 106
Hartley, R. M., Paper No. 33, Vol. 3 97	
Hayes, C., Paper No. 29, Vol. 2 467	Tai, T. C., Paper No. 30, Vol. 2 468
Hensch, M. J., Paper No. 4, Vol. 1 97	
	Voisinet, R. L. P., Paper No. 37, Vol. 3 240
Jenkins, B. Z., Paper No. 19, Vol. 2 149	Ward, J. R., Paper No. 35, Vol. 3 175
Jernell, L. S., Paper No. 6, Vol. 1 197	Werback, W. J., Paper No. 39, Vol. 3 294
Kalivretenos, C. A., Paper No. 13, Vol. 4, 52	Xerikos, J., Paper No. 32, Vol. 3 1
Paper No. 15, Vol. 4 113	Zien, Tse-Fou, Paper No. 20, Vol. 2 174
Keel, A. G., Jr., Paper No. 38, Vol. 3 279	
Keirse, J. L., Paper No. 28, Vol. 4 159	
Krens, F., Paper No. 14, Vol. 4 83	

GREETINGS

The Navy Aeroballistics Advisory Committee (NAAC) provides valuable assistance to the Naval Air and Naval Sea Systems Commands. It is extremely active in promoting the exchange of technical information among Naval activities, Navy contractors, and other government agencies. It also provides effective guidance by recommending aeroballistics research investigations and identifying the new aeroballistic facilities necessary for future weapons development. We hope that this Symposium, as in the past, will provide for a stimulating exchange of information and will be of value to all participants. Best wishes for a successful Symposium.



A. B. McCaulley
Captain, USN
Assistant Commander
for Research & Technology
Naval Air Systems Command



R. W. King
Rear Admiral, USN
Deputy Commander
for Research & Technology
Naval Sea Systems Command

10th Navy Symposium on Aeroballistics

Vol. 3

WELCOME

On behalf of the Dahlgren Laboratory of the Naval Surface Weapons Center, we are pleased to welcome you to the Tenth U. S. Navy Symposium on Aeroballistics.

The Navy Aeroballistics Advisory Committee, established jointly by the Naval Air Systems Command and the Naval Sea Systems Command, has prepared an excellent program covering diverse technical disciplines in the field of aeroballistics. It is noted that the Symposium brings together speakers and guests with special competence in aeroballistics from the Navy, Air Force, Army, other government agencies, universities, and from industry. It is our hope that we can provide a pleasant atmosphere for you during the Symposium.



C. J. Rorie
Captain, USN
Commander
Naval Surface Weapons Center

U S. NAVY SYMPOSIUMS ON AEROBALLISTICS

FIRST SYMPOSIUM – NOVEMBER 1950

Hosted by Defense Research Laboratory
Held at University of Texas
Austin, Texas

SECOND SYMPOSIUM – MAY 1952

Hosted by Naval Weapons Center
Held at Huntington Hotel
Pasadena, California

THIRD SYMPOSIUM – OCTOBER 1954

Hosted by Applied Physics Laboratory
The Johns Hopkins University
Held at Applied Physics Laboratory
The Johns Hopkins University
Silver Spring (Howard County Location), Md.

FOURTH SYMPOSIUM – NOVEMBER 1957

Hosted by Naval Weapons Laboratory
Held at Department of Commerce Auditorium
Washington, D. C.

FIFTH SYMPOSIUM – OCTOBER 1961

Hosted by Naval Ordnance Laboratory
Held at Naval Ordnance Laboratory
White Oak, Md.

SIXTH SYMPOSIUM – OCTOBER-NOVEMBER 1963

Hosted by Naval Ship Research and
Development Center
Held at National War College
Fort McNair, Washington D. C.

SEVENTH SYMPOSIUM – JUNE 1966

Hosted by Naval Missile Center
Held at Naval Missile Center
Point Mugu, Calif.

EIGHTH SYMPOSIUM – MAY 1969

Hosted by Naval Weapons Center
Held at NWC Corona Laboratories
Corona, Calif.

10th Navy Symposium on Aeroballistics

Vol. 3

NINTH SYMPOSIUM – MAY 1972

Hosted by Applied Physics Laboratory
The Johns Hopkins University
Held at Applied Physics Laboratory
The Johns Hopkins University
Silver Spring (Howard County Location), Md.

TENTH SYMPOSIUM – JULY 1975

Hosted by Naval Surface Weapons Center
Dahlgren Laboratory
Dahlgren, Virginia
Held at Sheraton Fredericksburg Motor Inn
Fredericksburg, Va.

NAVAL AEROBALLISTICS ADVISORY COMMITTEE

MEMBERS AND ALTERNATE MEMBERS FOR 1975

Members	Alternate
S. de los Santos, Chairman (NSRDC)	S. Gottlieb
L. Schindel (NAVSURFWPCEN/WOL)	K. Enkenhaus
L. L. Cronvich (APL/JHU)	E. T. Marley
R. D. Cuddy (NAVSURFWPCEN/DL)	F. G. Moore
J. W. Rom (NMC)	M. R. Marson
R. W. Van Aken (NWC)	R. E. Meeker
W. A. Langan (NADC)	V. C. Dailey

ASSOCIATES

- W. C. Volz, Executive Secretary (NAVAIRSYSCOM)
- H. Andrews (NAVAIRSYSCOM)
- L. Pasiuk (NAVSEASYSKOM)
- C. Wheeler (NAVSEASYSKOM)

NAAC PANELS AND PANEL CHAIRMAN
FOR 1975

Aeroelasticity and Structures	E. L. Jeter (NWC)
Air Inlets and Diffusers	R. L. Rumpf (APL/JHU)
Gas Dynamics	G. Pick (NSRDC)
Heat Transfer	W. C. Lyons (NSWC/WOL)
Missile Stability and Performance	T. A. Clare (NSWC/DL)
Launch Dynamics	G. Cooper (NMC)

PAST NAAC CHAIRMEN

Feb 1949-Nov 1949	CDR H. M. Mott-Smith (BuOrd)
Dec 1949-Oct 1950	CDR L. G. Pooler (BuOrd)
Oct 1950-Feb 1953	CDR L. G. Pooler (NOL)
Mar 1953-Jul 1953	A. I. Moskovits (Acting) (BuOrd)
Sep 1953-Jul 1955	E. A. Bonney (APL/JHU)
Aug 1955-Aug 1957	H. H. Kurzweg (NOL)
Sep 1957-Jul 1959	W. R. Haseltine (NWC)
Aug 1959-Jul 1961	R. A. Niemann (NSWC/DL)
Jul 1961-Jan 1963	R. E. Wilson (NOL)
Jan 1963-Jan 1965	S. T. de los Santos (NSRDC)
Jan 1965-Jan 1967	R. H. Peterson (NMC)
Jan 1967-Jan 1969	W. A. Kemper (NSWC/DL)
Jan 1969-Jan 1971	L. L. Cronvich (APL/JHU)
Jan 1971-Jan 1973	W. R. Haseltine (NWC)
Jan 1973-Jan 1975	R. E. Wilson (NAVSURFWPCEN/WOL)

10th Navy Symposium on Aeroballistics

Vol. 3

PAPER SELECTION COMMITTEE

R. W. Van Aken, ChairmanNWC
T. C. Tai NSRDC
R. Rumpf APL/JHU
L. SchindelNAVSURFWPNCEN/WOL
F. G. MooreNAVSURFWPNCEN/DL
J. RomNMC
W. C. VolzNAVAIRSYSCOM
L. PasiukNAVSEASYSKOM

ACKNOWLEDGEMENTS

Thanks to all who have contributed to the Tenth Navy Symposium on Aeroballistics:
The host organization, the Dahlgren Laboratory of the Naval Surface Weapons Center.
Dr. T. A. Clare, Chairman of the Symposium; and Mrs. Mitzi Lumpkin and Miss Virginia Scott of NAVSURFWPNCEN for their administrative and secretarial assistance.
Mr. E. T. Marley (APL), Mr. W. C. Volz (NAVAIRSYSCOM), Mr. L. Pasiuk (NAVSEASYSKOM) for their advice and assistance regarding arrangements and technical matters relating to the Symposium.
Mr. R. W. Van Aken, Chairman of the paper selection committee, and the committee members for their efforts in paper selection and session organization.
Mr. Amos Clary, Public Affairs Director at the Dahlgren Laboratory, Mr. C. Philbrick, Director of Security for the Symposium, and Mrs. Judy Kinnaman, Sheraton Fredericksburg Motor Inn, for their assistance in arrangements for the Symposium.
Session chairman, opening speakers and honored guests, for their contributions to the Symposium.
And, finally, the authors and presenters of the technical papers, without whom the Symposium would not be possible, for their excellent literary and oral presentation of technologies in the field of Aeroballistics.

SYMPOSIUM ATTENDEE LIST

- ANDERSON, C. W., JR.
Atlantic Research Corp.
Guinesville, VA 22065
(703) 754-4111 - Ext. 279
- ATHA, L. C.
Ballistic Missile Defenses
Advanced Technology Center
P. O. Box 1500
Huntsville, AL 35807
(205) 895-3431
- BAILIE, J. A.
Lockheed Missiles & Space Co.
D81-12, B154
Box 504
Sunnyvale, CA 94088
(408) 742-9226
- BARNARD, H. R.
Texas Instruments
P. O. Box 6015
M/S 96
Dallas, TX 75222
(214) 238-3582
- BAUER, R. L.
Raytheon Co.
Missile Systems Division
Hartwell Road
Bedford, MA 01730
(617) 274-7100 - Ext. 2849
- BECKER, M.
Naval Surface Weapons Center
Dahlgren Laboratory
Code DK-21
Dahlgren, VA 22448
(703) 663-8107
- BELL, R. W.
Naval Postgraduate School
Dept. of Aeronautics
Monterey, CA 93940
- BELSKY, R. C.
Naval Surface Weapons Center
Dahlgren Laboratory
Code DK-70
Dahlgren, VA 22448
(703) 663-8835
- BENSIMON, M.
NASA-Goddard Space Flight Center
Code 742
Greenbelt, MD 20771
(301) 982-4865
- BERGSTEN, B.
Wright-Patterson AFB, OH 45433
(513) 225-2449
- BOLICK, R. G.
Naval Surface Weapons Center
Dahlgren Laboratory
Code DG-40
Dahlgren, VA 22448
(703) 663-7646
- BOURGEOIS, B. M.
Naval Surface Weapons Center
Dahlgren Laboratory
Code DN-10
Dahlgren, VA 22448
(703) 663-8565
- BRAZZEL, C. E.
AMSMI-RDK
Bldg. 5400
Reustone Arsenal, ALA 35809
(205) 876-7276
- BRIGGS, M. M.
McDonnell Douglas Astronautics Co.
Dept. A3-203, M/S 11-2
5301 Bolsa Ave.
Huntington Beach, CA 92647
(714) 896-3352

10th Navy Symposium on Aeroballistics

Vol. 3

SYMPOSIUM ATTENDEE LIST

- BROOKS, W. B.**
McDonnell Douglas Astronautics Co.
P. O. Box 516
Dept E241, Bldg. 10614, M/S 39
St. Louis, MO 63166
(314) 232-7479
- BROWNE, P. E.**
LTV Aerospace Corp.
Vought Systems Division
Unit 2-53364
P. O. Box 5907
Dallas, TX 75222
(214) 266-3237
- BRUCE, C. F.**
MIT-Lincoln Laboratory
Rm. D-382
P. O. Box 73
Lexington, MA 02173
(617) 862-5500 - Ext. 7872
- BRUNSVOLD, R. S.**
Naval Surface Weapons Center
White Oak Laboratory
Silver Springs, MD 20910
(202) 394-2080
- BURNS, G. P.**
Naval Surface Weapons Center
Dahlgren Laboratory
Code DK-22
Dahlgren, VA 22448
(703) 663-8368
- CARTER, S. K.**
Naval Weapons Center
Code 4063
China Lake, CA 93555
(714) 939-2627
- CAVALLERI, R.**
Atlantic Research Corp.
5390 Cherokee Avenue
Alexandria, VA 22314
(703) 354-3400 - Ext. 288
- CAYWOOD, W. C.**
Johns Hopkins University
Applied Physics Laboratory
8621 Georgia Avenue
Silver Spring, MD 20910
(202) 953-7100 - Ext. 7408
- CHALK, J. B.**
Naval Intelligence Support Center
4301 Suitland Road
Washington, D. C. 20390
- CHAPMAN, G. T.**
NASA - Ames Research Center
Moffet Field, CA 94035
- CLARE, T. A.**
Naval Surface Weapons Center
Dahlgren Laboratory
Code DK-20
Dahlgren, VA 22448
(703) 663-8829
- COOPER, G. F.**
Pacific Missile Test Center
Code 1241
Point Mugu, CA 93042
(805) 982-8941
- CORLETT, W. A.**
NASA-Langley Research Center
Mail Stop 406
Hampton, VA 23665
(804) 827-3181
- CRESCI, R. J.**
Polytechnic Institute of N. Y.
Route 110
Farmingdale, NY 11735
(516) 694-5500
- CRONVICH, L. L.**
Johns Hopkins University
Applied Physics Laboratory
8621 Georgia Avenue
Silver Spring, MD 20910
(202) 953-7100 - Ext. 7475

SYMPOSIUM ATTENDEE LIST

- CURRY, W. H.**
Sandia Laboratories
Division 5625
Albuquerque, NM 87115
(505) 264-8500
- DAHLKE, C. W.**
U. S. Army Missile Command
AMSMI-RDK
Redstone Arsenal, AL 35809
(205) 876-7753
- DAILEY, V. C.**
Naval Air Development Center
Warminster, PA 18974
(215) 672-9000 - Ext. 2316
- DANIEL, D. C.**
AFATL/DLDD
Eglin AFB, FL 32542
- DANIELS, P.**
Naval Surface Weapons Center
Dahlgren Laboratory
Code DK-21
Dahlgren, VA 22448
(703) 663-8107
- DE LOS SANTOS, S.**
Naval Ship Research & Development Center
Carderock Laboratory
Aviation & Surface Effects Dept. (1606)
Bethesda, MD 20084
(202) 227-1463
- DENYSYK, B.**
Naval Surface Weapons Center
Dahlgren Laboratory
Code DK-55
Dahlgren, VA 22448
(703) 663-8615
- DEVAN, L.**
Naval Surface Weapons Center
Dahlgren Laboratory
Code DK-21
Dahlgren, VA 22448
(703) 663-8107
- DILLENUS, M. F.**
Nielsen Engineering & Research, Inc.
510 Clyde Avenue
Mountain View, CA 94043
(415) 968-9457
- DRAGOWITZ, C. J.**
Grumman Aerospace Corp.
Dept. 393, Plant 35
Bethpage, NY 11714
(516) 575-3671
- DUNBAR, L.**
Science Applications, Inc.
101 Continental Bldg.
Suite 310
El Segundo, CA 90245
(213) 640-0480
- DUP. DONALDSON, C.**
Aeronautical Research Association
of Princeton, Inc.
50 Washington Rd.
P. O. Box 2229
Princeton, NJ 08540
(609) 452-2950
- EAVES, R. H., JR.**
ARO, Inc.
VKF-Tunnel F Bldg.
Arnold Air Force Station, TN 37389
(615) 455-2611 - Ext. 650
- ENKENHUS, K.**
Naval Surface Weapons Center
White Oak Laboratory
Flight Measurement Div.
Bldg. 430-109
Silver Spring, MD 20910
(202) 394-1939
- FARLEY, H. C.**
Naval Surface Weapons Center
Dahlgren Laboratory
Code DG-44
Dahlgren, VA 22448
(703) 663-7481

SYMPOSIUM ATTENDEE LIST

FELDHUHN, R. H.
*Naval Surface Weapons Center
White Oak Laboratory
Aerodynamics & Structural Branch
WA-21
Silver Spring, MD 20910
(202) 394-1675, 2890*

FIDLER, J. E.
*Martin Marietta Aerospace
Orlando Division
P. O. Box 5837, MP-88
Orlando, FL 32805
(305) 352-2204*

FISHER, P. D.
*Atlantic Research Corp.
P. O. Box 38
Gainesville, VA 22065
(703) 754-4111 - Ext. 258*

FORTUNATO, E.
*Naval Surface Weapons Center
White Oak Laboratory
Code 312
Silver Spring, MD 20910
(202) 394-2070*

FRIERSON, J. L.
*Naval Surface Weapons Center
Dahlgren Laboratory
Code DG-44
Dahlgren, VA 22448
(703) 663-7481*

GARNER, J. P.
*Naval Surface Weapons Center
Dahlgren Laboratory
Code DK-21
Dahlgren, VA 22448
(703) 663-8107*

GILLERLAIN, J. D.
*Naval Surface Weapons Center
White Oak Laboratory
Silver Spring, MD 20910
(202) 394-2086*

GIRAGOSIAN, P. A.
Wright-Patterson AFB, OH 45433

GNAGY, J. R.
*Pacific Missile Test Center
Code 1241
Point Mugu, CA 93042
(805) 982-8941*

GORECLAD, A. J.
*Naval Surface Weapons Center
White Oak Laboratory
Silver Spring, MD 20910
(202) 394-1651*

GOTTLIEB, S. M.
*Naval Ship Research & Development Center
Bethesda, MD 20084*

GRACEY, C.
*Naval Surface Weapons Center
Dahlgren Laboratory
Code DK-21
Dahlgren, VA 22448
(703) 663-8107*

GRAFF, G. Y.
*Naval Surface Weapons Center
Dahlgren Laboratory
Code DG-44
Dahlgren, VA 22448
(703) 663-7481*

GUIOU, CAPT M.
*Arnold Air Force Station
AEDC/DYR
Arnold AFS, TN 37389
(615) 455-2611 - Ext. 7834*

GURKIN, L. W., III
*NASA - Wallops Island Flight Cntr.
Wallops Island, VA 23337
(804) 3411 - Ext. 2566, 2200*

SYMPOSIUM ATTENDEE LIST

- HALDEMAN, C. W.**
Massachusetts Inst. of Technology
560 Memorial Drive
Cambridge, MA 02139
(617) 253-2602
- HALL, R. B.**
Naval Weapons Center
Code 4576
China Lake, CA 93555
(714) 939-7395
- HARRIS, T. B.**
General Electric Company
Valley Forge Space Techn. Center
Rm. U-3217
King of Prussia, PA 19406
(215) 962-1340
- HARTLEY, R. M.**
Naval Ship Research & Development Center
Code 166
Bethesda, MD 20084
- HASTINGS, S. M.**
Naval Surface Weapons Center
White Oak Laboratory
Silver Spring, MD 20910
(202) 394-1669
- HAYES, C.**
NASA - Langley Research Center
Mail Stop 406
Hampton, VA 23665
(804) 827-3181
- HERRON, R. D.**
ARO, Inc.
PWT-4T
Arnold Air Force Station, TN 37389
(615) 455-2611 - Ext. 7150, 7433
- HESSMAN, F. W.**
Rockwell International
Missile Systems Division
4300 East Fifth Avenue
Columbus, OH 43216
(614) 239-2667
- HOLESKI, D. E.**
Pacific Missile Test Range
Code 1232
Point Mugu, CA 93042
(805) 982-8403
- HUANG, S. L.**
Naval Air Development Center
Code 3033
Worminister, PA 18974
(215) 672-9000 - Ext. 2041
- HUMPHREYS, D. E.**
Naval Coastal Systems Laboratory
Code 710.2
Panama City, FL 32401
(904) 234-4213
- INGALLS, R.**
Pacific Missile Test Center
Point Mugu, CA 93042
(805) 982-8941
- INGRAM, C. W.**
Systems Research Lab., Inc.
28000 Indian Ripple Rd.
Dayton, OH 45440
(513) 426-8961
- JENKINS, B. Z.**
U. S. Army Missile Command
AMSMI-RKD
Redstone Arsenal, AL 35809
(205) 876-7278

SYMPOSIUM ATTENDEE LIST

JOHNSON, G. G.

*LTV Aerospace Corp.
Unit 2-53363
P. O. Box 5907
Dallas, TX 75222
(214) 266-7494*

KALIVRETENOS, C. A.

*Naval Surface Weapons Center
White Oak Laboratory
Silver Spring, MD 20910
(202) 394-4267*

KATZ, W. M.

*Naval Surface Weapons Center
Dahlgren Laboratory
DK-21
Dahlgren, VA 22448
(703) 663-8107*

KAUFMAN, L. G., III

*Grumman Aerospace Corp.
Research Dept. - Plant 35
Bethpage, NY 11714
(516) 575-2323*

KEARNS, J. P.

*Johns Hopkins University
Applied Physics Laboratory
8621 Georgia Avenue
Silver Spring, MD 20910
(202) 953-7100 - Ext. 646*

KEMPER, W. A.

*P. O. Box 129
Dillon, Colorado 80435*

KING, RADM R. W.

*Naval Sea Systems Command
SEA 03
Washington, D. C. 20362
(202) 692-8696*

KRENS, F. J.

*Naval Surface Weapons Center
Dahlgren Laboratory
Code DG-40
Dahlgren, VA 22448
(703) 663-7646*

KUSTER, F. A.

*Advanced Missile Project Office
Naval Air Development Center
Code 30P4
Warminster, PA 18974
(215) 674-9000 - Ext. 2574*

KUTSCHINSKI, C. R.

*Hughes Aircraft Co.
8433 Fallbrook Avenue
Bldg. 265/X35
Canoga Park, CA 91304
(213) 883-2400 - Ext. 3618*

KYRISS, C. L.

*General Electric Co.
Room U-3217, VFSTC
P. O. Box 8555
Philadelphia, PA 19101
(215) 962-5725*

LA GRANGE, D. E.

*Naval Ammunition Depot
Code 5041
Crane, IN 47522
(812) 854-1603*

LANDO, D. W.

*Naval Surface Weapons Center
Dahlgren Laboratory
Code DK-55
Dahlgren, VA 22448
(703) 663-8359*

LARSEN, K. A.

*Pacific Missile Test Center
Code 1241
Point Mugu, CA 93042
(805) 982-8941*

SYMPOSIUM ATTENDEE LIST

- LEE, K. W.
Naval Air Development Center
AVTD-3014
Warminster, PA 18974
(215) 672-9000 - Ext. 2344 or 2166
- LEWIS, C. H.
*Virginia Polytechnic Inst. &
State University*
214 Randolph Hall
Blacksburg, VA 24061
(703) 951-6126 - Ext. 6742
- LINDORM, C. A.
Naval Surface Weapons Center
Dahlgren Laboratory
Code DN-30
Dahlgren, VA 22448
(703) 663-8731
- LUCERO, E. F.
Johns Hopkins University
Applied Physics Laboratory
11100 Johns Hopkins Road
Laurel, MD 20810
(301) 953-7100 - Ext. 7450
- LYNCH, J. P., III
Naval Surface Weapons Center
Dahlgren Laboratory
Code DG-50
Dahlgren, VA 22448
- MADDOX, A. R.
Naval Weapons Center
Code 40604
China Lake, CA 93555
(714) 939-2935
- MARKARIAN, C. F.
Naval Weapons Center
Aerothermodynamics Branch
Code 4061
China Lake, CA 93555
(714) 939-2824
- MARLEY, E. T.
Johns Hopkins University
Applied Physics Laboratory
11100 Johns Hopkins Road
Laurel, MD 20810
(301) 953-7100 - Ext. 7477
- MAYER, W. E.
Boeing Aerospace Corp.
Seattle, WA 98124
(206) 655-3479
- MATTHEWS, M. L.
Boeing Aerospace Corp.
P. O. Box 3999
Seattle, WA 98124
(206) 773-1525
- MCCABE, E. F., JR.
Naval Ship Research & Development Center
Code 166
Bethesda, MD 20084
(202) 227-1670
- MARSHALL, J. R.
Naval Weapons Center
Code 4063
China Lake, CA 93555
(714) 939-2820
- MCCAULLEY, CAPT H. B./USN
*Assistant Commander for Research
and Technology*
AIR-03
Naval Air Systems Command
Washington, D. C. 20361
(202) 692-7439
- MASON, L. A.
Naval Surface Weapons Center
Dahlgren Laboratory
Code DK-21
Dahlgren, VA 22448
(703) 663-8107

SYMPOSIUM ATTENDEE LIST

MASSEY, J. M.

*Naval Surface Weapons Center
Dahlgren Laboratory
Code DK-63
Dahlgren, VA 22448
(703) 663-8468*

MEEKER, R. E.

*Naval Weapons Center
Code 4063
China Lake, CA 93555
(714) 939-2820*

MATTHEWS, M. L.

*Boeing Aerospace Corp.
P. O. Box 3999
Seattle, WA 98124
(206) 773-1525*

MILTON, J. E.

*University of Florida
Graduate School
P. O. Box 1918
Eglin AFB, FL 32542
() 882-5614*

MOFFAT, R. J.

*Leland Stanford Junior University
Dept. of Public Safety
711 Serra Street
Stanford, CA 94305*

MOGAVERO, M. A.

*Computer Science Center
221-C Preston Court
Baltimore, MD 21228
(301) 788-5832*

MONTAG, W. H.

*NASA-Goddard Space Flight Center
Code 742
Greenbelt, MD 20771
(301) 982-4865*

MORRISSETTE, R. C.

*Naval Surface Weapons Center
Dahlgren Laboratory
Code DG-30
Dahlgren, VA 22448
(703) 663-8411*

MOORE, F. G.

*Naval Surface Weapons Center
Dahlgren Laboratory
Code DG-40
Dahlgren, VA 22448
(703) 663-7481*

MURPHY, C. H.

*Aberdeen Proving Ground
Exterior Ballistics Laboratory
R. H. Kent Bldg. (120)
Aberdeen Proving Ground, MD 21005
(301) 278-3109*

NARDACCI, J. L.

*McDonnell Douglas Astronautics Co.
5301 Bolsa Avenue
Huntington Beach, CA 92647
(714) 896-5223*

NESTLER, D. E.

*General Electric Company
P. O. Box 8555
Philadelphia, PA 19101
(215) 962-6090*

NEWQUIST, J. C.

*Naval Surface Weapons Center
Dahlgren Laboratory
Code DG-50
Dahlgren, VA 22448
(703) 663-8586*

NIELSEN, J. N.

*Nielsen Engineering and
Research, Inc.
510 Clyde Avenue
Mountain View, CA 94043
(415) 968-9457*

SYMPOSIUM ATTENDEE LIST

OBERKAMPF, W. L.

*University of Texas at Austin
Austin, TX 78712
(512) 471-4585*

OHLMEYER, E. J.

*Naval Surface Weapons Center
Dahlgren Laboratory
Code DG-40
Dahlgren, VA 22448
(703) 663-7481*

OSBOURNE, B. P., JR.

*Defense Research & Engineering
Rm. 3D1089
The Pentagon
Washington, D. C. 20301
(202) OX-5-0552*

OSKAY, V.

*Director, U. S. Army Ballistic
Research Laboratories
Attn: AMXBR-EB
Aberdeen Proving Grounds, MD 21005
(301) 278-3405*

O'CONNOR, J. S.

*Johns Hopkins University
Applied Physics Laboratory
Johns Hopkins Road
Laurel, MD 20810
(301) 953-7100 - Ext. 7416*

ON, T. J.

*Naval Surface Weapons Center
Dahlgren Laboratory
Code DK-21
Dahlgren, VA 22448
(703) 663-8107*

PARRY, E. M.

*Naval Surface Weapons Center
Dahlgren Laboratory
Code DG-30
Dahlgren, VA 22448
(703) 663-8411*

PASIERB, J. J.

*Johns Hopkins University
Applied Physics Laboratory
8621 Georgia Avenue
Silver Spring, MD 20910
(301) 953-7100 - Ext. 3260*

PASIUK, L.

*Naval Sea Systems Command
SEA-03513
Washington, D. C. 20362
(202) 692-1151*

PEPITONE, T. R.

*Naval Surface Weapons Center
Dahlgren Laboratory
Code DK-21
Dahlgren, VA 22448*

PERPER, D. N.

*Hughes Aircraft Co.
Missile Division
Bldg. 268/W83
Canoga Park, CA 91304
(213) 883-2400 - Ext. 1294*

PICK, G. S.

*Naval Ship Research & Developm. Cntr.
Code 1660
Bethesda, MD 20084
(202) 227-1670*

PLATZER, M. F.

*Naval Postgraduate School
Dept. of Aeronautics
Monterey, CA 93940
(408) 646-2944*

RAUSCH, J. R.

*General Dynamics Corporation
5001 Kearny Villa Road
P. O. Box 80847
San Diego, CA 92138*

SYMPOSIUM ATTENDEE LIST

REDING, J. P.

*Lockheed Missiles & Space Co.
Dept. 81-11, Bldg. 154
P. O. Box 504
Sunnyvale, CA 94088
(408) 742-1944*

ROM, J. W.

*Pacific Missile Test Center
Code 0101
Point Mugu, CA 93042
(804) 982-7831 - Ext. 7833*

RUMPF, R. L.

*Johns Hopkins University
Applied Physics Laboratory
8621 Georgia Avenue
Silver Spring, MD 20910
(202) 953-7100 - Ext. 7440*

SANDERS, D. K.

*Naval Ammunition Depot
Code 5041
Crane, IN 47522
(812) 854-1603*

SCHINDEL, L. H.

*Naval Surface Weapons Center
White Oak Laboratory
Silver Spring, MD 20910
(202) 394-1245*

SCHMIDT, L. V.

*Naval Air Systems Command
Code AIR-3200
Washington, D. C. 20361
(202) 692-7417*

SHEA, G. C.

*Naval Surface Weapons Center
Dahlgren Laboratory
Code DN-30
Dahlgren, VA 22448
(703) 663-8731*

SHEETZ, N.

*Naval Surface Weapons Center
White Oak Laboratory
Code 323
Silver Spring, MD 20910
(202) 394-2323*

SINGLETON, R. E.

*U. S. Army Research Office
Box 12211
Research Triangle Park, N. C. 27709
(919) 549-0641*

SLYKER, R. W.

*Pacific Missile Test Center
PMTC 2144
Point Mugu, CA 93042
(805) 982-8063*

SMITH, R. E.

*Naval Weapons Center
Code 4063
China Lake, CA 93555
(714) 939-2477*

SMITH, R. H.

*NASA OAST Headquarters
600 Independence Avenue
Washington, D. C. 20546
(202) 755-2383*

SOKOL, C. R.

*Naval Surface Weapons Center
Dahlgren Laboratory
Code DG-40
Dahlgren, VA 22448
(703) 663-7481*

SOLIS, R. E.

*Naval Surface Weapons Center
Dahlgren Laboratory
Code DK-21
Dahlgren, VA 22448
(703) 663-8107*

SYMPOSIUM ATTENDEE LIST

STEVENS, F. L.
*Naval Surface Weapons Center
Dahlgren Laboratory
Code DK-21
Dahlgren, VA 22448
(703) 663-8107*

STOEHR, G.
*Naval Surface Weapons Center
Dahlgren Laboratory
Code DK-55
Dahlgren, VA 22448
(703) 663-8359*

SUN, J.
*Naval Surface Weapons Center
Dahlgren Laboratory
Code DK-21
Dahlgren, VA 22448
(703) 663-8107*

SWANSON, R. C.
*Naval Surface Weapons Center
Dahlgren Laboratory
Code DG-10
Dahlgren, VA 22448
(703) 663-7561*

TAI, T. C.
*Naval Ship Research & Developm. Center
Code 1606
Bethesda, MD 20084
(202) 227-1462*

TALBOT, J. F.
*Naval Ship Research & Developm. Center
Bethesda, MD 20084
(202) 227-1670*

TISSERAND, L. E.
*Johns Hopkins University
Applied Physics Laboratory
11100 Johns Hopkins Road
Laurel, MD 20810
(301) 953-7100 - Ext. 7452, 7477*

VAN AKEN, R. W.
*Naval Weapons Center
Code 406
China Lake, CA 93555
(714) 939-3374*

VAN TUYL, A. H.
*Naval Surface Weapons Center
White Oak Laboratory
Code 331
Silver Spring, MD 20910
(202) 394-2265*

VAS, I. E.
*Gas Dynamics Laboratory
Forrestal Campus
Princeton University
Princeton, NJ 08540
(609) 452-5135*

VOISINET, R. L. P.
*Naval Surface Weapons Center
White Oak Laboratory
Silver Spring, MD 20910
(202) 394-2061*

VOLZ, W. C.
*Naval Air Systems Command
AIR-320C
Washington, D. C. 20361
(202) 692-7417*

WERBACK, W. J.
*Naval Weapons Center
Code 4062
China Lake, CA 93555
(714) 939-3348*

WILSON, G. G.
*Sandia Laboratories
Division 5625
Albuquerque, NM 87115
(505) 264-3939*

SYMPOSIUM ATTENDEE LIST

WING, L. D.

*NASA-Goddard Space Flight Center
Code 742
Greenbelt, MD 20771
(301) 982-4865*

ZIEN, T. F.

*Naval Surface Weapons Center
White Oak Laboratory
Bldg. 402, Rm. 204
Silver Spring, MD 20910
(202) 394-2082*

XERIKOS, J.

*McDonnell Douglas Astronautics, Co.
Space Systems Center
5301 Bolsa Avenue
Huntington Beach, CA 92647
(714) 896-3563*

THE IMPACT OF CONTEMPORARY FLUID MECHANICS
COMPUTATIONAL TECHNIQUES ON MISSILE DESIGN TECHNOLOGY

I. Inviscid Methods and Rapid Design Codes

J. Xerikos, Chief-Aerodynamics Branch
Flight Mechanics Department
McDonnell Douglas Astronautics Company-West
Huntington Beach, California

SUMMARY

The computational methods currently used in the design of tactical and strategic vehicles are assessed in terms of their application to specific aspects of missile sizing. The relative success in treating slender supersonic and hypersonic configurations (typically found in strategic applications), as opposed to transonic and supersonic wing-body-tail configurations (more representative of tactical vehicles) is discussed. An attempt is made to characterize qualitatively the principal elements of representative computational methods, pointing out the seemingly subtle differences in analyses that can strongly affect the utility of fluid mechanic codes.

The current status of sophisticated "rapid design" codes that rival finite-difference codes in terms of the methodology incorporated is discussed. The relationship between these contemporary aerodynamic design computer programs and the so-called exact methods is indicated by example.

Supporting computational processes which are peripheral to the fluid mechanics numerical analyses but essential components of the total

design process are identified. These range from geometric description subroutines using parametric interpolation methodology to innovative mechanizations of complex sizing exercises in which flow field analyses are nested.

The paper concludes with a discussion of the applicability of current as well as developing computational methodology in the design of contemporary vehicles.

INTRODUCTION

In a preface to a mathematical text on existence theorems in partial differential equations which was published in 1950 (Reference 1), C. Tompkins noted that "...it was apparent to a large and vociferous set of engineers that the electronic digital calculating machines they were then developing would replace all mathematicians and, indeed, all thinkers except the engineers building more machines." Tompkins, who advised the Navy during the post-World War II years on the capabilities of and requirements for computational equipment, then discussed

"...problems involving partial differential equations. The solution, in many cases, was to be brought about (according to the vociferous engineers) by:

- (1) buying a machine;
- (2) replacing the differential equation by a similar difference equation with a fine but otherwise arbitrary grid;
- (3) closing the eyes, mumbling something about truncation error and round-off error; and
- (4) pressing the button to start the machine."

He provided an example of a numerical solution of a simple linear, second-order partial differential equation where (using the above procedure) an arbitrary refinement of the finite-difference grid could lead from an accurate to an invalid solution. Tompkins concluded on a positive note, conceding that, in the absence of exact mathematical procedures there was a need for computations which amount to "experimental arithmetic," particularly when there is a reasonable empirical basis for judging whether the resulting numerical solution is an adequate approximation.

Tompkins' preface encouraged an intelligent use of the relevant mathematical literature in formulating numerical methodology. In the absence of this approach, he assumed that one would have to rely on "luck, prayer or further thought."

During the past 25 years, the educational distinction between engineers and applied mathematicians, to whom the text was originally addressed, has narrowed considerably. The mathematical prowess of engineering graduates has contributed to dramatic progress in the development of rational computational methods for the solution of engineering problems. In particular, progress in the area of fluid mechanics has tended to occur in quantum jumps as the result of concerted efforts dictated at times by national priorities. For example, the recent NASA Conference on Aerodynamic Analyses Requiring Advanced Computers, held at Langley Research Center in March 1975, featured 50 papers on important computational fluid mechanics topics.

The time involved in the development of new fluid mechanic computational methods for a given problem area has decreased from decades to

years (and under highly favorable circumstances, even months). The subsequent application of these methods to a specific missile design study, however, remains a highly subjective process which varies with parameters ranging from mission objectives (translated into design constraints) to the design philosophy and resources of the particular organization involved.

SOURCES OF AERODYNAMIC DESIGN DATA

The most significant change in missile design practice in recent years has been an increasing awareness of the value of computational methods which were previously regarded as useful but not essential elements of the design process. The change in attitude has resulted from a combination of advances in computer technology and economic and data accuracy considerations associated with experimental programs.

The extent to which computational codes have supplanted more traditional methods in contemporary configuration development design studies depends largely on:

1. The accuracy requirements imposed by the totality of vehicle design constraints.
2. The applicability and reliability of the codes over the GAMA (geometry/attitude/Mach number/altitude) range of interest.
3. The inability of experimental facilities to provide adequate simulation of all flight conditions.
4. The resources dedicated to the design study.
5. The degree of constructive interaction between technology- and design-oriented personnel.

Since the cost of both computational and experimental data acquisition is continuing to increase, economic considerations alone do not neces-

sarily dictate the level of involvement of computational methods (e. g. , dominant versus supporting). It is not likely that a missile configuration development program will proceed to flight-test status without the design first being validated in ground-test facilities. Consequently, from a practical standpoint, the determining factor is likely to be the degree of uncertainty associated with experimental data relative to the uncertainty bounds that are considered acceptable from the standpoint of satisfying vehicle performance requirements.

These requirements may be translated into, for example, accurate resolution of the vehicle static margin behavior as a function of angle of attack at flight conditions that may not be fully simulated in contemporary ground test facilities. In spite of continuing development of experimental facilities, typified most recently by the Naval Surface Weapons Center hypervelocity wind tunnel (T9), the parallel and more accelerated development of computer software and hardware has already led to knotty design decisions involving conflicting computational and experimental data with comparable uncertainty factors.

In the preceding discussion, the computational techniques were not classified as to their level of analytical sophistication, e. g. , finite-difference versus semiempirical codes. So-called rapid design codes that employ combinations of analytical approximations and empirical data have been used extensively to make aerodynamic predictions in vehicle preliminary design. In view of the gap between the potential and realized benefits of these approaches in obtaining aerodynamic design data, outlined in Figure 1, it would be useful to briefly review the development and current status of both "exact" and approximate computational methodology. The discussion of finite-difference codes

10th. Navy Symposium on Aeroballistics

Vol. 3

SOLUTION OF FINITE-DIFFERENCE ANALOG OF GOVERNING FLUID MECHANIC EQUATIONS.	DESIGN CODE COMBINING RATIONAL ANALYTICAL APPROXIMATIONS AND EMPIRICISM	GROUND TEST FACILITY/FLIGHT TEST
IN PRINCIPLE: PROVIDES DEFINITIVE DESCRIPTION OF NONLINEAR FLOW PROCESSES TO ARBITRARY LEVEL OF REFINEMENT	PROVIDES REASONABLE PHYSICAL DESCRIPTION OF FLOW FIELD IF SUFFICIENT DATA BASE IS AVAILABLE	PROVIDES DEFINITIVE FLOW FIELD DESCRIPTION AND/OR AERODYNAMIC COEFFICIENTS TO LEVEL OF REFINEMENT CONSISTENT WITH AVAILABLE SIMULATION AND MEASURE- MENT TECHNIQUES
IN FACT: NUMERICAL DATA ARE TYPICALLY ALTERED BY METHOD-PECULIAR ASPECTS OF COMPUTATIONAL PROCESSES WHICH ARE NON- CONSERVATIVE IN NATURE MATHEMATICAL MODELING OF FLOW FIELDS IS NOT UNIFORMLY VALID (I.E., SUCCESSFUL) FOR ALL VEHICLE GEOMETRIES AND SPEED REGIMES	OFTEN MISUSED IN TERMS OF APPLICATION OUTSIDE RANGE OF VALIDITY CANNOT BE CONFIDENTLY EXTRAPOLATED TO YIELD NONLINEAR TRENDS IN AERODYNAMIC DATA	ACCURACY OF DATA CAN BE COMPROMISED BY FACILITY FLOW QUALITY, INSTRU- MENTATION, OR SCALING CONSIDERATIONS GROUND TEST FACILITIES DO NOT PROVIDE FULL-SCALE REYNOLD'S NUMBER SIMULA- TION FOR ALL TACTICAL AND STRATEGIC FLIGHT ENVIRONMENTS

Figure 1. Sources of Aerodynamic Design Data

will be limited to solutions of the inviscid governing equations. Viscous methods will be reviewed in Part II of this paper.

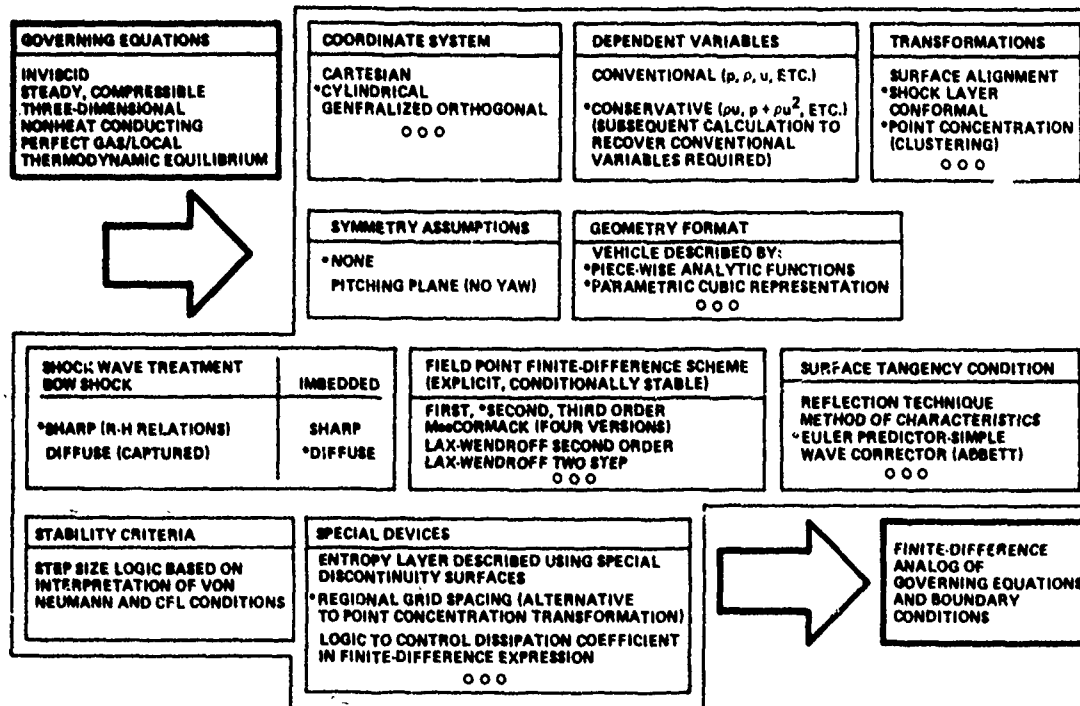
Inviscid Finite-Difference Codes

In 1947, the generation of the well-known "Tables of Supersonic Flow around Cones" by Kopal represented a significant computational achievement which involved the solution of an ordinary nonlinear, second-order differential equation. While inconvenient to use in design practice, the tables provided a definitive and unique source of pointed cone shock-layer data. In 1953, the ubiquitous NACA Report TN 1135 provided "Tables and Charts for Compressible Flow" which included a more accessible graphical version of the Kopal cone data. The extensive use of the NACA report in design activities for a number of years points up the importance of accessibility and utility factors in evaluating the

potential impact of new computational tools on design. In the past, the prodigious computational fluid mechanics output of government, academia, and industry has not been applied to vehicle design to an extent commensurate with the resources expended on these efforts. However, an increasing number of organizations are realizing the potential of advanced computational design methods.

Beginning in the late 1950's and continuing at an accelerated pace during the 1960's, numerous computational methods were developed in an attempt to provide tools for solving increasingly sophisticated design problems which were previously approached on a more approximate or wholly empirical basis. A significant number of these methods were two-dimensional in their original formulation. The usual claim of a straightforward extension to three dimensions was rarely realized. Consequently, the impact of these codes on the design process was minimal owing to their limited applicability to actual vehicle configurations; however, the intensive efforts of many investigators in government and industry are currently being applied to the development of more definitive three-dimensional codes that include the successful fluid mechanic modeling and numerical simulation features of previous computational analyses. These codes have been particularly successful when applied to slender configurations traveling at supersonic to hypersonic speeds.

The schematic diagram in Figure 2 shows representative options which are encountered in traversing the path from the governing inviscid, supersonic steady three-dimensional fluid mechanic equations to their finite-difference analog. Starting with the selection of a coordinate



EXAMPLE: *DENOTES SHOCK-CAPTURING CODE OPTIONS

Figure 2. Supersonic/Hypersonic Finite-Difference Codes, Representative Options

system and the introduction of symmetry assumptions, if appropriate, a choice must be made between use of conventional and conservative variables. The latter, for example, allows direct treatment of imbedded secondary shock waves within the vehicle shock layer since these variables are conserved across flow-field discontinuities. The results are generally satisfactory given adequate finite-difference mesh density to resolve the numerically diffused shock-wave description. One or more transformations of the governing equations can be used to vary preferentially the mesh density as well as to effect geometric simplifications which eventually can be translated into more tractable finite-difference expressions. The selection of a given finite-difference scheme (within even the restricted category of explicit, conditionally stable relations) can be made from a number of options, depending on

their demonstrated success in treating related physical problems. The surface tangency condition represents a particularly important element of the overall numerical process. An improperly formulated finite-difference relationship in the immediate vicinity of the vehicle surface can either suppress or exaggerate the effects of flow-field gradients associated with nose bluntness (e. g. , entropy layer phenomena) or surface slope discontinuities. In some instances, special devices have been introduced to improve computational stability or provide better resolution of a portion of the flow field; for example, the aforementioned blunt nose-induced entropy layer.

At present, several supersonic and hypersonic finite-difference codes are being employed in vehicle design studies leading to flight test programs. These include the Shock Capturing Technique (SCT) code developed by P. Kutler at NASA-Ames (Reference 2). The essential features of the MDAC version of the SCT code are identified in Figure 2 by asterisks. The core size requirements are compatible with CDC 6500 equipment with typical run times ranging from 1 to 5 minutes as angle of attack is increased from 0 to 20 degrees.

Rapid Design Codes

The computer provides two different types of design capability. The more dramatic type just discussed encompasses the use of finite-difference analogs of nonlinear partial differential equations to obtain detailed descriptions of vehicle flow fields. The direct type of capability makes use of the data handling and processing features of contemporary computers in assembling design codes which can combine approximate methods and empirical data to yield meaningful engineering solutions for vehicle aerodynamic characteristics. A rational

Vol. 3

combination of the two approaches is to use the results of validated finite-difference codes to provide "benchmark" data while conducting parametric studies using the more approximate (but more economical) design methods. The design code can thus be calibrated over the range of interest and deficiencies identified.

In some instances, extremely accurate design tools are needed from preliminary to final missile design. In these circumstances, use of approximate screening procedures may lead to either a nonoptimum design or to the conclusion that mission requirements cannot be met employing a given generic configuration class, control concept, and guidance logic.

The development of rapid design codes has followed two distinct paths: (1) the "assembly of methods" approach characterized by the automated USAF DATCOM code, and (2) the "unified methodology" approach typified in its simplest form by Newtonian hypersonic codes. The former represents a programmed source of design methods for vehicle components as well as for complete vehicle configurations; however, while the user is relieved of much tedious computational effort, he must still exercise considerable engineering judgment in selecting the combination of methods that will yield meaningful aerodynamic design data. In addition, holes often exist in the GAMA (geometry/attitude (α , β , ϕ)/Mach number/altitude (Re)) ranges for a given vehicle and mission profile.

The unified methodology codes, on the other hand, typically concede some degree of generality in terms of geometry and/or speed regime in order to provide uniformly accurate aerodynamic predictions

throughout their specified range of validity. Since these codes are often developed in response to a specific set of design requirements, they are usually well understood within the originating organization; however, because of their ability to generate data outside of their validated GAMA range, nothing short of a fail-safe mechanism will prevent their occasional misuse during subsequent design exercises.

An aerodynamic design code developed for the Mach number range from 0 to 3 is described in Reference 3. The theoretical and empirical procedures employed allow a component build-up approach to the prediction of the static aerodynamics of projectiles and missiles up to 15 degrees angle of attack. The procedure used is shown in schematic form in Figure 3. The code was developed to provide data "accurate enough to replace preliminary and intermediate wind-tunnel

WD2533

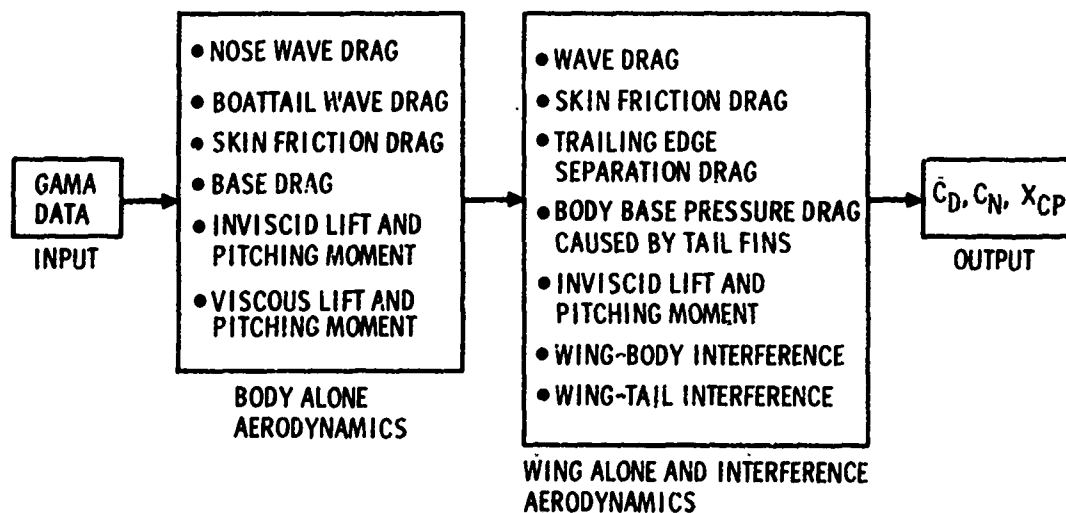


Figure 3. NSWC Missile Aerodynamics Computer Code: $0 < M_{\infty} < 3$

Vol. 3

testing." For those cases where this accuracy is realized, the code is a highly cost-effective design tool.

An obvious advantage of the computational resources available today is the ability to include subroutines in design codes which represent significant computational achievements by the standards of the previous decade. This has led to the development of second-generation supersonic/hypersonic aerodynamic design codes whose structure is typified by the block diagram shown in Figure 4.

Computational processes which are peripheral to the fluid mechanics analyses employed in this class of codes but which are essential elements of the total design process range from geometric description subroutines to innovative mechanizations of complex vehicle sizing exercises. For example, in the field of multidimensional interpolation methodology, efficient numerical procedures have been developed over the past decade to describe vehicle geometries to almost arbitrary levels of refinement and process multiparameter data in the form of n-dimensional surface fits for use as special data access subroutines in a design code. For example, Figure 5 is a computer-generated plot of aerodynamic data which has been processed for use by a 6 degree-of-freedom trajectory code in order to avoid use of inefficient tabular storage.

The utility of contemporary interpolation methods can be illustrated by considering a simple but widely used rapid design technique for predicting inviscid aerodynamic loads at supersonic and hypersonic speeds. Using a combination of tangent wedge or tangent cone and modified Newtonian methods, the pressure on the windward surface of

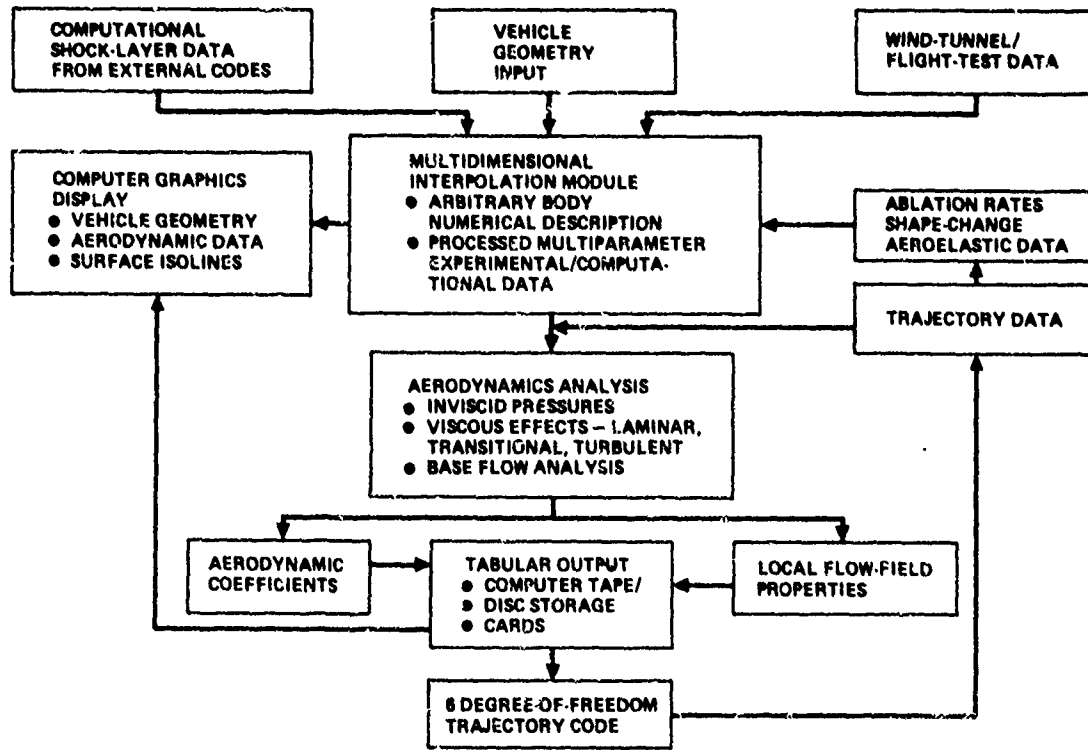


Figure 4. Supersonic/Hypersonic Aerodynamic-Design Computer Code

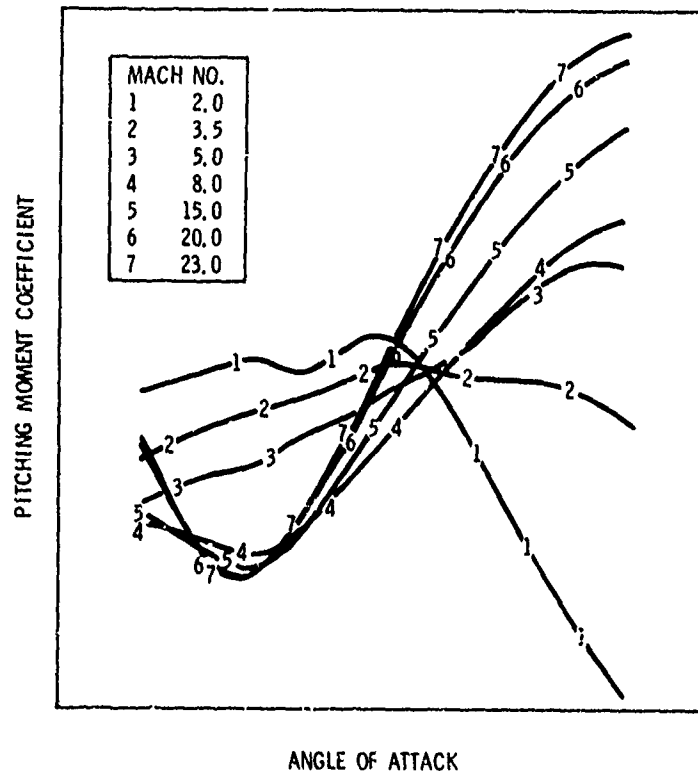


Figure 5. Computer-Processed Aerodynamic Data

Vol. 3

an arbitrary body at angle of attack can be determined primarily on the basis of the angle between the local surface normal and the free-stream direction (hence, its classification as a "local slope" technique).

Using a parametric cubic geometry description method which can accurately provide local curvatures as well as slopes, it becomes possible to automate the method selection process by using longitudinal and transverse body curvature data to distinguish between wedge-like and cone-like body elements. Consequently, an expression for surface pressures can be developed that uses the geometric data to combine the elementary methods in a rational manner so that results are exact, for example, in the limiting cases of a pure cone or wedge at small incidence.

For certain generic classes of vehicles such as blunt-nosed biconic configurations, a more accurate prediction procedure can be developed by using a blunt body/rotational method-of-characteristics code to generate surface pressure distributions for blunt cones at zero incidence as a function of axial coordinate, cone angle, and Mach number. Four-dimensional interpolation surfaces developed from these data can subsequently be used in a tangent-cone sense to provide bluntness-induced pressures on a slender body of revolution at angle of attack. This procedure is shown in schematic form in Figure 6 where θ is an equivalent cone angle which varies circumferentially at angle of attack. Figure 7 displays representative output from the subroutine. The correlation parameter employed served to increase the efficiency of the interpolation processes, e. g., for $\xi > 0.4$, surface pressures closely approximate sharp cone values over a wide range of θ and M_∞ .

For biconic configurations, additional logic in the form of exact inviscid relations relating properties upstream and downstream of the

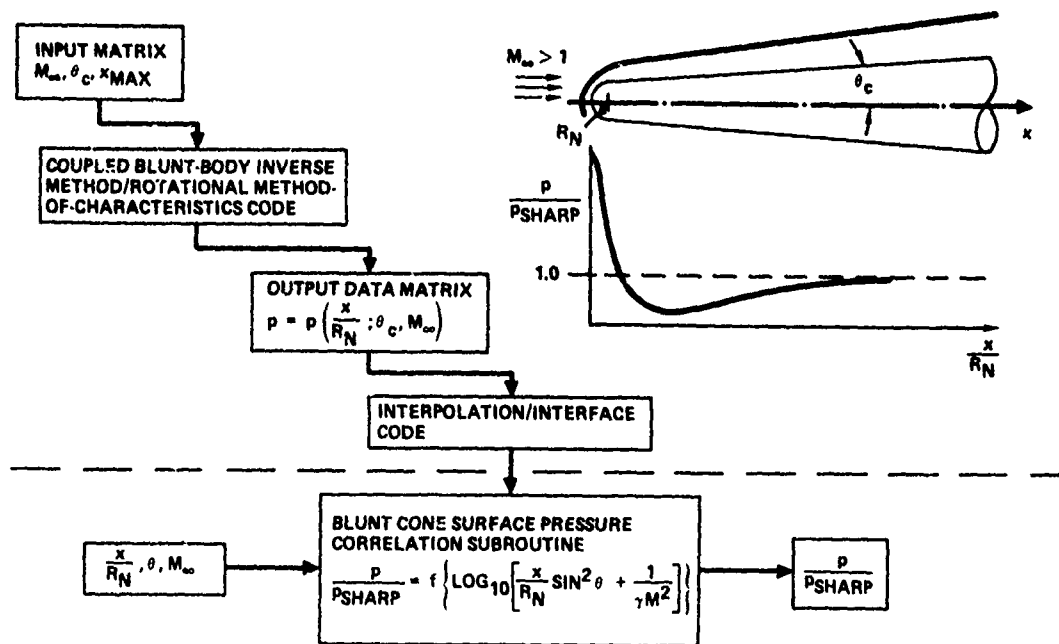


Figure 6. Design Data Synthesis – Blunt Cone Surface Pressure Correlation

WD2533

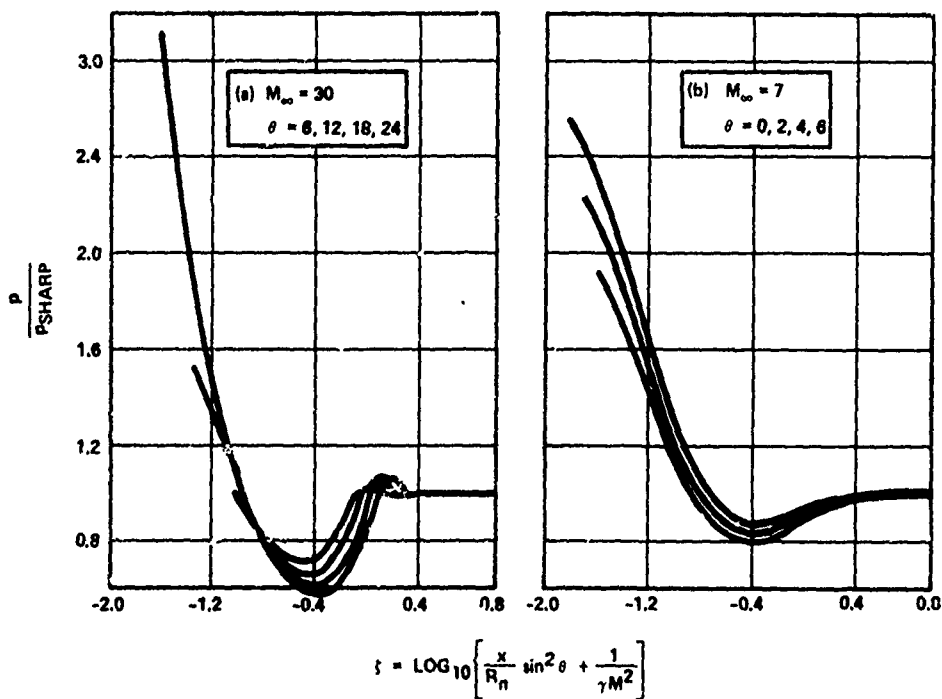


Figure 7. Blunt Cone Surface Pressure Correlation

cone-cone juncture can be introduced to treat conical frustrums. Results generated by this procedure are compared with those yielded by an exact inviscid finite-difference code in Figure 8. In view of the indicated uncertainty in the experimental data and the highly expanded center-of-pressure scale, the SCT code predictions recently reported in Reference 4 were considered quite reasonable. The excellence of the superimposed aerodynamic design code predictions, which may benefit from some degree of fortuity, gives ample evidence of the potential of advanced design techniques that employ a logical blend of analysis and empiricism. The design code results were generated with the expenditure of approximately 1/70th of the computer time required by the finite-difference code.

WD2533

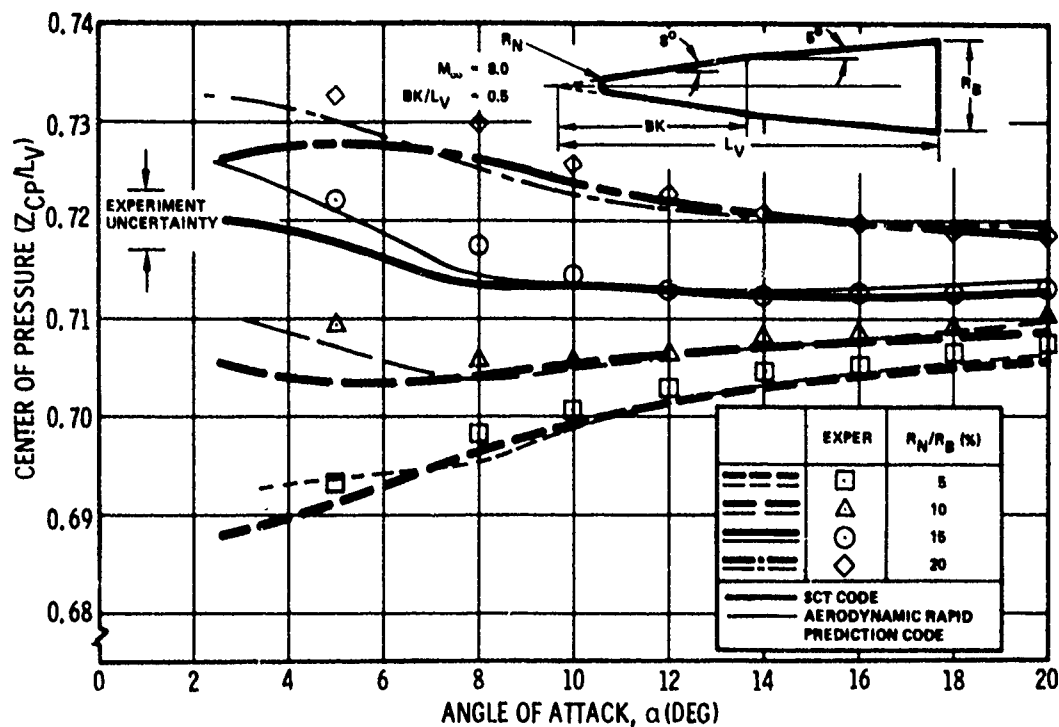


Figure 8. Effect of Nose Bluntness on Center of Pressure

When validated for a specified range of geometric and flight parameters, techniques such as those described above can play a highly useful role in design studies requiring a sufficiently large number of iterations to preclude direct use of finite-difference codes. These techniques represent an extremely useful compromise between conventional rapid design codes and finite-difference computer programs.

SUPERSONIC/HYPERSONIC VEHICLE DESIGN TOOLS

As speed and maneuver levels escalated for strategic reentry and interceptor vehicles, requirements for simple geometric configurations developed from the vehicle design. Thermal protection considerations prevented use of conventional fin-like control surfaces while high maneuver levels called for small center-of-pressure travel with angle of attack. As a result of the design constraints associated with maneuvering hypersonic vehicles, the blunt cone and variations thereof became a workhorse configuration. The variations include biconics and elliptic cones, with the latter obviously having higher lateral acceleration maneuver capabilities.

A representative configuration development design cycle for maneuvering hypersonic vehicles is shown in Figure 9. The indicated design activities involve a number of complex iterative procedures which serve to vary parametrically the vehicle geometry subject to a hierarchy of constraints. Contemporary strategic mission requirements are generally satisfied only after the development of highly innovative aerodynamic, guidance, and control design concepts. Cost is not initially a driving factor (within reasonable limits) unless the production of a significant number of vehicles is anticipated.

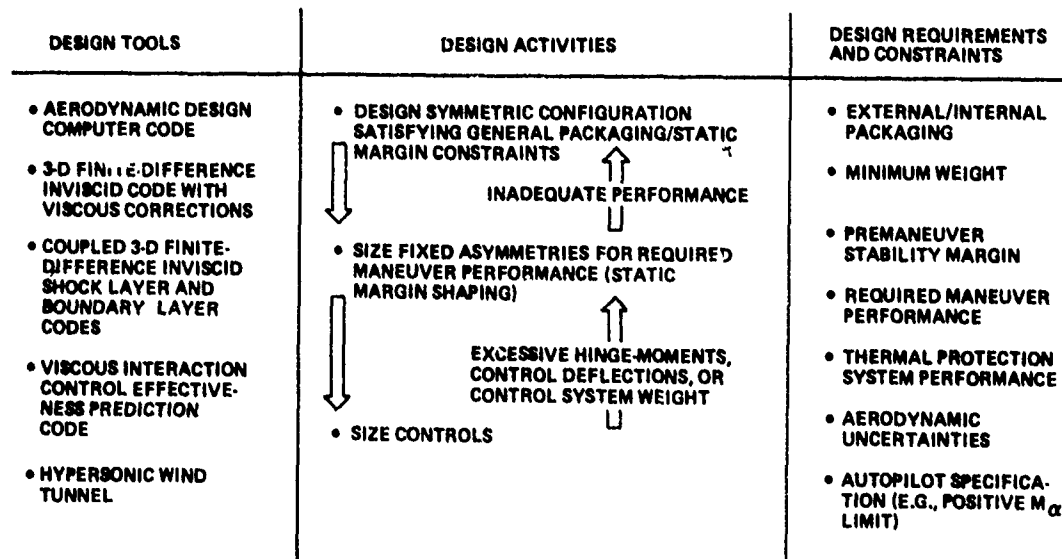


Figure 9. Representative Configuration Development Design Cycle – Maneuvering Hypersonic Vehicle

The computational tools required for an accurate definition of the aerodynamic characteristics as well as the inviscid shock layer properties for blunt cones at arbitrary incidence have been developed during the past 15 years. The development has been somewhat uneven and has featured announcements of definitive methods which in retrospect appear to be either significant contributory milestones or "computational millstones." The failure of many promising analyses proved again that seemingly straightforward applications of finite-difference analogs of governing nonlinear partial differential equations can lead to anomalous results.

The chronology of supersonic shock layer code development for slender blunt-nosed cones is indicated in Figure 10. For zero incidence, the

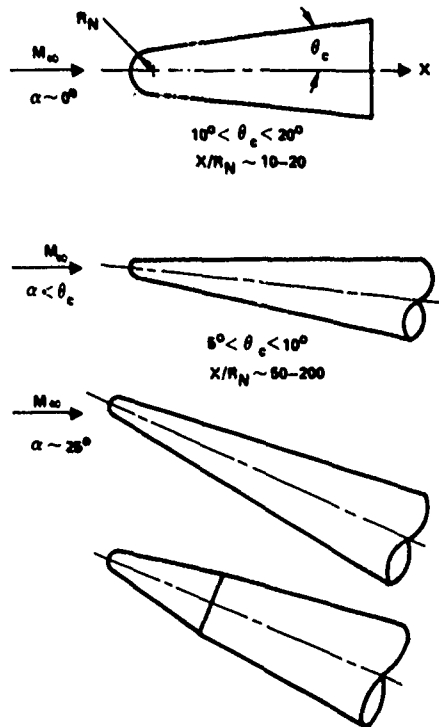


Figure 10. Development of Supersonic Shock Layer Codes

method of characteristics could be used to obtain downstream supersonic flow-field descriptions provided that a reasonable starting solution was available. The development of blunt nose solutions consequently became a principal activity of numerical gasdynamicists for several years with both steady-state and time-dependent solutions resulting. The computational difficulties introduced by increasing angle-of-attack requirements were largely anticipated, if only in terms of the three-dimensional bookkeeping involved. The effect of decreasing nose bluntness was somewhat more subtle, since in some instances nonconservative aspects of early numerical methods created cumulative computational errors which only became evident as the calculation progressed far downstream of the nose. Treatment of nonspherical nose geometry including asymmetric nose shapes arising

STATUS OF COMPUTATIONAL TOOLS

1966

- DEVELOPMENT OF BLUNT-BODY SOLUTIONS BEGINS IN RESPONSE TO NEED FOR ROTATIONAL METHOD-OF-CHARACTERISTICS STARTING SOLUTIONS

1980

- TREND TOWARD SLENDER VEHICLES WITH SMALL NOSE BLUNTNES REVEALS FLAWS IN METHOD-OF-CHARACTERISTICS NUMERICAL PROCESSES AS CALCULATIONS PROGRESS DOWNSTREAM. MORE REFINED (E.G., SECOND-ORDER) RMOC CODES ARE CONSEQUENTLY DEVELOPED

1986

- BLUNT-BODY CODE DEVELOPMENT CONTINUES WITH INVERSE AND INTEGRAL TECHNIQUES PLAYING PROMINENT ROLES

1986

- TIME-DEPENDENT METHODS ARE DEVELOPED TO SOLVE STEADY-STATE MIXED FLOW PROBLEMS
- 3-D RMOC CODES ARE APPLIED TO TREATMENT OF BLUNT CONES AT MODERATE α . EARLY ATTEMPTS ARE LIMITED BY ANOMALOUS BEHAVIOR AS CALCULATION PROGRESSES DOWNSTREAM.

1970

- NEW 3-D FINITE-DIFFERENCE MARCHING AND TIME-DEPENDENT CODES APPEAR AS 3-D RMOC CODES ARE IMPROVED TO ENABLE CALCULATIONS TO PROCEED TO ARBITRARY DOWNSTREAM STATIONS

1970

- STARTING SOLUTIONS FOR NONSPHERICAL NOSE ARE PROVIDED BY 3-D BLUNT-BODY CODES FOR RESTRICTED CLASS OF GEOMETRIES

1975

- FURTHER PROGRESS IN FINITE-DIFFERENCE MARCHING TECHNIQUES ALLOWS TREATMENT OF BODIES AT HIGHER INCIDENCE

- CURRENT CODES GENERALLY YIELD ACCURATE AERODYNAMIC COEFFICIENTS FOR BLUNT-NOSED SLENDER VEHICLES

Vol. 3

from passive nose-tip ablation processes is a more recent consideration which will require further development.

During the development process just described, the lag between the validation of a computational method and the subsequent application of the method in missile design has decreased dramatically. In fact, in some instances computer codes undergo effective shakedown tests during their initial use on a design study. Under these circumstances, the true utility of the method is rapidly established.

TACTICAL MISSILE DESIGN TOOLS

Missiles designed for the subsonic through supersonic regimes range from aerodynamically controlled wing-body-tail vehicles that fly at moderate angles of attack to thrust-vector-controlled axisymmetric configurations that may operate at angles of attack up to 180 degrees. The highly configuration-dependent aspects of the three-dimensional flow fields encountered make it extremely difficult to develop analytical models which can adequately treat a significant portion of the tactical missile GAMA range. For example, leeward flow fields, unlike in the hypersonic case, are dominated by vortex phenomena which contribute significantly to the generation of normal and yawing forces at angles of attack in excess of 10 degrees. Fortunately, in many instances, the leeward flow field can be modeled using an inviscid representation of the shed vortices (e. g. , see Reference 5). This approach is not uniformly successful in treating the leeward flow field of wing-body-tail missiles since the predicted interaction between trailing body and wing vortices and the tail surfaces may not quantitatively (or in some cases, even qualitatively) describe aerodynamic forces and moments resulting from, for example, pitch-roll coupling phenomena.

Most of the aerodynamic prediction methods currently available are represented by one of the categories given below:

- A. Linear and nonlinear finite-element lifting-surface-theory methods (analytical).
- B. Inviscid-vortex-modeling methods (slender body theory)
 - 1. Shedding from sharp leading or side edges of wings (analytical).
 - 2. Symmetric and alternate shedding from smooth-contoured bodies (semiempirical).
- C. Superposition-of-component-contributions method including interference effects (semiempirical).
- D. Viscous cross-flow methods (empirical).
- E. Leading-edge-suction-analogy method (empirical).

Numerical analyses based on the first two categories can impose computer storage and speed requirements that may tax current computational resources, depending on such factors as finite-element density or the complexity of the vortex modeling.

Design activities that are characteristic of a tactical missile configuration development study are indicated in Figure 11. The design requirements and constraints shown are a composite and include consideration of more than one class of missiles. Unlike reentry vehicles, for example, end-cost is a dominant factor throughout the design cycle.

The superposition-of-component-contributions methods, based on a blend of small-perturbation theories and appropriate empiricism as well as viscous cross-flow methods, are key elements of contemporary

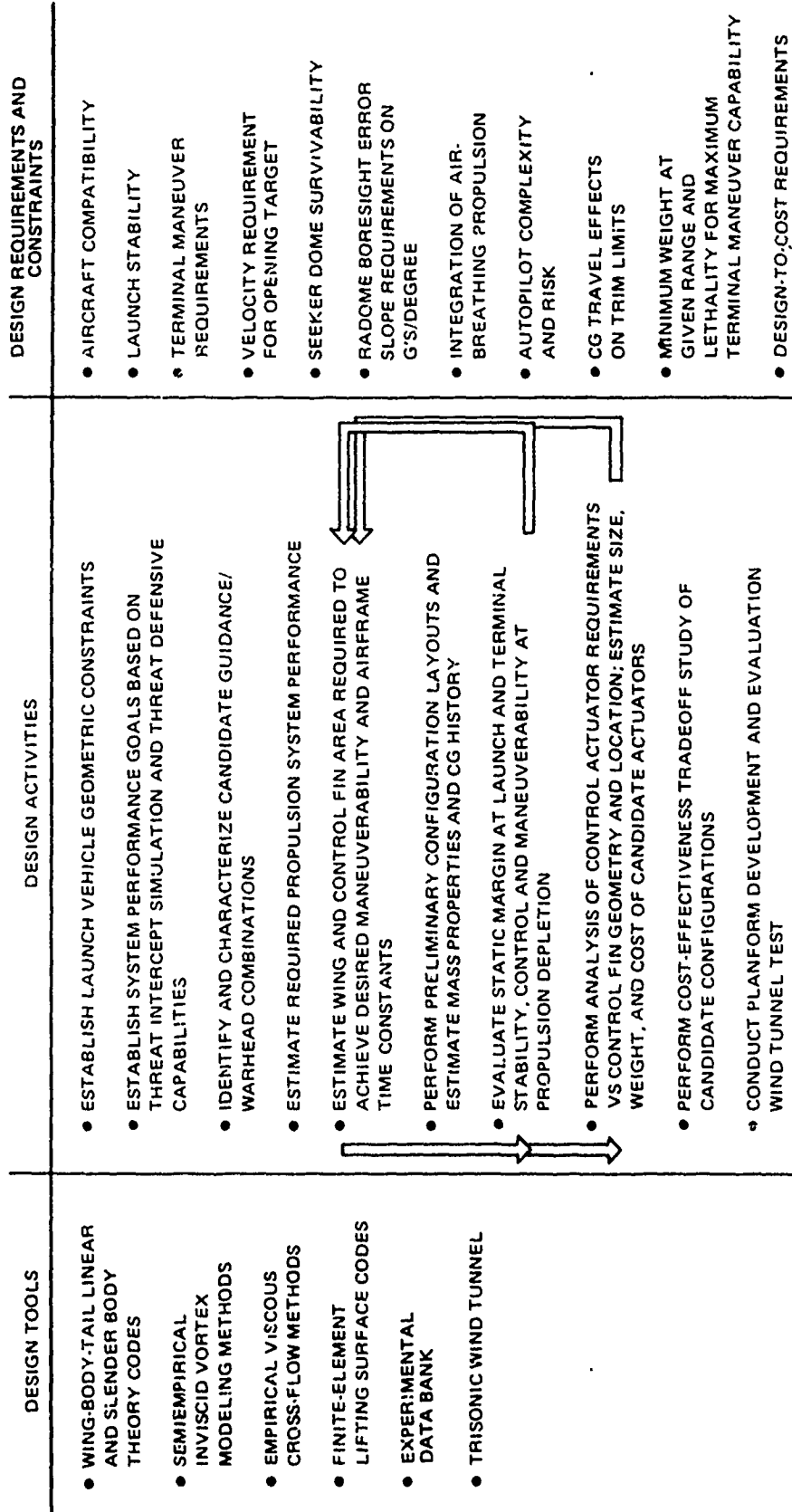


Figure 11. Representative Tactical Missile Design Approach

automated codes used to predict missile static aerodynamic characteristics during preliminary design. Finite-element or panel-type influence coefficient methods which treat both incompressible and compressible potential flow about vehicle components have undergone significant development during the past several years. An obvious advantage of these methods is their ability to provide more accurate surface pressure distributions in addition to force and moment coefficients. Computational analyses based on the inviscid-vortex-modeling approach have been coupled to potential flow codes in both additive and interactive modes. The prediction of nonlinear vortex lift for slender bodies and lifting surfaces with sharp leading edges has been reasonably successful up to moderate angles of attack ($\alpha \sim 20$ degrees). In spite of the progress achieved, however, tactical missile design will continue to depend on the availability of relevant experiment data for treating the highly nonlinear phenomena encountered in maneuvering flight through the transonic flight regime.

CONCLUSIONS

Among current missile design programs, development of reentry vehicle configurations involves rather extensive use of second-generation rapid design codes and three-dimensional inviscid finite-difference codes, coupled with appropriate viscous analyses. The combination of increased code efficiency and computer speed has already advanced these finite-difference programs beyond the status of benchmark codes that are used sparingly to establish the credibility of more approximate methods. The extremely accurate prediction of reentry vehicle aerodynamic characteristics required during design-cycle iterations has served as a forcing function which has significantly

Vol. 3

extended both computational and experimental (hypersonic wind tunnel) capabilities during the past several years. Although supersonic and hypersonic three-dimensional inviscid codes have yielded impressive results in terms of experimental data comparisons, certain problem areas remain in supersonic inviscid shock layers. Some anomalous results continue to be obtained within the reentry vehicle GAMA range, indicating the need for improved analytical modeling, particularly in the presence of vehicle asymmetries and surface discontinuities.

In the area of tactical missile design, the most evident application of the computer has been to automate the more commonly used analytical and semiempirical methods for efficient utilization within iterative design exercises. Inviscid-vortex-modeling and finite-element lifting-surface theoretical methods continue to show promise in treating missile components; however, application of the more advanced computational techniques to wing-body-tail configurations, for example, is still in the developmental stage. In addition, the complex nature of transonic flow will continue to be difficult to model analytically as well as to simulate experimentally.

In the future, there will continue to be problems whose complexity in terms of the necessary mathematical modeling of the physical processes involved will not allow anything less than the full utilization of computer capacities and speed; however, the computer should not be used indiscriminately when a logical engineering approach can yield an adequate solution utilizing modest computational resources. As these resources continue to increase, a real challenge will be to employ the computational tools at hand as highly useful and sometimes essential elements of the engineering design process rather than as a substitute for inventive thought.

REFERENCES

1. Bernstein, Dorothy L. Existence Theorems in Partial Differential Equations. Annals of Mathematics Studies. Princeton University Press, 1950.
2. Kutler, P., H. Lomax, and R. F. Warming. Computation of Space Shuttle Flow Fields Using Noncentered Finite Difference Schemes. AIAA Paper 72-193, 1972.
3. Moore, F. G. Static Aerodynamics of Missile Configurations for Mach Number Zero to Three. AIAA Paper 74-538 June 1974.
4. Chaussee, D. S., T. Holtz, and P. Kutler. Inviscid Supersonic/Hypersonic Flowfields and Aerodynamics from Shock-Capturing Technique Calculations. McDonnell Douglas Astronautics Company, Paper WD 2446, May 1975 (presented to the AIAA 8th Fluid and Plasma Dynamics Conference, Hartford, Connecticut, June 1975).
5. Wardlaw, A. B., Jr. Multivortex Model of Asymmetric Shedding on Slender Bodies at High Angle of Attack. AIAA Paper 75-123, January 1975.

THE IMPACT OF CONTEMPORARY FLUID MECHANICS COMPUTATIONAL TECHNIQUES ON
MISSILE DESIGN TECHNOLOGY, Part II: Viscous Flows

Clark H. Lewis, Professor
Aerospace and Ocean Engineering Department
Virginia Polytechnic Institute and State University
Blacksburg, Virginia

A unified approach is presented based on an implicit finite-difference method to compute two-dimensional and axisymmetric first-order boundary layers for both internal and external flows, three-dimensional boundary-layer flows over sharp and blunt cones at angle of attack, and two-dimensional and axisymmetric fully viscous shock-layer flows over non-analytic and analytic shapes at zero angle of attack in supersonic and hypersonic streams. Examples are given of the application of the finite-difference method applied to two-dimensional and three-dimensional parabolic partial differential equations including effects of gas chemistry and surface mass transfer. The methods presented are applicable to a wide class of problems in research and development and in the complete vehicle design process. Accurate results are obtained in reasonable computing times on currently available computing systems. Current status of boundary-layer and viscous shock-layer development is reviewed, and the needs for further research are indicated.

PREFACE

In recent years, finite-difference methods have become powerful tools for solving viscous flowfield problems. This paper is a brief survey of methods and techniques which have been developed in the Aerospace and Ocean Engineering Department at Virginia Polytechnic Institute and State University, Blacksburg, Virginia for the solution of viscous flows. Results from some of the applications of these methods are included to show the validity of the methods. The first technique developed dealt with laminar and/or turbulent two-dimensional or axisymmetric flows of a perfect gas or reacting mixtures of gases in chemical equilibrium. This method was later extended to include tangential slot injection of nonreacting binary gas mixtures to turbulent supersonic flows. The next development was directed toward the solution of three-dimensional boundary-layer flows for either perfect gas or binary gas mixtures. The latest technique developed has been a two-dimensional or axisymmetric fully viscous shock-layer model for seven species air or dissociating oxygen.

ACKNOWLEDGEMENT

The methods described in this paper were developed by several people in collaboration with the author, viz. Dr. E. C. Anderson, Dr. E. W. Miner, Mr. M. C. Frieders and Mr. A. L. Murray. Special thanks are due Messrs. Murray and Frieders for their assistance in the preparation of this paper.

NOMENCLATURE

A_q	coefficient used in calculating the turbulent Prandtl number, $A_q = 34.4$
A_0-A_5	coefficients in the partial differential equation
C_f	skin-friction coefficient
C_{f0}	skin-friction coefficient on a flat plate
C_q	normal injection parameter, $C_q = \rho_w v_w / \rho_e u_e$
C_h	heat-transfer coefficients
C_i	mass fraction of species i
C_p	specific heat of mixture, $\text{ft}^2/(\text{sec}^2 - ^\circ\text{R})$
\hat{C}_{pi}	specific heat of species i
D_{if}	binary diffusion coefficient, ft^2/sec
E	scalar velocity function used in the Van Driest inner eddy-viscosity law
ECW	denotes equilibrium catalytic wall
f	stream function
FVSL	denotes fully viscous shock layer
g	function of transformed coordinates
G_{if}	parameter in Wilke's mixture law
H	stagnation enthalpy, ft^2/sec^2
\hat{H}_i	enthalpy of species i
h	static enthalpy
\bar{h}	heat-transfer coefficient, $-\dot{q}_w/(T_0 - T_w)$
\bar{h}_{ref}	reference heat-transfer coefficient based on a 0.21 inch nose radius
I_f	transition intermittency factor
J_i	diffusion mass flux term of species i

k	thermal conductivity
k_h	coefficient in expression for turbulent Prandtl number, $k_h = 0.44 + 0.22/(1 + 0.42 z^2)$
k_m	coefficient in expression for turbulent Prandtl number, $k_m = 0.4 + 0.19/(1 + 0.49 z^2)$
k_q	coefficient in Pr_t expression, $k_q = 0.447$
k_t	turbulent thermal conductivity
L	length of the body
l, l_{st}	mixing length
Le	molecular Lewis number
Le_t	turbulent Lewis number
M	Mach number
M_i	molecular weight of species i
M_f	molecular weight of freestream gas
NSS	no shock slip
p, P	pressure
Pr	molecular Prandtl number
Pr_t	turbulent Prandtl number
\dot{q}	heat-transfer rate
\dot{q}_s	heat-transfer rate at stagnation point
r	body radius
r_n	nose radius
Re	Reynolds number
s	coordinate measured along the body surface
SS	shock slip
T	temperature
TVSL	thin viscous shock layer
u	tangential component of velocity

Vol. 3

u_f	friction velocity, $(\tau_w/\rho)^{1/2}$
V	transformed normal velocity
v	normal velocity component
\dot{w}	species production term
w	transverse velocity component
x	surface distance in body coordinate system
x'	axial distance in a velocity oriented coordinate system
y	normal distance in body coordinate system
y'	normal distance in velocity oriented coordinate system
y^+	$y u_f/\nu$
y_δ	boundary-layer thickness as used in the outer eddy-viscosity law
α	angle of attack
γ	ratio of specific heat
ϵ	eddy viscosity
ϵ^+	ϵ/μ
ϵ_i	inner region eddy viscosity
δ	boundary-layer thickness
λ	blowing parameter, $\rho_s u_s / \rho_e u_e$
Φ_{ij}	parameter in Wilke's mixture law
ϕ	transverse coordinate
κ	surface curvature
μ	viscosity
ρ	density
θ_c	cone angle
τ	local skin friction
ξ	transformed streamwise coordinate

η transformed normal coordinate

Subscripts

e outer edge of boundary layer

f freestream species property

i species i

o stagnation conditions

s slot condition

t turbulent quantity

w wall conditions

∞ freestream conditions

INTRODUCTION

The equations of motion of a fluid form a complex system of partial differential equations which can be solved analytically for only a few restricted cases. Numerical methods have existed for quite some time which are capable of providing solutions for complex sets of equations. Until the development of large-scale, high-speed computers, many numerical methods were not feasible to use; however, with the computer hardware available today, solutions of practical problems in engineering are becoming common place. Numerous methods have been developed in recent years which deal with the solution of various flowfield problems by some of these numerical techniques. This paper is a review of work that has been done in the Aerospace and Ocean Engineering Department at Virginia Polytechnic Institute and State University in applying finite-difference techniques to the study of viscous flowfields. The first method was developed by Anderson and Lewis (Ref. 1) and considered two-dimensional or axisymmetric boundary-layer flows of either perfect gases or reacting gases in chemical equilibrium. This method was later extended by Miner and Lewis (Ref. 2) to treat slot injection flowfields with nonreacting binary gas mixtures. The next step in the development of techniques for solving boundary-layer flows was done by Frieders and Lewis (Ref. 3) and considered nonreacting binary gas mixtures in a three-dimensional boundary layer. In the approach most commonly used, the flowfield over the body is treated in two parts, an inviscid outer flow and a viscous boundary layer. Many methods have been developed for solving the inviscid outer flowfield, for example, the methods Inouye, Rakich and Lomax (Ref. 4) Rizzi and Inouye (Ref. 5) and Kutler, Reinhardt and Warming (Ref. 6).

This classical approach to the problem generally worked quite well. It is, however, most appropriate for supersonic, high Reynolds number flows. As interest in hypersonic, low Reynolds number flows increased (for example, for reentry applications, including the space shuttle), problems were encountered in applying first-order boundary-layer theory to such flows. Some of the problems, such as displacement-thickness interaction, were partially met by using second-order boundary-layer theory, see e.g. Lewis (Ref. 7). Another problem of the boundary-layer methods is determining the edge conditions. For supersonic, high Reynolds number flows, in which the boundary-layer is thin compared to the shock-layer thickness and more specifically the entropy-layer thickness, it is generally adequate to consider the conditions at the boundary-layer edge to be the same as given by the inviscid solution at the body surface. For hypersonic, low Reynolds number flows in which the boundary layer is not thin, determining the edge conditions for the boundary layer can be most difficult. In the method of Blottner (Ref. 8), edge conditions were optionally determined by tracking streamlines from the shock crossing point to the boundary-layer edge or by entropy-layer swallowing.

Many of the problems (including those mentioned above) associated with computing viscous, hypersonic flows over blunt bodies have been overcome by the viscous shock-layer approach in which the entire flowfield from the body to the shock was treated in a unified manner. Knowledge of the shock shape was still required (to determine the flow properties behind the shock), but problems such as those of streamline tracking and displacement-thickness interaction were avoided. A viscous shock-layer model was developed by Miner and Lewis (Ref. 9) which can solve viscous flowfields over nonanalytic blunt bodies. This method was

developed for nonequilibrium, multicomponent, ionizing air or for dissociating oxygen. A separate shock-layer program was developed which used a perfect gas model. These programs are capable of modeling two-dimensional or axisymmetric, laminar shock-layer flows.

Two-Dimensional or Axisymmetric Boundary-Layer Flows

The governing equations for turbulent, 2-D or axisymmetric boundary-layer flows are:

Continuity:

$$\frac{\partial \rho u r^j}{\partial x} + \frac{\partial}{\partial y} \left[(\rho v + \overline{\rho'v'}) r^j \right] = 0 \quad (1)$$

Momentum:

$$\rho u \frac{\partial u}{\partial x} + (\rho v + \overline{\rho'v'}) \frac{\partial u}{\partial y} = \rho e u_e \frac{du_e}{dx} + \frac{\partial}{\partial y} \left[\mu \frac{\partial u}{\partial y} + \rho \epsilon + \frac{\partial u}{\partial y} \right] \quad (2)$$

Energy:

$$\rho u \frac{\partial H}{\partial x} + (\rho v + \overline{\rho'v'}) \frac{\partial H}{\partial y} = \frac{\partial}{\partial y} \left[\frac{\mu}{Pr} \frac{\partial H}{\partial y} + \frac{\rho C_p \epsilon^+}{Pr} \frac{\partial H}{\partial y} + \mu \left(1 - \frac{1}{Pr} \right) \right] \quad (3)$$

Species:

$$\rho u \frac{\partial C_i}{\partial x} + \rho v \frac{\partial C_i}{\partial y} = - \frac{\partial}{\partial y} (J_i) \quad (4)$$

where

$j = 0$ for two-dimensional flow

$j = 1$ for axisymmetric flow

These equations were nondimensionalized as proposed by Van Dyke (Ref. 10) and expressed in Levy-Lees variables. The resulting equations were then in parabolic form necessary for the solution procedure. The finite-difference

scheme used to solve the boundary-layer equations was an implicit method of the Crank-Nicolson (Ref. 11) type and has been used by a number of other authors such as Davis (Ref. 12), Blottner (Ref. 13) and Harris (Ref. 14).

This method has been used to solve external and internal boundary-layer flows of perfect gases, reacting gas mixtures in chemical equilibrium, or nonreacting binary gas mixtures. For the perfect gas solution, density was calculated from the equation of state and the viscosity was calculated by Sutherland's formula. The transport properties were defined by setting $Pr = 0.71$, $Pr_t = 0.9$, $Le = 1.0$ and $Le_t = 1.0$. For the chemical equilibrium solution, tables of the thermodynamic and transport properties were calculated using modified versions of a computer program developed by Lordi et al. (Ref. 15). Local values of temperature, density, viscosity, specific heat and Prandtl number were found by interpolation in these property tables. For the nonreacting, binary gas mixtures, property data were taken from Jaffe, Lind and Smith (Ref. 16) for the enthalpy, specific-heat, viscosity and binary diffusion coefficients.

To close the system of turbulent boundary-layer equations, a turbulence model must be specified. The model used was based on Prandtl's mixing length concept given by

$$\epsilon = \rho l^2 \left| \frac{\partial u}{\partial y} \right| \quad (5)$$

The mixing length was defined by one of three models. Two of these models consisted of two layers and used an inner and outer law in these regions. Both models used Klebanoff's (Ref. 17) modification of Clauser's law in the outer region, but the first used Van Driest's (Ref. 18) inner law and the second used Reichardt's law (Ref. 19) in the region near the wall. The third model was developed by Beckwith and Bushnell (Ref. 20)

and consisted of a number of separate layers with the mixing length defined in each of these layers as in Ref. 20.

Anderson and Lewis (Ref. 1) applied this method to flows around various geometries including flat plates, nozzles, hyperboloids and sphere cones. A few of the results obtained by the method are presented in this paper. The first case considered flow through a nozzle as reported by Boldman et al. (Ref. 21). The nozzle configuration consists of a 30° conical convergent section, a circular arc throat section and a 15° conical divergent section. The throat radius is 0.746 in., and the stagnation pressure and temperature were 300 psia and 970°R , respectively.

The predicted heat-transfer coefficient using the present method of solution is compared with the experimental data and the solutions obtained using the Elliott, Bartz and Silver (Ref. 22) integral method in Fig. 1. The present method of solution is in excellent agreement with the experimental data in the throat region and downstream. Differences of up to 20% between the predicted and experimentally determined heat-transfer coefficient are noted in the subsonic region of the nozzle. The near discontinuous change in the experimental value of the heat-transfer coefficient at $z \approx 1.97$ is the result of the temperature tabulated in this region, and also the experimental pressure data were not smooth in this region. For the present calculations, these data were smoothed in the region $1.9 \leq z \leq 2.5$. The integral method of solution is seen to reflect a strong dependence upon the starting condition assumptions. The two solutions presented using the integral method differ from each other by as much as 50%.

A 10° half-angle hyperboloid at an altitude of 100,000 ft. with a wall temperature of 1400°K was considered for a freestream Mach number and temperature of 20.178 and 226.98°K . This case corresponds to Case A of the AGARD test cases (Ref. 23). A plot of the Stanton number distribution is shown in Fig. 2 where the present method is in good agreement with Adams' (Ref. 24) results for all s/r_n .

For the equilibrium air solution, the present method is in excellent agreement with Blottner's (Ref. 13) solution for the Stanton number distribution. The maximum differences between Blottner's and Keltner and Smith's (Ref. 25) and the present results are less than 5%.

Three flat-plate solutions are presented for air-into-air mass transfer and one case with no mass transfer corresponding to the experimental data referred to as run numbers 8, 11, 15 and 19 by Danberg (Ref. 26). The freestream Mach number for these cases was approximately 6.3 and the temperature was approximately 59°K . The injection parameter $c_q = \rho_w v_w / \rho_e u_e$, varied from 0 to 25.8×10^{-4} . The ratio of the wall-to-edge static temperature was approximately 4.0. The predicted heat-transfer distribution, shown in Fig. 3, is in good agreement with the experimental data. It should be noted that the experimental heat-transfer data were determined indirectly by the use of thermocouples imbedded in the plate.

Calculations have been made with the present finite-difference method as modified by Miner and Lewis (Ref. 2) for two sets of data for supersonic flows with tangential slot injection; the experimental data and the finite-difference predictions of Cary (Ref. 27) and the experimental data of Kenworthy and Schetz (Ref. 28).

Vol. 3

Cary and Hefner (Ref. 29) reported the results of a series of experiments in which air was tangentially injected into a Mach 6 turbulent boundary layer. Also presented in Ref. 29 are finite-difference predictions for six of the experimental cases using the method of Ref. 20. In the experimental investigation, three slot heights were considered ($s = 0.158$ cm, 0.475 cm and 1.116 cm or $1/16$, $3/16$ and $7/16$ in.), and for each slot height the total enthalpy of the slot flow was varied over a range of values. Additionally, the mass flow from the slot, λ , was varied from 0.0165 to 1.6 . For these mass-flow rates, the ratio of wall static pressure with slot injection to wall static pressure without the slot present, $P_w/P_{w,0}$, ranged from $P_w/P_{w,0} = 0.3$ to $P_w/P_{w,0} = 2.8$. The finite-difference predictions given in Ref. 29 were for $P_w/P_{w,0} = 1.0$ and were made using initial velocity and total enthalpy profiles obtained from the experimental data. The initial species concentration profiles used by Cary were modified step functions with some smoothing of the step corners.

The predicted skin-friction distributions for Cary's Cases III and IV are shown in Fig. 4. The Beckwith-Bushnell eddy-viscosity model was used, and both wall and local properties were used in y^+ . Also shown for each case is the predicted C_{f_0} (flat plate) distribution, and the experimental skin-friction distributions obtained by Cary.

When wall properties were used in y^+ , the results predicted by the present method consistently agreed well with the results of the calculations Cary made with the method of Ref. 20 using wall properties in y^+ . However, when local properties were used in y^+ , the predicted C_f was consistently 10 percent higher than the results of Cary, and the predicted C_f approached more rapidly the flat-plate value C_{f_0} . For

these cases, predictions of drag reduction were strongly influenced by the choice of flow properties in the Van Driest damping function.

In the experiments conducted at Virginia Polytechnic Institute and State University by Kenworthy and Schetz (Ref. 28), air was tangentially injected through a 0.25 in. slot into a Mach 2.4 turbulent boundary layer. Two mass-flow rates were considered; for the higher mass-flow rate $\lambda = 0.2027$ and the Mach number of the slot flow was $M_j = 0.66$. For the lower mass-flow rate, $\lambda = 0.0764$, $M_j = 0.31$. For $M_j = 0.66$ (matched-pressure injection), the wall-pressure distribution was nearly constant and equal to the test section static pressure for $M = 2.37$. For the low pressure injection, $M_j = 0.31$, the wall static pressure dropped about 20% at the slot and recovered to the freestream value in about eighteen slot heights.

Predicted and experimental Mach number profiles at Stations 3 and 4 are shown in Fig. 5 for low pressure injection. Good agreement was obtained between the experimental and predicted profiles. At station 3, the predicted profiles were for $x = 12.7$ cm (5.0 in.) and at station 4, the predicted profiles were for $x = 17.78$ cm (7.0 in.). For low pressure injection, the predicted profiles agreed well with the experimental profiles. Miner and Lewis (Ref. 2) included as an option an iterative procedure for the pressure interaction effects. The pressure interaction model was a global iteration procedure which made the first boundary-layer calculation with the initial pressure distribution. A new distribution was computed from the calculated displacement-thickness distribution using Prandtl-Meyer theory to calculate the Mach number and the isentropic flow relations to calculate a p/p_0 distribution.

For the Cary slot injection cases, comparison between experimental and predicted pressure distributions was not possible, but such comparisons could be made for the Kenworthy and Schetz low pressure injection case. The experimental and predicted pressure distributions are shown in Fig. 6. The agreement was very good and the present method correctly predicted the pressure distribution throughout the interaction region.

THREE-DIMENSIONAL BOUNDARY LAYERS

A three-dimensional boundary-layer computer program has been developed to simulate the reentry of sharp and blunt cones. The program includes the effects of surface mass transfer to simulate ablation during reentry, and also includes laminar, transitional and turbulent boundary-layer analysis. A program with these capabilities is necessary because wind tunnels capable of duplicating the correct flight conditions for reentering bodies at supersonic or hypersonic conditions are nonexistent. There is also a need for validated computer codes, tested at perfect gas wind tunnel conditions, which can be used for the accurate scaling of wind tunnel results to free-flight conditions including chemistry and mass transfer.

The turbulent boundary layer has been modeled by using an invariant model of three-dimensional turbulence which employs the two-layer eddy-viscosity mixing-length approach. An intermittency factor has been used through the transition regime to express the probability of the flow being turbulent at each point.

The resulting boundary-layer equations are integrated using a marching implicit finite-difference scheme.

Background

The three-dimensional, compressible, turbulent boundary-layer equations have been presented by Vaglio-Laurin (Ref. 30) and by Braun (Ref. 31). In addition, the laminar, compressible three-dimensional equations were presented by Moore (Ref. 32). The laminar three-dimensional equations were integrated using a marching finite-difference scheme by McGowan and Davis (Ref. 33) for sharp cones at angle of attack.

Vol. 3

The McGowan and Davis report puts the governing equations in similarity variable form, reducing the number of independent variables from three to two in the transformed equations. Therefore their method becomes a two-dimensional scheme.

Adams (Ref. 34) extended the method of McGowan and Davis and a transformation similar to that used by Dwyer (Ref. 35) to include turbulent boundary layers with a variable normal grid spacing. The Adams method, however, was still a locally similar solution representing the patching together of local solutions for sharp cones in hypersonic flow. Adams presented detailed, hypersonic, three-dimensional, turbulent boundary-layer profiles around a sharp cone at incidence which are compared to the results of the present investigation.

Frieders and Lewis (Ref. 36) developed a computer program for fully three-dimensional laminar boundary layers based on the method of McGowan and Davis mentioned above and on the two-dimensional method of Anderson and Lewis (Ref. 1). This program extended the two-dimensional nature of the McGowan and Davis method to a true three-dimensional method for use on blunt cones at angle of attack and for use in nonuniform flow-fields. The Frieders and Lewis program (Ref. 36) used two different coordinate systems and transformations in order to patch together full three-dimensional solutions for blunt cones at incidence.

Mayne (Ref. 37) also used the method of McGowan and Davis to study streamline swallowing on blunt cones at angle of attack. His study was limited to the windward streamline and also involved the use of two different coordinate systems. Mayne also split the solution method for a blunt cone into three parts; 1) the stagnation point, 2) the axisymmetric sphere where the cross-flow momentum equation is not solved

and 3) the fully three-dimensional afterbody behind the sphere-cone tangent point.

Mass transfer has been investigated for two-dimensional boundary-layer flows over cones by a number of authors. Jaffe, Lind and Smith (Ref. 16) investigated the binary diffusion of He, Ar and CO₂ into air as well as air-into-air for sharp cones at zero incidence. However, the species boundary condition at the wall was incorrectly stated. The correct wall boundary condition for the species equation was used by Lewis, Adams and Gilley (Ref. 38), and by Mayne, Gilley and Lewis (Ref. 39). These two reports dealt with mass-transfer effects on slender blunted cones and sharp cones at zero incidence to hypersonic flow. The results of these reports are compared to present results for zero incidence cones.

Mass transfer in turbulent boundary layers was investigated by Miner and Lewis (Ref. 2) for two-dimensional flow using a modified version of the computer program reported in Miner, Anderson and Lewis (Ref. 40). The species equation wall boundary condition is also incorrect as reported in Miner and Lewis. The transformation of the governing equations in the present paper is identical to that used by Miner and Lewis. The present computer program can be thought of as the three-dimensional analog of the program used by Miner and Lewis with the exception of the species wall boundary condition.

Two recent papers by Adams (Ref. 41) and by Watkins (Ref. 42) make use of the Levy-Lees transformation to the governing equations. Adams developed an implicit finite-difference analysis of sharp cone windward streamline flows including transition and turbulence. Adams used the suggestion by Moore (Ref. 43) for dealing with the crossflow

Vol. 3

momentum equation at the windward streamline. The same method is used in the present investigation. Adams also develops the variable spaced grid system for the normal coordinate which is also found in the present program.

Watkins developed the full three-dimensional laminar boundary-layer equations in a modified Levy-Lees coordinate system for use in studying spinning sharp bodies at angle of attack. The form of his transformed equations is very similar to the laminar version of the transformed equations as described in this report.

A report by Blottner and Ellis (Ref. 44) describes a computer program very similar to the present program in terms of numerical solution method but is limited to laminar, incompressible boundary layers over blunt bodies.

The present analysis is the first to the author's knowledge to express the full three-dimensional compressible, turbulent boundary-layer equations including the effects of heat and mass transfer. The equations have been transformed using the Levy-Lees transformation equations. The finite-difference method follows the method of McGowan and Davis, utilizing an implicit scheme similar to that used by Dwyer (Ref. 35) as modified by Krause (Ref. 45).

Results of the present investigation have been compared to available experimental and numerical data. The full three-dimensional solution of a sharp cone at angle of attack with transition to turbulence has been calculated. Solutions have also been calculated to show the effects of using different turbulent Prandtl number profiles as provided for in the program.

The laminar compressible three-dimensional boundary-layer equations were presented by Moore (Ref. 32). Following Moore's laminar equations the governing equations have been developed for turbulent compressible flows and are presented here without derivation in terms of mean physical variables.

Continuity Equation:

$$\frac{\partial}{\partial x} (\rho u r) + \frac{\partial}{\partial y} (\rho V r) + \frac{\partial}{\partial \phi} (\rho w) = 0 \quad (6)$$

Streamwise Momentum Equation:

$$\rho u \frac{\partial u}{\partial x} + \rho V \frac{\partial u}{\partial y} + \rho \frac{w}{r} \frac{\partial u}{\partial \phi} - \rho \frac{w^2}{r} \frac{\partial r}{\partial x} = \frac{-\partial P}{\partial x} e + \frac{\partial}{\partial y} \left[\mu \frac{\partial u}{\partial y} - \rho u' v' \right] \quad (7)$$

Transverse Momentum Equation:

$$\rho u \frac{\partial w}{\partial x} + \rho V \frac{\partial w}{\partial y} + \rho \frac{w}{r} \frac{\partial w}{\partial \phi} + \rho \frac{uw}{r} \frac{\partial r}{\partial x} = \frac{-1}{r} \frac{\partial P}{\partial \phi} e + \frac{\partial}{\partial y} \left[\mu \frac{\partial w}{\partial y} - \rho v' w' \right] \quad (8)$$

Normal Momentum Equation:

$$\frac{\partial P}{\partial y} = 0 \quad (9)$$

Energy Equation:

$$\rho u \frac{\partial H}{\partial x} + \rho V \frac{\partial H}{\partial y} + \rho \frac{w}{r} \frac{\partial H}{\partial \phi} = \frac{\partial}{\partial y} \left[\mu \left(\frac{\partial H}{\partial y} + \frac{1-\text{Pr}}{\text{Pr}} \frac{\partial h}{\partial y} \right) - \rho v' H' \right] \\ + \frac{\partial}{\partial y} \left[\frac{\mu}{\text{Pr}} (\text{Le}-1) (h_f - h_i) \frac{\partial C_f}{\partial y} + \sum_i h_i \rho v' C_i' \right] \quad (10)$$

Species Equation:

$$\rho u \frac{\partial C_i}{\partial x} + \rho V \frac{\partial C_i}{\partial y} + \rho \frac{w}{r} \frac{\partial C_i}{\partial \phi} = \frac{\partial}{\partial y} \left[\text{Le} \frac{\mu}{\text{Pr}} \frac{\partial C_i}{\partial y} + \rho v' C_i' \right] \quad (11)$$

where $V = v + \rho'v'/\rho$. The equation of state for each species is:

$$P_i = \frac{\rho_i}{M_i} RT \quad (12)$$

where R is the universal gas constant. Only one species equation is necessary since in a two-component mixture the mass fractions sum to unity:

$$\sum_i c_i = 1 \quad (13)$$

The viscosity and thermal conductivity are related by the Prandtl number:

$$Pr = \mu C_p / k \quad (14)$$

where

$$C_p = \sum_i c_i C_{p_i}$$

Similarly, diffusion and thermal conductivity are related by the Lewis number:

$$Le = \rho D_{if} C_p / k \quad (15)$$

The boundary conditions on the above equations are as follows:

Momentum Equations:

$$y = 0 : u = w = u'v' = v'w' = \rho'v' = 0, v = v_w$$

$$y \rightarrow \infty : u = u_e, w = w_e$$

$$u'v' = v'w' = \rho'v' = 0$$

Energy Equations:

$$y = 0 : H = H_w, v'H' = 0$$

$$y \rightarrow \infty : H = H_e, v'H' = 0$$

Species Equations:

$$y = 0 \quad : \quad C_f = C_{f_w} = \left(\frac{D_{if}}{v} \frac{\partial C_f}{\partial y} \right)_w, \quad v' C_i' = 0$$

$$y \rightarrow \infty \quad : \quad C_f = 1.0, \quad v' C_i' = 0$$

In the derivation of the conservation equations the usual assumptions regarding the fluctuating quantities have been employed. These are:

1) the turbulent level is small and therefore terms having the mean square of the velocity fluctuation are dropped from the equations

2) molecular transport parameters are approximated by the mean flow counterparts

3) the rate of change of mean flow properties in the normal direction is an order of magnitude greater than the rates of change in the streamwise and transverse directions.

The solution of the governing equations requires the expression of the turbulent shear terms and the turbulent flux of total enthalpy in terms of the mean flow quantities. A popular concept used to obtain these expressions is the eddy viscosity, eddy-conductivity analogy with the molecular viscosity and conductivity where:

$$-\rho u'v' = \epsilon_x \partial u / \partial y \quad (16)$$

$$-\rho v'w' = \epsilon_\phi \partial w / \partial y \quad (17)$$

and
$$-\rho v'H' = k_t \partial H / \partial y \quad (18)$$

and where the dimensionless transport parameters are:

$$Pr_t = C_p \epsilon / k_t \quad (19)$$

$$Le_t = \rho D_t C_p / k_t \quad (20)$$

Windward Plane Conservation Equations:

On the windward plane of a cone, the transverse (crossflow) velocity, w , and $\partial P_e / \partial \phi$ vanish due to symmetry; however, the crossflow velocity gradient does not vanish and still appears in the continuity equation. Under these conditions the transverse momentum equation would vanish completely at the windward plane where initial profiles are generated for the remaining integration of the governing equations. To avoid this problem, Moore (Ref. 43) has suggested that the transverse momentum equation first be differentiated with respect to ϕ before neglecting terms which vanish at the windward streamline. This procedure results in the following transverse momentum equation at the windward plane:

$$\begin{aligned} \rho u \frac{\partial}{\partial x} \left(\frac{\partial w}{\partial \phi} \right) + \frac{\rho}{r} \left(\frac{\partial w}{\partial \phi} \right)^2 + \rho v \frac{\partial}{\partial y} \left(\frac{\partial w}{\partial \phi} \right) + \rho \frac{u}{r} \frac{\partial w}{\partial \phi} \frac{\partial r}{\partial x} \\ = \frac{-1}{r} \frac{\partial^2 p_e}{\partial \phi^2} + \frac{\partial}{\partial y} \left[(\mu + I_f \epsilon) \frac{\partial}{\partial y} \left(\frac{\partial w}{\partial \phi} \right) \right] \end{aligned} \quad (21)$$

The remaining conservation equations are reduced to a quasi-two-dimensional form at the windward plane where $w = 0$. The continuity equation serves as the only coupling between the transverse momentum equation and the remaining governing equations. For cones at zero angle of attack the transverse momentum equation in either form vanishes identically leaving a completely axisymmetric problem.

A more convenient form of the governing equations for numerical solution is obtained by introducing two stream functions defined as follows:

$$\psi(x, y) = \sqrt{2\xi} f(\xi, \eta) \quad (22)$$

$$\psi(x, y) = \sqrt{2\xi/r} g(\xi, \eta) \quad (23)$$

where ξ , η are the Levy-Lees transformed coordinates defined as follows:

$$\xi(x) = \int_0^x \rho_r \mu_r u_r r^2 dx \quad (24)$$

$$\eta(x, \phi, y) = \rho_e u_e r / \sqrt{2\xi} \int_0^y \frac{\rho}{\rho_e} dy \quad (25)$$

This coordinate transformation removes the singularity at $x = 0$ and stretches the normal coordinate. Accordingly, the transformed derivatives become:

$$\frac{\partial}{\partial x} = \rho_r \mu_r u_r r^2 \frac{\partial}{\partial \xi} + \frac{\partial \eta}{\partial x} \frac{\partial}{\partial \eta} \quad (26)$$

$$\frac{\partial}{\partial \phi} = \frac{\partial}{\partial \phi} + \frac{\partial \eta}{\partial \phi} \frac{\partial}{\partial \eta} \quad (27)$$

$$\frac{\partial}{\partial y} = \rho u_e r / \sqrt{2\xi} \frac{\partial}{\partial \eta} \quad (28)$$

Satisfying the continuity equation with above stream functions the following relations are obtained:

$$\rho u r = \frac{\partial \Psi}{\partial y} \quad (29)$$

$$\rho w = \frac{\partial \psi}{\partial y} \quad (30)$$

$$\rho v r = -\frac{\partial \Psi}{\partial x} - \frac{\partial \psi}{\partial \phi} \quad (31)$$

Using equations 31, 26 and 28 results in the following expression:

$$\frac{\rho v r \sqrt{2\xi}}{\rho_r \mu_r u_r r^2} + \eta_x \delta r f' + \eta_\phi \delta g' + 2\xi \frac{\partial f}{\partial \xi} + f + \delta \frac{\partial g}{\partial \phi} = 0 \quad (32)$$

or

$$V + 2\xi \frac{\partial f}{\partial \xi} + f + \delta \frac{\partial g}{\partial \phi} = 0 \quad (33)$$

Vol. 3

where

$$V = \rho v r \sqrt{2\xi} / \rho_r u_r \mu_r r^2 + \eta_x \delta r f' + \eta_\phi \delta g' \quad (34)$$

and

$$\delta = 2\xi / \rho_r u_r \mu_r r^3 \quad (35)$$

Differentiation of equation (29) with respect to y using equation (28) gives the expression for f' :

$$f' = \frac{u}{u_e} \quad (36)$$

Similarly, differentiation of equation (30) with respect to y using equation (28) gives the expression for g' :

$$g' = \frac{w}{u_e} \quad (37)$$

Evaluating the momentum equations (7) and (8) at the outer edge gives the pressure gradients as:

$$-\frac{\partial P_e}{\partial x} = \rho_e u_e \frac{\partial u_e}{\partial x} + \frac{\rho_e w_e}{r} \frac{\partial u_e}{\partial \phi} - \frac{\rho_e w_e^2}{r} \frac{\partial r}{\partial x} \quad (38)$$

$$-\frac{1}{r} \frac{\partial P_e}{\partial \phi} = \rho_e u_e \frac{\partial w_e}{\partial x} + \frac{\rho_e w_e}{r} \frac{\partial w_e}{\partial \phi} + \frac{\rho_e u_e w_e}{r} \frac{\partial r}{\partial x} \quad (39)$$

Using equations (26) - (39) the governing conservation equations are now expressed in terms of transformed variables.

To obtain the transformed equations at the windward streamline, two new stream functions are introduced in order to satisfy the windward plane continuity equation, as follows:

$$\psi = \sqrt{2\xi} f \quad (40)$$

$$\psi = \sqrt{2\xi} g \quad (41)$$

The transformed equations are then obtained in the same manner as for the general three-dimensional case. For a cone at zero angle of attack, the system of transformed equations reduces to a fully axisymmetric system without a transverse momentum equation.

Equations at the Stagnation Point

At the stagnation point of a blunt cone, the boundary-layer equations have a removable singularity. In the limit as $\xi \rightarrow 0$ the expressions for ξ and η are:

$$\xi(x) = \rho_e \mu_e \frac{du_e}{dx} x^4 / 4 \quad (42)$$

and

$$\eta(x,y) = \left[2\rho_e / \mu_e \frac{du_e}{dx} \right]^{1/2} \int_0^y \rho / \rho_e dy \quad (43)$$

Also at the stagnation point of a blunt cone the expression for V in the windward plane continuity equation becomes:

$$V = \frac{\rho v}{\left[2\rho_e \mu_e \frac{du_e}{dx} \right]^{1/2}} \quad (44)$$

Eddy-Viscosity Models

Prandtl's mixing length hypothesis states that the eddy viscosity is the product of some characteristic length and the normal velocity gradient. For two-dimensional flow this concept leads to:

$$e \approx \rho l_*^2 \left| \partial u / \partial y \right| \quad (45)$$

Prandtl's studies assumed that the eddy viscosity should depend only on local eddy scale and on the properties of turbulence. Adams (Ref. 41) extended this concept to the three-dimensional case by assuming that the

Vol. 3

eddy viscosity is also independent of coordinate direction. In the three-dimensional case ϵ becomes:

$$\epsilon = \epsilon_x = \epsilon_\phi = \rho l_*^2 \left[\partial u / \partial y^2 + \partial w / \partial y^2 \right]^{1/2} \quad (46)$$

which reduces to the two-dimensional form when $w = 0$. This is referred to as the invariant turbulence model by Hunt, Bushnell and Beckwith (Ref. 46) and was used with success by Adams (Ref. 41).

The model used in this investigation is the common two-layer inner-outer model which uses the Prandtl mixing length theory and the Van Driest or Reichardt damping near the wall. Following Patankar and Spalding (Ref. 47) and Adams (Ref. 41) the mixing length distribution is as follows:

$$\begin{aligned} l_* &= k_* y & \{0 < y \leq \lambda y_\ell / k_*\} \\ l_* &= \lambda y_\ell & \{\lambda y_\ell / k_* < y\} \end{aligned} \quad (47)$$

where

$$k_* = 0.435$$

$$\lambda = 0.09$$

$$y_\ell = y \text{ when } \left[(u^2 + w^2) / (u_e^2 + w_e^2) \right]^{1/2} = 0.99$$

The inner law is damped near the wall so as to yield the exact laminar shear stress term at the wall. To accomplish this, two different damping factors have been used in this investigation, Van Driest's with local shear stress and Reichardt's (Ref. 19) damping term.

Cebeci (Ref. 48) developed a mass transfer correction to Van Driest's inner eddy-viscosity law by modifying the damping constant A^* .

For turbulent flows with mass transfer Cebeci determined the damping constant to be

$$A^* = 26 \exp(-5.9 v_w^+)$$

where

$$v_w^+ = v_w / (\tau_w / \rho)^{1/2}$$

Reichardt's expression for the inner eddy-viscosity law was obtained by curve fitting experimental pipe flow data. The expression is:

$$\epsilon_i = \mu k_* \left[\frac{y \sqrt{\tau_w \rho}}{\mu} - 11.0 \tanh \left(\frac{y \sqrt{\tau_w \rho}}{11 \mu} \right) \right] \quad (48)$$

As can be seen, this expression does not involve the velocity gradient terms. For this reason it is preferred for use in numerical solutions, since it usually requires fewer iterations to converge.

Following Eqs. (46) and (47), the outer eddy-viscosity law is:

$$\epsilon_o = \lambda^2 y_\delta^2 \partial E / \partial y \quad (49)$$

The outer eddy-viscosity law is used in conjunction with the Klebanoff (Ref. 17) intermittency factor which assures a smooth approach of ϵ_o to zero as $y \rightarrow \delta$. The modified law is:

$$\epsilon_o = \lambda^2 y_\delta^2 \gamma \partial E / \partial y \quad (50)$$

where γ is Klebanoff's intermittency factor:

$$\gamma = \left[1 + 5.5 (y/\delta)^6 \right]^{-1} \quad (51)$$

Transition Models

Two models of transition from laminar to turbulent flow have been used in our studies. One model is simply instantaneous transition to turbulent flow, and there really is no transition region or zone at all. In the second case a smooth transition to turbulent flow occurs over a prescribed distance. This distance is known as the transition zone and is defined as the distance between the onset of transition at $x = X_t$ and the beginning of fully turbulent flow at $x = X_T$ at some point downstream.

The probability of turbulent flow at any point is expressed by a model by Dhawan and Narasimha (Ref. 49) as:

$$I_f(x) = 1 - \exp \left[0.412 (2.917)^2 \left(\frac{x - X_t}{X_T - X_t} \right)^2 \right] \quad (52)$$

The transition intermittency factor is employed as a simple multiplier of the eddy viscosity in the governing equations and therefore acts as a damping coefficient for the fully turbulent eddy viscosity.

Turbulent Prandtl Number Laws

Five different turbulent Prandtl numbers have been considered in our investigation. One of the models employs a constant Prandtl number:

$$Pr_t = 0.9$$

as recommended by Patankar and Spalding (Ref. 47) for two-dimensional boundary-layer flows. Other authors have derived models for the distribution of the turbulent Prandtl number normal to the wall. These models show the Prandtl number varying from near 0.8 at the wall to nearly 1.4 at the outer edge. The models presented here are by Rotta; Shang; Meier, Voisinet and Gates; and by Cebeci.

Rotta (Ref. 50) has suggested an empirical formula for the turbulent Prandtl number distribution as follows:

$$\text{Pr}_t = 0.95 - 0.45 (y/\delta)^2 \quad (53)$$

which gives a value of 0.5 at the outer edge and 0.95 near the wall.

A similar empirical formula was developed by Shang (Ref. 51) to study the sensitivity of a solution to the turbulent Prandtl number:

$$\text{Pr}_t = \text{Pr}_1 \exp (-10 (y/\delta)) + \text{Pr}_2 (1 - 0.2 (y/\delta)) \quad (54)$$

where

$$0.2 \leq \text{Pr}_1 \leq 0.4 \text{ and } 0.8 \leq \text{Pr}_2 \leq 1.0$$

Shang's formula allows the user to specify the constants in the formula, so that the difference in the values at the wall is between 1.0 and 1.4 and between 0.65 and 0.95 at the outer edge. Both Rotta's and Shang's formulas fall within the turbulent Prandtl number uncertainty envelope as established by Simpson et al. (Ref. 52). Shang's data follow the boundaries of Simpson's envelope very well at both the upper and lower boundaries while Rotta's formula falls between the boundaries in the outer region and undershoots Simpson's lower boundary at the wall.

Meier et al. (Ref. 53) applied Prandtl's mixing length concept as modified by Van Driest to define a mixing length for both turbulent momentum and energy transport. Writing the turbulent Prandtl number based on mixing lengths, Meier et al. produced the following expression:

$$\text{Pr}_t = \left[\frac{k (1 - \exp (-y^+/A))}{k_q (1 - \exp (-y^+/A_q))} \right]^2 \quad (55)$$

Vol. 3

Using this Prandtl number model, Meier et al. found they could accurately describe experimental temperature distributions from the wall up to the fully turbulent part of the boundary layer.

Cebeci (Ref. 54) based his model of the turbulent Prandtl number on the considerations of a Stokes type flow. In Cebeci's model the Prandtl number is strongly affected by the molecular Prandtl number near the wall and is a constant away from the wall. Cebeci's model for the turbulent Prandtl number is:

$$Pr_t = \frac{k_m (1 - \exp(-y/A))}{k_h (1 - \exp(-y/B))} \quad (56)$$

Cebeci's study using this Prandtl number model showed good agreement with experiment and also confirmed that mass transfer has no significant effect on the turbulent Prandtl number.

Fluid Properties

The development of the fluid property calculations in our investigation follows closely those of Jaffe, Lind and Smith (Ref. 16). Fluid properties are developed for a binary gas mixture consisting of either helium, argon, or carbon dioxide being injected into a freestream of air.

The fluid properties necessary to this investigation are C_{p_f} , C_{p_i} , C_p ; C_{v_f} , C_{v_i} , C_v ; h , h_i , h_f ; k_f , k_i , k ; μ_i , μ_f , μ ; and D_{f_i} .

The mixture of gases is composed of perfect gas species where the total pressure is equal to the sum of the partial pressures of the individual species and where the specific enthalpies are functions of temperature only. Individual species molecular weights are necessary to calculate the mixture density from the following expression.

$$\rho = \frac{P}{RT} \left[\frac{M_f M_i}{C_f (M_i - M_f) + M_f} \right] \left(\frac{\text{slugs}}{\text{ft}^3} \right) \quad (57)$$

The specific heat capacities at constant pressure or volume are obtained from fifth degree polynomials. Similar polynomials are used to calculate the individual species viscosities, enthalpies and binary diffusion coefficients. For monotonic gases the specific heats and specific enthalpies are calculated from thermodynamic considerations.

The mixture values of enthalpy and specific heats are calculated from the specific properties and the relative mass fractions of the individual species. The viscosity of a mixture is calculated from Wilke's (Ref. 55) formula.

The thermal conductivity of a mixture is also obtained from Wilke's formula in which the individual species viscosities are replaced with the individual conductivities. The individual species thermal conductivities are calculated with the Eucken (Ref. 56) equation.

The coefficients for the polynomial fits were taken from tables developed by Lewis, Adams and Gilley (Ref. 38), and by Jaffe, Lind and Smith (Ref. 16). Lewis et al. extended the data of Jaffe et al. to a maximum temperature of 12,600°R for helium and argon. The original data of Jaffe et al. for carbon dioxide to 6300°R has been used in our investigation.

Finite-Difference Method

The finite-difference method used in our investigation follows the method used by McGowan and Davis (Ref. 33) which is similar to the method developed by Dwyer (Ref. 35) with modifications by Krause (Ref. 45). The method has been further modified to include variable spacing for the normal coordinate. The accuracy of this method is second order. The method is stable for negative transverse velocities when proper step sizes are chosen.

The momentum, species and energy equations are written in standard parabolic form as:

$$A_0 \frac{\partial^2 w}{\partial \eta^2} + A_1 \frac{\partial w}{\partial \eta} + A_2 w + A_3 + A_4 \frac{\partial w}{\partial \xi} + A_5 \frac{\partial w}{\partial \phi} = 0 \quad (58)$$

where w is the dependent variable in each case. The coefficients A_0 through A_5 are determined from the transformed governing equations.

The derivatives in Eq. 58 are replaced with finite-difference expressions and the finite-difference grid is shown in Fig. 7.

The finite-difference form of the Eqs. 58 results in simultaneous linear algebraic equations of tridiagonal form which are solved by a method developed by Richtmyer (Ref. 57). The boundary conditions at both the wall and the outer edge must be specified for this method.

The ability to variably space the normal grid allows closer placing of grid points near the wall where variations in properties are greater. The method used is taken from Cebeci, Smith and Mosinskis (Ref. 58) and has been successfully used by Anderson and Lewis (Ref. 1) and Adams (Ref. 41).

Using this procedure results in a constant ratio of succeeding normal grid intervals such that:

$$k = \frac{\Delta \eta_n}{\Delta \eta_{n-1}}$$

where the value of n at infinity is given by

$$\eta_\infty = \Delta \eta_1 \frac{k^N - 1}{k - 1}$$

where N is the total number of intervals across the layer.

Boundary-Layer Parameters

Local boundary-layer parameters are determined at a given point following the converged solution of the boundary-layer equations at each point. These parameters include heat transfer, heat-transfer coefficients, skin-friction coefficients, displacement thicknesses and momentum thicknesses.

The heat transfer at the wall is given by:

$$-\dot{q}_w = \left[k \frac{\partial T}{\partial y} + (h_f - h_i) \rho D_{fi} \frac{\partial C_f}{\partial y} \right]_w \left(\frac{\text{ft-lb}}{\text{ft}^2\text{-sec}} \right) \quad (59)$$

The compressible two-dimensional boundary-layer displacement thickness, δ^* , is used to obtain the displacement thickness in each of the two directions, x and ϕ . Neither δ_x^* or δ_ϕ^* completely define the actual displacement thickness at any point. For axisymmetric bodies, Cebeci and Mosinskis (Ref. 59) define a δ^* as a function of δ_x^* . For a sharp cone at angle of attack an expression for δ^* on the windward streamline only was developed by Moore (Ref. 60) as a function of both δ_x^* and δ_ϕ^* .

Momentum thicknesses have been defined similar to the displacement thicknesses for both directions. Heat-transfer and skin-friction coefficients have been defined in the conventional manner.

Discussion

The computer program has been developed to solve a large class of boundary-layer flows. The geometries included in the program are those of a sharp and a spherically blunted cone. For these two geometries the program has full three-dimensional solution capabilities for cases where these cones are at an angle of attack. When either geometry is in an

axisymmetric flowfield (zero angle of attack) the program will solve only the windward streamline of the vehicle. Figure 8 is a flow chart of the boundary-layer solution procedure.

Figures 9 through 12 present some solutions from the computer program. Figure 9 shows calculations made for a sharp cone at zero angle of attack in hypersonic laminar flow. This is the same cone solved by Jaffe, Lind and Smith in Ref. 16; however, the species equation wall boundary condition has been corrected in the current calculations. The current results are compared to results obtained from the program of Miner, Anderson and Lewis (Ref. 40) which also uses the corrected boundary condition for the species equation. For cases of mass transfer, significant decreases in wall heat transfer and skin friction are indicated. These effects are dependent on both the molecular weights and specific heats of the injected gases.

Figures 10 and 11 show the comparison of fully three-dimensional solutions using the present program and the experimental data of Cleary (Ref. 61). Cleary presented rather complete heat-transfer data for both sharp and blunt cones at angle of attack in laminar flow. Points were chosen on the afterbody, and comparison is made in the circumferential direction for the heat-transfer rate at the wall. Reasonably good agreement has been obtained for these cases. These figures show the dropping of the leeward solution plane for the sharp cone flow and for the blunt cone flow far downstream. Similar problems were reported by McGowan and Davis (Ref. 33) and Adams (Ref. 34). Difficulties on the leeward ray have been attributed to defects in the boundary-layer model as applied to leeward ray flows of cones at angle of attack. This problem is discussed by Moore (Ref. 43).

Data in Fig. 12 are presented in two different directions; 1) data versus ϕ , the transverse coordinate at three different values of S/L , and 2) data versus S/L , the streamwise coordinate at three different values of ϕ . The Stanton number and the transverse skin-friction coefficient are shown in both directions for a sharp cone at angle of attack with transition to turbulence.

The present program has been used to predict full 3-D flow problems with transition and/or mass transfer and is considered to be a useful engineering code. Further development of the program should include the following improvements;

- 1) an internally adjustable transverse stepsize
- 2) a three-dimensional transition-zone model including transverse variation of the transition onset distance and the transition intermittency factor
- 3) transverse variation of the wall temperature and injection rate distributions
- 4) equilibrium gas capability.

TWO-DIMENSIONAL OR AXISYMMETRIC VISCOUS
SHOCK-LAYER FLOWS

The governing equations for the viscous shock-layer flows follow the formulation of Davis (Refs. 62,63) and Moss (Ref. 64). The shock-layer equations were derived from the governing equations for reacting gas mixtures (such as given by Bird, Stewart and Lightfoot (Ref. 65)) written for a body oriented coordinate system. The equations are first nondimensionalized by variables of order one at the body surface (corresponding to high Reynolds number, boundary-layer flows). The equations are also nondimensionalized by variables of order one in the outer inviscid flow (corresponding to the shock region). A single set of equations is then obtained by retaining terms from the equations in each set to second order. The resulting set of shock-layer equations is uniformly second-order accurate in the inverse Reynolds number parameter ϵ from the body to the shock. Both longitudinal and transverse curvature are included. As given by Davis, the governing viscous shock-layer equations were specialized for a perfect gas (Ref. 62) or a binary, reacting mixture of oxygen atoms and molecules (Ref. 63). Moss (Ref. 64) gave the shock-layer equations for a multicomponent mixture of reacting gases.

The equations for shock-layer flows of multicomponent gases are given below.

Continuity Equation:

$$\frac{\partial}{\partial s} \left[(r + y \cos \phi)^j \rho u \right] + \frac{\partial}{\partial y} \left[(1 + \kappa y) (r + y \cos \phi)^j \rho v \right] = 0 \quad (60)$$

s-Momentum Equation:

$$\frac{1}{1+\kappa y} \rho u \frac{\partial u}{\partial s} + \rho v \frac{\partial u}{\partial y} + \rho uv \frac{\kappa}{1+\kappa y} + \frac{1}{1+\kappa y} \frac{\partial P}{\partial s} = \epsilon^2 \frac{\partial}{\partial y} \left[\mu \left(\frac{\partial u}{\partial y} - \frac{\kappa u}{1+\kappa y} \right) \right] + \epsilon^2 \mu \left(\frac{2\kappa}{1+\kappa y} + \frac{j \cos \phi}{r + y \cos \phi} \right) \left(\frac{\partial u}{\partial y} - \frac{\kappa u}{1+\kappa y} \right) \quad (61)$$

y-Momentum Equation:

$$\frac{\partial P}{\partial y} = \frac{\kappa}{1+\kappa y} \rho u^2 - \frac{1}{1+\kappa y} \rho u \frac{\partial v}{\partial s} - \rho v \frac{\partial v}{\partial y} \quad (\text{FVSL}) \quad (62)$$

which becomes

$$\frac{\partial P}{\partial y} = \frac{\kappa}{1+\kappa y} \rho u^2 \quad (\text{TVSL}) \quad (63)$$

if the thin shock-layer approximation is made.

Energy Equation:

$$\frac{1}{1+\kappa y} \rho u C_p \frac{\partial T}{\partial s} + \rho v C_p \frac{\partial T}{\partial y} - \frac{1}{1+\kappa y} u \frac{\partial P}{\partial s} - v \frac{\partial P}{\partial y} = \epsilon^2 \frac{\partial}{\partial y} \left(k \frac{\partial T}{\partial y} \right) + \epsilon^2 \left(\frac{\kappa}{1+\kappa y} + \frac{j \cos \phi}{r + y \cos \phi} \right) k \frac{\partial T}{\partial y} - \epsilon^2 \sum_{i=1}^{ns} J_i C_{p_i} \frac{\partial T}{\partial y} + \epsilon^2 \mu \left(\frac{\partial u}{\partial y} - \frac{\kappa u}{1+\kappa y} \right)^2 - \sum_{i=1}^{ns} h_i \dot{w}_i \quad (64)$$

Species Conservation Equations:

$$\frac{1}{1+\kappa y} \rho u \frac{\partial C_i}{\partial s} + \rho v \frac{\partial C_i}{\partial y} = \dot{w}_i - \epsilon^2 \frac{\partial}{\partial y} (J_i) - \epsilon^2 \left(\frac{\kappa}{1+\kappa y} + \frac{j \cos \phi}{r + y \cos \phi} \right) J_i \quad (65)$$

The specific heat C_p and static enthalpy h are required for each of the species considered and for the gas mixture. Also required are the viscosity μ and the thermal conductivity k . Since the multicomponent gas mixture is considered to be a mixture of thermally perfect gases, the thermodynamic and transport properties for each species were calculated using the local temperature. The properties for the gas mixture were then determined in terms of the individual species properties.

The enthalpy and specific heat of the species were obtained from the thermodynamic data tabulated by Browne (Refs. 66-68).

The viscosity of each of the individual species was calculated from the curve fit relation

$$\mu_i = \exp(C_i) T_k^{(A_i \ln T_k + B_i)}; \frac{\text{gm}}{\text{cm-sec}} \quad (66)$$

where A_i , B_i and C_i are the curve fit constants for species from Blottner (Ref. 69) and T_k is the local temperature in degrees Kelvin.

The thermal conductivity of the individual species was calculated from the Eucken (Ref. 56) semi-empirical formula using the species viscosity and specific heat.

After the viscosity and thermal conductivity of the individual species were calculated, the viscosity and thermal conductivity of the mixture were calculated using Wilke's semi-empirical relations.

In the present work, the diffusion model is limited to binary diffusion with the binary diffusion coefficients specified by the Lewis number which was set to 1.4.

A measure of the validity of a theory is the agreement with experimental data. For the shuttle configuration, flight heat-transfer data are some years in the future and, in general, wind-tunnel data for shuttle

configurations are not readily available outside of the NASA and some contractors. One set of experimental hypersonic wind tunnel data which has been published is that of Pappas and Lee (Ref. 70) at the NASA Ames Research Center for flow over a 7.5° sphere-cone with $r_n = 1$ in. In the experimental program, surface pressure and heat-transfer distributions were measured at Mach 13 with varying rates of injection of foreign gases. Included in the experimental data were distributions for the no injection case. Experimental and present predictions of the heat-transfer distributions are shown in Fig. 13. Also shown in this figure is the previous first-order boundary-layer theory of Lewis, Adams and Gilley (Ref. 38) including transverse curvature and displacement-thickness interaction for the Ames conditions. The results from Ref. 38 were obtained using a global iteration for determining the displacement-thickness interaction effects, and the inviscid body pressure for the effective body was obtained using a blunt body, method of characteristics procedure similar to that of Ref. 62. The present theory did not compare as well with the experimental data as did the previous boundary-layer theory with viscous interaction included. In the present viscous shock-layer method, the effect of the discontinuity in surface curvature, κ , was most distinct immediately upstream of the sphere-cone tangent point and for a short distance downstream. The sphere-cone considered by Pappas and Lee (Ref. 70) ended at $s \approx 5$, and almost all of this body was within the length affected by the discontinuity in κ . Despite the effect of the discontinuity in κ , the agreement between the experimental data and the predictions of the present viscous shock-layer theory was quite good.

The RAM C flights were part of a program conducted by the NASA Langley Research Center for studying flowfield electron concentrations under reentry conditions. The body for each RAM C flight was a 9° sphere-cone with a 6 in. nose radius.

While the RAM C, 230 Kft, conditions were quite different from the Ames conditions, the Reynolds numbers were of the same order ($Re_\infty/r_n = 4315$ for the RAM C conditions and $Re_\infty/r_n = 1515$ for the Ames conditions). The shock Reynolds numbers were also similar (RAM C, $Re_s = 269$; Ames, $Re_s = 190$) and the values of the Reynolds number parameter were nearly the same (RAM C, $\epsilon = 0.0965$; Ames, $\epsilon = 0.0980$). The Reynolds number similarity between the two cases should allow comparison of the normalized heat-transfer distributions. The present predictions for the RAM C and Ames conditions were in quite good agreement even though there was a difference in cone angle (and thus in the location of the sphere-cone tangent points). Further, the present viscous shock-layer results for the RAM C conditions agreed well with the Ames experimental data. The results of Kang and Dunn (Ref. 71) for the RAM C are also shown in Fig. 13 in normalized form. Figure 13 clearly shows that for $s > 3$ the results of Kang and Dunn were higher by an order of magnitude or more than the present results (see Refs. 72-74). A comparison of the results of Kang and Dunn for the RAM C with the Ames experimental data showed a difference by a factor of 11 or 12 at $s = 4$ or 4.5. The values of Re_∞/r_n and Re_s given above indicate that the Ames conditions were at least as much in a viscous shock-layer regime as the RAM C, 230 Kft, conditions.

The viscous shock-layer results were also compared with data from an experimental study of the shuttle orbiter conducted by Adams et al. (Ref. 75), Martindale (Ref. 76) and Carter and Martindale (Ref. 77).

Three tests of the 139 Orbiter were conducted in the AEDC/VKF Hypersonic Wind Tunnel. The first case was the OH9 test where the edge conditions were measured by flowfield probe surveys. The other two cases were for the OH4B heat-transfer tests and correspond to the maximum and minimum Reynolds number available in the AEDC/VKF Tunnel B.

Adams et al. (Ref. 75) used a 31-deg asymptotic half-angle hyperboloid to approximate the windward streamline of the 139 Shuttle Orbiter at a 30-deg angle of attack. The equation of the hyperboloid was:

$$r_n = \frac{y'^2}{2x'} - \frac{x' \tan^2 31^\circ}{2}$$

where x' and y' are the coordinates in a freestream velocity orientated system. Figure 14 compares the wall pressure distribution with the calculated results of Inouye, Rakich and Lomax (Ref. 4) and the experimental data from test 1T (Ref. 76). The fully viscous shock-layer (FVSL) results were in excellent agreement with the predictions of Inouye et al. and in relatively good agreement with the experimental data. Use of the thin viscous shock-layer approximation resulted in a lower prediction of the wall pressure. Comparisons with the OH4B heat-transfer tests are shown in Fig. 15 which compares the heat-transfer distribution for the 3T test conditions at a low Reynolds number. The results of the present method were slightly lower than either the experimental data or the predictions of Adams, Martindale, Mayne and Marchand, and the TVSL approximation predicted an even lower heat-transfer distribution than did the FVSL model.

The shock-layer method was also used to make predictions of the flow around a 0.01 scale model of the shuttle orbiter at conditions similar to those attainable in the CAL Shock Tunnel (Ref. 78). The

Vol. 3

Mach number was 19.15 and the freestream temperature and pressure were 76.0°R and 0.00173 psia, respectively. The body geometry differed slightly from the 31-deg half-angle hyperboloid used in the study by Adams et al. (Ref. 75).

The predicted heat-transfer distribution along the windward streamline of the orbiter model is shown in Fig. 16. Comparison of the perfect gas, seven species and binary oxygen solutions show that when normalized by the stagnation heat-transfer rate, the distributions as predicted by the three solutions were in reasonable agreement.

Calculations have been made for comparison with profile data taken by Carter and Martindale (Ref. 77) in the AEDC/VKF Tunnel B. In Fig. 17, predictions of the pitot pressure profiles are compared with the experimental profiles at four stations along the windward streamline. The agreement between the calculations and the experimental data is good and the predicted location of the shock agrees well with the measured location.

Boudreau (Ref. 79) conducted experiments on another shuttle configuration in the AEDC/VKF Tunnel F. Tunnel F is an arc-driven wind tunnel of the hot-shot type and is capable of providing Mach numbers up to 20. In this experiment, nitrogen was the test gas. Predictions of the stagnation heat transfer, reference enthalpy and stagnation temperature were made using the perfect gas viscous shock-layer program. These predictions are compared with the experimental data of Boudreau in Table I. Differences between the nitrogen gas used in the tunnel and the perfect gas solution may cause the differences between the experiment and the numerical solution. The method could be improved by adding the

capability of an equilibrium nitrogen solution to determine the effect of differences in the gas properties.

CONCLUDING REMARKS

Over the past several years, numerical techniques have been developed to predict two-dimensional and axisymmetric laminar, transitional and/or turbulent boundary-layer flows of perfect gases, binary gas mixtures and air in chemical equilibrium. A complete method has been developed to predict three-dimensional laminar, transitional and/or turbulent boundary-layer flows over sharp or blunt cones at angle of attack in supersonic and hypersonic streams including the effects of surface mass transfer. Methods have also been developed to predict two-dimensional and axisymmetric fully viscous shock-layer flows over analytic and nonanalytic bodies with perfect gas, binary reacting oxygen or multicomponent finite rate chemically reacting gas mixtures. Central to all of these methods is the use of an implicit finite-difference scheme to solve the governing parabolic partial differential equations. Results are presented in this paper which indicate that the method has been successfully used in a variety of practical problems for both internal and external flows. The method is generally second-order accurate in the numerical solutions of the governing partial differential equations. The method is also versatile in its range of applicability as demonstrated by the results contained in this paper.

The applicability and limitations of classical boundary-layer theory are indicated by the results contained herein. The viscous shock-layer approach has many advantages over the classical boundary-layer approach and is recommended as the method to actively pursue for solution of practical flowfield problems. It seems entirely possible and practical that development-type engineering codes can and will be developed using the shock-layer approach to replace many of the currently

used finite-difference methods and even more widely used integral methods for engineering design and research applications.

While computing times have not been emphasized in the present paper, it can be stated that the computing requirements of viscous shock-layer solutions are of the same order as those of two-dimensional or axisymmetric boundary-layer solutions for the same problems. When one considers the complications involved in properly treating the higher-order boundary-layer effects such as displacement and vorticity interactions, it seems natural that a method which treats these effects to second-order accuracy as a fundamental part of the theory should be very attractive, not only to researchers but also to designers in the field of reentry aerodynamics.

REFERENCES

1. Anderson, E. C. and Lewis, C. H., "Laminar or Turbulent Boundary-Layer Flows of Perfect Gases or Reacting Gas Mixtures in Chemical Equilibrium," NASA CR-1893, 1971.
2. Miner, E. W. and Lewis, C. H., "A Finite-Difference Method for Predicting Supersonic Turbulent Boundary-Layer Flows with Tangential Slot Injection," NASA CR-2124, 1972.
3. Frieders, M. C. and Lewis, C. H., "Effects of Mass Transfer into Laminar and Turbulent Boundary Layers Over Cones at Angle of Attack," College of Engineering Report VPI-AERO-031, VPI & SU, Blacksburg, Virginia, March 1975; also AEDC-TR-75-55 to be published, 1975.
4. Inouye, M., Rakich, J., and Lomax, H., "A Description of Numerical Methods and Computer Programs for Two-Dimensional and Axisymmetric Supersonic Flow over Blunt Nosed and Flared Bodies," NASA TN D-2970, August 1965.
5. Rizzi, A. W. and Inouye, M., "A Time-Split Finite-Volume Technique for Three-Dimensional Blunt-Body Flow," AIAA Paper 73-133, January 1973.
6. Kutler, P., Reinhardt, W. A., and Warming, R. F., "Multishocked, Three-Dimensional Supersonic Flowfields with Real Gas Effects," AIAA Journal, Vol. 11, No. 5, May 1973, pp. 657-664.
7. Lewis, Clark H., "First Order Treatment of Higher-Order Boundary-Layer Effects," The Physics of Fluids, Vol. 13, No. 12, December 1970, pp. 2939-2949.
8. Blottner, F. G., "Finite-Difference Methods of Solution of the Boundary-Layer Equations," AIAA Journal, Vol. 8, No. 2, February 1970, pp. 193-206.
9. Miner, E. W. and Lewis, Clark H., "Hypersonic Ionizing Air Viscous Shock-Layer Flows Over Nonanalytic Blunt Bodies," NASA CR-2550, May 1975; also College of Engineering Report VPI-AERO-030, VPI & SU, Blacksburg, Virginia, October 1974.
10. Van Dyke, M., "Second-Order Compressible Boundary-Layer Theory with Application to Blunt Bodies in Hypersonic Flow," Stanford University Report SUDAER No. 112, 1961.
11. Crank, J. and Nicolson, P., "A Practical Method for Numerical Evaluation of Solutions of Partial Differential Equations of the Heat Conduction Type," Proc. Camb. Phil. Soc., Vol. 43, 1947, p. 50.
12. Davis, R. T., "The Hypersonic Fully Viscous Shock Layer Problem," Sandia Laboratories Report SC-RR-68-840, December 1968.

13. Blottner, F. G., "Finite Difference Solution of the First-Order Boundary Layer Equations," Nonreacting and Chemically Reacting Viscous Flows Over a Hyperboloid at Hypersonic Condition, Lewis, C. H., ed., AGARDograph No. 147, NATO, Paris, September 1970, pp. 13-36.
14. Harris, J. E., "Numerical Solution of the Compressible Laminar, Transitional, and Turbulent Boundary Layer Equations," PhD Dissertation, VPI & SU, Blacksburg, Virginia, 1970.
15. Lordi, J. A., Mates, R. E., and Moselle, J. R., "Computer Program for the Numerical Solution of Nonequilibrium Expansions of Reacting Gas Mixtures," Cornell Aeronautical Laboratory, Inc., CAL Report No. AD-1689-A-6, October 1965.
16. Jaffe, N. A., Lind, R. C., and Smith, A. M. O., "Solution to the Binary Diffusion Laminar Boundary Layer Equations Including the Effect of Second Order Transverse Curvature," Report LB 32613, January 1966, Douglas Aircraft Company.
17. Klebanoff, P. S., "Characteristics of Turbulence in a Boundary Layer with Zero Pressure Gradient," NASA TN-3178, 1954.
18. Van Driest, E. R., "On Turbulent Flow Near a Wall," J. A. S., Vol. 23, No. 11, November 1956, pp. 1007-1011, 1036.
19. Reichardt, H., "Vollständige Darstellung der Turbulenten Geschwindigkeitsverteilung in glatten Lutungen," ZAMM 31, 1951, pp. 208-219.
20. Beckwith, I. E. and Bushnell, D. M., "Calculation by a Finite-Difference Method of Supersonic Turbulent Boundary Layers with Tangential Slot Injection," NASA TN D-6221, 1971.
21. Boldman, D. R., Newmann, H. E., and Schmidt, J. F., "Heat Transfer in 30° and 60° Half-Angle of Convergence Nozzles with Various Diameter Uncooled Pipe Inlets," NASA TN D-4177, 1967.
22. Elliott, D. G., Bartz, D. R., and Silver, S., "Calculation of Turbulent Boundary Layer Growth and Heat Transfer in Axisymmetric Nozzles," JPL TR-32-387, 1963.
23. Lewis, C. H. ed. (1970): Nonreacting and Chemically Reacting Viscous Flows Over a Hyperboloid at Hypersonic Condition, AGARDograph No. 147, NATO, Paris, September 1970, pp. 37-54.
24. Adams, J. C. , "Higher Order Boundary-Layer Effects for the AGARD Engineering Applications Body and Flow Conditions," Nonreacting and Chemically Reacting Viscous Flows Over a Hyperboloid at Hypersonic Condition. Lewis, C. H. ed., AGARDograph No. 147, NATO, Paris, September 1970, pp. 121-134.

10th Navy Symposium on Aeroballistics

Vol. 3

25. Keltner, G. L. and Smith, A. M. O., "Laminar Boundary-Layer Calculations on Bodies of Revolution in Hypersonic Flow," Nonreacting and Chemically Reacting Viscous Flows Over a Hyperboloid at Hypersonic Condition, Lewis, C. H. ed., AGARDograph No. 147, NATO, Paris, September 1970, pp. 121-134.
26. Danberg, J. E., "Characteristics of the Turbulent Boundary Layer with Heat Transfer: Data Tabulation," NOLTR 67-6, January 1967.
27. Cary, Aubrey M., Jr. and Hefner, Jerry N., "Film Cooling Effectiveness in Hypersonic Turbulent Flow," AIAA Journal, Vol. 8, No. 11, November 1970, pp. 2090-2091.
28. Kenworthy, M. A. and Schetz, J. A., "An Experimental Study of Slot Injection into a Supersonic Stream," NASA CR-2128, January 1973.
29. Cary, A. M., Jr. and Hefner, J. N., "An Investigation of Film-Cooling Effectiveness and Skin Friction in Hypersonic Turbulent Flow," AIAA Paper No. 71-599, June 1971.
30. Vaglio-Laurin, R., "Turbulent Heat Transfer on Blunt Nosed Bodies in Two-Dimensional Flow," J. Aero. Sci., Vol. 27, No. 1, pp. 27-36, January 1960.
31. Braun, W. H., "Turbulent Boundary Layer on a Yawed Cone in a Supersonic Stream," NASA TR R-7, 1959.
32. Moore, F. K., "Three-Dimensional Boundary-Layer Theory," Advances in Applied Mechanics, Vol. 4, pp. 160-228, 1956.
33. McGowan, J. J. and Davis, R. T., "Development of a Numerical Method to Solve the Three-Dimensional, Compressible, Laminar Boundary-Layer Equations with Application to Elliptical Cones at Angle of Attack," Aerospace Research Laboratories, ARL 70-0341, Wright-Patterson AFB, December 1970.
34. Adams, J. C., Jr., "Analysis of the Three-Dimensional Compressible Turbulent Boundary Layer on a Sharp Cone at Incidence in Supersonic and Hypersonic Flow," AEDC-TR-72-66, June 1972.
35. Dwyer, H. A., "Boundary Layer on a Hypersonic Sharp Cone at Small Angle of Attack," AIAA Journal, Vol. 9, No. 2, pp. 277-284, February 1971.
36. Frieders, M. C. and Lewis, C. H., "Boundary-Layer Flows Over Sharp and Spherically Blunted Cones at Angle of Attack to Supersonic Nonuniform Free Streams," Aerospace Research Laboratories, ARL 73-0123, August 1973.
37. Mayne, A. W., "Calculation of the Boundary-Layer Flow in the Windward Symmetry Plane of a Spherically Blunted Axisymmetric Body at Angle of Attack, Including Streamline-Swallowing Effects," AEDC-TR-73-166, October 1973.

38. Lewis, C. H., Adams, J. C., and Gilley, G. E., "Effects of Mass Transfer and Chemical Nonequilibrium on Slender Blunted Cone Pressure and Heat Transfer Distributions at $M_\infty = 13.2$," AEDC-TR-68-214, December 1968.
39. Mayne, A. W., Gilley, G. E., and Lewis, C. H., "Binary Boundary Layers on Sharp Cones in Low Density Supersonic and Hypersonic Flow," AEDC-TR-68-275, February 1969.
40. Miner, E. W., Anderson, E. C., and Lewis, C. H., "A Computer Program for Two-Dimensional and Axisymmetric Nonreacting Perfect Gas and Equilibrium Chemically Reacting Laminar, Transitional and/or Turbulent Boundary-Layer Flows," VPI Engr. Report E-71-8, VPI & SU, 1971.
41. Adams, J. C., "Implicit Finite-Difference Analysis of Compressible Laminar, Transitional, and Turbulent Boundary Layers along the Windward Streamline of a Sharp Cone at Incidence," AEDC-TR-71-235, December 1971.
42. Watkins, C. B., "Numerical Solution of the Three-Dimensional Boundary Layer on a Spinning Sharp Body at Angle of Attack," Symposium on the Application of Computers to Fluid Dynamics Analysis and Design, Farmingdale, N. Y., January 3-4, 1973.
43. Moore, F. K., "Laminar Boundary Layer on a Cone in Supersonic Flow at Large Angle of Attack," NACA TN 2844, November 1952.
44. Blottner, F. G. and Ellis, M., "Three-Dimensional Incompressible Boundary Layer on Blunt Bodies," Sandia Laboratories Research Report SLA-73-0366, Albuquerque, N. M., April 1973.
45. Krause, E., "Comment on 'Solution of a Three-Dimensional Boundary-Layer Flow with Separation'," AIAA Journal, Vol. 7, No. 3, March 1969.
46. Hunt, J. L., Bushnell, J. M., and Beckwith, I. E., "Finite Difference Analysis of the Compressible Turbulent Boundary Layer on a Blunt Swept Slab with Leading Edge Blowing," NASA TN D-6203, March 1971.
47. Patankar, S. V. and Spalding, D. B., Heat and Mass Transfer in Boundary Layers, CRC Press, Cleveland, Ohio, 1968.
48. Cebeci, T., "Behavior of Turbulent Flow Near a Porous Wall with Pressure Gradient," AIAA Journal, Vol. 8, No. 12, December 1970.
49. Dhawan, S. and Narasimha, R., "Some Properties of Boundary Layer Flow during the Transition from Laminar to Turbulent Motion," J. Fluid Mech., Vol. 3, No. 4, April 1958, pp. 418-426.
50. Rotta, J. C., "Temperaturverteilungen in der Turbulenten Grenzschicht and der Ebenen Platte," Int. Journal of Heat Transfer, Vol. 7, 1964, pp. 215-228.

10th Navy Symposium on Aeroballistics

Vol. 3

51. Shang, J. S., "A Parametric Study of Hypersonic Turbulent Boundary Layers with Heat Transfer," Aerospace Research Laboratories, ARL TR 74-0003, Wright-Patterson AFB, January 1974.
52. Simpson, R. L., Whitten, D. G., and Moffat, R. J., "An Experimental Study of the Turbulent Prandtl Number of Air with Injection and Suction," Int. Journal of Heat Transfer, Vol. 13, 1970, pp. 125-143.
53. Meier, H. U., Voisinnet, R. L. P., and Gates, D. F., "Temperature Distributions using the Law of the Wall for Compressible Flow with Variable Turbulent Prandtl Number," AIAA Paper No. 74-596, June 1974.
54. Cebeci, T., "A Model for Eddy Conductivity and Turbulent Prandtl Number," J. of Heat Transfer, May 1973, pp. 227-234.
55. Wilke, C. R., "A Viscosity Equation for Gas Mixtures," J. Chem. Physics, Vol. 18, No. 4, April 1950, pp. 517-519.
56. Eucken, A., Physik Z., Vol. 14, 1913, pp. 324-332.
57. Richtmyer, R. D., Difference Methods for Initial-Value Problems, Interscience Publishers Inc., N. Y., 1957.
58. Cebeci, T., Smith, A. M. O., and Mosinskis, G., "Calculation of Compressible Adiabatic Turbulent Boundary Layers," AIAA Paper No. 69-687, June 1969.
59. Cebeci, T. and Mosinskis, G., "Prediction of Turbulent Boundary Layers with Mass Addition, Including Highly Accelerating Flows," ASME Paper No. 70-HT/SpT-19, June 1970.
60. Moore, F. K., "Displacement Effect of Three-Dimensional Boundary Layer," NACA TN 2722, June 1952.
61. Cleary, J. W., "Effects of Angle of Attack and Bluntness on Laminar Heating Rate Distributions of a 15° Cone at a Mach Number of 10.6," NASA TN D-5450, Ames Research Center, Moffett Field, California, 1969.
62. Davis, R. T., "Numerical Solution of the Hypersonic Viscous Shock-Layer Equations," AIAA Journal, Vol. 8, No. 5, May 1970, pp. 843-851.
63. Davis, R. T., "Hypersonic Flow of a Chemically Reacting Binary Mixture Past a Blunt Body," AIAA Paper No. 70-805, July 1970.
64. Moss, J. N., "Solutions for Reacting and Nonreacting Viscous Shock Layers with Multicomponent Diffusion and Mass Injection," PhD Dissertation, VPI & SU, Blacksburg, Virginia, October 1971.

65. Bird, R. B., Stewart, W. E., and Lightfoot, E. N., Transport Phenomena, John Wiley and Sons, Inc., 1950.
66. Brown, W. G., "Thermodynamic Properties of Some Atoms and Atomic Ions," MSD Engineering Physics TM2, General Electric Co., Philadelphia, PA.
67. Brown, W. G., "Thermodynamic Properties of Some Diatomic and Linear Polyatomic Molecules, MSD Engineering Physics TM3, General Electric Co., Philadelphia, PA.
68. Brown, W. G., "Thermodynamic Properties of Some Diatoms and Diatomic Ions at High Temperature," MSD Advanced Aerospace Physics TM8, General Electric Co., Philadelphia, PA, May 1962.
69. Blottner, F. G., "Non-Equilibrium Laminar Boundary Layer Flow of Ionized Air," General Electric Report R64SD56, November 1964.
70. Pappas, C. C. and Lee, G., "Heat Transfer and Pressure on a Hypersonic Blunt Cone with Mass Addition," AIAA Journal, Vol. 8, No. 5, May 1970, pp. 954-956.
71. Kang, S.-W. and Dunn, M. G., "Hypersonic Viscous Shock Layer with Chemical Nonequilibrium for Spherically Blunted Cones," AIAA Journal, Vol. 10, No. 10, October 1972, pp. 1361-1362.
72. Miner, E. W. and Lewis, C. H., "Hypersonic Ionizing Air Viscous Shock-Layer Flows Over Sphere Cones," AIAA Journal, Vol. 13, No. 1, January 1975, pp. 80-88.
73. Kang, S.-W. and Dunn, M. G., "Comment on 'Hypersonic Ionizing Air Viscous Shock-Layer Flows over Sphere Cones'," AIAA Journal Vol. 13, No. 1, January 1975, pp. 118-121.
74. Miner, E. W. and Lewis, C. H., "Reply by Authors to S.-W. Kang and M. G. Dunn," AIAA Journal, Vol. 13, No. 1, January 1975, pp. 121-125.
75. Adams, J. C., Jr., Martindale, W. R., Mayne, A. W., Jr., and Marchand, E. V., "Real Gas Scale Effects on Laminar Boundary-Layer Parameters Including Effects of Entropy-Layer Swallowing," AEDC-DR-74-59, 1974.
76. Martindale, W. R., "Test Results from the NASA/Rockwell International Space Shuttle Test (OH4B) Conducted in the AEDC/VKF Tunnel B," AEDC-DR-74-8, January 1974.
77. Carter, L. D. and Martindale, W. R., "Test Results from the NASA/Rockwell International Space Shuttle Test (OH9) Conducted in the AEDC/VKF Tunnel B," AEDC-DR-74-9, January 1974.

10th Navy Symposium on Aeroballistics

Vol. 3

78. Murray, A. L., Lewis, C. H., and Miner, E. W., "Viscous Shock-Layer Predictions for the Windward Streamline of a Shuttle Orbiter at 30-deg Angle of Attack," College of Engineering Report VPI-AERO-Q35, VPI & SU, Blacksburg, Virginia, May 1975; also NASA CR to be published.
79. Boudreau, A. H., "Test Results From the NASA/RI Shuttle Heating Test OH-11 in the AEDC-VKF Tunnel F," AEDC-DR-74-16, February 1974.

TABLE I
 COMPARISON OF AEDC TUNNEL F EXPERIMENT AND
 VPI PERFECT GAS VISCOUS SHOCK LAYER SOLUTION

Conditions	Q_0 (EXP) BTU/FT ² -SEC	Q_0 (VSHL) BTU/FT ² -SEC	H_{ref} (EXP) BTU/FT ² -SEC-°R	H_{ref} (VSHL) BTU/FT ² -SEC-°R	T_0 (EXP) °R	T_0 (VSHL) °R
$\alpha = 25^\circ$ $M_\infty = 11.18$ $T_\infty = 155.4^\circ R$ $P_\infty = 0.0214$ psia	131.1	122.6	0.0426	0.0350	3618	4040.2
$\alpha = 30^\circ$ $M_\infty = 10.74$ $T_\infty = 90.8^\circ R$ $P_\infty = 0.0654$ psia	94.3	91.4	0.0639	0.0556	2016	2185.5
$\alpha = 35^\circ$ $M_\infty = 11.15$ $T_\infty = 148.9^\circ R$ $P_\infty = 0.0196$ psia	117.9	111.9	0.0403	0.0338	3465	3851.2
$\alpha = 35^\circ$ $M_\infty = 14.10$ $T_\infty = 90.2^\circ R$ $P_\infty = 0.0182$ psia	133.7	126.2	0.0493	0.0402	3250	3676.7
$\alpha = 45^\circ$ $M_\infty = 11.42$ $T_\infty = 123.3^\circ R$ $P_\infty = 0.0481$ psia	155.1	137.8	0.0626	0.0492	3016	3339.4

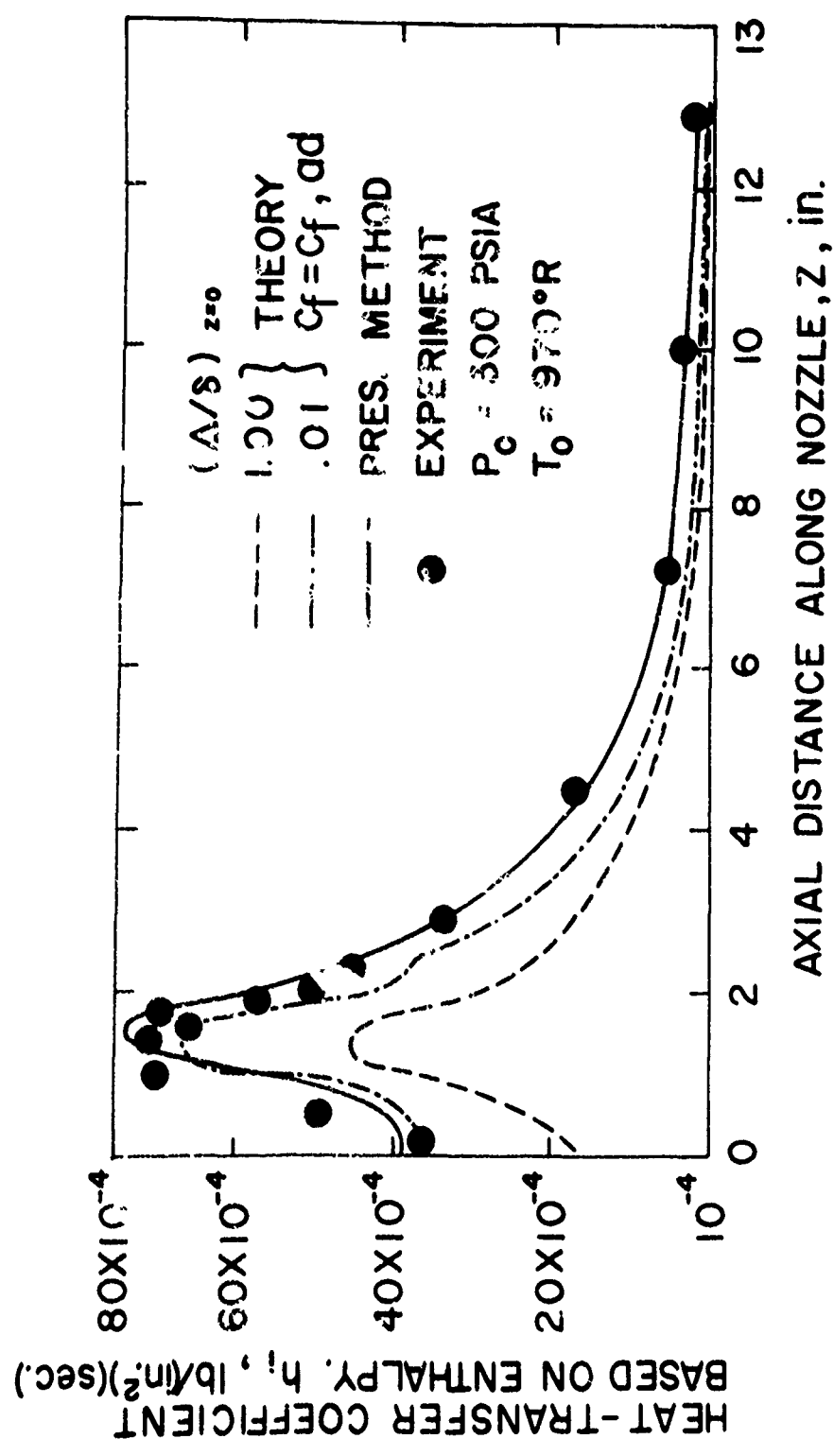


Figure 1: Heat-Transfer Distribution for the NASA-Lewis Nozzle

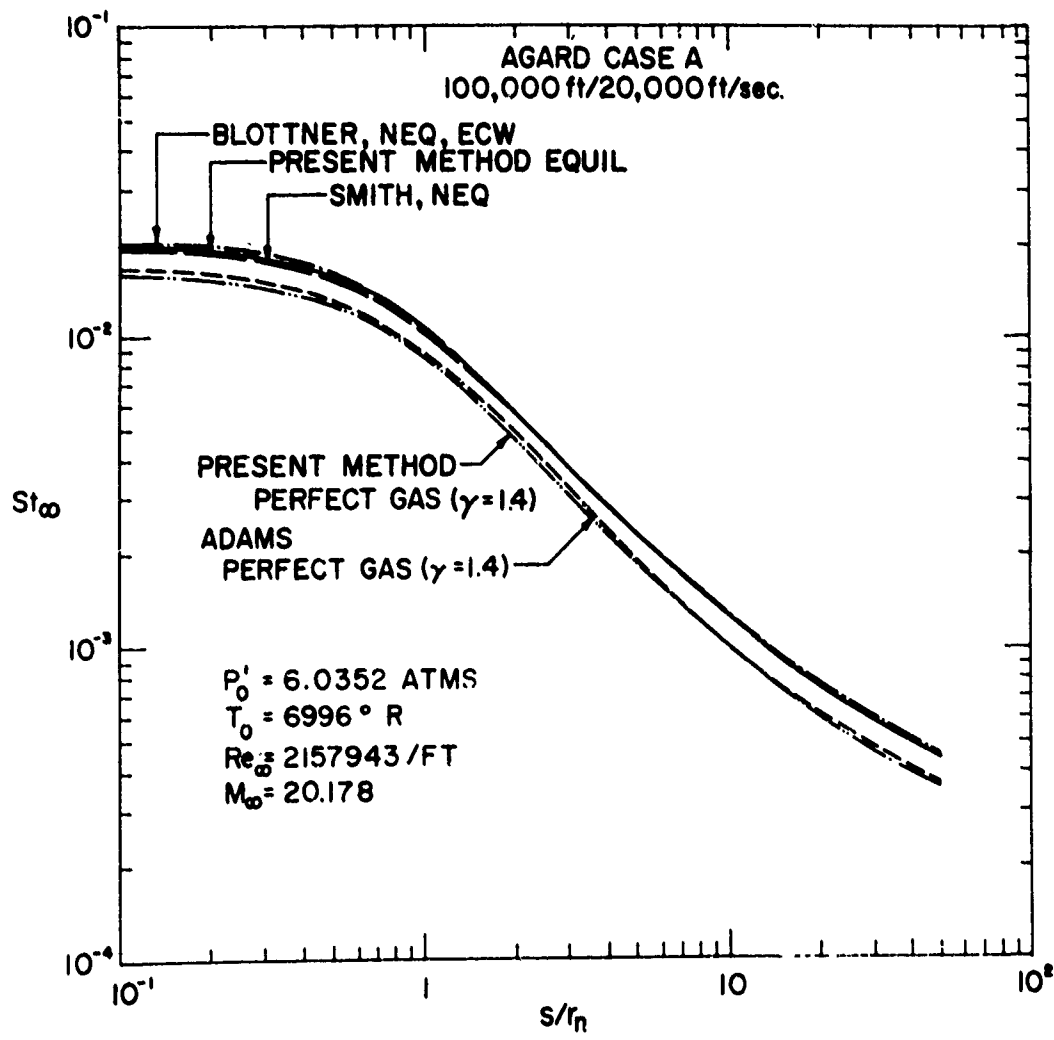


Figure 2: Stanton Number Distribution for a 10° Half-Angle Hyperboloid AGARD Case A

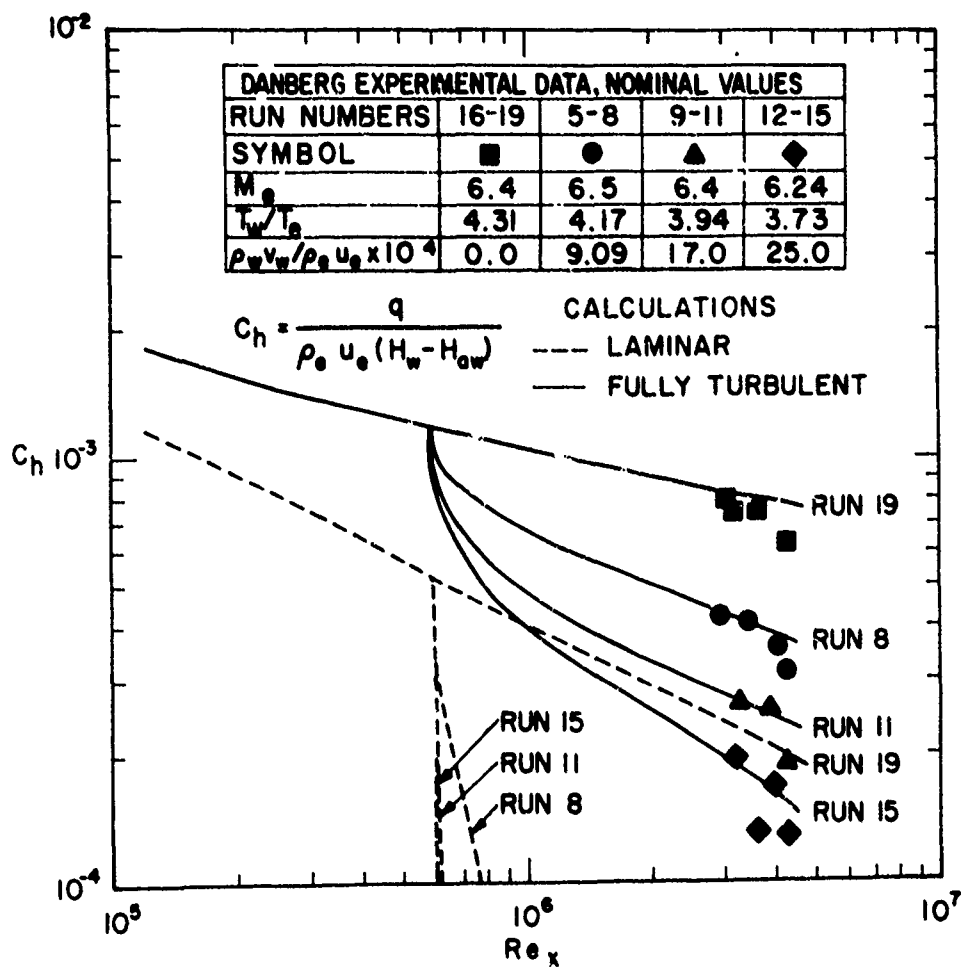


Figure 3: Stanton Number Distribution for a Flat Plate with Mass Injection
 Danberg's Data

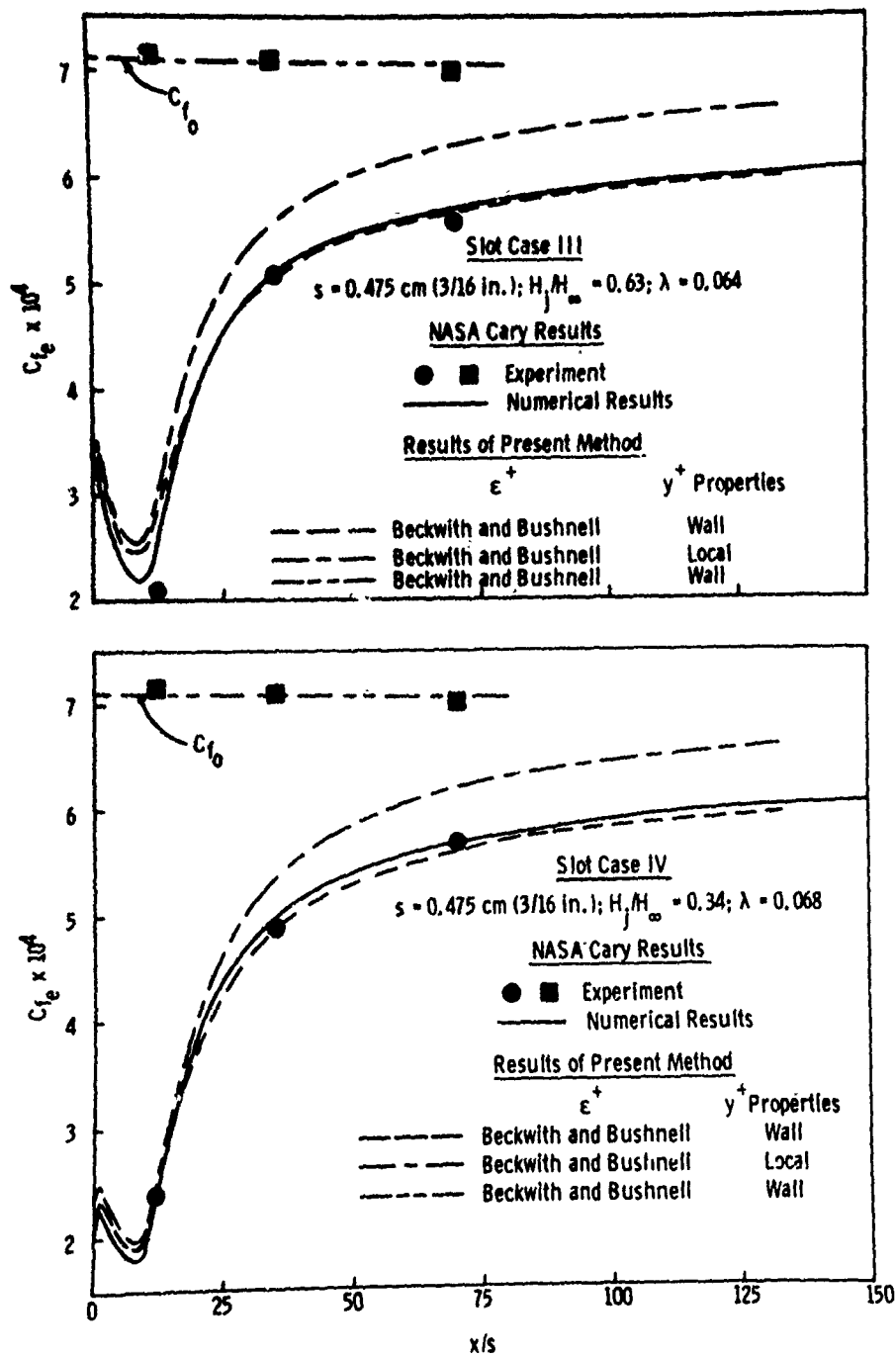


Figure 4: Skin-Friction Distributions with Slot Injection, NASA Cary Conditions

● VPI Experiment of Kenworthy and Schetz
 — Results of Present Method with Beckwith and Bushnell ϵ

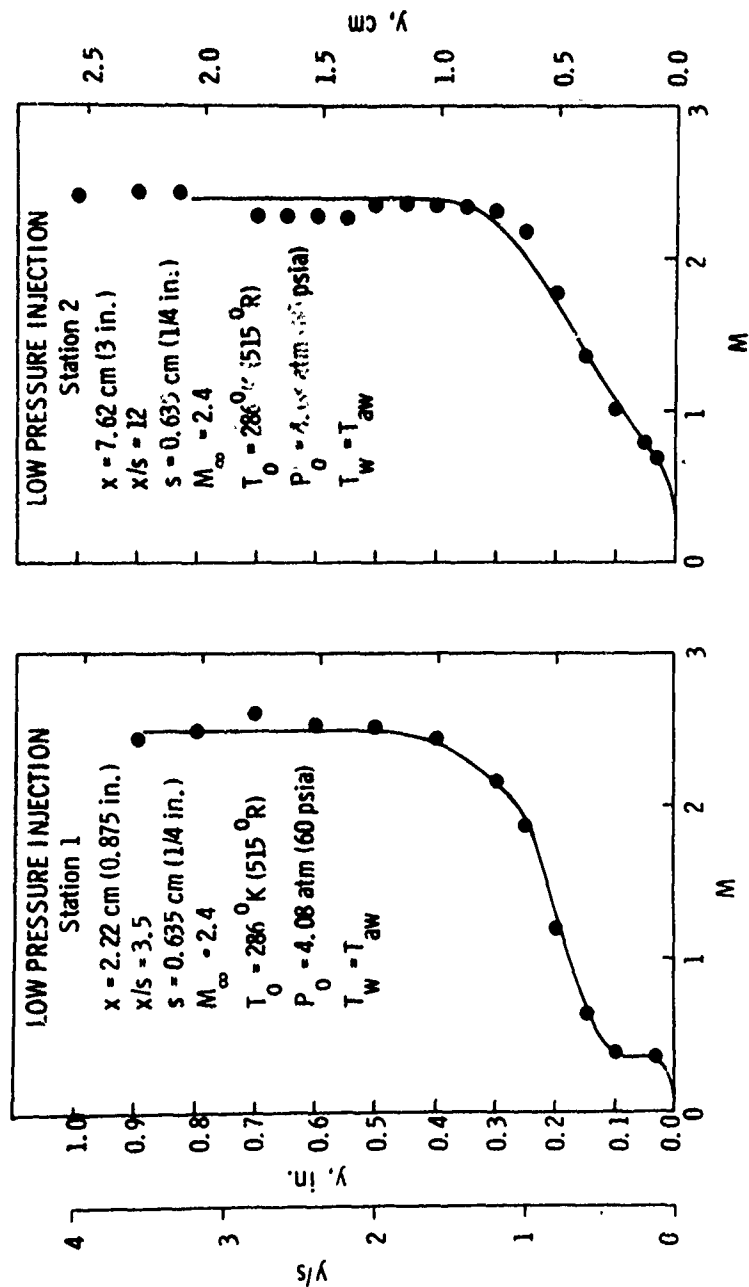


Figure 5: Comparison of Mach Number Profiles, Low Pressure Injection, VPI Conditions

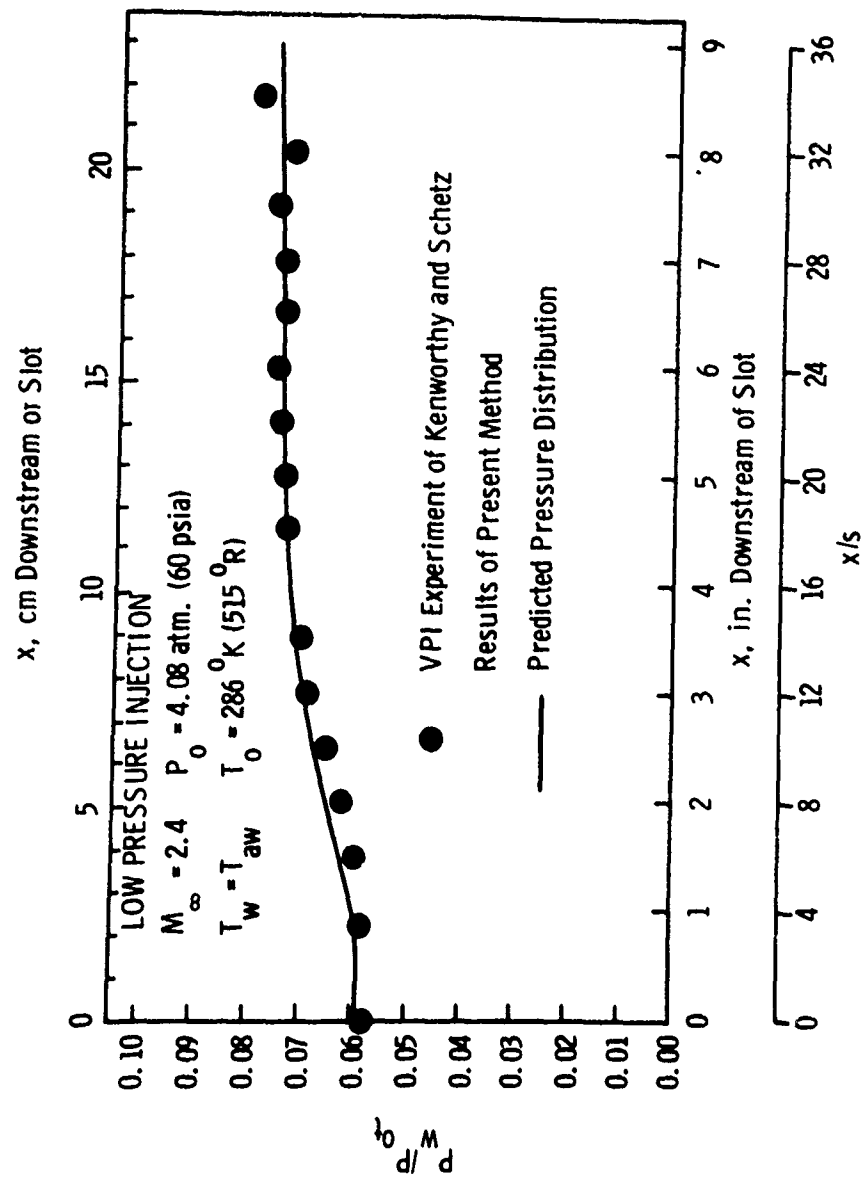


Figure 6: Comparison of Experimental and Predicted Wall Static Pressure Distributions, VPI Conditions

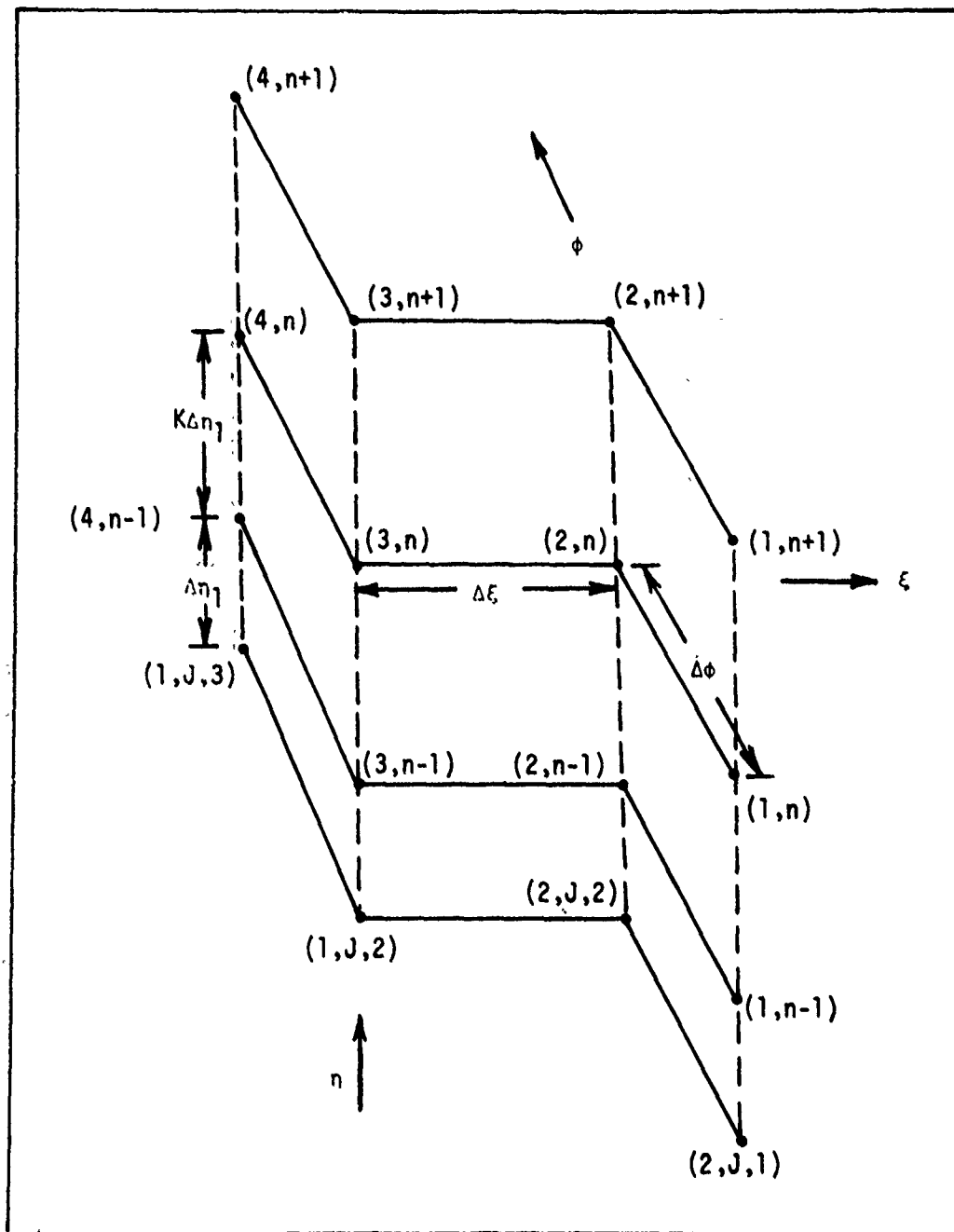


Figure 7: Finite-Difference Grid and Notation
 Bottom grid shows notation used in the computer program

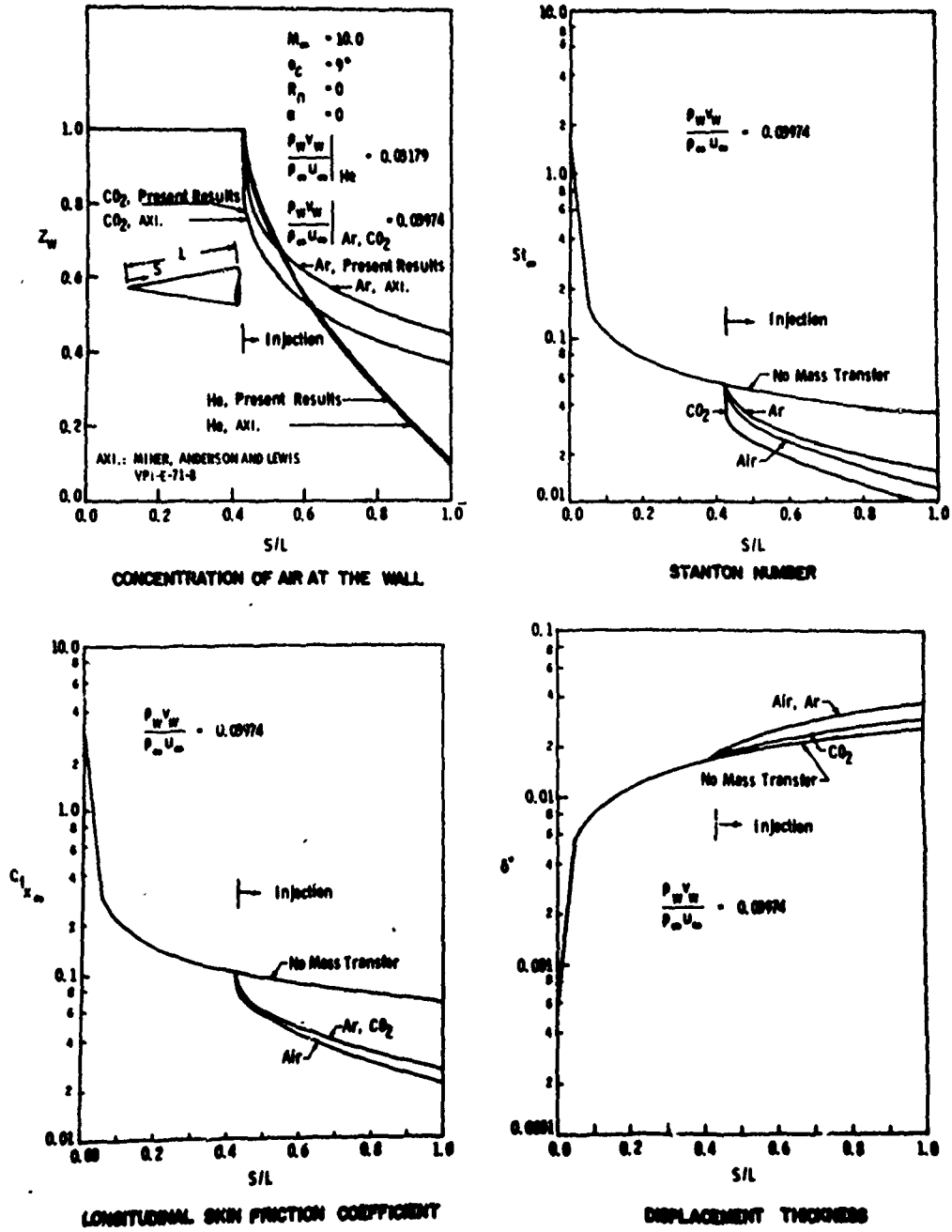


Figure 9: Comparison of Present Results with Previous Numerical Data Mass Transfer Over a Sharp Cone at Zero Angle of Attack

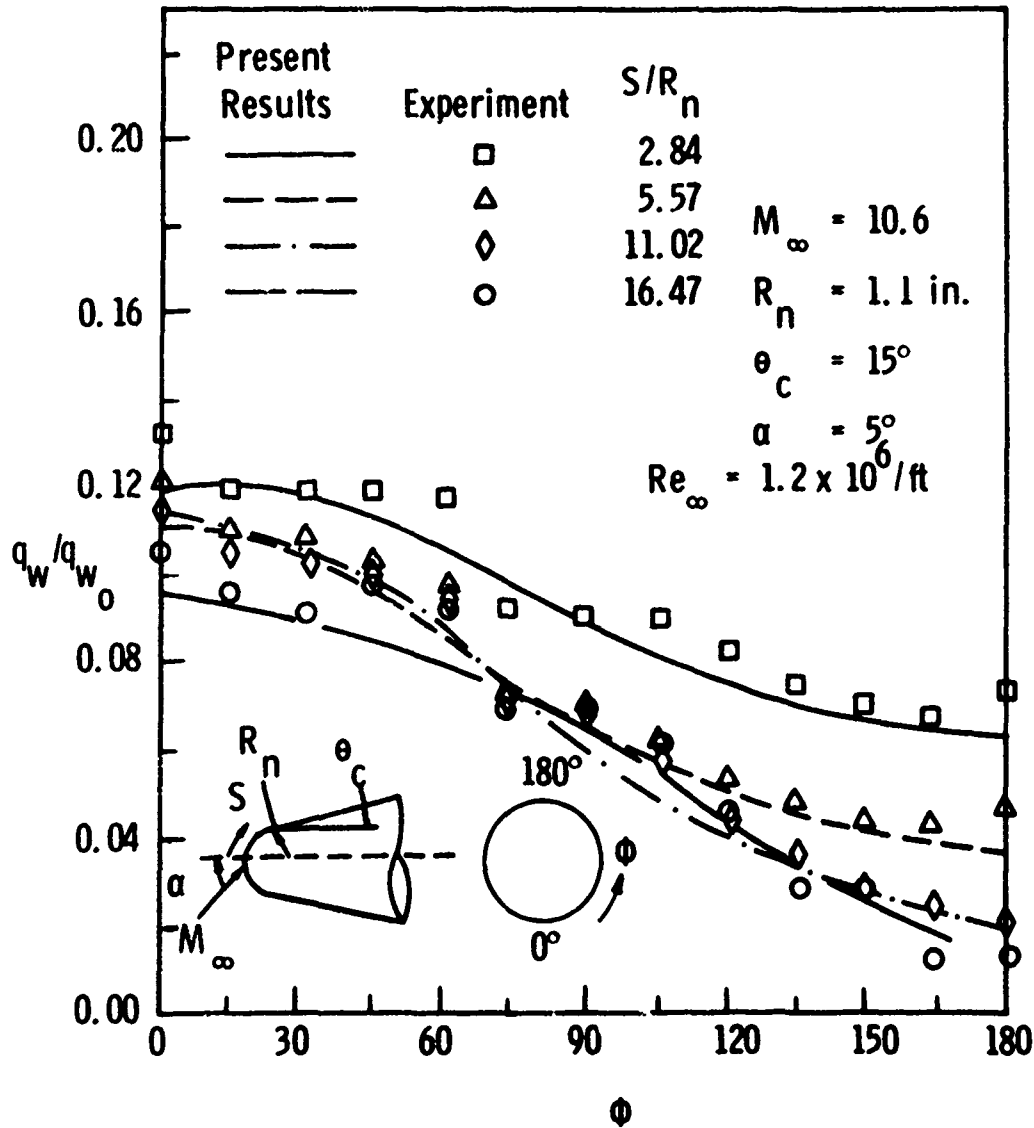


Figure 10: Wall Heat-Transfer Rate over a Blunt Cone at Angle of Attack; Present Results versus Experiment of Cleary

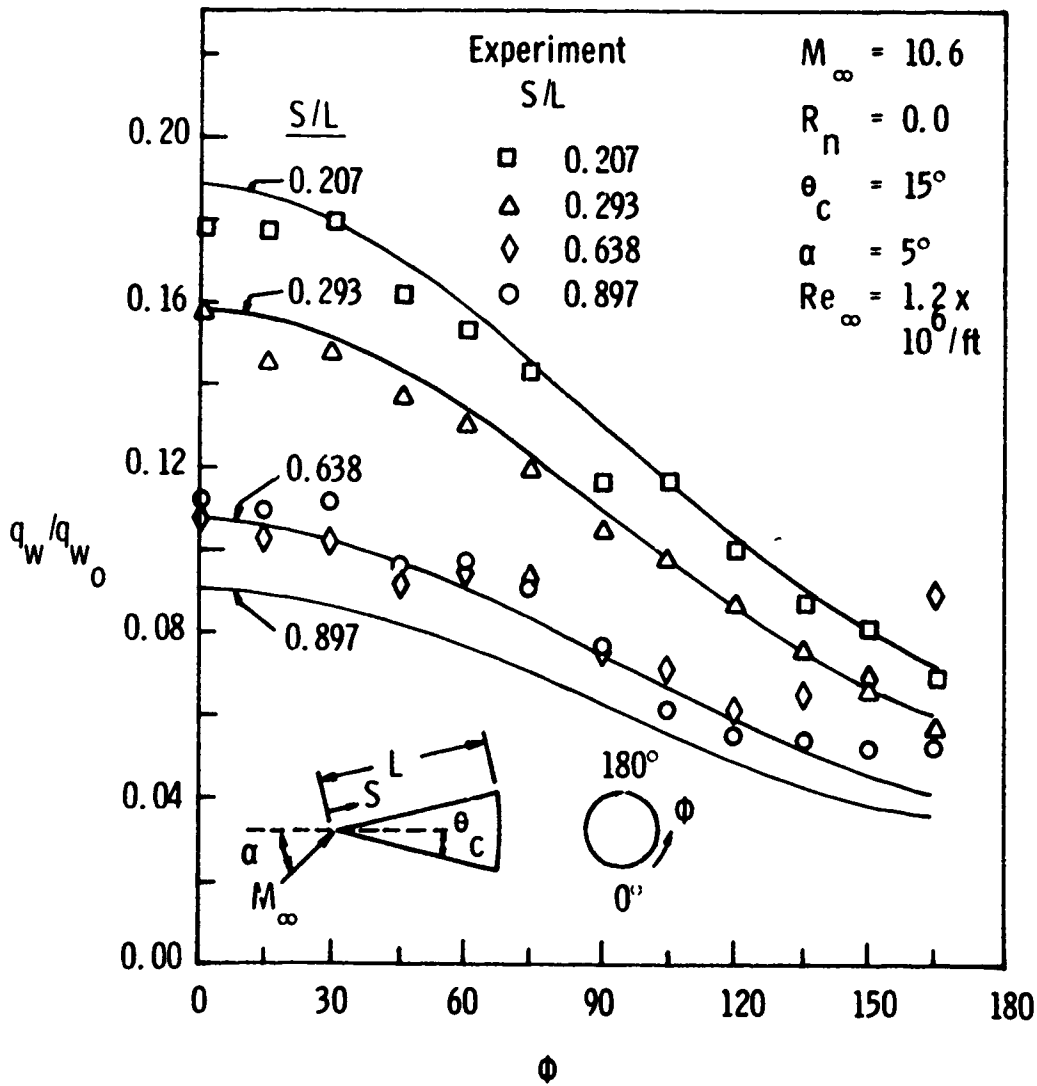
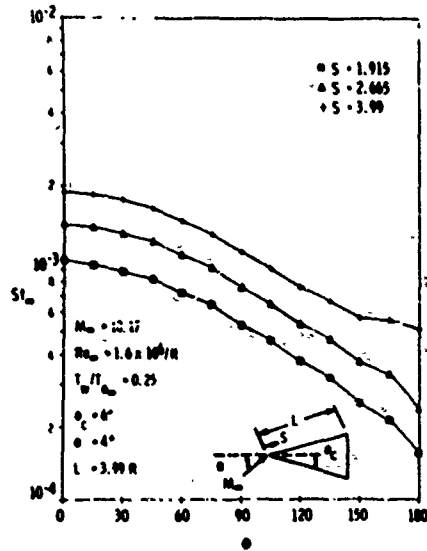
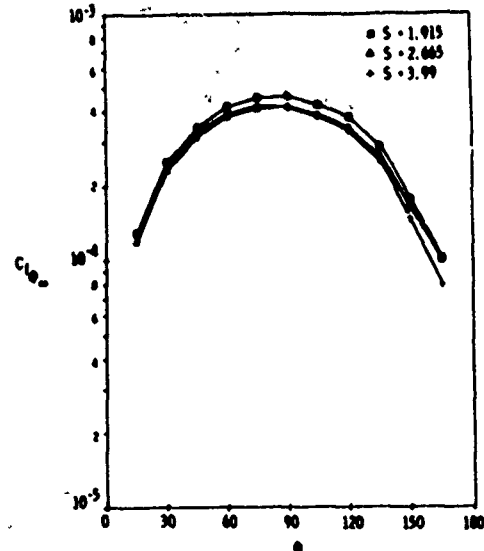


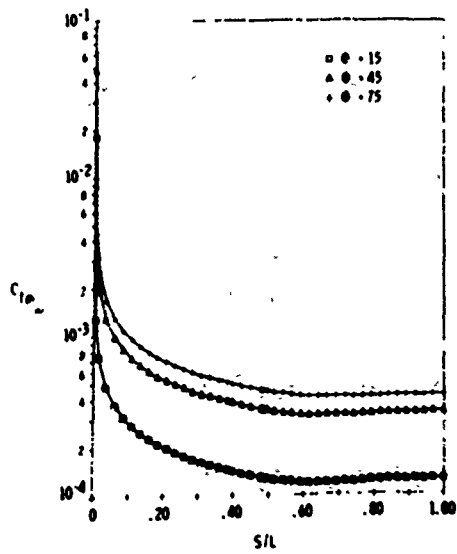
Figure 11: Wall Heat-Transfer Rate over a Sharp Cone at Angle of Attack; Present Results versus Experiment of Cleary



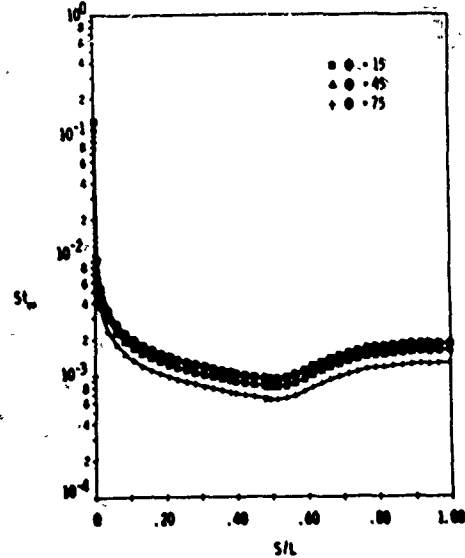
TRANSVERSE VARIATION OF THE STANTON NUMBER



TRANSVERSE SKIN FRICTION COEFFICIENT



LONGITUDINAL VARIATION OF THE TRANSVERSE SKIN FRICTION COEFFICIENT



LONGITUDINAL VARIATION OF THE STANTON NUMBER

Figure 12: Three-Dimensional Solution of a Sharp Cone at Angle of Attack with Transition; Program Generated Plots

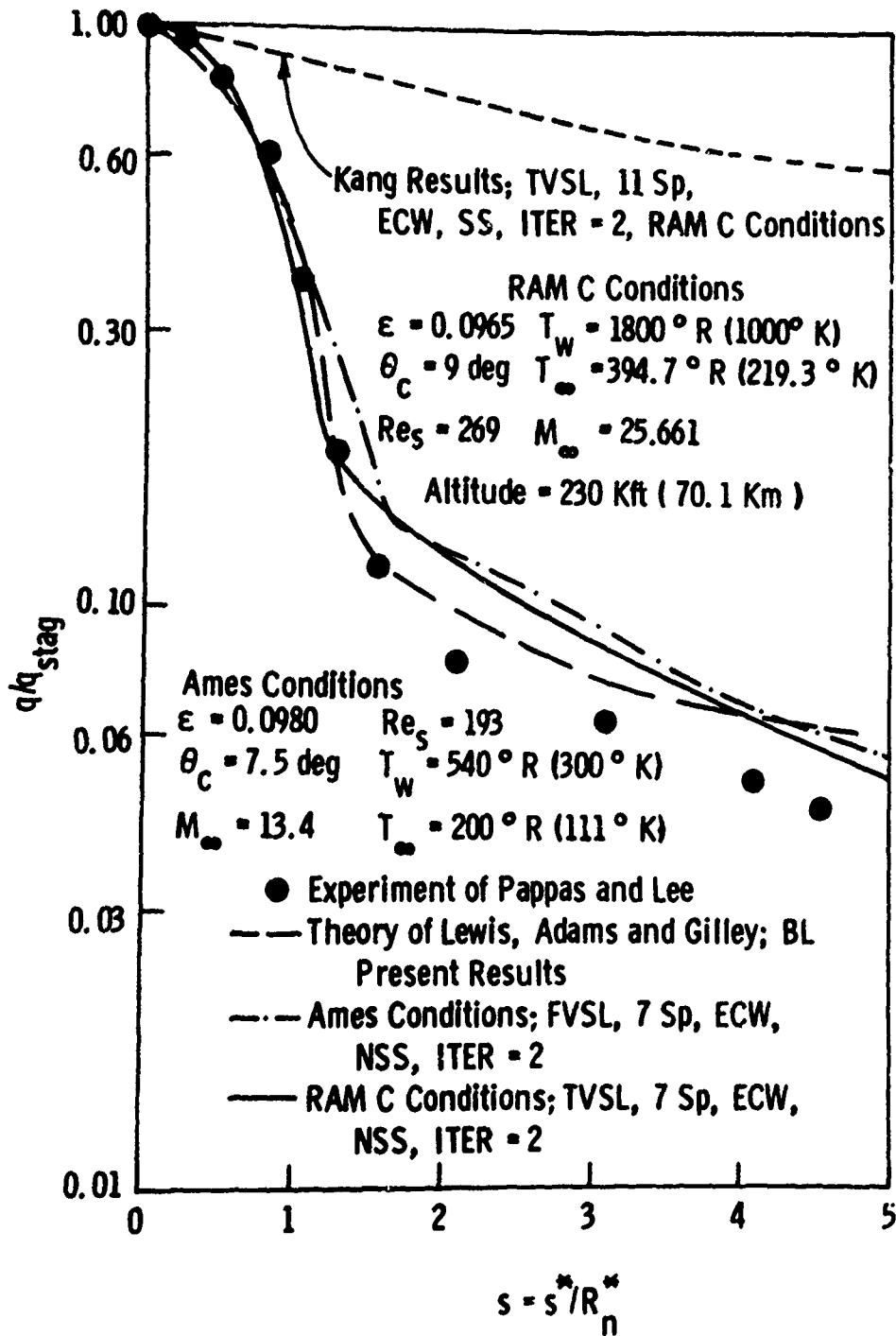


Figure 13: Normalized Heat-Transfer Distributions for 7.5° Sphere-Cone, Ames Conditions

● Experimental Data, AEDC/VKF Tunnel B,
139 Orbiter, $\alpha = 30$ deg, OH9 Test

----- Inouye, M., Rakich, J. V., Lomax, H. and
Aungier, R. H. Results, AEDC Inviscid
Calculation, 31-deg Hyperboloid

Present Results

———— Perf, FVSL, ITER = 3

----- Perf, TVSL, ITER = 1

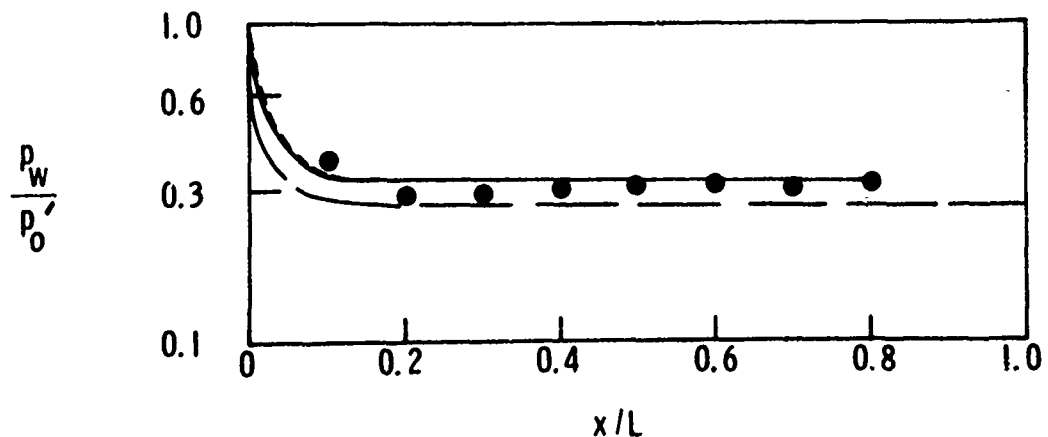


Figure 14: Surface Pressure Distribution at AEDC Conditions

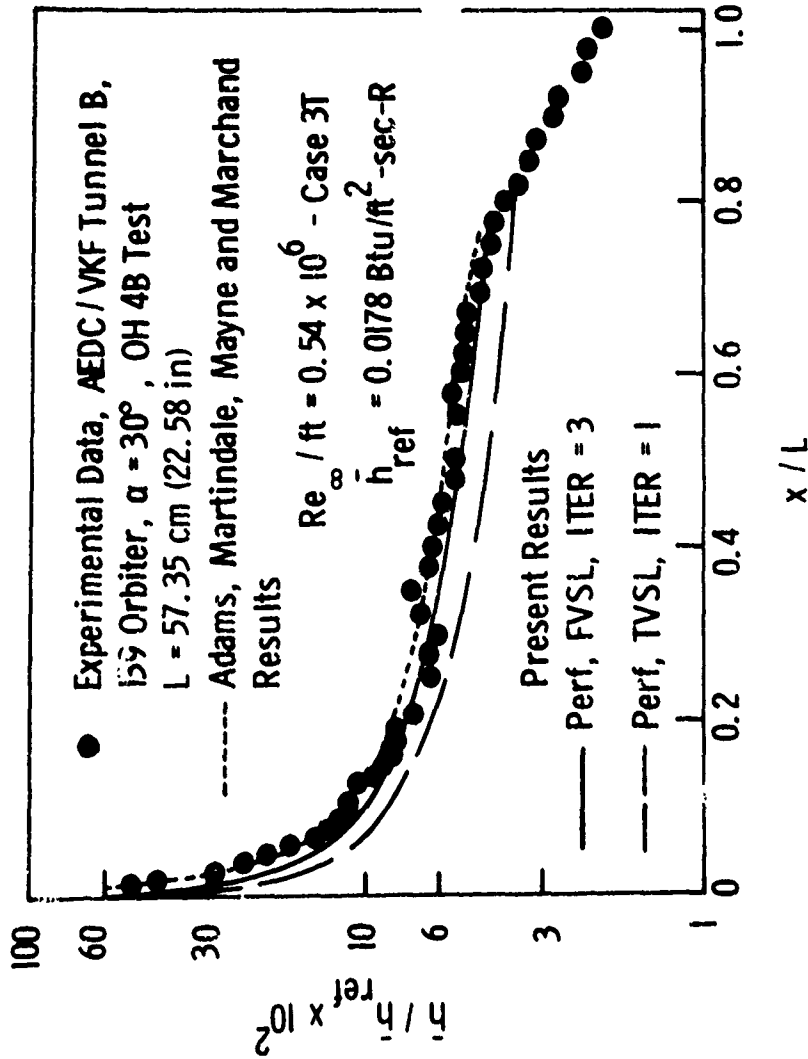


Figure 15: Heat-Transfer Distributions Predicted by the VPI Perfect Gas Shock Layer Theory and AEDC Boundary Layer with Entropy Layer Swallowing Compared with Experimental Data

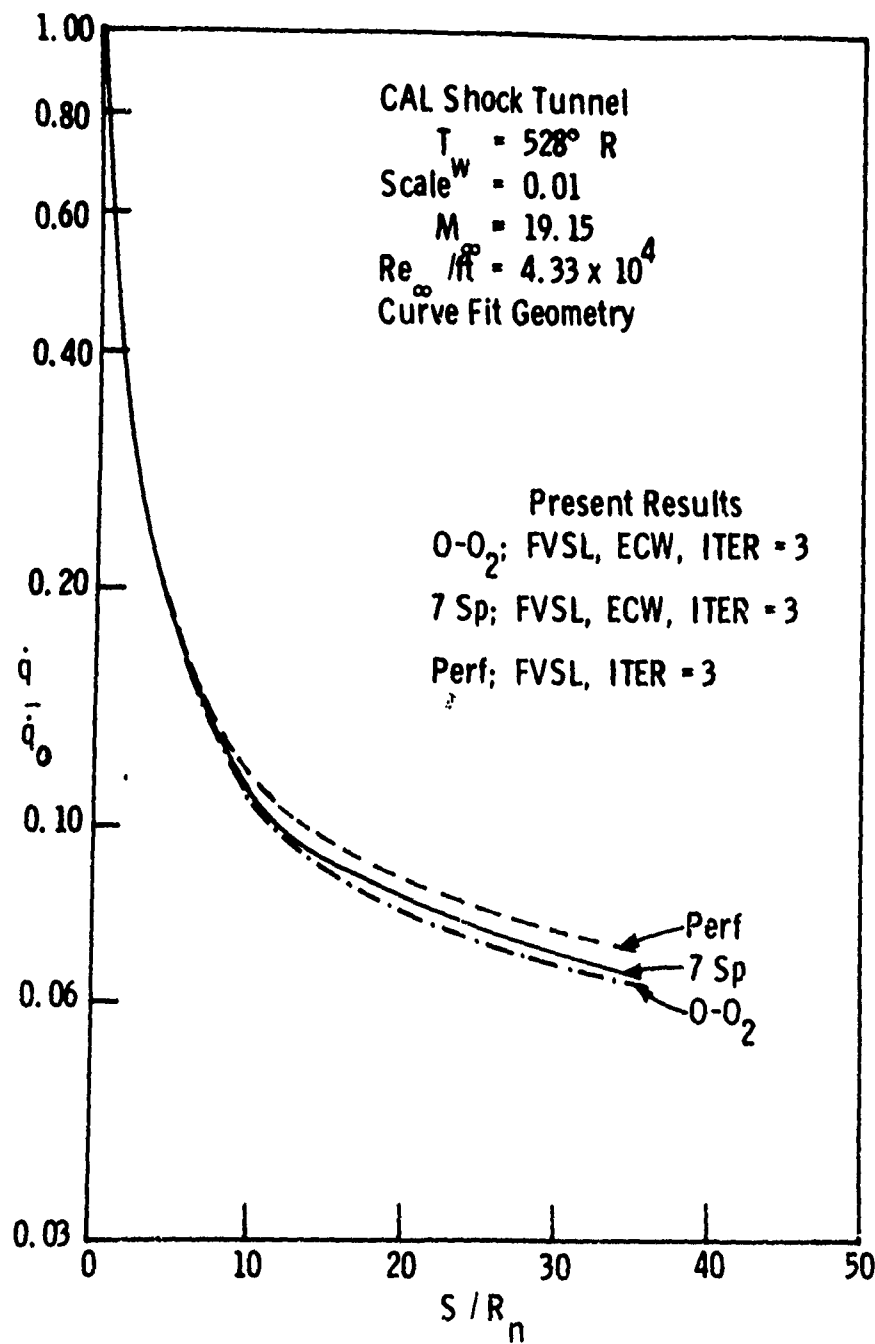


Figure 16: Normalized Heat-Transfer Distributions along the Windward Streamline of a 0.01 Scale Model of the Shuttle Orbiter at CAL Shock Tunnel Conditions

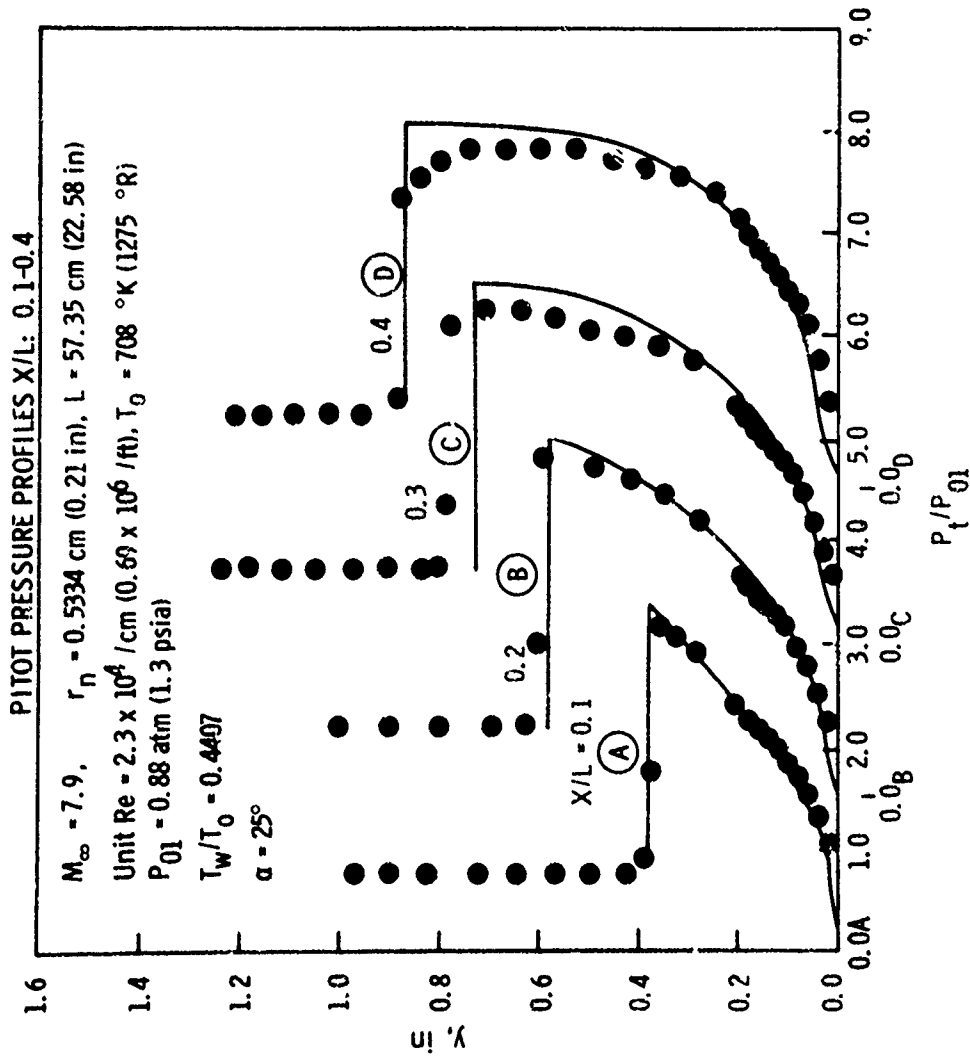


Figure 17: Comparison of Pitot Pressure Profiles Predicted by the VPI Perfect Gas Shock-Layer Theory and AEDC Experimental Data

PAPER NO. 33

SURVEY OF THREE DIMENSIONAL FLOW FIELDS
IN THE PRESENCE OF WINGS AT $M = 2.48$

by

George S. Pick and Richard M. Hartley
Naval Ship Research and Development Center (NSRDC)
Bethesda, Maryland 20084

(Paper UNCLASSIFIED)

ABSTRACT

In order to obtain detailed information about the flow field behind movable wing control surfaces a survey investigation was conducted, involving parametric models of the Generic Ordnance Ramjet Engine (GORJE) vehicle. The objective of the investigation was to determine the effects of wing planform, thickness ratio and deflection angle on total and static pressure and local Mach number distributions at possible locations for inlet installations. In all phases the free stream wind tunnel conditions were identical at $M = 2.48$ and at unit Reynolds number of about $3.05 \times 10^6/\text{ft}$.

The first phase of the investigation involved a sting mounted 1/10 scale model. The survey indicated that an interdigitated inlet location is preferable on the basis of flow field total pressure recovery in both "+" and "x" wing orientations for angles of attack to ± 4 deg and for wing deflections less than about ± 6 deg.

A rather complex flow field was revealed in the second phase of the investigation which involved a wall mounted model. There was an interaction between the incipient conical body shock wave and the wing wake. It was found that the wing wake was narrow at $\delta = 0$ deg without much tendency to spread in width, but the pressure recovery levels varied both streamwise and spanwise. The wake structure showed several pressure defect cells whose location and number varied from wing to wing. In general the energy losses for the thinner wing were smaller than those of the thick wing. However, the inlet losses were greater for the thinner wing at $\delta = 0, 5$ deg, where the center of an inboard low pressure recovery (or pressure defect) cell coincided with the inlet location. The

pressure recovery for all wings improved with wing deflection at the inlet location because the wake was deflected away from the air capture region. The wing downwash and wake width increased with increasing deflection. Moreover a viscous interaction region was generated close to the wing-body junction as a result of wing unporting. Wing tip vortex strength was larger for the clipped delta wing than for the thick wing. The inlet recovery for the clipped delta wing was slightly lower than for the thick wing.

The above study provides a data base from which it is possible to select inlet locations with acceptable pressure recovery. However, caution must be exercised to stay within the limitations of the measured parameters.

NOMENCLATURE

Symbol	Definition	Dimension
M	Free-Stream Mach Number	----
M_l	Local Mach Number	----
P	Local Measured Static Pressure	psia
P_∞	Free-Stream Static Pressure	psia
P_C	Cone Surface Pressure	psia
P_N	Normalized Local Static Pressure	psia
P_T	Local Total Pressure	psia
\bar{P}_T	Numerically Averaged Total Pressure	psia
P_{TN}	Normalized Local Total Pressure	psia
P_{T2}	Local Measured Pitot Pressure	psia
P_{T_∞}	Free-Stream Total Pressure	psia
P_{T2N}	Normalized Local Pitot Pressure	psia
r	Radial Position of Total Pressure Probe	in.
Re	Free-Stream Unit Reynolds Number	1/ft
Y_s	Static Rake Position	in.
Y_T	Total Pressure Rake Position	in.
α	Angle of Attack	deg
ϕ	Model Roll Angle	deg
ϕ_p	Total Pressure Probe Local	deg.
	Circumferential Angle	
γ	Specific Heat Ratio ($\gamma = 1.4$)	----

INTRODUCTION

A rocket ramjet is capable of extending the range and maneuverability of existing rocket-powered missiles without large increases in missile size and weight. In order to be cost competitive with conventional rocket-powered vehicles, however, the rocket ramjet requires aft-mounted inexpensive inlets which must perform satisfactorily in the flow field of the missile forebody and control surfaces. The first step in determining satisfactory performance is to map the flow field at possible locations of the inlets.

This paper compares and analyzes flow field survey data obtained in a parametric study involving models derived from the Generic Ordnance Ramjet Engine (GORJE) configuration. Two wind tunnel models were designed for the program, one sting mounted and the other wall mounted. The objective of the investigation was to determine the effects of wing planform, thickness ratio, and deflection on total and static pressure and local Mach number distributions at possible locations for the inlets. The study was conducted at $M = 2.48$ and $R_e = 3.05 \times 10^6/\text{ft}$.

The results can be applied to similar systems and thus are useful for the selecting of inlet locations, estimating inlet performance, and selecting of wing/inlet configurations.

WIND TUNNEL FACILITY

The experiments were conducted in the 18-inch supersonic tunnel at the Naval Ship Research and Development Center (NSRDC). This indraft facility operates in the Mach number range of 0.3 to 4.5 with a nominal run time of 20 sec. A contoured two-dimensional nozzle was used throughout the experiment. Tunnel flow is established in about 2 sec between the intake settling chamber at atmospheric pressure and temperature, and an exit reservoir evacuated to a pressure of about 1.5 psia.

The Mach number survey of the empty test section showed that flow uniformity was within ± 0.5 percent of the nominal Mach number ($M = 2.48$). Wall static pressure readings revealed that the free-stream flow field changed less than ± 2.0 percent, even at angles of attack and at high angles of wing deflection. Since the supply pressure of the tunnel was substantially constant, the free-stream unit Reynolds number varied only between $2.98 \times 10^6/\text{ft}$ and $3.11 \times 10^6/\text{ft}$. Details of the test facility may be found in Reference 1.

DESCRIPTION OF MODELS

Sting-Mounted Model

The wind-tunnel model used in the first phase of the investigation was a 10-percent scale model of the GORJE vehicle. The overall view of the installed model is shown in Fig 1. The forebody section was an ogive nose cylinder. Just aft of the wing hingeline, the body diameter was increased by means of a 10-deg flare. Two sets of four wings each were

fabricated for the model. Both wings had identical planform areas but the root chord of Wing 2 was only half as thick as that of Wing 1. Fig 2 gives the pertinent dimensions of these wings. The model was designed so that each wing could be deflected independently. Provision was also made for rotating the entire forebody/wing section relative to the aft section; this enabled both in-line and interdigitated inlet locations to be surveyed. Boundary layer trips were installed close to the nose tip and parallel to the leading edge of the wings to ensure fully turbulent boundary layer on the model surface.

Instrumentation for the pressure survey consisted of an automatically movable total pressure probe which surveyed a circular area at the designated inlet location, a stationary 15 deg half-angle cone probe located 180 deg away from the total pressure probe in the geometric center of the inlet, and a static tap on the surface of the model in the same axial plane as the total pressure and cone probes. Fig 3 is a closeup view of the two probes. The total pressure probe, moved by a cam system, surveyed an 0.3 in. diameter area in three concentric circles (0.10, 0.20 and 0.30 in. in diameter) for a total of 36 pressure measurements in each run. Fig 4 is the exploded view of the cam and drive mechanism and the various components of the model.

Wall-Mounted Model

A 40-percent scale, wall-mounted half model was used for the second phase of the investigation in order to obtain detailed information on the effect of wing planform, thickness, and deflection on the distribution of the wing wake pressure. The forebody (a blunt faired cone cylinder) was designed to reach into the subsonic upstream portion of the supersonic

Vol. 3

nozzle and caused less than 0.5-percent blockage in the throat.

Although the geometry of the model forebody did not scale exactly to vehicle geometry, the approaching boundary layer and free-stream conditions were nearly duplicated ahead of the wing without a large primary nose shock and excessive tunnel flow distortions. Since the primary purpose of the investigation was to survey the flow field behind the wing, this forebody distortion ahead of the wing did not materially affect the data except that ahead of the wing, the Mach number was about 8.5 percent higher than would be expected under normal flight conditions.

Separate total and static pressure surveys were conducted with a 20-prong total pressure and a 7-prong static pressure rake for each wing configuration, wing deflection, and axial body station. A 9- by 10-in. area perpendicular to the free-stream direction was surveyed in each 20-sec run. The probe support mechanism in the wind tunnel was converted from manual to semiautomatic motorized operation by using a precision, variable-speed gear motor. A high quality potentiometer was geared to the probe mechanism and used to monitor the precise position of the rake at any instant. In all, either 600 pitot pressures or 210 static pressures were measured in the survey area during each test run. The vertical distance between adjacent points was 0.5 in. and the horizontal distance about 0.3 in. for the total pressure measurements. The vertical distance between adjacent static pressure points was 2.0 in. with the same horizontal spacing as in the total pressure measurement. Large vertical spacing was used between static probes to avoid shock interference from adjacent tubes. This was not a problem for the total rake. The overall view of the model and total pressure probe is shown in Fig 5.

Four wings were used in the second phase of the investigation.

Table 1 gives their pertinent dimensions, and Fig 6 shows the planforms. Wings 1 and 2 had the same planform and thickness distribution as Wings 1 and 2 in the previous phase. Wing 3 had the same planform and thickness distribution as Wing 2 but its area was only 50 percent as large. Wing 4 was a clipped delta wing identical to the lower panel of Wing 1 and truncated at the crank.

TEST PROGRAM

Sting-Mounted Model

The test program for the sting-mounted 1/10-scale model is outlined in Table 2. All test runs were conducted at $M = 2.48$. Two wings of identical planform areas but differing thickness ratios were used with inline and interdigitated probe positions in the "x" configuration. In addition, the "+" configuration was also tested with Wing 1 only. As special cases, the inlet areas at $\phi = 0$ and 45 deg were also surveyed without wings in order to determine the influence of the body boundary layer on the inlet. The survey area was at a constant distance of 5.6 in. downstream from the wing hingelines; 101 runs were conducted.

The pressure instrumentation consisted of a 10-psid transducer for the total pressure and 2.5-psia transducers for the static probe and tap. In addition to the model instrumentation, the tunnel test conditions were also monitored. All transducers were calibrated and found to be linear and accurate within ± 1 percent full scale. In terms of local to free-stream static pressure ratio, the maximum error of the measured data was ± 5.8 percent. The maximum error of the measured total pressure to free-stream pressure ratio was ± 4 percent.

Vol. 3

Wall-Mounted Model

The test program for the wall-mounted 40 percent scale model is outlined in Table 3. All test runs were conducted at $M = 2.48$. Four wings were used with survey probes oriented in the vertical position and traversing in the horizontal plane parallel with the wing hingeline. The 102 survey runs included four for the body alone configuration. Prior to the survey runs, preliminary runs were conducted to determine the effect of the model on the free-stream Mach number, the maximum sweep speed of the probes, and the relationship of the static flow field to model surface pressure. Conclusions from these preliminary studies are discussed later. In addition to the standard tunnel monitoring equipment, the pressure instrumentation for this test phase, consisted of twenty 10-psid transducers for the total pressure rake and ten 5-psia transducers for the static rake and three model taps. All transducers were calibrated and found to be linear and accurate to within 0.9 percent full scale. In terms of local to free-stream static pressure ratio, the maximum error of the measured data was ± 7.6 percent and for P_T/P_{T_∞} the error was ± 4 percent.

DATA REDUCTION TECHNIQUES

Sting-Mounted Model

For the first phase of the investigation, the data reduction program utilized the measured pitot and static pressures to compute the total pressure ahead of the bow shock of the total pressure probe at each probe position. This was accomplished by employing an iterative procedure to determine the local Mach number at each location. In fact, the local Mach number was determined by two independent measurements, one based on

the cone probe and the other on the model wall static pressure.

Reference 2 gives equations for computing local Mach number based on cone probe measurements. The equation for the 15 deg cone probe, which was used in the experiment, is given as:

$$M_{\ell} = 1.19998 + 0.73956 x - 0.41043 x^2 + 10.33126 x^3 \\ - 59.10989 x^4 + 188.67195 x^5 - 352.88729 x^6 \\ + 387.49722 x^7 - 231.20630 x^8 + 58.17087 x^9$$

where: $x = -2.07297 (P_c/P_{T_{\infty}}) + 1.11920$. The local Mach number computation based on the wall static pressure utilized the standard equations given in Reference 3. This involved knowledge of the flow conditions ahead of the wings, but behind the nose-generated conical shock. However the flow conditions in that region were essentially unknown. Accordingly, the iterative matching procedure utilized known free-stream conditions, the measured probe station conditions, and the implicit energy relationships across the various shock wave systems. Comparison of local Mach numbers for the two computations indicates that and in no case did the difference exceed ± 0.5 percent.

Once the local Mach number ahead of the total pressure probe is known, the total pressure ahead of the probe bow shock may be calculated by application of the Rayleigh-Pitot equation:

$$\frac{P_T}{P_{T_2}} = \left[\frac{2\gamma}{\gamma + 1} M_{\ell}^2 - \frac{\gamma - 1}{\gamma + 1} \right] \frac{1}{\gamma - 1} \left[\frac{(\gamma - 1) M_{\ell}^2 + 2}{(\gamma + 1) M_{\ell}^2} \right]^{\frac{\gamma}{\gamma - 1}}$$

The probe position was determined by the electronic output of the two scanvalve motors that moved the total pressure probe mechanism.

Vol. 3

The output of one motor determined the radial probe position, and that of the second motor provided the angular position.

Output from the computed data included probe position, angle of attack, free-stream conditions, the ratio of total pressure to pitot pressure across the probe bow shock (P_T/P_{T_2}), the ratio of local static pressure to free-stream total pressure (P/P_{T_∞}), the ratio of local total pressure to free-stream total pressure (P_T/P_{T_∞}), and the absolute values of all measured and computed pressures in psia.

In addition to the numerical output, a plot program was also developed to graphically illustrate either the local total to free-stream total pressure distribution [$P_T/P_{T_\infty} = f(r, \phi_p)$] and the local Mach number [$M_x = f(r, \phi_p)$], or the local static to free-stream static pressure ratio [$P/P_\infty = f(r, \phi_p)$] in a polar coordinate system. The program can print the values of the various pressure ratios or local Mach number at scaled probe locations. The program is also capable of plotting constant pressure ratio contours for specified values and increments by interpolating among the measured values and determining the location of the specified ratio.

Wall-Mounted Model

The data reduction program utilized the measured local pitot and static pressures to compute the total pressure ahead of the bow shock of the total pressure probe and the local Mach number at each probe position. Since both local static and pitot pressures were measured the computation did not involve any iteration. However, two modifications had to be made to the actual measured data in order to perform the necessary calculations:

1. Standard free-stream conditions were applied to all data ($P_{T_\infty} = 14.7$ psia, $P_\infty = 0.887$ psia) the actual measurements were scaled

and normalized. This was necessary because the actual free-stream conditions changed slightly from run to run. This normalizing procedure did not alter the pressure ratios or the local Mach number, it merely changed the absolute values. Therefore, since the objective of the investigation was to obtain the distribution of local pressure ratios and local Mach number, the above modification did not influence the qualitative or quantitative accuracy of the data.

2. As mentioned earlier, the pressure probes were spaced 2 in. apart to avoid shock interaction. Therefore, the measured static pressure values had to be interpolated to match the location of the total pressure probes. This procedure introduced some additional errors, but it is estimated that they were no larger than about 2 percent of the measured static pressure values.

The probe position was determined by the output of the potentiometer directly geared with the probe support mechanism.

The computed data output included probe position, free-stream tunnel conditions, measured actual pressures and normalized pressures both in psia, the ratios of total pressure to free-stream pressure, static to free-stream static pressure, and pitot to total pressure as well as local Mach number.

In addition to the numerical output, a plot program graphically illustrated the local to free-stream total pressure distribution, the local static to free-stream static pressure distribution, and the local Mach number distribution in a Cartesian coordinate system [i.e., $P_T/P_{T_\infty} = f(z,y)$]. The program can print the values of the pressure ratios and M_∞ at scaled probe locations relative to the model. It is also capable of plotting contours of pressure ratios or local Mach numbers for specified

values and increments.

PRELIMINARY STUDIES

Sting-Mounted Model

Two tasks had to be performed prior to the test runs in the first phase of the investigation:

1. Positive calibration of the movable survey probe, more specifically, the actual diameters of the circular paths along which the probe moved when taking pitot pressure data. This calibration was repeated when adjustments had to be made to the mechanism. Table 4 summarizes these calibrations.

2. Determination of the total pressure sensor system settle-out time. This, in turn determined the trigger rate with which the probe mechanism moved (the trigger rate was the length of time the probe stayed on any one station to take data). Testing of several trigger rates indicated that in terms of data accuracy, the difference between the 2-sec maximum and the 0.5-sec minimum rates was less than 1.5 percent. Accordingly, it was decided to use the minimum trigger rate in order to sweep the survey area within 20 sec.

Wall-Mounted Model

For the second phase of the investigation, it was necessary:

1. To determine the effect of the wall-mounted model on tunnel free-stream Mach number. It was found that the presence of the model did not affect free-stream conditions in the wind tunnel ahead of the conical shock wave generated by the 10-deg flare between the forebody and afterbody. There was no shock reflection within the test rhombus.

2. To calibrate the rake position. This calibration showed a repeatable slope linearity to within ± 1.6 percent. However, because of the gear backlash and tunnel starting and stopping shock effects on the mechanism, it was necessary to determine the starting point coordinate from the wall of the tunnel before each run.

3. To determine (a) whether model surface taps would provide sufficient definition to give total pressure and local Mach number distribution or (b) whether it was necessary to measure the static pressure in the flow field. The preliminary survey revealed the presence of a nonlinear static pressure field behind the wing and so local pressures in the flow field could not be related to the model pressure taps. Accordingly, it was necessary to measure the static pressure field in order to determine the wind wake flow field characteristics.

4. To determine the sweep rate of the static and total pressure rakes. The sweep rate of about 0.6 in./sec did not affect total or static pressure data substantially. The error due to the moving pressure probe was less than ± 0.5 percent of the measured value for a stationary probe. However, sweep showed dependency on pressure gradient in the case of static pressure. Compared to values for a stationary probe, the measured values were off by about ± 0.9 percent for low pressure gradient regions and by about ± 3 percent for high pressure gradient regions.

RESULTS AND DISCUSSION

STING-MOUNTED MODEL

These results are available in the form of numerically averaged total pressure recovery ($P_T/P_{T\infty}$) as functions of wing deflection for various configurations, angle of attack, and probe position (inlet position in the physical sense). Total pressure ratio profiles are also available to explain gross behavior at the inlet location. The detailed analysis was presented in Reference 4. Here the summary of results are discussed along with data which pertain to the second phase of the investigation.

Fig 7 presents the total pressure contours for the case of the in-line inlet location at zero angle of attack. With no wings, the uniform pressure recovery gradient was characteristic of a fully developed, turbulent boundary layer. With the addition of undeflected wings, a low recovery wing wake area occurred that was roughly symmetrical and in-line with the wing. The body boundary layer was still apparent in the lower portion of the profile, and the suggestion of a centered low recovery region--possibly from a vortex shed from the wing--appeared in the upper portion. The average total pressure recovery and Mach number dropped with the addition of wings. In general, the pressure recovery losses were smaller in the wake of the thinner wing (Wing 2). However, the thinner wing did demonstrate lower recovery in the in-line, zero angle of attack case. This phenomenon will be discussed later.

When the wing directly in front of the probe was deflected +5 deg (+ is trailing edge to left, looking forward), the wing wake moved to the left. The boundary layer and vortex regions were still evident and

the average pressure recovery and Mach number were approximately the same as for the undeflected case. When the wing was deflected to ± 11 deg, wing wake was deflected out of the inlet area and the average pressure recovery increased to the no-wing value.

When both the vertical (in-line) and horizontal wings were deflected simultaneously (at $\alpha = 0$ deg), the flow fields for positive wing deflections were similar to those shown in Fig 7. The situation was somewhat different for negative wing deflections. Although at $\delta = -5$ deg the profile was similar to $\delta = +5$ deg and the wing wake was deflected to the right, at $\delta = -11$ deg the wake from the horizontal wing was deflected toward the inlet and interacted with the vertical wake, producing a uniform pressure recovery gradient. The average total pressure recovery decreased for negative wing deflections.

When the location of the probe was interdigitated with the wing at $\alpha = 0$ deg, the pressure of the wing at $\delta = 0$ deg had little effect on the surveyed flow field compared to the body alone configuration. For positive wing deflections, there was a slight increase in pressure recovery when both wings were deflected. For negative deflections, there was a uniform pressure recovery that decreased markedly with wing deflection and dropped to approximately 50 percent at $\delta = 11$ deg. The low pressure recovery resulted from a confluence of the two wing wakes.

For angle of attack, the pressure recovery at the leeward side was improved by the addition of undeflected wings in the interdigitated position as compared to the no wing case. The wings broke up the lee-side vortices and straightened the flow. As at zero angle of attack, the average total pressure recovery decreased when both wings were deflected toward the surveyed area. This decrease was evident at positive

Vol. 3

deflections for the windward side and at negative deflections for the leeward side.

The flow field for the in-line position at angle of attack exhibited (as at $\alpha = 0$ deg) an increase in pressure recovery resulting from deflection of the wing at the windward inlet location in the "+" wing orientation. At the leeward location, viscous losses eliminated this gain. In the "x" wing orientation, both in-line and interdigitated locations demonstrated large losses in total pressure recovery for positive wing deflections but not for negative deflections. This may be explained by considering the contributions of wing deflections and crossflow. The crossflow resulting from the angle of attack always tended to push the wing wake above the surveyed area. A negative wing deflection, with trailing edges upward, directed the wing wake in the same direction. Positive wing deflection opposed the crossflow, causing the wing wake to be directed toward the surveyed area with a resultant decrease in total pressure recovery.

Measurements showed that higher pressure recoveries were achievable with a thin wing than with a thick wing (except at $\alpha = 0$ deg and $\delta = 0$ deg in the in-line position). Furthermore, the interdigitated position was preferable on the basis of the flow field total pressure recovery in both "+" and "x" wing configurations for $\delta < \pm 6$ deg within the range of angles of attack investigated.

WALL-MOUNTED MODEL

Selection of engine inlet locations for a given system may be determined by factors not necessarily related to optimum inlet per-

formance. For instance, launch constraints, structural design, vehicle stability and external aerodynamics may necessitate locating the inlet in the relatively disadvantageous in-line position. In order to understand the consequences of such a proposition, it was decided to obtain detailed flow field information in the entire wing wake region, rather than in only a small selected area and to study the effects of the wing planform thickness and wing deflection. A further goal of the second phase of the investigation was to try to explain the causes of the anomaly mentioned in the previous section (namely that pressure recovery behind Wing 2 at $\alpha = 0$ deg, $\delta = 0$ deg in-line position was lower than for the thick wing under the same flow conditions) based on more insight into the details of the flow field. The results of the second phase of the investigation are presented in Figs 8-26.

Fig 8 shows the total pressure distribution of the body alone. At the first and second survey stations (Fig 8a, and 8b, corresponding to the axial distances of 5.5 and 12.5 in. behind the wing hingeline when the wing is installed), the pressure field consisted mainly of the compression wave which is generated by the 10 deg flare which connects the fore and aft bodies and which results from the change of body slope at the flare-cylindrical-aft-body junction. This compression wave was conical in shape, and its angle was such that it fell outside the boundaries of the surveyed area at the third survey station (see Fig 8c at $x = 19.5$ in.). This description is further substantiated by examination of the local Mach number and the static pressure distributions at the second survey station ($x = 12.5$ in.), shown in Figs 9b and 9c. For reference purposes, the total pressure distribution at the same location is also shown (Fig 9a). The local Mach number distribution exhibited

Vol. 3

sharp gradients perpendicular to the flow direction in the horizontal plane with a lower than free stream Mach number region ($M = 2.40$). Correspondingly in the same vicinity, the static pressure distribution showed values that were 10 to 20 percent higher than the measured free-stream static pressure outside of the affected region.

Fig 10 presents the total pressure distribution behind Wing 1 at $\delta = 0$ deg. The wing wake at each survey station was confined to a relatively narrow, symmetrical region relative to the wing chord line. The wake extended outboard approximately the same distance as the span of the wing, and its structure did not change downstream within the surveyed region ($x = 5.5$ to $x = 22.4$ in. from the wing hingeline as shown in Figs 10a to 10d). Directly in-line and behind the wing, three distinct low pressure recovery cells were apparent: one close to the wing tip, one at the crank, and one at the midpoint of the inboard portion of the wing. The low pressure recovery cell along the inboard part of the wing increased slightly in vertical extent downstream. Strong interaction between the conical compression wave and the wing wake on the leeward side was evident in Figs 10a and 10b, but as it propagates downstream, the compression wave passed outside of the wake boundary, and therefore no interaction was encountered further downstream (see Figs. 10c and 10d).

The extent of the various shock-wake interactions downstream of the wing are well illustrated in Fig 11 which shows the total pressure distributions in the vertical plane near the wing tip (Fig 11a), at the crank (Fig 11b), and at mid-panel of the inboard section of the wing (Fig 11c). The wake width increased downstream; this increase was most pronounced at midpanel and at the outboard panel wake was virtually unchanged from $x = 19.5$ to $x = 22.4$ in. The pressure recovery levels in the wake varied both with the downstream distance from the wing

(increasing with increasing distance) and along the span (exhibiting the greatest losses inboard and gradually diminishing toward the tip) as shown in Fig 11. The wing generated shock is clearly shown at the survey stations $x = 5.5$ and 12.5 in. downstream from the wing hingeline.

At a wing deflection angle of 5 deg the shock strength increased as shown by the lower level of total pressure recovery; see Fig 12. The wake expanded in width and wing downwash was evident on the leeward side as the wake evolved downstream. The pressure recovery at the inlet location was somewhat improved since wing deflection caused the wake to move away from the area of the inlet. At the larger wing deflection ($\delta = 11$ deg), the wing wake almost completely deflected away from the air capture region, as shown in Fig 13. The wake was then much wider than previously, the downwash angle increased as expected, and the wake shock strength increased. These are all well illustrated in Fig 14 where the wing wake total pressure distributions in the vertical plane are shown for $\delta = 11$ deg at three different span locations. The strong interaction of the incipient body cone shock and wake shock systems on the leeward side of the wing are shown in Fig 13 as well as Fig 14. At $\delta = 11$ deg, the wing tip vortex strength was sufficient to cause measurable pressure disturbances, in fact at $\delta = 5$ deg small areas of vortex activity are discernible in Fig 12 at $x = 19.5$ and $x = 22.4$ in. The effects of unporting (caused by the wing deflection) close to the body-wing junction are shown on the leeward side for $\delta = 5$ deg and $\delta = 11$ deg in Fig 12b, 12c, 13c and 13d.

Since the maximum thickness ratio of Wing 2 was only half that of Wing 1, its energy losses in the wake were generally smaller than those of Wing 1. Consequently the total pressure recovery was higher for Wing 2

than for the thicker wing with identical planform area. The total pressure distributions for Wing 2 at $\delta = 0, 5$ and 11 deg are illustrated in Fig 15-17. At $\delta = 0$ deg the wake widths of both wings was almost the same. The location of the low pressure recovery cell near the tip was identical for Wings 1 and 2 but the losses were higher for Wing 1. The pressure recovery loss at the crank of both wings was the same. Wing 1 had one inboard cell compared to two for Wing 2. The pressure recovery loss of the inboard cell was higher for Wing 1 than for Wing 2. The center of the inboard cell of Wing 1 was located several inches above the inlet, but the center of the second inboard cell of Wing 2 intersects the inlet location thereby causing large inlet losses (as was pointed out in the discussion of Fig 7). This is evident by comparing Fig 10 and 15. For convenience, Figs 10d and 15d are replotted as Figs 18a and 18c. The possible causes of this phenomenon may be explainable by the small differences in the spanwise geometric parameters. At $\delta = 0$ deg the only spanwise parameters that differ between Wings 1 and 2 are the taper (included angles of 5.2 and 2.6 deg respectively) and the wing-ridge-body intersection angle (100.7 and 95.4 deg respectively). In general, acute wing-body intersection angles are avoided because they tend to promote flow separation. By turning that statement around, it is conceivable that the more obtuse angle of the thick-wing-body-intersection produced a more streamlined flow near the body in the vicinity of the inlet location.

The other gross features of the flow near the vicinity of Wings 1 and 2, namely, the leeside interaction between the conical wave and the wing wakes, look very similar. At $\delta = 5$ deg, Wing 2 showed lower pressure recovery losses on the leeward side with smaller pressure gradients in the

vertical plane than Wing 1 (compare Fig 12 and 16). The wing downwash effects were roughly comparable. In the compression region, Wing 2 had higher pressure recovery levels than Wing 1.

At $\delta = 11$ deg, the gross features of the flow behind Wings 1 and 2 were similar, although the tip vortex was more clearly discernible for Wing 2 than for Wing 1. The wake width, the downwash and the compression regions were nearly identical for both wings. The overall pressure recovery losses at the inlet locations were comparable for both wings. Again, for convenience, the total pressure distributions for Wings 1 and 2 at $x = 22.4$ in. and $\delta = 11$ deg are replotted as Figs 18b and 18d.

The recovery pressure loss region for Wing 3 (which had the same planform as Wings 1 and 2 and a thickness distribution similar to Wing 2 but with only 50 percent wing area) extended along the entire span (similar to Wing 2) as shown in Fig 19, 20 and 21 for $\delta = 0, 5,$ and $\delta = 11$ deg, respectively. At $\delta = 0$ deg there were between three and four wake low-pressure recovery cells. Since the span of Wing 3 was small, the wing wake did not interact with the conical body shock-expansion system as is evident from Fig 19b. The wake width was similar to that of Wing 2 at $\delta = 0$ deg. The pressure recovery at the inlet was generally improved as wing deflection increased because the wake was deflected away from the air capture region as shown in Fig 20 and 21. The pressure loss region exhibited on the leeward side of the inboard panel is attributed to wing-body interaction. At $\delta = 11$ deg the improvement in pressure recovery was not as great for Wing 3 as for Wing 2 in the vicinity of the inlet. This may be attributable to the fact that the wing-body interaction region (which was closer to the body with the smaller area wing) was drawn into the capture area, with an accompanying increase in viscous losses. The viscous wing-body interaction losses on

Vol. 3

the leeward side may also have affected the lift distribution of the wing. The shape of the wing wake and downwash for Wings 3 and 2 were similar as were their windward compression regions. Wing tip vortices were not as noticeable as for Wing 2. As with the previous wings, the downwash effect was more pronounced in the vicinity of the crank and the inboard portion of the wing. The above discussion is illustrated in Fig 22 which compares the total pressure distribution for Wings 2 and 3 at $x = 19.5$ in. for $\delta = 0$ and $\delta = 11$ deg.

Wing 4 is a clipped delta wing identical to the lower panel of Wing 1 and truncated at the crank plane. The total pressure distributions behind Wing 4 at $\delta = 0, 5$ and 11 deg are shown in Fig 23, 24, and 25, respectively. The wake for this wing extended outboard along the span to the wing tip. For all wing deflections, Wing 4 had two low-recovery cells at $x = 22.4$ in. The lower recovery cell (30 percent loss) was outboard at the 67 percent span location at $\delta = 0$ deg. The inlet recovery was slightly lower and the pressure distortion level higher for Wing 4 compared to Wing 1. The wing deflection improved in the recovery of pressure loss at the capture area location, similar to the other three wings. In essence, the wake region was deflected away from the vicinity of the inlet by the deflected wing. The conical body wave and the wing wake did not interact since the wing span was too short. However, since the aspect ratio of this wing was small, the tip vortex was stronger than for Wing 1. This is shown in Fig 26 which compares the total pressure distribution for Wings 1 and 4 at $x = 19.5$ in. for $\delta = 0$ and $\delta = 11$ deg.

Extensive flow field measurements, for a 10-percent scale sting-mounted model and a 40-percent scale wall-mounted model were conducted behind movable wing surfaces. In order to analyze and assess the gross flow field behavior in the wing wake region use was made of local total static pressure recovery maps and local Mach number distribution maps. These measurements identified unique flow field characteristics which would affect the performance of installed inlets.

The first phase of the investigation, indicated that an interdigitated inlet location was preferable on the basis of total pressure recovery in both "+" and "x" wing orientations, for $\alpha = \pm 4$ deg and for wing deflections less than about ± 6 deg.

A rather complex flow field was revealed in the second phase of the investigation. First of all there was a complex interaction between the incipient conical body shock wave and the wing wake. It was found that the wing wake was narrow at $\delta = 0$ deg without much tendency to spread in width, but the pressure recovery levels varied both streamwise and spanwise. The wake structure showed several pressure defect cells whose location and number varied from wing to wing. In general, the energy losses were smaller for Wing 2 than for Wing 1. However, its inlet losses at $\delta = 0$ and 5 deg where the center of an inboard low pressure recovery (or pressure defect) cell coincided with the inlet location, exceeded those of Wing 1. When the wings were deflected, the pressure recovery for all wings improved at the inlet location because the wake was deflected away from the air capture region. The wing downwash and wake width increased with increasing deflection. Likewise a viscous interaction region was generated close to the wing-body junction as a result

of wing unporting. Wing tip vortex strength was larger for Wing 4 than for Wing 1. The inlet recovery for Wing 4 was slightly lower than for Wing 1.

The above study provides a data base from which it is possible to select inlet locations with acceptable pressure recovery. However, caution must be exercised to stay within the limitations of the measured parameters.

The inlet locations of air-breathing missiles are sensitive to upstream influences, these can not be predicted theoretically. Therefore, very careful preliminary studies (similar to the present one) must be conducted on the case by case basis prior to the selection of acceptable inlet location.

REFERENCES

1. Ziegler, N. G., "The David Taylor Model Basin Wind-Tunnel Facility", DTMB Aero Rpt 1027, 1963.
2. Volluz, R. J., "Handbook of Supersonic Aerodynamics. Section 20. Wind Tunnel Instrumentation and Operation", NAVORD Rept 1488, Vol 16. 1961 (Sections 2.4, 3.2).
3. Anon. , "Equations, Tables, and Charts for Compressible Flow", NACA Rept 1135, 1953.
4. Hall, R. B., G. S. Pick, "Investigation of Vehicle Flow field at Inlet Locations in the Presence of Wings", Proceedings of the JANNAF 1974 Propulsion Meeting, 1974.

TABLE 1 - WING GEOMETRY OF WALL-MOUNTED MODEL

Wing Number	Chord Length -in-	Span -in-	Thickness at Chord -in-	Leading Edge
1	6.73	6.78	0.566	Cranked
2	6.73	6.78	0.284	Cranked
3	4.76	4.79	0.200	Cranked
4	6.73	4.36	0.566	Straight

TABLE 2 - TEST PROGRAM FOR STING-MOUNTED MODEL
 (All tests were conducted at zero and ± 4 -deg angles of attack)

Axial Station -in-	Wing Number	Wing Deflection -deg-	Wing Configuration	Probe Position
5.6	1	0; ± 5 ; ± 11	+	In-line
5.6	1	0; ± 5 ; ± 11	x	In-line
5.6	1	0; ± 5 ; ± 11	+	Interdigitated
5.6	1	0; ± 5 ; ± 11	x	Interdigitated
5.6	2	0; ± 11	x	In-line
5.6	2	0; ± 11	x	Interdigitated
5.6	No Wing	--	-	$\phi_p = 0$ deg
5.6	No Wing	--	-	$\phi_p = 45$ deg

TABLE 3 - TEST PROGRAM FOR THE WALL-MOUNTED MODEL
 (All tests were conducted at zero angle of attack)

Axial Station -in-	Wing Number	Wing Deflection -deg-	Wing Configuration	Probe Position
5.5	1, 2, 3, 4	0; 5; 11	+	In-line
12.5	1, 2, 3, 4	0, 11	+	
19.5	1, 2, 3, 4	0; 5; 11	+	
22.4	1, 2, 3, 4	0; 5; 11	+	
5.5	No Wing	--	-	--
12.5		--	-	--
19.5		--	-	--
22.4		--	-	--

TABLE 4 - CALIBRATION OF TOTAL PRESSURE PROBE
 POSITION FOR
 STING-MOUNTED MODEL

Run Number	Actual Diameter -in-
2-23	0.290
	0.198
	0.104
24-97	0.252
	0.172
	0.090
99-101	0.300
	0.204
	0.108

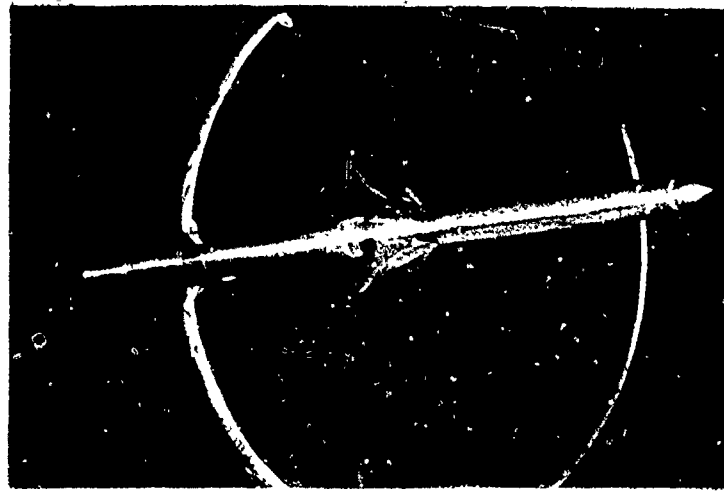
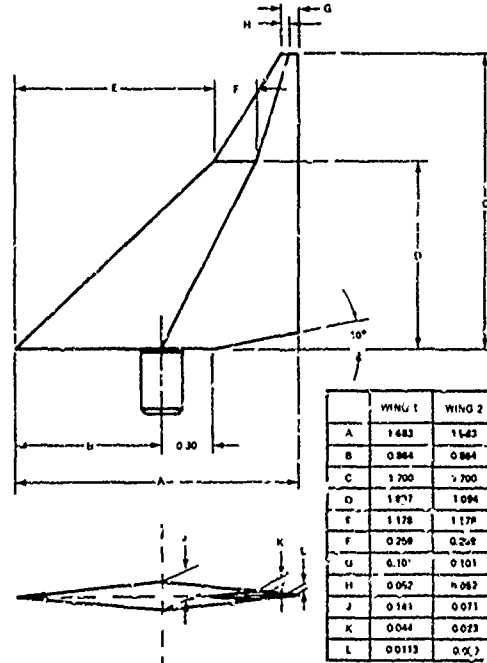


Figure 1 - Overall View of the Sting Mounted Model in the Supersonic Wind Tunnel



	WING 1	WING 2
A	1.683	1.683
B	0.864	0.864
C	1.700	1.700
D	1.877	1.894
E	1.178	1.177
F	0.258	0.258
G	0.107	0.101
H	0.052	0.082
J	0.181	0.071
K	0.044	0.023
L	0.0113	0.007

Figure 2 - Geometry and Dimensions of the Wing Configurations of the Sting-Mounted Model

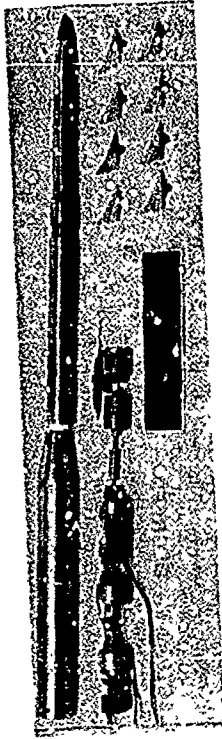


Figure 4 - Exploded view of the Survey Probe Drive Mechanism and Various Model Components

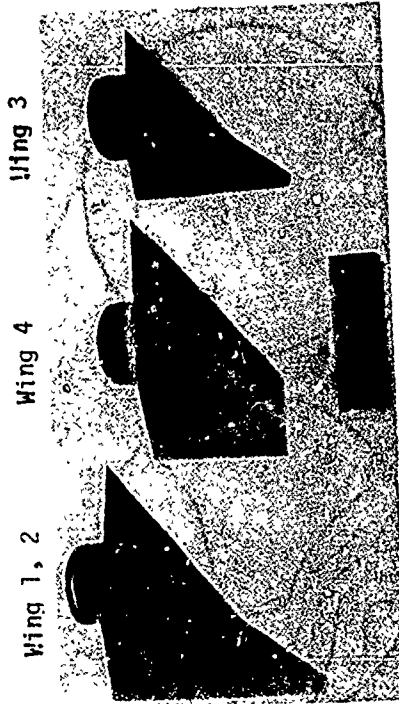


Figure 6 - Wing Configurations of the Wall-Mounted Model



Figure 3 - Close-up View of the Total and Static Probes on the Sting-Mounted Model

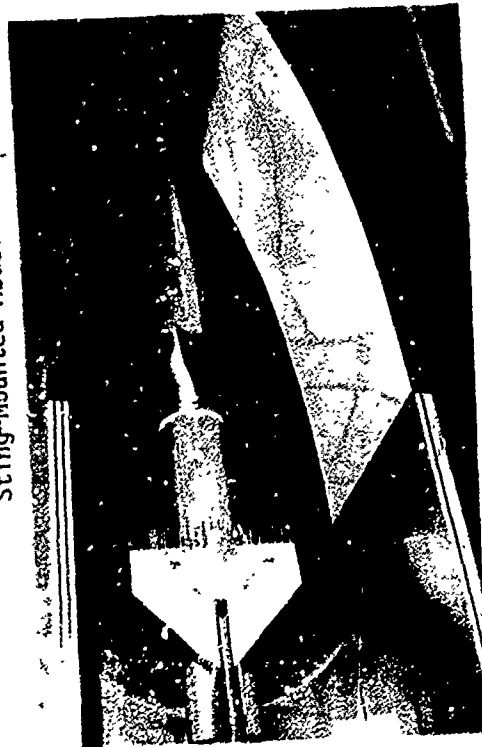


Figure 5 - Overall View of the Wall-Mounted Model and Probe in the Supersonic Wind Tunnel

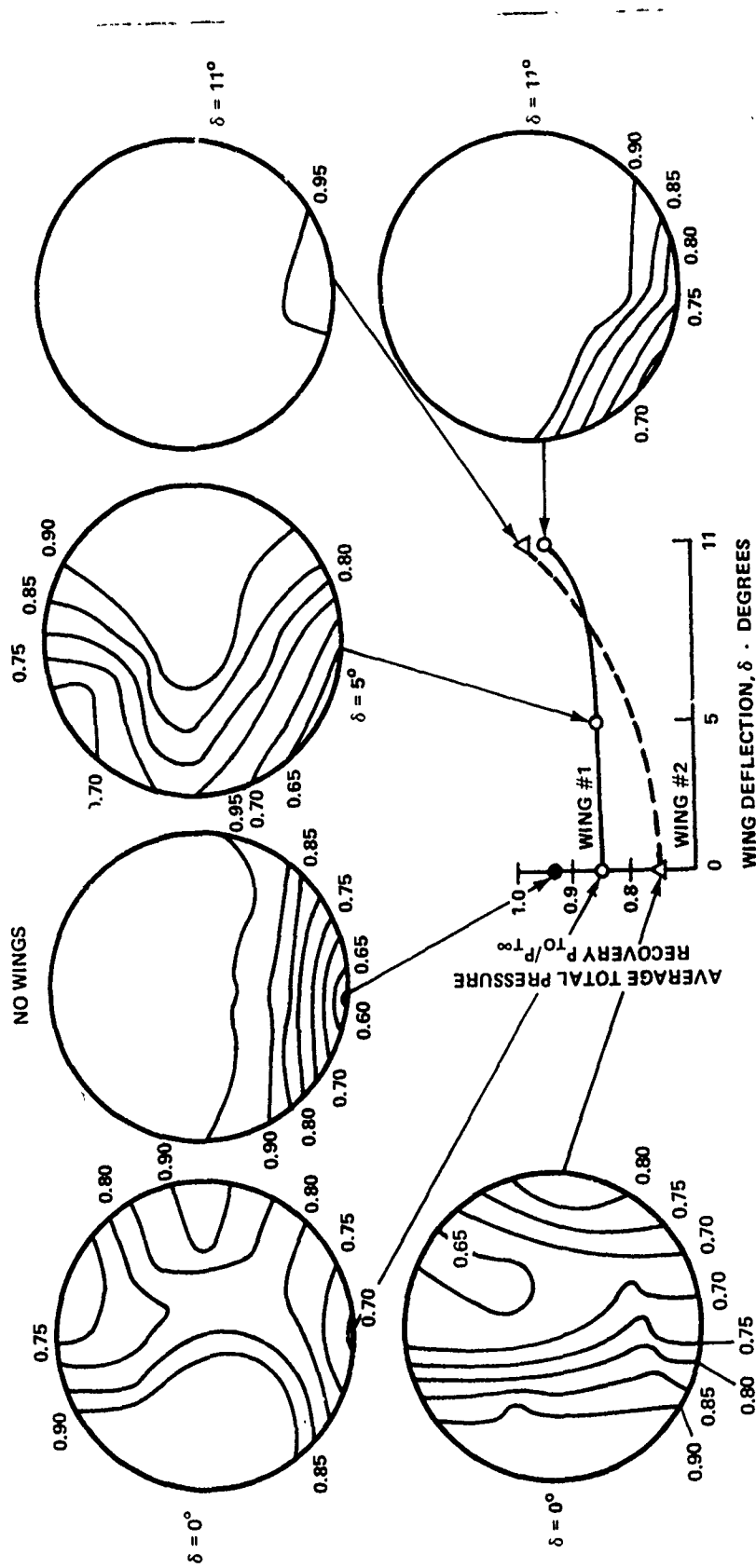
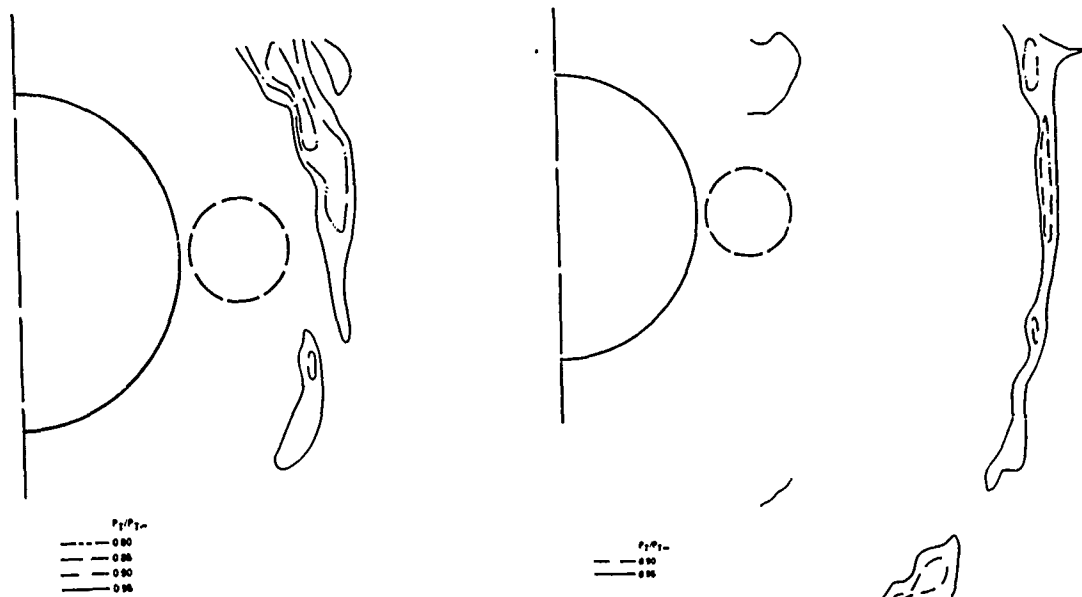
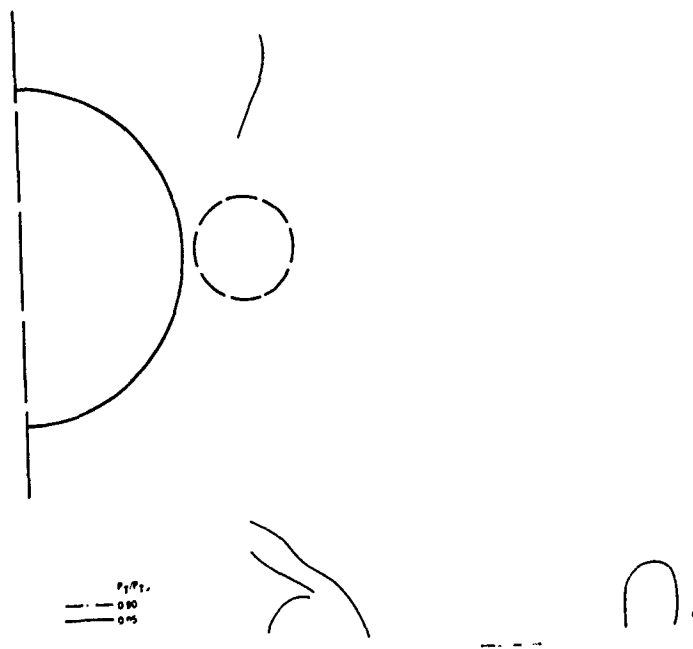


Figure 7 - Total Pressure Recovery as Function of Wing Deflection Angle for Wings 1 and 2 for Inline Location at $\alpha = 0^\circ$



a) $x = 5.5$ inches

b) $x = 12.5$ inches



c) $x = 19.5$ inches

Figure 8 - Total Pressure Distribution Body Alone

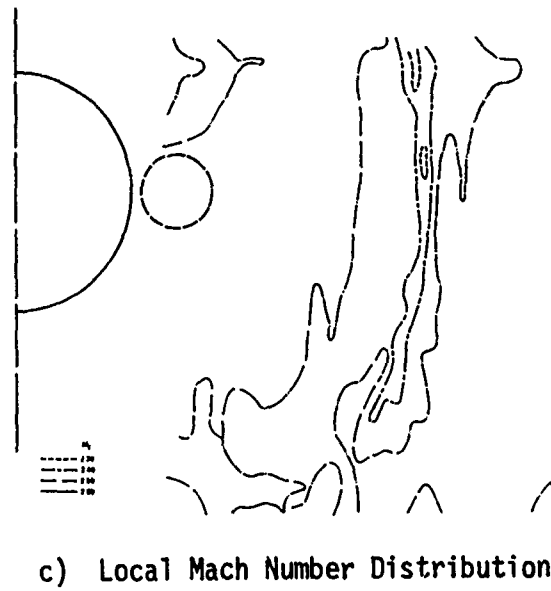
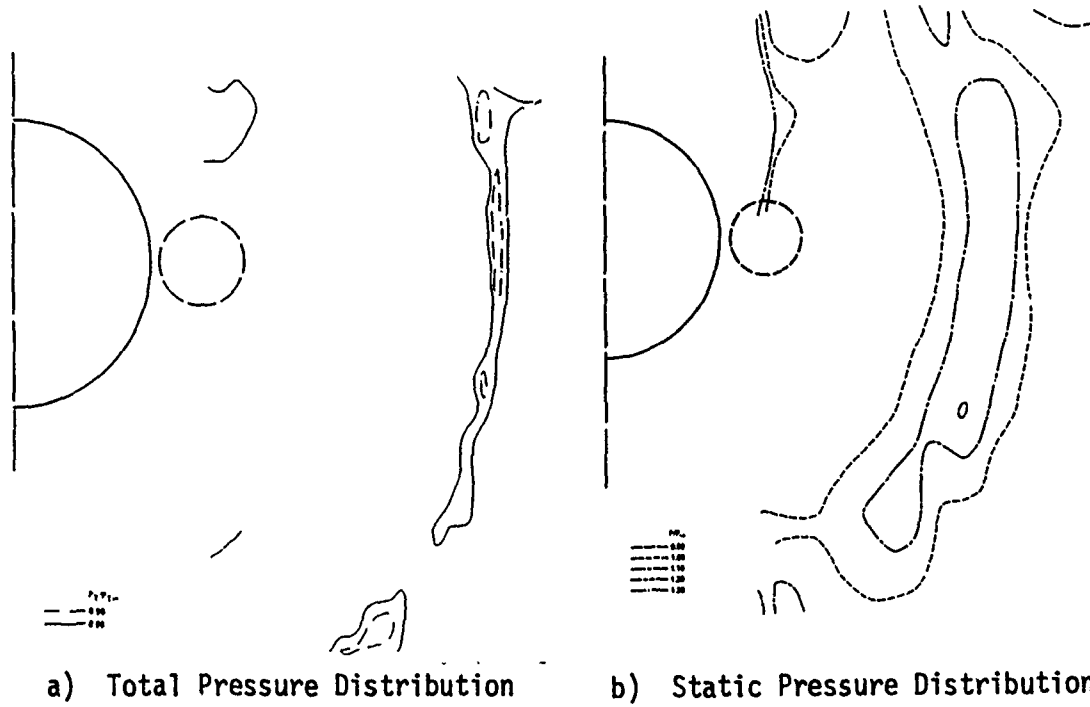


Figure 9 - Total, Static and Local Mach Number Distributions
Body Alone at $x = 12.5$ inches

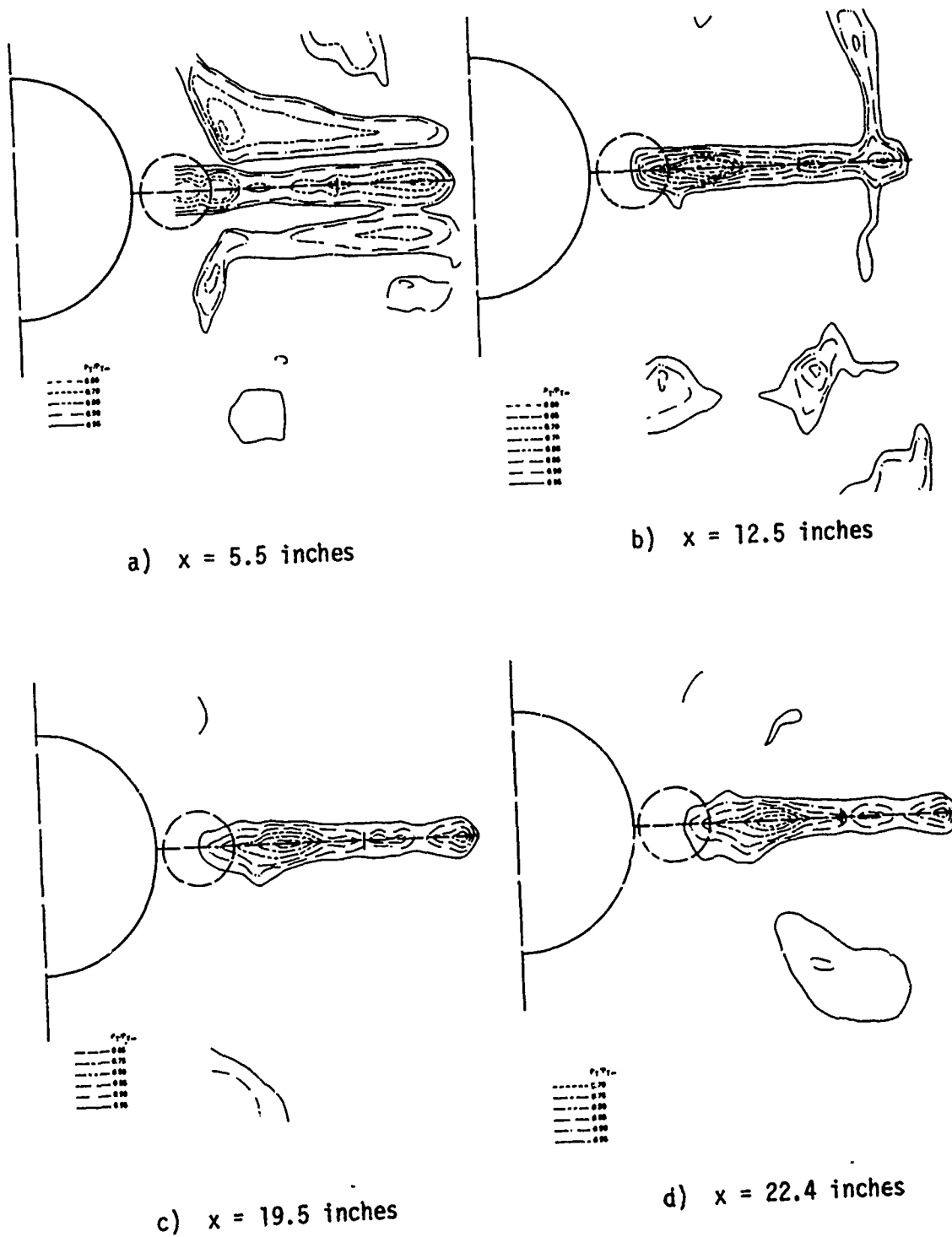


Figure 10 - Total Pressure Distribution Behind Wing 1 at $\delta = 0^\circ$

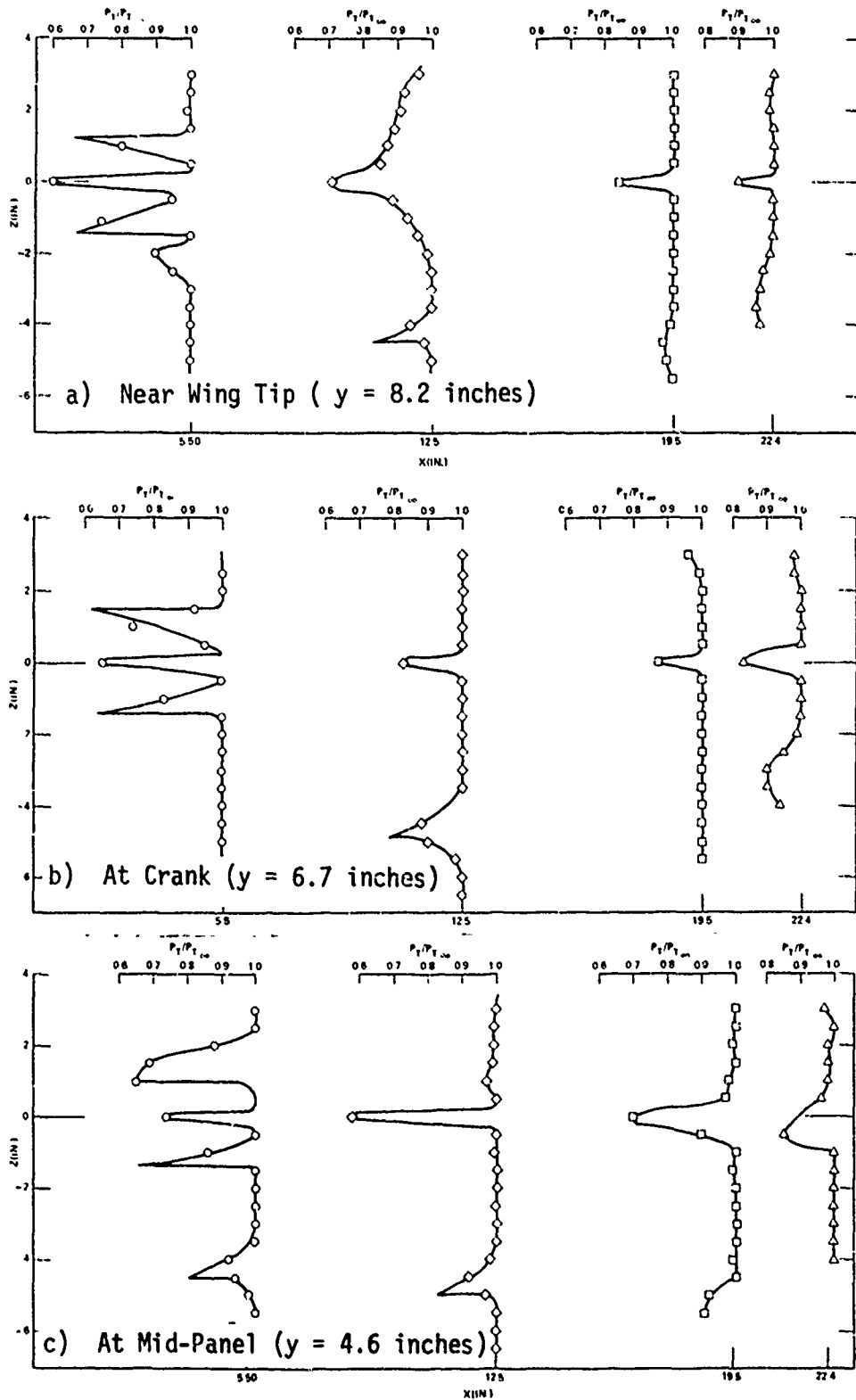


Figure 11 - Wing Wake Total Pressure Distribution Behind Wing in the Vertical Plane for $\delta = 0^\circ$

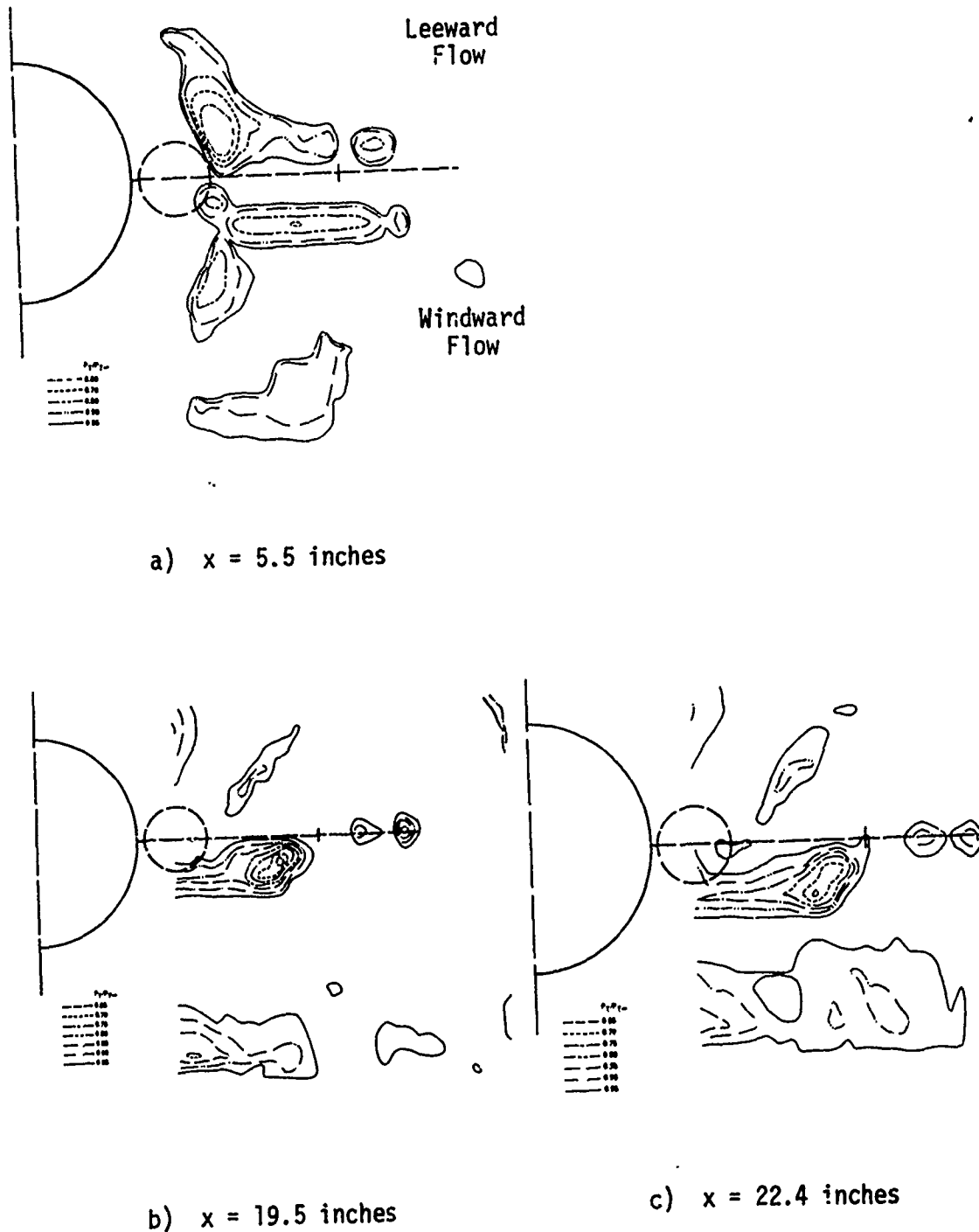


Figure 12 - Total Pressure Distribution Behind Wing 1 at $\delta = 5^\circ$

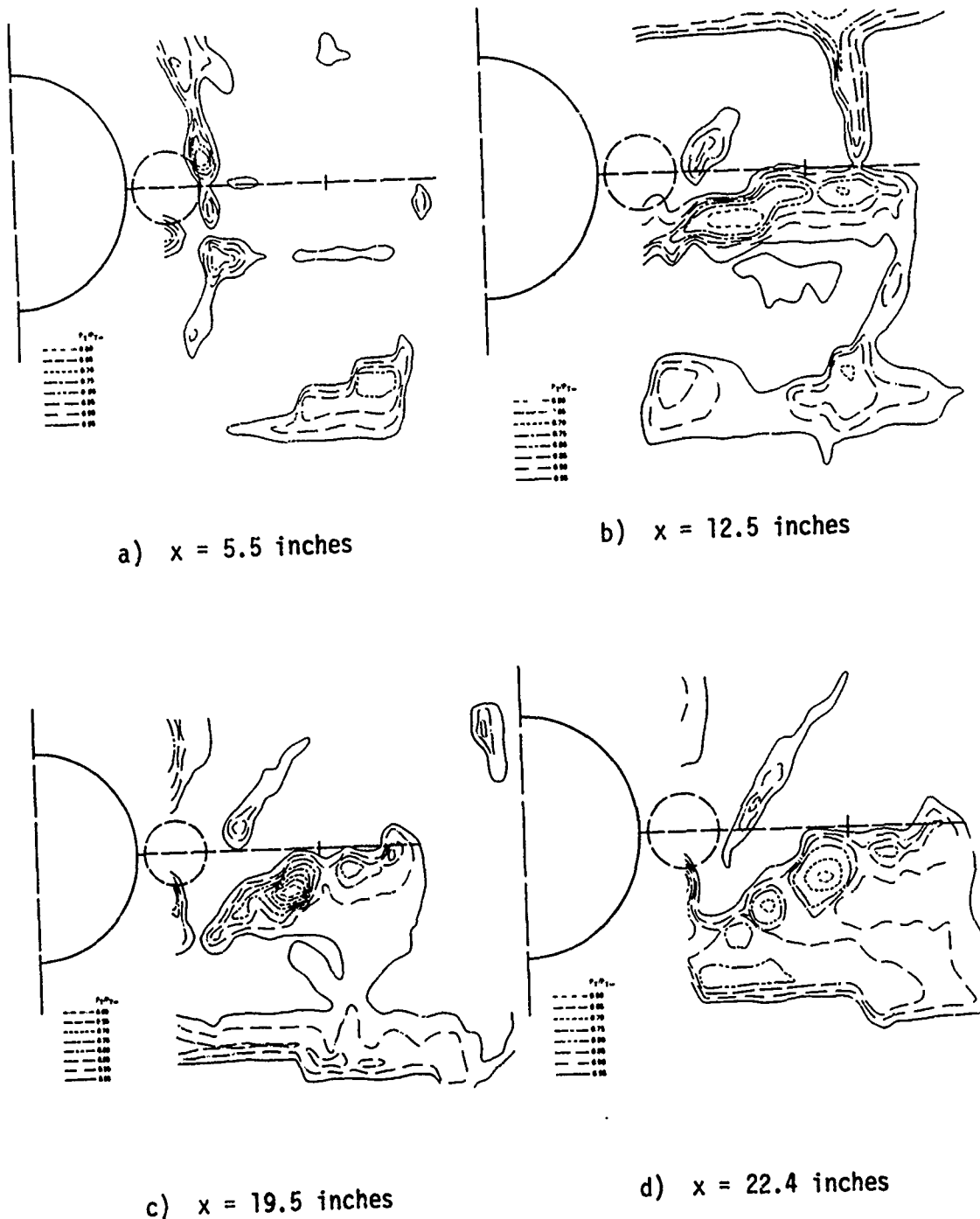


Figure 13- Total Pressure Distribution Behind Wing 1 at $\delta = 11^\circ$

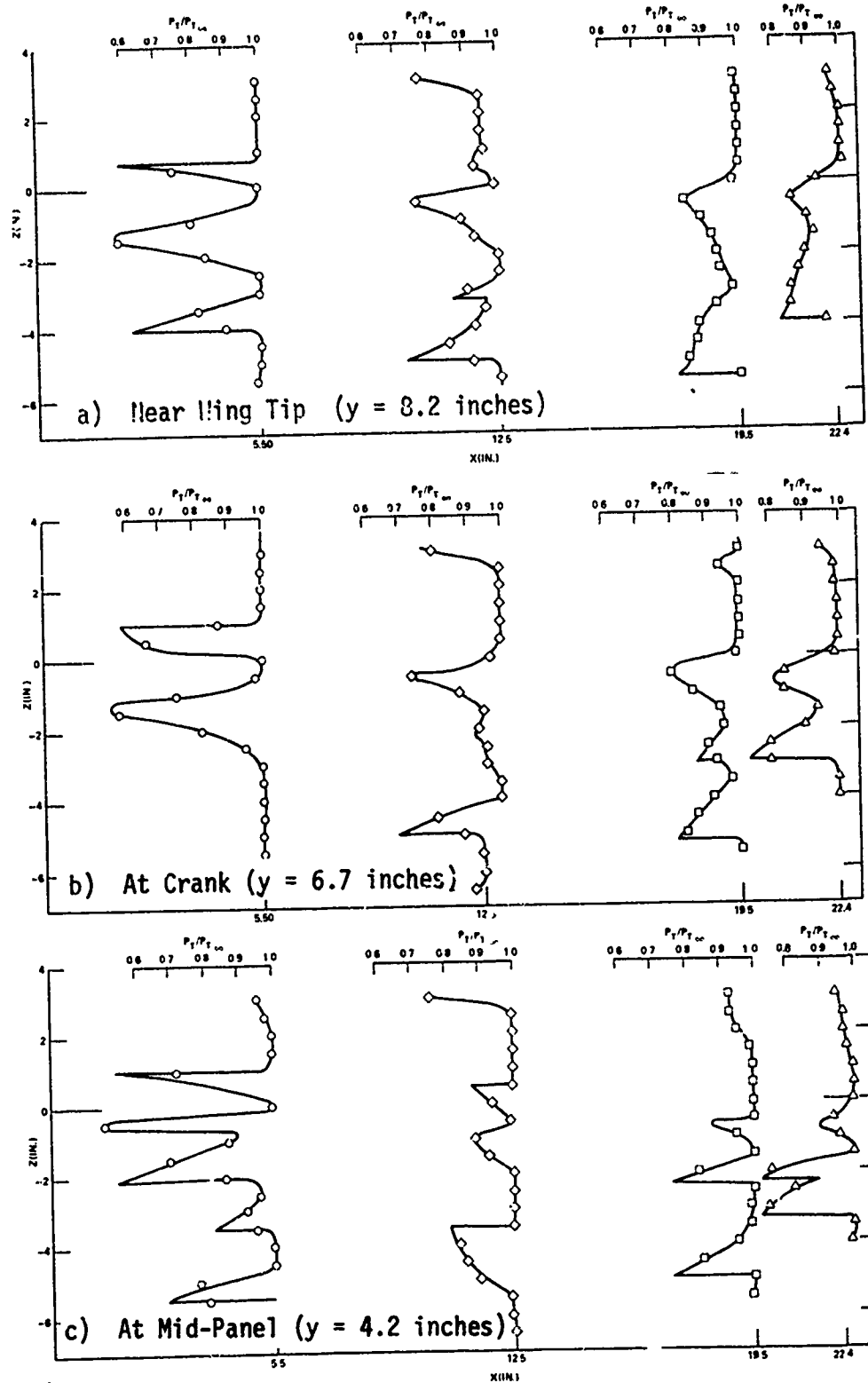


Figure 14 - Wing Wake Total Pressure Distribution Behind Wing 1 in the Vertical Plane for $\alpha = 11^\circ$

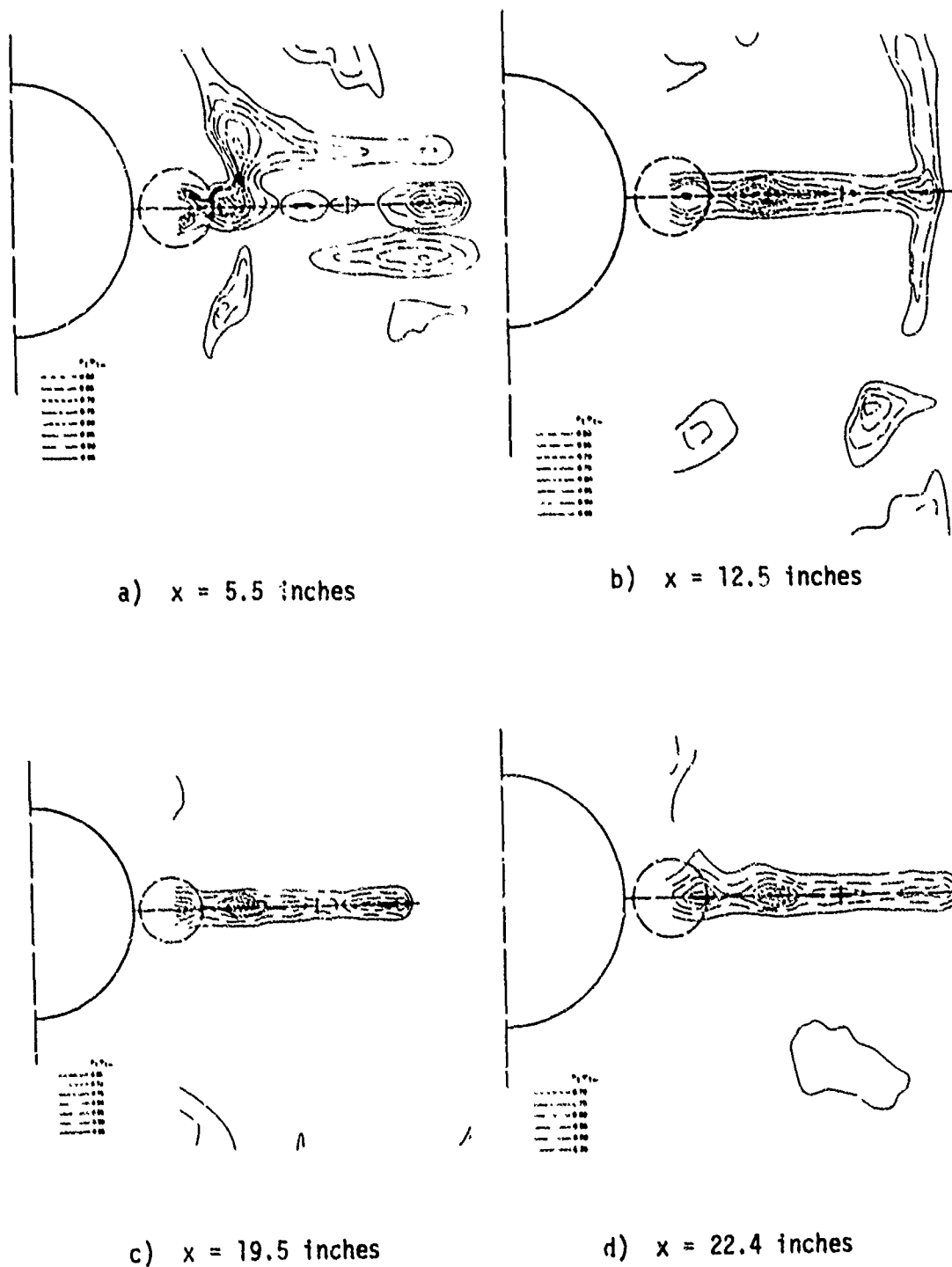
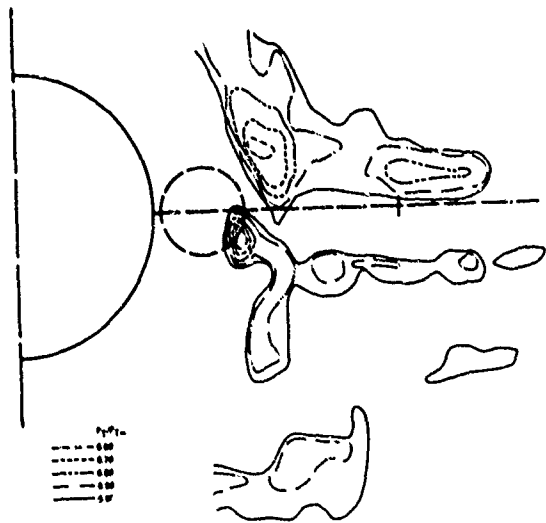
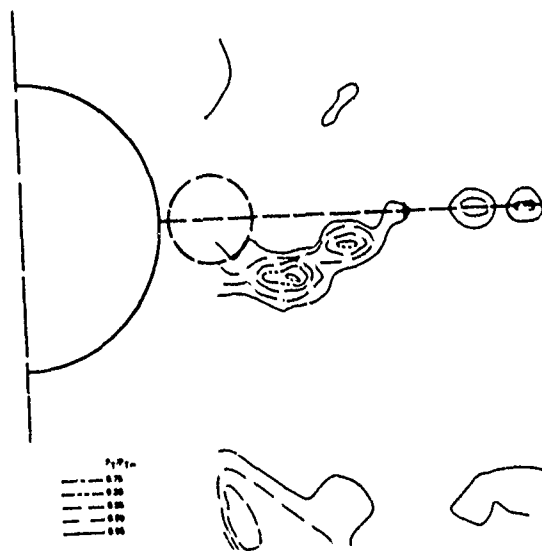


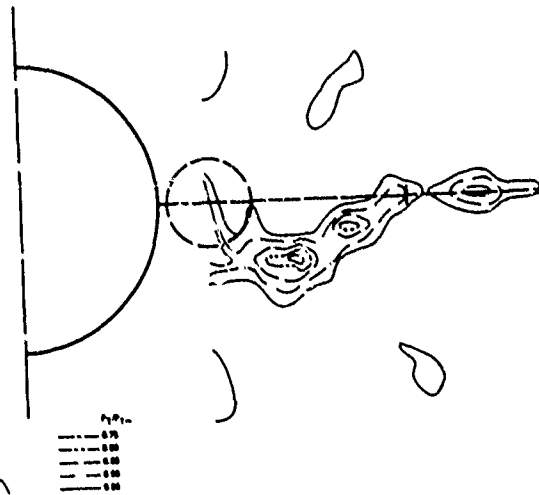
Figure 15 - Total Pressure Distribution Behind Wing 2 at $\delta = 0^\circ$



a) $x = 5.5$ inches



b) $x = 19.5$ inches



c) $x = 22.4$ inches

Figure 16 - Total Pressure Distribution Behind Wing 2 at $\delta = 5^\circ$

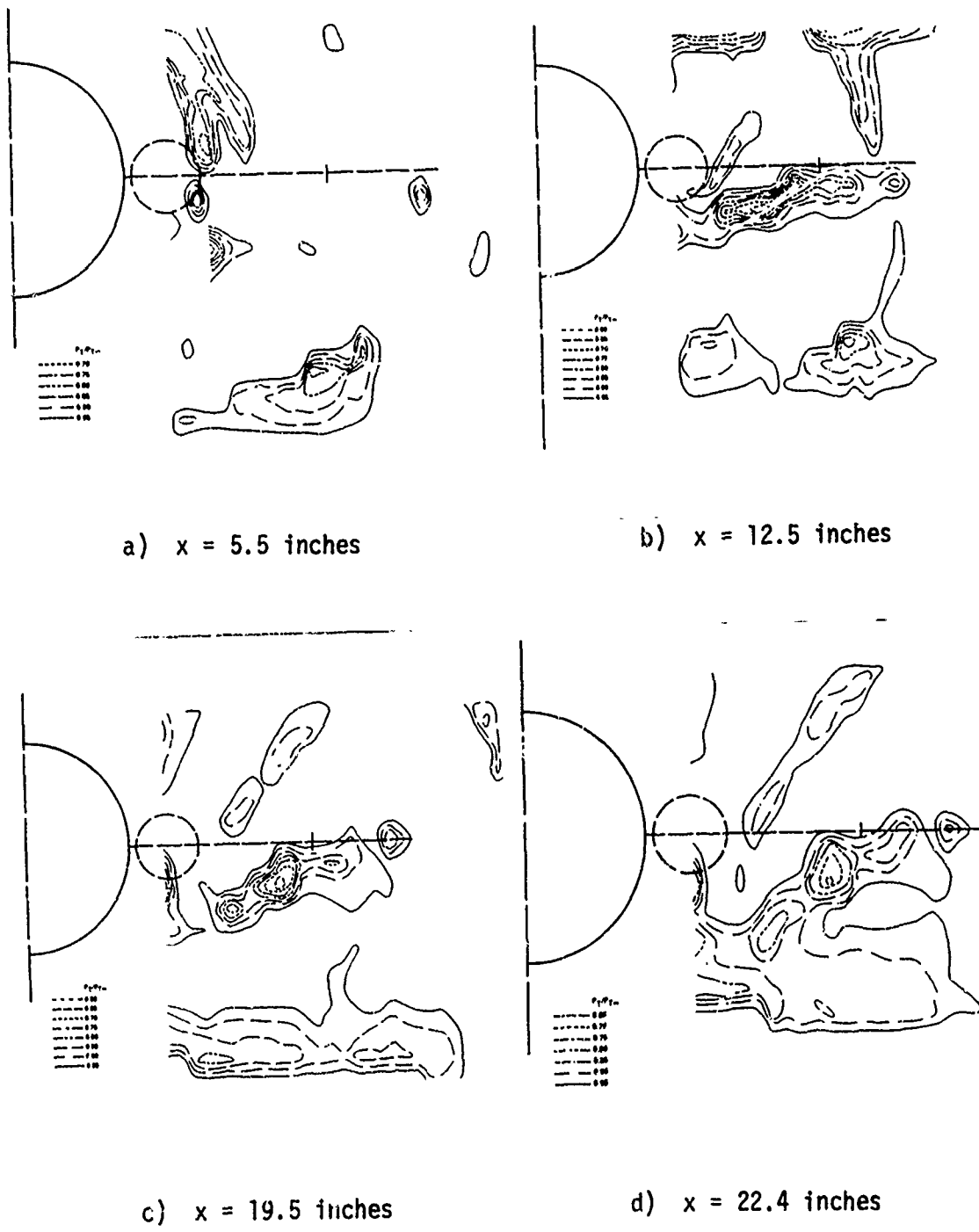


Figure 17 - Total Pressure Distribution Behind Wing 2 at $\delta = 11^\circ$

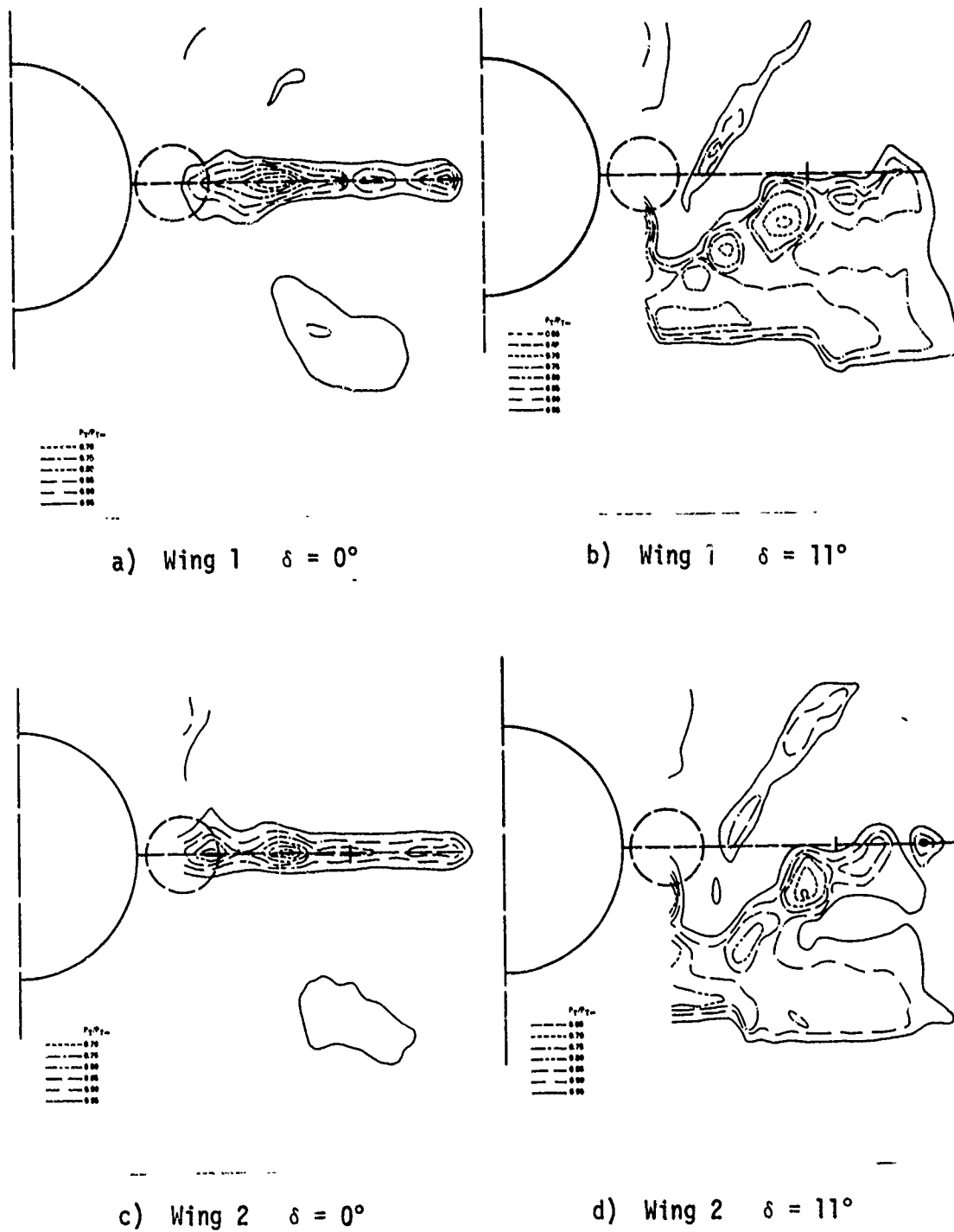


Figure 18 - The Effect of Thickness Ratio on Total Pressure Distribution for Wings 1 and 2 at $x = 22.4$ inches

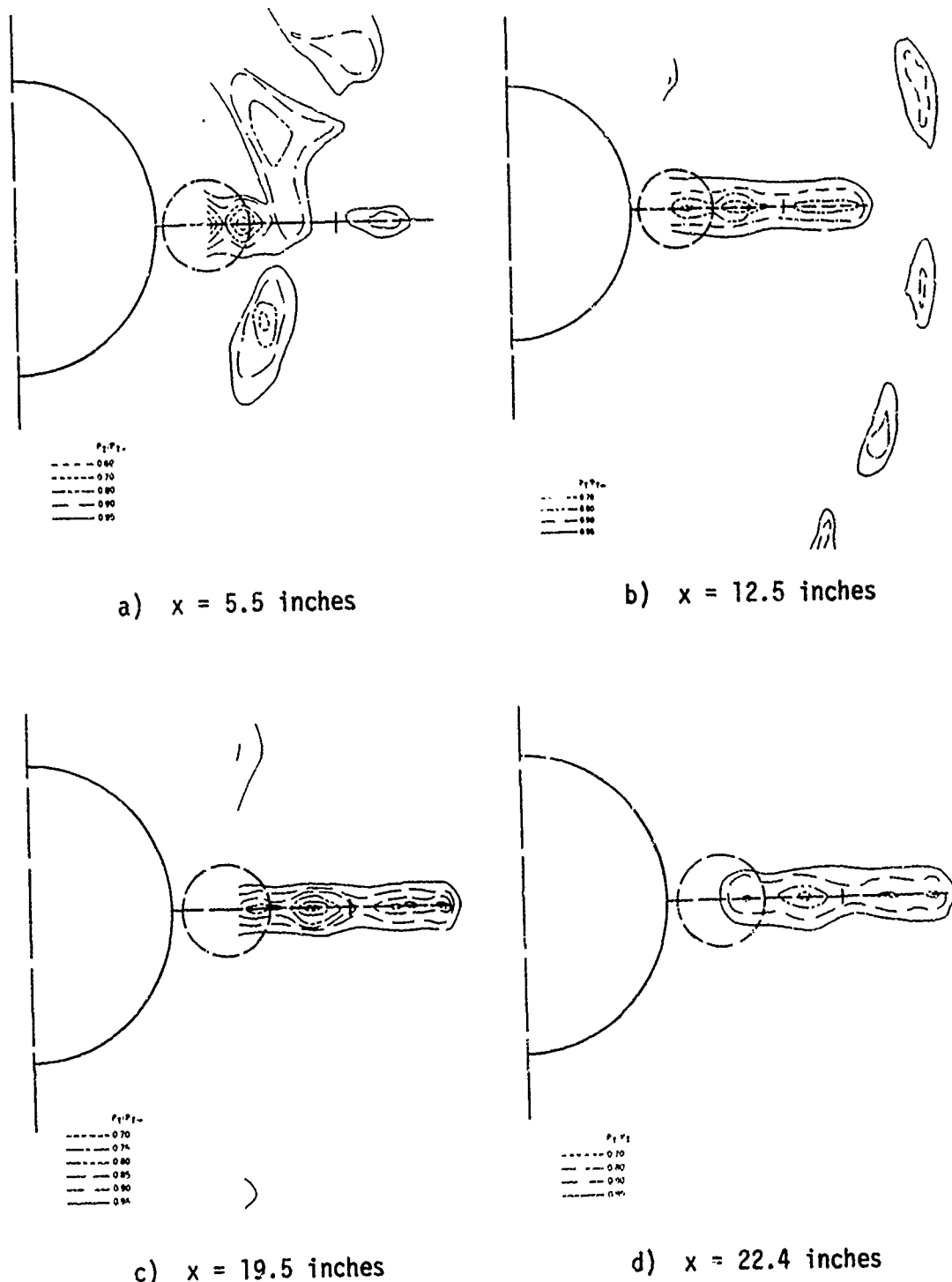
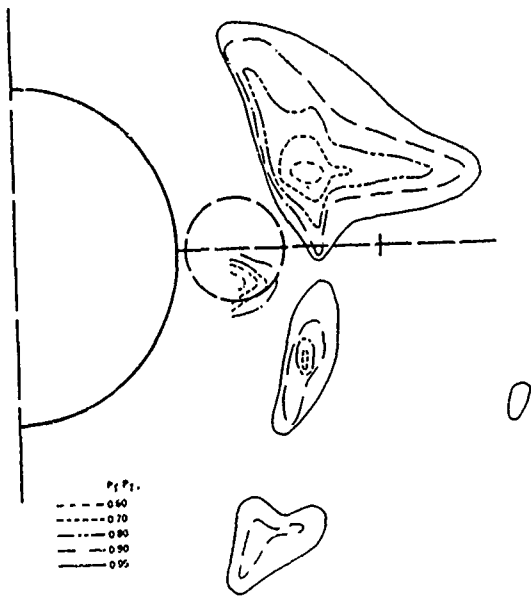
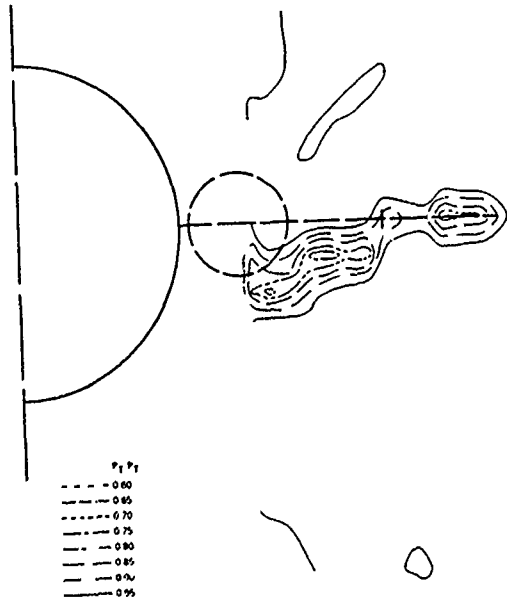


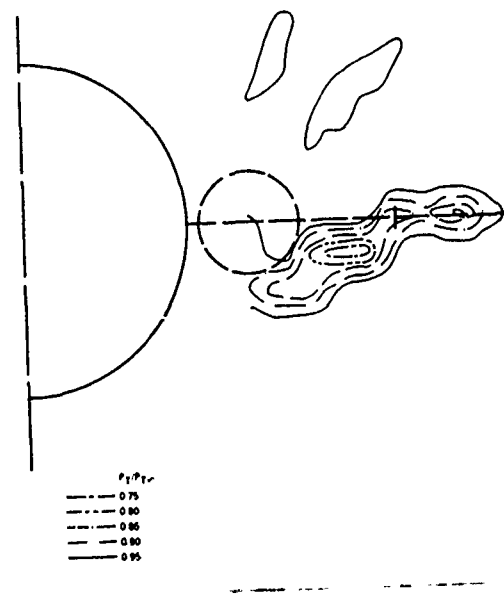
Figure 19 - Total Pressure Distribution Behind Wing 3 at $\delta = 0^\circ$



a) $x = 5.5$ inches

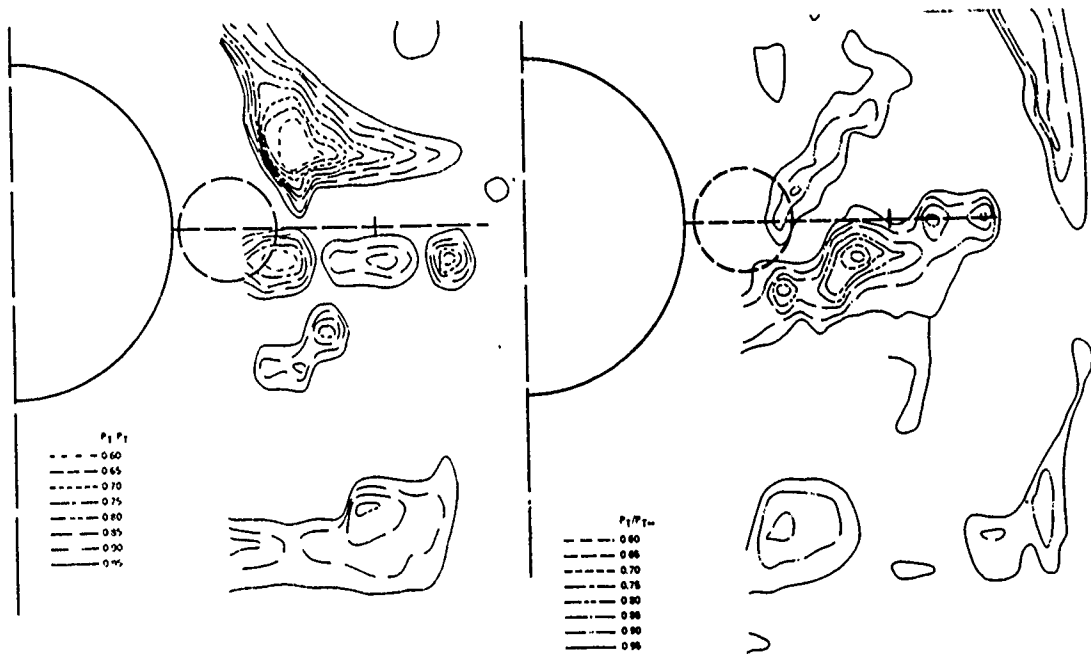


b) $x = 19.5$ inches



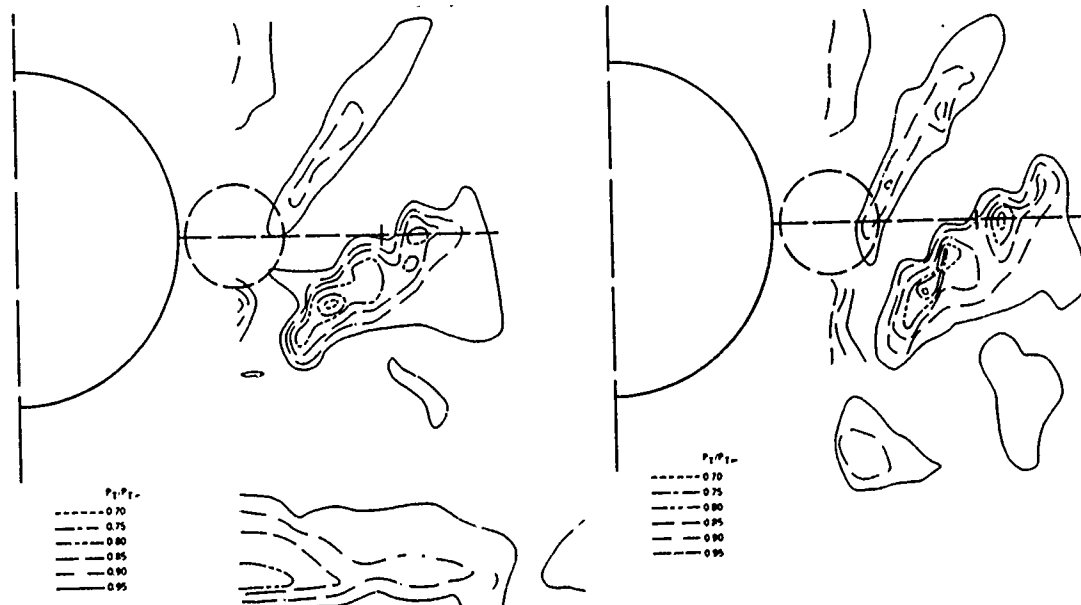
c) $x = 22.4$ inches

Figure 20 - Total Pressure Distribution Behind Wing 3 at $\delta = 5^\circ$



a) a) $x = 5.5$ inches

b) $x = 12.5$ inches



c) $x = 19.5$ inches

d) $x = 22.4$ inches

Figure 21 - Total Pressure Distribution Behind Wing 3 at $\delta = 11^\circ$

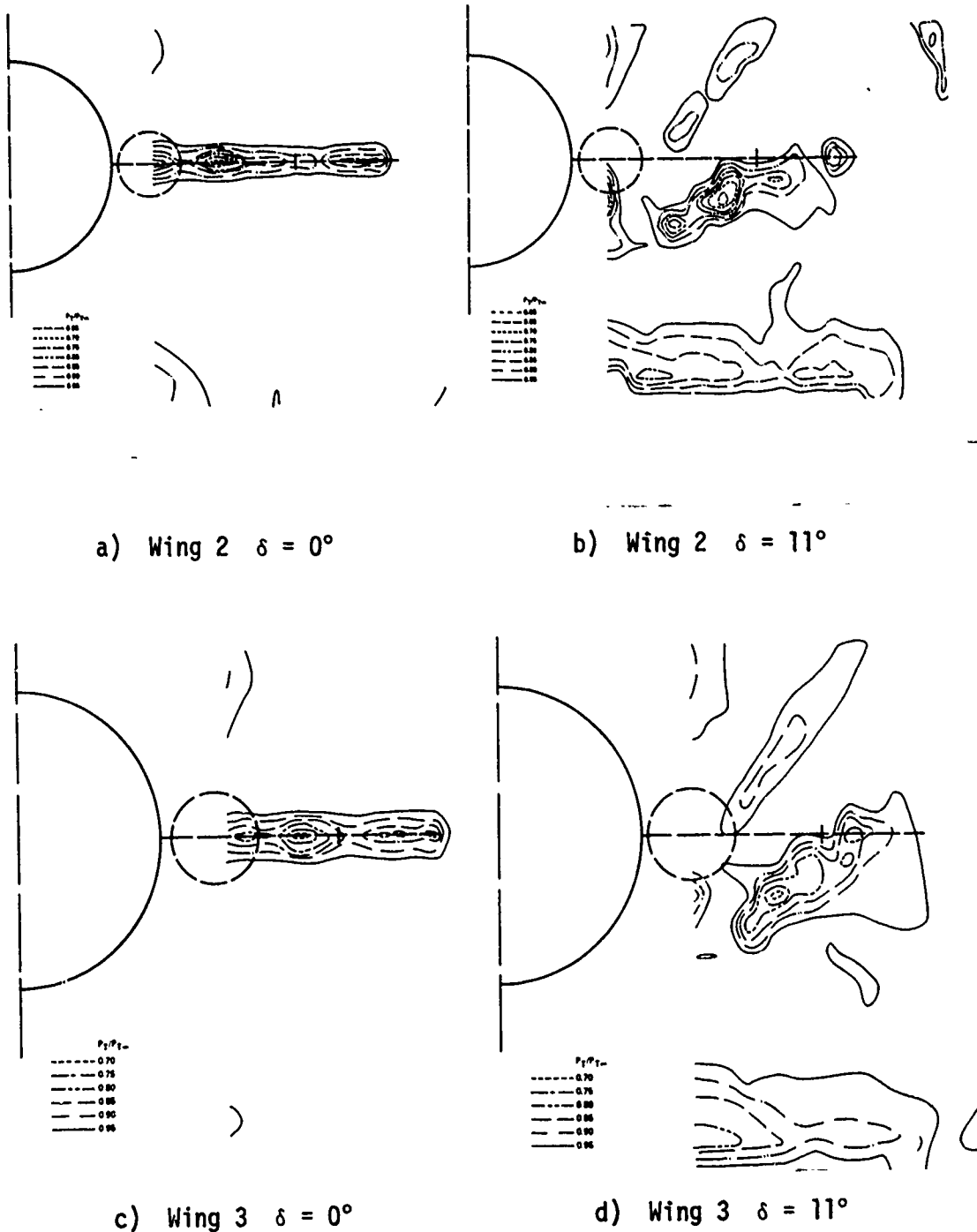


Figure 22 - Effect of Wing Deflection and Wing Planform on Total Pressure Distribution for Wings 2 and 3 at $x = 19.5$

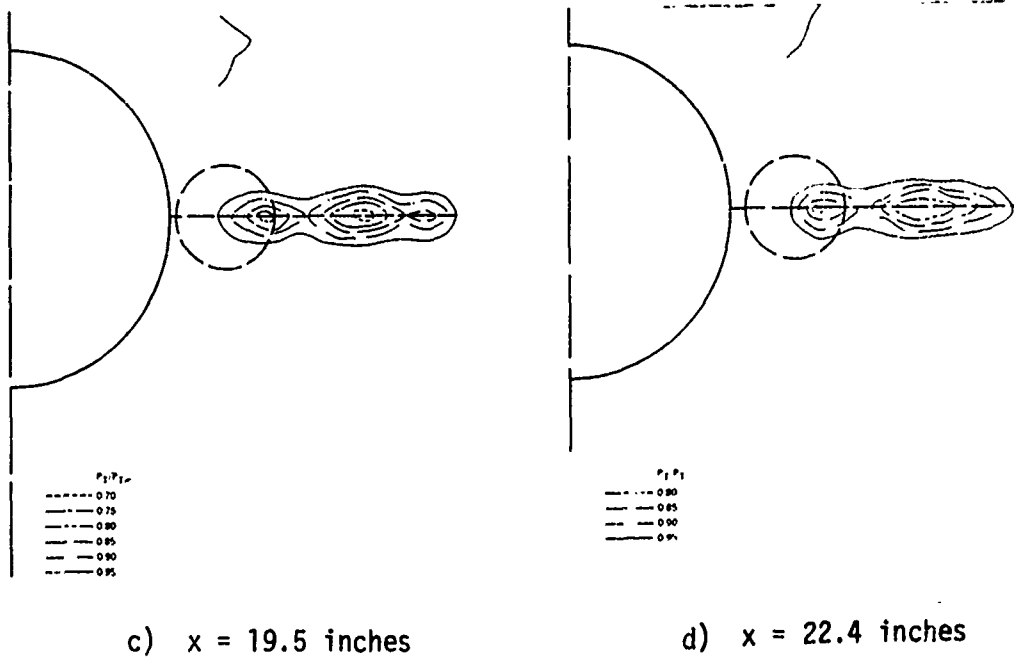
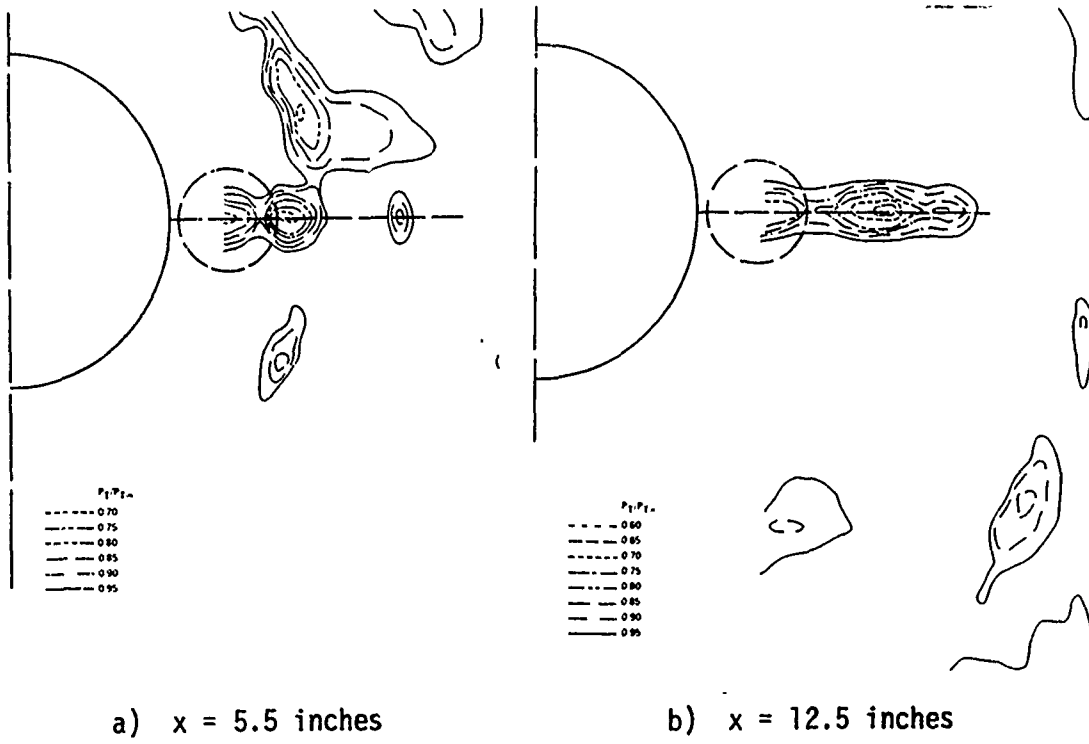
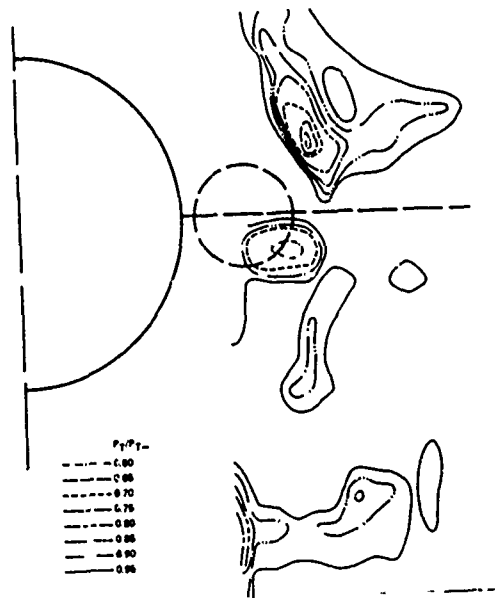
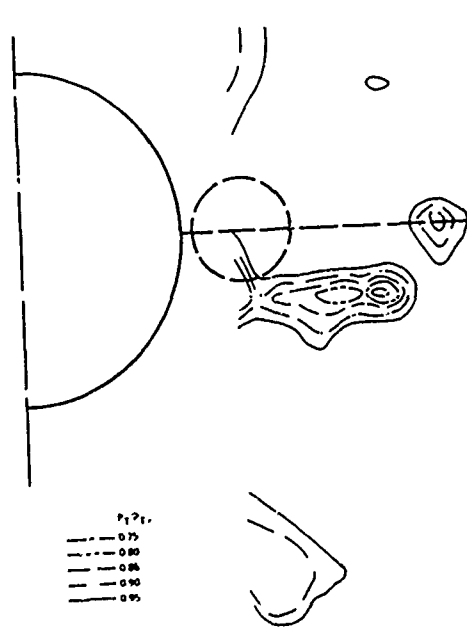


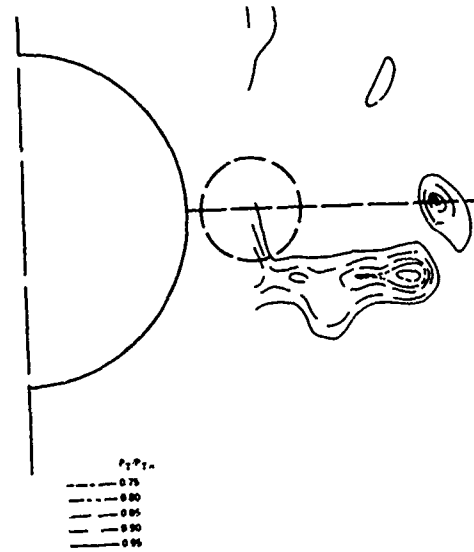
Figure 23 - Total Pressure Distribution Behind Wing 4 at $\delta = 0^\circ$



a) $x = 5.5$ inches



b) $x = 19.5$ inches



c) $x = 22.4$ inches

Figure 24 - Total Pressure Distribution Behind Wing 4 at $\delta = 8^\circ$

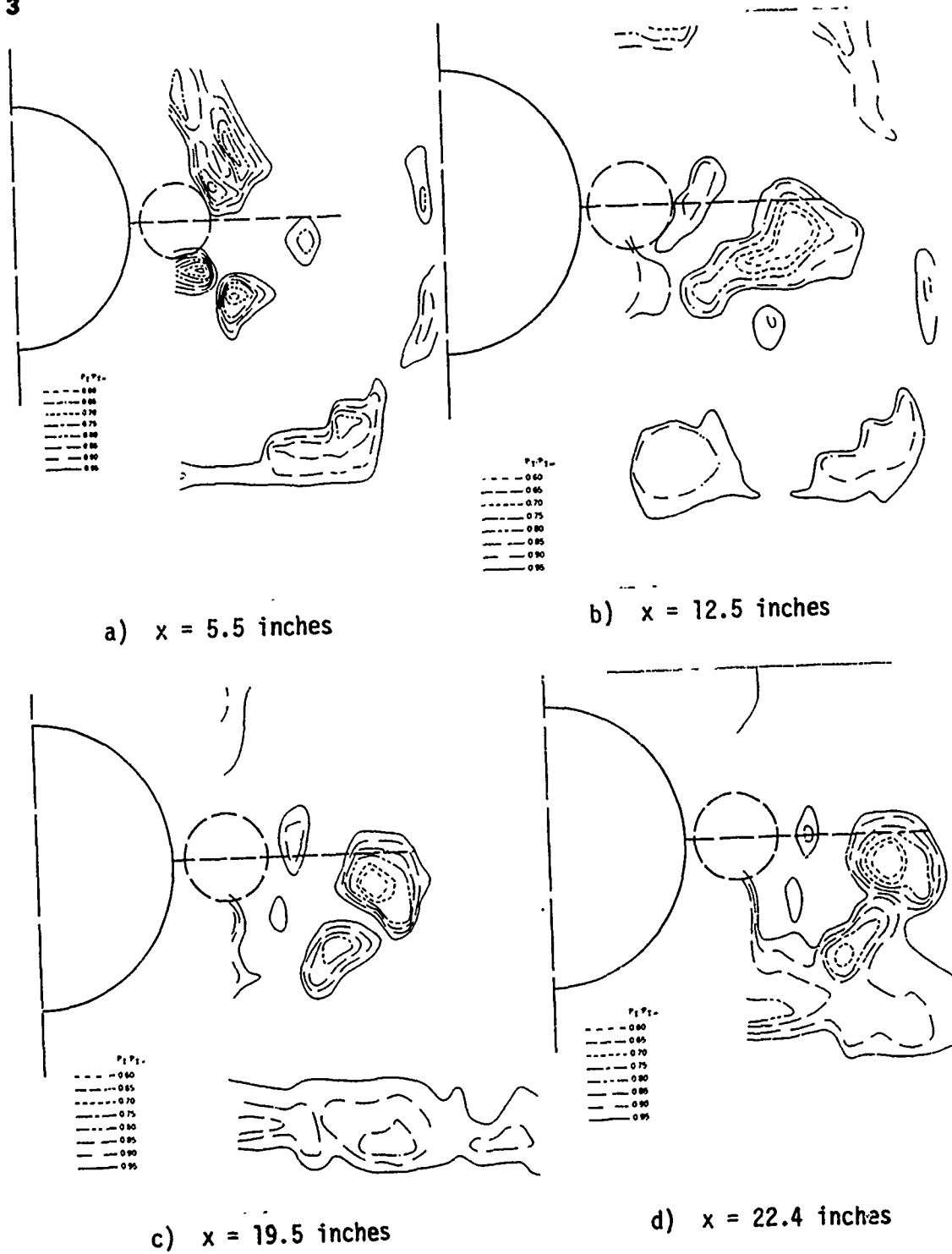
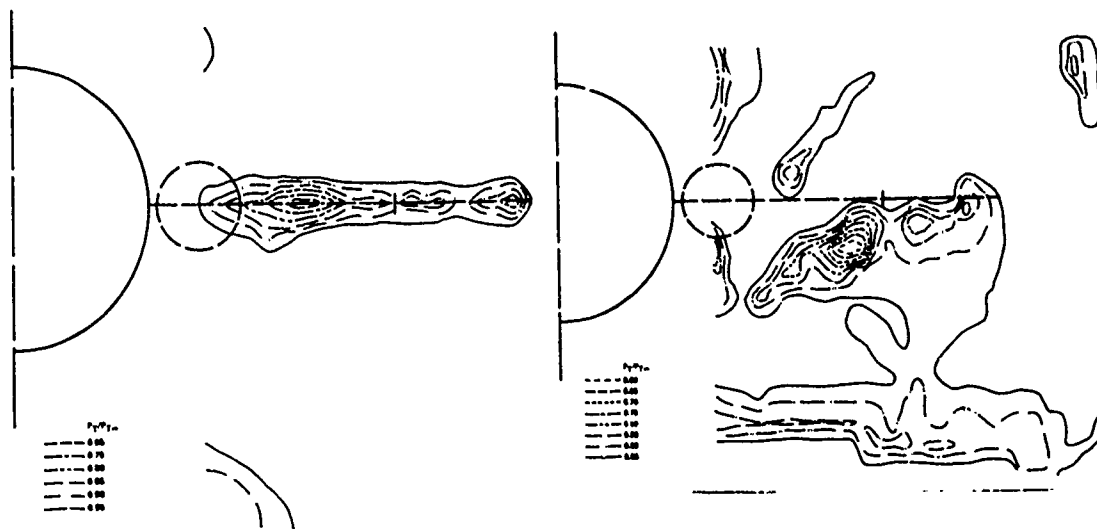
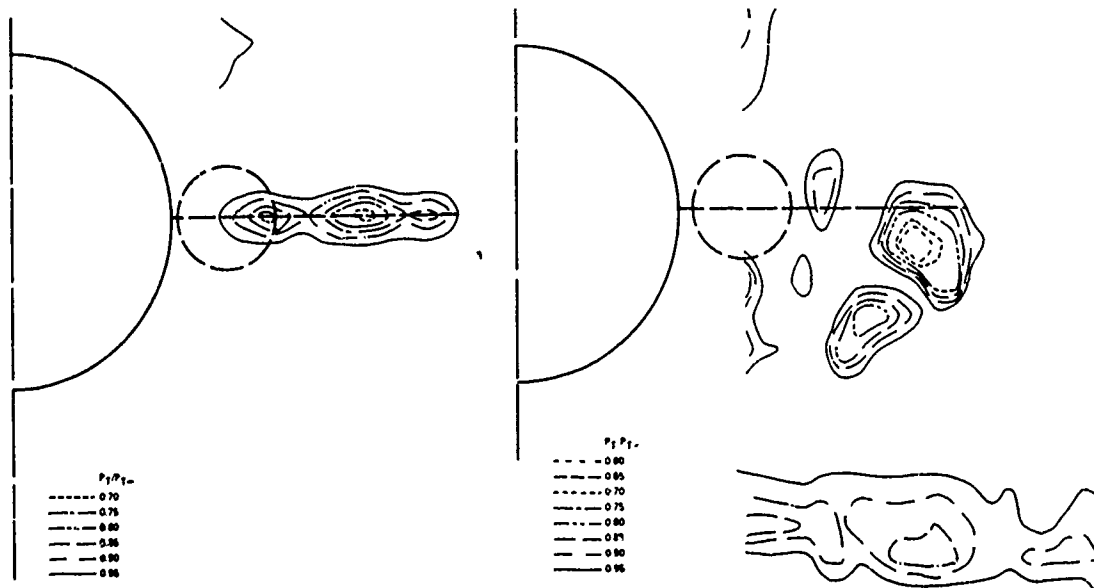


Figure 25 - Total Pressure Distribution Behind Wing 1 at $\delta = 11^\circ$



a) Wing 1 $\delta = 0^\circ$

b) Wing 1 $\delta = 11^\circ$



c) Wing 4 $\delta = 0^\circ$

d) Wing 4 $\delta = 11^\circ$

Figure 26 - Effect of Wing Deflection and Wing Planform on Total Pressure Distribution for Wings 1 and 4 at $x = 19.5$

PAPER NO. 34

TWO DIMENSIONAL ANALYSIS OF BASE DRAG
REDUCTION USING EXTERNAL BURNING

by

Robert J. Cavalleri

ATLANTIC RESEARCH CORPORATION
Alexandria, Virginia

NOMENCLATURE

- p - Static pressure
- p_0 - Total pressure
- T_0 - Total temperature
- M - Mach number
- μ - Mach angle
- θ - Flow angle
- x, y - Cartesian co-ordinates
- h_0 - Total enthalpy
- \bar{s} - Entropy divided by gas constant ($\frac{S}{R}$)
- W - Velocity divided by stagnation sound speed ($\frac{q}{a_t}$)
- γ - Ratio of specific heats
- q - Velocity
- a - Speed of sound
- \bar{h}_0 - Total enthalpy divided by stagnation sound speed ($\frac{h_0}{a_t^2}$)
- \dot{m} - Fuel flow rate
- δ_0 - Distance to zero velocity line
- η - y/δ_0
- u - Axial velocity
- v - Vertical velocity

Subscripts

- ∞ - Free stream
- b - Base
- o - Zero velocity line

INTRODUCTION

The concept of supersonic base drag reduction using external burning has been previously investigated by using a simplified, one-dimensional, analytical model¹ or by using a more-complicated, two-dimensional analysis² of a mixing and reacting flow. A similar problem, supersonic base flow, has led to analytical techniques which appear capable of treating the pertinent flow field phenomena. The intent of the work presented in this article is to use approaches and techniques similar to those developed for the supersonic base-flow problem in conjunction with experimental, external-burning, wind-tunnel tests as a basis for a two-dimensional theoretical analysis and for interpreting some of the data.

In the analytical model under consideration, the flow is divided into three regions as illustrated in Figure 1. These three regions consist of an outer inviscid flow region, an inner recirculating flow region and an intermediate region that connects the base flow and inviscid flow regions. An appropriate analytical technique for the intermediate region has not been selected, however, and thus will not be discussed in this article. In order to simplify the outer inviscid flow analysis, the assumption is made that the combustion is complete at the model lip. This assumption is valid providing that the mixing and combustion occur in a relatively short distance. The initial lip conditions required for the inviscid outer flow were obtained using the results and models of jet penetration into a supersonic stream^{3,4}. The flow model for the recirculating base region uses an integral technique based on experimental and theoretical base-flow results.

EXPERIMENTAL MODEL AND TEST DATA

The experimental external burning data was obtained on an eight-inch diameter, axisymmetric body. The body extended into the nozzle and actually was an integral part of the nozzle. The experimental test configuration and the configuration of the model are illustrated in Figures 2 and 3. The fuel was injected through 16 ports equally spaced around the periphery of the model. The ports were located 1.5 inches upstream of the model lip. The instrumentation consisted of static pressure taps on the model upstream of the lip, pressure taps and thermocouples on the base, pressure taps on the wind tunnel wall, a pitot static probe and a base sting with static pressure taps and thermocouples. The centerline pressure distribution on the base sting for a fuel flow rate of .6 lbm/sec is shown in Figure 4*. The free stream conditions for this case are $p_{0\infty} = 35$ psia, $T_{0\infty} = 710^\circ\text{R}$, and $M_\infty = 2$, whereas the motor chamber pressure for this case is 320 psia. Also shown in Figure 4 is the centerline pressure distribution for the case of no fuel flow and the centerline static pressure distribution of reference 5. The test conditions for reference 5 were for a model diameter of .93 inches and a freestream Mach number of 2.4. The measured boundary layer profile 26.5 inches upstream of the model base is shown in Figure 5. This profile was used as an initial input profile to the turbulent boundary layer analysis of reference 6, so that the boundary layer with no fuel flow at the model lip could be determined. The results of this calculation are also shown in Figure 5.

* There is some question as to the validity of the data that was obtained due to the possibility of interference effects of the downstream flow in the diffuser on the model base pressure. Thus, the specific impulse and thrust coefficient values that are mentioned later on may, to some extent, be in error.

OUTER INVISCID FLOW ANALYSIS

As mentioned previously, the method of characteristics for a non-isentropic (rotational), non-adiabatic flow is employed in the outer flow region. An approach similar to this (rotational characteristics) has been applied by other investigators⁷ to the supersonic base flow problem. The equations employed in this analysis are:

Characteristics directions

$$\frac{dy}{dx} = \tan(\theta + \mu) \quad \text{uprunning characteristics}$$

$$\frac{dy}{dx} = \tan(\theta - \mu) \quad \text{downrunning characteristics}$$

Compatibility equations

along an uprunning characteristic

$$d\theta = \frac{dW}{W \tan \mu} + \frac{\sin 2\mu d\bar{s}}{2\gamma} - \frac{d\bar{h}_0}{W^2 \tan \mu} - \frac{\epsilon \sin \theta \sin \mu dx}{\cos(\theta + \mu) y}$$

along a downrunning characteristic

$$d\theta = \frac{-dW}{W \tan \mu} - \frac{\sin 2\mu d\bar{s}}{2\gamma} + \frac{d\bar{h}_0}{W^2 \tan \mu} + \frac{\epsilon \sin \theta \sin \mu dx}{\cos(\theta - \mu) y}$$

along a streamline

$$\bar{s} = \text{entropy} = \text{constant}$$

$$\bar{h}_0 = \text{total enthalpy} = \text{constant}$$

where $\epsilon = 0$ for two dimensional flow and $\epsilon = 1$ for axisymmetric flow.

The inherent restriction in the above approach is that there is no chemical reaction occurring at the location where the analysis is initiated. Thus, the combustion must be essentially complete in a short distance downstream of the injection station. It is believed that this restriction is not unrealistic since in order for the combustion region to efficiently reduce the base drag, the bulk of the combustion region

Vol. 3

should be upstream of the model lip.

The case for the data presented in Figure 4 for $\dot{m} = 0$ and for the data from reference 5 was analyzed first so as to estimate the level of confidence in the approach. The initial profile used for the method of characteristics calculation includes the supersonic portion of the boundary layer; thus the data of Figures 5 and 6 were used as initial conditions for the characteristics calculations. The results of these two calculations are shown in Figures 7 and 8. The work of reference 5, which is exceptionally detailed, experimentally determined the location of the dividing streamline and the zero velocity line. This data is presented in Figure 7 along with the results of the method-of-characteristics calculation. As can be seen from the figure, the agreement between the calculation and the experiment is very good. The data obtained in the current tests was not as detailed as that of reference 5; thus no definitive statement can be made concerning the accuracy of the results of Figure 8. The overall shape of the centerline pressure distribution and the dividing streamlines have the same overall shape even though the models differed in size by an order of magnitude. In general, the theoretical results indicate that, for distances in the x direction of one base diameter, the method of characteristics gives good agreement with the data.

The analysis was then used to do a parametric study to determine the effect of the initial external burning profile on the flow field using the experimental centerline pressure distribution for a fuel flow rate of .6 lbm/sec. The initial data used in the calculation was obtained using the empirical results of references 3 and 4 to obtain a value for the Mach number and total pressure in the vicinity of the

fuel jet core region at the model lip; these values are 1.5 and 17 psia, respectively. The initial profiles used are shown in Figure 9. The results of the calculations are illustrated in Figures 10 and 11. The maximum total temperature that could be used without the program stopping was 1100°R . Values higher than this resulted in extreme distortions of the flow field with the flow going subsonic slightly downstream of the model lip. The implication of this is that either the method of analysis is inappropriate at the higher temperatures or that the maximum temperature that produces the measured pressure distribution is around 1100°R . To get an estimate for the lower limit of the temperature, thermochemistry calculations were made for fuel-to-air ratios of 30 and 15. The fuel-to-air ratio of 30 corresponds to the situation when the maximum amount of air captured by the area wetted by the fuel combusts with the fuel. The total temperature for these two fuel ratios, 30 and 15, are 1429°R and 2178°R , respectively. Thus, using a value of 1100°R for the total temperature is not unrealistic providing that the combustion occurs in a short distance.

The results of the calculations indicate that the combustion-generated compression field tends to force the dividing streamline towards the centerline. The presence of the boundary layer at the model lip tends to relieve some of the effect of the compression. The most interesting result of the calculation is that the compression that impinges on the wake pressure boundary is reflected as an expansion. This effect is opposite to that of a non-external-burning flow field where the corner expansion reflects as a compression which can eventually result in the so-called lip shock.

The case for the profile labeled 3 in Figure 9 was intended to determine the effect of a lower Mach number profile. This case, however, resulted in the flow going subsonic slightly downstream of the model lip.

Since the compression field impinging on the recirculating region is reflected as an opposite family expansion, there exists the possibility of increasing the base pressure by extending the body. This results in the compression field impinging on a solid wall where it is reflected as a compression. The results for an extended body using profile 2 (the lower profile shape is due to the presence of a boundary layer) are shown in Figure 12. At a distance of .37 inches downstream from the initial data line the flow goes subsonic while the pressure reaches a value of 9.17 psia. If the base pressure increases by a corresponding amount, then the specific impulse would increase from a value of 300 for $p_b = 5.98$ to a value of 547 for $p_b = 7.31$ psia, likewise the thrust coefficient would increase from a value of .288 to a value of .525.

INNER BASE FLOW REGION

Previous methods of analysis of the supersonic base flow region have employed either an integral technique⁸ or the solution of the Navier Stokes Equations.⁷ In an attempt to employ a somewhat simpler technique a slightly different approach is adapted. Rather than using the dividing streamline as a dividing boundary between the inner and outer flow regions, the zero velocity line as illustrated in Figure 1 is employed. The motivation behind this approach is that if the velocity is low enough in the recirculating flow region, the flow

can be assumed to be either incompressible or at least the energy equation and momentum equation can be decoupled. This results in requiring a velocity profile for only the velocity. Also, the pressure can be considered at most to be only a function of x .

The equations employed for the recirculating flow region are the boundary layer equations. The velocity profile used in this region is

$$u = -a \left(1 - \frac{3}{2} \eta^2 + \frac{1}{2} \eta^3 \right)$$

$$\text{where } \eta = \frac{y}{\delta_0}$$

This profile satisfies the following boundary conditions:

$$\eta = 0 \quad \frac{\partial u}{\partial \eta} = 0$$

$$\eta = 1 \quad u = 0 \quad \frac{\partial^2 u}{\partial \eta^2} = 0$$

This profile is substituted into the continuity equation for an axisymmetric flow to determine an equation for the vertical v velocity component. This result and the u velocity profile are then substituted into the x -momentum equation. The resulting equation is then integrated with respect to η . This yields an ordinary differential equation for $a(x)$ which is

$$\frac{5453}{7840} a \frac{da}{dx} = \frac{\tau_0}{\rho \delta_0} - \frac{dp}{dx} \left(\frac{1}{\rho} + \frac{47}{224} \frac{a^2}{p} \right)$$

where τ_0 is the shear stress at the upper boundary δ_0 .

It should be mentioned that in the above equation the temperature has been assumed to be constant, thus $\rho = \frac{p}{RT}$ and the quantity RT is constant. The experimental results tend to verify that T is constant in the base flow region. There is one empirical constant that must be

Vol. 3

determined in the above equation, namely the stress τ_0 . The stress was assumed to be given by the relationship

$$\tau_0 = K \mu_L \left(\frac{\partial u}{\partial y} \right)_{y = \delta_0}$$

where μ_L = laminar viscosity and K = empirical constant.

The data of reference 5 was used to determine an empirical value of K . The results of the calculations are shown in Figures 13a, 13b and 13c, for a value of K equal to 525, the value giving the best agreement with the experiment.

The integral technique, given above, was then used to determine the velocity profiles in the recirculating flow region for the external burning tests. The results for no fuel injection are shown in Figure 14, whereas the results for $\dot{m} = .6$ lbm/sec are shown in Figure 15. The velocity in this region is not small and approaches a value of $M = .8$. The results of Figure 14 also indicate that the extent of the predicted recirculating flow region is about one-half base diameter, whereas the results of Figure 13 indicate that the measured recirculating flow region for a smaller model is about one base diameter. This discrepancy may be due to the fact that the value of K and thus the turbulent shear stress at the zero velocity line is related to the scale of the experiment.

The results of Figure 15 indicate that the effect of the pressure gradient imposed by the external burning is to lengthen the extent of the recirculating flow field. The maximum velocity in the base region is reduced from 800 feet/second to 600 feet/second and the extent of the region increases by a factor of two. The experimental data obtained from a pitot static probe located 20 inches downstream

of the base indicated a decrease in centerline Mach number as fuel flow increased. This tends to agree with the trend indicated in Figures 14 and 15.

CONCLUSIONS AND RECOMMENDATIONS

All of the above calculations except for the cases of the data of reference 5 were obtained for initial data lines that have not been experimentally verified. Thus the above results can only be viewed as indications of what the flow field might actually be and should be considered as being qualitative. The calculations yield results, however, which tend to agree with the experimentally observed trends. This suggests that the approach forms a good analytical basis upon which a simplified predictive model can be developed.

The basic limitations of the above analyses lie in the uncertainty of the assumed initial-data line and the turbulent stress in the recirculating region. Any further experimental work that can eliminate these areas of uncertainty would result in a calibration of - and thus a higher degree of confidence in - the ability to analyze an external-burning flow field. These analytical techniques could then be used to optimize a particular configuration to obtain improved performance.

REFERENCES

- ¹ Strahle, W.C., "Theoretical Consideration of Combustion Effects on Base Pressure in Supersonic Flight," Twelfth Symposium on Combustion, Combustion Institute, Pittsburgh, Pennsylvania (1969).
- ² Fein, H.L. and Shelor, D.W., "An Investigation of External Burning Propulsion for the 75 mm Projectile," AFRPL-TR-72-133 (January 1973).
- ³ Billing, F.S., Orth, R.C., and Lasky, M., "A Unified Approach to the Problem of Gaseous Jet Penetration into a Supersonic Stream," AIAA Paper 70 - 93.
- ⁴ Hsia, H.T., "Equivalence of Secondary Injection to a Blunt Body in Supersonic Flow," AIAA Journal, Vol. 4, No. 10, pp 1832 - 1834 (October 1966).
- ⁵ Hong, Y.S., "A Study of Axially Symmetric Supersonic Base Flow with a Turbulent Initial Boundary Layer," Doctoral Thesis, Mechanical Engineering Department, University of Washington (1968).
- ⁶ Szsmen, P.K. and Cresci, R.J., "Compressible Turbulent Boundary Layer with Pressure Gradient and Heat Transfer," AIAA Journal, Vol. 4, No. 1, pp 19 - 25 (January 1966).
- ⁷ Weiss, R.F. and Weinbaum, S., "Hypersonic Boundary Layer Separation and the Base Flow Problem," AIAA Journal, Vol. 4, No. 8, pp 1321 - 1330 (August 1966).
- ⁸ Baum, E. and Denison, M.R., "Interacting Supersonic Laminar Wake Calculations by a Finite Difference Method," AIAA Journal, Vol. 5, pp 1224 - 1230 (1967).

FLOW FIELD MODEL

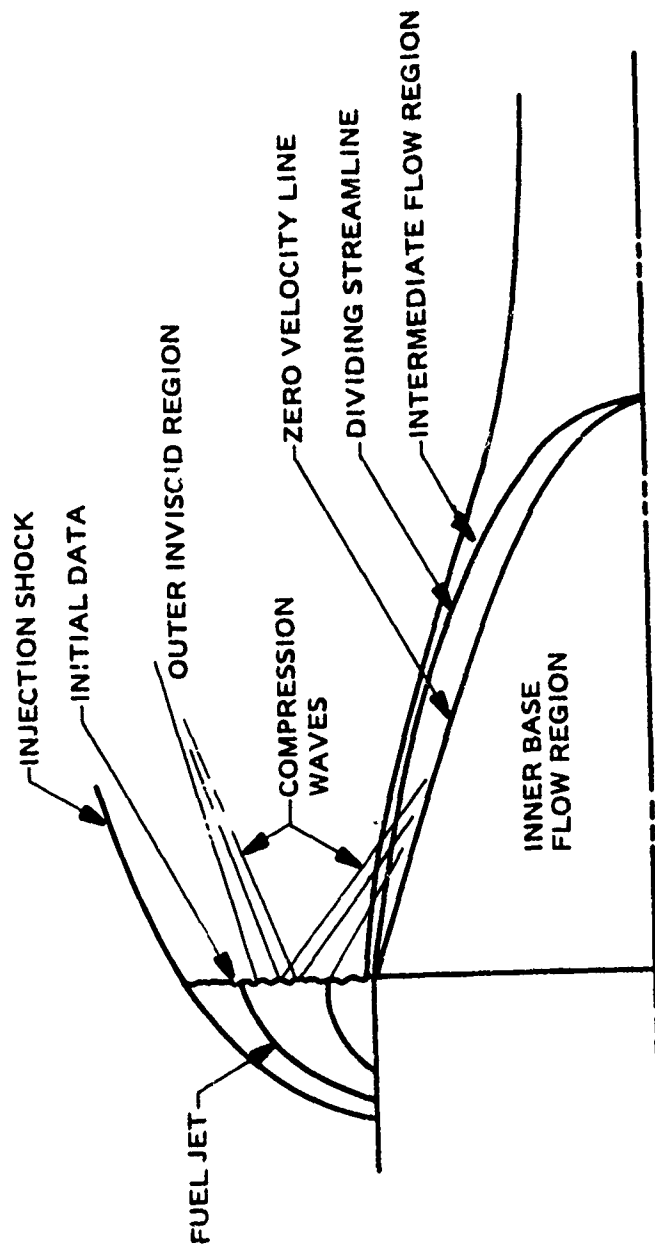


Figure 1. Flow Field Model.

TEST CONFIGURATION

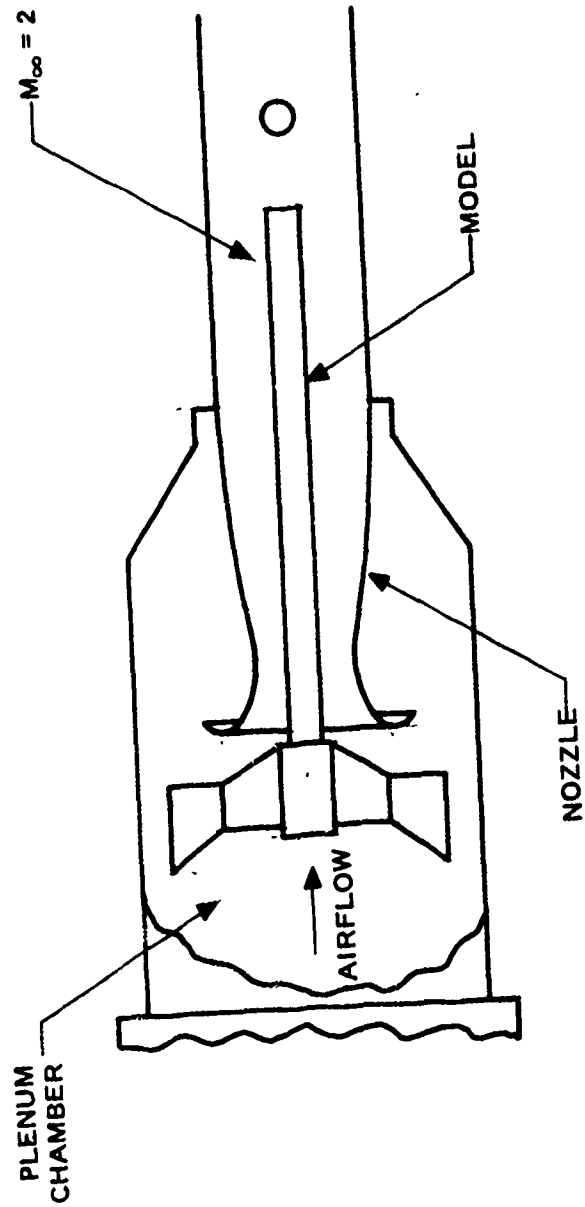


Figure 2. Test Configuration.

MODEL CONFIGURATION

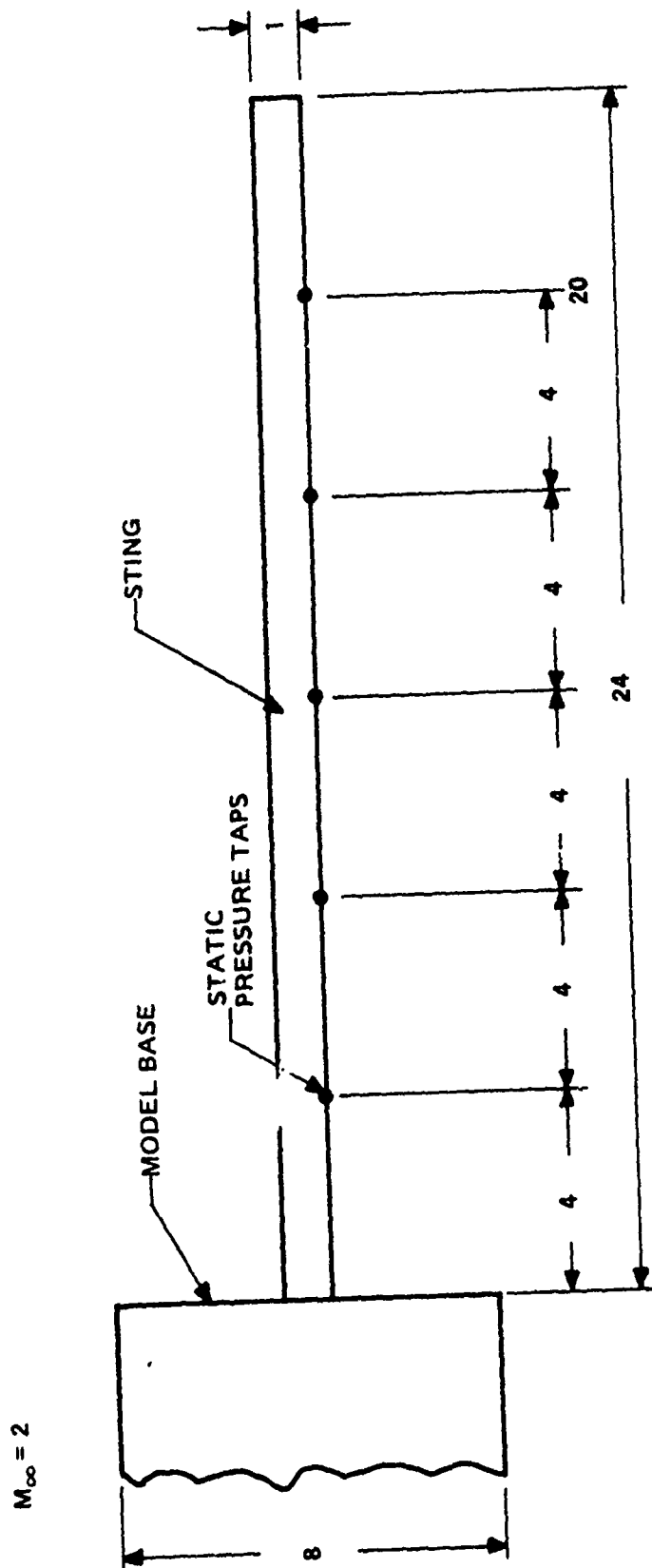


Figure 3. Model Configuration.

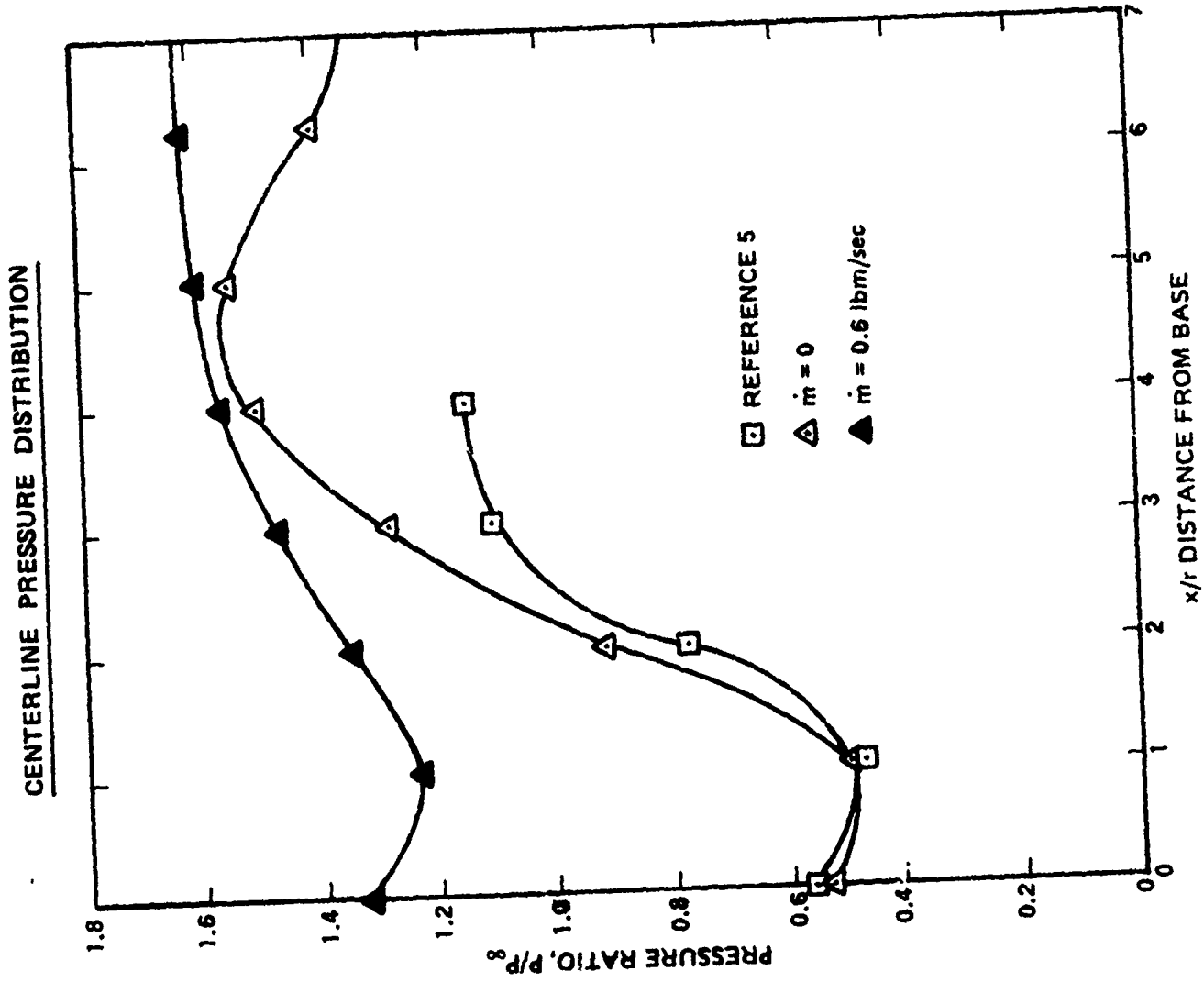


Figure 4. Centerline Pressure Distribution.

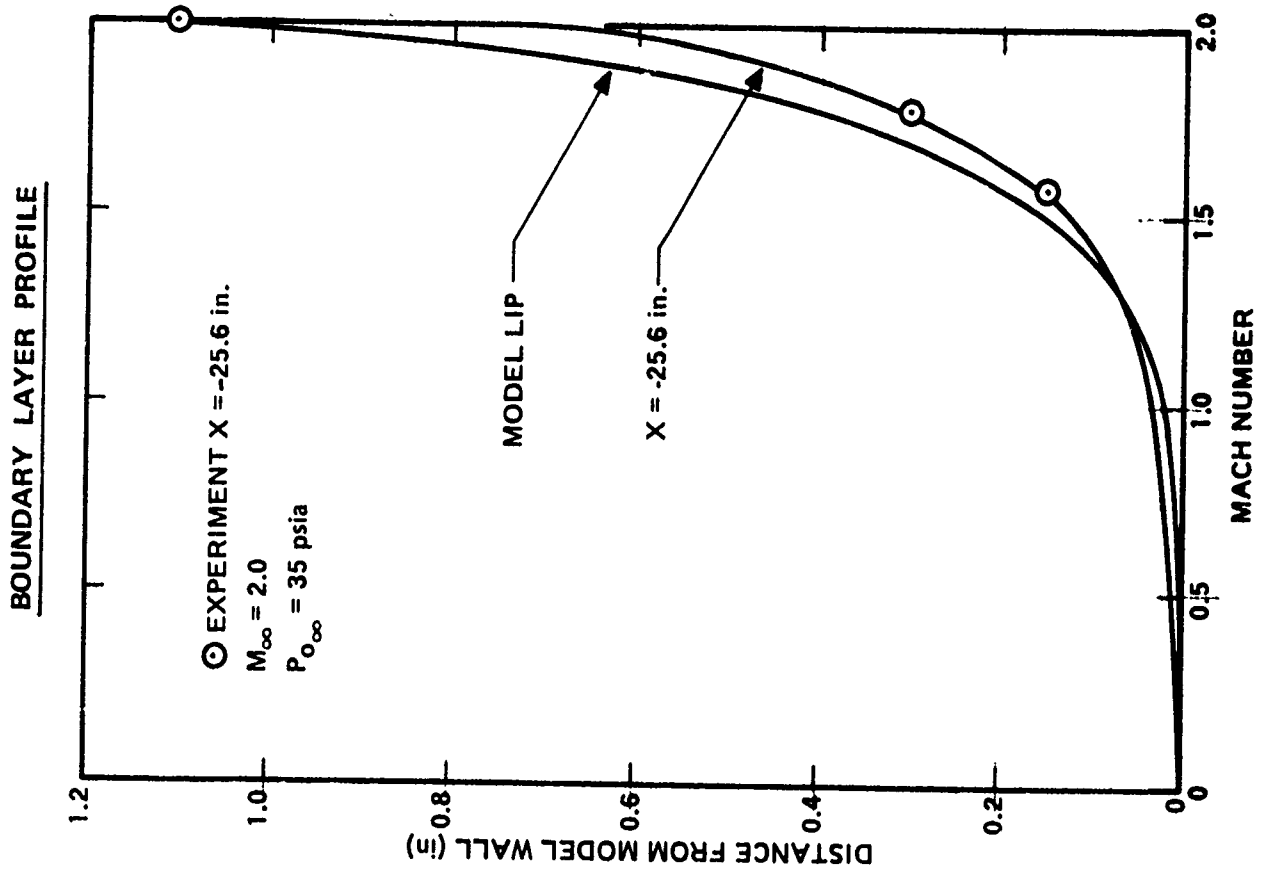


Figure 5. Boundary Layer Profile.

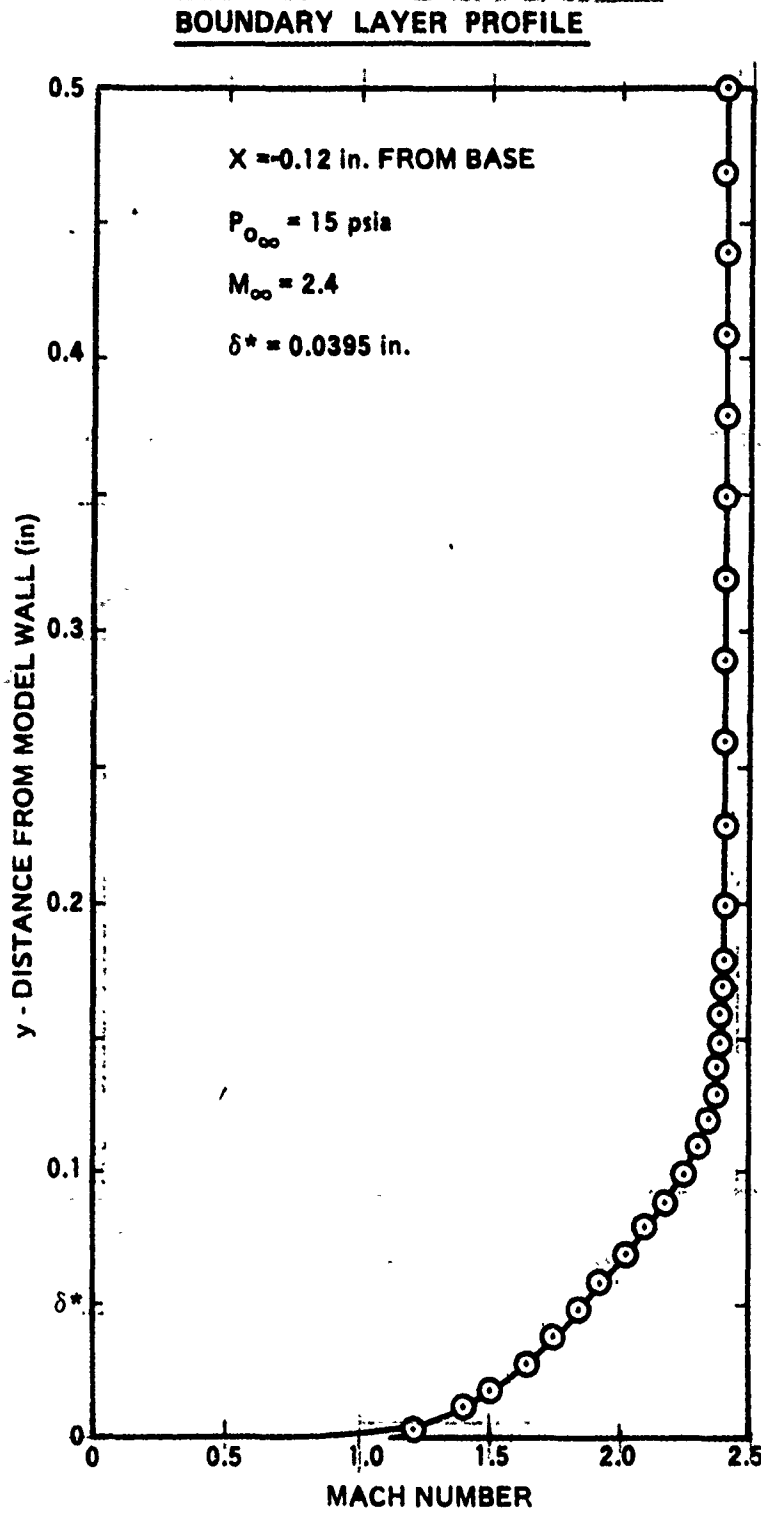


Figure 6. Boundary Layer Profile.





DIVIDING STREAMLINE CALCULATION AND WAVE DIAGRAM

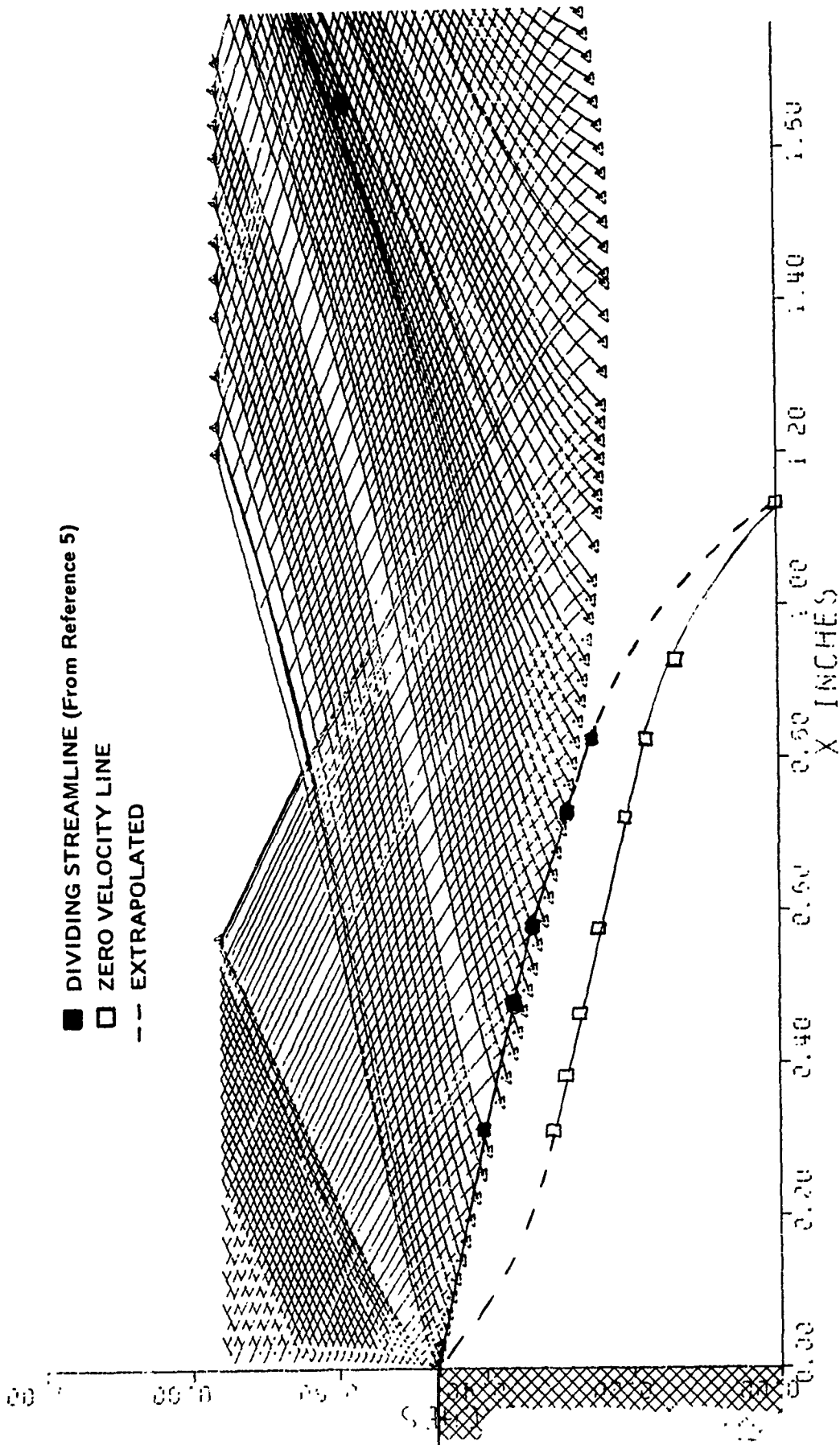


Figure 7. Dividing Streamline Calculation and Wave Diagram.



DIVIDING STREAMLINE CALCULATION AND WAVE DIAGRAM FOR NO FUEL FLOW

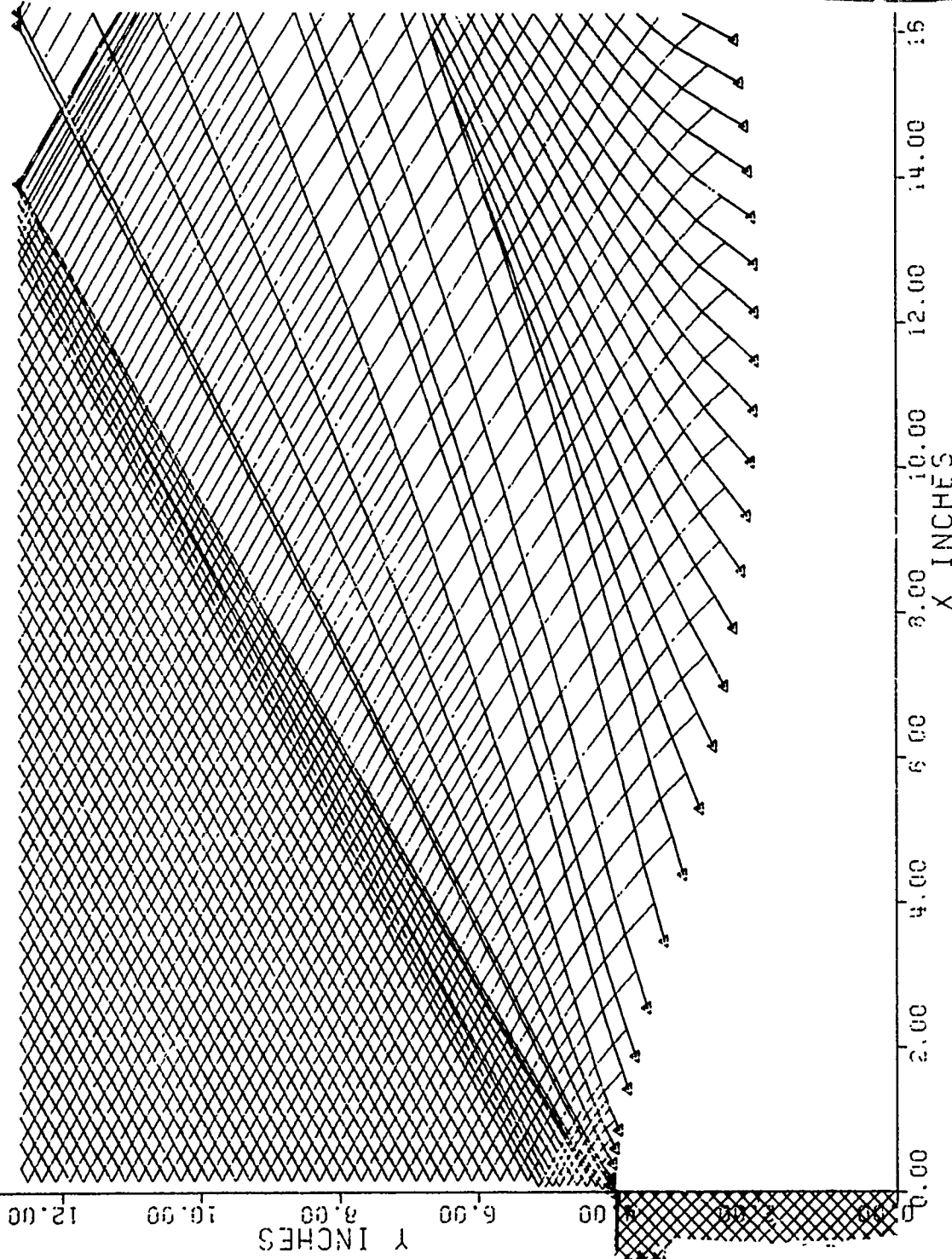


Figure 8. Dividing Streamline Calculation and Wave Diagram for no Fuel Flow.



INITIAL PROFILES FOR $\dot{m} = 0.6$ lbm/sec

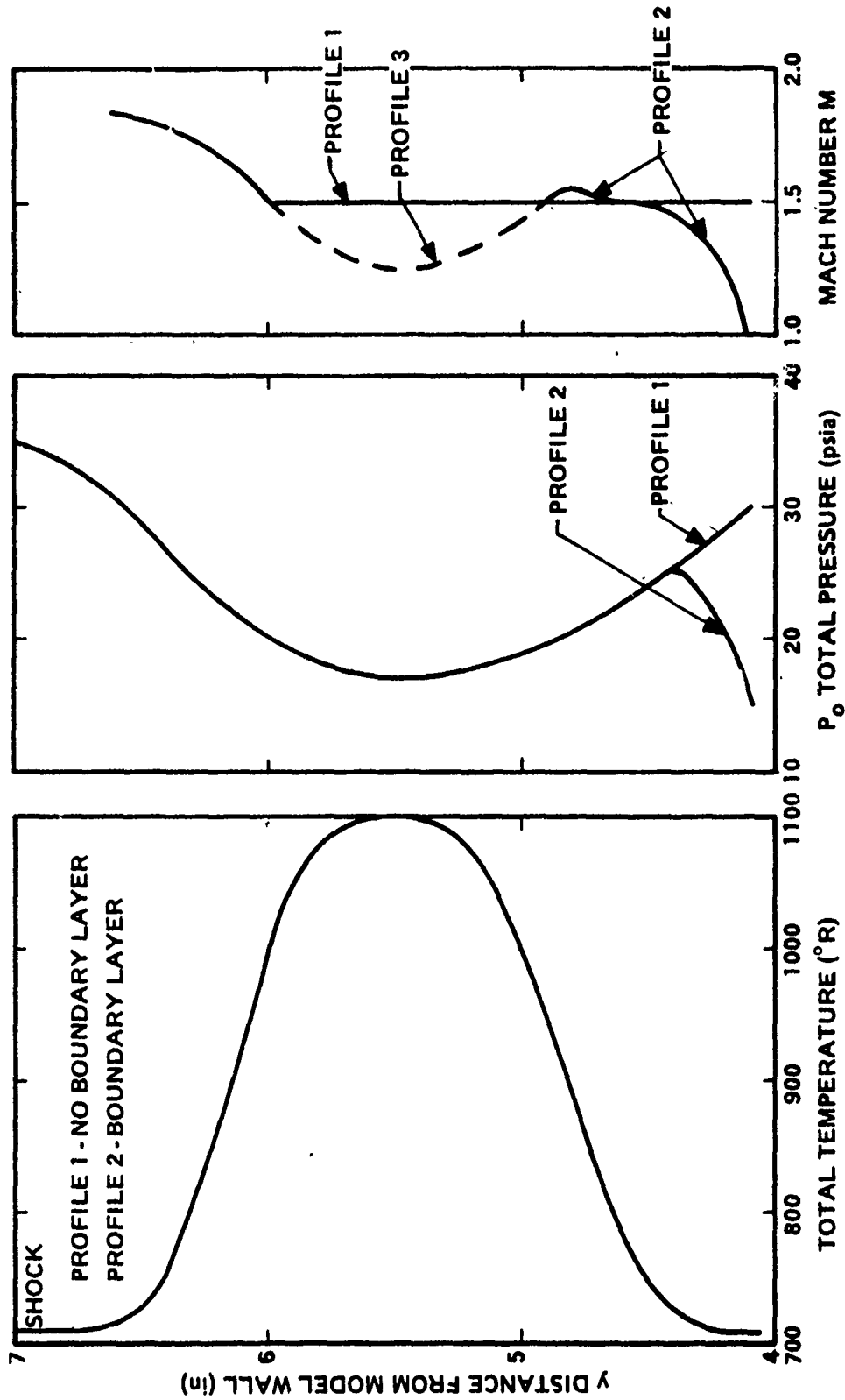


Figure 9. Initial Profiles for $\dot{m} = 0.6$ lbm/sec.



BASE REGION WAVE DIAGRAM FOR NO BOUNDARY LAYER

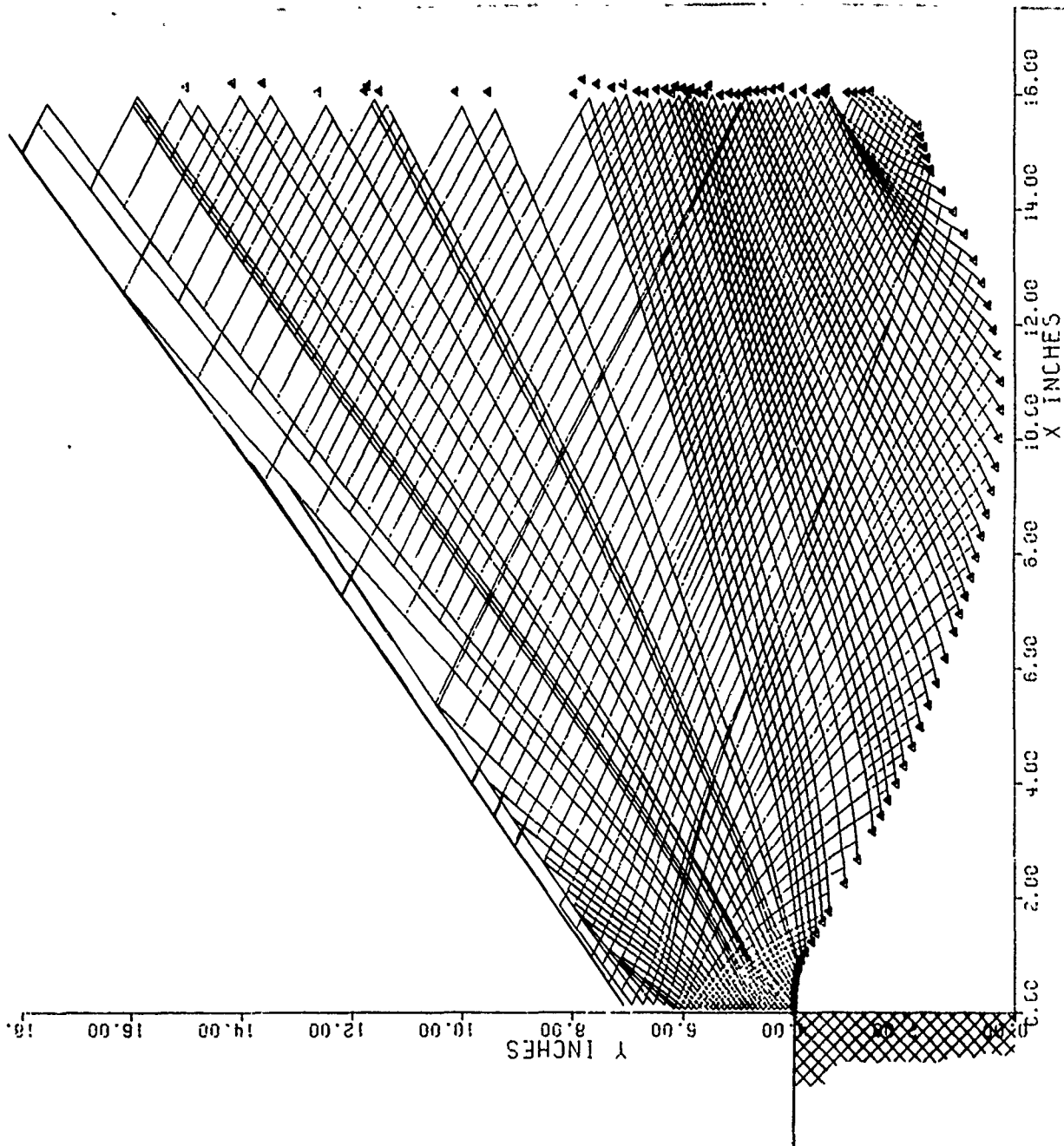


Figure 10. Base Region Wave Diagram for no Boundary Layer.



BASE REGION WAVE DIAGRAM WITH AN INITIAL BOUNDARY LAYER

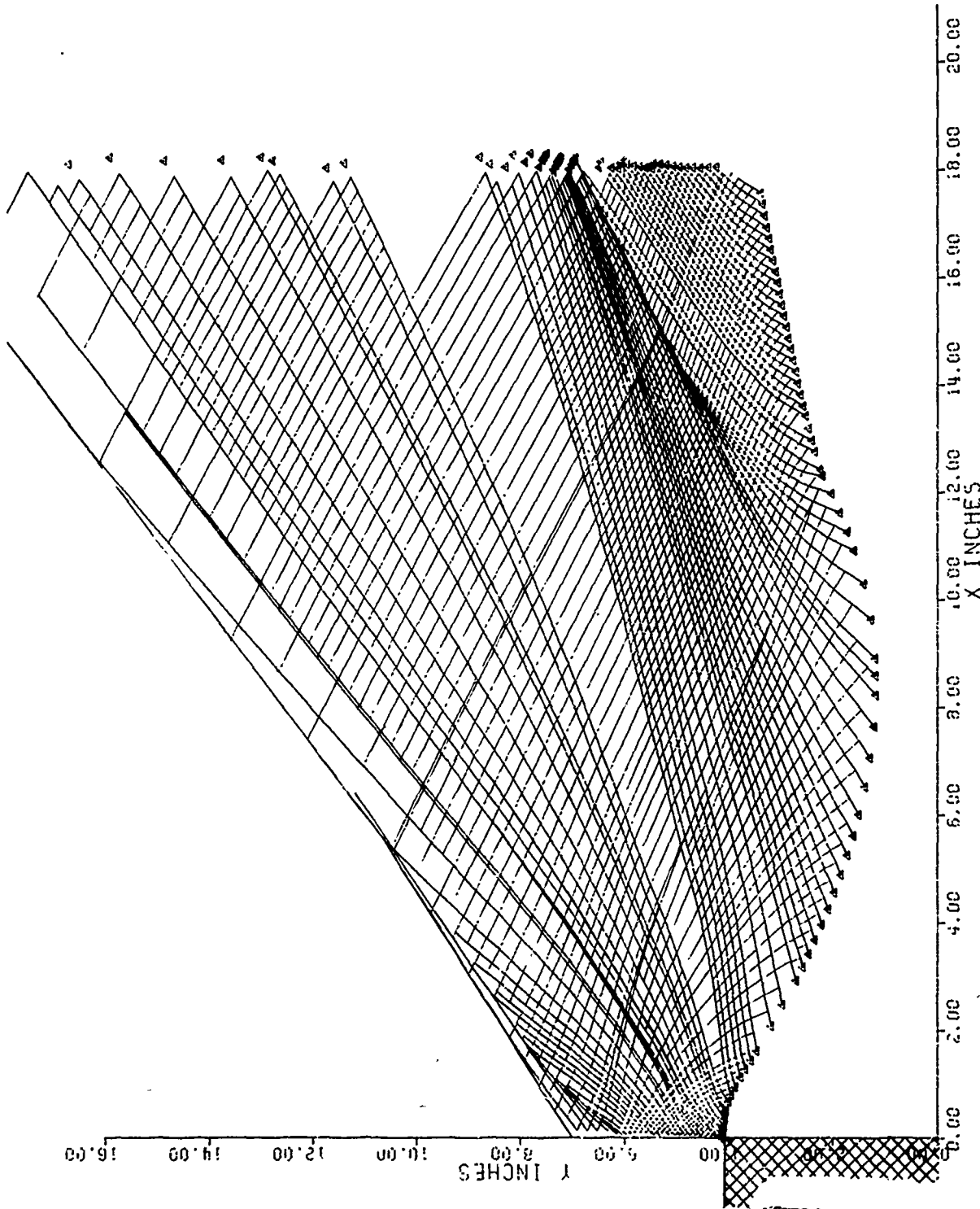


Figure 11. Base Region Wave Diagram with an Initial Boundary Layer.



BASE REGION WAVE DIAGRAM FOR AN EXTENDED BODY

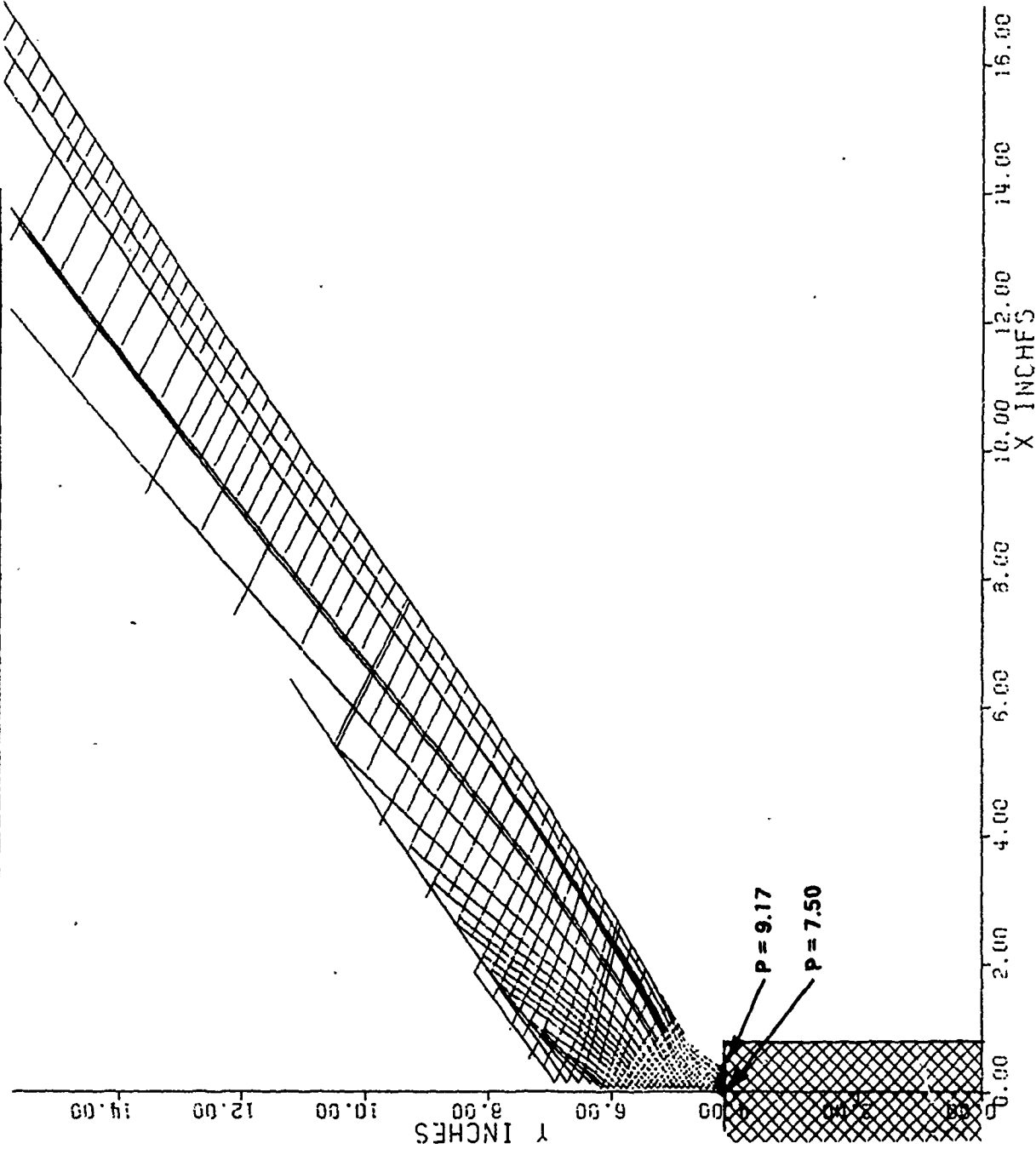


Figure 12. Base Region-Wave Diagram for an Extended Body.



RECIRCULATING FLOW PROFILES

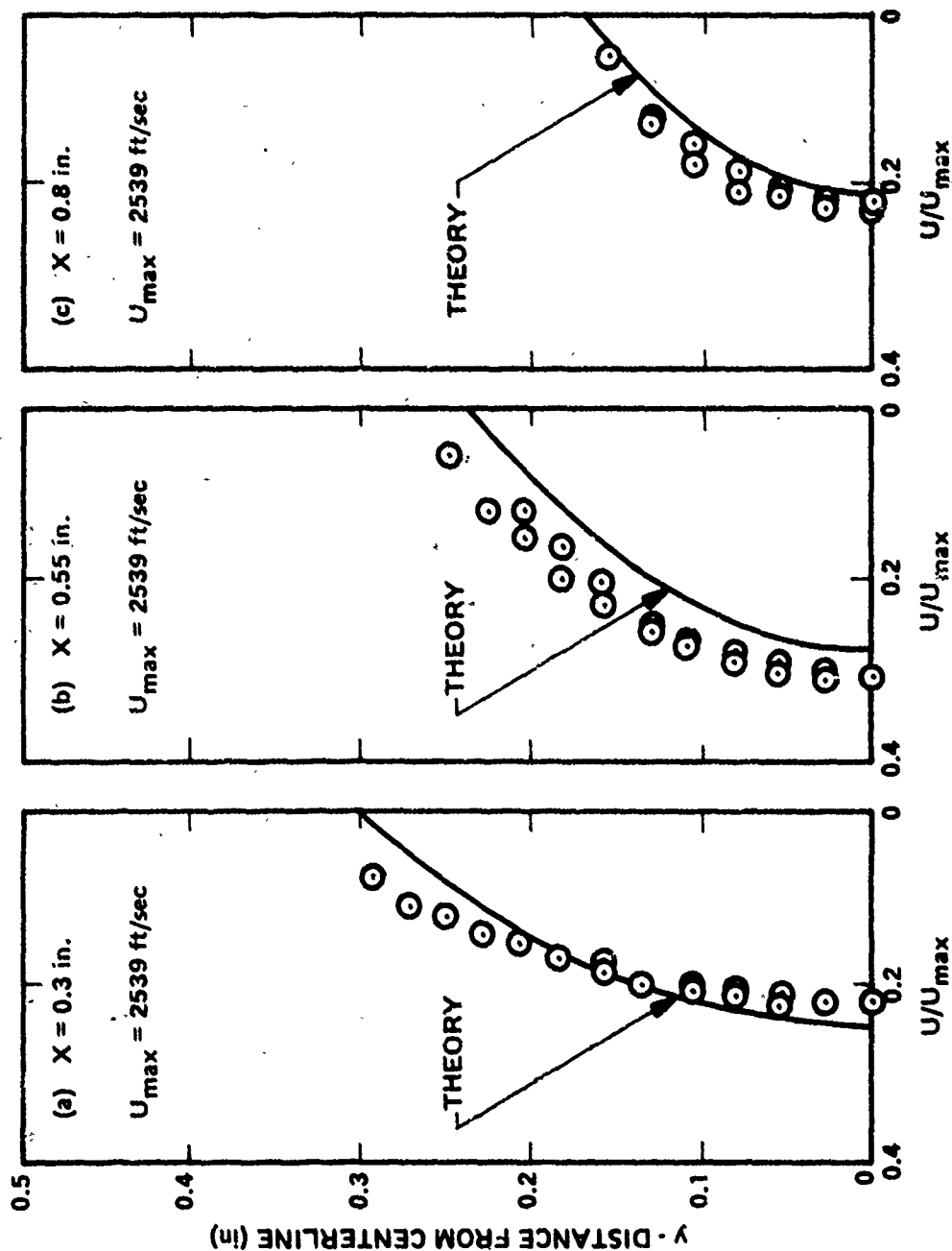


Figure 13. Recirculating Flow Profiles.



RECIRCULATING FLOW PROFILE

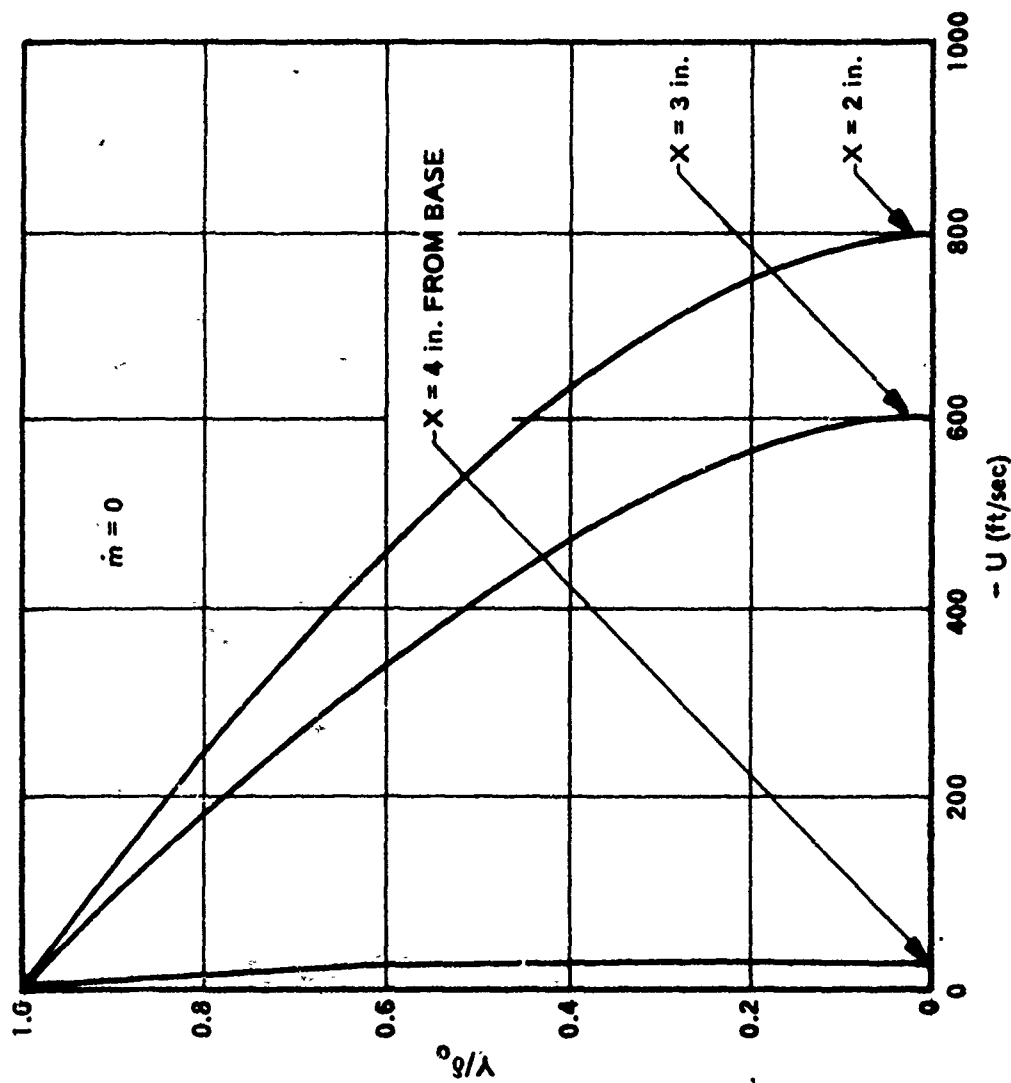


Figure 14. Recirculating Flow Profile.

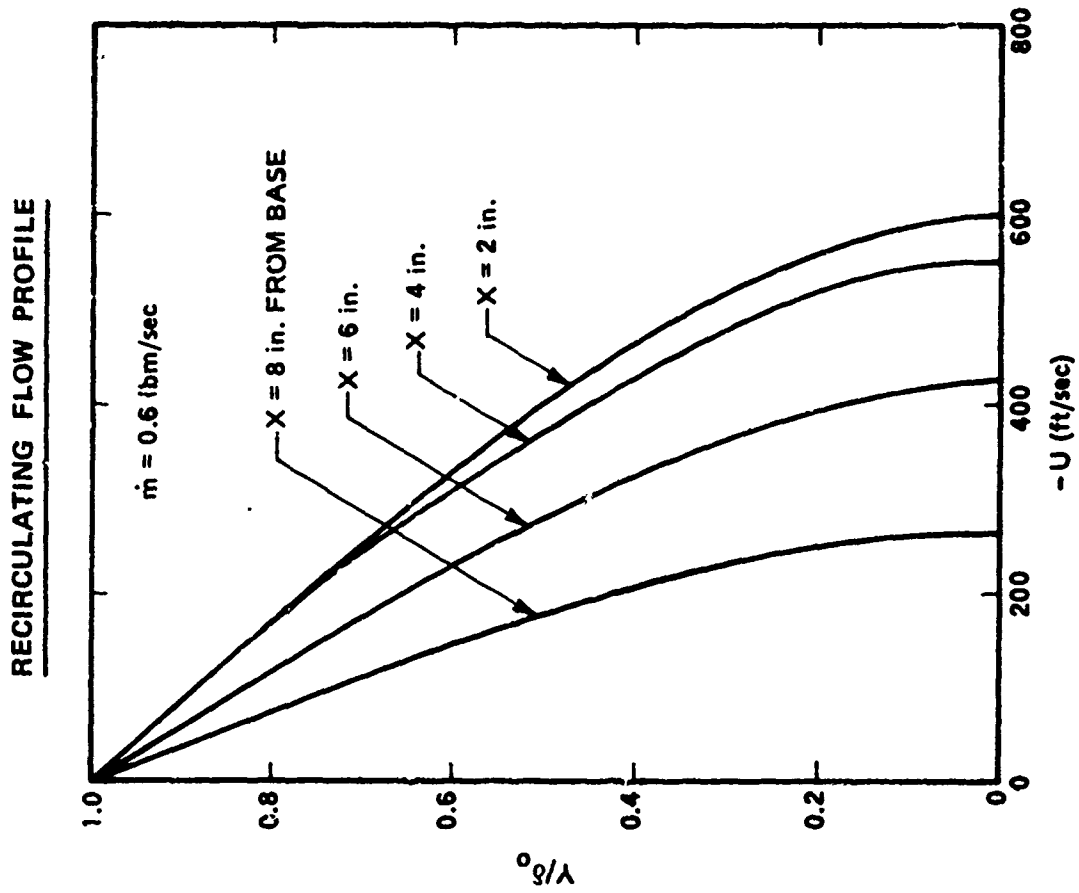


Figure 15. Recirculating Flow Profile.

PAPER NO. 35

WIND-TUNNEL STUDY OF PROJECTILE
BASE DRAG REDUCTION THROUGH
COMBUSTION OF SOLID, FUEL-RICH PROPELLANTS*

By

Frank P. Baltakis

Naval Surface Weapons Center

White Oak Laboratory

Silver Spring, Maryland

and

J. Richard Ward

Ballistic Research Laboratories

Aberdeen Proving Ground, Maryland

*This work was supported by the Army Materiel Command.

ABSTRACT

The effectiveness of a combustible injectant to reduce projectile base drag was investigated in a wind tunnel at simulated low altitude projectile flight conditions. The injectant was generated by burning a solid, fuel-rich propellant in an open base cavity. Base drag reduction was determined from base pressure data and, for selected runs, from direct force measurements. Centerbody-type nozzles were used to provide interference-free base flow.

A large number of candidate propellant compositions have been evaluated and a base drag reduction of 50 percent achieved while maintaining the fuel specific impulse of over 500 seconds. Projectile spin is found to significantly increase propellant burning rate thus increasing base pressure rise but severely reducing specific impulse. Various additives are shown to be very effective for controlling propellant burning rate and also for enhancing performance.

INTRODUCTION

A simple technique is being sought to reduce projectile base drag which at transonic or low supersonic speeds may be in excess of 50 percent of the overall drag (Figure 1). Approaches used by different investigators have included base geometry optimization, boundary-layer bleed into the base region and the addition of mass and heat.

Base geometry methods such as boat-tailing or short, cylindrical protuberances have been shown to reduce the base drag component by about 25 percent (references 1 and 2). Use of the boundary-layer bleed method (reference 3) also results in about a 25 percent reduction of the base drag component. Further reduction seems to require addition of mass or energy into the flow (reference 4).

Two types of energy addition are considered of interest in gun projectile development: (1) combustion in the base cavity (Base Burning) and (2) combustion in the main stream, external to the wake flow (External Burning). Analytical predictions indicate that the base pressure increase of up to the free-stream static pressure is possible with the Base Burning method and up to several times the free-stream value with the External Burning method (reference 5). Experimental data show that both methods have good propulsive efficiency but only at low heat input rates (references 5 and 6).

The purpose of the present study is to explore the feasibility and potential of burning solid, fuel-rich propellants in the base cavity of gun-fired projectiles. Of the many areas requiring study, the main attention here is given to: (1) selection of a suitable propellant, (2) evaluation of combustion and propulsive characteristics of this propellant, and (3) evaluation of the effects of projectile spin and flight parameters. The study was conducted in a wind tunnel under closely simulated projectile flight conditions.

TEST FACILITY

Test Conditions

The experiments were conducted in a wind tunnel at Mach numbers of 1.56, 1.98, and 2.49 at duplicated sea-level pressure and temperature conditions. The facility used was NAVSURFWPNCEN Hypersonic Tunnel which has large capacity air supply and heating systems. Normally this tunnel is operated at Mach numbers 5 to 10. Recently it has been equipped with two additional stilling chambers which permit its operation at supersonic Mach numbers at duplicated sea-level pressure and temperature conditions. The flow nozzles used in this study were of centerbody-type design, six-inch or twelve-inch exit diameter and were procured specifically for projectile base flow studies. The tunnel test section and the new stilling chamber are shown on Figure 2. The test setup is illustrated on Figure 3.

Model and Instrumentation

Projectile base flow was simulated using a bluff cylindrical model which was supported in the stilling chamber and extended through the nozzle throat into the test section (Figure 3). Two sizes, one-inch and 2.5-inch diameter models were used. Model lengths, measured from the nozzle throat, were 10.5 and 18 inches for the one-inch and the 2.5-inch diameter models respectively.

Both models were equipped with air turbines capable of spin rates of up to 50 KRPM and with force balances for

direct base drag measurements (Figure 4). Six pressure orifices were provided near the model periphery (Figure 4) for base drag determination during tests with spin.

The propellant for each run was contained in a separate steel capsule (Figure 4) and was ignited with a laser light beam. A 250-watt CO₂ gas laser was used arranged as shown on Figure 3. The light beam diameter at the plane of impingement was about 3/8-inch and the exposure ranged from two to five seconds.

Propellants

In the base burning technique the propellant must ignite while in the gun and it must sustain combustion when in flight at atmospheric pressure. To have high performance the propellant should produce fuel-rich combustion products which would rapidly burn with air in the projectile near-wake. Since conventional propellants do not meet these requirements, the first step in this study was to select the most suitable propellants. The approach was empirical with the tracer compositions or constituents serving as initial guides.

Table 1 shows compositions that have been evaluated in this study. It includes 92 different combinations with the dominant constituents being magnesium or aluminum as fuels and strontium peroxide or strontium nitrate as oxidizers. Major parametric variations included fuel/oxidizer ratio, fuel grain size and a number of additives. Particle sizes of the tracer compositions B-44 and B-45 were as specified

Vol. 3

in MIL SPEC 382, GRADE 12 and the compositions B-37, B-41, B-42, B-43 and B-74 as specified in MIL SPEC 382, GRADE 11. The diameter of the magnesium particles in the binary compositions was 74 to 100 μ except where specified otherwise. In P-1 to P-10 propellants the aluminum particles had an average diameter of 6 μ and the sodium nitrate and the manganous carbonate 2.5 and 1 μ respectively.

The compositions designated as B-1 to B-76 (Table 1) were recommended and supplied by Frankford Arsenal, those designated as P-1 to P-10, by Picatinny Arsenal.

RESULTS AND DISCUSSION

Wind-tunnel tests were conducted in three series and included 92 different propellants. Some of these did not burn; some were tested very recently (May 1975) and the data have not been fully reduced. Table 1 lists all the compositions tested to date. Those which did not burn are so indicated. Those whose performance data have not been fully reduced are indicated by a blank space in the specific impulse column.

The performance parameters of primary interest in Base Burning are base pressure increase and propellant specific impulse. The base pressure increase was recorded directly versus time. The specific impulse was obtained by integrating the base pressure increase with respect to time and base area and then dividing it by the mass of the propellant.

Base Pressure Increase

The base pressure increase was found to vary considerably with time. End-burning propellants which ignited quickly generally yielded a step-type pressure pulse. Propellants which were shaped to burn radially, or which ignited slowly, yielded gradual pressure changes (Figure 5). Detailed pressure data of the first two series of tests are presented in references 7 and 8. Complete data are being summarized and will be published shortly. It may be worth noting here that peak values of about 95 percent of the free-stream static pressure have been measured for radially burning propellants (P-5 and P-6).

In this paper, propellant performance comparisons are made primarily on the basis of the specific impulse. Base pressure increase, when referred to, is an average value defined as $\Delta P_B = (\Delta t)^{-1} \int (P_B - P_{BI}) dt$ where P_{BI} is base pressure without combustion and Δt is the time period during which the pressure rise is 25 percent or greater of the maximum.

Specific Impulse

The specific impulse (I_{SP}) for the propellants tested is found to range from 60 to about 700 seconds ($lb_f\text{-sec}/lb_m$). The value of 700 seconds was achieved with an $Mg/Sr(NO_3)_2$ type propellant (B-76, Table 1) at a base drag reduction level of approximately 40 percent. This propellant was tested in the most recent series and the data are preliminary. Also no opportunity was available for determining

its sensitivity to various parameters or its potential for further optimization.

A second propellant with a very high specific impulse is an $Al/KClO_4$ type (P-9, Table 1). It yielded 550 seconds at a base drag reduction of approximately 50 percent. This one also was tested in the last series and the data are preliminary.

Effects of Spin

The effects of spin were investigated at rates of up to 50,000 RPM with a one-inch-diameter model and at rates of up to 15,000 RPM with a 2.5-inch model. (The latter data have not been fully reduced.) Both end-burning and radially burning propellants were included.

The primary effect of spin is to increase the burning rate. This, in turn, increases the base pressure and reduces the specific impulse. For a one-inch diameter model, end-burning propellants strong dependence was measured at spin rates below 10,000 RPM. At higher rates, as may be seen in Figures 6, 7, and 8, the burning rate and, consequentially, the base pressure and specific impulse varied very little.

Effects of Free-Stream Mach Numbers

The Mach number effect on the specific impulse is illustrated on Figure 9. The effect on base pressure rise and on percentage of base drag reduction is illustrated on Figures 10 and 11. The specific impulse and the base pressure rise increase relatively linearly with increasing Mach

number. At least in part, this is due to the initial base pressure being lower at higher Mach numbers. Base drag reduction, in percent of the total base drag, decreases from Mach 1.56 to 1.98. At Mach 2.5 it seems to increase again, although the data are not sufficient to draw a more definite conclusion.

Effect of Propellant Grain Size

The effect of grain size was investigated in the range of 44 to 250 μ with Mg/Sr(NO₃)₂ type propellant (B-46 to B-49, Table 1). The data have not been fully reduced. A cursory comparison shows a slight increase in burning rate, base pressure rise and also in specific impulse with decreasing grain size.

Effects of Additives

Binary compositions, which dominated propellant samples in the first series, proved to be poor performers. Particularly, their limits of combustion in terms of fuel/oxidizer ratio were very narrow. In the second and third series of tests a number of additives and binders were introduced to enhance performance and also to control the burning rate.

The types of additives investigated are given in Table 1. Some of these were used to increase low molecular weight gas content of the combustion products, others as additional fuel constituents, binders and burning rate modifiers. A detailed description of the additives tested and the results will be included in the final report to be published

shortly. An illustration of the effect of some of the additives on specific impulse is given on Figure 12.

CONCLUSIONS

Over 90 candidate propellant compositions have been tested in a projectile base cavity in a supersonic stream. Base drag reduction of over 90 percent has been measured at peak propellant burning rates. Propellant specific impulse of approximately 700 seconds has been attained at a base drag reduction level of 40 percent.

Projectile spin significantly increased propellant burning rate thus increasing base pressure rise but severely reducing specific impulse.

Additives to binary compositions had a very pronounced effect on propellant performance. Varying propellant grain size produced only a relatively minor effect.

Sensitivity of the performance parameters to propellant additives suggests a strong possibility for further improvement. Additives (or basic constituents) producing large quantities of gaseous combustibles and those enhancing rapid combustion in the near-wake (Figure 13) should offer the greatest potential.

SYMBOLS

B-1 to B-76	Propellant designation, see Table 1
CaRes	Calcium resinate
C_D	Drag coefficient
D	Projectile base diameter
D_B	Base drag
DOP	Diethylphthalate
E.B.	Ensign Bickford Co.
HES	Hercules Experimental Sample
I_{SP}	Specific impulse, $lb_f\text{-sec}/lb_m$
M_∞	Free-stream Mach number
PVC	Polyvinylchloride
P_B	Base pressure, psia
P_{BI}	Base pressure before combustion, psia
ΔP_B	Base pressure change due to combustion, psi
P_∞	Free-stream pressure, psia
RDX	Cyclonite (explosive)
t	Time, sec
Δt	Combustion time during which the pressure rise is 25 percent or greater of the maximum
TNT	Trinitrotoluene
VAAR	Vinylalcoholacetate resin
VITON A	A fluorinated polymer

REFERENCES

1. MacAllister, L. C., Reiter, B. J. et al, "A Compendium of Ballistic Properties of Projectiles of Possible Interest in Small Arms", BRL Report No. 1532, Feb 1971.
2. Merz, R. A. and Quintenz, T. E., "Drag Reduction by Short Base Protuberances", Rutgers University, NSF Summer Program and Senior Project, May 1970.
3. Regan, F. J. and Schermerhorn, V. L., "The Effect of Base Bleed on the Drag and Magnus Characteristics of a Rotating Body of Revolution", NOLTR 72-204, Aug 1972.
4. Murthy, S. N. B. and Osborn, J. R., "Base Flow Data With and Without Injection: Bibliographic and Semi-Rational Correlations", Purdue University, Contract No. DAAD 05-72-C-0342, Ballistic Research Laboratories, Aberdeen Proving Ground, May 1973.
5. Strahle, W. C., "Combustion Effects on the Base Pressure in Supersonic Flight and Applications", IDA, Institute for Defense Analyses, Research Paper P-389, Feb 1970, (C).
6. Baltakis, F. P., "Wind Tunnel Study of Projectile Drag Reduction Through External Burning", NOLTR 72-71, Apr 1972.
7. Ward, J. R., Baltakis, F. P, and Pronchick, S. W., "Wind Tunnel Study of Base Drag Reduction by Combustion of Pyrotechnics", BRL R 1745, Oct 1974.
8. Ward, J. R., Baltakis F. P., Elmendorf, T., and Mancinelli, D., "Wind Tunnel Experiments of the Effect of Near-Wake Combustion on the Base Drag of Supersonic Projectiles", BRL IMR 379, May 1975.

TABLE 1 PROPELLANT COMPOSITIONS

Designation		Constituents (Percent by Weight)	¹ _{SP} Sec
NSWC	BRL or Picat.		
B-1		Mg(10), SrO ₂ (90)	No combustion
B-2		Mg(15), SrO ₂ (85)	No combustion
B-3		Mg(16.9), SrO ₂ (83.1)	No combustion
B-4		Mg(20), SrO ₂ (80)	130
B-5		Mg(25), SrO ₂ (75)	120
B-6		Mg(30), SrO ₂ (70)	147
B-7		Mg(35), SrO ₂ (65)	No combustion
B-8		Mg(40), SrO ₂ (60)	
B-9		Mg(50), SrO ₂ (50)	
B-10		Mg(20), SrO ₂ (80), Grain dia. 150-200μ	156
B-11		Mg(20), SrO ₂ (80), <44μ	No combustion
B-12		Mg(20), Sr(NO ₃) ₂ (80)	No combustion
B-13		Mg(30), Sr(NO ₃) ₂ (70)	No combustion
B-14		Mg(36.5), Sr(NO ₃) ₂ (63.5)	465
B-15		Mg(40), Sr(NO ₃) ₂ (60)	No combustion
B-16		Mg(50), Sr(NO ₃) ₂ (50)	No combustion
B-17		Mg(22.3), BaO ₂ (77.7)	
B-18		Mg(41.2), KClO ₄ (58.8)	
B-19		MgH ₂ (24), Sr(NO ₃) ₂ (76)	No combustion
B-20		MgH ₂ (70), Na(NO ₃) ₂ (30)	
B-21		Mg(14.7), SrO ₂ (83.3), CaRes*(2)	157
B-22		Mg(14.4), SrO ₂ (81.6), CaRes(4)	212
B-23		Mg(14.1), SrO ₂ (79.9), CaRes(6)	225
B-24		Mg(13.8), SrO ₂ (78.2), CaRes(8)	300
B-25		Mg(13.5), SrO ₂ (76.5), CaRes(10)	304
B-26		Mg(12.8), SrO ₂ (72.2), CaRes(15)	253
B-27		Mg(14.3), SrO ₂ (80.7), Gelatin(5)	192
B-28		Mg(13.5), SrO ₂ (76.5), Gelatin(10)	231
B-29		Mg(12.8), SrO ₂ (72.2), Gelatin(15)	351
B-30		Mg(14.3), SrO ₂ (80.7), Oxamide(5)	138

*See list of symbols

10th Navy Symposium on Aeroballistics

Vol. 3

TABLE 1 (Continued)

Designation	BRL or NSWC Pat.	Constituents (Percent by Weight)	I _{SP} Sec
B-31		Mg(13.5), SrO ₂ (76.5), Oxamide(10)	166
B-32		Mg(12.8), SrO ₂ (72.2), Oxamide(15)	193
B-33		Mg(14.3), SrO ₂ (80.7), Polyvinylchloride(5)	170
B-34		Mg(13.5), SrO ₂ (76.5), Polyvinylchloride(10)	278
B-35		Mg(12.8), SrO ₂ (72.2), Polyvinylchloride(15)	372
B-36		Mg(13.5), SrO ₂ (76.5), Polyethylene(10)	60
B-37	F-4	Mg(33.2), Sr(NO ₃) ₂ (57.7), CaRes(9.1)	
B-38		Mg(31.2), Sr(NO ₃) ₂ (54.2), CaRes(8.6), Binder(6)	339
B-39		Mg(28.2), Sr(NO ₃) ₂ (49.1), CaRes(7.7), Binder(15)	--
B-40		Mg(26.6), Sr(NO ₃) ₂ (46.2), CaRes(7.2), Binder(20)	
B-41	F-1	Mg(8.1), SrO ₂ (78.8), C(4), CaRes(9.1)	330
B-42	F-13	Mg(29.9), Sr(NO ₃) ₂ (51.9), CaRes(8.2), Gelatin(10)	No combustion
B-43	F-14	Mg(7.3), Sr(NO ₃) ₂ (70.9), C(3.6), CaRes(8.2), Gelatin(10)	464
B-44	R284	Mg(28), Sr(NO ₃) ₂ (55), Polyvinylchloride(17)	
B-45	R20C	Mg(21.5), SrO ₂ (65.7), CaRes(6), PbO ₂ (3.4), BaO ₂ (3.4)	325
B-46		Mg(33.2), Sr(NO ₃) ₂ (57.7), CaRes(9.1), 149-250μ	
B-47		Mg(33.2), Sr(NO ₃) ₂ (57.7), CaRes(9.1), 74-100μ	
B-48		Mg(33.2), Sr(NO ₃) ₂ (57.7), CaRes(9.1), 44-100μ	
B-49		Mg(33.2), Sr(NO ₃) ₂ (57.7), CaRes(9.1), <44μ	
B-50		Mg(29.9), Sr(NO ₃) ₂ (51.9), CaRes(8.2), HES(10)	

TABLE 1 (Continued)

Designation		Constituents (Percent by Weight)	I _{SP} Sec
B-51	BRL or NSWC Picat.	Mg(31.9), Sr(NO ₃) ₂ (55.4), CaRes(B.7), TNT(4)	450
B-52		Mg(31.9), Sr(NO ₃) ₂ (55.4), CaRes(8.7), RDX(4)	
B-53		Mg(37.1), KClO ₄ (52.9), CaRes(10)	
B-54		Mg(29.9), Sr(NO ₃) ₂ (51.9), CaRes(8.2), Azocel(10)	
B-55		Mg(14.3), KClO ₄ (80.7), CaRes(5)	165
B-56		Mg(13.8), BaO ₂ (76.5), CaRes(10)	232
B-57		Mg(12.8), BaO ₂ (72.2), CaRes(15)	290
B-58		B(15), BaCrO ₄ (85)	No combustion
B-59		B(31), KClO ₄ (69)	260
B-60		Ti(33), KClO ₄ (77)	No combustion
B-61		Ti(36), Sr(NO ₃) ₂ (64)	No combustion
B-62		Ti(29.7), KClO ₄ (69.3), CaRes(10)	
B-63		Ti(32.4), Sr(NO ₃) ₂ (57.6), CaRes(10)	190
B-64		Zr(52), Sr(NO ₃) ₂ (48)	110
B-65		Zr(57), KClO ₄ (43)	130
B-66		Zr(51.3), KClO ₄ (38.7), CaRes(10)	450
B-67		Zr(46.8), Sr(NO ₃) ₂ (43.2), CaRes(10)	420
B-68		ZrH ₂ (70), Sr(NO ₃) ₂ (30)	No combustion
B-69		ZrH ₂ (50), Sr(NO ₃) ₂ (50)	No combustion
B-70		NaBH ₄ (15), Sr(NO ₃) ₂ (85)	
B-71		NaBH ₄ (25), Sr(NO ₃) ₂ (75)	
B-72		NaBH ₄ (35), Sr(NO ₃) ₂ (65)	
B-73		NaBH ₄ (40), Sr(NO ₃) ₂ (60)	
B-74	F-3	Al(27.1), Sr(NO ₃) ₂ (63.8), CaRes(9.1)	No combustion
B-75	I-136	CaRes(10), SrO ₂ (90)	
B-76	E.B.	Mg(25+5), Sr(NO ₃) ₂ (35+5), PVC(10), DOP(10), NH ₄ ClO ₄ (20)	700

10th Navy Symposium on Aeroballistics

Vol. 3

TABLE 1 (Continued)

Designation	BRL or Picat.	Constituents (Percent by Weight)	I _{SP} Sec
P-1		Al(84.1), NaNO ₃ (9.3), MnCO ₃ (1.9), VITON A(4.7)	No combustion
P-2	1558	Al(83.3), NaNO ₃ (9.8), MnCO ₃ (2.0), VITON A(4.9)	No combustion
P-3		Al(78), NaNO ₃ (15), MnCO ₃ (2.0), VITON A(5.0)	
P-4	1744	Al(73.5), NaNO ₃ (9.8), MnCO ₃ (2.0), C(9.8), VITON A(4.9)	
P-5	1745	Al(68.6), NaNO ₃ (24.5), MnCO ₃ (2.0), VITON A(4.9)	115
P-6	1689	Al(63.7), NaNO ₃ (9.8), MnCO ₃ (2.0), C(19.6), VITON A(4.9)	220
P-7	1747	Al(63.7), NaNO ₃ (19.6), MnCO ₃ (2.0), C(9.8), VITON A(4.9)	No combustion
P-8	1746	Al(53.9), NaNO ₃ (39.2), MnCO ₃ (2.0), VITON A(4.9)	
P-9	1748	Al(53.9), KClO ₄ (39.2), MnCO ₃ (2.0), VITON A(4.9)	550
P-10	1749	Al(30), KClO ₄ (60), MnCO ₃ (2.0), VITON A(8.0)	
P-11		Mg(90), NaNO ₃ (5), VITON A(5.0)	No combustion
P-12		Mg(80), NaNO ₃ (15), VITON A(5.0)	105
P-13		C(97), VAAR(3.0)	
P-14		C(55), NaNO ₃ (40), VAAR(5.0)	--
P-15		C(34), NaNO ₃ (63), VAAR(3.0)	--
P-16		Ti(43), MoO ₃ (57)	129

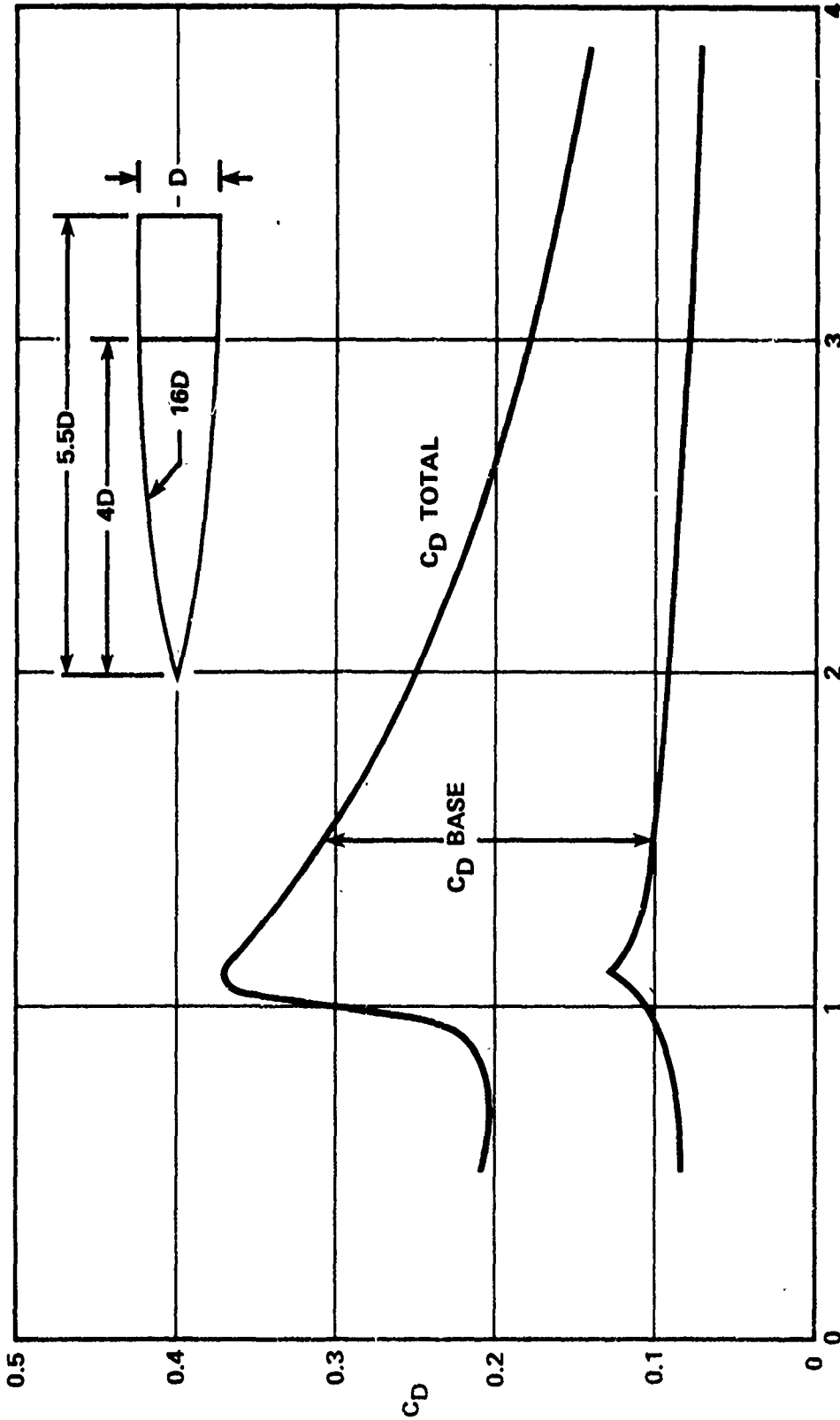


FIG. 1 PROJECTILE DRAG COEFFICIENT VERSUS MACH NUMBER

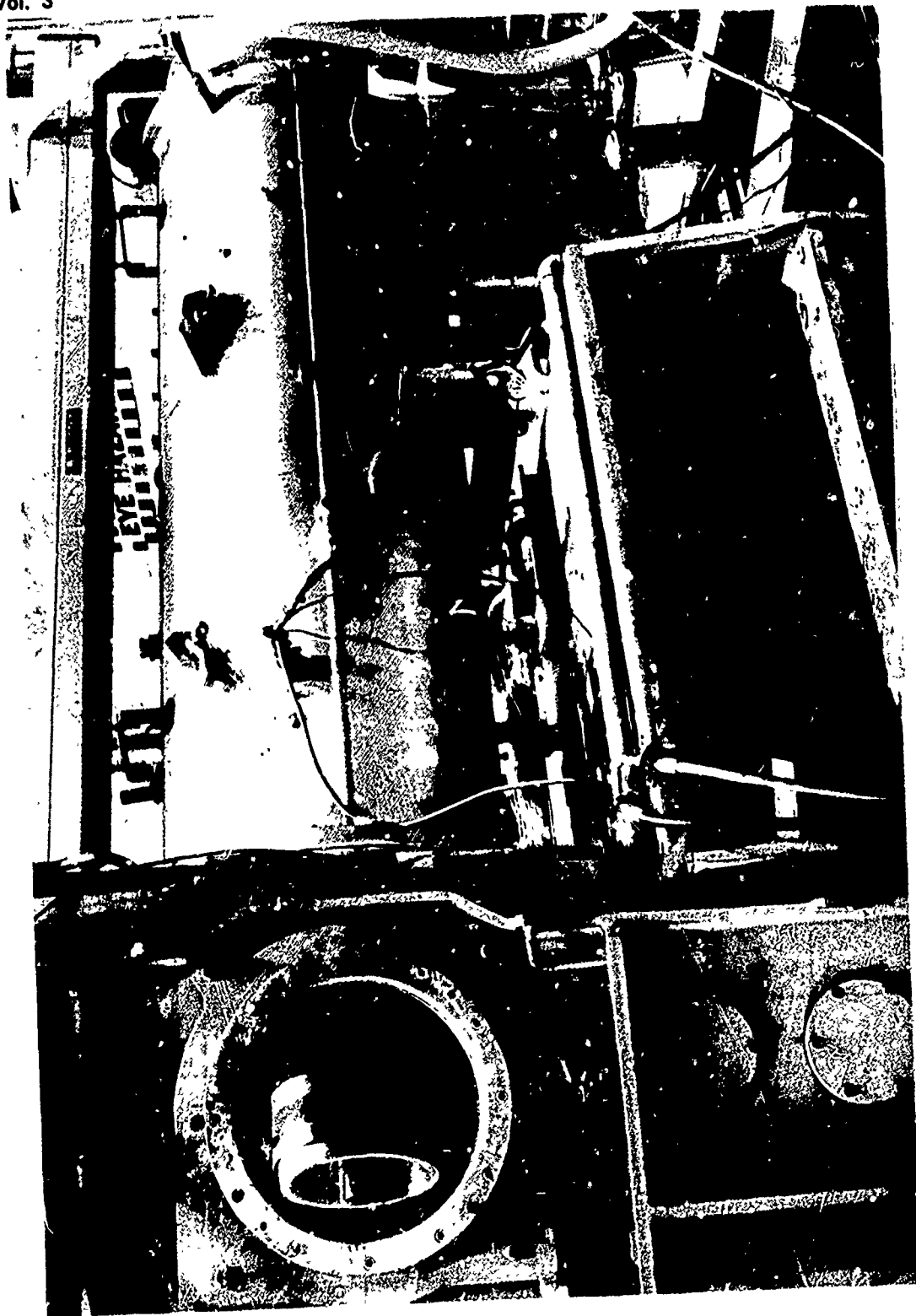


FIG. 2 TUNNEL TEST SECTION AND STILLING CHAMBER

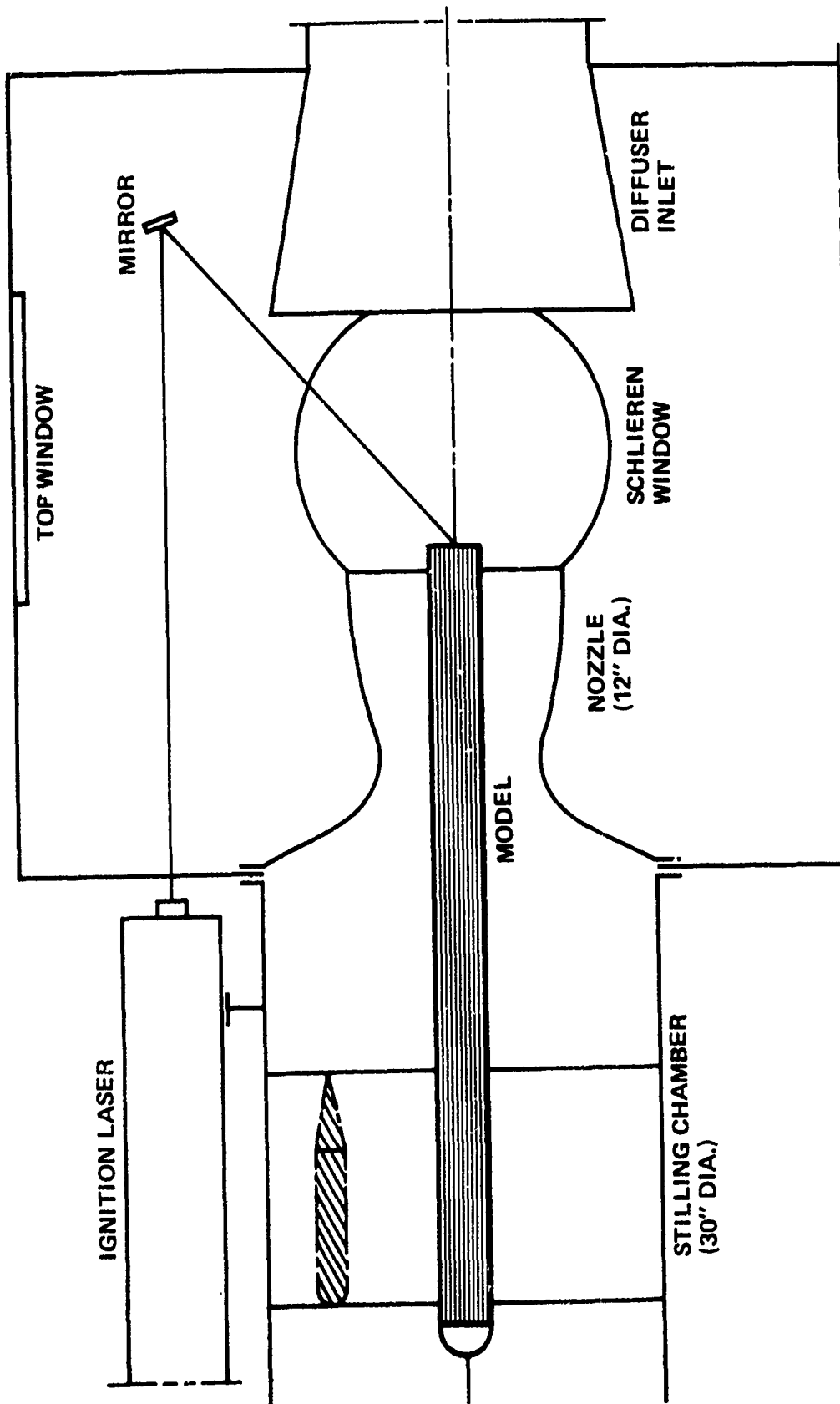


FIG. 3 TEST SETUP DIAGRAM

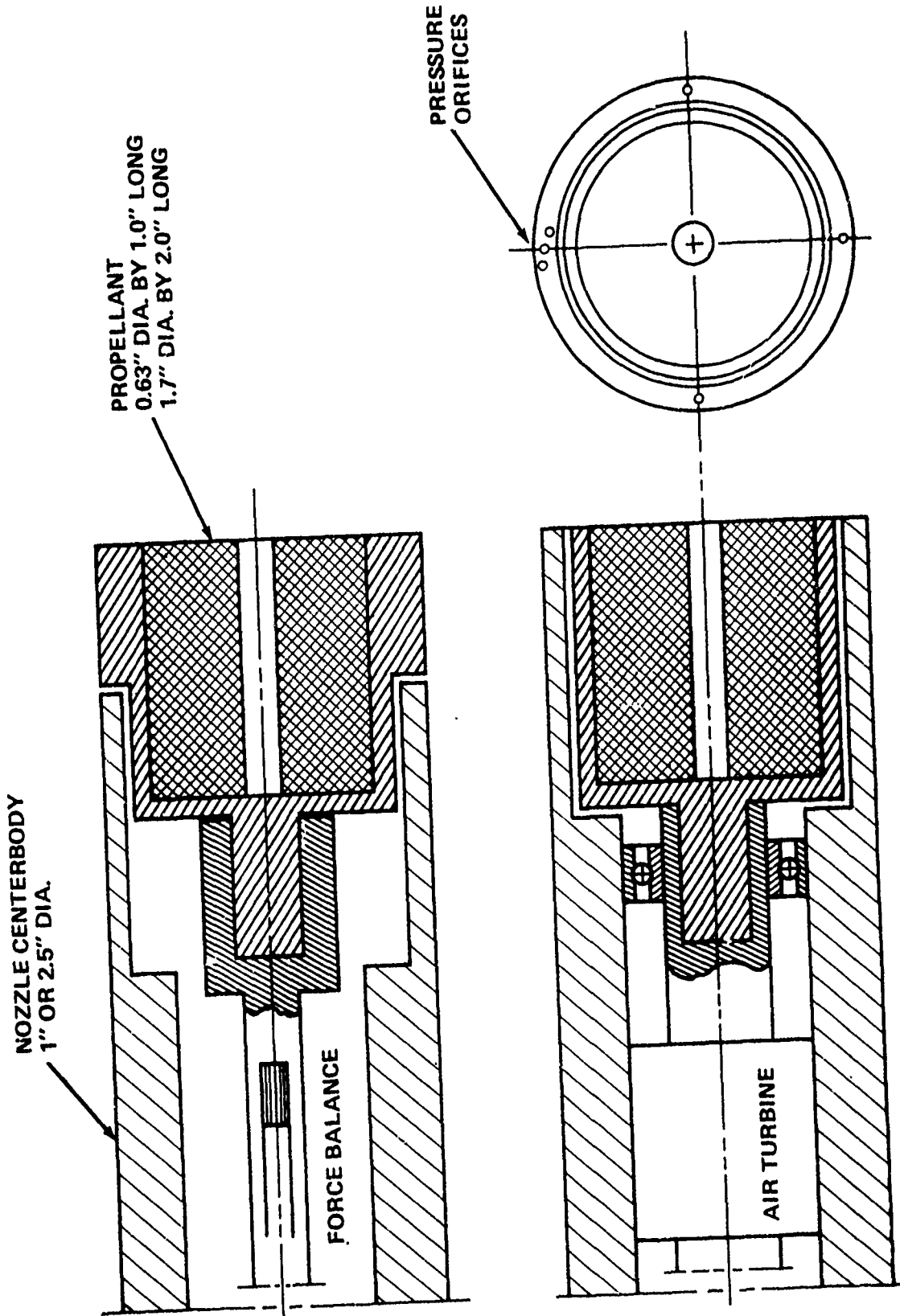
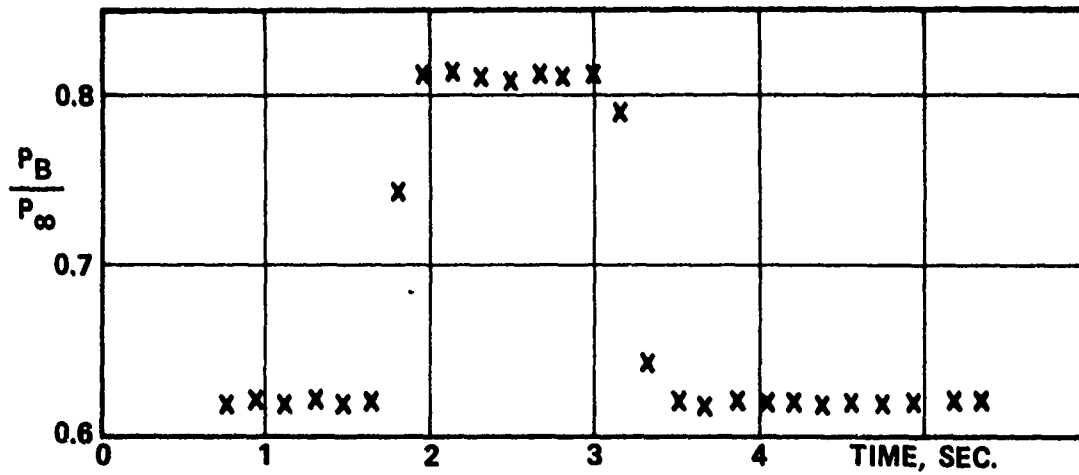
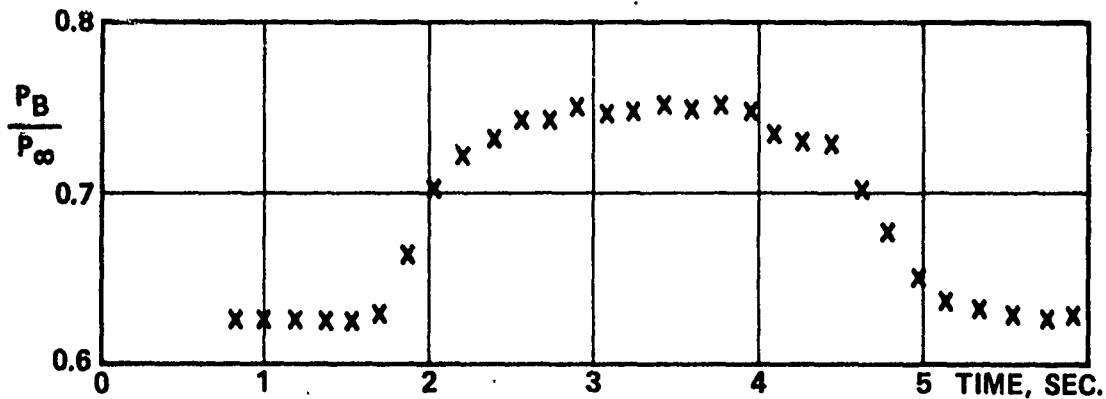


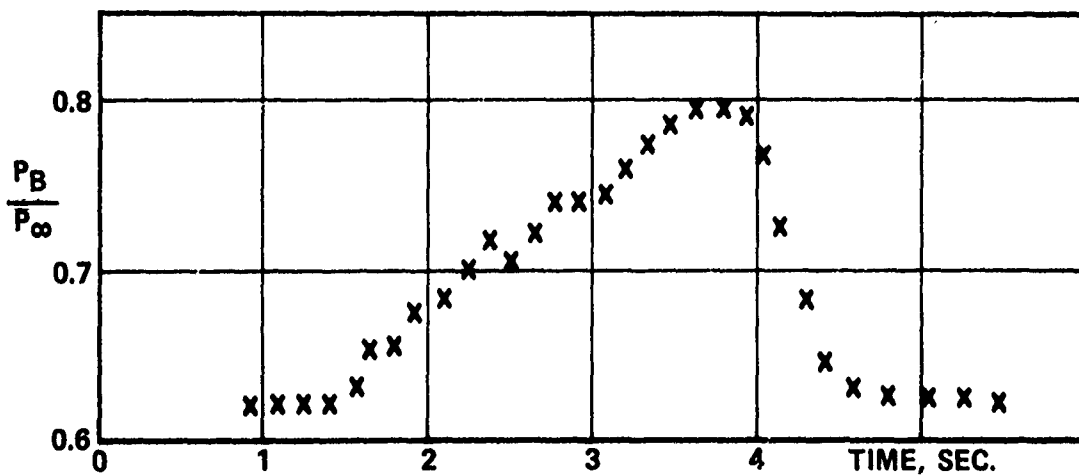
FIG. 4 PROPELLANT CAPSULE INSTALLATION METHODS FOR FORCE AND SPIN TESTS



A. END-BURNING PROPELLANT; NO SLAG FORMATION



B. END-BURNING PROPELLANT



C. RADIALLY-BURNING PROPELLANT

FIG. 5 TYPICAL PRESSURE-TIME HISTORIES

END-BURNING
B-45 PROPELLANT
1" DIA. MODEL
 $M_\infty = 1.98$

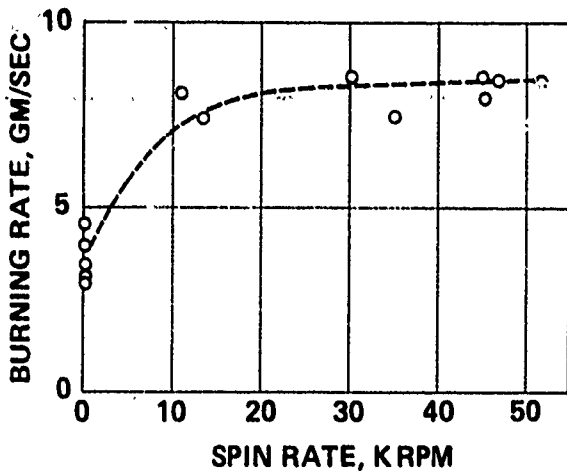


FIG. 6 EFFECT OF SPIN ON PROPELLANT BURNING RATE

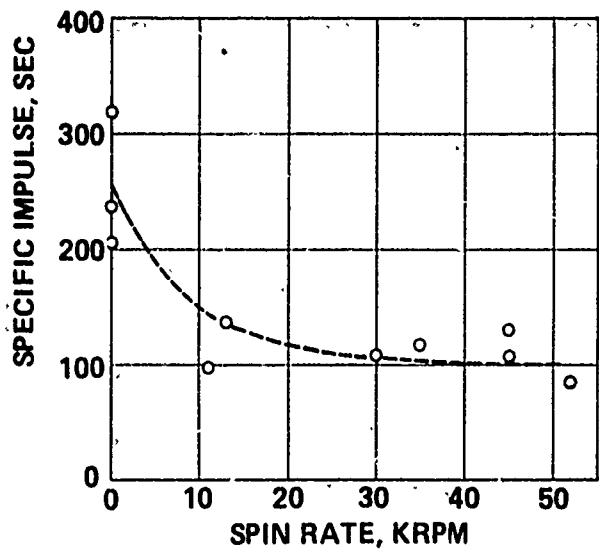


FIG. 7 EFFECT OF SPIN ON SPECIFIC IMPULSE

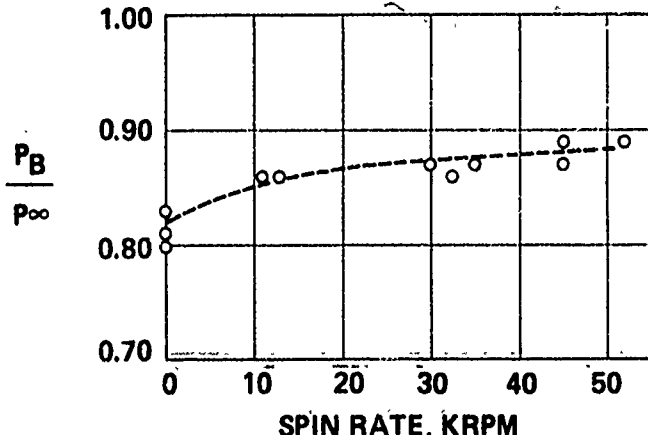


FIG. 8 EFFECT OF SPIN ON PROJECTILE BASE PRESSURE

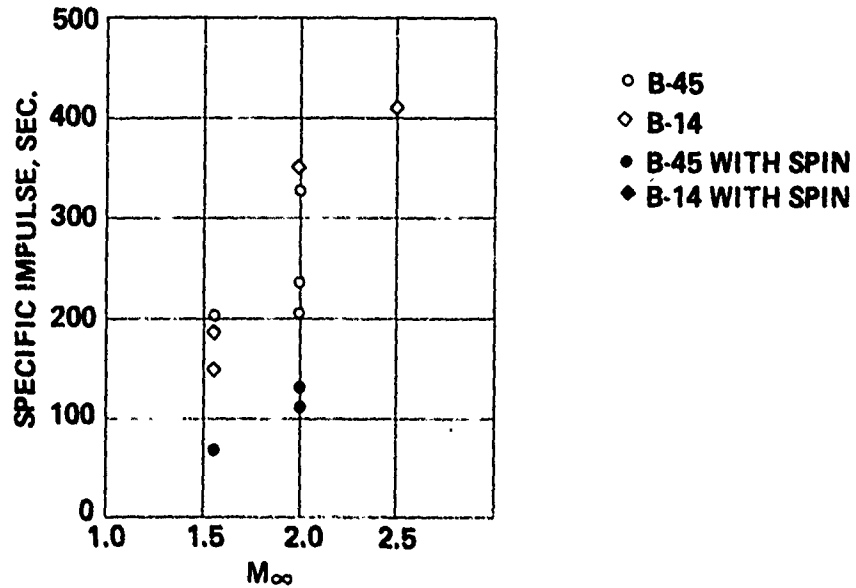


FIG. 9 EFFECT OF FLOW MACH NUMBER ON SPECIFIC IMPULSE

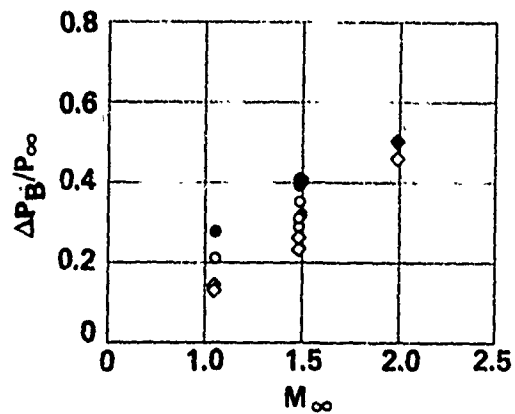


FIG. 10 EFFECT OF FLOW MACH NUMBER ON BASE PRESSURE RISE

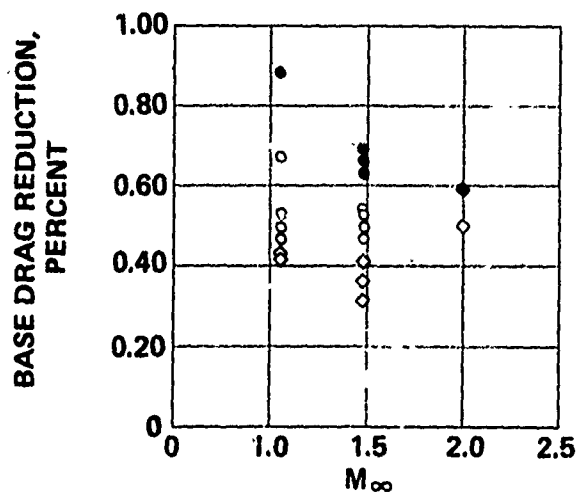


FIG. 11 EFFECT OF FLOW MACH NUMBER ON BASE DRAG REDUCTION

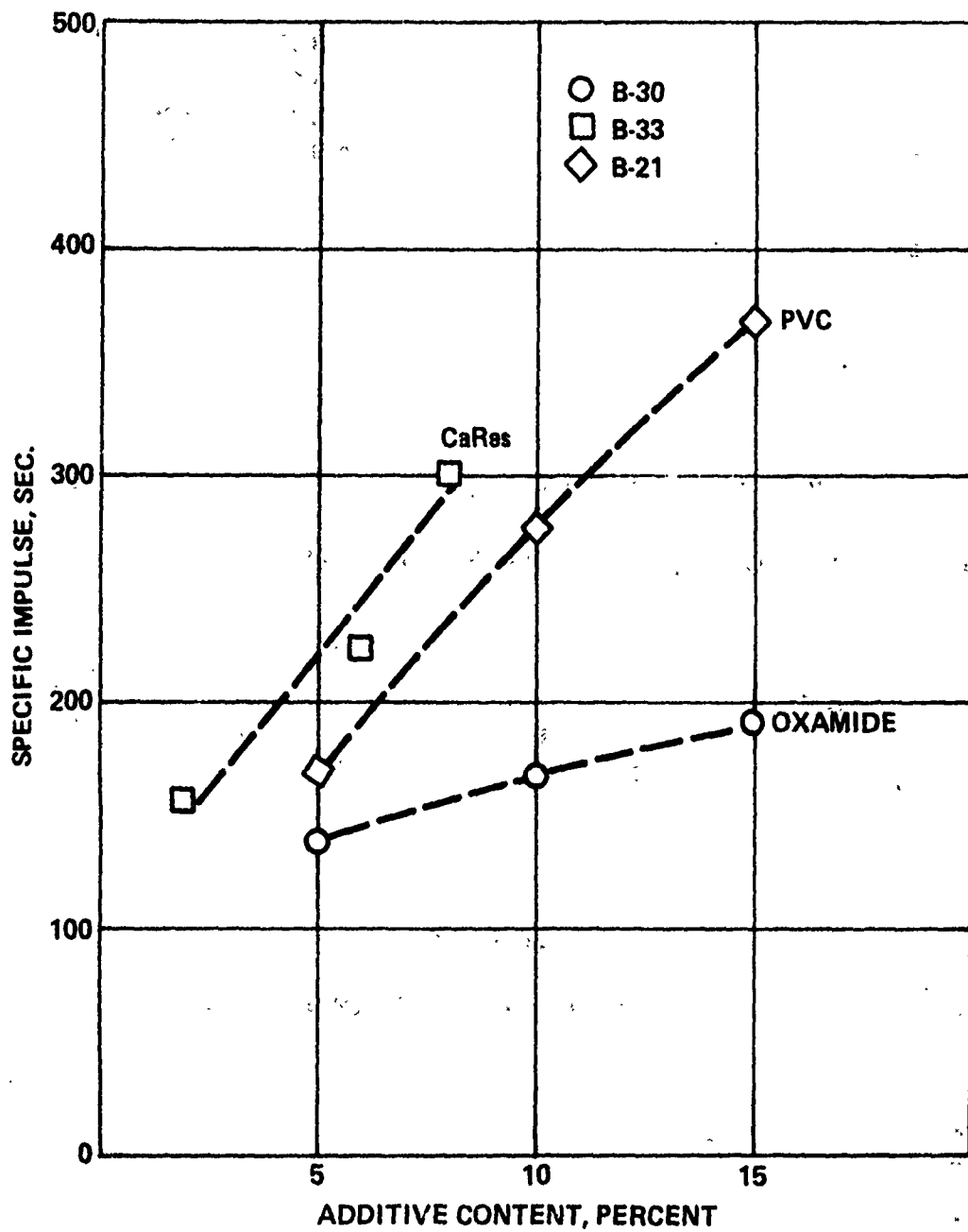


FIG. 12 EFFECT OF PROPELLANT ADDITIVES ON SPECIFIC IMPULSE



A. NEAR-WAKE COMBUSTION, B-76 PROPELLANT, $I_{sp} = 700$ SEC.



B. EXTENDED COMBUSTION, B-63 PROPELLANT, $I_{sp} = 190$ SEC.

FIG. 13 SCHLIEREN PHOTOGRAPHS SHOWING NEAR-WAKE AND EXTENDED COMBUSTION ZONES

PAPER NO. 36

**A THREE-DIMENSIONAL FLOW FIELD COMPUTER PROGRAM
FOR
MANEUVERING AND BALLISTIC RE-ENTRY VEHICLES**

C. L. Kyriss, Supervising Engineer

T. B. Harris, Research Engineer

To be presented at the: TENTH USN SYMPOSIUM ON AEROBALLISTICS

JULY 15-17, 1975

**GENERAL ELECTRIC COMPANY
RE-ENTRY AND ENVIRONMENTAL SYSTEMS DIVISION
Post Office Box 8555
Philadelphia, Pennsylvania 19101**

ABSTRACT

A numerical solution for determining the three-dimensional inviscid supersonic flow about maneuvering re-entry vehicles has been developed. The solution is a direct one in which the shock wave shape and the flow properties in the shock layer are determined automatically for a specified body shape and freestream conditions. A time-dependent technique is used to obtain the solution in the subsonic-transonic region surrounding the stagnation point; and a forward marching, finite-difference technique is employed in the supersonic region. Predictions have been shown to be in excellent agreement with ground and flight test experimental data. In addition, operating costs are small enough that the program can be used in preliminary design tradeoff studies as well as in detailed design studies.

1.0 INTRODUCTION

The design of high performance re-entry vehicles, both ballistic and maneuvering, requires a knowledge of the three-dimensional flow field about the body. The vehicle's aerodynamic performance, thermal protection requirements, and structural requirements are all dependent upon the surrounding flow field. Aerothermal performance is generally critical in the lower altitude portion of the re-entry trajectory where the shock layer flow is characterized by an outer inviscid flow impressed upon a thin viscous boundary layer. In this critical region, aerodynamic and thermodynamic analyses require an accurate prediction for the inviscid flow, since it provides boundary conditions for boundary layer calculations and is generally the primary influence in determining a vehicle's aerodynamic characteristics - drag, lift and stability. This paper presents a numerical solution which has been developed to calculate the three-dimensional inviscid flow field about maneuvering or ballistic re-entry vehicles.

The solution is determined using a time-dependent technique in the subsonic-transonic region surrounding the vehicle nosetip, and a forward marching, finite-difference technique in the supersonic (afterbody) region. The computer program is operational for general body shapes, both in the subsonic and supersonic flow domains. It has been successfully applied to many maneuvering and ballistic vehicle designs - including sphere cones and biconics, bodies with bent axes, elliptic cones, sliced bodies, and vehicles with flaps. Angles of sideslip as well as angles of attack may be accepted. The only restriction on total angle of incidence is that (excluding the stagnation region) the flow remain supersonic everywhere. Both real gas and ideal gas calculations are possible.

The program has important applications. Since the actual flight environments for re-entry vehicles, i. e. high Mach number and high Reynolds number, usually cannot be fully simulated in ground test facilities, an analytical method is necessary to predict the vehicle's aerodynamic characteristics. The present program furnishes this technique. In addition, because run times are short, usage is not limited to final detailed design analyses. The program may be used in preliminary aerodynamic design and tradeoff studies as well.

Section 2.0 of this paper presents the analytical background for the program, including a review of the governing equations, presentation of the finite difference scheme, identification of boundary conditions and their treatment, and descriptions of the body geometry definition and treatment of special problems (e. g. entropy layers, and leeside computation at large angles of attack). Section 3.0 presents numerical results for several re-entry configurations. Results are compared with ground and flight test data. A further discussion of the applications of the program is given in Section 4.0, and conclusions are presented in Section 5.0.

2.0 ANALYSIS

The inviscid flow field surrounding a hypersonic re-entry vehicle is characterized by a region of subsonic flow near the stagnation point which becomes supersonic as it expands around the body. The complete flow field is determined using a time-dependent technique in the subsonic-transonic region and a forward marching, finite-difference technique in the supersonic region. The overall solution is a direct one in which the shock wave shape and the flow properties in the shock layer are determined automatically for a specified body shape and free-stream conditions. The bow shock wave is treated as a sharp discontinuity using the Rankine-Hugoniot jump conditions and the body surface is assumed to be impermeable.

2.1 Governing Equations

For an inviscid, adiabatic flow in chemical equilibrium, the governing (Euler) equations can be written as:

$$\left. \begin{aligned} \frac{Dp}{Dt} + \gamma \nabla \cdot \bar{q} &= 0, \\ \frac{D\bar{q}}{Dt} + \frac{p}{\rho} \nabla p &= 0, \\ \frac{Ds}{Dt} &= 0, \end{aligned} \right\} \quad (1)$$

where

$$p = \ln p, \quad (2)$$

and

$$\left. \begin{aligned} \frac{p}{\rho} &= F(p, s), \\ \gamma &= \frac{\partial(\ln p)}{\partial(\ln \rho)} \Big|_s = \gamma(p, s). \end{aligned} \right\} \quad (3)$$

The symbols p , ρ , s , t , ∇ , and $\frac{D}{Dt}$ have their usual meaning; \bar{q} denotes the velocity vector; and F and γ are known, tabular functions for a given gas composition. For steady flow, the mathematical character of these equations depends upon whether the flow is subsonic (elliptic) or supersonic (hyperbolic). For this reason, the computation is divided into a subsonic-transonic region and a supersonic region. The method of solution in each of these regions is given below.

2.2 Method of Solution

The solution in each region is obtained from a well posed, initial-boundary value problem. In the transonic (nosetip) region, the steady state solution to the time dependent Euler equations is sought. This solution provides the initial data for the supersonic (afterbody) region solution. Coordinate transformations are used to map the irregular physical space (shock layer) into a regular computational space. The partial derivatives in the resulting equations are then approximated by finite-differences of second order accuracy where the difference operators are chosen to preserve the physics of the flow.

2.2.1 Transonic Region Flow Field

The steady state solution in the transonic region (Figure 1), which includes the entire subsonic flow field near the stagnation point and a portion of the downstream supersonic flow, is found as the asymptotic limit of an unsteady flow process. The present method is a simple extension of the program developed by Moretti⁽¹⁾ to include asymmetric nosetips and real gas effects.

The body geometry is specified in cylindrical coordinates in tabular form, in selected circumferential (meridional) planes, viz. $r = r_b(\theta, \Phi)$. For axisymmetric shapes, the body geometry may also be specified analytically as a combination of simple geometric shapes (e. g. sphere-cone). The body geometry and flow are assumed to be symmetric about the pitch plane. For the selected computational network in spherical coordinates, the body radii, $R_b = R_b(\theta, \Phi)$ are determined through a second order interpolation. The body and shock surfaces are then represented by

$$F_b = R - R_b(\theta, \Phi) = 0, \quad (\text{body}) \quad (4a)$$

and

$$F_s = R - R_s(\theta, \Phi, t) = 0, \quad (\text{shock}) \quad (4b)$$

with the shock radius, R_s , to be determined as part of the solution.

The shock layer in the transonic region (Figure 1) is mapped into a rectangular parallelepiped through the transformation:

$$\left. \begin{aligned} X &= \Phi \\ Y &= \pi - \theta \\ Z &= \frac{R - R_b}{R_s - R_b} \\ T &= t \end{aligned} \right\} \quad (5)$$

In terms of the new independent variables, the governing equations (1) can be written in vector-matrix representation as:*

$$\bar{f}_T = - (\tilde{F} \bar{f}_z + \tilde{A} \bar{f}_y + \tilde{N} \bar{f}_x + \bar{H}), \quad (6)$$

where

$$\bar{f} = (P, u, v, w, S). \quad (7)$$

At interior points in the field, the solution is advanced using MacCormack's predictor-corrector scheme⁽³⁾ on P and \bar{q} . The convective transport of entropy is treated using convective differences in the radial direction, as outlined in Reference 4, to eliminate numerically induced waves. This scheme (due to Moretti) maintains the second order accuracy of the computation by approximating the radial derivative with the difference approximation:

$$S_z = (-S_{n+2} + 3S_{n+1} - 2S_n) / \Delta z \quad (8a)$$

in the predictor cycle and

$$S_z = (S_{n+1} - S_n) / \Delta z \quad (8b)$$

in the corrector cycle, when the radial velocity relative to the mesh is inward.

When the relative radial velocity is outward (positive), the standard MacCormack scheme is used.

At the shock and the body, characteristic compatibility relations are used in conjunction with the Rankine-Hugoniot relations and the body surface tangency conditions to close the system. The unit normal to the shock (positive inward),

* The details containing the final form of the coefficient matrices in (6) will be given in Reference 2.

Vol. 3

represented by (4b), is given by

$$\vec{e}_{N_s} = \frac{-\nabla F_s}{|\nabla F_s|} = \frac{-\vec{e}_R + \frac{1}{R_s} \frac{\partial R_s}{\partial \theta} \vec{e}_\theta + \frac{1}{R_s \sin \theta} \frac{\partial R_s}{\partial \phi} \vec{e}_\phi}{|\nabla F_s|} \quad (9)$$

$$= e_{N_1} \vec{e}_R + e_{N_2} \vec{e}_\theta + e_{N_3} \vec{e}_\phi,$$

where

$$|\nabla F_s| = [e_{N_1}^2 + e_{N_2}^2 + e_{N_3}^2]^{1/2} \quad (10)$$

and the e_{N_i} are direction cosines. The freestream velocity vector is

$$\vec{q}_\infty = U_\infty \vec{e}_R + V_\infty \vec{e}_\theta + W_\infty \vec{e}_\phi, \quad (11)$$

where

$$\left. \begin{aligned} U_\infty &= q_\infty (\sin \alpha \sin \theta \cos \phi + \cos \alpha \cos \theta) \\ V_\infty &= q_\infty (\sin \alpha \cos \theta \cos \phi - \cos \alpha \sin \theta) \\ W_\infty &= q_\infty (-\sin \alpha \sin \phi). \end{aligned} \right\} \quad (12)$$

Then the total velocity relative to the shock along the inward normal is

$$\vec{U}_\infty = \vec{e}_{N_s} \cdot \left(\vec{q}_\infty - \frac{\partial R_s}{\partial t} \vec{e}_R \right) = e_{N_1} U_\infty + e_{N_2} V_\infty + e_{N_3} W_\infty - e_{N_1} \frac{\partial R_s}{\partial t}. \quad (13)$$

If $R_s(\theta, \phi, t)$ is known, the properties downstream of the shock are completely specified through the Rankine-Hugoniot conditions. The determination of $R_s(\theta, \phi, t)$ is outlined below.

The new shock position is determined by

$$\bar{R}_s(t+\Delta t) = R_s(t) + \left. \frac{\partial R_s}{\partial t} \right|_t \Delta t \quad (14a)$$

in the predictor cycle and

$$R_s(t+\Delta t) = \frac{1}{2} \left[R_s(t) + \bar{R}_s(t+\Delta t) + \left. \frac{\partial \bar{R}_s}{\partial t} \right|_{t+\Delta t} \Delta t \right] \quad (14b)$$

in the corrector cycle. The spatial derivatives of R_s appearing in equations (9) and (10) are evaluated by finite differences. The temporal derivative of R_s appearing in (13) and (14) is determined by simultaneously satisfying the Rankine-Hugoniot conditions and a characteristic compatibility relation written in the direction of the normal to the shock, viz.

$$\frac{DP}{Dt} + \gamma \nabla \cdot \vec{q} - \frac{\gamma}{\alpha} \vec{e}_{N_s} \cdot \left(\frac{D\vec{q}}{Dt} + \frac{p}{\rho} \nabla p \right) = 0. \quad (15)$$

This equation provides a relationship between P_T and $\tilde{U}_T = \frac{\partial}{\partial t}(\tilde{e}_{N_3} \cdot \tilde{q})$ of the form

$$P_T - \frac{\gamma}{\alpha} \tilde{U}_T = \text{RHS}, \quad (16)$$

which is integrated using a predictor-corrector scheme. The consistent difference approximation

$$\left. \begin{aligned} f_T &= \frac{\bar{f}(T+\Delta T) - f(T)}{\Delta T} && \text{(predictor)} \\ \bar{f}_T &= \frac{2f(T+\Delta T) - f(T) - \bar{f}(T+\Delta T)}{\Delta T} && \text{(corrector)} \end{aligned} \right\} (17)$$

is used on the temporal derivatives, and the spatial derivatives are approximated by the usual alternating, one-sided derivatives, except in the radial direction where a scheme like that given by equation (8) is used. To eliminate repeated and time consuming solutions of the Rankine-Hugoniot relations, a shock table is constructed at the beginning of the run which relates \tilde{U}_b , P , and \bar{U} (where $\bar{U} = \tilde{U} - e_{N_1} \frac{\partial R_s}{\partial x}$).

On the body surface represented by equation (4a), the velocity component normal to the surface must vanish, i. e.

$$\tilde{U} = \tilde{e}_{N_b} \cdot \tilde{q} = e_{N_1} U + e_{N_2} V + e_{N_3} W = 0, \quad (18)$$

where the unit normal to the body (positive outward) is given by

$$\left. \begin{aligned} \tilde{e}_{N_b} &= \frac{\nabla F_b}{|\nabla F_b|} = \frac{\tilde{e}_R - \frac{1}{R_b} \frac{\partial R_b}{\partial \theta} \tilde{e}_\theta - \frac{1}{R_b \sin \theta} \frac{\partial R_b}{\partial \phi} \tilde{e}_\phi}{|\nabla F_b|} \\ &= e_{N_1} \tilde{e}_R + e_{N_2} \tilde{e}_\theta + e_{N_3} \tilde{e}_\phi, \end{aligned} \right\} (19)$$

and

$$|\nabla F_b| = [e_{N_1}^2 + e_{N_2}^2 + e_{N_3}^2]^{1/2}. \quad (20)$$

A characteristic compatibility relation in the direction of the normal to the body can now be written in the form (see (15) and (16) and note that $\tilde{U}_T = 0$):

$$P_T = \text{RHS}. \quad (21)$$

An independent equation can also be written for the projection of the momentum equation along the intersection of the plane tangent to the body surface and the ϕ -plane. The unit vector in this direction is given by

$$\vec{e}_T = \vec{e}_{N_b} \times \vec{e}_\phi / |\vec{e}_{N_b} \times \vec{e}_\phi|, \quad (22)$$

and the projection of the momentum equation along this direction is

$$\vec{e}_T \cdot \left(\frac{D\vec{q}}{Dt} + \frac{p}{\rho} \nabla P \right) = 0, \quad (23)$$

which can be written as

$$\tilde{V}_T = \text{RHS}. \quad (24)$$

Equations (21) and (24) are now integrated along with the crossflow momentum equation and the equation for entropy convection using MacCormack's predictor-corrector scheme with special radial derivatives (equation (8)). This system of equations is closed by the kinematic condition (18).

The allowable time step for the computation is chosen according to the Courant-Fredricks-Lewy (CFL) necessary condition for stability as the minimum of the allowable time step at each mesh point. The solution is then advanced in time until a suitable steady-state condition has been reached. The resulting numerical method becomes an iterative scheme in which a discrete iterative index is replaced by a continuous time variable, and the unsteady Euler equations provide a universal rule for improving the solution.

The transonic program provides the inviscid forces and moments acting on the nose-tip and the initial data to be used in the supersonic solution. The provision has been made to allow misalignment of the body axes in the nosetip and afterbody regions. For spherically blunted configurations, the initial data for the supersonic analysis can be determined from an axisymmetric transonic solution in wind-fixed coordinates so that this one solution suffices for all angles of attack and sideslip.

2.2.2 Supersonic Region Flow Field

In the supersonic region (Figure 2), the governing steady flow equations are hyperbolic in the z direction. Therefore, the solution can be determined by a forward marching process in z , similar to that used in the transonic region where t was hyperbolic. In a certain sense, the problem in the supersonic region is simpler than the general three-dimensional, unsteady transonic problem because the additional time dimension is no longer needed. However, special problems must be considered in the supersonic region downstream of the nose related to large gradients in the

flow properties. For example, entropy gradients through the shock layer (due to nose bluntness and angle of attack effects) are given special consideration because, if improperly treated, they eventually destroy the computation. Also, at large angles of attack, the inviscid model begins to break down on the leeward side. Since this does not occur before the crossflow becomes supersonic, the windward side is unaffected and the computation can be continued by properly truncating the solution on the leeside. An outline of the resulting method and some of the details are given below.*

The 3D supersonic (3DS) program, like the 3D transonic (3DT) program, is currently operational for general asymmetric shapes. The vehicle geometry is defined by specifying cross-sectional shapes in tabular form, at selected longitudinal (z) stations; i. e., x, y coordinates relative to the body axis defined by $y = d(z)$. The associated "cylindrical" coordinates (Figure 2) are spline fit circumferentially where provisions have been made to allow segmentation of the cross-section as would be necessary on bodies having maneuvering control surfaces (slices and flaps). At the present time, the cross-sections are assumed to be conically connected. To simplify the geometry specification, special options are available for circular and elliptic cross-sections and for complete vehicle configurations comprised of simple geometric shapes (e. g., sphere-cone-cone, etc.).

The final form of the governing equations is reached through a sequence of independent variable transformations. The equations (1) are first written in Cartesian coordinates (x, y, z) and then transformed to "cylindrical" coordinates (r, θ , z) with velocity components (u, v, w), where the origin is given by $y = d(z)$.** The steady flow equations become:

$$\bar{u} P_r + \frac{\bar{v}}{r} P_\theta + w P_z + \gamma \left[u_r + \frac{v_\theta}{r} + \frac{u}{r} + w_z - d'(C w_r - \frac{d}{r} w_\theta) \right] = 0, \quad (25a)$$

$$\bar{u} u_r + \frac{\bar{v}}{r} u_\theta + w u_z - \frac{v}{r} \bar{v} + \frac{p}{\rho} P_r = 0, \quad (25b)$$

* A more complete description will be given in Reference 2. Related work on this subject is given in References (5-7).

** The authors are indebted to Prof. G. Moretti for having suggested this coordinate system since it is particularly well suited to vehicles with misaligned axes.

Vol. 3

$$\bar{u} \bar{u}_r + \frac{\bar{v}}{r} v_\theta + w w_z + \frac{u}{r} \bar{v} + \frac{p}{\rho} \frac{1}{r} P_\theta = 0, \quad (25c)$$

$$\bar{u} w_r + \frac{\bar{v}}{r} w_\theta + w w_z + \frac{p}{\rho} \left[P_z - d' (G_r - \frac{d}{r} P_\theta) \right] = 0, \quad (25d)$$

$$\bar{u} S_r + \frac{\bar{v}}{r} S_\theta + w S_z = 0, \quad (25e)$$

where:
$$\left. \begin{aligned} \bar{u} &= u - w \theta d' \\ \bar{v} &= v + w r d' \end{aligned} \right\} \quad (26)$$

$$d = \sin \theta, \quad \theta = \cos \theta. \quad (27)$$

Next the shock layer, bounded by the body and the shock, is mapped into a rectangle in the computational plane through the transformation:

$$\left. \begin{aligned} x &= \frac{r - r_b}{r_s - r_b} \\ y &= G(\theta) \\ z &= z \end{aligned} \right\} \quad (28)$$

where the body and shock are represented by

$$F_b = r - r_b(\theta, z) = 0, \quad (29a)$$

and
$$F_s = r - r_s(\theta, z) = 0, \quad (29b)$$

with r_b being known and r_s to be determined. The governing equations (25) can now be written in the form

$$\vec{f}_z = -(\tilde{A} \vec{f}_x + \tilde{B} \vec{f}_y + \vec{C}), \quad (30)$$

where
$$\vec{f} = (P, u, v, S), \quad (31)$$

and
$$w = [2(H-h) - u^2 - v^2]^{1/2}, \quad (32)$$

$$h = h(P, S). \quad (33)$$

As in the transonic region, the solution in the field in the supersonic region is advanced using MacCormack's predictor-corrector scheme with convective differences in the radial direction for entropy transport (see equation (8), for example). The region to be computed is dependent upon whether the flow is symmetric or asymmetric, as shown in Figure 3. The symmetric case requires that the body be symmetrical with respect to the y-z plane and that the sideslip angle be zero. As indicated in Figure 3, a non-uniform grid network is allowed (in both X and Y) in addition to the $Y = G(\Theta)$ transformation which can be used to refine the mesh in large circumferential gradient regions. Presently, the $G(\Theta)$ transformation is modeled after the transformation to elliptic-cylindrical coordinates. The inverse transformation is

$$\theta = \tan^{-1}(-K \sin Y / \cos Y), \quad (34)$$

where K is an ellipticity parameter.

At the shock, represented by (29b), the unit normal (positive inward) is given

by

$$\vec{e}_{n_s} = \frac{-\nabla F_s}{|\nabla F_s|} = \left\{ -\vec{e}_r + \frac{1}{r_s} \frac{\partial r_s}{\partial \theta} \vec{e}_\theta + \left[\frac{\partial r_s}{\partial y} + d \left(G + \delta \frac{1}{r_s} \frac{\partial r_s}{\partial \theta} \right) \right] \vec{e}_z \right\} / |\nabla F_s| \quad (35)$$

$$= e_{n_1} \vec{e}_r + e_{n_2} \vec{e}_\theta + e_{n_3} \vec{e}_z,$$

where

$$|\nabla F_s| = \left[e_{n_1}^2 + e_{n_2}^2 + e_{n_3}^2 \right]^{1/2}, \quad (36)$$

and the e_{n_i} are the direction cosines of the normal to the shock. The freestream velocity vector in (r, θ, z) is

$$\vec{q}_\infty = u_\infty \vec{e}_r + v_\infty \vec{e}_\theta + w_\infty \vec{e}_z, \quad (37)$$

where the components are

$$\left. \begin{aligned} u_\infty &= q_\infty (\sin \beta \delta + \cos \beta \sin \alpha G) \\ v_\infty &= q_\infty (\sin \beta G - \cos \beta \sin \alpha \delta) \\ w_\infty &= q_\infty (\cos \beta \cos \alpha) \end{aligned} \right\} \quad (38)$$

and where α and β are the angle of attack and angle of sideslip, respectively.

Vol. 3

Then the freestream velocity normal to the shock is

$$\tilde{u}_{\infty} = \tilde{q}_{\infty} \cdot \tilde{e}_{n_s} = e_{n_1} u_{\infty} + e_{n_2} v_{\infty} + e_{n_3} w_{\infty} = q_{\infty} \cos \sigma, \quad (39)$$

where σ is the inclination of the normal to the shock with respect to the freestream velocity vector. A shock table can be constructed from the conservation relations, with σ as a parameter, which relates \tilde{u} , P and S. This table is constructed only once at the beginning of the solution, and eliminates repeated and time consuming real gas solutions of the Rankine-Hugoniot relations. The range of the table is $0 \leq \sigma \leq \sigma^*$, where $\Delta \sigma = 0.5$ degrees, and $\sigma^* = \cos^{-1}(1/M_{\infty})$. For $\sigma \geq \sigma^*$, \tilde{u} , P, and S are equal to their freestream counterparts. The velocity downstream of the shock is

$$\tilde{q} = \tilde{u} \tilde{e}_{n_s} + \tilde{v}, \quad (40)$$

where \tilde{v} is the tangential velocity, which remains unchanged across the shock, viz.

$$\tilde{v} = \tilde{v}_{\infty} = \tilde{q}_{\infty} - \tilde{u}_{\infty} \tilde{e}_{n_s}. \quad (41)$$

The velocity vector downstream of the shock can now be written as

$$\tilde{q} = \tilde{q}_{\infty} + (\tilde{u} - \tilde{u}_{\infty}) \tilde{e}_{n_s} = u \tilde{e}_r + v \tilde{e}_{\theta} + w \tilde{e}_z, \quad (42)$$

where the downstream components are:

$$\left. \begin{aligned} u &= u_{\infty} + e_{n_1} (\tilde{u} - \tilde{u}_{\infty}) \\ v &= v_{\infty} + e_{n_2} (\tilde{u} - \tilde{u}_{\infty}) \\ w &= w_{\infty} + e_{n_3} (\tilde{u} - \tilde{u}_{\infty}). \end{aligned} \right\} \quad (43)$$

Now if $r_s(\theta, z)$ is known, the properties downstream of the shock are completely specified through the relationships given above. The determination of $r_s(\theta, z)$ is outlined below.

The position of the shock at the new downstream location, $z + \Delta z$, is determined by

$$\bar{r}_s(z + \Delta z) = r_s(z) + \left. \frac{\partial r_s}{\partial z} \right|_z \Delta z \quad (44a)$$

in the predictor cycle and

$$r_s(z + \Delta z) = \frac{1}{2} \left[r_s(z) + \bar{r}_s(z + \Delta z) + \left. \frac{\partial r_s}{\partial z} \right|_{z + \Delta z} \Delta z \right] \quad (44b)$$

in the corrector cycle. Once the shock position has been specified through the relations (44), the derivative $\frac{\partial \xi}{\partial \theta}$ appearing in (35) and (36) is evaluated by finite differences.

The derivative $\frac{\partial \xi}{\partial \theta}$ is determined by simultaneously satisfying the Rankine-Hugoniot relations and a reference plane characteristic compatibility relation of the form

$$\frac{dP}{dl_+} - \frac{\gamma}{a^2 \beta} \left[\left(u - \frac{v}{r_3} \frac{\partial \xi}{\partial \theta} \right) \frac{dw}{dl_+} - w \frac{du}{dl_+} \right] = \text{RHS}, \quad (45)$$

where

$$\beta = \left[\frac{w^2}{a^2} - 1 + \left(u - \frac{v}{r_3} \frac{\partial \xi}{\partial \theta} \right)^2 / a^2 \right]^{1/2}, \quad (46)$$

and

$$\frac{d}{dl_+} = \frac{\partial}{\partial z} + \lambda \frac{\partial}{\partial x} \quad (47)$$

is the directional derivative along the reference plane characteristic $\frac{dx}{dz} = \lambda$.

Equation (45) can be written as

$$P_z - \frac{\gamma}{a^2 \beta} \left[\left(u - \frac{v}{r_3} \frac{\partial \xi}{\partial \theta} \right) w_z - w u_z \right] = \text{RHS}, \quad (48)$$

where the right hand side contains derivatives of X and Y. This expression is integrated using a predictor-corrector scheme. The X derivatives are approximated by

$$f_x = (2f_n - 3f_{n-1} + f_{n-2}) / \Delta X \quad (49a)$$

in the predictor cycle and

$$f_x = (f_n - f_{n-1}) / \Delta X \quad (49b)$$

in the corrector cycle. The Y derivatives are approximated by the usual alternating, one-sided finite differences in the predictor and corrector. The Z derivatives on the left hand side of (48) are replaced by

$$f_z = \frac{\bar{f}(z+\Delta z) - f(z)}{\Delta z} \quad (50a)$$

in the predictor and

$$f_z = \frac{2f(z+\Delta z) - f(z) - \bar{f}(z+\Delta z)}{\Delta z} \quad (50b)$$

in the corrector. An iteration is now carried out to determine $\frac{\partial \bar{r}_s}{\partial z} \Big|_{z+\Delta z}$ in the predictor and $\frac{\partial \bar{r}_s}{\partial z} \Big|_{z+\Delta z}$ in the corrector, such that

$$|\text{LHS}(48) - \text{RHS}(48)| \Delta z < \epsilon^*, \quad (51)$$

where the properties at $Z + \Delta Z$ in the LHS of (48) are given by the Rankine-Hugoniot relations. After the corrector cycle, the final shock position is given by

$$r_s(z+\Delta z) = r_s(z) + \frac{1}{2} \left[\frac{\partial r_s}{\partial z} \Big|_z + \frac{\partial r_s}{\partial z} \Big|_{z+\Delta z} \right] \Delta z. \quad (52)$$

On the body surface, represented by (29a), the normal velocity must vanish, i. e.

$$\tilde{u} = \tilde{e}_{n_b} \cdot \tilde{q} = e_{n_1} u + e_{n_2} v + e_{n_3} w = 0, \quad (53)$$

where the unit normal to the body (positive outward) is given by

$$\tilde{e}_{n_b} = \frac{\nabla F_b}{|\nabla F_b|} = \left\{ \tilde{e}_r - \frac{1}{r_b} \frac{\partial r_b}{\partial \theta} \tilde{e}_\theta - \left[\frac{\partial r_b}{\partial z} + d' \left(\phi + \delta \frac{1}{r_b} \frac{\partial r_b}{\partial \theta} \right) \right] \tilde{e}_z \right\} / |\nabla F_b| \quad (54)$$

$$= e_{n_1} \tilde{e}_r + e_{n_2} \tilde{e}_\theta + e_{n_3} \tilde{e}_z,$$

with

$$|\nabla F_b| = \left[e_{n_1}^2 + e_{n_2}^2 + e_{n_3}^2 \right]^{1/2}. \quad (55)$$

The kinematic condition (53) can then be written as

$$u - \frac{1}{r_b} \frac{\partial r_b}{\partial \theta} v - \left[\frac{\partial r_b}{\partial z} + d' \left(\phi + \delta \frac{1}{r_b} \frac{\partial r_b}{\partial \theta} \right) \right] w = 0. \quad (56)$$

An equation is now written for the conservation of tangential momentum. The unit vector which lies along the intersection of the plane tangent to the body surface and the z plane is given by

$$\tilde{e}_t = \tilde{e}_z \times \tilde{e}_{n_b} / |\tilde{e}_z \times \tilde{e}_{n_b}| = \left(\frac{1}{r_b} \frac{\partial r_b}{\partial \theta} \tilde{e}_r + \tilde{e}_\theta \right) / \nu = e_{t_1} \tilde{e}_r + e_{t_2} \tilde{e}_\theta, \quad (57)$$

* The method of false position is used with ϵ usually taken as 10^{-5} .

where

$$v = [e_{t_1}^2 + e_{t_2}^2]^{1/2} = [1 + (\frac{1}{r_b} \frac{\partial r_b}{\partial \theta})^2]^{1/2}. \quad (58)$$

Then the projection of the momentum equation along the \hat{e}_t direction is

$$\hat{e}_t \cdot \left(\frac{D\bar{q}}{Dt} + \frac{P}{\rho} \nabla P \right) = 0, \quad (59)$$

which can be written as

$$w \tilde{v}_z + \frac{\bar{v}}{r_b} G' \tilde{v}_y + \frac{\bar{v}}{r_b} (u e_{t_2} - v e_{t_1}) + \frac{P}{\rho} \frac{e_{t_2}}{r_b} G' P_y = \text{RHS}, \quad (60)$$

where the right hand side contains body curvature terms. This equation is solved for \tilde{v}_z and integrated using the usual predictor-corrector scheme except that convective differences are used on \tilde{v}_y . Similar arguments hold for the entropy conservation equation:

$$S_z = -\frac{\bar{v}}{r_b} G' S_y / w. \quad (61)$$

Finally, the body surface pressure is determined from a reference plane characteristic compatibility relation (similar to that used at the shock) which is simplified by making use of the kinematic condition (56) to give an equation of the form:

$$P_z = \text{RHS}. \quad (62)$$

The right hand side of this equation contains only X and Y derivatives of the variables and known derivatives of the body geometry and is integrated using the usual predictor-corrector scheme at boundaries. After some algebraic manipulation, the expressions for the determination of the velocity components at the body can be written as

$$\left. \begin{aligned} w &= \sqrt{q^2 - \hat{v}^2} v / |\nabla r_b|, \\ u &= \hat{u} e_{t_2} + \hat{v} e_{t_1}, \\ v &= -\hat{u} e_{t_1} + \hat{v} e_{t_2}, \end{aligned} \right\} \quad (63)$$

where

$$\hat{u} = \frac{1}{v} \left[\frac{\partial r_b}{\partial \theta} + d' \left(G + d \frac{1}{r_b} \frac{\partial r_b}{\partial \theta} \right) \right] w, \quad \hat{v} = \tilde{v}, \quad (64)$$

$$q^2 = 2(H-h), \quad (65)$$

with H being the total enthalpy.

The procedure outlined above provides an accurate and efficient method for the determination of the inviscid flow field about the body. In an attempt to provide a more realistic assessment of the real flow about the body, and in particular the forces which act upon it, certain options have been implemented which are motivated by physical and operational considerations.

The first deals with the treatment of the vortical layer, which for a blunted body becomes singular as the length becomes infinite. The emphasis in the current work is not to focus on this phenomenon, which is a manifestation of the assumption of an inviscid flow and which would not exist in a real (viscous) fluid, but to simply ensure that the overall procedure is not adversely affected. The problem is not resolved, for example, by coordinate stretching alone,⁽⁵⁾ and although it can be treated by special considerations,⁽⁶⁾ this unduly complicates the analysis. It was found that the problem is effectively treated by using convective differences;⁽⁸⁾ and with second order accurate convective schemes, the required accuracy is achieved as well. In addition, maintaining the surface entropy at the stagnation value for a blunt body does not allow the flow to completely relax to the conical pattern as the length becomes infinite. This is not only physically unrealistic but also impedes the rate at which the explicit solution is allowed to advance.* Consequently, an option has been provided to relax the surface entropy in the windward plane in the following manner. The data at the longitudinal station, z , are linearly extrapolated to the body in the windward meridian at the downstream location, $z + \Delta z$.** This entropy is then convected around the body (Equation (61)). The net result is that for a blunted cone the solution will ultimately approach a conical flow if continued sufficiently far downstream. This provides not only a more realistic physical model, but also a more efficient numerical method, particularly for vehicles of small bluntness.

* The allowable step size for the computation is taken as the minimum of the allowable step size at each mesh point according to the CFL criterion.

** The entropy ordinarily does not begin to relax for 50 nose radii or more downstream of the nose.

Another problem which arises is that at large angles of attack ($\alpha \gg 2\theta_0$) a crossflow shock forms on the leeward side and the flow separates. In this case, an inviscid analysis of the leeside region without viscous displacement interaction effects is somewhat academic. Since the crossflow is supersonic, the flow on the windward side ahead of the separation region is unaffected by the leeside flow. Also, the pressures which exist on the leeside are at least an order of magnitude less than those on the windward side. Consequently, for purposes of determining the forces and moments acting on the vehicle, a detailed treatment of the leeside region is not necessary because the windward flow can be determined separately and the leeside pressure is essentially negligible. An option has therefore been provided to truncate the solution along a ray upstream of where the flow separates when the crossflow becomes supersonic. The crossflow derivatives along this ray are then approximated by one-sided finite differences. In the determination of the forces and moments acting on the vehicle, a correlation of leeside pressures is used to complete the specification of the surface pressure. The resulting method has the desirable feature of eliminating computations on the leeside which are of questionable validity, thereby providing a more efficient aerodynamic design and analysis tool.

The 3DFF program has been successfully applied to a variety of configurations. Results showing comparisons with flight and ground test data are given in the next section.

3.0 RESULTS

The three-dimensional flow field program has been operational for nearly three years. During this period, its results have been extensively compared with ground and flight test experimental data, and the predictions of other numerical solutions. These comparisons have demonstrated the program to be extremely accurate. Typical results will be presented here for several ballistic and maneuvering re-entry vehicle designs -- including sphere cones and biconics, a bent axis vehicle, a sliced body, and vehicles with simulated ablated nose tip shapes. Most comparisons will present center of pressure variations, as this is the parameter of primary interest in the aerodynamic design of maneuvering vehicles. Comparisons of surface pressure distributions will also be presented which indicate that the details of the flow field are being calculated accurately.

Figure 4 presents the predicted center of pressure and normal force coefficient derivative variations with bluntness ratio for a nine degree sphere cone, near zero angle of attack, at three different freestream Mach numbers. Also presented are test data obtained at Mach 10, and the agreement with the numerical results is excellent. Figure 4 illustrates that both the force coefficient and center of pressure are strong functions of Mach number. The importance of a reliable technique which can be applied to predict aerodynamic characteristics throughout the entire flight Mach number regime is then evident (see Applications Section 4.0). Real gas as well as ideal gas calculations are possible with the 3DFF program, and Figure 4 presents predictions at Mach 20 employing the two equations of state. The real gas calculation corresponds to 60,000 feet altitude. The effect of the gas law on stability is as large as one to two percent of the apex length for some configurations. This can have a significant impact upon the design of maneuvering, and also ballistic vehicles.

The next case considered is a sphere biconic, with and without a bent longitudinal axis. Figure 5 presents a sketch of the geometry, and compares the predicted center of pressure values with test data. The agreement between the analytical and experimental results is excellent. Corresponding pressure distributions are

presented in Figure 6 for the bent axis configuration at a particular angle of attack. The high initial pressures are due to the larger nose cone angle and the deflected axis. The predicted and measured pressure distributions are in very good agreement along the windward and side rays. On the leeward side, the comparison is not as favorable, however, this is not surprising since the inviscid flow model loses validity on the leeward side at high angles of attack. The flow becomes separated in this region, and viscous effects become significant. Despite the fact that the leeward pressures are not calculated very accurately, there are no serious consequences. The magnitude of the leeside pressures is about an order of magnitude smaller than the windward pressures (at this particular angle of attack and Mach number); consequently, they are a second order influence in determining the vehicle's integrated force and moment characteristics. At high angles of attack, it is the pressure distribution in the windward half-plane that is usually primarily responsible for determining a configuration's aerodynamic characteristics. This is evidenced in Figure 5 where it can be seen that the predicted center of pressure location at 8 degrees angle of attack is in excellent agreement with the data.

Nose shape change effects due to ablation can dramatically affect the performance of ballistic and maneuvering vehicles. Figure 7 illustrates the ability of the 3DFF program to predict these effects. Two basic shapes are considered: a bluff shaped nose associated with ablation in the high altitude, laminar flow regime; and a pointed nose associated with lower altitude turbulent flow. Predictions have been generated for both symmetric and asymmetric shapes; the basic body considered is the bent axis biconic discussed previously. The agreement between the predictions and data is excellent: the trim angles of attack and normal force coefficients are accurately predicted for all four nose shapes.

Predictions for another maneuvering concept are presented in Figure 8. This is a sliced body, i. e. a symmetric configuration except for an aft slice on the windward side. A sketch of this concept is shown in Figure 8 along with comparisons of the predicted and measured longitudinal stability characteristics for both the sliced and unsliced bodies. The agreement is again very good.

Typical sideslip comparisons are presented in Table I. The predicted and measured yaw center of pressure locations are presented for three different vehicles at various combinations of angle of attack and sideslip angle. In all cases, the predictions are in excellent agreement with the data. Note the significant change in yaw stability that a vehicle may experience with angle of attack, and that the 3DFF program accurately predicts this effect.

In Figure 9, a 3DFF prediction is compared to actual flight test data. This figure presents the pre-flight predicted and derived trim angle of attack histories. The agreement is very good. The maximum difference between the analytical and experimental results is about one degree, occurring in the Mach 11 to Mach 16 flight range. This discrepancy is believed to be due primarily to the difference between the predicted and actual nose tip recession rates.

4.0 APPLICATIONS

A fundamental problem faced by the re-entry vehicle industry has been that of predicting the aerodynamic characteristics of vehicles in the flight environment, i. e. high Mach number and high Reynolds number flow. This is due to the fact that ground test facilities cannot fully simulate flight conditions. Existing high Mach number wind tunnels ($M_{\infty} > 10$) operate at relatively low Reynolds number. The boundary layers which exist on models tested in these facilities are responsible for significant induced pressure and/or skin friction effects, and consequently detract from the significance of test results. This is a serious limitation if some aspect of vehicle stability or performance is critical at the high Mach number condition. In particular, maneuvering vehicles are usually designed with low stability margins in order to maximize their performance. This requires an accurate prediction of the stability level, since errors may lead to either decreased performance or total failure. Given the limitations associated with existing wind tunnels, the best method to predict aerodynamic characteristics of vehicles in the high Mach number, high Reynolds number flight environment is to analytically determine the inviscid flow over the body. This is precisely the function of the Three Dimensional Flow Field program. One of its most important applications, then, is to predict re-entry body characteristics in the full-scale flight environment. Due to its accuracy, the program's domain of applicability includes high performance maneuvering vehicles. In fact, the program was developed to enable accurate predictions to be generated for these vehicles.

Another aspect of the program's ability to uniquely simulate the flight environment is its ability to include real gas effects. In most aerodynamic ground test facilities, the total enthalpy of the flow is not sufficient to produce dissociation or ionization of the shock layer gases. In the high Mach number flight environment, however, these real gas effects become important; therefore, they must be simulated analytically. As indicated in Section 3, Figure 4 presents the 3DFF center of pressure predictions for a nine degree sphere cone, subject to ideal and real gas flows at Mach 20, 60,000 feet altitude. The difference in stability is as large as

Vol. 3

one to two percent of the apex length for some configurations. This effect is significant for maneuvering vehicles whose stability must be known quite accurately, and may be significant for some ballistic vehicles as well.

The other primary application of the program is to perform preliminary design and tradeoff studies. This is possible due to its small operating cost. Run times for the supersonic solution are on the order of about 2 to 5 minutes on the Honeywell 6060 computer which is equivalent to about 10 seconds or less on a CDC 7600. Since the run times are short, program usage is not limited to final detailed design studies, and the program may be used economically to perform parametric tradeoffs to arrive at an optimum configuration. A typical study of the sensitivity of vehicle stability to small changes in frustum angle for a biconic body at Mach 20 is shown in Figure 10. To obtain similar information from a wind tunnel experiment would have been much more costly. The outcome of such a study would be a definition of the optimum basic body (no control surfaces), which would then be the subject of further analyses. These applications establish the 3DFF program as an extremely powerful aerodynamic design tool.

5.0 CONCLUSIONS

The Three Dimensional Flow Field program has proven to be a valuable design technique. Prior to its development, no reliable technique existed for the prediction of aerodynamic characteristics of re-entry vehicles in the full scale flight environment. The 3DFF program has provided this essential capability. Due to its accuracy and efficiency, the program is now applied on a daily basis to the design of ballistic and maneuvering vehicles, and the analysis of ground and flight test data. In other words, it is the fundamental aerodynamic prediction technique.

The capability of the program is now being extended 1) to include the explicit calculation of embedded shocks, and 2) to treat complications introduced by vehicles with circumferential discontinuities (e. g. sliced or flapped vehicles). These developments will provide an even greater applicability for the program.

ACKNOWLEDGEMENTS

The authors express their sincere thanks to Professor G. Moretti and F. Bosworth. Professor Moretti has pioneered the numerical solution of three-dimensional hypersonic flows, and the success of the present program is due in a large part to his efforts and guidance. F. Bosworth is responsible for assembling the resulting procedures into a logical and efficient computer program.

NOMENCLATURE

a	sound speed
Θ	$\cos \Theta$
d	normal coordinate of body axis, see Figure 2
e	direction cosine
f	dependent variable
F	surface function
G	coordinate transformation function, eqn (28)
h	enthalpy
H	total enthalpy
l_+	characteristic coordinate
M	Mach number
p	pressure
P	$\ln p$
q	velocity modulus
r, R	radial coordinates
S	$\sin \Theta$
S	entropy
t, T	time
u, v, w	velocity components in circular cylindrical coordinate system
U, V, W	velocity components in spherical coordinate system
\tilde{u}, \tilde{U}	normal velocity component (to shock or body)
\tilde{v}, \tilde{V}	tangential velocity component (to shock or body)
z	axial coordinate
X, Y, Z	transformed coordinates, eqns. (5), (28)
α	angle of attack
β	angle of sideslip; also eqn. (46)
γ	isentropic exponent
Θ	polar angle, see Figures 1 and 2

10th Navy Symposium on Aerballistics

Vol. 3

NOMENCLATURE (CONTD.)

K	ellipticity parameter, eqn. (34)
λ	characteristic slope in reference plane, see eqn. (47)
ρ	density
σ	angle between shock normal and freestream velocity vector
Φ	spherical angle

SUBSCRIPTS

b	body
n, N	normal
r, θ, z	circular cylindrical coordinates, or partial derivatives with respect to these directions
R, Θ, Φ	spherical coordinates
s	shock
t, T	time; time derivative; tangential
X, Z	derivatives with respect to these coordinates

SUPERSCRIPTS

$\vec{}$	vector
\sim	matrix; particular velocity component
$\bar{}$	particular velocity component: value in MacCormack scheme
$\langle \rangle$	particular velocity component
\prime	derivative

REFERENCES

1. Moretti, G. , "Three-Dimensional Inviscid Flow about Supersonic Blunt Cones at Angle of Attack - II. Improved Time-Dependent Techniques for the Blunt-Body Problem," General Applied Science Laboratories, Inc. , SC-CR-68-3728, September, 1968.
2. Kyriss, C. , Hall, D. , and Harris, T. , "A Description of the Three-Dimensional Inviscid Transonic and Supersonic Flow Field Programs," General Electric Co. , Re-Entry and Environmental Systems Div. , to be published.
3. MacCormack, R. W. , "The Effect of Viscosity in Hypervelocity Impact Cratering," AIAA Paper 69-354, 1969.
4. Moretti, G. , "A Pragmatical Analysis of Discretization Procedures for Initial - and Boundary - Value Problems in Gas Dynamics and Their Influence on Accuracy, or, Look Ma, No Wiggles!," Polytechnic Institute of New York, POLY-AE/AM Report No. 74-15, September, 1974.
5. Thomas, P. D. , Vinokur, M. , Basianon, R. , and Conti, R. J. , "Numerical Solution for the Three-Dimensional Hypersonic Flow Field of a Blunt Delta Body," AIAA J. , Vol. 10, No. 7, July, 1972.
6. Moretti, G. , and Pandolfi, M. , "Analysis of the Inviscid Flow about a Yawed Cone. Preliminary Studies," Polytechnic Institute of Brooklyn, PIBAL Report No. 72-18, May, 1972.
7. Kutler, P. , Reinhardt, W. A. , and Warming, R. F. , "Multishocked, Three-Dimensional Supersonic Flow Fields with Real Gas Effects," AIAA J. , Vol. II, No. 5, p. 657-664, May, 1973.
8. Kyriss, C. L. , "Flow Fields About Arbitrary Shapes," GE-IR&D Project No. 72-9D, December, 1972.

TABLE I. SIDESLIP RESULTS

CONFIGURATION	α/θ	β	M_∞	YAW CENTER OF PRESSURE	
				DATA	3DFF
SPHERE BICONIC	0	1.5°	8	.717	.716
	2	1.5°	8	.699	.697
SLICED BODY	2	1.5°	16	.650	.647
BENT AXIS	1.6	2°	8	.708	.711
	1.6	2°	18	.712	.710

FIGURE 1. TRANSONIC FLOW FIELD REGION

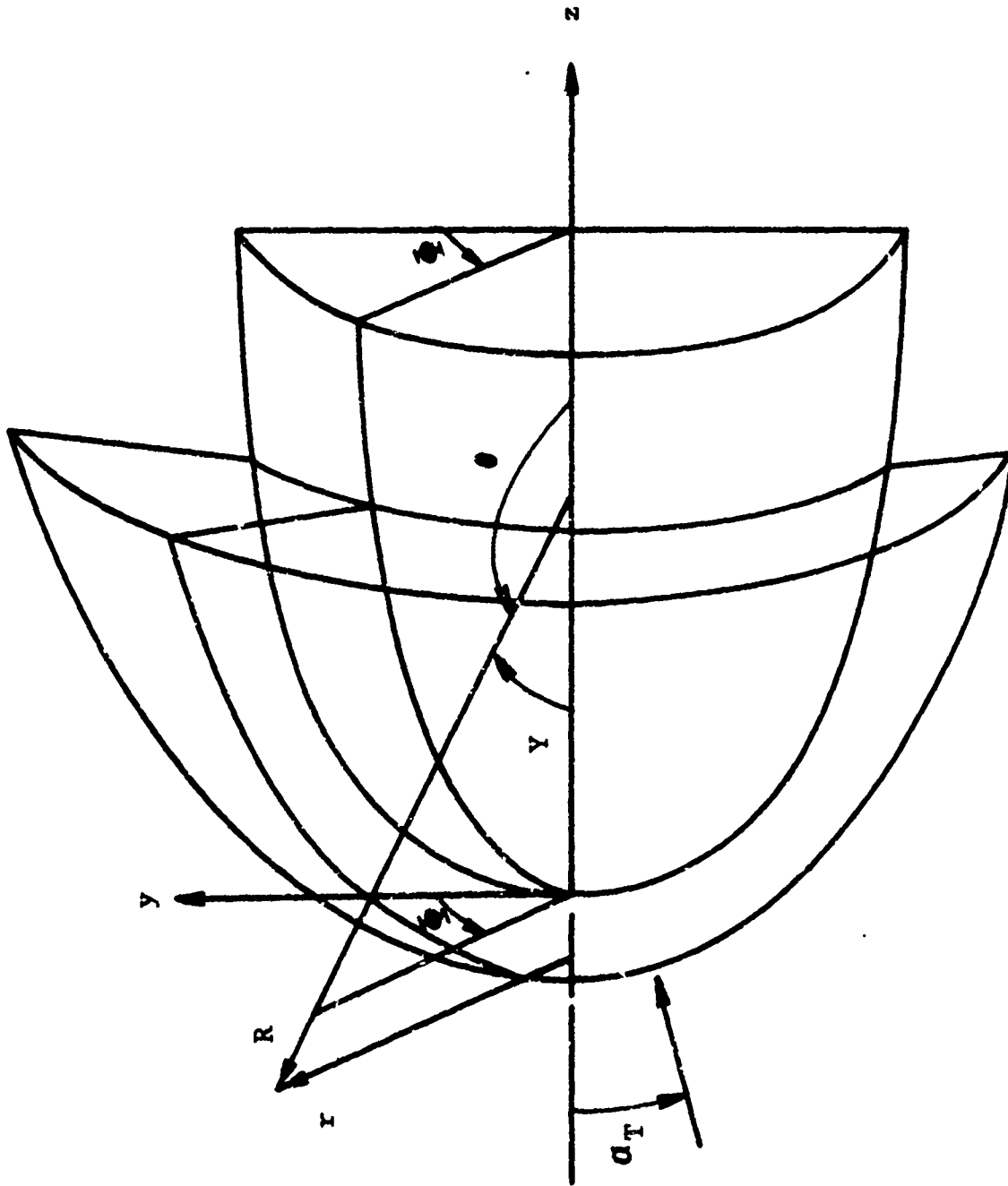


FIGURE 2. SUPERSONIC FLOW FIELD REGION

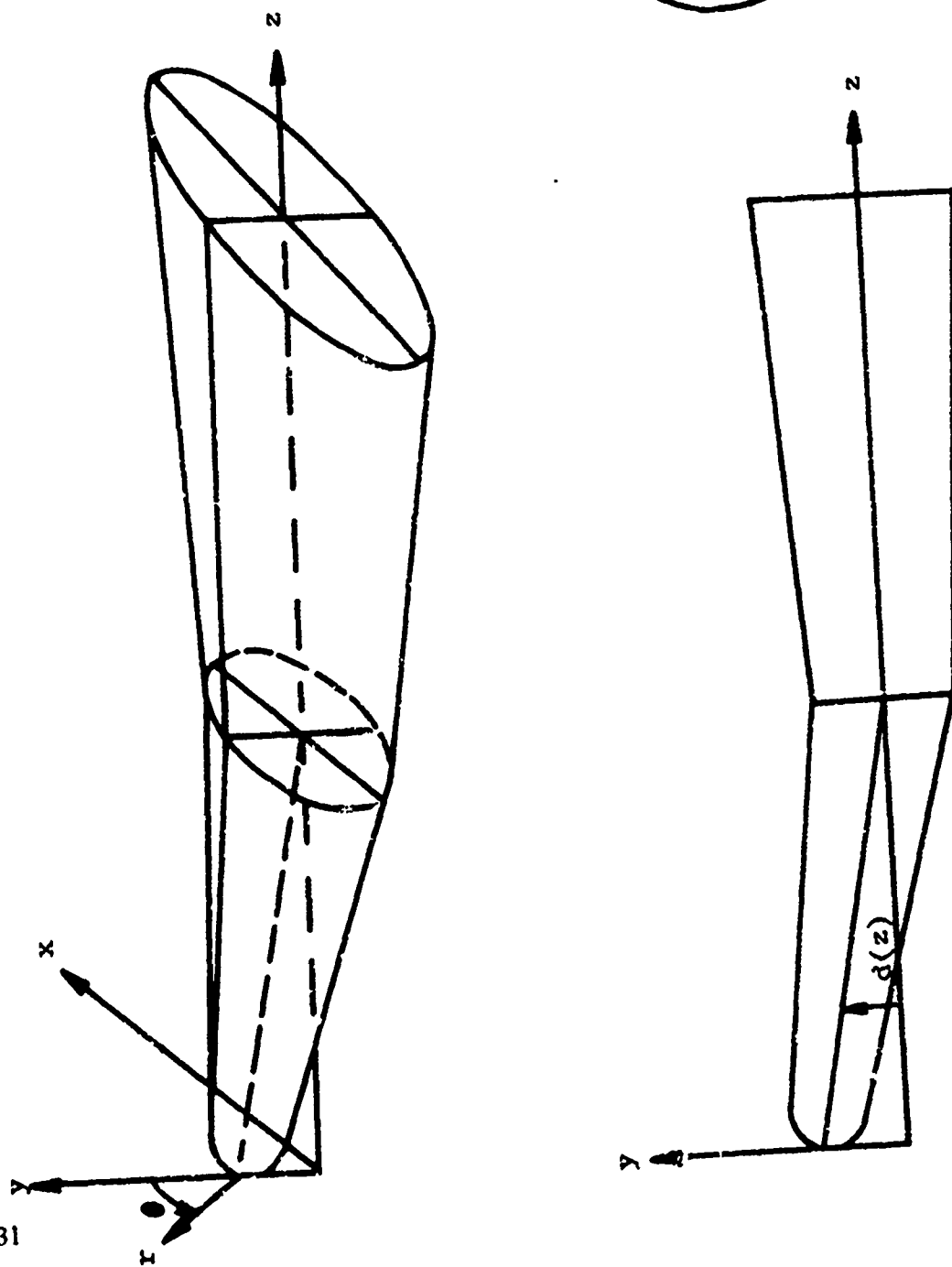


FIGURE 3. PHYSICAL AND COMPUTATIONAL PLANES IN THE SUPERSONIC REGION

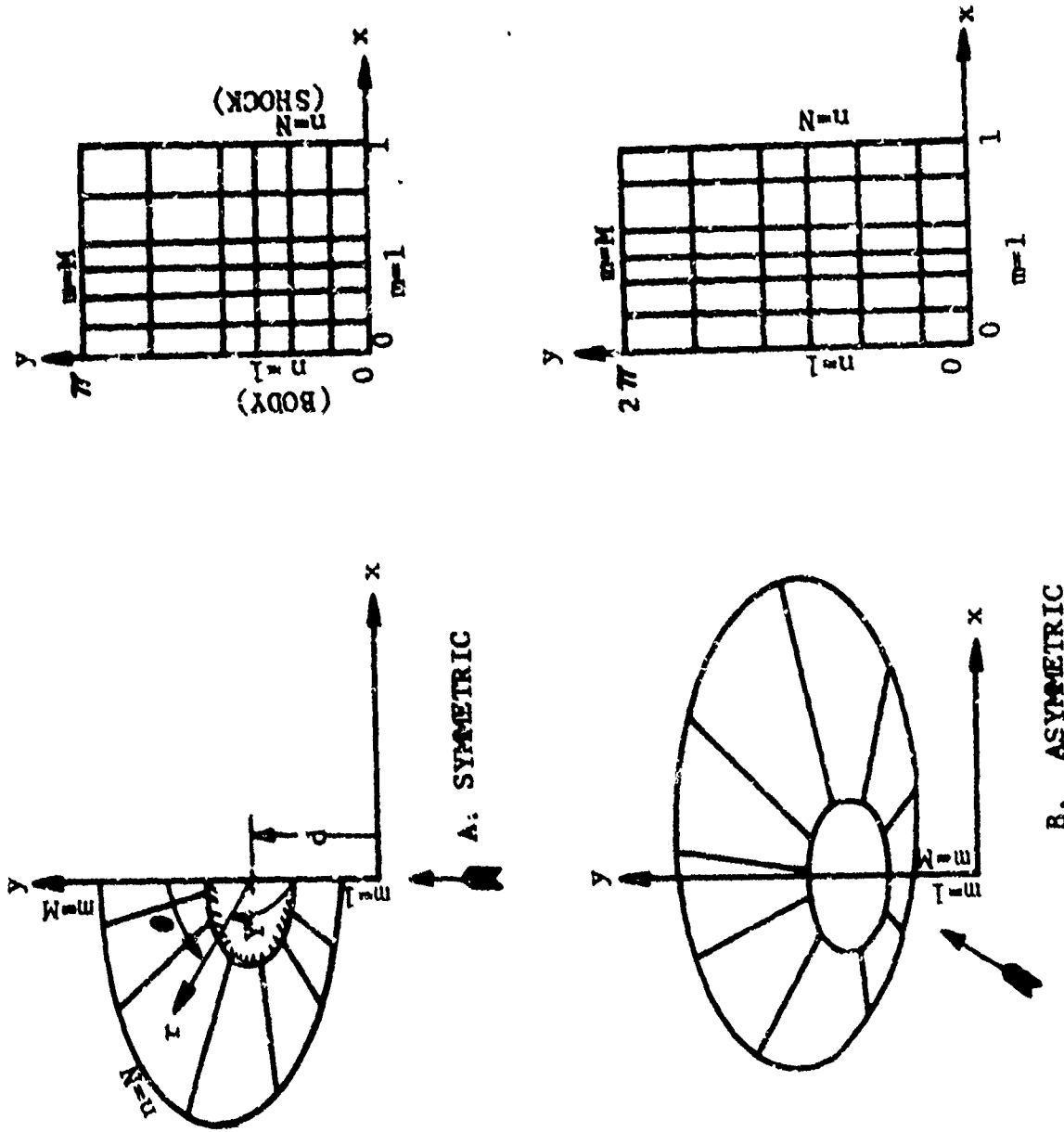
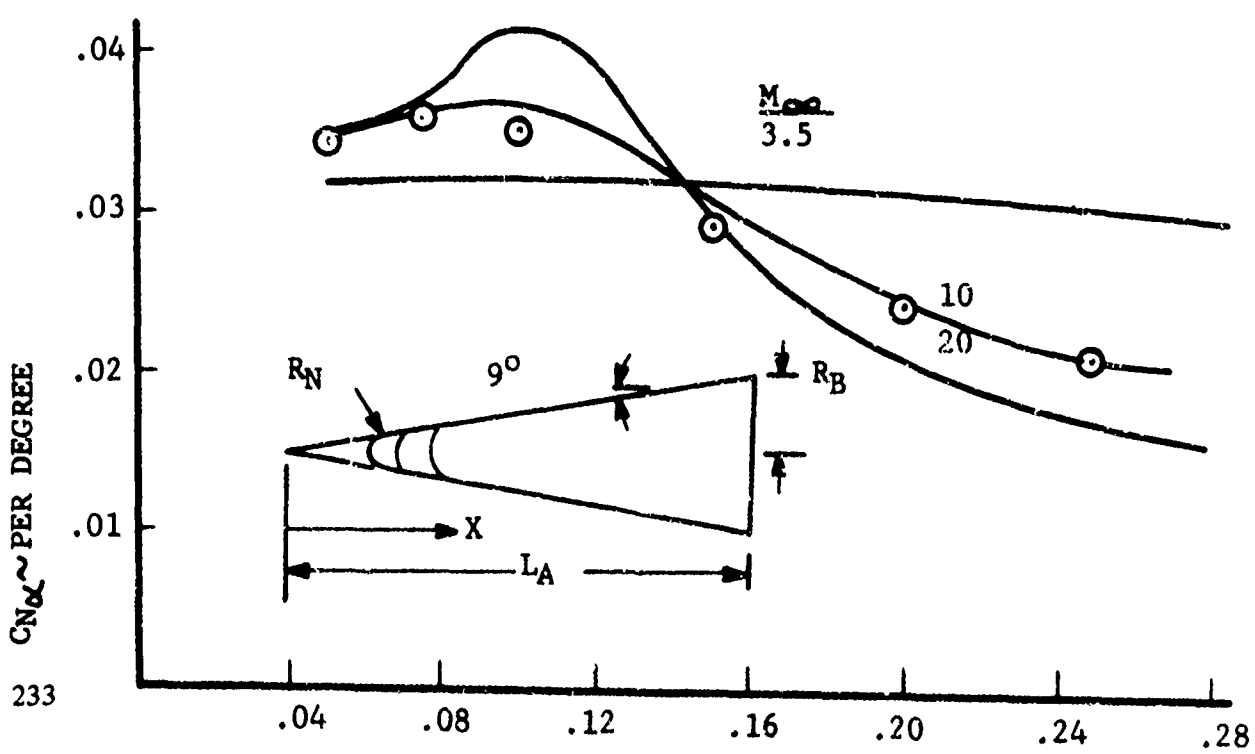
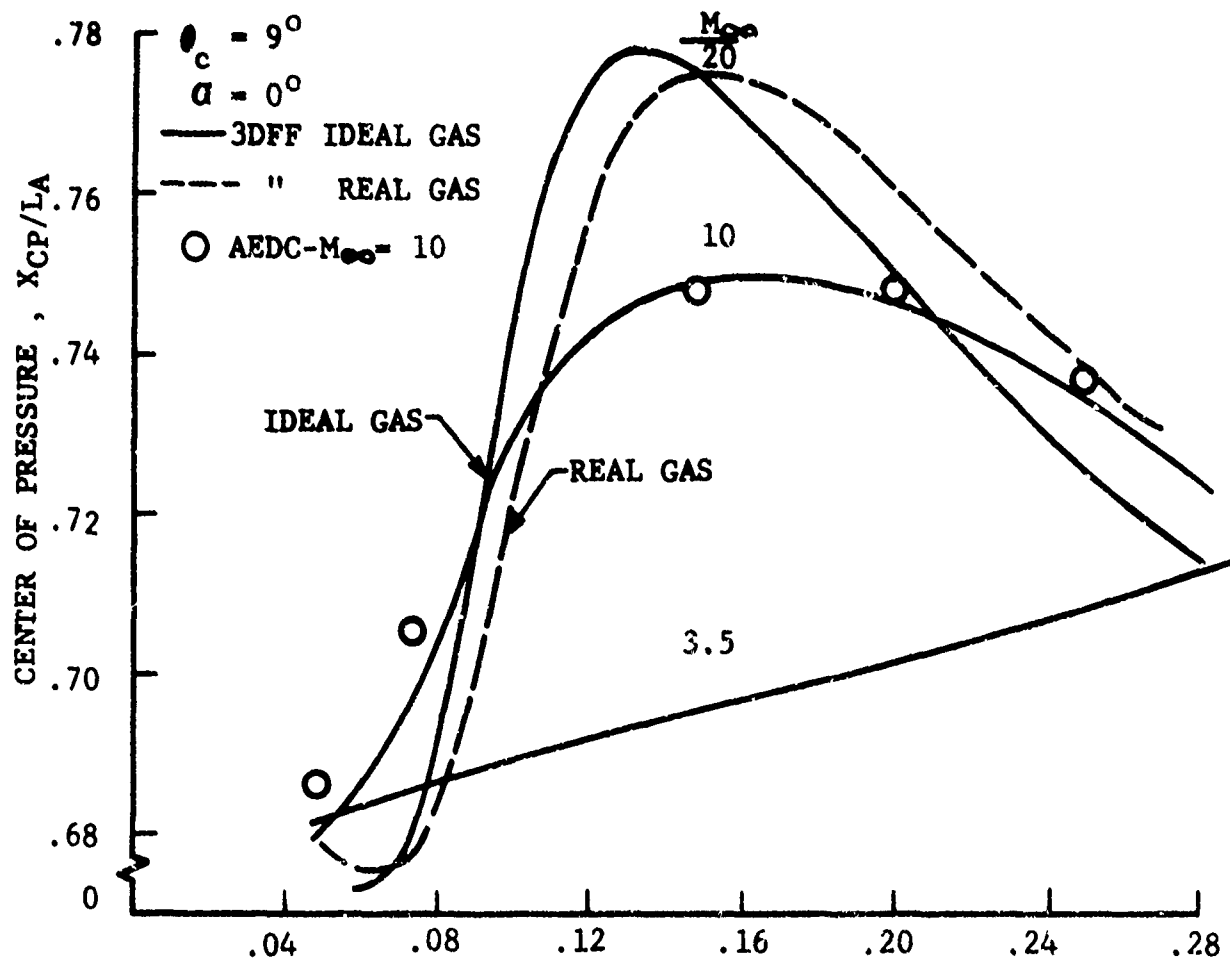


FIGURE 4. 3DFF PREDICTIONS FOR SPHERE CONE



BLUNTNESS RATIO $\sim R_N/R_B$

FIGURE 5. 3DFF PREDICTION FOR BICONIC GEOMETRY

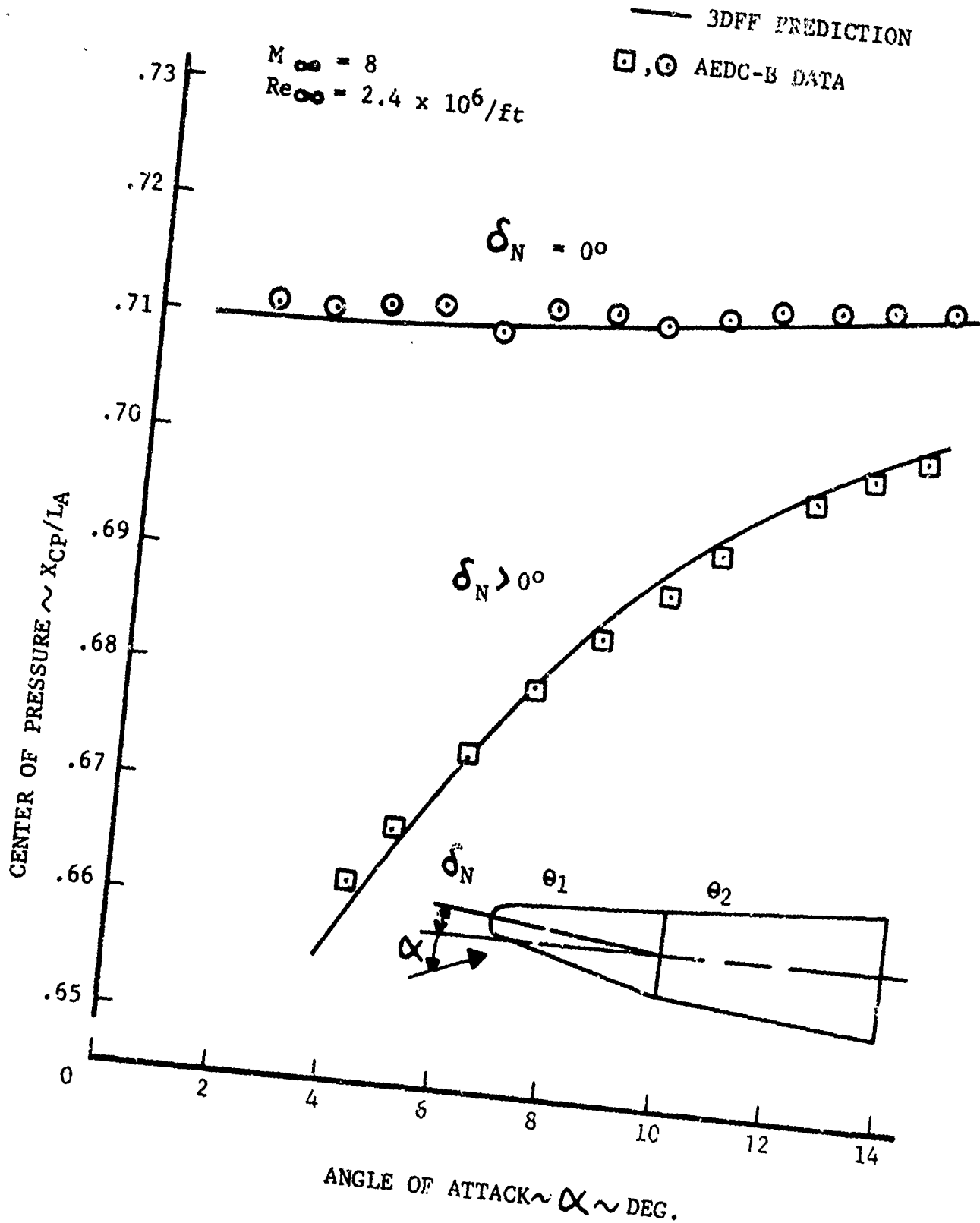


FIGURE 6. BICONIC SURFACE PRESSURE DISTRIBUTION

$M_\infty = 8$
 $\alpha = 8^\circ$
 $Re_\infty = 2.4 \times 10^6/FT$
 $\delta_N > 0^\circ$

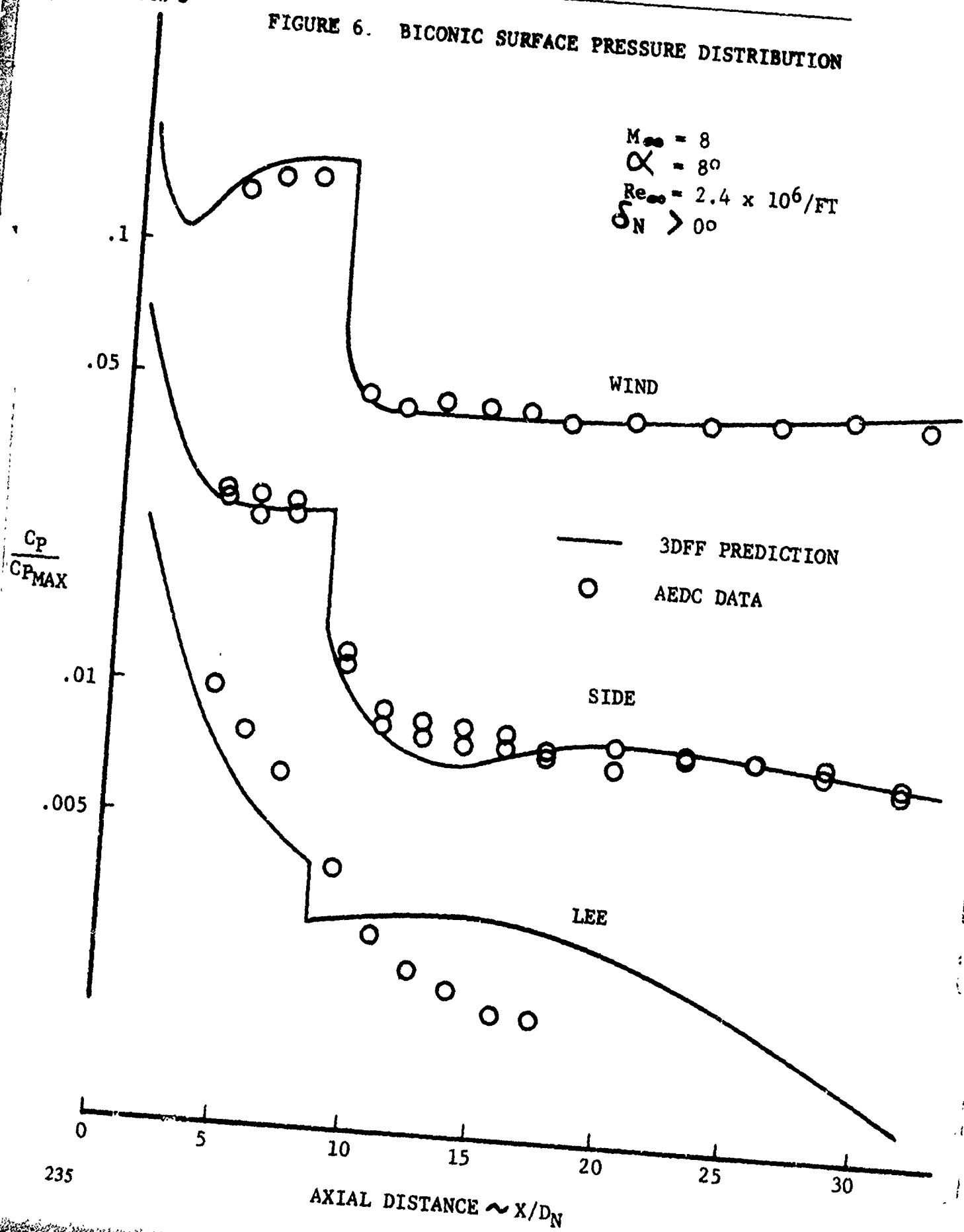


FIGURE 7. SYMMETRIC AND ASYMMETRIC NOSE SHAPE EFFECTS ON NORMAL FORCE AND PITCHING MOMENT COEFFICIENTS

BENT AXIS CONFIGURATION

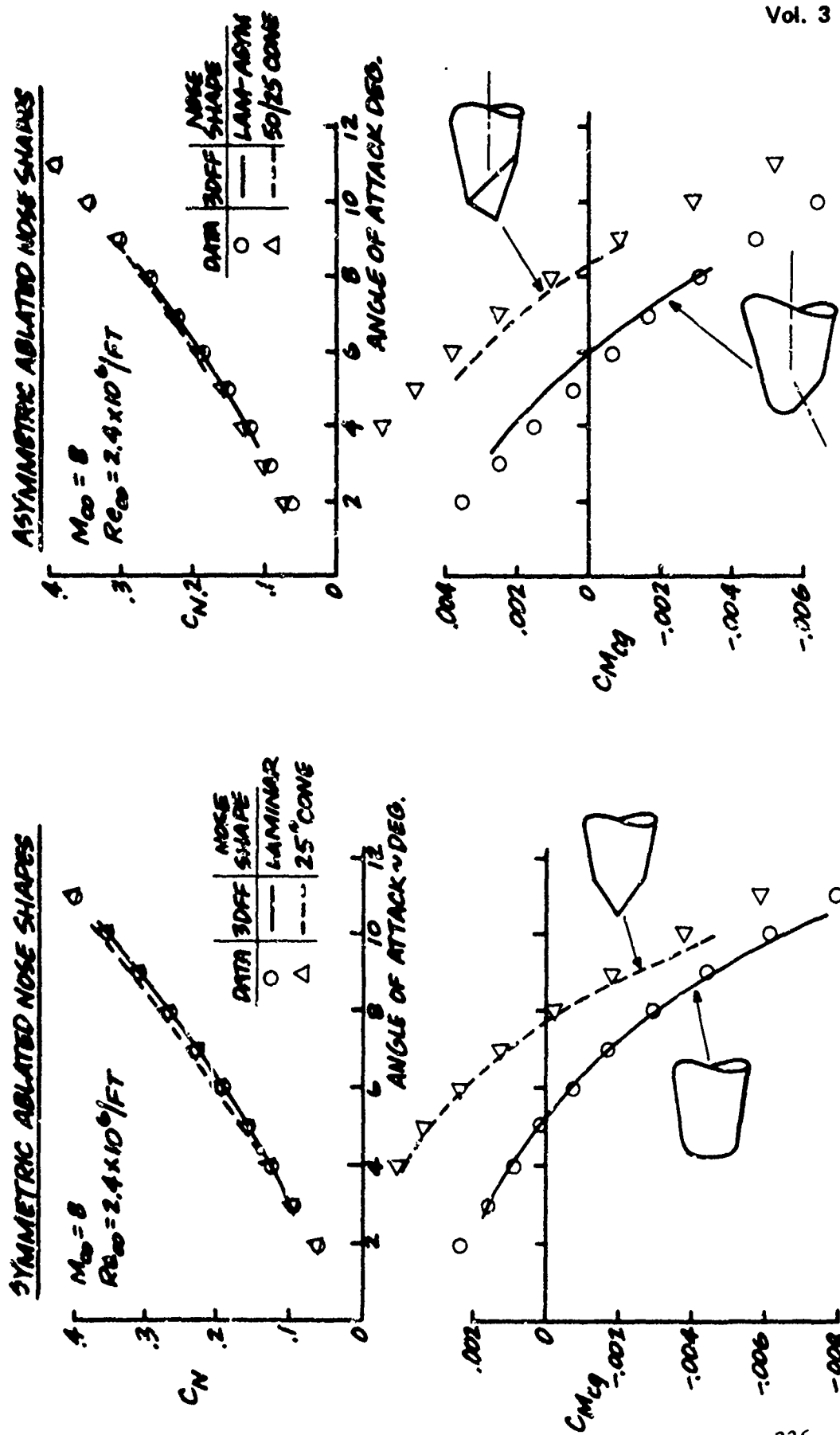


FIGURE 8. COMPARISON OF 3DFF PREDICTIONS WITH SLICED BODY DATA

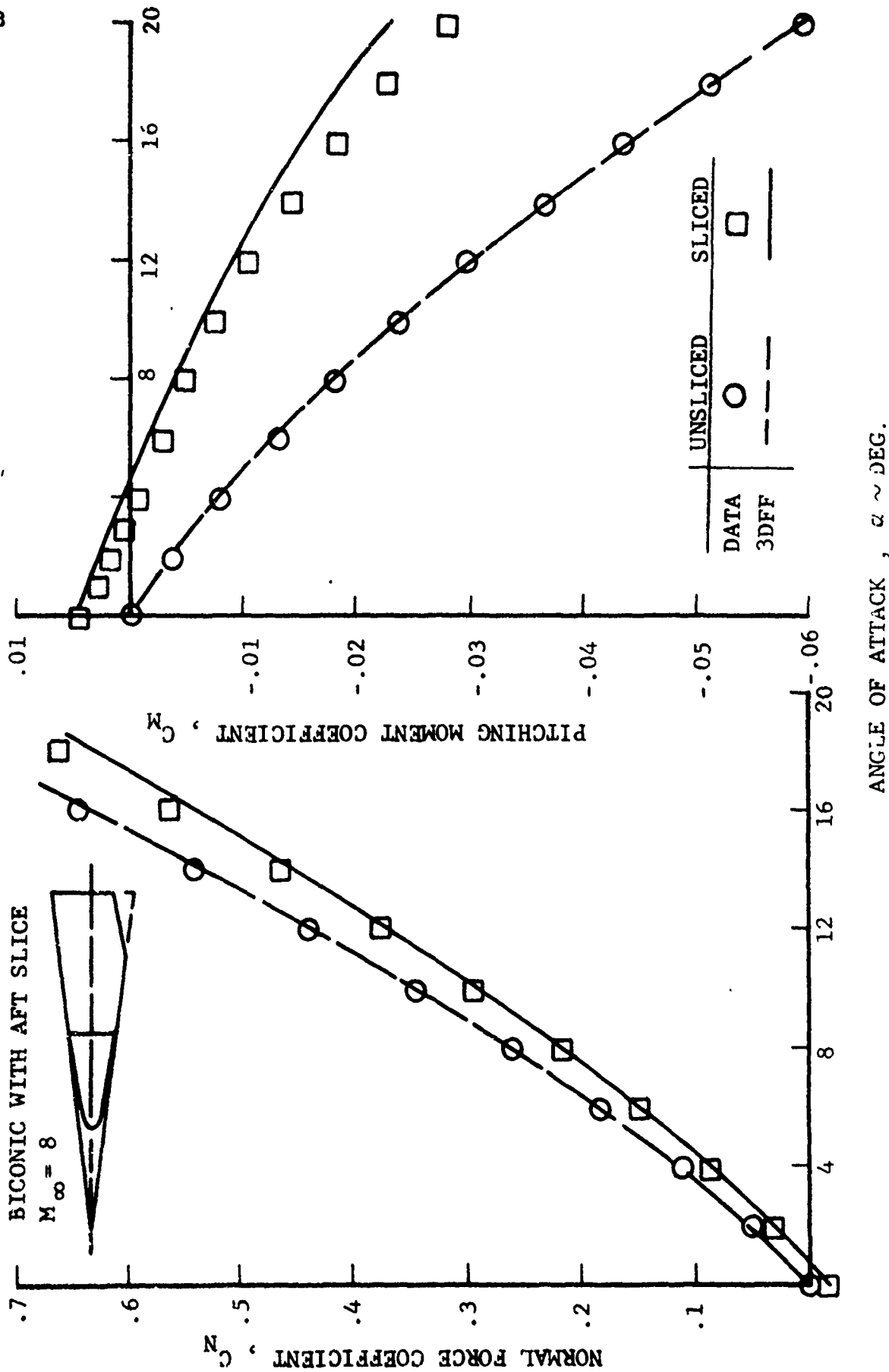


FIGURE 9. COMPARISON OF 3DFF PREDICTION WITH FLIGHT TEST DATA

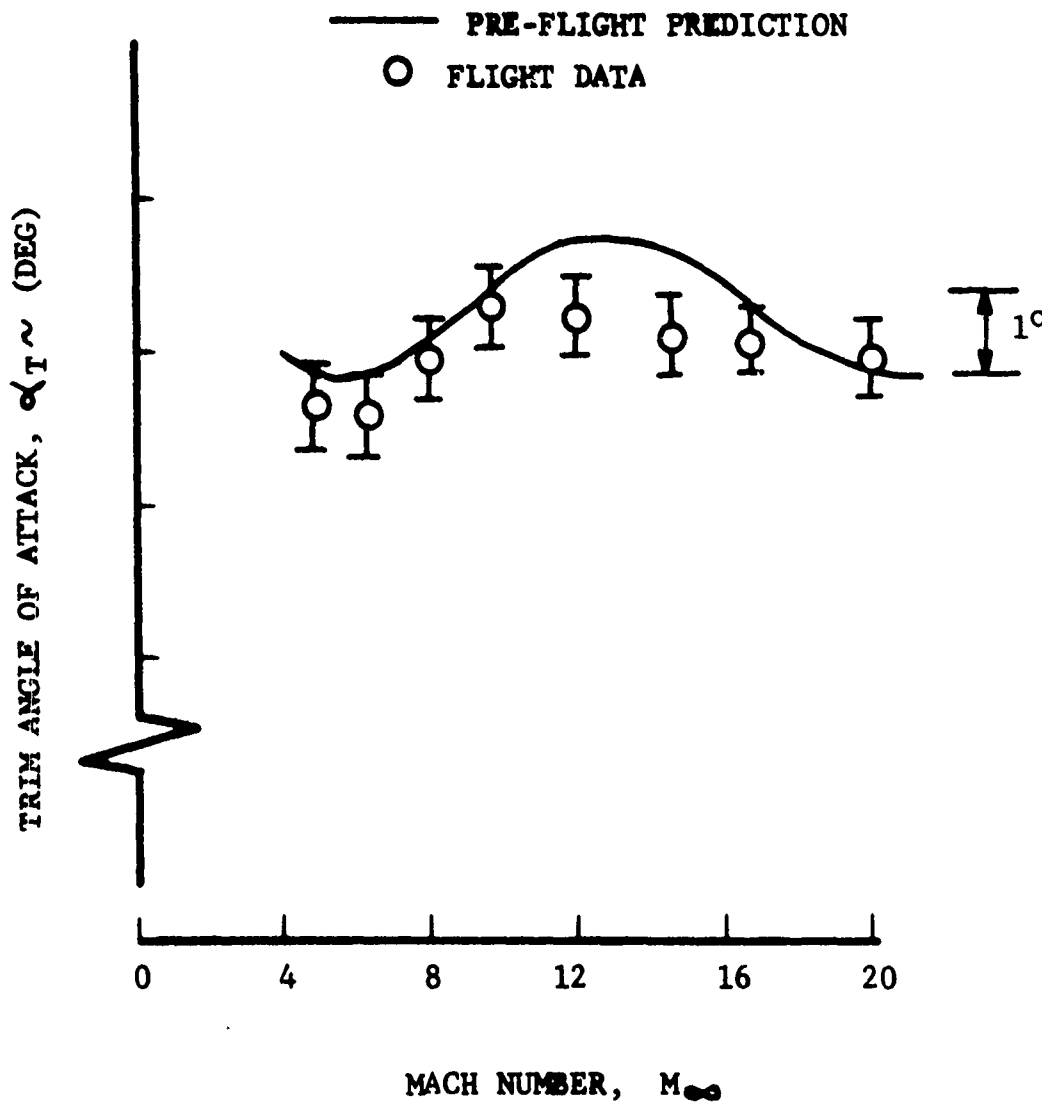
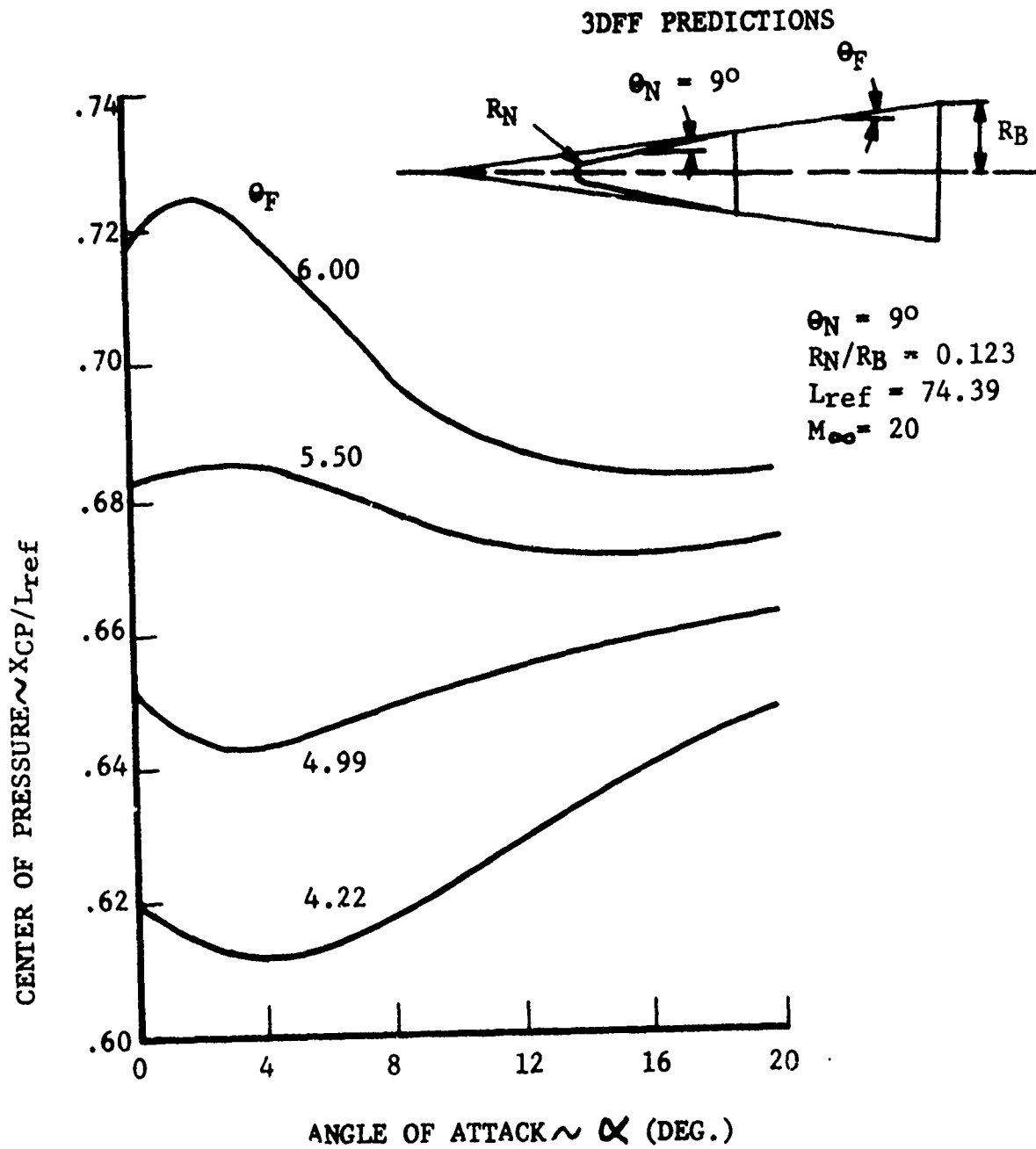


FIGURE 10 STABILITY CHARACTERISTICS



PAPER NO. 37

MACH 4.9 TURBULENT BOUNDARY LAYER SEPARATION
INDUCED BY A CONTINUOUS FLOW COMPRESSION

Robert L. P. Voisinet

Naval Surface Weapons Center
White Oak Laboratory
Silver Spring, Maryland 20910

SUMMARY

Flow-field measurements of a compressible turbulent boundary-layer separation are presented. The boundary layer chosen for investigation was formed on the nozzle wall of the Naval Surface Weapons Center Boundary Layer Channel. A continuous compression of the nozzle flow was imposed on the thick nozzle-wall boundary layer to produce a streamwise pressure rise of sufficient strength to cause separation. This manner of separating the boundary layer produced a separated flow field which was free of incident shock waves, wall discontinuities, and wall curvature.

Tests were conducted at an adiabatic-wall condition, for a nominal initial Mach number of 4.9, and Reynolds numbers based on initial boundary-layer thickness from 1.4×10^5 to 1.4×10^6 . Comprehensive flow-field measurements included wall static-pressure distributions, boundary-layer surveys of static pressure, Pitot pressure and stagnation temperature, wall shear-stress distributions and wall heat-transfer measurements throughout the entire region of interaction.

The effects of Reynolds number on the separation phenomena are presented. For Reynolds numbers below 8×10^5 the separation length was found to increase with increasing Reynolds number, whereas for Reynolds numbers above 8×10^5 the reverse trend was observed.

This reversal in the separation length versus Reynolds number trend was consistent with the reversal observed for incipient separation versus Reynolds number correlations.

NOTATION

- C_f - skin-friction coefficient
- d - diameter of skin-friction balance sensing element
- h - heat-transfer coefficient
 $q/(T_w - T_{aw})$
- M - Mach number
- P - pressure
- r_f - recovery factor
- Re/ft - unit Reynolds number per foot = $\rho_e u_e / \mu_e$
- Re_δ - Reynolds number based on δ
- t - thickness of skin-friction balance sensing element
- T - temperature
- u - velocity
- u_τ - shear velocity = $\sqrt{\tau_w / \rho_w}$
- u^* - Van Driest transformed velocity (Eqn. 1)
- x - distance along test plate from nozzle throat
- y - distance normal to test plate
- δ - boundary-layer thickness
- δ^* - displacement thickness
- θ - momentum thickness
- μ - dynamic viscosity

Vol. 3

- ν - kinematic viscosity
- ρ - density
- τ - shear stress

Subscripts

- aw - adiabatic-wall conditions
- e - boundary-layer edge conditions
- I - conditions at start of interaction
- inc - incipient separation conditions
- o - tunnel supply conditions
- oil - determined from oil flow
- PK - peak pressure-rise conditions
- PP - determined by Preston probe
- R - reattachment conditions
- S - separation conditions
- t - stagnation conditions
- w - wall conditions

Superscripts

- ' - "ideal" properties calculated from P , P_t , T_t

1. INTRODUCTION

Compressible turbulent boundary-layer separation is a phenomenon of such complexity that its analysis has been primarily empirical in nature. The need for experimental data has been great and continues to grow with each new theory and numerical technique which is introduced. However, the requirement is not only for more data but for more comprehensive data. With this

objective in mind, an experimental investigation was conducted for the purpose of obtaining more comprehensive measurements of a separated flow field with particular attention given to the evaluation of the boundary-layer flow structure and its interaction with the external flow field. A thick nozzle-wall boundary layer was chosen for investigation in order that detailed measurements could be obtained for a large-scale interaction.

Tests were conducted at an adiabatic-wall condition for a nominal Mach number of 4.9. The Reynolds number, the only parameter systematically varied in the tests, ranged from 1.4×10^5 to 1.4×10^6 . Data in this Reynolds number range are of particular interest because they lie between the comprehensive low Reynolds number data of Kuehn¹ and high Reynolds number data of Thomke and Roshko.²

The boundary-layer separation was accomplished by imposing a continuous compression of the nozzle flow onto the boundary layer so as to produce a continuous streamwise pressure rise of sufficient magnitude to cause separation. This technique of separating the boundary layer differs from shock-induced separations in that the incident compression is isentropic and occurs over a finite distance. Curved ramp models produce similar isentropic compressions; however, longitudinal curvature effects are present in these configurations.

Vol. 3

The present test provided for a separated flow field which was free of incident shock waves, wall discontinuities and wall curvature. Presumably, the analytical modeling of such a flow would be simplified because of the elimination of these factors.

2. EXPERIMENTAL SETUP AND TEST CONDITIONS

The experiment was performed in the White Oak Laboratory Boundary Layer Channel³ shown in Figure 1. The two-dimensional supersonic half nozzle, the main component of the facility, has for one wall a flat test plate, eight feet long and twelve inches wide, along which the boundary-layer measurements were made. The test plate boundary layer developed naturally along the smooth flat nozzle wall to a thickness of between two and three inches. This boundary-layer flow has been investigated extensively in the past and is well documented for a range of Reynolds number, heat-transfer, and pressure-gradient conditions.^{4,5,6} The opposite nozzle wall, a flexible contoured plate, was adjusted to produce a strong adverse-pressure-gradient flow along the flat test plate downstream of the initial flow expansion. The influence of the flexible nozzle wall contour on the opposite wall pressure distribution is illustrated in Figure 2. The nozzle contour provided for an initial expansion of the flow to Mach 4.9 as in conventioned supersonic nozzles, followed by a region of zero pressure gradient. The nozzle flow then

underwent a continuous flow compression of sufficient strength to cause separation of the flat test plate boundary layer. This was followed by a flow expansion to meet nozzle exit conditions. The nozzle contour was designed using a method-of-characteristics computer program together with a correction for the boundary-layer displacement thickness. Provision was made for a smooth transition between the various pressure-gradient regimes with no shock-wave interference. The nozzle configuration was not changed during the test. Therefore, the strength of the compression imposed on the boundary layer remained essentially the same for all test conditions. Figure 3 illustrates how the boundary layer responded to this incident compression.

Tests were conducted at tunnel supply pressures between 10 and 150 psia. The tunnel supply temperature was 595°R and the wall temperature was ambient (535°R) except for the region of the nozzle throat where the nozzle wall was heated to the local adiabatic-wall temperature. These conditions provided a range of Reynolds number per foot from 5.6×10^5 to 8.5×10^6 at a wall-to-adiabatic-wall temperature ratio very near 1.0. Boundary-layer profiles ahead of the interaction, wall-pressure distributions, and separation lengths were measured for the range of Reynolds numbers investigated. However, the comprehensive

boundary-layer and flow-field measurements and the wall shear-stress and heat-transfer measurements through the interaction were only obtained at an intermediate Reynolds number of $Re_{\delta I} = 7.7 \times 10^5$.

3. TRAVERSING TEST PLATE MODEL

With the realization that flow measurements were to be made at many incremental streamwise locations throughout the separation region, a special traversing plate model was designed and fabricated. The model, pictured in Figure 4, consisted of a flat test plate replacement for the existing nozzle wall of the facility. The model was fitted with aerodynamic fences which were necessary for the elimination of the cross flow emanating from the thick sidewall boundary layers (see discussion later). One distinctive feature of the model was the eight-inch wide central strip of the test plate which could be traversed 8.5 inches in the streamwise direction. The leading edge of this strip slid under a 0.030-inch thick stainless steel sheet. Appropriate sealing was provided on all surfaces to eliminate leakage from the tunnel plenum chamber to the flow surface. With this model, the need for duplication of instrumentation was minimized and the streamwise measuring resolution was greatly increased. For example, continuous wall static-pressure distributions were obtained by monitoring

only four static-pressure orifices along the test plate during a traverse. Access ports along the traversing test plate provided for the installation of a variety of instrumentation.

4. INSTRUMENTATION

Continuous distributions of wall shear stress and heat transfer were obtained by direct measurement using skin-friction balances and a heat-transfer gage installed in the traversing test plate instrumentation ports. Figure 5 pictures the balances used in this investigation. The large White Oak Laboratory balance⁷ and the small balance of DRL design⁸ provided redundancy in measuring instrument. In addition, the effect of sensing element size was tested by masking off portions of the sensing area and substituting smaller sensing elements.

Heat-transfer measurements were made using a thermopile gage mounted on the surface of an instrumentation port insert. The thermopile consisted of two thermocouples connected in series and located on opposite sides of a thin thermal barrier. The heat flux measured was proportional to the temperature across the thermal barrier. Since the test conditions were near adiabatic, a heater button was mounted to the back of the gage to produce selected heat flux conditions. This allowed for the measurement of the heat-transfer coefficient in addition to the measurement of the adiabatic-wall temperature and recovery factor.

Vol. 3

A Preston probe was traversed through the interaction region to establish the location of the separation and reattachment points. A 0.040-inch diameter probe was mounted in both a forward and rearward facing mode. The points of flow reversal were determined when the pressure differential between the probe and wall static pressure became zero. An oil flow technique was also used to determine these points. A small amount of oil was allowed to flow from a static pressure orifice in the test plate. The separation and reattachment points were determined by traversing the test plate and orifice beneath the interaction and observing when the direction of oil flow changed from the streamwise to rearward direction.

In addition to the measurements of wall properties, surveys of the boundary layer and external flow field were made by using a boundary-layer traverse and probes which were inserted through the test plate instrumentation ports. Generally, boundary-layer surveys were obtained at one-inch increments in the streamwise direction in the region of interaction. Surveys of Pitot pressure, static pressure, and total temperature were obtained using a variety of instrumentation as shown in Figure 6. Typically, Pitot-pressure probes were of the flattened-tip configuration with a 0.003 x 0.100-inch rectangular opening. The static-pressure probe consisted of a 0.750-inch diameter flat-surfaced disc with a sharp,

10-degree bevel on its edge and a static orifice at its center. The total temperature through the boundary layer was measured using the fine-wire probe design of Yanta⁹ with a 0.002-inch diameter x 0.127-inch long sensing wire exposed to the flow. Probe supports were of varying design with extensions provided for the probes when sting support interference was suspected.

All boundary-layer traverses were made from the free stream toward the plate with a maximum movement of 4.5 inches. Data were recorded with the probes at rest and only when the probe pressures and/or temperatures were observed to have reached equilibrium conditions. The data acquisition system simultaneously recorded eight channels of data on digital voltmeters and converted the information directly to a computer card output.

5. DATA REDUCTION

The data-reduction schemes used in this test were very nearly identical to those reported earlier by the author;^{4,5,6} therefore, only a brief description will be given here. The introduction of the static-pressure variation normal to the test plate into profile and integral parameter definitions was of utmost necessity for this flow field. The procedure used was to define "ideal" flow properties which are calculated from the local static pressure, total pressure and stagnation temperature using isentropic relations. These properties

represent the "inviscid" flow field which would exist if the boundary layer was not present. The boundary-layer thickness was defined as the distance from the wall where $M/M' = 0.995$, i.e., the point where the viscous and inviscid distributions differed by half a percentage. The primed (') quantities refer to the "ideal" flow parameters.

6. TWO-DIMENSIONALITY

Measurements of boundary-layer flows in a two-dimensional facility of this type are usually questioned as to the two-dimensionality of the flow. This question is always intensified when any mention of separation is made.¹⁰ Two investigations into identifying the two-dimensionality of the present flow were conducted. The first was by observation of surface oil flow patterns. Figure 7 shows oil flow patterns on the test plate in the region of interaction for test configurations with and without aerodynamic "fences." As can be seen, fences were found to be a necessity in eliminating the cross flows which were emanating from the thick sidewall boundary layers and feeding the separation process. With the introduction of the fences the flow field became more nearly two-dimensional. The incoming flow did not exhibit cross-flow tendencies and the separation and reattachment lines were well defined and straight across a good portion of the test plate.

(It should be noted that these photographs were obtained in preliminary shakedown tests. The detached flow at the leading edge of the fences was eliminated in the final tests by an improved fence design.) It should be further noted that the boundary layer would not separate when the fences were installed until the strength of the pressure rise imposed on the boundary layer was increased.

The second evaluation of two-dimensionality was made by comparing the wall static-pressure distributions on and two inches off centerline of the test plate as shown in Figure 8. Differences between the on and off centerline distributions were slight for both configurations, indicating how insensitive the lateral distribution of wall pressure is to cross-flows and three-dimensional effects. However, the streamwise position of the interaction and the overall degree of separation did differ significantly between the configurations with and without fences indicating the strong influence of cross-flows on separation lengths and incipient separation criteria. These findings are consistent with the studies of Reda and Murphy^{10,11} on shock-induced separations.

7. FLOW-FIELD DEFINITION

The complex flow field encountered in this test is illustrated in Figure 9 through schlieren photographs

and an isobar mapping of the interaction region. The isobar mapping was compiled from many static-pressure surveys through the flow field. Strong static-pressure gradients were observed through the interaction except for the region of the subsonic separation bubble where the static pressure normal to the wall appeared to be constant. The schlieren photographs showed the separation shock emanating from deep within the boundary layer.

Boundary-layer velocity profiles ahead of the interaction are shown in Figure 10 for the range of Reynolds numbers tested. The profiles are presented in law-of-the-wall coordinates using the Van Driest¹² transformed velocity, u^* , in the form

$$u^* = \frac{u_e}{A} \left\{ \sin^{-1} \left(\frac{2A^2 \left(\frac{u}{u_e} \right) - B}{\sqrt{B^2 + 4A^2}} \right) + \sin^{-1} \left(\frac{B}{\sqrt{B^2 + 4A^2}} \right) \right\} \quad (1)$$

where:

$$A = \sqrt{\frac{T_e}{T_w}} r_f 0.2 M_e^2 \quad \text{and} \quad B = \frac{T_{aw}}{T_w} - 1$$

The shear velocity, u_τ , was determined from a best fit of the transformed profile data in the logarithmic region of the boundary layer to the relation

$$\frac{u^*}{u_\tau} = 2.5 \ln \frac{y u_\tau}{\nu} + 5.1 \quad (2)$$

All the profiles exhibited the usual turbulent boundary-layer characteristics of a laminar sublayer, a logarithmic region, and a wake region. A summary of the boundary-layer parameters is given in Table 1 for the range of Reynolds numbers tested. For Reynolds numbers per foot below 4.5×10^5 , the flow was below the turbulent flow limit of the facility.

8. WALL-PRESSURE DISTRIBUTIONS

The wall-pressure distributions through the interaction region are shown in Figure 11. Shown for comparison is a best approximation of the "inviscid" pressure field which was imposed on the boundary layer. This "inviscid" distribution was computed using a method-of-characteristics solution from measured streamwise static-pressure distributions outside the boundary layer and ahead of the interaction. An overall "inviscid" pressure rise of between 8 and 10 was imposed on the boundary layer from the incident compression. The "inviscid" pressure drop which followed the compression was caused by the subsequent expansion of the nozzle flow. For this

reason, the actual pressure rise through the interaction only reached about half the peak "inviscid" value.

Of particular interest in Figure 11 is the effect of the Reynolds numbers per foot above 3.4×10^6 , the upstream propagation decreased with increasing Reynolds number, whereas for Reynolds numbers per foot below 3.4×10^6 , the opposite trend was observed. This trend reversal becomes more vivid in Figures 12, 13 and 14, where the location of the separation and reattachment points, the non-dimensional separation distance, and the location of the separation shock are plotted respectively versus Reynolds number. The reverse phenomenon can best be explained with the use of Figure 15 which shows incipient separation pressure-rise data for different Mach numbers and Reynolds numbers. Shown on the figure are the data of Kuehn,¹ Thomke and Roshko² and Sterrett and Emery¹³ together with the correlation of Elfstrom.¹⁴ Consider the test conditions of this study in terms of the reversal trend in the incipient separation pressure rise-Reynolds number correlation. As the Reynolds number is increased for a constant $P/P_I = 9$ and $M_I = 4.9$, the state of the boundary layer transforms from being unseparated to being incipiently separated and strongly separated; then it reverts back to being incipiently separated and unseparated. Over the limited Reynolds number range of

the present study the flow acted as predicted with the degree of separation increasing and then decreasing with increasing Reynolds number. Although it has been argued that the geometry of the experiment and the choice of a criterion for detection of incipient separation could account for the reversal trend seen in Figure 15, the present tests tend to discount these arguments because of the single test configuration and measurement technique. The reversal trend appears genuine.

The free-interaction concept as proposed by Chapman, Kuehn and Larson¹⁵ states that certain characteristics of the separated flow should not depend on the object shape or mode of inducing separation. This concept requires the fulfillment of two criteria. The ratio of the separation-point pressure to the initial pressure must remain invariant and the shape of the distribution of pressure up to the separation point must be the same. Figures 16 and 17 show that the first criterion was fulfilled for the Reynolds numbers tested with $P_S/P_I = 2.18$. Similarly a type of free interaction appeared in the reattachment region with $P_R/P_{PK} = 0.67$. These pressure values were based on the separation and reattachment points determined from Preston probe measurements. Oil flow measurements of the separation and reattachment point locations were also obtained (see Figure 12), but they were not considered as a valid indication of the flow reversal points based on the low P_S/P_I value

(1.2 to 1.5) which was indicated. This discrepancy in the oil flow results was also noted by Driftmyer¹⁶ for a similar test configuration.

The second free-interaction criterion, the invariance in the shape of the pressure distribution up to the separation point, was not fulfilled according to the guidelines of Reference 15. Although the pressure distributions were similar in shape, a scaling factor appeared necessary in the length parameter. Zukoski¹⁷ proposed that the length coordinate be non-dimensionalized to the boundary-layer thickness providing for a ratio $(X_S - X_I)/\delta_I$ which is constant and equal to a value of 2.5. Values of $(X_S - X_I)/\delta_I$ for this investigation varied from 1.15 to 1.73 for decreasing Re_{δ_I} over the Reynolds number range tested. Because the parameters X_S and X_I are difficult to measure and subject to varying interpretation, the maximum pressure gradient in the free interaction appeared to be an easier and more consistent parameter to evaluate. It would seem logical that the larger the pressure gradient the smaller the free-interaction length, $X_S - X_I$. Figure 18 shows pressure-gradient data compiled from a number of experiments plotted versus Reynolds number for several Mach numbers. Although there was a sizeable scatter in the data, the maximum pressure gradient in the interaction region showed a consistent trend of increasing with increasing Reynolds number for a given Mach number. This pressure

gradient appeared to be independent of the overall pressure rise after the free interaction,^{2,16} the heat-transfer condition,¹⁴ and the mode of separation. The concept of a free-interaction region appears valid; however, proper scaling of the length parameter must be found to correlate the variation with Mach number and Reynolds number.

9. WALL HEAT-TRANSFER AND SHEAR-STRESS

The recovery-factor and heat-transfer coefficient distributions through the separation region are presented in Figure 19. The value of the local recovery factor was observed to increase sharply at separation, remain somewhat constant through the separation region, and relax back to its original value after reattachment. The value of the heat-transfer coefficient also showed a sharp increase at separation; however, the value thereafter decreased to a lower value at the center of the separation region before increasing again through the reattachment.

Wall shear-stress measurements are presented in Figure 20. The data were obtained by direct measurement using skin-friction balances. Large corrections to the data were needed to compensate for pressure-gradient effects on the shear balances; consequently, results can only be considered in qualitative terms. The pressure-gradient effects resulted primarily from the integral

pressure force acting on the edge of the measuring element. This pressure force was proportional to the local pressure gradient and thickness of the measuring element; therefore, the greatest errors occurred in the separation and reattachment regions where the pressure gradients were strongest. Since the wall shear stress was small in these same regions, it is questionable whether skin-friction balances can be considered as valid and accurate tools to the evaluation of separation criteria.

10. CONCLUSIONS

An experimental investigation of a compressible turbulent boundary-layer separation was conducted with emphasis placed on the collection of a comprehensive set of flow-field measurements. A continuous compression of a nozzle flow provided a separated flow field which was free of incident shock waves, wall discontinuities and wall curvature. The compression-induced-separation data could be correlated with data obtained for other test configurations and models. A traversing plate model was shown to be of great advantage in minimizing instrumentation duplication and increasing streamwise measuring resolution. Aerodynamic fences were found to be a necessity for the elimination of cross-flows emanating from large sidewall boundary layers.

The important conclusions reached in this study are:

1. The separation length, $(X_R - X_S)/\delta_I$, was found to increase with increasing Reynolds number for $Re_{\delta_I} < 8 \times 10^5$, whereas the opposite trend was found for $Re_{\delta_I} > 8 \times 10^5$. This reversal in the separation length versus Reynolds number trend is consistent with the reversals observed for incipient separation versus Reynolds number correlations.

2. The pressure rise to separation was found to be invariant with Reynolds number for a given Mach number. The free-interaction length, $(X_S - X_I)/\delta_I$, and the maximum pressure gradient in the free-interaction region, $[d(P/P_I)]/[d(X/\delta_I)]$, were found to be a function of Reynolds number and Mach number. No reversals were observed in the interaction length versus Reynolds number trend; $(X_S - X_I)/\delta_I$ decreased for increasing Re_{δ_I} .

ACKNOWLEDGEMENTS

The author is grateful for the support and encouragement of the members of the Boundary Layer Group-- Dr. Roland E. Lee, Chief, and Drs. William J. Yanta and David F. Gates. The assistance of Messrs. F. W. Brown and F. C. Kemerer is also gratefully acknowledged for their efficient operation of the facility and preparation of instrumentation.

This research was performed under the sponsorship of the Naval Air Systems Command, Washington, D. C., Task No. A 32 320/292/69/R009-02-030.

REFERENCES

1. Kuehn, D. M., "Experimental Investigation of the Pressure Rise Required for the Incipient Separation of Turbulent Boundary Layers in Two-Dimensional Supersonic Flow," NASA Memo 1-21-59A, Feb 1959
2. Thomke, G. J. and Roshko, A., "Incipient Separation of a Turbulent Boundary Layer at High Reynolds Number in Two-Dimensional Supersonic Flow Over a Compression Corner," NASA CR-73308, 1969
3. Lee, R. E., Yanta, W. J., Leonas, A. C. and Carner, J., "The NOL Boundary Layer Channel," NOLTR 66-185, Nov 1966
4. Voisinet, R. L. P. and Lee, R. E., "Measurements of a Mach 4.9 Zero-Pressure-Gradient Turbulent Boundary Layer with Heat Transfer - Part 1, Data Compilation," NOLTR 72-232, Sep 1972
5. Voisinet, R. L. P. and Lee, R. E., "Measurements of a Supersonic Favorable-Pressure-Gradient Turbulent Boundary Layer with Heat Transfer - Part 1, Data Compilation," NOLTR 73-223, Dec 1973
6. Voisinet, R. L. P., Lee, R. E. and Yanta, W. J., "An Experimental Study of the Compressible Turbulent Boundary Layer with an Adverse Pressure Gradient," Paper No. 9, Turbulent Shear Flows, AGARD CP-93-71, Sep 1971
7. Bruno, J. R., Yanta, W. J. and Risher, D. P., "Balance for Measuring Skin Friction in the Presence of Heat Transfer," NOLTR 69-56, Jun 1969
8. Fenter, F. W., "The Turbulent Boundary Layer on Uniformly Rough Surfaces at Supersonic Speeds," DRL Report 437, CM 941, Jan 1960
9. Yanta, W. J., "A Fine-Wire Stagnation Temperature Probe," NOLTR 70-81, Jun 1970
10. Reda, D. C. and Murphy, J. D., "Shock Wave-Turbulent Boundary Layer Interactions in Rectangular Channels," AIAA Paper 72-715, Jun 1972

11. Reda, D. C. and Murphy, J. D., "Shock Wave-Turbulent Boundary Layer Interactions in Rectangular Channels - Part II, The Influence of Sidewall Boundary Layers on Incipient Separation and Scale of the Interaction," AIAA Paper 73-234, Jan 1973
12. Van Driest, E. R., "Turbulent Boundary Layer in Compressible Fluids," JAS, Vol. 18, No. 3, Mar 1951
13. Sterrett, J. R. and Emery, J. C., "Experimental Separation Studies for Two-Dimensional Wedges and Curved Surfaces at Mach Numbers of 4.8 to 6.2," NASA TN D-1014, 1962
14. Elfstrom, G. M., "Turbulent Separation in Hypersonic Flow," I.C. Aero Report 71-16, Sep 1961
15. Chapman, D. R., Kuehn, D. M. and Larson, H. K., "Investigation of Separated Flows in Supersonic and Subsonic Streams with Emphasis on the Effect of Transition," NACA Report 1356, 1958
16. Driftmyer, R. T., "A Forward Facing Step Study - The Step Height Less Than The Boundary-Layer Thickness," NOLTR 73-98, May 1973
17. Zukoski, E. E., "Turbulent Boundary-Layer Separation in Front of a Forward-Facing Step," AIAA Journal, Vol. 5, No. 10, Oct 1967

P_o psia	Re/ft $\times 10^{-6}$	δ inches	δ_w^* inches	$0_w'$ inches	Re_δ $\times 10^{-5}$	C_f $\times 10^3$
150.	8.5	2.0	0.68	0.058	14.16	0.636
105.	6.0	2.1	0.73	0.062	10.5	0.665
75.	4.2	2.2	0.79	0.066	7.7	0.703
60.	3.4	2.26	0.83	0.070	6.4	0.733
45.	2.5	2.36	0.88	0.074	4.92	0.786
30.	1.7	2.5	0.94	0.078	3.54	0.835
25.	1.4	2.57	0.98	0.081	3.00	0.804
20.	1.12	2.65	1.02	0.086	2.47	(0.860)
15.	0.85	2.75	1.09	0.090	1.95	0.895
12.	0.67	(2.85)	(1.15)	(0.094)	(1.59)	(0.980)
10.	0.56	2.95	1.19	0.098	1.38	1.07

() Interpolated Values

TABLE 1 - BOUNDARY LAYER PROPERTIES AHEAD OF THE INTERACTION,
X = 67 INCHES

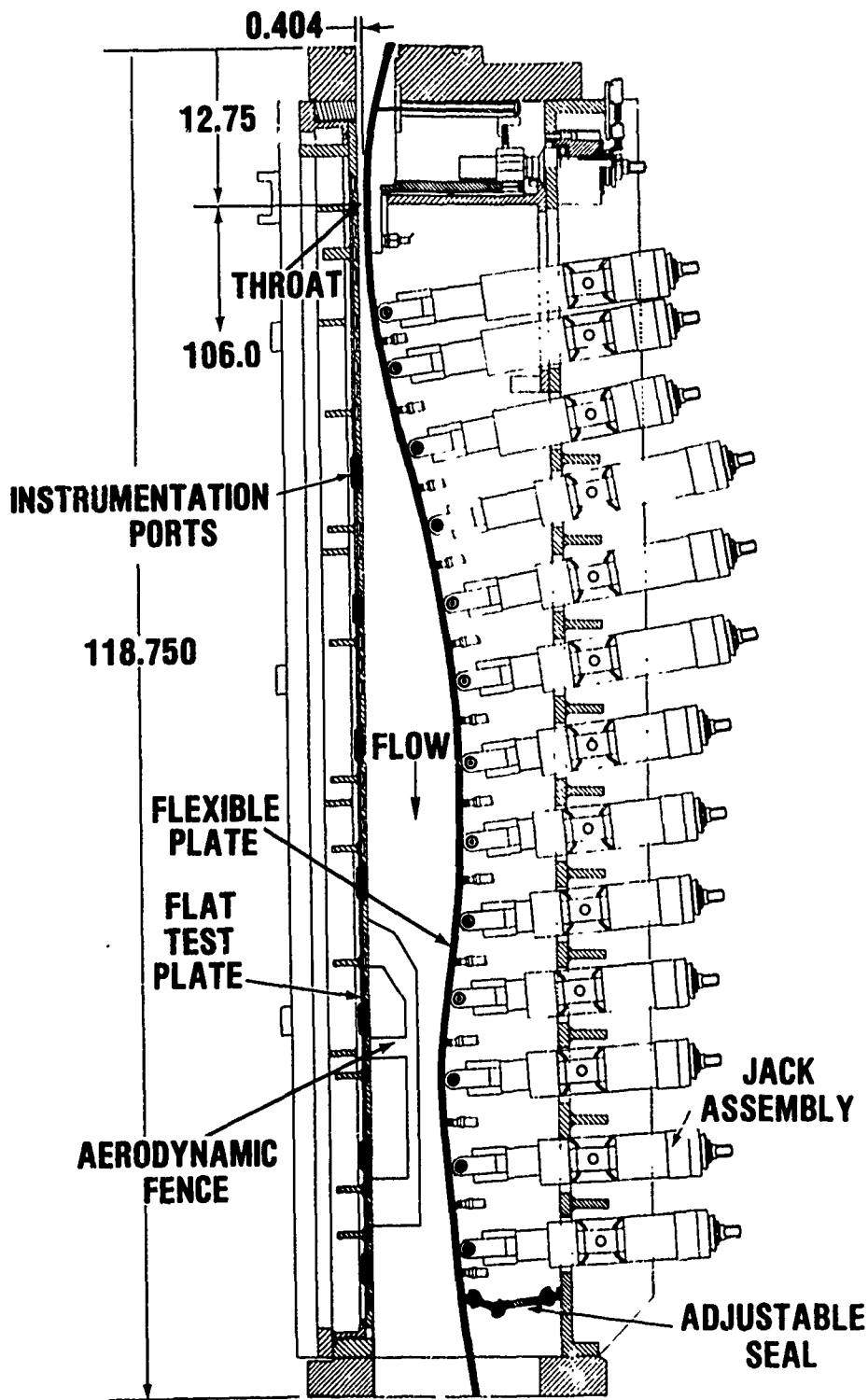


FIG. 1 - NSWC BOUNDARY LAYER CHANNEL

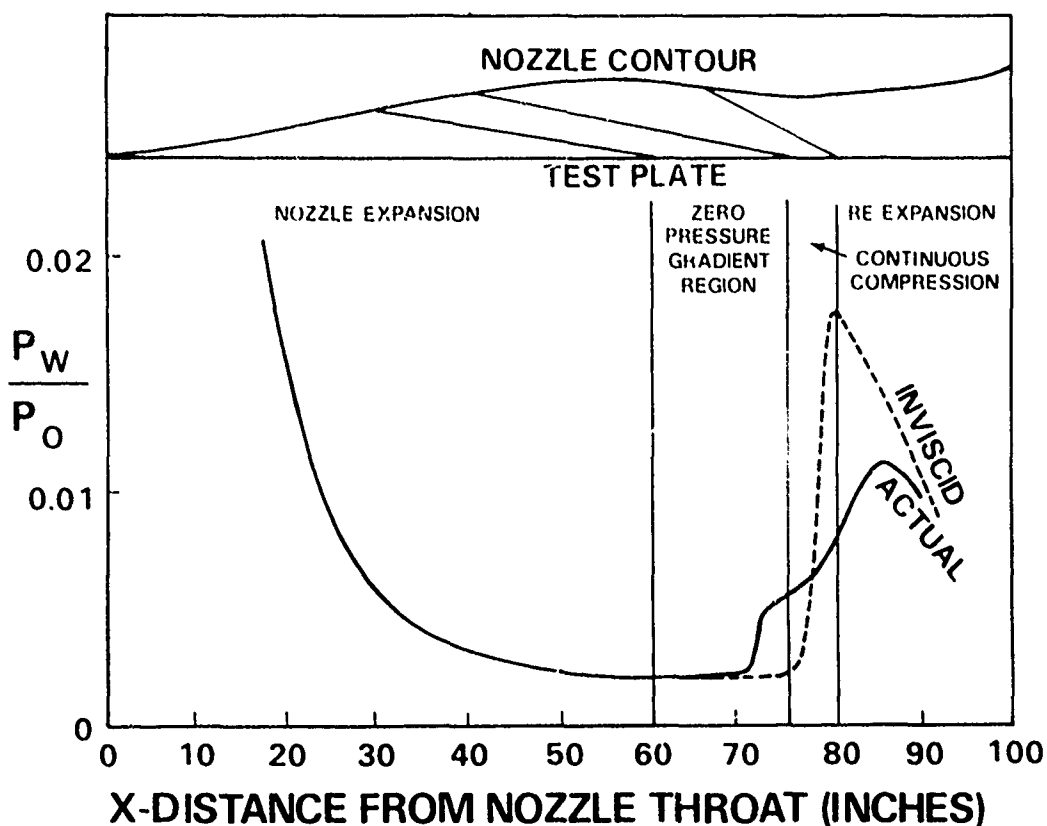


FIG. 2 - NOZZLE CONTOUR INFLUENCE ON TEST PLATE PRESSURE DISTRIBUTION

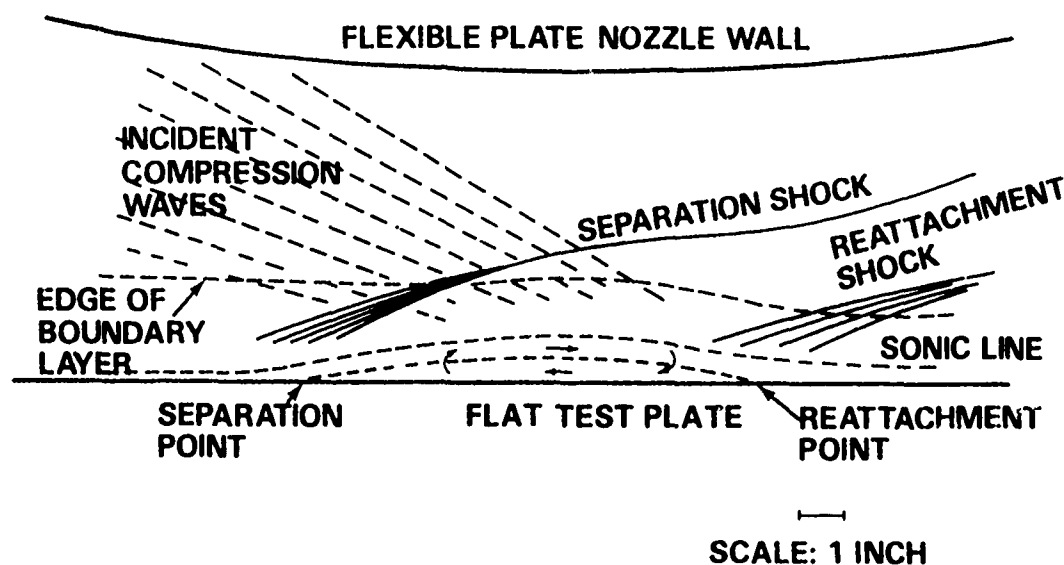


FIG. 3 - FLOW SEPARATION INDUCED BY A CONTINUOUS NOZZLE FLOW COMPRESSION

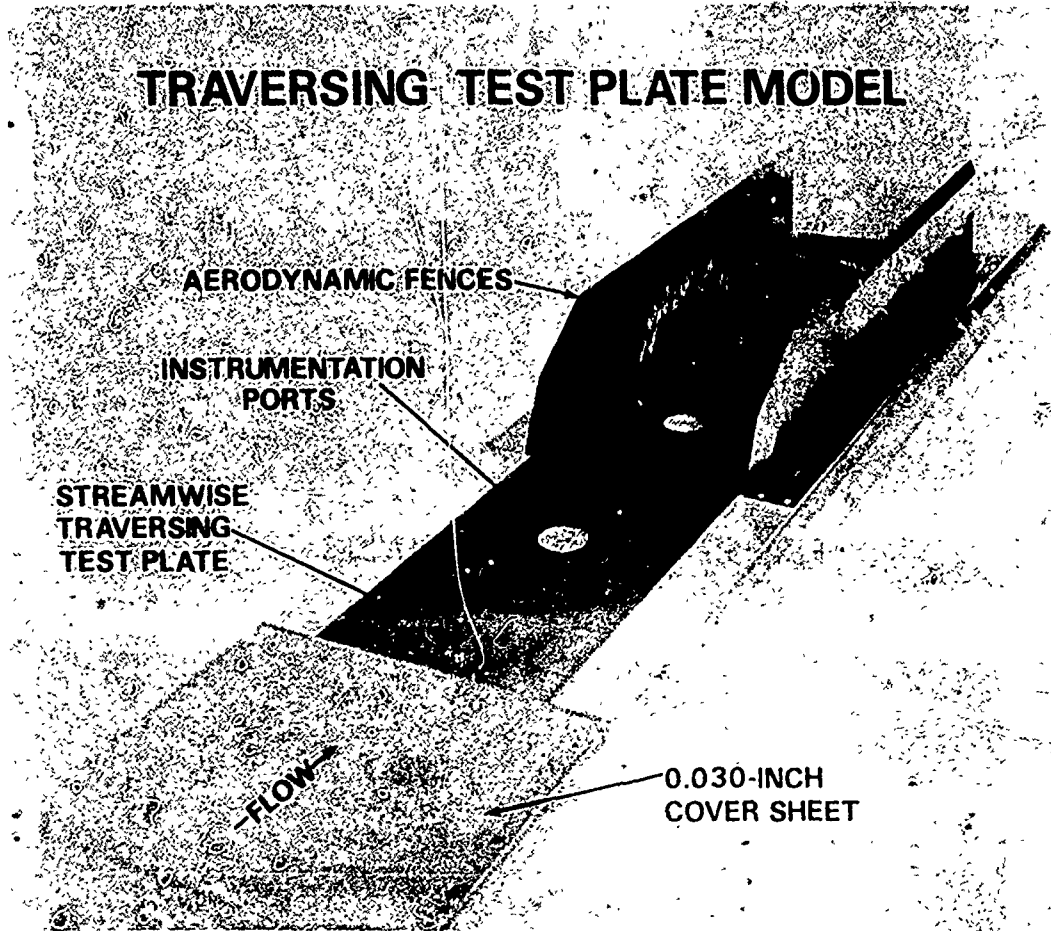


FIG. 4 - TRAVERSING TEST PLATE MODEL

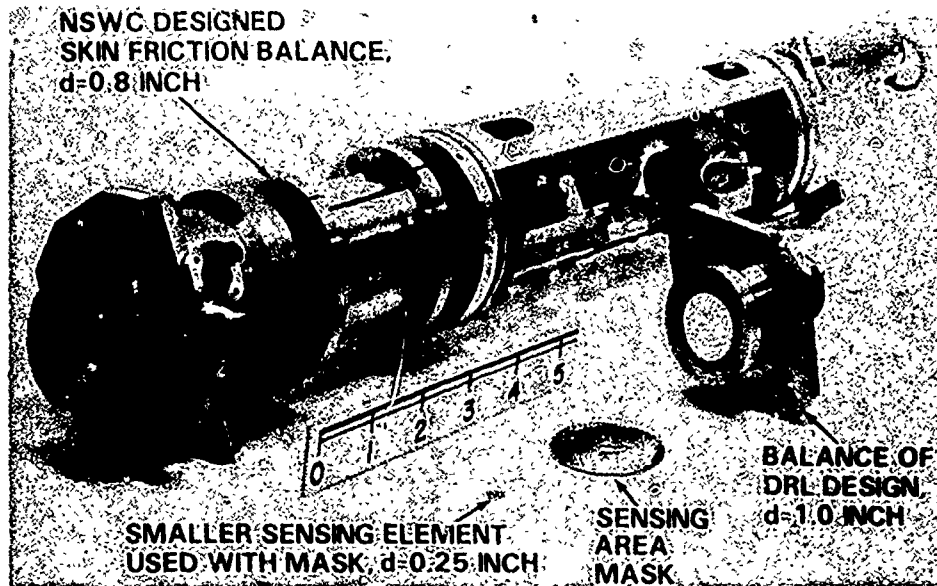
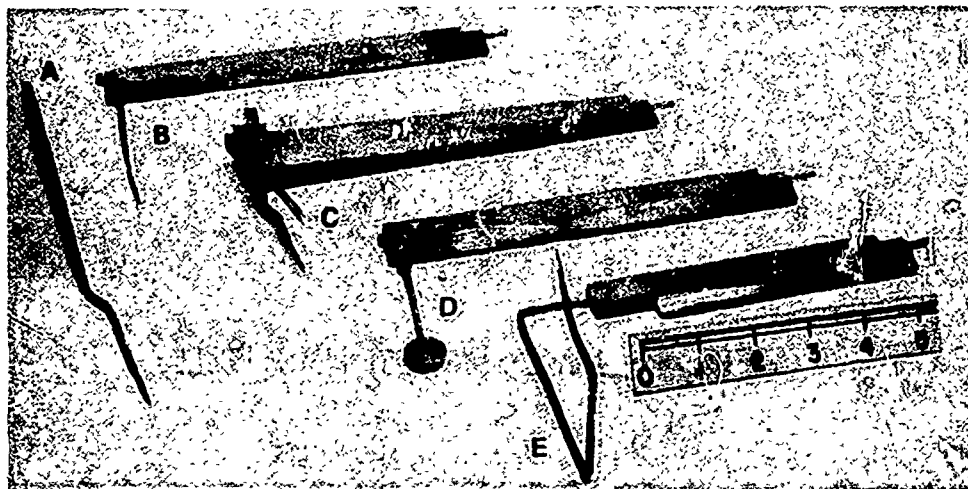


FIG. 5 - SKIN-FRICTION BALANCES



- A. FLATTENED TIP PITOT PROBE WITH EXTENSION
- B. FLATTENED TIP PITOT PROBE
- C. DOUBLE PROBE HOLDER WITH PITOT AND FINE WIRE STAGNATION TEMPERATURE PROBE
- D. 0.75-INCH DIAMETER DISC STATIC PRESSURE PROBE
- E. REVERSE FLOW PITOT PROBE

FIG. 6 - BOUNDARY-LAYER PROBES



OIL FLOW PATTERN
WITHOUT AERODYNAMIC
FENCES

OIL FLOW PATTERN
WITH AERODYNAMIC
FENCES

FIG. 7 - SURFACE OIL FLOW PATTERNS

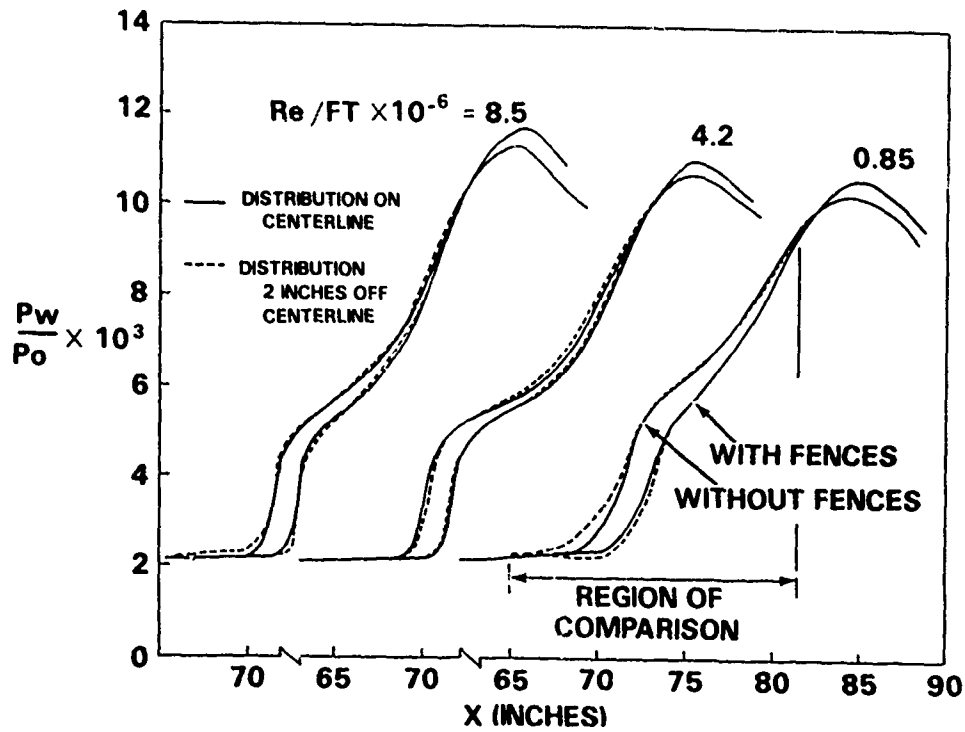


FIG. 8 - STREAMWISE WALL-PRESSURE DISTRIBUTIONS ON AND OFF CENTERLINE WITH AND WITHOUT FENCES

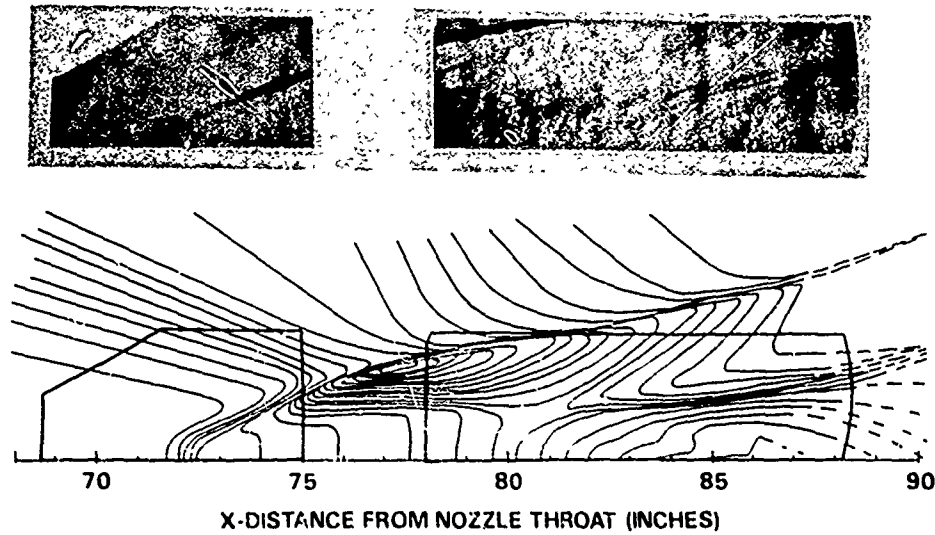


FIG. 9 - SCHLIEREN PHOTOGRAPHS AND STATIC-PRESSURE ISOBAR MAPPING, $Re_{\delta I} = 7.7 \times 10^5$

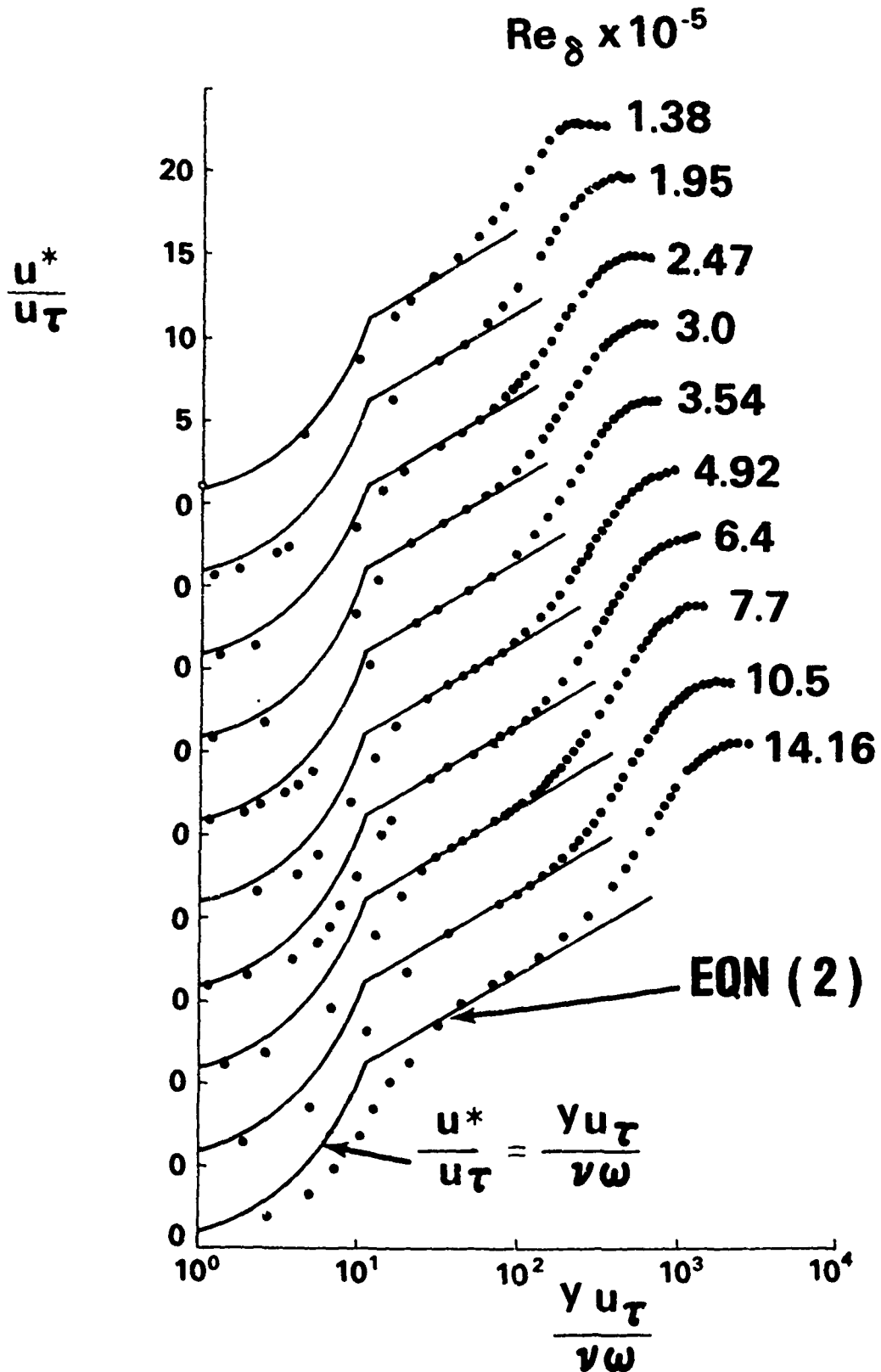


FIG. 10 - REYNOLDS NUMBER EFFECT ON THE LAW-OF-THE-WALL VELOCITY CORRELATION AHEAD OF THE INTERACTION, X = 67 INCHES

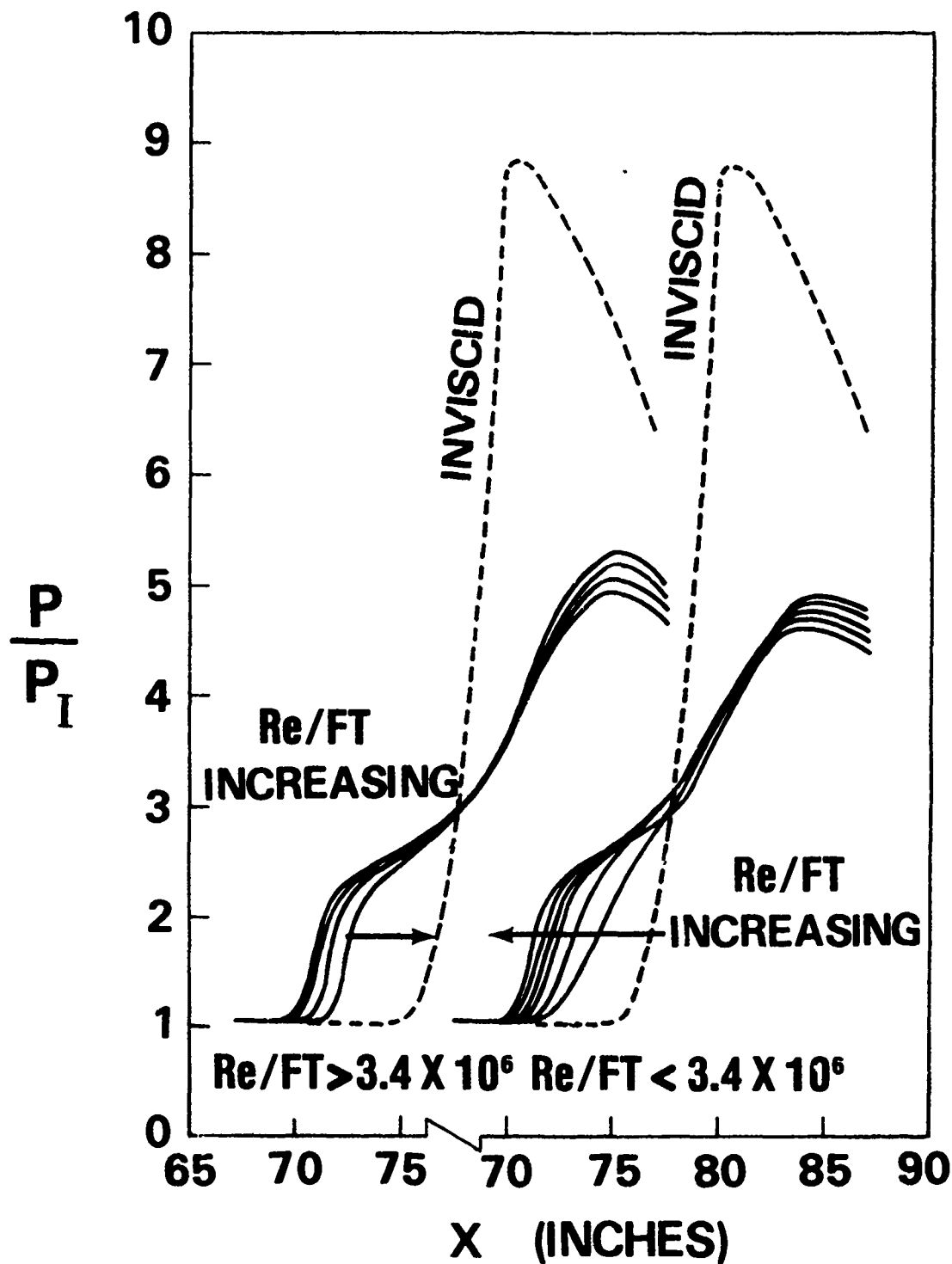


FIG. 11 - REYNOLDS NUMBER EFFECT ON THE WALL-PRESSURE DISTRIBUTION

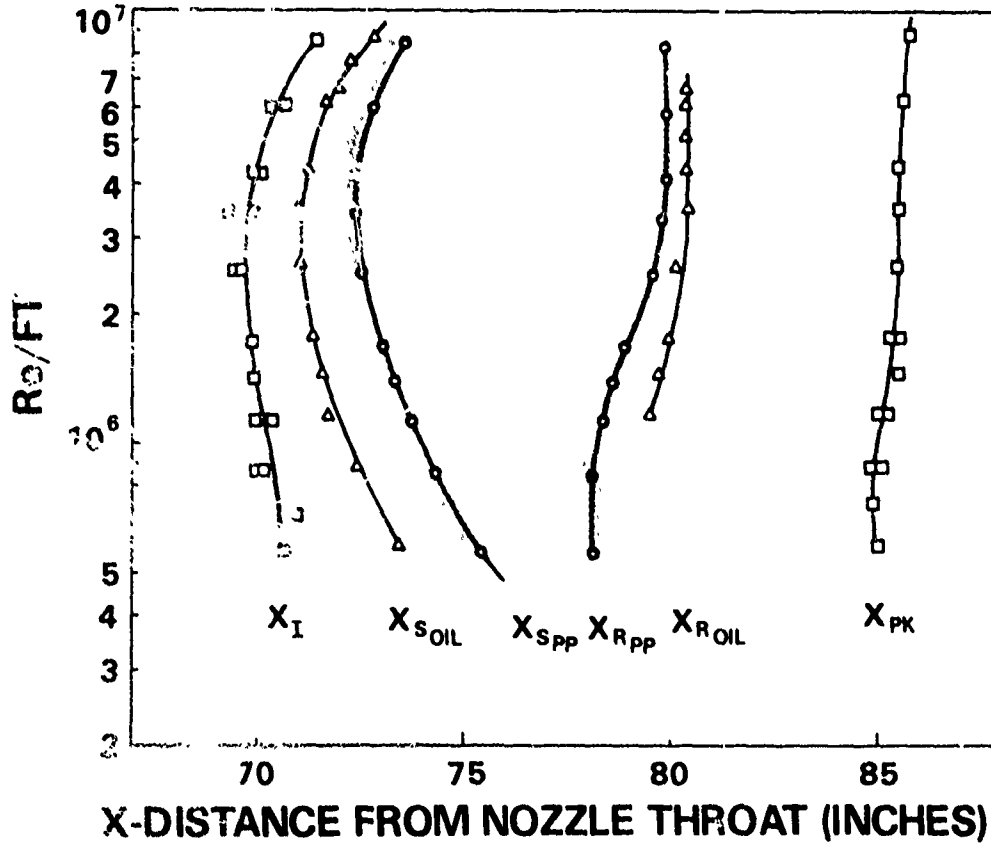


FIG. 12 - VARIATION OF SEPARATION AND REATTACHMENT LOCATIONS WITH REYNOLDS NUMBER

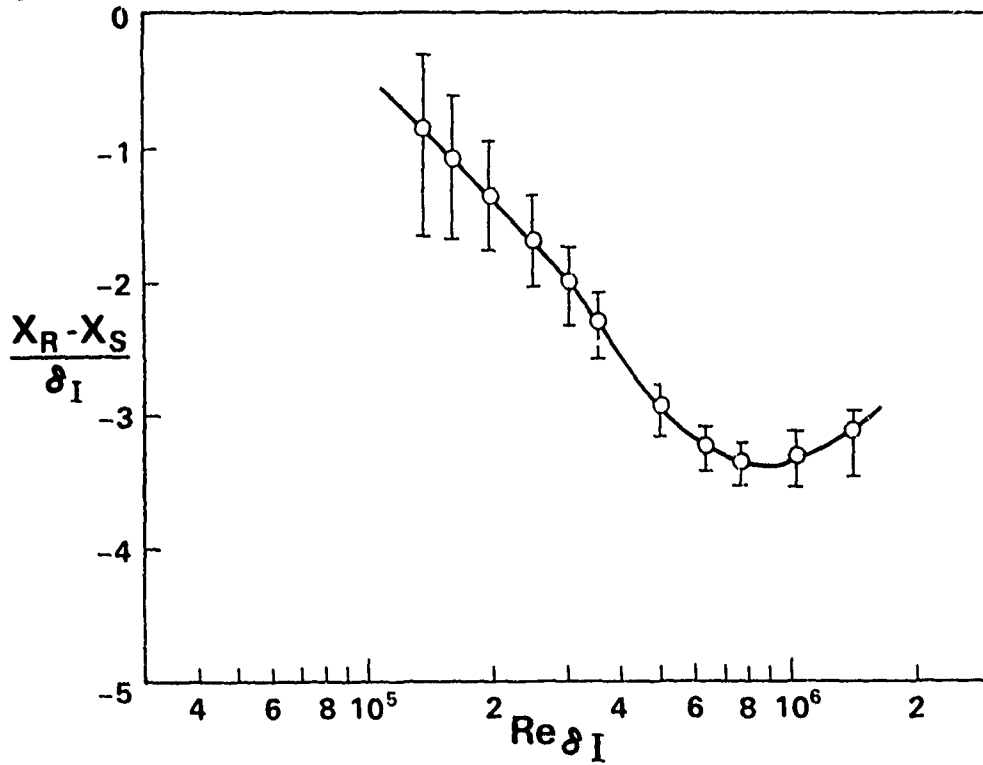


FIG. 13 - VARIATION OF SEPARATION LENGTH WITH REYNOLDS NUMBER

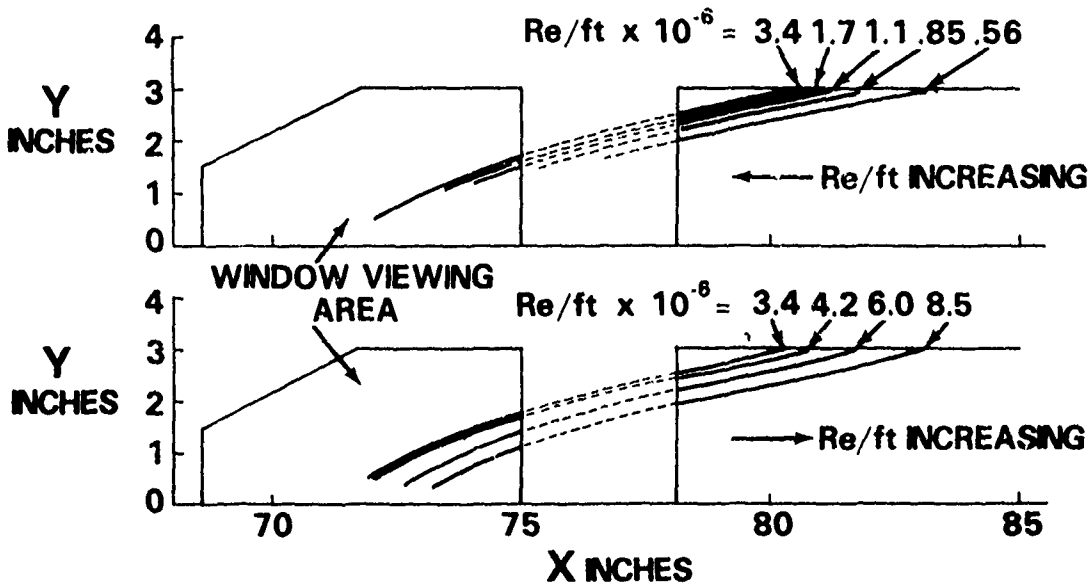


FIG. 14 - VARIATION OF SEPARATION SHOCK LOCATION WITH REYNOLDS NUMBER

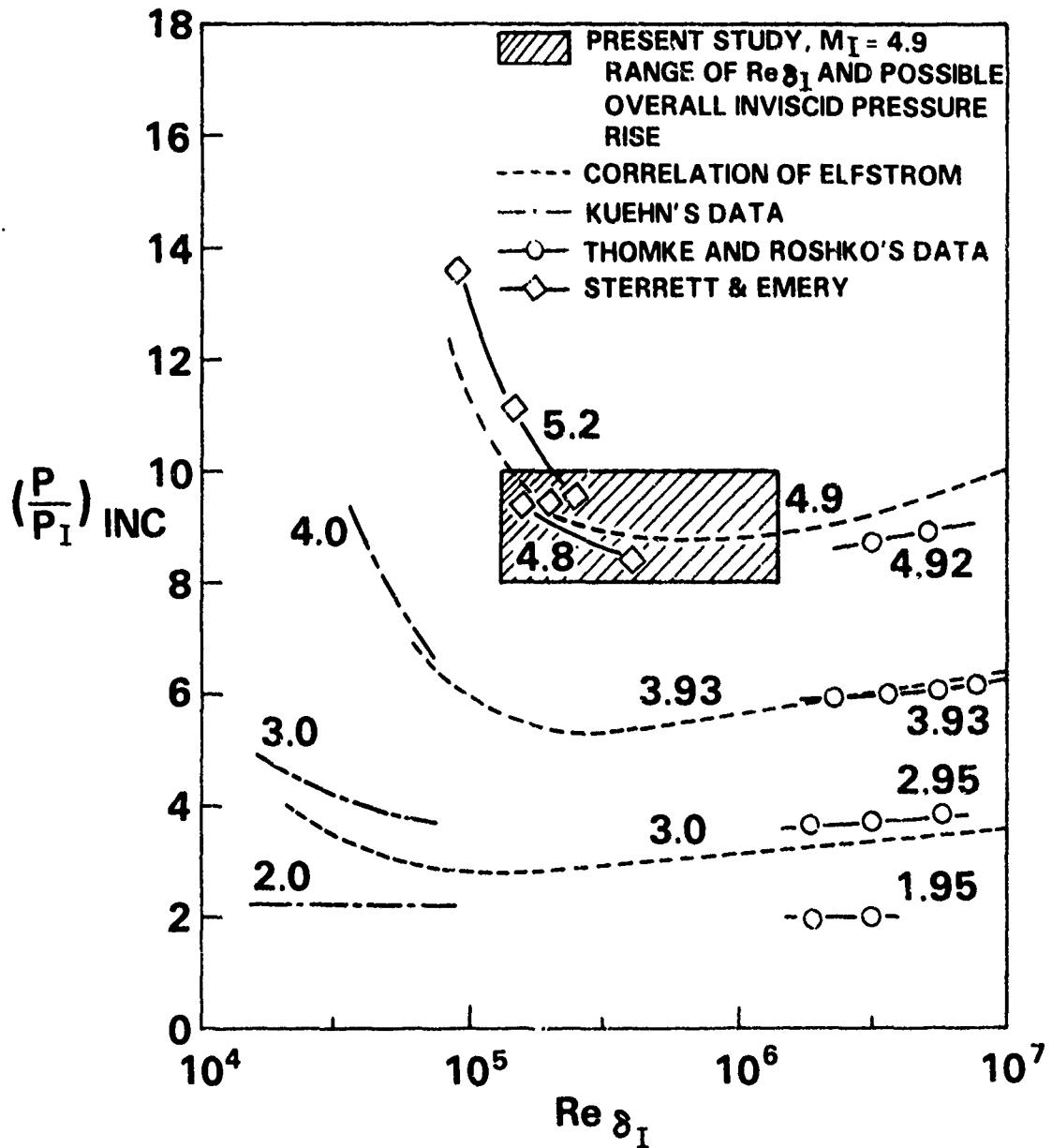


FIG. 15 - REYNOLDS NUMBER EFFECT ON THE PRESSURE RISE TO INCIPIENT SEPARATION

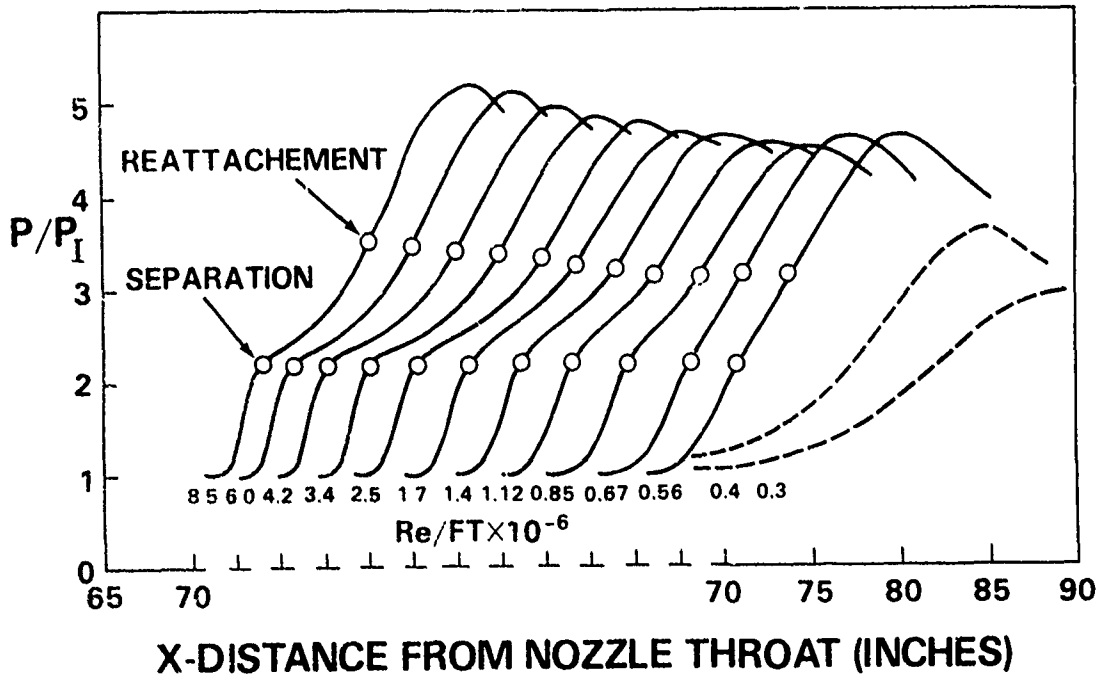


FIG. 16 - REYNOLDS NUMBER EFFECT ON THE WALL-PRESSURE DISTRIBUTION

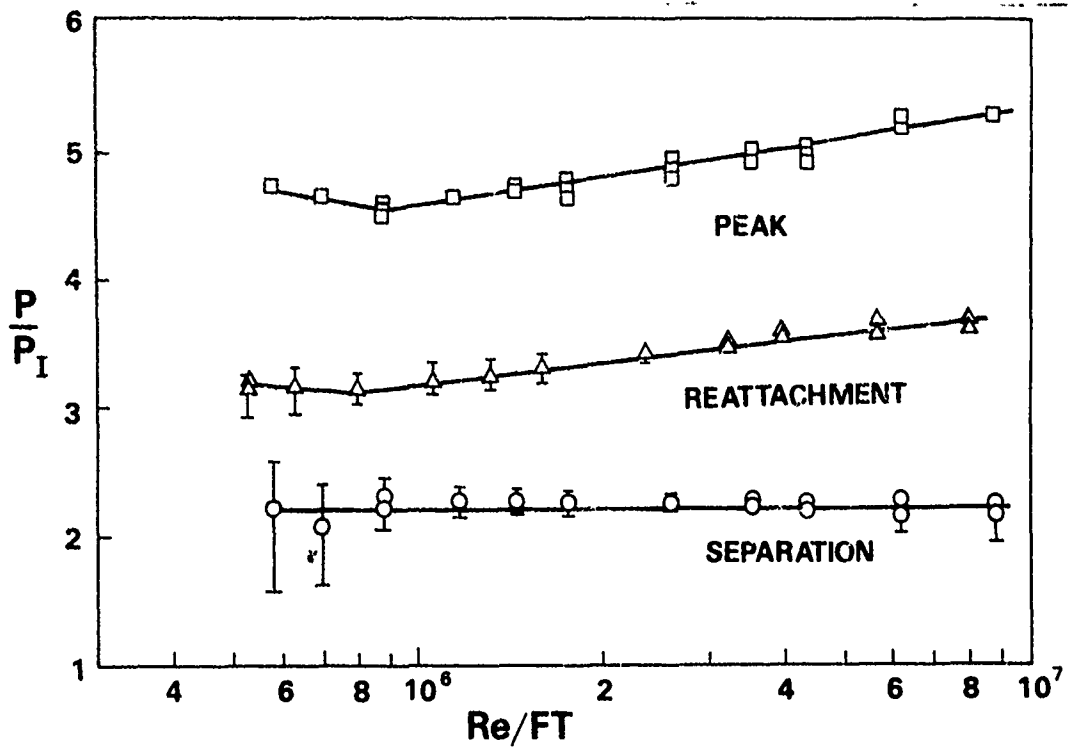


FIG. 17 - VARIATION OF THE PRESSURE RISE WITH REYNOLDS NUMBER

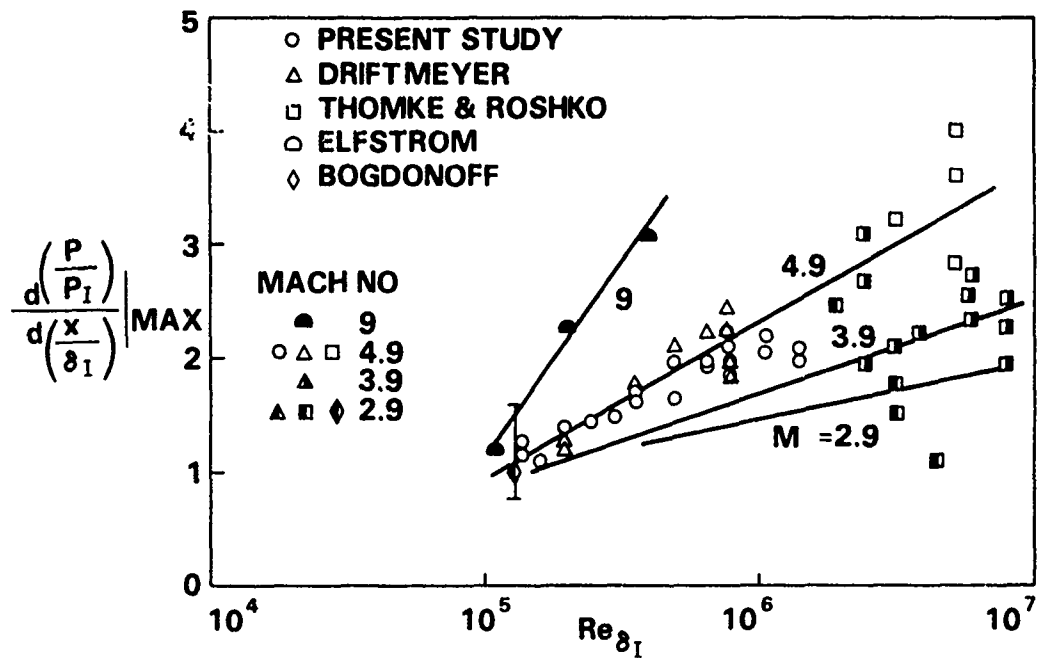


FIG. 18 - VARIATION OF THE MAXIMUM PRESSURE GRADIENT IN THE FREE-INTERACTION REGION WITH REYNOLDS NUMBER

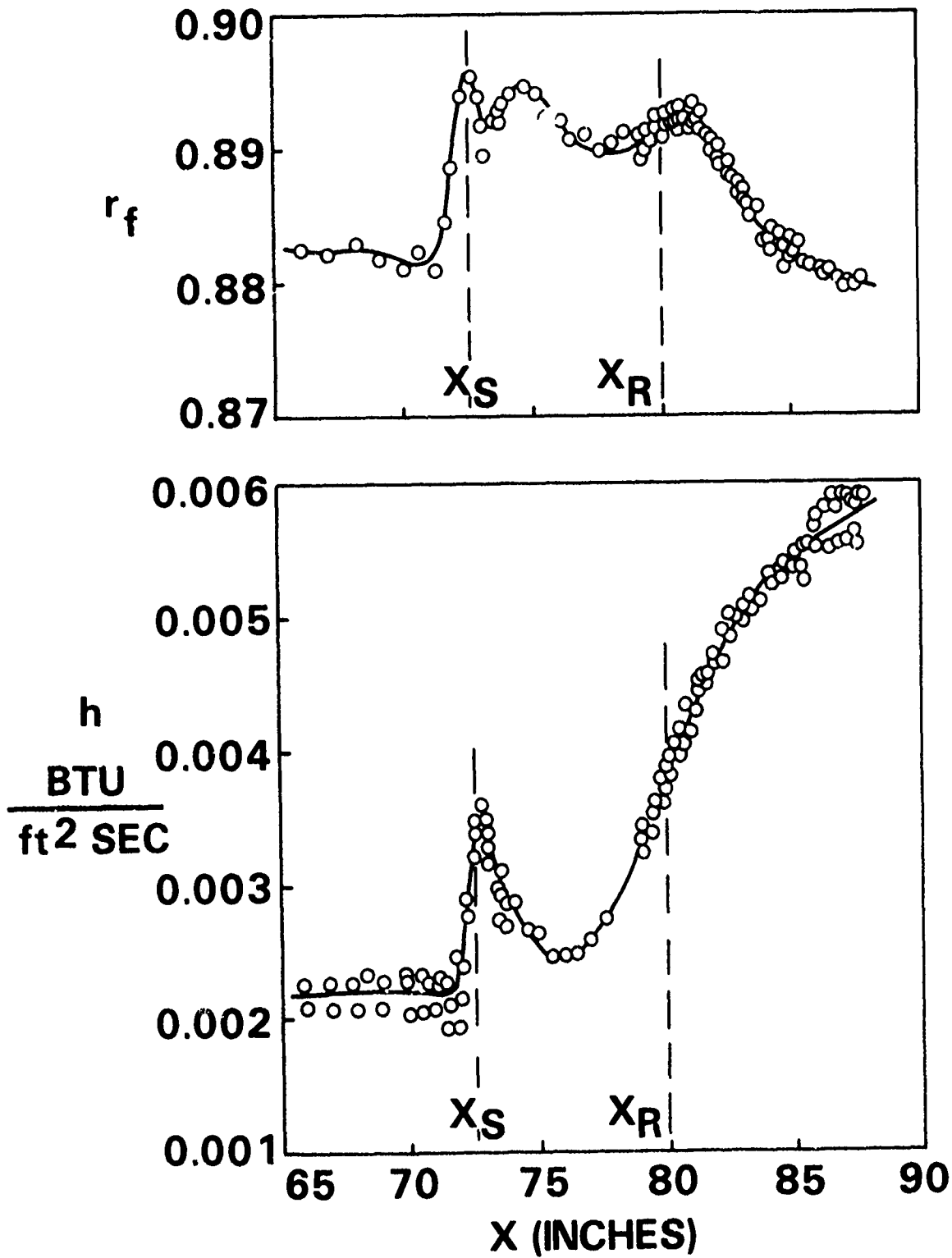


FIG. 19 - RECOVERY FACTOR AND HEAT-TRANSFER COEFFICIENT DISTRIBUTIONS, $Re_{q1} = 7.7 \times 10^5$

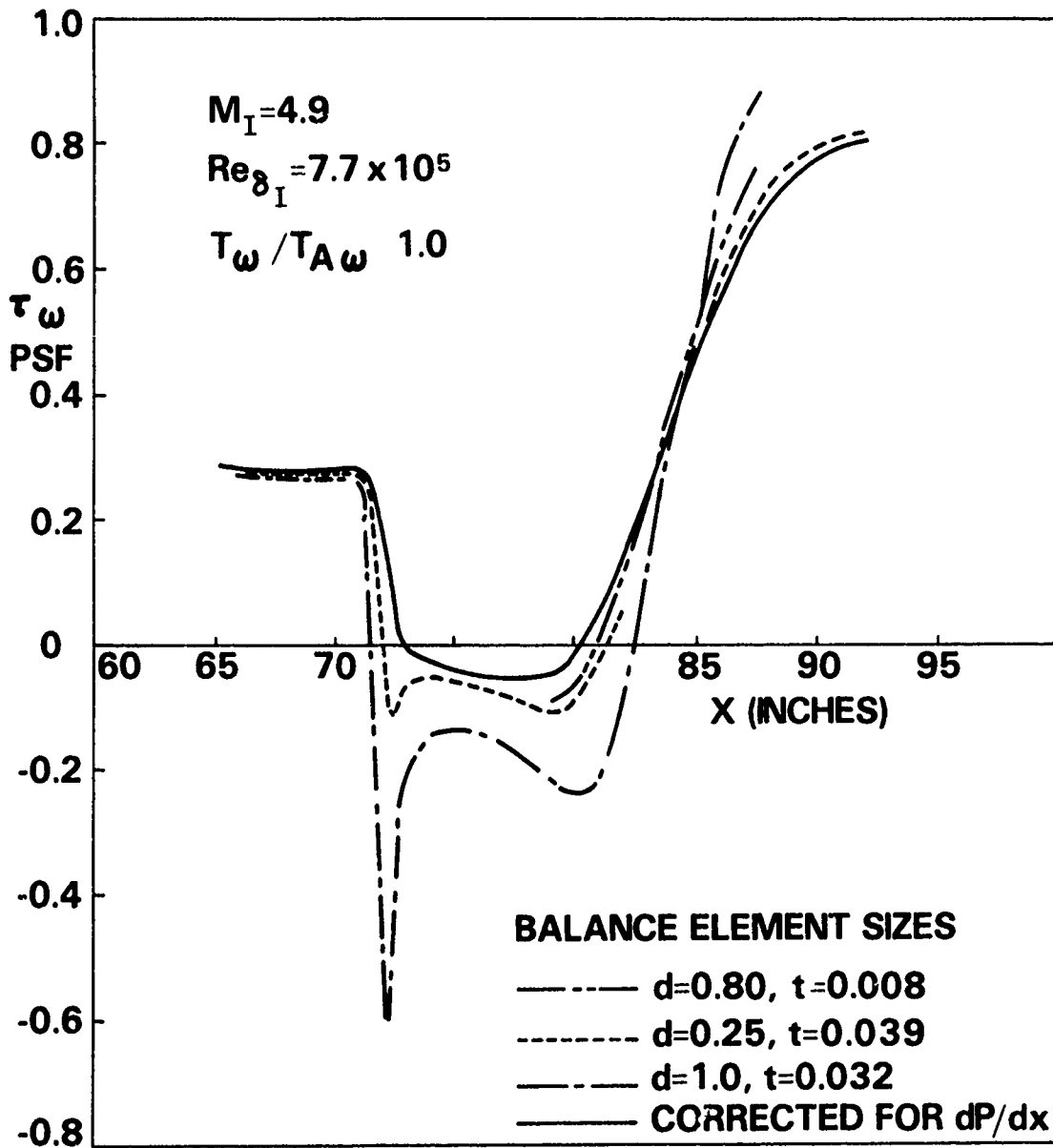


FIG. 20 - WALL SHEAR-STRESS DISTRIBUTIONS, $Re_{\delta_I} = 7.7 \times 10^5$

PAPER NO. 38

EFFECTS OF HYPERSONIC VISCOUS INTERACTION ON
THE CENTER OF PRESSURE OF SHARP AND BLUNT CONES
AS A FUNCTION OF ANGLE OF ATTACK

By

A. G. Keel, Jr.

J. A. Darling

Naval Surface Weapons Center

White Oak Laboratory

Silver Spring, Maryland

ABSTRACT

Advanced re-entry vehicle designs demand knowledge of the center-of-pressure location to within 0.5 percent of vehicle length. This requirement necessitates a new emphasis on delineation of viscous effects peculiar to high Mach number facilities in which flight Reynolds numbers cannot be duplicated. To resolve this question of viscous influence, particularly with regard to the White Oak Mach 18 Hypervelocity Research Tunnel, normal-force and pitching-moment data have been obtained for seven- and ten-degree sharp and blunt cones at a unit Reynolds number of $0.5 \times 10^6/\text{ft}$ for angles of attack from -6 to +12 degrees. A special high-resolution, four-component internal strain-gage balance was designed and built in-house to make these measurements. Similar static coefficient data obtained in the White Oak Hypersonic Tunnel at Mach 9 are also considered.

For the most blunt case, the results of three-dimensional inviscid computations are in exceptional agreement with the measured variation of center of pressure with angle of attack. For sharp cones, a consistent trend in the viscous influence is demonstrated: at low angles of attack, viscous interaction has a stabilizing effect on center of pressure; with increasing angle of attack, the viscous influence decreases with the center of pressure asymptotically approaching the inviscid value.

NOMENCLATURE

C_∞	$\frac{\mu_\infty T_w}{\mu_w T_\infty}$	= Chapman-Rubesin viscosity coefficient
F_N		aerodynamic normal force
l_v		sharp cone length
M_∞		free-stream Mach number
Re_ℓ		free-stream Reynolds number scaled to actual model length
\bar{V}_∞	$M_\infty \left(\frac{c_\infty}{Re_\ell} \right)^{1/2}$	= hypersonic viscous parameter
X_{CP_v}		center-of-pressure location measured from sharp cone vertex
α		angle of attack
γ		ratio of specific heats
θ_c		semivertex cone angle
μ_∞, μ_w		viscosity based on free-stream static temperature (T_∞), based on model wall temperature (T_w)
ψ		nose radius/base radius = bluntness ratio

INTRODUCTION

Advanced re-entry vehicle designs now demand knowledge of the center-of-pressure location to within 1/2 percent of model length. In applying wind-tunnel test data to flight conditions, this requirement necessitates a more critical assessment of possible viscous effects peculiar to the high Mach number facilities in which flight Reynolds numbers

Vol. 3

cannot be simulated. New emphasis has been placed on the development of inviscid and viscous flow-field computational techniques. However, the uncertainty of these techniques is yet to be rigorously established. It is apparent that for these high Mach number conditions, more accurate experimental results are required. These results must have sufficient resolution to delineate possible viscous effects on center-of-pressure location and to establish parametric trends. A means of comparative evaluation of the computational results would thus be provided. The purpose of this paper is to present newly acquired experimental results that serve as partial fulfillment of these needs.

EXPERIMENTAL RESULTS

Sharp and spherically blunted cones have been tested in the Naval Surface Weapons Center, White Oak Laboratory, Mach 18 Hypervelocity Research Tunnel¹ at a unit Reynolds number of 0.5×10^6 per foot. An in-house designed, high-resolution strain-gage balance, mounted internal to the model, was used to obtain normal force and center-of-pressure location. Data are acquired under steady-state conditions for a continuous variation of angle of attack from -6 to +12 degrees.

Center-of-pressure data for a sharp ($\psi = 0$) seven-degree cone are presented in Figure 1. The center-of-pressure location measured from the cone vertex and normalized with respect to the sharp cone length is shown versus angle of attack. The Mach 18 results correspond to a Reynolds number based on model length of 6×10^5 yielding a value of the

so-called hypersonic viscous parameter, \bar{V}_∞ , equal to 0.023. The accuracy of these experimental results for the center-of-pressure location is within ± 0.2 percent of model length. The inviscid analytic result for the center-of-pressure location of a sharp cone is easily derived, by use of conicity, as

$$\frac{x_{cpV}}{l_v} = \frac{2}{3 \cos^2 \theta_c} \quad (1)$$

which is independent of Mach number, angle of attack, and flow species (γ). Deviation of the present results at low angles of attack from the inviscid prediction for $\theta_c = 7$ degrees is apparent. The viscous influence has a stabilizing effect with an aft shift of approximately one percent of model length occurring near zero angle of attack for the present conditions ($\theta_c = 7^\circ$, $\psi = 0$, $M_\infty = 18$, $\bar{V}_\infty = 0.023$). As the angle of attack increases, the viscous effect decreases and the center-of-pressure location asymptotically approaches the inviscid prediction within the experimental uncertainty.

Recent numerical results have been obtained by Lubard² for the high Mach number viscous flow about a seven-degree "sharp cone" at angles of attack of 1, 5 and 10 degrees. A solution to an approximate form of the full Navier-Stokes equations is achieved. Lubard's center-of-pressure results are included in Figure 1 for comparison to the present data. In addition to the "sharp" cone results for the principal

Vol. 3

Reynolds number condition of interest in Reference 1, results for the same Re_ρ and, alternatively, for the same \bar{V}_∞ as the present case are shown. This is possible only at the expense of slightly increased bluntness (ψ) since results are computed as a function of model length for a fixed spherical nose radius. The calculation predicts the same behavior with angle of attack for the viscous influence on center of pressure as that exhibited by the experimental results. The quantitative agreement is within estimates of the combined uncertainties³ of the numerical and experimental results. More definitive interpretation of the comparison is thus precluded.

Additional evidence of this behavior of the viscous influence is illustrated in Figure 2 with sharp cone results ($\theta_c = 6, 7, \text{ and } 8 \text{ degrees}$) obtained at Mach 9 in White Oak Laboratory's Hypersonic Tunnel with a conventional six-component force and moment balance. Data presented are for a range of Reynolds numbers corresponding to \bar{V}_∞ from 0.004 to 0.014. Consistent with the $M_\infty = 18$ results of Figure 1, increasing \bar{V}_∞ (decreasing Reynolds number) produces an aft shift in center of pressure at low angles of attack. With increasing angle of attack the low Reynolds number data and high Reynolds number data merge, adopting the inviscid value within the experimental uncertainty of these Mach 9 results (± 0.4 percent). However, it should be noted that the expected strong coupling for these lower Mach number data between the leeward-side separation region and the base flow at the higher angles of attack ($\alpha > 2\theta_c$) clearly must alter

but, moreover, augment the influence of the leeward side, perhaps more noticeably sustaining a center-of-pressure location at high angle of attack other than the analytic inviscid prediction. That the high Reynolds number $\theta_c = 6$ and 7 degrees results lie systematically above the inviscid prediction might be attributable to the above occurrence. An unequivocal conclusion cannot be reached since, as previously stated, the deviation of these data from the inviscid value is within the experimental uncertainty.

As a final consideration of the center of pressure for a sharp cone, high Mach number experimental results obtained in other facilities^{4,5} for a seven-degree cone are compared to the present data in Figure 3. The similarity of the trend with angle of attack of the viscous influence on center of pressure is apparent, especially between the present results and the Aerospace Research Laboratories' (ARL) data. However, the ARL results achieve the inviscid value at an angle of attack approximately twice that required for the present results. The AEDC measurements for high angles of attack indicate a center of pressure below the inviscid prediction. These differences likely arise as much from bias or systematic uncertainty inherent to each facility as to actual difference in case.

The blunt cone, Mach 18 center-of-pressure data are presented in Figures 4(a)-(d). Results for 10-degree, spherically blunted cones with bluntness ratios of 0.0167, 0.10, and 0.252 and for a seven-degree cone with a bluntness of 0.20 are illustrated. For each bluntness, the behavior

Vol. 3

of the center-of-pressure location with angle of attack is well established by the experimental results. The viscous parameter, \bar{V}_∞ , as indicated on the figures, varied slightly due to changing model length. Inviscid computations have been performed* for each case at angles of attack of 1, 3, 5, 10, and 15 degrees using a three-dimensional, finite-difference program. Comparisons are included in Figures 4(a)-(d). Excellent agreement is seen for the most blunt case for each cone angle. The detailed angle-of-attack dependence established by the experiments is well predicted by the theory. For the 10-degree cone with smaller bluntnesses, the experimental results diverge from the inviscid prediction as angle of attack decreases--an apparent viscous effect. Note, however, that for the lower angles of attack this effect on center of pressure is nonmonotonic with bluntness. For example, Figure 5 compares the present 10-degree cone results for $\alpha = 1$ degree to the inviscid prediction of the variation of center of pressure with bluntness. Agreement is found between the experiment and the calculation for $\psi = 0.25$. For $\psi = 0.10$, the experimental results indicate a center-of-pressure location approximately two percent of model length further aft; whereas, for $\psi = 0.0167$ a shift aft of about 0.5 percent is indicated. Note additionally, that Figure 5 reveals that the $\psi = 0.10$ bluntness is within the range where the inviscid computation predicts a quite sensitive dependence of center of pressure on bluntness, especially

*The author gratefully acknowledges the cooperation of Dr. J. M. Solomon (NAVSURFWPCEN/WOL) in performing the inviscid computations.

in relation to the sensitivity predicted near $\psi = 0.0167$. It seems plausible that for the intermediate bluntness, which is not sufficiently blunt to overwhelm the viscous influence, the greater observed effect on center of pressure is a consequence of the above.

In summary, hypersonic viscous interaction is observed to have a stabilizing influence on center of pressure for sharp, slender cones at low angles of attack ($\alpha \lesssim \theta_c$), in that, an aft shift relative to the analytic inviscid prediction is observed. As angle of attack increases, the viscous effect decreases and the center of pressure asymptotically approaches the inviscid prediction (within the experimental uncertainty) for $2\theta_c \lesssim \alpha \lesssim 3\theta_c$. Analogously, for the less-blunt spherically blunted cones, the experimental results deviate from the numerical inviscid calculations as the angle of attack decreases. This apparent viscous effect is nonmonotonic with bluntness.

Future plans are to obtain center-of-pressure data at Mach 18 over a range of the viscous parameter, \bar{V}_∞ (or equivalently Reynolds number), for additional bluntnesses. Further comparisons to viscous and inviscid computations are intended.

REFERENCES

1. Cornett, R. H. and Keel, A. G., Jr., "NOL Mach 18 Hypervelocity Research Tunnel," NOLTR 74-158, Aug 1974, NAVSURFWPCEN/WOL, Silver Spring, Md.

10th Navy Symposium on Aeroballistics

Vol. 3

2. Lubard, S. C., "Calculation of the Hypersonic Flow on a Sharp 7° Cone at Angle of Attack," RDA-TR-5004-002, Jul 1974, R&D Associates, Santa Monica, Calif.
3. Lubard, S. C., private communication, R&D Associates, Santa Monica, Calif.
4. Stetson, K., private communication, Aerospace Research Laboratories, Wright-Patterson Air Force Base, Ohio.
5. Pate, S. R. and Eaves, R. H., Jr.: "Recent Advances in the Performance and Testing Capabilities of the AEDC-VKF Tunnel F (HOTSHOT) Hypersonic Facility," AIAA Paper No. 74-84, Jan 1974

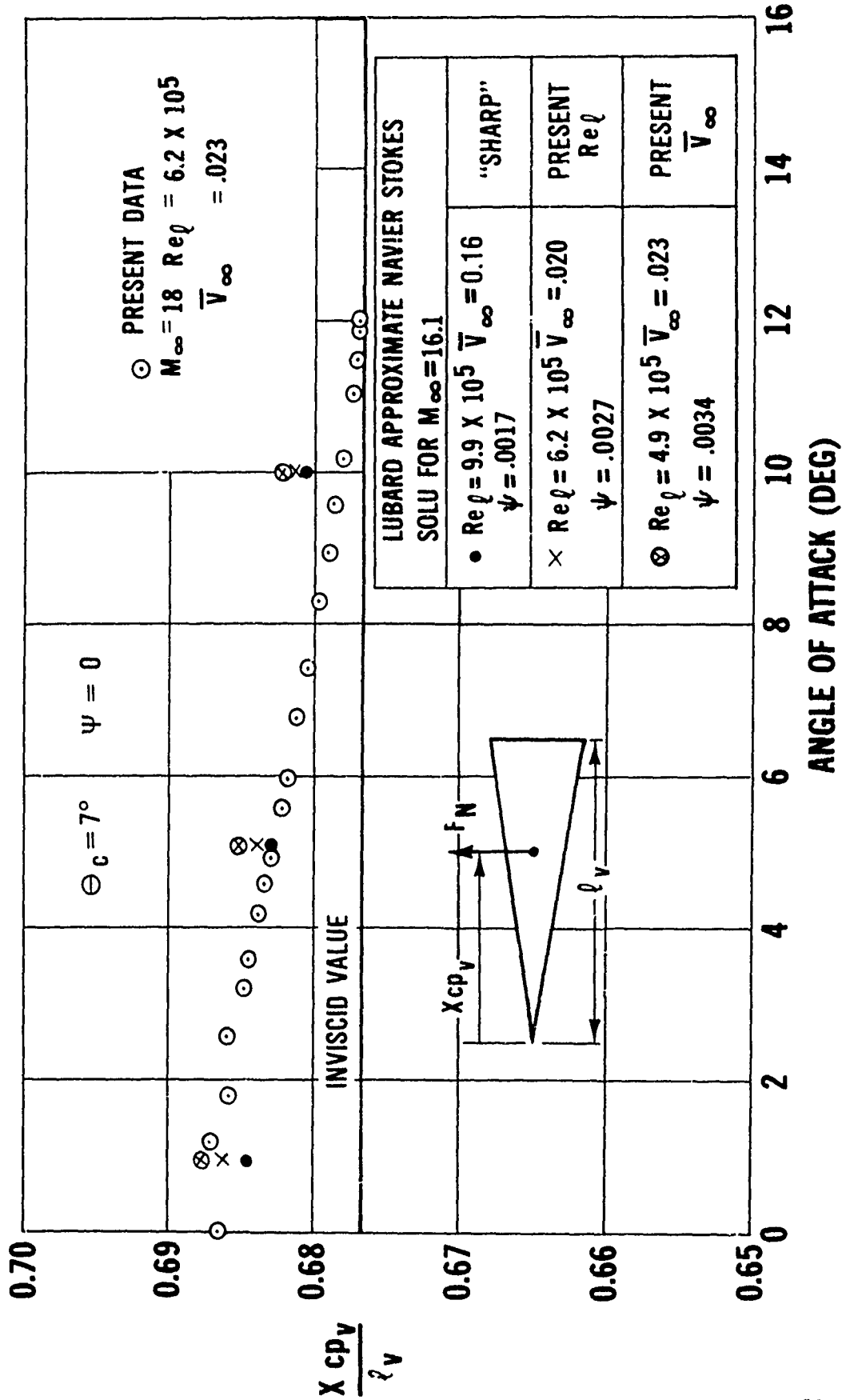


FIGURE 1 MACH 18 EXPERIMENTAL DATA FOR CENTER OF PRESSURE OF SHARP CONE

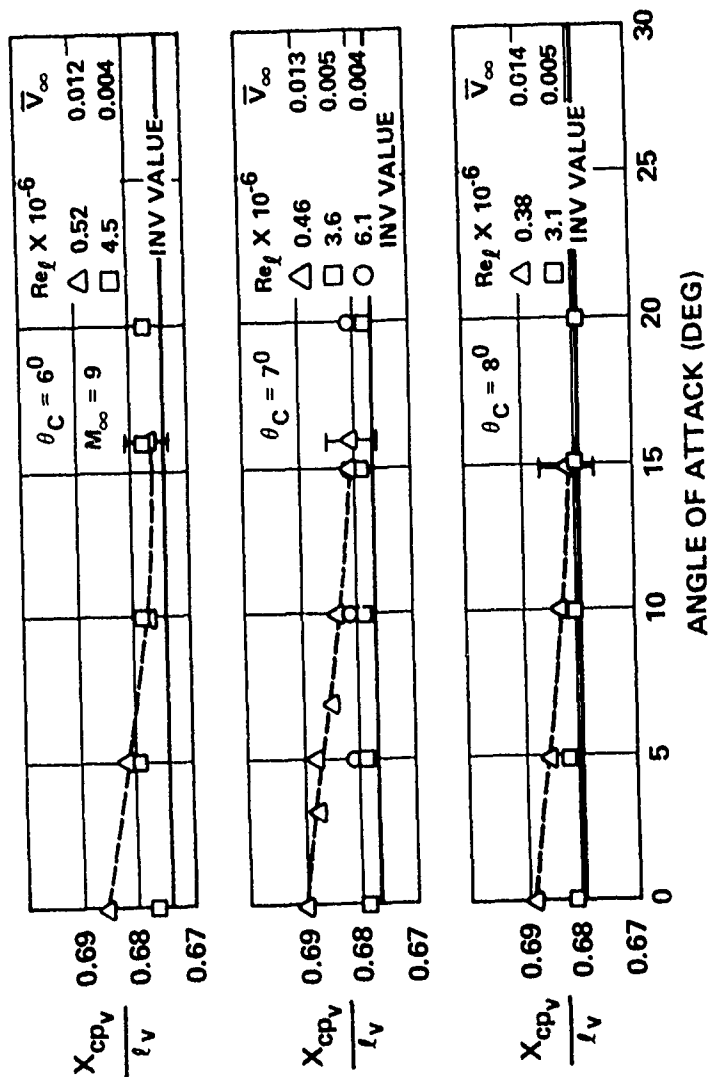


FIGURE 2 MACH 9 EXPERIMENTAL DATA FOR CENTER OF PRESSURE OF SHARP CONES

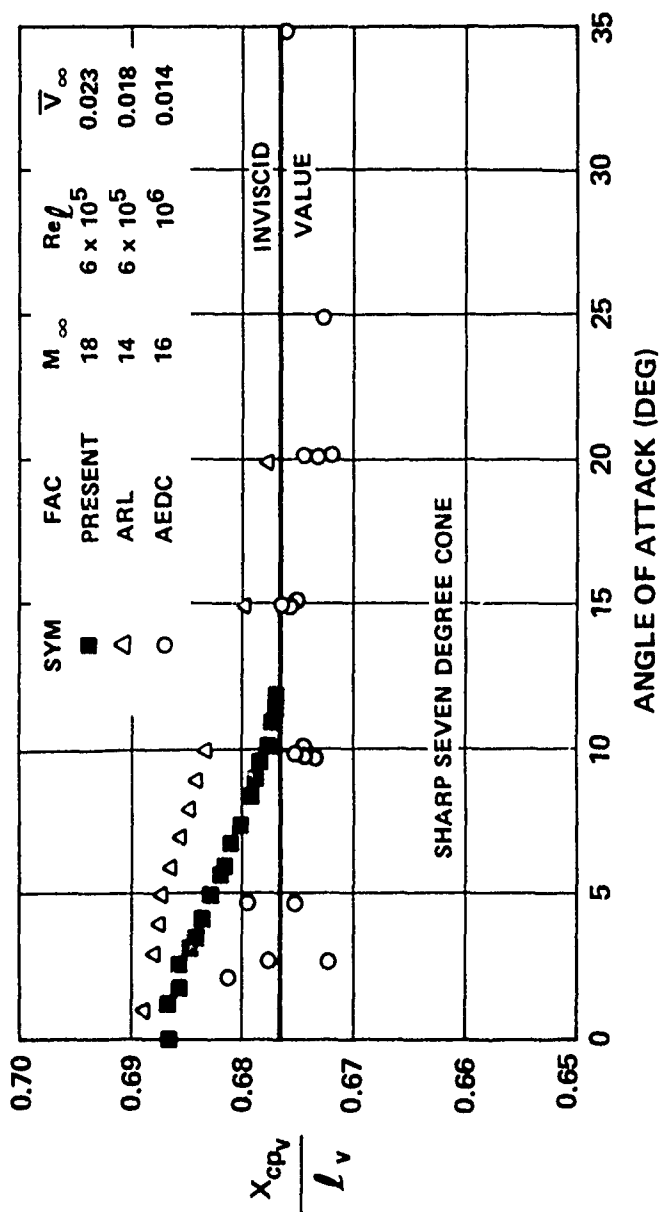


FIGURE 3 COMPARISON OF HIGH MACH NUMBER CENTER-OF-PRESSURE DATA FOR SHARP SEVEN-DEGREE CONE

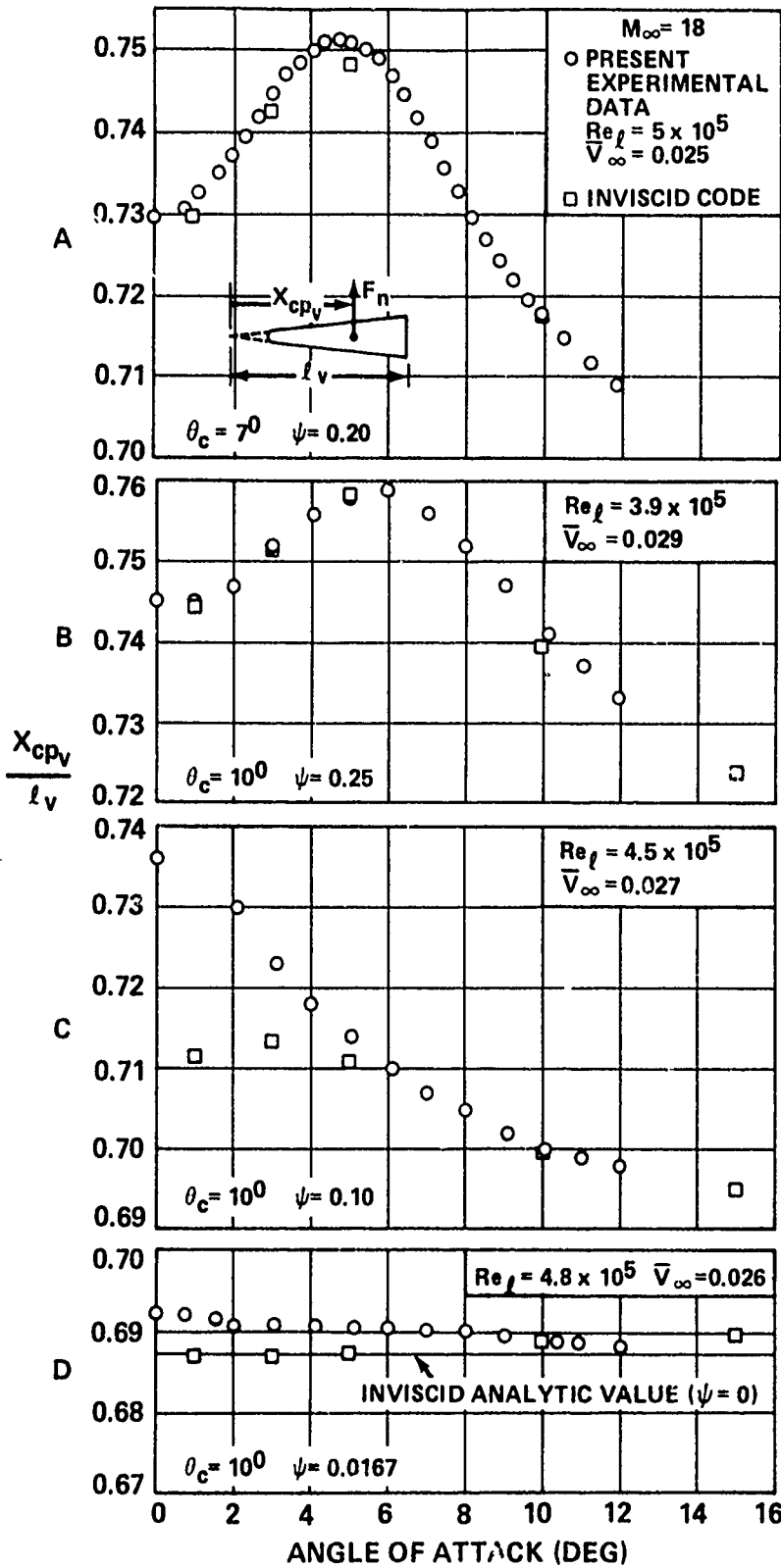


FIGURE 4 MACH 18 EXPERIMENTAL DATA FOR CENTER OF PRESSURE OF BLUNT CONE

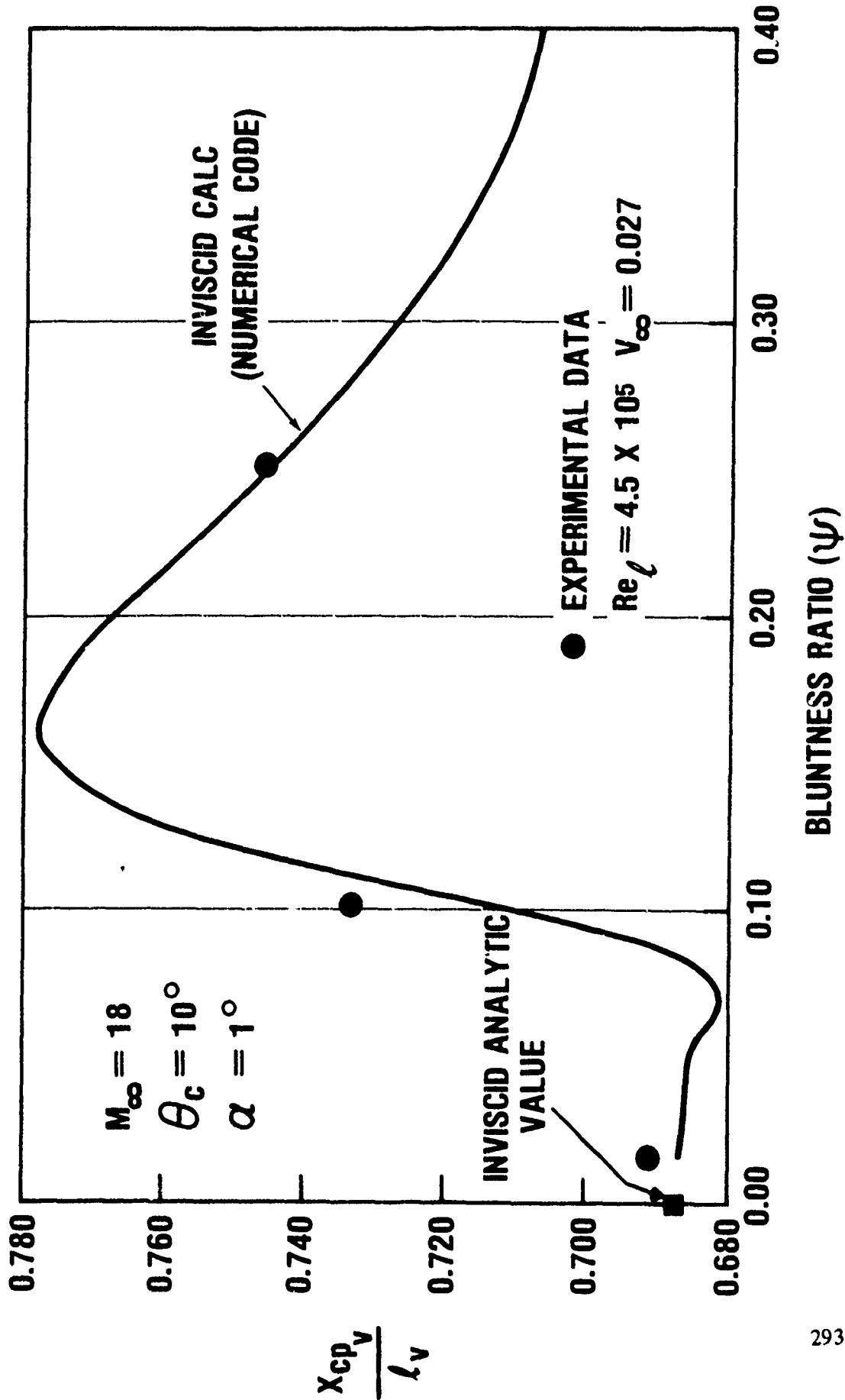


FIGURE 5 CENTER-OF-PRESSURE DEPENDENCE ON BLUNTNESS

PAPER NO. 39

A State-of-the Art Review of Methods
in Aeroelasticity and Structural Analyses
for Guided Weapons

G. Dailey, JHU/APL
R. J. Oedy, Hughes Missile Division
W. J. Werback, Naval Weapons Center

INTRODUCTION

The ability to conduct valid aeroelastic and structural analyses will become increasingly important in future Naval guided weapons as the demands for improved performance continue to increase. As an aid in determining the "where are we" and "where should we be going" in these fields within the engineering design community, members of the Structural and Aeroelasticity Panel of the Naval Aeroballistics Advisory Committee recently prepared position reports on these subjects. These reports form the basis of this paper.

WHERE ARE WE IN AEROELASTICITY

In the following discussion, this broad question is explored from the point of view of the needs of advanced tactical Naval missiles. The discussion will hopefully give an overview of the current state of knowledge, indicate the problems currently being encountered, point out the limitations of the tools of analysis, and focus on the technical areas in need of further development.

A missile flutter analysis requires consideration of four technical fields: structural dynamics, unsteady aerodynamics, thermoelasticity, and servoelectricity. The hardware involved in the analysis can be grouped into three categories: fixed lifting surfaces, missile bodies, and movable control surfaces. The question "Where are we in aeroelastic analysis?" will first be explored from the point of view of the hardware involved. The limitations in the analytical tools available to solve particular hardware problems will be discussed so as to lead to an understanding of specific topics in need of further work. Later, the particular limitations of analysis and the specific topics needing further development will be brought together and grouped by technical fields.

Fixed Lifting Surfaces

Fixed lifting surfaces do not appear to be causing any current serious aeroelastic problems. This is attributed more to the inherently large flutter stability margins for these surfaces resulting from other design requirements (such as strength requirements for high maneuver loads) than any deliberate aeroelastic design effort. A possible exception of this generalization is when thermal stresses associated with transient aerodynamic heating play a significant role in the modal response characteristics of the surface.

As regards structural dynamic modeling of fixed lifting surfaces, there is no difficulty, per se, in predicting their elastic behavior since powerful and reliable methods have been developed over the past ten years for analyzing continuous structures. There are some difficulties, however, in modeling quick-attachment designs for such surfaces. The stiffness properties of the attachments are difficult to analyze with confidence due to uncertainties regarding the degree of engagement of the attachments with the surfaces, the free play which will occur, and the nonlinear behavior of the attached surfaces under load. Experience with similar attachment designs provides the best guidance for developing early analytical models.

The limitations in the unsteady aerodynamic representations for fixed lifting surfaces appear to be more in the low reduced-frequency range than at the higher reduced-frequencies. This leads to a greater confidence in the unsteady aerodynamic representations likely to cause flutter of the elastic modes of the surfaces than to those reduced-frequencies likely to cause servocontrol instabilities.

Rapid transient heating may cause future lifting surfaces to have a tendency toward instability caused by unequal thermal expansion of structural

Vol. 3

components. This expansion may result in a loss of stiffness leading to instability. Analytical methods are available for performing thermoelastic studies for lifting surfaces, but good thermoelastic test methods are lagging the analytical tools. Desired results from a transient thermoelastic test would include such things as the time-history of the mode shapes, frequencies, and damping.

Missile Bodies

The missile body is involved indirectly in the flutter of aerodynamic surfaces through mass and stiffness coupling. The body is involved directly in autopilot/aeroelastic mode coupling instability, since the sensing elements (gyros, accelerometers, etc.) are body mounted. For investigating either type of instability, it is necessary that reasonably accurate estimates of body modes, frequency, and damping be made.

Here again, limitations in structural dynamic modeling are the primary source of design uncertainty. Mechanical joints are the most difficult design feature to analyze with any confidence. Structural discontinuities, the internal elastic behavior of sensor platforms, and the coupled multi-plane response of nearly-axial symmetric configurations are also difficult to model. Experience on similar body designs is often the best guide in modeling short of an actual dynamic test. Some sort of statistical modeling is often needed to establish the probable range of the upper and lower bounds of the frequencies, modal slopes, and deflections.

Much work has recently been done in testing and analyzing missile joint configurations to determine their stiffness characteristics in bending and shear. There is still a lack, however, of simple analytical tools to determine these characteristics for joints connecting materials of different thicknesses and elastic properties, taking into account the number

of fasteners, spacing, and preload. In addition, there is a need to predict the torsional stiffness characteristics.

The limitations in unsteady aerodynamic representations for missile bodies will be discussed later as it relates to the analysis of servo-control instabilities and static aeroelastic effects.

Autopilot/Movable Control Surfaces

Movable control surfaces and their actuator/control systems are the major source of aeroservoelastic instabilities encountered in advanced missile design. When a flutter problem is encountered with a control surface, it is almost invariably the result of starting with a flutter prone design (i.e., an adverse mass/stiffness/area distribution) dictated by other design considerations. Control surface design features which often create problems include:

1. Planforms with sweepback to minimize hinge moment variations with Mach number and/or a forward pitch axis for stable hinge moments. The resulting configurations have inherently strong elastic and inertial coupling between bending and torsion modes.
2. Structural compliance and nonlinearities associated with folding-hinge requirements. If the structural nonlinearity has a hardening spring characteristic with increasing amplitude (due to inadequate preload or free-play at mechanical interfaces), this condition may lead to limit cycle flutter and structural fatigue problems, particularly under captive flight conditions. If structural nonlinearities with a softening spring characteristic are present, estimates of control surface frequencies based on low amplitude laboratory

Vol. 3

test behavior may be unrealistically high and result in grossly unconservative flutter speed predictions.

3. Planforms attached to forward mounted wings. Not only are the wing and control surface coupled elastically, inertially, and aerodynamically, but the control surface often has strong bending/torsion coupling due to a forward hinge position. This condition may lead to structural fatigue problems under captive flight conditions, and flutter during free flight conditions.

Actuator/control/system design features which may create instability include:

1. Pitch-free control surface operation (no mechanical constraint) during the initial flight phase to enhance vehicle stability. This requirement may result in bending/pitch mode frequency ratios both above and below 1.0 — a difficult dual flutter stability condition to achieve.
2. Design with large amplitude and other parameter-dependent variations in effective mechanical impedance. This characteristic leads to difficulties in developing an adequate structural dynamic model for control studies.
3. Designs with control system response frequencies extending into the spectrum of structural frequencies. For these designs the stability analyses of the motion must include aeroelastic coupling.
4. Systems with torque-balance control. Such systems may need to provide large viscous damping in the torsion mode to compensate for a possible lack of stiffness available to suppress flutter.

5. Design in which subtle hardware production changes may cause significant variations in control system stiffness and damping.

Control surfaces and autopilots having the above design features tend to have small stability margins. Under these conditions, the limitations in aeroelastic analysis tools are more likely to result in unconservative predictions leading eventually to instability during flight test.

As in the case of lifting surfaces acting alone, the major limitation in control surface dynamic modeling is in simulating the structural compliance and nonlinearities associated with surface attachment, including folding-hinge designs. There are limitations also in dynamic modeling actuator/control systems to properly account for their amplitude and frequency dependent characteristics. The models are often more accurate at low frequencies than at high frequencies. Their nonlinearities may be of sufficient magnitude to cast doubt on the use of linearized models for aeroservoelastic stability studies.

The limitations in the unsteady aerodynamic representations for control surfaces is similar to that stated for fixed lifting surfaces. There are limitations in the aerodynamic representations at reduced-frequencies likely to cause servocontrol instability. Since aft-mounted control surfaces operate in a more turbulent flow region than do fixed lifting surfaces, unsteady aerodynamic representations for control surfaces are less reliable than for fixed lifting surfaces.

The need to investigate autopilot/aeroelastic mode coupling instability has increased in recent years as control reaction times have decreased and system response frequencies have extended into the range of structural frequencies. The investigations seek to determine if the flexible modes and their associated aerodynamic forces can destabilize a system whose low frequency rigid-body representation may be stable.

Vol. 3

When the choice is to use some sort of control system filtering (notch or otherwise), then reasonably accurate estimates of the system modes and frequencies are required. It should be noted here that, although filters can be used to decouple and stabilize a system, they have little if any effect on the structural response. Hence, vibration environments will remain which may cause serious damage to guidance and other components. Here the limitations in modeling the body and the aerodynamic surfaces can have serious consequences.

When autopilot/aeroelastic mode coupling instability is suspected, and structural and/or actuator/control system nonlinearities are known to be, dynamic testing of the complete missile should be conducted over the entire operational load range. In many cases, with presently available test methods, this is difficult to accomplish and better test approaches need to be developed. The proper simulation of aerodynamic forces and moments is particularly difficult.

Tests to evaluate autopilot/aeroelastic mode coupling often show:

- a) A substantial portion of the vibratory input energy is transferred to other than the input plane.
- b) Rather subtle changes in the location of sensing elements such as gyros and accelerometers can produce significant changes in gain.
- c) The autopilot energy and damping is not consistent from unit to unit.

To properly account for such effects in analysis requires an adequately detailed simulation of the control system considering the nonlinear characteristics and the significant feedback paths. The limitations in modeling the actuator/control system and the airframe lead to difficulties correlating with and confirming the interpretation of the test results.

Topics Needing Further Development

The preceding material has indicated the limitations in current aeroelastic analysis capability as it relates to specific hardware items. These limitations will now be brought together and grouped by technical fields.

In structural dynamics the major limitation is in modeling the stiffness and damping of body joints, wing attachments, and control surface hinges. Of these, the development of simple methods to analyze body joints and wing attachments is most needed.

The major limitation in unsteady aerodynamics is in the representation of the aerodynamic loads at the reduced-frequencies likely to cause autopilot/aeroelastic mode coupling. There are also limitations in the aerodynamic representations for the evaluation of static aeroelastic effects. These limitations will now be discussed in more detail.

For missile autopilot/aeroelastic mode coupling studies in which the flexible modes of the missile are an important consideration, it is necessary to know in detail the changes in aerodynamic load over the missile. This is in contrast to missile autopilot stability studies in which the missile is treated as a rigid body in flight, for which it suffices to know the changes in resultant forces and moments, and to represent the aerodynamic loads by stability derivatives.

In expanding the rigid body studies to include the flexible modes of the missile, the concept of aerodynamic derivatives is often taken over and aerodynamic terms are generated for the flexible and rigid body motions of the missile. When this is done, aerodynamic force and moment resultants, rather than distributed aerodynamic loads, are used to compute the generalized forces for the elastic modes.

Two sources of error in the stability results are thus present. First, extending the use of aerodynamic derivatives to unsteady motions is theoretically in error since the derivatives are functions of frequency. Second, the generalized forces for the missile modes are not based on the distributed aerodynamic loads. The more accurate approach is to use unsteady aerodynamic forces and to investigate autopilot/aeroelastic mode coupling by considering the frequency dependent generalized forces. Unfortunately, however, accurate unsteady aerodynamic forces for a complete missile are not readily obtained from existing computer programs for transonic and supersonic cases.

One finds, for example, that theoretical estimates of the resultant aerodynamic forces and moments for rigid control surface modes are, for low reduced frequencies, less accurate than those predicted by aerodynamic derivatives. This indicates the need for refining the unsteady force predictions, possibly through the use of empirical factors, to match the aerodynamic derivative results which have a greater measure of experimental verification.

Improved aerodynamic representations are also needed for evaluating static aeroelastic effects. This class of aeroelastic problems involves only the interaction of aerodynamic forces and structural deformation without significant contribution from inertial forces.

For certain types of tactical missile airframes -- generally of high fineness ratio, comparatively flexible, and which operate at high dynamic pressure -- static aeroelastic effects may have a first order influence on vehicle flight stability and control. The aeroelastic effects may reflect a change in stability derivatives which in a practical sense is a more important consideration than divergence since the missile may become unstable and essentially uncontrollable.

Total lift and moment contributions of various tactical missile components are generally well known. However, reliable pressure distribution data, chordwise and spanwise, and body carryover lift, are often a great deal more uncertain with configurations in which body lift plays a significant role and the lifting surfaces are of very low aspect ratio. Uncertainties in estimating static aeroelastic effects, consequently, may be directly traceable to uncertainties in three dimensional airload distribution.

As regards wind tunnel testing for missile static aeroelastic behavior, this is frequently difficult "full scale" because of limited dynamic pressure capabilities. In this case, modal deflection characteristics must be exaggerated considerably to achieve the same effect at low dynamic pressures. Improvements are needed in wind tunnel test methods to establish three-dimensional airload distributions for tactical missile components.

The major limitation in thermoelasticity is simulating by test the transient heating of aerodynamic surfaces as occurs during free-flight. Good experimental methods are needed to measure the transient mode shapes, frequencies, and damping.

In servoelasticity, limitations exist in modeling the amplitude and frequency-dependent characteristics of actuator/control systems. Improvements are needed in simulating aerodynamic forces and moments during autopilot/aeroelastic mode coupling tests.

Specific Recommendations

The purpose of reviewing the limitations in current aeroelastic analysis tools was to focus on the technical areas in need of further development so that recommendations could be made concerning the promotion and direction of research in this field. Before making these recommendations, however,

Vol. 3

it should be noted that even with the limitations stated, there are steps the aeroelastician can take at this time to minimize aeroelastic problems and these steps are quite straight-forward. For example:

- a) The aeroelastician should identify aeroservoelastic and flutter-prone design features early, and help identify design alternatives.
- b) An adequately detailed simulation of the aeroelastic system should be constructed considering all potentially significant coupling mechanisms, nonlinear characteristics, and operations conditions.
- c) Early dynamic tests should be conducted on hardware, and later dynamic tests (including wind tunnel or sled tests) should be made as needed to correlate with and correct the analytical simulation. Tests should be performed over the operational load range.
- d) Using the updated analytical simulation, upper and lower bounds of the parameters should be established and used in the analysis along with their probability of occurrence. Statistical modeling should be used in evaluating the aeroelastic stability of the system

The effort spent following these steps needs, of course, to be related to the particular design under consideration and the seriousness of the adverse flutter predictions.

The following items are specifically recommended for emphasis based on current needs as described in the preceding discussion.

1. The continuation of the development of simple methods to analyze the stiffness characteristics of missile joints and attachment of aerodynamic surfaces.
2. The development of improved analytical and wind-tunnel techniques for establishing quasi-steady and low reduced-frequency airload distributions on missiles.

3. The development of test methods for autopilot/aeroelastic mode coupling tests to achieve response levels comparable to flight conditions.
4. The continuation of the development of analytical methods to perform aeroelastic analyses taking into account autopilot/aeroelastic mode coupling.

WHERE ARE WE IN STRUCTURAL ANALYSIS

The field of structural analysis is very broad. It includes everything from simple static problems to shock response of complex structures, from linear elasticity to complicated nonlinear effects. Even restricting the field to the area of aeroballistics removes very little. Reference (1) is a recent source for the state of the art of structural analysis methods and contains 1105 pages. Obviously, time and resources does not permit a complete survey of the field in this paper. Instead, the field has been broken down into a number of smaller areas. Each of these is commented on according to experience and needs of analysts as well as reference material. Recommendations are then given indicating the areas where more research work is needed, particularly for aeroballistics structures.

Classification of Structural Analysis Problems

In order to properly assess the state of the art to structural analysis, Table 1 has been prepared. The breakdown in this table is not unique, and there may be some areas which are omitted and some areas of overlap between categories. The table does illustrate the broad nature of the field of structural analysis and serves as a basis for discussion.

TABLE 1

CLASSIFICATION OF STRUCTURAL ANALYSIS PROBLEMS

TYPE OF STRUCTURE (GEOMETRY)

- Lumped parameter
- Frames and trusses
- Plane (Two dimensional)
 - Plane stress
 - Plane strain
- Axisymmetric solids
 - Symmetrical loading
 - Nonsymmetrical loading
- Shells
 - Shell of revolution
 - Symmetrical loading
 - Nonsymmetrical loading
- Arbitrary shells
 - Thick
 - Thin
 - Stiffened
- Solid bodies (Three dimensional)
- General (Combinations of the above)

STATIC OR DYNAMIC

- Static
 - Equilibrium
 - Buckling
- Dynamic
 - Transient
 - Vibrations (Normal modes)
 - Wave propagation
 - Shock response
 - Aeroelasticity
 - Random vibrations

MATERIAL PROPERTIES

- Elastic
 - Isotropic
 - Anisotropic
- Plastic
- Creep
- Viscoelastic
- Temperature dependent
- Composite materials
- Fracture

LINEARITY

- Linear
- Nonlinear
 - Geometrical (Large deflection, small strains)
 - Large strain
 - Material nonlinearities

The different areas are discussed individually in the following. Some which are of little interest in the field of aerballistics are omitted. There is, of course, a difference between the state-of-the-art in general and the capability in a certain area at a given installation. Even though an analyst is familiar with the state-of-the-art, he may not have a computer program on hand which contains the latest methods. For example, the widely used program NASTRAN is behind the state-of-the-art in many areas but it is still the best tool available to many people. The development of the finite-element method is probably the most important advance in structural mechanics in recent years.

Plane Structures

Many structural problems can be approximated by plane-stress or plane-strain conditions. The solution of plane-stress or -strain problems by the finite element method is routine for linear elasticity. Methods are also available for material nonlinearity, such as plasticity, but are not widely used and require more research. Probably the best method for plane problems is to use isoparametric elements with consistent stresses.

Axisymmetric Bodies

Many finite element programs which can solve plane problems can also solve axisymmetric bodies under symmetric loading, hence the preceding paragraph on plane problems also applies in this instance. In the case of nonsymmetrical loading the analyst can either expand the load into a Fourier series or treat the problem as a solid body. For the type of loads which can be expanded into a Fourier series of a few terms, this procedure works quite well. Treating the solid or revolution as a general solid is, of course, much more expensive.

Shells

Shell structures are widely used, resulting in much interest in their analysis. The topic of shell analysis is in itself a very broad subject. Reference (2) is a survey of shell structure computer programs. Much research has been done in the analysis of shell problems with both finite-difference and finite-element methods being used for their solution. In particular, many different shell finite-elements have been developed.

An important subclass of shell structures, into which many shell structures fall, is shells of revolution. Three methods have been used successfully in the analysis of shells of revolution:

1. Finite-differences
2. Finite-elements
3. Forward integration

Each method has its pros and cons, but the method of forward integration is probably the best. Linear and nonlinear as well as static and dynamic analyses are possible with all methods. More work is needed in the nonlinear solutions in order to improve the efficiency and accuracy of the solution.

Arbitrary shell configurations have been solved by three methods:

1. Finite-differences
2. Finite-elements
3. Integral equations

Of these, the finite-element method is the most attractive since it is easiest to model an arbitrary geometry by this method. The earliest shell elements were simply flat triangular and quadrilateral elements, but they were found to have mathematical convergence difficulties. This led to the development of curved elements, but it is not an easy task to develop curved

shell elements which satisfy the conditions of convergence. Many curved shell elements have been developed, but the ideal element has not been invented yet (and may never be). One class of shell structure which appears in aero-structures is interesting shells. At present there is no advanced shell element which is useful for this type structure.

There is also renewed interest in the use of the method of finite-differences to solve arbitrary shells. New approaches are being taken that show some promise. Some of these actually combine the methods of finite-elements and finite-differences.

Solid Bodies

Before the development of the isoparametric elements, analysis of three-dimensional bodies often required many extra nodes not needed for accuracy just to model the shape of the body. This led to long computer running times. The curved isoparametric element has made the modeling of complex shapes much easier and more economical (at the expense of more computation effort) in the calculation of the element stiffness matrix. In solid bodies the number of unknowns as well as the amount of input data becomes quite large. Thus the limiting factor appears to be computing time, although efforts are being made to improve the efficiency of three-dimensional calculations. Some sort of graphic preprocessor or data generator becomes a necessity for three-dimensional analysis in order to generate and check the data, since errors in input can be difficult to detect and can be costly if not found.

Static Problems

Linear static problems are, of course, the simplest. Once this case is solved, the extension to nonlinear effects can be carried out according

10th Navy Symposium on Aerballistics

Vol: 3

to appropriate theory. The areas of plasticity and geometrical nonlinearities are, of course, complex and undergoing constant research.

Dynamic Problems

There are a variety of methods available for dynamic work. The choice depends on the characteristics of the problem. One area in which further work is needed is the area of high frequency (above 1 KHz).

Material Properties

Once beyond the limits of linear elasticity, the field of structural analysis seems almost boundless. There are many possibilities -- plasticity, creep, viscoelasticity, etc., to name but a few. There are many methods of representing plastic deformation of materials; some are simple mathematically and some are complex. The analyst must choose a method which represents most clearly the actual material behavior. The problem here is that seldom is there sufficient material data to make an intelligent choice. However, numerical methods have permitted significant advances to be made in the analysis of nonlinear structures.

Linearity

There has been much work done in the past few years on geometrical nonlinearities. Usually, different methods do not get the same result for the same problem since each may be based on different assumptions. There is a great amount of capability in current computer programs, but no best method for all types of problems has developed. Since nonlinear problems sometimes take a long time to run, more efficient numerical methods are needed in order to reduce computing costs.

Conclusions

It has been impossible to cover every facet of structural analysis in

this survey. An attempt has been made to cover each main area, and those which most need further work have been pointed out. The field of linear elastic analysis is the most highly developed, although some of its areas (such as shells) need further research. The field of dynamics is well covered although further research is needed, particularly with regard to high frequency response. The area of plasticity, creep, etc., is very active, and much work remains to be done. This also applies to the field of geometrical nonlinearity.

It can be concluded after reading Reference 1 that much capability exists in the area of structural analysis, and that a broad range of problems can be solved. The large general purpose computer programs are usually not up to date in the state-of-the-art, but can solve a wide variety of problems; whereas smaller special purpose programs sometimes contain very advanced methods. Of course, one of the biggest problems is matching the problem with the capability to solve it. Even if the capability to solve a problem exists, it may be unknown or inaccessible to those responsible for solving it.

Recommendations

Although there are some areas in structural analysis in which the analyst may easily solve nearly any problem, there are no areas in which no future research is needed. In the field of aeroballistics, the following have been identified as needing further work:

1. Better dynamic analysis methods for predicting response in the 1 KHz to 10 KHz range. Present methods are good only up to about 1 KHz.

Vol. 3

2. Better characterization of nonlinear material properties.

As stated in Reference 3:

"To a large extent, the technology of the numerical methods has exceeded the ability to characterize materials. In addition, the material models in many cases do not capture the basic behavior of the material"

Reference 4 plays the same tune:

"The level of structural analysis capability that has been achieved has outstripped our ability to describe accurately complex material behavior such as cyclic, time, and temperature dependent plasticity".

Also the NAAC Aeroelasticity and Structures Panel in the years 1971 and 1972 noted the lack of material design data at high temperatures for short durations. Reference 5 also points this fact out:

"The field of creep analysis is dominated by high temperature analysis of components for nuclear steam supply systems".

Thus we see the need for materials research to support the structural analysis capability that already exists. In particular, work is needed in high temperatures for short time durations such as exist in high performance missile trajectories.

3. Further research work is needed in analysis of complex shell structures such as appear in missile structures. In particular there is a need for a doubly curved shell element for arbitrary geometry which satisfies necessary consistency conditions and yet is not so complex as to be uneconomical for all but very simple problems (Reference 2).

References

1. Pilkey, W., et al., "Structural Mechanics Computer Programs", University Press of Virginia, Charlottesville, Virginia, 1974
2. Hartung, R. F., "An Assessment of Current Capability for Computer Analysis of Shell Structures", AFFDL-TR-71-54, 1971
3. Von Riesenmann, W. A., et al., "Nonlinear Continua" in "Structural Mechanics Computer Programs", University Press of Virginia, Charlottesville, Virginia, 1974
4. Arman, H. A., Jr., "Plastic Analysis" in "Structural Mechanics Computer Programs", University Press of Virginia, Charlottesville, Virginia, 1974
5. Nickell, R. E., "Thermal Stress and Creep" in "Structural Mechanics Computer Programs", University Press of Virginia, Charlottesville, Virginia, 1974

THE JOHNS HOPKINS UNIVERSITY
APPLIED PHYSICS LABORATORY
SILVER SPRING MARYLAND

Survey of Structural Materials Technology
for Navy Tactical Missiles*

W. C. Caywood and J. S. O'Connor
Johns Hopkins University
Applied Physics Laboratory

ABSTRACT

An industry survey has been conducted to assess the status of advanced technology in the field of materials and fabrication techniques for use in Navy tactical missiles ranging in speed from subsonic to hypersonic. The survey addresses a broad spectrum of structural materials with special emphasis on the advanced composite materials presently under development. In this paper the findings of the survey are reported and projections are made regarding the application of new technology to the structures of the Navy's advanced tactical missiles. The results of the survey indicate that present emphasis is on cost reduction with secondary consideration given to weight reduction and resulting performance gains. However, examples are cited where even the most expensive materials are cost effective because of their increased performance.

INTRODUCTION

During 1974 a series of studies were conducted at the Johns Hopkins University, Applied Physics Laboratory with the objective of learning how to increase the defensive and offensive capability of the Navy's surface fleet during the 1980's. This program of study was called Project 80. As part of this study, an industry survey was conducted to assess the current status and the projections for advanced technology in the field of materials and fabrication techniques for Navy surface-launched tactical

* This information was derived from a Project 80 survey supported by the NAVSEASYSKOM under Contract N00017-72C-4401.

Vol. 3

missiles. For this technical review, visits were made to eight aerospace companies, one rocket motor company, three research facilities, and four technical conferences as noted in Table 1.

The significant findings of the survey are covered in this paper. Although the survey specifically addressed surface-launched missile technology, the findings should have application to air and sub-surface launched missiles. The survey clearly revealed that cost is of major concern, that composite materials offer the most promise of significant breakthroughs in missile structural design, and that little or no work is going on that has application to the critical structural problems associated with hypersonic airbreathing tactical missiles.

REVIEW OF STRUCTURAL REQUIREMENTS

The Navy's tactical missiles that are currently operational or in engineering development are listed in Fig. 1. There are two airbreather missiles in this group: the subsonic Harpoon which is powered by a turbojet engine, and the Mach 2.0 - 2.5 Talos which is powered by a subsonic burning ramjet. The remaining missiles are rocket propelled and have average speeds no greater than about Mach 2.5, but may reach peak speeds as high as Mach 3.8. The flight environments for these missiles are relatively mild and structural integrity problems are usually isolated to a few specific areas. The significant design challenges are associated with weight and cost reduction.

Improvements in performance and firepower will be required in future Navy tactical missiles if they are to be capable of intercepting the threats postulated for the 1980's. Cruise speeds as high as Mach 6.0 at sea level and Mach 8.0 at altitudes of 80,000 to 100,000 feet can be expected of supersonic combustion ramjet (SCRAM) missiles. A major problem area will be combustor design, where peak temperatures of 6000°F

Table 1
Sources of Information on Advanced Structural Materials

Source	Location
Areospace Companies:	
Boeing Aerospace Co.	Seattle, Washington
General Dynamics	Ft. Worth, Texas
General Dynamics	San Diego, California
Hughes Aircraft Co.	Los Angeles, California
LTV Aerospace	Ft. Worth, Texas
Martin-Marietta	Orlando, Florida
Mc Donnell Douglas Astronautics Co.	St. Louis, Missouri
Northrop Aircraft	Los Angeles, California
Rocket Motor Companies:	
Hercules Inc.	Ridgeley, West Virginia
Research Laboratories:	
Battelle Memorial Institute	Columbus, Ohio
U.S. Air Force Flight Dynamics Laboratory	Wright-Patterson Air Force Base, Ohio
U.S. Air Force Materials Laboratory	Wright-Patterson Air Force Base, Ohio
Technical Conferences:	
DOD Structures Technology Conference	Columbus, Ohio (April 2-4, 1974)
ASTM Composite Reliability Conference	Las Vegas, Nevada (April 15-16, 1974)
AIAA Structures, Structural Dynamics and Materials Conference	Las Vegas, Nevada (April 17-19, 1974)
SAMPE Meeting	Los Angeles, California (April 22-25, 1974)

Missile Category	Missile Name	
Surface-to-Surface	Harpoon Standard Active	Standard Arm
Surface-to-Air	Standard Missile MR Standard Missile ER Terrier	Tartar Talos Sea Sparrow
Air-to-Surface	Bullpup Condor Walleye Harpoon	Standard Arm Shrike Harm
Air-to-Air	Phoenix Sparrow	Sidewinder Agile
Surface-to-Subsurface	Asroc	

Fig. 1 Current Navy Surface and Air Launched Tactical Missiles

and peak pressures of 2000 psi exist in an oxidizing, high-shear-flow atmosphere. Another major problem area will be the leading edges of air inlets and aerodynamic surfaces where sharp, distortion-free structures at temperatures to 4000°F are required. Sensor window materials will need to be developed to withstand the hypersonic thermal and rain erosion environment without structural failure or excessive electrical losses.

Maneuverability will influence the capability to intercept targets, and intercept maneuvers as high as 40 g's are not an unreasonable expectation. All-weather capability and multi-mode guidance requirements will also dictate structural requirements.

Improvements in structural design efficiency will also be required. Since many of the advanced system concepts will require tube or box launchers for high firepower, volumetrically efficient means of folding the aerodynamic surfaces will be required. The missile design must also consider the missile's vulnerability to hostile environments, such as radar detection and nuclear and laser effects. Steps must be taken to reduce the radar signature and the vulnerability to nuclear and laser environments. For improved performance or size reduction, lightweight construction is a necessity.

STATUS OF ADVANCED METALLIC MATERIALS

Relatively few significant developments in metals have been made during the past 10 or 15 years for tactical missile structures. The development of aluminum and magnesium alloys have been static and little change is expected in the future. Some improvements have been made in the use of steels, particularly maraging steels and these could result in improved motor cases.

Vol. 3

The use of titanium in aircraft structures is increasing primarily because a number of fabrication problems have been solved. Several new alloys such as Ti-11 (Ti-6Al-2Sn-1.5Zr-1.0Mo-0.35Bi-0.1Si) and Ti-6Al-2Sn-4Zr-2Mo have improved temperature capabilities and show promise of use to 1300 to 1400°F.

The new developments in superalloys and refractory metals for tactical missile airframes have been few. Candidate alloys are still the nickel base Inconels, nickel base Rene 41, and cobalt base L-605. These alloys should be suitable for temperatures up to 1600 to 2000°F. A group of dispersion - strengthened alloys were developed that showed promise for use at temperatures up to 2400°F but these alloys are not commercially available. The most promising refractory metals remain the columbium and tantalum alloys for use in the 3000 to 4000°F temperature range. The need for protective coatings, high cost, and poor strength to weight ratio continue to be pacing items limiting the use of refractory metals. Molybdenum alloys appear to be receiving little consideration, mainly due to the lack of a satisfactory coating. Fabricating costs for refractory alloys are about 1½ those of superalloys, and raw material costs are about 1/3 of the total hardware cost.

Although emphasis is on cost reduction, the lowest cost material may not be the most cost effective when the overall system requirements are considered. An example is in the design of the Advanced Terminal Interceptor (ATI), a high performance successor to SPRINT. The ATI has projected loads of 400g longitudinal and 600g lateral. With this maneuver requirement, a high stiffness to density material is required. Parametric tradeoff studies have indicated that beryllium is the most cost effective material followed by high modulus graphite. The weight and dollar savings result from decreased booster requirements.

STATUS OF ADVANCED COMPOSITE MATERIALS

The single most significant development in structures technology within the past ten years is the progress made in the field of advanced composite materials. Structural composites consist of high-strength fibers held together by a matrix material. The fibers may be continuous and selectively oriented as to direction, chopped and randomly oriented, or fabricated into a cloth material by weaving or braiding. The fibers carry the major loads through the material while the matrix carries the shear forces and loads the fibers. The matrix material usually has the lower temperature limit and therefore sets the temperature limit for the composite.

Composite materials are usually described by giving the fiber material first, followed by the matrix material. Figure 2 indicates the status of the various composites which are discussed below. Both cost and weight savings are projected through their use. Some improvements have been largely due to fabrication techniques rather than material properties. Many of the developments have been for aircraft, strategic missile, and space shuttle applications and there has been limited application of composite materials to tactical missile design.

Glass/Epoxy and Glass/Phenolic

Glass cloth and chopped glass fiber composites have been in existence for many years but have seen limited application to missile and aircraft structures. Missile applications have generally been limited to radomes for low-speed missiles and ablative-type thermal insulation for higher-speed missiles. An exception to this is the molded glass-reinforced phenolic tails of the SRAM missile. Also, molded chopped-glass has been considered for the Maverick missile airframe and for Harpoon aerodynamic surfaces.

Maverick is a 12-inch diameter air-to-ground missile with a speed of Mach 1.2. The existing structure is aluminum. However, in the late 1960's

Material	Max. Operating Temp. (°F)	Operational	Engineering Development	Advanced Development	Exploratory Development
Glass/Epoxy	350-400	X			
Boron/Epoxy	350-400	X		X	
Boron/Aluminum	800-1000			X	
Boron/Titanium	1400				
Boron/Polyimide	600-2000		X		
Kevlar 49/Epoxy	350-400		X		
Graphite/Epoxy	350-400				X
Graphite/Aluminum	800-1000			X	
Graphite/Polyimide	600-2000			X	
Carbon/Carbon	> 5000			X	

The Column Headings, as Applied to Either Missile or Aircraft Structures, can be Defined as Follows:

- Operational — Production Hardware
- Engineering Development — In Service Testing
- Advanced Development — Component Hardware Testing
- Exploratory Development — Small Specimen Testing

Fig. 2 Status of Composite Materials for Application to Tactical Missile Primary Structures

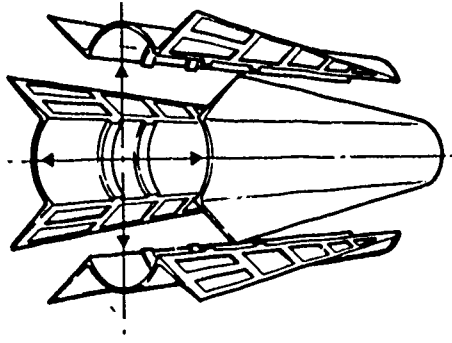
eight molded chopped-glass/epoxy airframes were built and tested and it was found that the composite design was both lighter and cheaper than the aluminum structure. Each airframe consisted of four identical parts which were bonded together as shown in Fig. 3. The final assembly contains rings and longitudinal stiffeners which were molded along with the skin. The assembly can be drilled and attached to the remaining structure by conventional methods. A 33% weight saving and a 35% cost saving (4000 units) were indicated. The molded design was not committed to production, however, since there was insufficient information on variations in material allowances and insufficient experience to anticipate production problems.

The newest of the surface-launched tactical missiles is the subsonic, turbojet-powered Harpoon. Solid aluminum castings are used for the control fins and an aluminum honeycomb assembly is used for the wing. Molded chopped glass/epoxy composites show promise of weight and cost savings for both of these aerodynamic surfaces, but this material is not presently the baseline configuration (Figure 4).

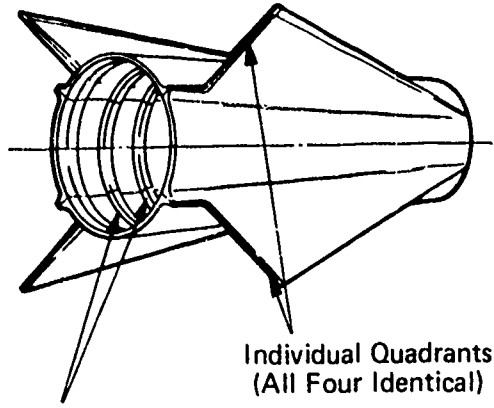
Glass/epoxy composites are also used extensively in RPV structures where radar transparency and low signature are required. In most cases the matrix binder has been a phenolic or epoxy resin. Molded chopped-glass/epoxy shows excellent potential for reducing cost. The resulting properties are similar to aluminum and magnesium castings.

One development that has seen widespread application in strategic missiles is filament winding of E-glass and S-glass/epoxy rocket motor cases. Most of the large strategic-missile motor cases have been fabricated by this technique and both weight and cost savings have been reported. Current cost of the material is \$8 per pound. One current tactical missile application is the Army's SPRINT. Both rocket motors of the Sprint Missile

Exploded View of Quadrant Concept



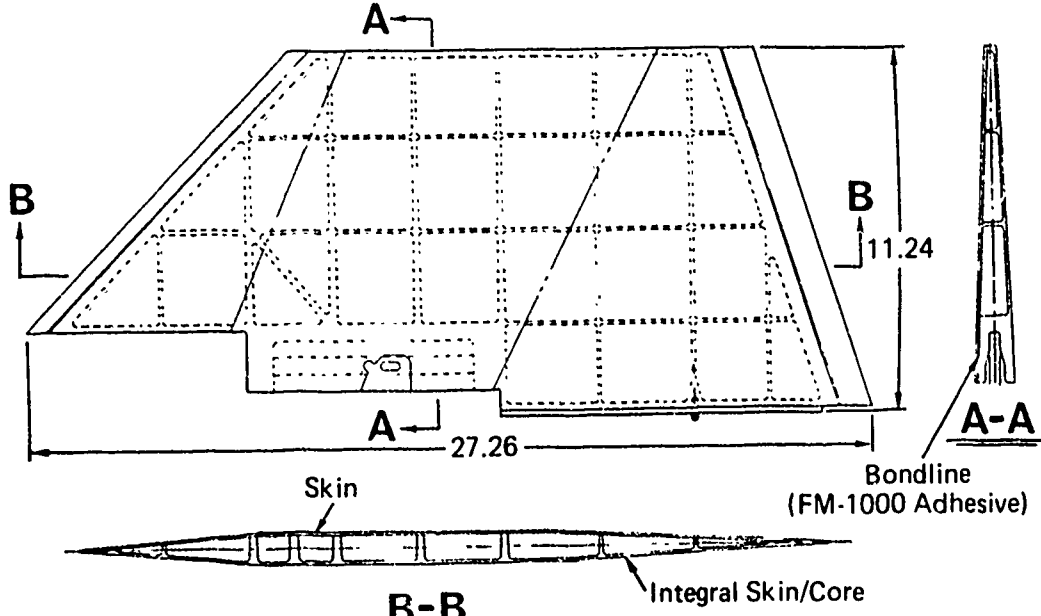
Bonded Quadrant Assembly



Molded-In Ribs, Bosses, etc.
Self-Indexing

Individual Quadrants
(All Four Identical)

(U) Fig. 3 Molded Chopped-Glass Maverick Airframe



Material: US Polymeric EM-7302 (1/2 Chopped Fiberglass Epoxy)

(U) Fig. 4 Molded Harpoon Wing Concept

are wound S-glass/epoxy; however, to date there has been little application of filament winding to Navy tactical missile motor cases.

Boron/Epoxy

One of the first "advanced" composites is Boron/Epoxy (B/Ep). The B/Ep composite has been extensively investigated by the military services and industry and a number of B/Ep structural components have been tested on aircraft including the F-14 and F-15. B/Ep has demonstrated lower cost as well as lower weight over the alternate metal structure. In these aircraft B/Ep cannot compete with the cost of aluminum, but was 4% less than the cost of titanium components. One reason is the amount of scrappage with each material. In the case of titanium, five pounds of material results in one pound of structure; for B/Ep the ratio is 1.2 to 1. Although the costs of boron filaments and B/Ep prepreg have decreased from \$350 per pound to \$175 per pound, there is little prospect of further cost reductions, and it is more likely costs may increase.

Boron/Aluminum

Boron/Aluminum (B/Al) composites are also being investigated, primarily for applications at temperatures to 800°F where weight savings are of prime importance. B/Al structures are being considered for the space shuttle where the present value of space shuttle weight is approximately \$30K per pound. Spars and panels have been built and tested at room temperature and 600°F. B/Al structures are likely to cost about twice as much as conventional metal structures, but weight savings of about 22% are possible. B/Al is not likely to be cost effective in tactical missile structures.

Boron/Titanium

Boron/Titanium (B/Ti) composites have characteristics similar to B/Al but are capable of withstanding temperatures up to about 1400°F. This material

Vol. 3

is not as advanced in development as B/A1. It is also a high-cost composite and is not likely to find application in tactical missile structures.

Boron/Polyimide

The polyimide resins permit the use of boron composite components at temperatures up to about 600°F. Limited test data indicates that they may be used at surface exposure temperatures of 1000°F for 5 minutes or less and exposure temperatures up to 2000°F for 2 minutes or less. In the latter two cases a sacrificial layer at the surface acts as an insulating layer without mechanical strength and the load is carried by the self-insulated low-temperature sublayer. Tests on other high-temperature polymer resins, PPQ (polyphenylquinoxaline), or PIQ (polyimidazoquinazolines) developed by Whittaker will permit structural temperatures up to about 700°F and surface exposure temperatures up to 4000 to 5000°F for a few minutes with no visible change in the surface appearance.

Kevlar 49/Epoxy

Kevlar 49 is an organic synthetic material developed by DuPont and is available in fiber rovings and a wide variety of woven fabrics. This material offers a significant improvement in weight, strength, and stiffness over glass fiber products and is currently being used in large rocket motors. Because of its low density and excellent strength and stiffness, its weight efficiency in these applications is greater than S-glass/Ep on the basis of both strength and strain limit. A number of other Kevlar 49/epoxy applications are being investigated. The C4 Trident motor cases will be filament wound with Kevlar 49/Ep. One tactical application is in the rocket motor case, nozzle, and launch tubes of the Advanced LAW (light Anti-Tank Weapon). Kevlar 49 was chosen because LAW is a man-carried weapon and has a severe weight limitation. The current cost of this

material is about \$20 per pound and its predicted 1980 cost is \$7 per pound.

Graphite/Epoxy

Gr/Ep structures are currently being extensively tested on military and commercial aircraft. One example is the Northrop YF-17 lightweight fighter (Fig. 5). The prototype aircraft contains 900 lbs. of Graphite/Epoxy material which replaces 1200 lbs. of aluminum structure. The graphite is used in 64 different elements including leading edge extensions, trailing edge flaps, speed brake panel, leading edge and rudders from the vertical tails, and various doors and access panels. Northrop plans to use more graphite on a production version of the YF-17. Two prototype YF-17's have been built in the production shop to demonstrate that production workers can work with the composites.

For missile applications, filament wound motor cases have been constructed from Gr/Ep. Currently these are slightly less efficient than S-glass/Ep and Kevlar-49/Ep when strength is the designing criterion but are more efficient when strain or case stiffness is the critical consideration.

In 1969, graphite filaments and Gr/Ep prepreg cost about \$400 per pound whereas prices of \$40 per pound are being quoted today and prices of \$5 per pound are being forecast for the future. At about \$20 per pound, Gr/Ep becomes cost competitive with aluminum.

Graphite/Aluminum

A promising metal matrix composite for use in tactical missile structures is Graphite/Aluminum (Gr/Al). This material is in the early exploratory development phase. It should cost less than B/Al and shows promise of becoming less expensive than Gr/Ep in that the transverse strength of the matrix material will make it unnecessary to use expensive multi-dimensional layups. Joints could be simpler, and existing tooling and fabricating methods for

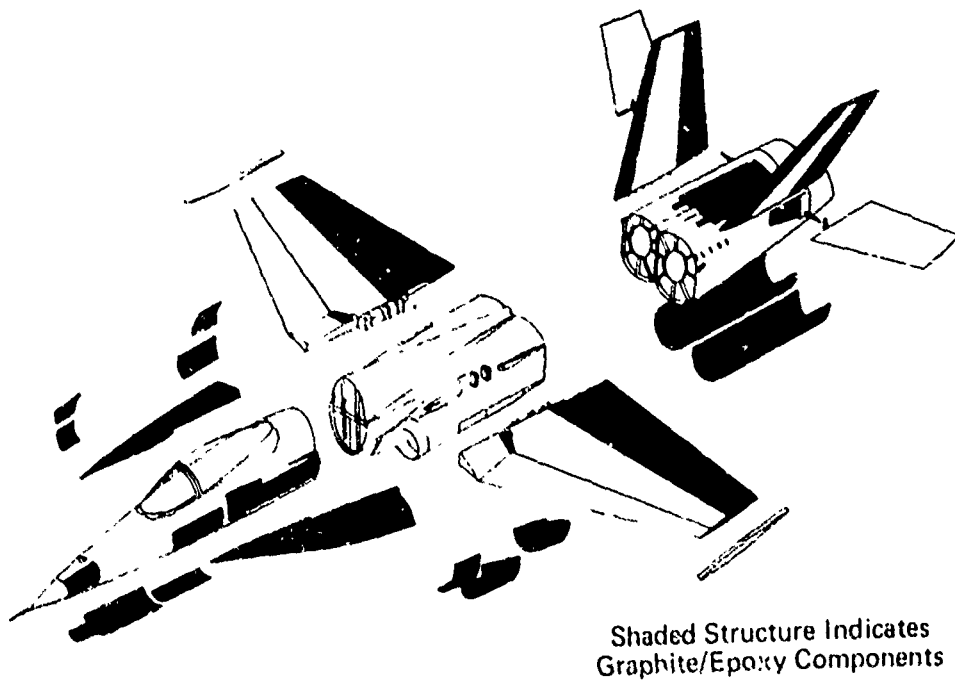


Fig. 5 Exploded View of YF-17 Fighter

metal structures would still be applicable.

Graphite/Polyimide

As with boron filaments, the use of polyimide resins should permit the use of graphite composite components up to about 600°F, and possibly up to 2000°F for exposures of less than 2 minutes. In the latter case, a sacrificial layer at the surface acts as an insulating layer without mechanical strength and the load is carried by self-insulated low-temperature sublayer. Polyimide composites have greater porosity than epoxy composites, are more difficult to process, and are more brittle. Polyimide composites require a 500-600°F autoclave for processing, which is a rare item in the industry.

Carbon/Carbon

Carbon/Carbon composites offer potential for very high temperature applications. Work on this material is in an advanced development state and is directed toward reentry vehicle nosecone and nozzle applications. The material shows very good erosion characteristics. Low erosion rates are significant in maintaining high chamber pressures in solid propellant rocket motors. This material may have application to the inlet leading edges of supersonic combustion ramjet missiles (SCRAM).

Other Composites

Thermoplastic resins as opposed to thermosetting resins are also receiving attention. Typical thermoplastic resin matrices are Polysulfone, Fiberite 1322A, and Fiberite 1334A. Epoxy is the most commonly used thermosetting resin matrix. The thermoplastics show promise of having higher strength and stiffness values at elevated temperature. Also thermoplastic construction eliminates the autoclave operation and may reduce cost considerably. NAVAIR is supporting work on thermoplastic composites.

Another area being investigated is the molding of components from 1/4 inch diameter graphite/nylon pellets. The resulting material has the

10th Navy Symposium on Aeroballistics

Vol. 3

strength, stiffness, and weight characteristics of magnesium. Precision molding of the pellets has been tried with excellent results. The lubricating characteristics of the graphite permit easy removal from the mold.

DEVELOPMENTS IN THERMAL PROTECTION SYSTEMS

Recent developments in low-density external insulation systems for tactical missiles have been few. Candidate materials are still cork and the silicone rubbers. Low-density insulators have been developed for the space shuttle, but these have little application to small tactical missiles. However, improvements have been achieved in the bonding adhesives.

Improvements have been made in the more dense ablative insulation materials such as the graphite and resin composites. Reliability has been increased and costs have been reduced. However, these materials will have limited application to tactical missiles.

For combustor liners of supersonic ramjet missiles, the silicone rubber, DC 93-104, developed by Dow Corning is most attractive. For the combustor liners of hypersonic ramjet missiles, the most promising system to date is a vacuum-codeposited, 30% silicone carbide-pyrolytic graphite coating on a graphite substrate.

Developments in protective coatings for refractory metals for use on hypersonic airbreathing missiles have been relatively few in recent years. One of the most promising systems for sharp leading edge (0.03 inch radii) structures is a hafnia-coated tantalum (T222) alloy. Silicone carbide appears attractive as an oxidation protective coating for the carbon leading edges of the space shuttle; however, this would not be sufficiently scalable for hypersonic missile leading edges.

DEVELOPMENTS IN METHODS OF FABRICATION

Manufacturing costs of a structure are closely related to its parts count, as assembly costs are high for built-up structures. Assembly costs

are being reduced by replacing complex built-up assemblies with castings. The reduced parts count of cocured composite structures is one of the main reasons that predictions are being made that composite structures will be cheaper than conventionally constructed metal structures.

Some interesting developments are taking place in two-dimensional braiding and three-dimensional weaving of composite materials. The braiding technique has application to nose cones, shell structures, ducts, etc., and can also be used to fabricate sheet material. Braided structures are relatively inexpensive and the braiding can accommodate cutouts better than filament windings. Three-dimensional woven composites have increased inter-laminate shear strength, and experimental reentry vehicle nose cones and thrust chambers have been fabricated using 3D woven graphite.

Molding of low-strength composites shows promise of sizable cost reductions. Reductions of about 74% have been reported for chopped glass/epoxy aerodynamic surfaces. The molding of graphite/nylon pellets into intricate shapes has also been investigated and the results are very encouraging.

Hydrostatic extrusion of composite materials is being investigated and looks promising. Gr/Al composites have been extruded into thin-wall rods and other shapes may be hydrostatically extruded. With this process structural stiffeners could be extruded and then bonded in place.

Adhesive bonding of structural parts has been limited, but increased use of structural adhesives is forecast. A technique called Weldbond is also an attractive method of joining. This technique is a combination of spot welding and adhesive bonding and aircraft parts fabricated by this method have shown increased strength over welded or bonded joints, reduced costs, and reduced sealing problems in tankage.

Increased use is being made of computers in design and manufacturing. Also, extensive use is made of tape-controlled machines for contour milling. The use of high-viscosity chemicals coupled with shot peening after chemical milling has resulted in thin-walled high strength castings of low cost. In the Harpoon program, a savings of 10% in weight and a cost savings of \$5 to \$35 per pound of weight saved is predicted for chemical milling of aluminum castings.

Computer-aided design and manufacturing of forging dies has also been developed. This technique should also be applicable to designing casting molds and extrusion dies and would reduce manufacturing costs.

Hot isostatic processing is being used for diffusion bonding, powder metal compaction, and healing defects in metals. The process extends autoclave operations to the 15,000 psi and 3000°F range. The process has been used to produce powdered metal parts of S-100 beryllium, Ti-6Al-4V, and A-286 with properties equal to or greater than those of wrought materials. Material scrapage is greatly reduced since the parts require little or no machining after the forming operation.

A manufacturing technique that looks attractive for motor cases and inlet ducts is the strip laminate process developed by Imperial Metals Industry of England for the Troy motor case for the Rapier missile. In this process, adhesive-coated thin-strip metal is lathe wrapped on a cylindrical mandrel. Curing is accomplished by passing steam through the mandrel. Head cap and nozzle are adhesively bonded to the strip-wound tube. The process, which is being further developed in this country, has demonstrated hoop strengths greater than 300 ksi with low-cost steels, low tooling and manufacturing costs, and excellent dimensional control.

PROJECTION OF THE 1980's

Emphasis will be given to reducing costs with secondary consideration given to weight. However, for high performance missiles, the lowest cost system may be designed using very expensive but very light materials.

The increasing cost of energy will affect the relative costs of materials, favoring those materials which do not require large amounts of energy for production.

Composites will receive wider acceptance in missile structural components. Cost and weight savings will be realized through their use. This is schematically illustrated in Fig. 6 for four components studied by the Navy. Here both cost and weight reductions are indicated. Projections on the relative weights and cost of various structural material systems are shown in Figures 7 and 8. From these data it is apparent that both cost and weight will be widely scattered and savings will be dependent upon structural applications.

Graphite/Epoxy and Graphite/Aluminum will see widespread application in both primary and secondary missile structures for use up to 600 to 800°F (Mach 3 at sea level). Boron composites will see little application because of cost. Molded chopped fiber composites will see increased applications in airframes and aerodynamic surfaces where there is no requirement for long-term high-temperature capability. In structures such as wings and tails, molded composites may be used for short times at temperatures exceeding the accepted allowables, relying on the transient thermal gradient to insure structural integrity.

For applications at temperatures of 800 to 1400°F (\approx M4.0 at sea level), titanium alloys will be used. Experience in fabrication of titanium aircraft parts and the introduction of new alloys have increased the use of titanium and decreased its cost.

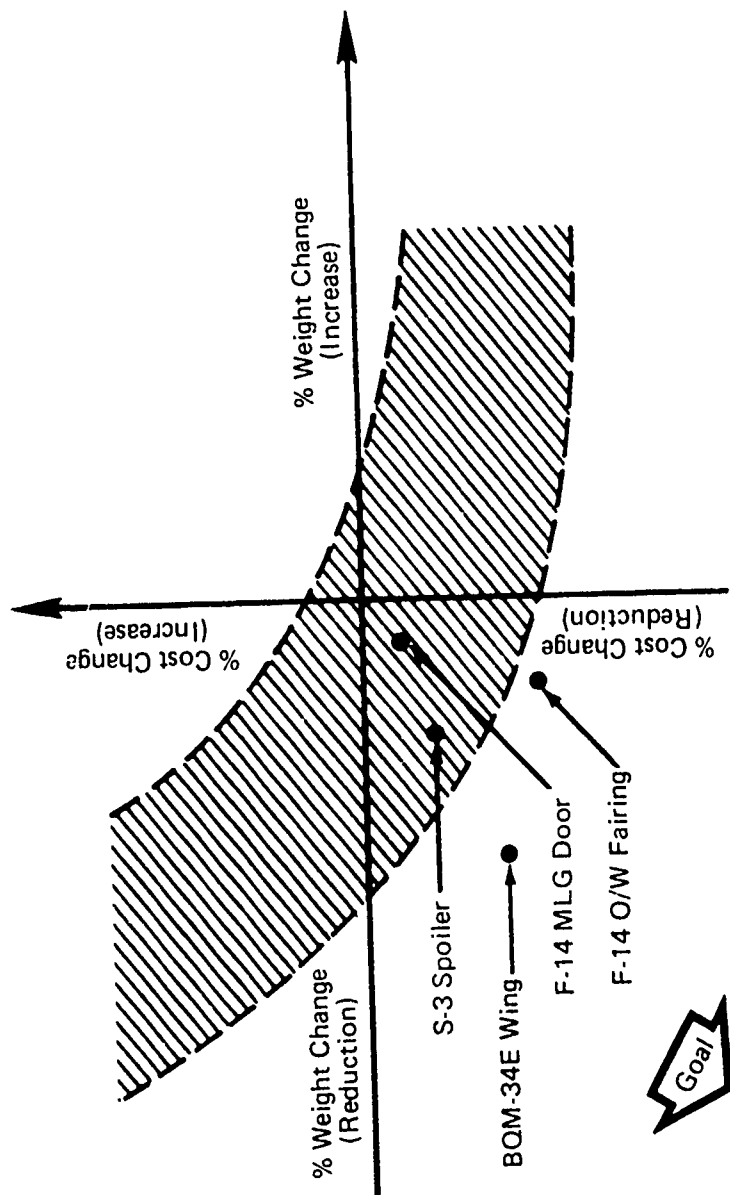
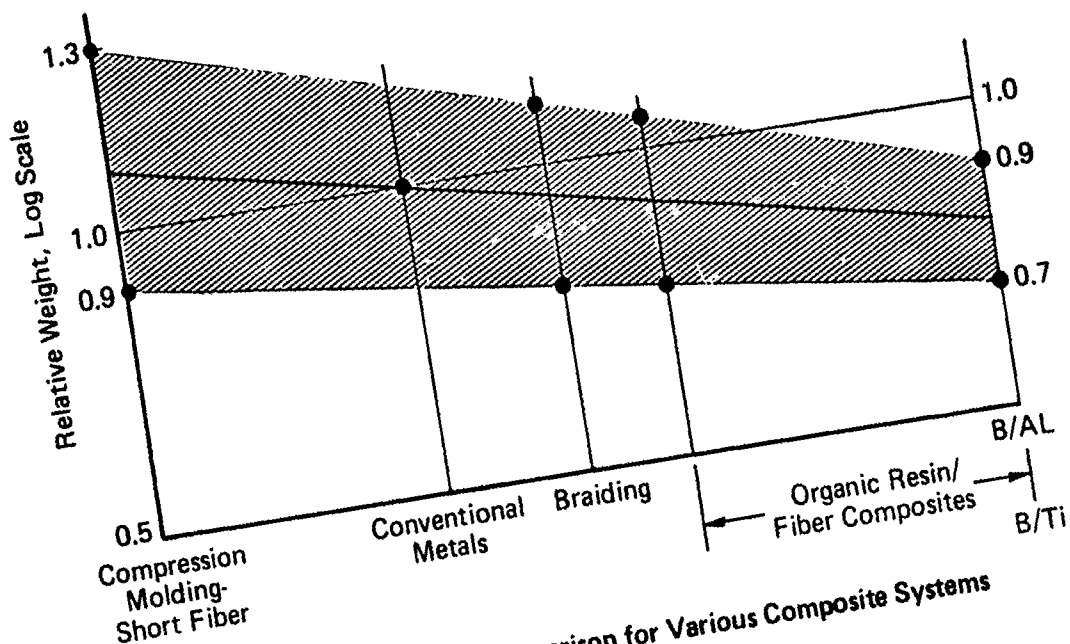
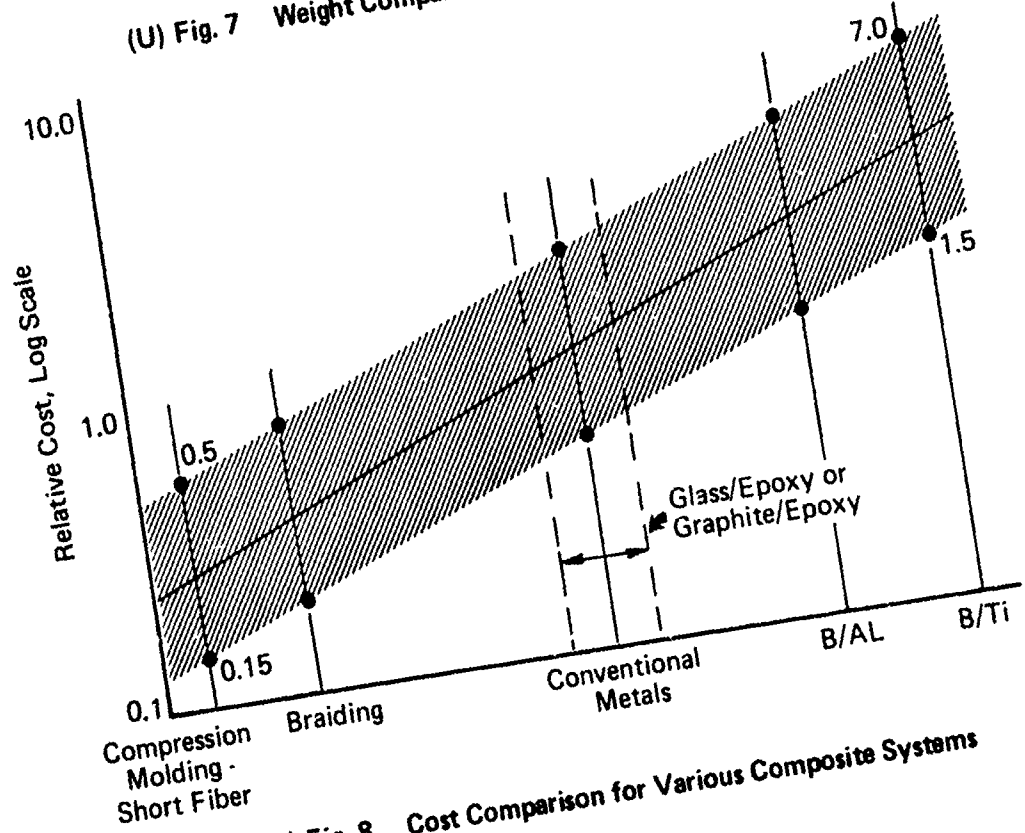


Fig. 6 Cost-Weight Tradeoff



(U) Fig. 7 Weight Comparison for Various Composite Systems



(U) Fig. 8 Cost Comparison for Various Composite Systems

Vol. 3

For missiles operating in the temperature range of 1800 to 2000°F (M4.5 - 4.75 at sea level) nickel and cobalt based alloys will continue to be used.

Refractory metals, carbon composites, and thermal protection systems will be required for the airframes of hypersonic airbreathing missiles. At Mach 6.0 sea level cruise conditions, temperatures will reach about 3500°F. For this environment tantalum and columbium alloys are attractive. Relatively few new developments have been made with these alloys but some new protective coatings have been developed.

The efficiency of metal structures will also improve. New extrusion, bonding and joining techniques will result in reduced cost and weight.

Design for reduced radar signatures and reduced vulnerability to nuclear and laser radiation environments will become increasingly important in future missile design. Materials and techniques capable of attenuating these signatures and withstanding hostile radiation environments will be required.

PAPER NO. 41

NONLINEAR HYPERSONIC AERO-THERMO-ELASTIC
EFFECTS ON MISSILE LIFTING SURFACES

By J. A. Bailie
B. Almroth
F. A. Brogan

NONLINEAR HYPERSONIC AERO-THERMO-ELASTIC EFFECTS
ON MISSILE LIFTING SURFACES*

by

J. A. Baillie⁽¹⁾
B. Almroth⁽²⁾
F. A. Brogan⁽³⁾

ABSTRACT

The problems of static and dynamic aeroelastic stability are considered for the case of tactical missile fins or wings in the range of hypersonic velocity. The reduction of structural stiffness due to thermal stresses and the reduction in material properties at elevated temperature are accounted for in the analysis. Since temperatures vary with time, the aeroelastic problem cannot be formulated in terms of current flight conditions. The classical linearized procedures for divergence or flutter analysis can still be formulated at any given point along the trajectory. These procedures are here evaluated with respect to efficiency and accuracy in comparison to direct integration of the quasistatic or dynamic equilibrium equations. Numerical results are obtained by use of a computer program package (here called STAGS-MOFA). Previously existing individual programs were modified as necessary and combined so that thermal, aerodynamic and elastic analyses can be obtained in the same runstream. Based on the numerical results, a procedure is recommended which is believed to represent the current state of the art.

*Paper Presented at the 10th Navy Symposium on Aeroballistics, Fredericksburg, Virginia, 15-17 July 1975. This paper is based on results obtained in a study made for the Naval Air Development Center, Warminster, Pennsylvania under Contract N62269-73C-0713.

- (1) Staff Engineer, Missile Systems Division, Lockheed Missiles and Space Company, Sunnyvale, California.
- (2) Staff Scientist, Senior, Structural Mechanics Research Laboratory, Lockheed Palo Alto Research Laboratory.
- (3) Research Scientist, Structural Mechanics Research Laboratory, Lockheed Palo Alto Research Laboratory.

INTRODUCTION

One of the features that distinguishes the aeroelastic behavior of lifting surfaces at subsonic and low supersonic speeds is that isothermal, linear theories generally suffice to define both structural and aerodynamic behavior. There are exceptions such as the nonlinear flow behavior at transonic speeds and nonlinearities caused by separated flow at all speeds. In most cases, however, the equations can be linearized making it possible to conduct the different phases of aeroelastic analyses independently. Since in the linearization process the effects of prestress and if small geometric imperfections are ignored, both strength and stiffness are invariant with time. This leads to a rather simple definition of critical loading conditions by means of the dynamic pressure and the velocity normal load factor. Response to gusts and turbulence can be considered separately. Above all, it is the removal of time as a variable in the definition of the aeroelastic environment which results in a greatly simplified analysis.

Once the flight regime is extended to high supersonic speeds, aerodynamic heating must be included and the analysis becomes more complicated. The temperatures vary with time and since thermal stresses change the structural stiffness, the aeroelastic problem cannot be formulated in terms of the current flight condition even if it were possible to assume linearity in structural behavior. The classic aeroelastic triangle of interacting Inertial, Elastic and Aerodynamic forces used by Collar (Ref. 1) becomes the aeroelastic

rectangle shown by Rogers (Ref. 2)

In the mid-fifties numerous studies were initiated on the influence of aerodynamic heating on aeroelastic behavior in the low supersonic speed range. The thermal, aerodynamic, or structural effects of the problem were usually considered separately. Only a few investigations were devoted to their interactions. A wide ranging study on static phenomena at Bell Aircraft took full advantage of the digital computer capability existing at that time (Refs. 3-7). With the aid of an early model digital computer, significant progress was also made at M.I.T. toward the understanding of the nonlinear effects of thermally induced stresses (Refs. 8-10). In addition to these and other similar studies with very limited distribution, numerous closed form solutions have been published. They are all based on simplifying assumptions such as infinite aspect ratio, zero chordwise flexibility, and idealized boundary conditions. Such solutions are satisfactory for demonstration of certain phenomena but their usefulness for analysis of practical flight structures is limited.

During the late fifties and early sixties, the Bell Aerospace Corporation, under Air Force Systems Command sponsorship, produced a series of reports on static aero-thermoelastic phenomena at hypersonic speeds (Refs. 11-13). In Ref. 13, geometrically nonlinear structural behavior and thermal stresses are accounted for. Various inviscid aerodynamic theories are presented in simple form, such as tangent wedge, modified Newtonian, shock expansion and blast wave theories. Simple means to correct for leading edge sweep, nose bluntness and boundary layer effects are provided.

One of the earlier studies of flutter of isothermal chordwise rigid sections in linearized supersonic flow was that by Garrick and Rubinow Ref. 14 who developed the framework upon which many succeeding authors built.

In 1956 (Ref. 15) Piston Theory was shown to reduce the complexity of many aerodynamic calculations associated with aeroelasticity and to make possible the routine inclusion of the effects of airfoil thickness and initial angle of attack. In succeeding parameter studies (Ref's 16 and 17) these effects were shown to reduce the flutter speed for the parameter ranges studied. These studies also demonstrated the marked influence structural parameters had on the flutter characteristics and that there is a danger in drawing conclusions of wide applicability from studies of simple models.

In one of the first studies to include thermal effects on the flutter speed Broadbent (Ref. 18) considered a rectangular wing with a 2% thickness/chord ratio biconvex section. He found that flutter does not occur if the wing is chordwise rigid, but that a finite flutter speed is obtained if the change in chamber induced by thermal effects is included. This verifies results obtained by Mansfield (Ref. 19) regarding the anticlastic bending that affects the streamwise slopes which govern the aerodynamic coupling terms. Using second order Piston Theory Harder et al (Ref. 20) considered a specific unswept, built up wing. They demonstrated various influences of thermal stress, but at that time computer technology had not reached a stage which would allow a generally applicable methodology to be developed. In Section V of Ref. 21 Zartarian and Hsu considered the effect of aerodynamic nonlinearities and

particularly initial angle of attack on the flutter of a typical section and showed it to be destabilizing.

The importance of the nonlinear effects of thermal stress and airfoil thickness were highlighted in Ref. 22 which showed good correlation with wind tunnel tests if the higher order aerodynamic terms were included. Omission of such terms is shown to lead to serious errors at Mach Number in excess of 3. Experiments reported in Ref. 23 showed aerodynamic heating produced a reduction in flutter velocity of as much as one third.

In three NASA reports, Refs. 24, 25 and 26 attention is devoted mainly to aerodynamic aspects of supersonic flutter of room temperature structures. They demonstrate the difficulty in drawing generally valid conclusions about optimum or even "best" methods of flutter analysis. These reports demonstrate that it is not always true that aerodynamic effects of thickness are destabilizing. They also demonstrate the influence of modes beyond the first torsional and bending modes and effects of differences in the treatment of the wing tip regions. Ref. 27 is based upon a study of single planform with 70° leading edge sweep whose thickness and frequency ratios were varied and tested over a Mach Number range from 5 to 8. As the stiffness properties of importance were controlled by springs mounted away from the airstream aerodynamic heating effects were practically precluded. The flutter analysis which utilized a direct analog computer model of a two degree of freedom (pitching and rolling) system indicated superiority of modified shock expansion theory relative to Piston Theory. Since angles of attack up to 25° were considered the "Hypersonic Similarity Parameter" $M\sqrt{c}$ reached values as high as 4.0 while the range of applicability of Piston Theory is restricted to

values of unity or less. Here again initial angle of attack was found to be slightly destabilizing. As is well known the reduced frequencies of flutter at hypersonic speeds are small, usually less than 0.1. Taking advantage of this fact Goetz (ref. 28) demonstrates the use of statically measured aerodynamic parameters in two degrees of freedom flutter analyses of chordwise rigid sections. An informative and useful review of many of the important aspects of the overall problem, which also draws attention to needed improvements is given in Ref. 29.

It is desirable to develop an aeroelastic analysis capability for the hypersonic range that includes all important nonlinear effects. Experience indicates that below hypersonic speeds mechanically induced stress can be neglected in aeroelastic analyses, as the geometric changes are small for flight velocities significantly below those that cause aeroelastic instability. This makes the structural and aeroelastic analyses relatively independent of each other, contrary to what is the case at hypersonic speeds.

Probably the most important of the interactions that can be neglected only at subsonic and low supersonic speeds arises from the nonlinear phenomena coupling structural deformation and aero-thermodynamic behavior. For example, in a symmetric airfoil section the inplane stresses do not produce any out-of-plane distortions, and hence no change in distribution of aerodynamic pressures, until thermal buckling or aeroelastic instability is encountered. In practical applications a number of complications arise. Symmetric profiles with imperfections as well as nonsymmetric, cambered or deliberately warped,

10th Navy Symposium on Aeroballistics

Vol. 3

sections experience thermally induced lateral deformations which cause the lift distribution to vary with time. The fact that any plate-like wing subjected to bending will exhibit chordwise curvature due to the Poisson effect also contributes to thermoelastic coupling, not present in linear theory.

Since in the hypersonic domain larger deformations must be allowed, the nonlinear interdependence between deformation, aerodynamic forces, and temperatures becomes continually stronger as the Mach number is increased. Consequently, it is necessary that a computer code for evaluation of aeroelastic stability integrates the thermal, aerodynamic and structural analyses. Here such a program for the analysis of a lifting surface on a tactical missile is presented. The computer program is built around the STAGS code (Ref. 30), which includes geometrically nonlinear structural effects. A modified STAGS code constitutes the heart of the analysis, with the other computer program attached to it. In the following a description is given of the adaptation of STAGS for aeroelastic analysis. Based on these results, a procedure for aeroelastic analysis of hypersonic tactical missile is formulated, which is believed to be the best possible within the current state of the art. Recommendations are made for further improvement of this analytic capability.

STRUCTURAL ANALYSIS

The thermoelastic analysis in the computer program is carried out by use of a combination of the STAGS program for elastic analysis and the program for determination of the temperature history in the structure. These two codes are briefly described in the following. Numerical results were obtained in order that it be verified that the codes are suitable for the particular purpose of aeroelastic analysis of tactical missiles. Some of these results are also presented in this section.

2.1 The STAGS Code

STAGS is intended for analysis of shell or plate type structures. The structure to be considered may consist of up to 30 different shell branches, each treated by use of finite difference discretization. In addition, the structure may include some finite elements: an elastic bar, a shear panel, a beam, and a nonlinear triangular plate element. The computer code is discussed in more detail in Ref. 30. Only a brief description of the code is presented here.

The analysis in STAGS is based on a finite difference energy method. That is, the total potential energy is expressed in terms of the displacement components at a number of node points and the applied mechanical or thermal loads. This is possible after derivatives occurring in the expression for the strain energy have been substituted by their finite difference equivalents and the energy has been numerically integrated over the entire structure. The total potential energy is minimized with respect to the

Vol. 3

degrees of freedom of the system

$$\partial V / \partial X_i = \partial / \partial X_i (U - \Omega) \quad (1)$$

Here U is the strain energy and Ω the work done by external (or thermal) forces and the X_i represent the displacement unknowns. The minimization leads to a set of equations of the form

$$K(X) = \{F\} \quad (2)$$

where K is a nonlinear algebraic operator (of the third order). The force vector F includes thermal and mechanical loads and also strains caused by inelastic deformation. The equilibrium equations for a system in motion are obtained through the addition of the effects of inertia and damping.

$$[M]\{\ddot{X}\} + [D]\{\dot{X}\} + K(X) = \{F\} \quad (3)$$

Options are given in the program that allow for omission or inclusion of the dynamic terms. The perturbation technique is used to formulate the eigenvalue problems for bifurcation buckling and small amplitude vibrations.

Consequently, the code can be used for:

- o Linear stress analysis
- o Geometrically nonlinear elastic stress analysis
- o Inelastic stress analysis, geometrically linear or nonlinear
- o Bifurcation buckling analysis with linear or geometrically nonlinear prestress (elastic)
- o Small vibration analysis with prestress based on linear or geometrically nonlinear analysis (elastic)

- o Transient response analysis, linear or geometrically non-linear, elastic or inelastic.

Any combination of point forces, line loads and distributed surface tractions can be applied. Loading by specification of displacements or thermal gradients (through the shell wall and over the shell surface) is also permitted. Any configuration of boundary conditions or other displacement constraints can be included in the analysis.

In the nonlinear static and in the transient analysis a restart capability is available. Intermediate data can be saved on tape or file so that the analysis may be continued later. The input data is automatically checked for certain errors or inconsistencies. If so desired, the user can suppress execution of the program and thus obtain a check on the input. The output from such a preliminary run may include a graphic presentation of the shell geometry with a display of the grid lines. The results of a STAGS run can be transferred to tape or disk file that can be used as input for a post-processor. Graphic displays of results are obtained from the post-processor. These include contour- or cross-plots of displacement, stress resultants and stresses. Displacement histories can be plotted in the case of transient or nonlinear static analysis.

Input for the STAGS analysis can be in two different forms, regular data cards and user written subroutines. The latter type of input may sometimes be more demanding of the user. However, it makes possible the definition of input parameters such as loads, temperatures, etc. by

Vol. 3

functional relationships. This tends to increase the generality of the computer code and also, in many cases provides for a more compact input deck with less time required for input preparation. User written sub-routines can be used for

- o Initial imperfections
- o Loads
- o Load factor history (for transient analysis)
- o Shell wall properties and temperatures
- o Reference surface geometry
- o Grid generation
- o Boundary conditions and other constraints
- o Stiffener geometry and temperature
- o External damping

Efficient execution of large problems generally requires an increase in the size of the computer central core memory available to the program. The choice of core size is governed by a user written routine.

The shell configuration is described by use of a reference surface. The shell itself can be offset from this reference surface by a small amount that may vary over the surface. The location of any point on the reference surface can be uniquely defined by use of a set of two independent parameters, X, Y. The geometry of the surface is given after a functional relationship that has been established that defines the coordinates in a Cartesian system x, y, z as functions of the values of these two parameters.

$$x = x(X, Y), \quad y = y(X, Y), \quad z = z(X, Y) \quad (4)$$

The parameters X and Y defining the position of a point on the surface are referred to as surface coordinates. For shell geometries not included as standards in STAGS the user must define the relation given in Eq. 4 in a user written subroutine.

Stiffeners are defined as structural elements that are attached to the shell surface and have such properties that effects of cross section warping or deformation can be neglected. Stiffeners can either be considered as discrete, in which case they are defined one by one, or their contribution to the shell wall stiffness can be "smeared" over the shell surface. Smeared stiffeners are used for convenience (to reduce the number of data cards) or in order to suppress the local deformation between the stiffeners.

Inelastic analysis can only be used with an initially isotropic material. It cannot be used with material properties that vary with the surface coordinates. The yield stress must be independent of temperature. Bifurcation buckling and small vibration analyses may not include plasticity.

2.2 The TRR-1D Program

For computation of temperatures in the shell the code TRR-1D developed by Compton and Schultz in Ref. 31 computes the transient thermal response of a body subject to arbitrary aerodynamic heating. The shell or plate under consideration is divided into a number of layers. The different layers can be of any different materials. Temperature variant thermal properties can be included for all layers. The inside surface of the geometry is assumed to be adiabatic, and the exterior surface is subjected to time-variant aerodynamic heating. Heat conduction into the body is one-dimensional, and radiation from the surface to the surroundings can be taken

Vol. 3

into account. The finite difference equations are derived by conventional energy balance considerations for each node using backward differences. The temperature response is determined by a tri-diagonal matrix solution at each time step.

The calculation of the aerodynamic heat transfer coefficient is performed at each time step based on updated fluid properties.

A summary of the aerothermodynamic techniques used is:

1. Stagnation point - Faye-Riddell method with calorically-imperfect gas properties
2. Flat plate - Blasius method for laminar flow and the Spalding-Chi method for turbulent flow
3. Conical flow - Flat-plate methods modified for conical flow as given by Van Driest in Ref. 32.

Transition from laminar to turbulent flow is assumed to occur instantaneously at a length Reynold's number of 500,000. No effort is made to compute a transition zone or to compute a virtual origin for the turbulent boundary layer. The resulting inaccuracies and the early transitions are on the conservative side.

2.3 Numerical Results

2.3.1 Comparison to Previously Obtained Results

An important function of STAGS in the aeroelastic analysis is to determine modes and frequencies of small vibration. The capability to perform such analyses was recently included and therefore STAGS results were obtained and compared with results from FLUENC, which is a sub-program of the MOFA system of computer programs of Ref. 33. The trend of the

results indicate that with sufficiently small grid size in both programs the nodes and frequencies from the two programs would be identical.

For minimum drag many plate-like wing structures subjected to hypersonic flow are designed so that they are very thin at the leading and trailing edges such as the parabolic and diamond shaped profiles. This results in temperature distributions with markedly higher temperatures at the edges and a minimum at midchord. The thermal expansion results in that case in spanwise compression at the edges and tension in the cooler midsection. Such temperature distributions can have a profound effect on the aeroelastic behavior of the wing. Consequently, the effect has been considered in several papers such as the well known analysis of Ref. 34. In the following we will compare results obtained from STAGS to the closed form solutions of Ref. 34 for constant thickness plates. However, a temperature distribution is used that is typical of a wing with a diamond shaped profile.

With the temperature distribution discussed above, compressive stresses at the edges are increasing with the temperature. At some temperature level thermal buckling will occur. According to Ref. 34 the critical value of the difference between edge and midchord temperature is

$$\Delta T_{\text{crit}} = 18.5 \frac{D}{E \alpha t a^2} \frac{(\xi + 1)(\xi + 3)}{\xi} \quad (5)$$

For quadratic chordwise temperature variation, with a minimum at midchord, $\xi = 2$. In that case, a square aluminum plate with a 20 in. side and 0.5 in. thickness will buckle at $\Delta T_{\text{crit}} = 153^\circ\text{F}$. With a discretized analytical model, as in the STAGS code, the results are accurate only if a sufficiently fine grid spacing is used. Therefore, for comparison with the analytical results, STAGS results were obtained for various grid sizes. With a

relatively coarse grid spacing, 2.0 in., the critical temperature difference is 118°F , far below the analytical results, 153°F . As the grid is refined, values of ΔT_{crit} closer to the value of Ref.34 are obtained. Thus, with a grid spacing of 1.0 in., $\Delta T_{\text{crit}} = 142^{\circ}\text{F}$.

With a sufficiently fine grid the STAGS results should be more accurate than those of Ref.34. The reason for this is that Eq. (5) is based on the assumption that in the buckling mode the chord r is straight. The STAGS results show some chordwise bending in the buckling mode. If essentially the same restriction is introduced in STAGS (by increasing the chordwise bending stiffness by a factor of 10^4) ΔT_{crit} increases to 147°F . Thus, the validity of the STAGS code may be considered verified for this type of application. A model with coarse grid spacing, 2.0 in., is somewhat inaccurate, but still reflects correctly the basic structural behavior. In the interest of computer economy, additional results were obtained with this grid size.

The temperature field under consideration here is symmetric about the midplane of the plate. Consequently for a perfectly flat plate there will be no out-of-plane deformation in the prebuckling stage, $\Delta T < \Delta T_{\text{crit}}$. Above the critical temperature this equilibrium configuration becomes unstable. With the temperature difference increasing above ΔT_{crit} , a new deformation mode gradually develops. This mode is essentially represented by pure twisting of the wing. The wing tip twist increases gradually in the post critical range.

The value of the twist at the wing tip is shown as a function of the temperature in Fig. 1. The temperature difference is normalized with

respect to ΔT_{crit} , so that thermal buckling occurs at $\lambda = 1.0$. The twist parameter ϕ is defined in Ref. 34. The results for the perfectly flat plate, as obtained in Ref. 34 are shown by the curve marked $\phi_i = 0$.

If the plate contains an imperfection in shape that is not orthogonal to the buckling mode, no equilibrium can exist without lateral displacements. By use of a nonlinear analysis it is possible to determine the growth of this lateral displacement with increasing values of λ . An initial imperfection in the form of a uniform twist of the wing was introduced in Ref. 34. The amplitude of the twisting mode was then determined as a function of λ . Results were obtained for different values of the initial twist as shown in Fig. 1.

For two values of the initial twist, $\phi_i = 0.05$ and 0.20 results were obtained by use of STAGS and are also shown in Fig. 1. At any finite value of λ the STAGS results indicate a lower value of the twist. It should be noted that the curves with STAGS results are normalized with respect to a lower value of ΔT_{crit} , 118°F . STAGS results normalized with respect to the critical load of Ref. 34, 153°F , would indicate higher values of the twist in comparison to results from Ref. 34, reflecting the fact that the discrete model is weaker due to the coarse spacing and also due to the inclusion of chordwise bending.

The variation of the torsional stiffness of the lifting surface with temperature and initial twist was also discussed in Ref. 34. STAGS results for the torsional stiffness are compared to those from Ref. 34 in Figure 2. The agreement between results from the two methods provides additional

Vol. 3

verification of the STAGS code. For a perfect plate the torsional stiffness (or the square of the corresponding vibration frequency) decreases linearly with increasing temperature, so that it becomes equal to zero at $\lambda = 1.0$. The imperfect plate retains a finite stiffness. The explanation of the fact that the imperfect shell retains a finite stiffness at $\lambda = 1.0$ is that the edges are stretching as the wing twists. This reduces the temperature induced spanwise compressive stress.

The ratio between the fundamental bending and torsional frequencies is one of the important parameters in flutter analysis. This ratio can readily be obtained from the results of the stiffness calculations with STAGS discussed above. Results are presented in Figure 3. As is to be expected, the frequency ratio changes markedly with the temperature and its behavior is strongly dependent on the initial imperfection amplitude. For a perfectly flat plate the frequency ratio becomes infinite at $\lambda = 1.0$ because the frequency of the torsional mode vanishes.

Lifting Surfaces with Diamond Shaped Profile

It was demonstrated above how the thermal stresses induced by aerodynamic heating dramatically reduce the torsional stiffness of the lifting surface. The example discussed illustrates a basic trend, although it is somewhat less than realistic, since a plate of uniform thickness is used in the elastic analysis with a temperature distribution typical of a surface with a diamond profile.

In other attempts at analysis, such as Refs. 35, 36, 37, 38, 39, 40, the variable thickness was accounted for in the elastic analysis. These

publications consider the effect on the torsional stiffness of spanwise thermal stresses in wings of rectangular planform. The wing, treated as a simple beam, is clamped at the root chord and generally considered to have an infinite aspect ratio. Singer (Ref. 40) is among those who introduces an approximate correction for finite aspect ratio.

Material property degradation with the temperature is another complication that cannot easily be accounted for in the analytic solutions. Only through use of numeric solution procedure is it possible to obtain reasonably accurate results. Still the analytic solutions are useful since they give an indication of what trends to expect in a computer solution of the governing partial differential equations.

With thin leading and trailing edges on the lifting surface it appears necessary also to consider local deformation modes. Mansfield (Ref. 41) presents a closed form solution for the thermal buckling of a lifting surface with a sharp leading edge. The critical load in that case depends only on the temperature gradient at the edge, the thermal expansion coefficient α , and the wedge angle β . With a quadratic chordwise temperature (symmetric) the critical temperature at the sharp edge is

$$\Delta T_{\text{crit}} = \frac{3 \beta^2}{5 \alpha (1+\nu)} \quad (6)$$

This simple closed form solution cannot take into account the effects of property degradation, nose bluntness, finite aspect ratio, or boundary conditions at the root. Neither is it possible to evaluate wing behavior as the critical temperature is exceeded. Nevertheless, the formula should be useful for a first estimate.

The STAGS program with the thermal analyzer of Ref. 31 was used in a study of the behavior of rectangular wings with diamond shaped cross-section under hypersonic flight conditions. The cross-section of the wing is shown in Fig. 4. The edges are somewhat blunted so that the thickness varies from 0.05 in. at the leading and trailing edges to 0.45 in. at midchord. Comparison with the analytical solutions above should be somewhat cleaner if in STAGS (as in the analytical solution) the spatial temperature distribution is held constant in time. The temperature distribution shown in Fig. 4 is typical for results obtained. In a STAGS analysis the four lowest vibration frequencies and corresponding modes were determined for different values of the amplitude of this distribution. The results are shown in Fig. 4 both for a wing clamped along the entire length of the root chord and one in which the displacements are constrained only at the node points 7,8,9 (see Fig. 4).

For the wing with complete root chord constraint the trends of the lowest frequencies agrees with that of the analytic solutions at the lower edge temperatures. The torsional stiffness, represented by the square of the frequency of the second mode, decreases linearly with the temperature. Extrapolation of the results obtained indicate that the stiffness would vanish at a temperature of about 1200°F . Analytic solutions, valid only for longer wings, indicate a critical temperature of only 760°F . The lowest frequency, corresponding to the first bending mode, is less sensitive to the temperature. The elementary beam theory does not predict any influence of thermal stress on the bending stiffness. However, higher order theories, such as those by Mansfield (Ref. 38) or Kochanski and

Argyris (Ref. 37) show the same trend as the STAGS solution.

The frequencies of the wing with only partial root chord constraint shows very little dependence on the temperature. This result certainly is to be expected since the thermal stresses at the leading and trailing edges will be less significant if points on the root chord are free to move in the spanwise direction. Thermal stresses computed for the rectangular wing are shown for three different boundary conditions in Fig. 5. The results in Fig. 4 also indicate the reduction in stiffness that is due to material property degradation. Since the thicker midsection of the wing stays relatively cool, the reduction is moderate.

The frequencies of the third and fourth modes are also shown in Fig. 4 as functions of temperature. These are local deformation modes with considerable chordwise bending. They appear to correspond to the leading edge buckling modes. We expect one of these frequencies to approach zero when the temperature reaches that for leading edge buckling. We notice that the frequencies for the wing with clamped root chord drop sharply, while the frequencies for the wing with partially supported root chord are relatively insensitive to the temperatures.

It is clear that the finite difference grid used is too coarse to give a good estimate of the critical load when the buckling mode is localized. With a 1.0 in. chordwise grid spacing the critical temperature (bifurcation buckling) is found to be 570°F. However, examination of the buckling mode indicates that a much finer grid is needed. A grid with a variable spacing as shown in Fig. 6 was introduced and with this grid the critical leading edge temperature was found to be 370°F. The corresponding buckling mode

Vol. 3

is also shown in Fig. 6. Beyond the 5th row, 0.75 in. from the leading edge, the lateral displacements are very small. According to Eq. (6) with $\beta = 0.08$, and a sharp edge, the critical temperature is 230°F .

The behavior of the plate in the postcritical temperature range was also determined. The nonlinear analysis does not distinguish between stable and unstable equilibrium configurations. Therefore, if buckled configurations are to be computed, it is necessary to introduce a small disturbance as a trigger. In this case a couple of lateral loads of one pound each and with opposite direction were applied at the leading edge near the root chord (rows 3 and 4). It is found that the amplitude of the buckle grows gradually with the temperature, so that the deformation still is very moderate at temperatures well beyond the critical. Modulus degradation with the temperature does not have a detrimental effect. In fact, with property degradation the increase in the buckle amplitude is somewhat retarded. This must be due to the fact that a reduced shear modulus allows the leading edge to expand more freely in comparison to the cooler material in the interior. It is noticed also that the progressing leading edge buckling has little effect on the overall stiffness of the wing.

Rather similar trends are evidenced by the tapered clipped delta wing whose lower frequency behavior as a function of the same chordwise uniform temperature distribution is shown in Figure 7. However we note this wing shows less sensitivity to thermal effects and with the 13 chordwise and 9 spanwise nodes there was no evidence of leading edge

buckling. Obviously the higher temperature results are of academic interest only because of their proximity to the material melting point.

In order to verify that STAGS and TRR1D work properly in combination, other cases were executed in which the spatial temperature distribution was allowed to vary with time as indicated by the results from TRR1D. It was observed that in that case convergence in the solution of the nonlinear equations (in STAGS) was considerably slower. This is tentatively attributed to the fact that the presently used extrapolated initial estimates are not suitable unless the temperatures vary proportionally with the aerodynamic pressure. It should be possible to remedy this situation.

It may be observed also that the temperatures corresponding to leading edge buckling and, to a lesser degree, the degradation of the torsional stiffness are determined in a conservative way by the STAGS-TRR1D combination. The reason for this is that heat transfer in the chordwise direction has been neglected. A two-dimensional thermal analysis would certainly produce more favorable results.

Finally, the results obtained with wings with different support at the root chord indicate that deformation of the missile body may have a substantial effect on the stiffness of a heated wing and consequently on its aeroelastic performance.

AEROELASTIC ANALYSIS

3.1 Approach

Over the past decade many studies have been made of the aeroelastic behavior of a wide range of vehicle configurations operating at hypersonic speed. Some of these are referred to in the Introduction which gives a brief summary of the state of the art in the field. Here an aeroelastic analysis system is presented for lifting surfaces on tactical missiles. Previously existing codes for aerodynamic, thermal, and elastic analysis have been utilized as much as possible, with modifications as necessary. The system of computer codes is intended to provide a method for solving a wide range of hypersonic aeroelastic problems for lifting surfaces in the Mach number range of roughly 3 to 6 and small angles of attack.

The equations governing a vehicle under flight conditions can, after reduction to a finite number of degrees of freedom, be written in the form

$$[M] \{\ddot{u}\} + [D] \{\dot{u}\} + P(\dot{u}) + K(u) + Q(u) = \{F\} \quad (7)$$

Here the vector u represents the "discretized" displacement field, $[M]$ and $[D]$ represent mass and structural damping matrices. The vector $\{F\}$ represents forces on the structure computed without consideration of structural deformation, but including thermal effects. The operations P and Q operate on nonlinear functions of u and \dot{u} , denoted by (u) and (\dot{u}) respectively to determine the components of aerodynamic forces caused by structural deformation. The operator $[K]$ determines the internal forces in terms of the displacement unknowns. In

the linear case it corresponds to the stiffness matrix. The components of F generally vary with time. Under stationary flight conditions, temperatures will still vary until thermal equilibrium is obtained.

A straight forward numerical integration of Eq. (7) over the trajectory, or a pertinent part of it, is in principle feasible. Such a solution would yield the answers to all questions about structural integrity, including possible aeroelastic instability. However, the time period over which the integration must be carried out is large (by orders of magnitude) in comparison to the period of free vibrations of a typical wing. Therefore, the procedure will in general not be economically feasible, and even in the presence of our days' high-speed digital computers, the classical methods of aeroelastic analysis survive as viable options.

The force vector F is generally a function that varies slowly with time, that is in comparison to the displacement velocity corresponding to free structural vibration. Consequently unless a vibration is excited the first three terms in equation (7) can be discarded, leaving us with the equation:

$$K(u) + Q(u) = \{F\} \quad (8)$$

Here K and Q are nonlinear algebraic operators, containing terms of first through third degree in u . The application of these operators to a function results in a vector with the number of elements N equal to that of the load vector $\{F\}$. Consequently we can write

$$K_i(u) + q Q_i(u) = F_i \quad i = 1, N \quad (9)$$

For reasons that will be clear from the subsequent discussion, we make the substitution

$$\{u\} = \{u_0\} + \{u_1\} \quad (10)$$

in which we assume that $\{u_0\}$ represents an equilibrium configuration and that $\{u_1\}$ is so small that all terms of higher than the first order in $\{u_1\}$ may be discarded.

After substitution of Eq (10) into Eq. (8) we can subtract the equation:

$$K(u_0) + qQ(u_0) = \{F\} \quad (11)$$

Then Eq. (8) takes the form

$$\bar{K} \{u_1\} + q \bar{Q} \{u_1\} = 0 \quad (12)$$

The elements of the matrices \bar{K} and \bar{Q} are in general functions of the displacement vector $\{u_0\}$

That is

$$\bar{K}_{ij} = (\partial K_i / \partial X_j) \text{ at } u = u_0 \quad (13)$$

and

$$\bar{Q}_{ij} = (\partial Q_i / \partial X_j) \text{ at } u = u_0$$

If

$$\text{Det} \left([\bar{K}] + q [\bar{Q}] \right) = 0 \quad (14)$$

then Eq. (13) has nonzero solutions. That is, $u = u_0$ represents a multiple solution to the nonlinear Eq (8), indicating that the fundamental branch in the

displacement/velocity diagram of that point is intersected by a branch representing secondary equilibrium.

If $\{F\} = 0$ (no thermal effects) and $\{h\} = 0$ (symmetric wing profile, and zero angle of attack) then $[\bar{K}] = [\bar{K}_1]$, $[\bar{Q}] = [Q_1]$ and Eq. (13) represents the classical formulation of the divergence problem (static aeroelasticity). With a symmetric wing profile, thermal effects cause only in-plane displacement components. The eigenvector obtained from Eq. (14) contains normal displacement components. In that case the solution still represents a bifurcation in the equilibrium path. The matrix $[K]$ represents the linear stiffness matrix for the prestressed structure. That is, it includes the effects of thermal stresses on the stiffness properties.

If the fundamental solution of Eq. (8) $\{u\} = \{u_0\}$ contains normal displacement components, the vanishing of the determinant (Eq. 14) generally represents a vertical tangent in a displacement/velocity or displacement/dynamic pressure diagram rather than a bifurcation point. In that case the eigenvalue approach to the divergence problem is not a rigorous solution. It is possible to linearize Eq. (8) for computation of u_0 but the solution then obtained from Eq. (14)) represents a more or less unconservative estimate of the critical velocity. The problem of static aeroelastic stability then can be approached either through solution of the eigenvalue problem defined by Eq. (14) or, in the more general case, through direct solution of the nonlinear Eq. (8).

Dynamic aeroelastic instability is said to occur if the flight conditions are such that the amplitude of a small vibration will increase

Vol. 3

with time. Solution to that problem, of course, requires that the "dynamic" terms in Eq. (7) are retained. The structural damping is often discarded since its magnitude is not well known and its exclusion results in only slightly conservative results.

The time step in the integration of Eq. (7) must be relatively small in comparison to the period for important vibration modes. Since the duration of a maneuver presumably is very large in comparison to a vibration period the direct approach is economically and numerically impractical. Somewhat better efficiency may be achieved if the quasi-static solution first is obtained from Eq. (8). The analysis can be restarted with excitation of small vibrations at appropriately selected points along the trajectory. The trajectory is safe if the vibration amplitude is decaying at all points.

A linearization of the dynamic aeroelasticity analysis allowing for thermal and aerodynamic prestress effects can also be achieved. Such a procedure is described in the following. In the equation

$$M\{\ddot{u}\} + K(u) + Q(u) = \{F\} \quad (15)$$

is substituted

$$\{u\} = \{u_0\} + a_i \{u_i\} \sin \omega_i t \quad (16)$$

where $\{u_0\}$ represents the quasi-static solution and a_i , $\{u_i\}$ and ω_i represent amplitude, deformation pattern (eigenvector), and frequency of the i -th vibration mode. It is assumed that a_i is so small that terms of higher order in a_i can be discarded. After subtraction of the terms

representing quasi-static equilibrium we obtain again a homogeneous equation system. Frequencies and modes of free vibration $\{u_i\}$ can be determined as eigenvalues and eigenvectors.

Frequencies and generalized masses corresponding to the few modes needed for aeroelastic analyses can be determined at appropriately chosen points along the trajectory. These results can be used in a classical flutter analysis. We refer to this procedure as linear dynamic aeroelasticity analysis, in which the first step is to compute the normal modes of the prestressed structure.

The information obtained from the linear eigensolution to extract the flutter speed is somewhat limited since it does not indicate the rate of growth of the vibration amplitude. However, it does not seem likely that a vehicle can be subjected to supercritical condition for a significant time interval without structural failure.

It is true also that the linearization of the analysis precludes effects of stiffening of the structure with finite deformation. For the cantilevered plates considered here such stiffening is insignificant within the range of tolerable deformation. It appears thus that the linear dynamic aeroelasticity analysis is quite satisfactory for the present purpose.

All options discussed above have been retained as capabilities in the computer program for aeroelastic analysis, STAGS-MOFA. In the case of linear divergence analysis the problem defined by Eq. (14) is not solved directly. The nonconservative nature of the aerodynamic matrices results in a matrix that is not symmetric. Eigenvalue routines for such problems are not

Vol. 3

available for problems of the size that may be required for accurate analysis of lifting surfaces. Therefore, the static aeroelastic analysis (as well as the dynamic) was based on the modal approach. In Eqs. (8) nonlinear terms are discarded. Linearized equations gives quasi-static solutions that are used as prestress in the free vibration analysis as described. The vibration modes and frequencies are used in a modal analysis of linear divergence.

The building blocks for the aeroelastic analysis then are

TRRID for thermal analysis

STAGS for elastic analysis

FLAM for computation of aerodynamic forces

MODIV for linear static aeroelastic analysis

MOFA for linear dynamic aeroelastic analysis

The manner in which those programs work together is indicated by the Flow Chart in Figure 8. Auxiliary storage is used for intermediate results, such as temperatures from TRRID. However, by proper choice of control cards it is possible to exercise the program in sequence during the same computer run.

The temperatures are first computed in TRRID at a number of time steps along the trajectory. The results are stored in a file and accessible so that the temperature distribution at any fixed value of the time can be obtained by interpolation. Subsequently the values of the aerodynamic force matrices are determined in FLAM. The information is available to STAGS as needed during

nonlinear quasi-static or possibly a complete nonlinear transient analysis. The quasi-static analysis gives the solution to the nonlinear divergence problem as well as a complete picture of stresses and strains in the structure during the trajectory.

For linear static aeroelasticity analysis the user will ask STAGS for a linear analysis. Modes and frequencies will be computed and stored so that for each preselected time step a computed critical velocity can be obtained by use of the MODIV program. The trajectory is safe if the computed critical velocity at all points exceeds the actual velocity.

Unless a STAGS analysis consists of direct integration of the nonlinear form of Eq. (7), a separate dynamic aeroelastic analysis is also needed. For this purpose the user can select to obtain either a linear or a nonlinear quasi-static solution. If the user chooses the option of nonlinear dynamic aeroelasticity analysis the transient analysis will be restarted at preselected steps with excitation of the vibration modes. If he chooses linear dynamic aeroelasticity analysis modes and frequencies will be stored on file and utilized by MOFA in a classical flutter analysis. If the computed flutter velocity exceeds the actual velocity at all time steps, the trajectory is safe.

The MOFA (Modal Flutter Analysis) Program (Ref. 33) was developed at Hughes Aircraft specifically to handle the flutter of tactical missile lifting surfaces, including interference effects between fore and aft surfaces at subsonic, transonic and low supersonic speeds. An isothermal, unprestressed structure is assumed throughout and a completely linear analysis. Aerodynamic thickness effects are neglected by the use of "Mach Box" theory at supersonic

10th Navy Symposium on Aeroballistics

Vol. 3

speeds. The flutter speed is extracted in the time honored manner by the solution of the complex eigenmatrix for a series of values of the reduced frequencies and plotting the structural damping against free stream velocity.

Necessary modifications were introduced in the MOFA program so that it could be used in conjunction with STAGS for hypersonic flutter analysis. The Generalized Aerodynamic Forces used in the MOFA program for hypersonic flutter analysis are based on nonlinear Piston Theory and on the modes of the prestressed structure.

Aerodynamic Forces

The present study represents a step towards the development of a complete and integrated system for analysis of the aeroelastic behavior of flight vehicles with thin lifting surfaces (wings and fins) operating in the lower hypersonic regime. For simplification of the aerodynamics, the analysis is limited to small angles of attack. Thus if fin strip aerodynamics only is considered the basic theory is essentially available. The moderate body or fuselage nose tip bluntness usually necessary in a hypersonic missile design generates a nonuniform flow field over the fins. Analytic means have been developed to account for the effect of missile body (Ref. 42). The capability is presently limited to hemispherical nose tips. The nonuniform dynamic pressure distribution generated over the fins by such a nose tip can be computed and is included in the program discussed here.

With the exception of this effect of nose bluntness, a significant simplification is introduced in hypersonic theory by the fact that the pressure at a point is a function of the local slope at that point only. This reduces the aerodynamic calculations to consideration of chordwise strips. It was shown in Ref. 42 for the very small angle of attack considered in the present study Third Order Piston Theory will provide a simple means for calculation of the aerodynamic influence coefficients with sufficient accuracy.

The geometry of a typical two-dimensional strip will be discussed with reference to Fig. 9 in which the important variables are illustrated and the derivation follows Ref. 43 very closely. It is noted that the slope at any point is the sum of five components; namely, the initial angle of attack of the airfoil, camber, control surface increment, a component due to thickness, distribution and one induced by deformation. Since the study presently excludes possible change in attitude of the vehicle, the first four components can be determined at the start of the analysis. All changes of slope occurring during an analysis are due to structural deformation. With the usual sign convention the different expressions for upper and lower surface slopes are:

$$\delta_u = \delta_{uR} - (\alpha + \delta_f) \quad (17)$$

$$\delta_l = \delta_{lR} + (\alpha + \delta_f)$$

Here δ_u and δ_l are upper and lower surface slopes with respect to the wind velocity. δ_{uR} and δ_{lR} are the rigid body slopes relative to the reference surface, α is the initial angle of attach of the reference surface, and δ_f is the change of slope arising because of structural deformation.

The pressure difference normal to a lifting surface is

$$\frac{\Delta p}{q} = (C_{pl} - C_{pu}) \quad (18)$$

Vol. 3

in which the pressure coefficient C_p is expressed in terms of the total slope, at a point as

$$C_p = \left(\frac{p - p^\infty}{q}\right) = \frac{2\delta}{M_\infty} + \left(\frac{\gamma + 1}{2}\right) \delta^2 + \left(\frac{\gamma + 1}{6}\right) M_\infty \delta^3 \quad (19)$$

On substituting Eq. (19) into Eq. (18) and distinguishing between upper and lower surface slopes one obtains

$$\frac{\Delta p}{q} = \frac{2}{M_\infty} (\delta_l - \delta_u) + \left(\frac{\gamma + 1}{2}\right) (\delta_l^2 - \delta_u^2) + \left(\frac{\gamma + 1}{6}\right) M_\infty (\delta_l^3 - \delta_u^3) \quad (20)$$

Inserting Eq. (17) into Eq. (20) and expressing the result in ascending powers of the slope $(\alpha + \delta_f)$ gives

$$\frac{\Delta p}{q} = Q_0 + Q_1 (\alpha + \delta_f) + Q_2 (\alpha + \delta_f)^2 + Q_3 (\alpha + \delta_f)^3 \quad (21)$$

in which the Q_i are the Aerodynamic Influence Coefficients (A.I.C.) as function of the total surface slope

$$\begin{aligned} Q_0 &= -\frac{2}{M_\infty} (\delta_{lR} + \delta_{uR}) + \left(\frac{\gamma + 1}{2}\right) (\delta_{lR}^2 - \delta_{uR}^2) - \left(\frac{\gamma + 1}{6}\right) M_\infty (\delta_{lR}^3 + \delta_{uR}^3) \\ Q_1 &= \frac{4}{M_\infty} - (\gamma + 1) (\delta_{lR} - \delta_{uR}) + \left(\frac{\gamma + 1}{2}\right) M_\infty (\delta_{lR}^2 + \delta_{uR}^2) \\ Q_2 &= -\left(\frac{\gamma + 1}{2}\right) M_\infty (\delta_{lR} + \delta_{uR}) \\ Q_3 &= (\gamma + 1) M_\infty / 3 \end{aligned} \quad (22)$$

Charts of these coefficients are given in Ref. 43 for many profiles. Expanding Eq. (21) to obtain an expression for the lifting pressure in terms of the perturbation or flexibility components of the streamwise surface slope gives

$$\frac{\Delta p}{q} = \bar{Q}_0 + \bar{Q}_1 \delta_f + \bar{Q}_2 \delta_f^2 + \bar{Q}_3 \delta_f^3 \quad (23)$$

in which the A.I.C.s are functions of the rigid body surface slopes are

$$\bar{Q}_0 = Q_0 + Q_1 \alpha + Q_2 \alpha^2 + Q_3 \alpha^3$$

$$\bar{Q}_1 = Q_1 + 2Q_2 \alpha + 3Q_3 \alpha^2$$

$$\bar{Q}_2 = Q_2 + 3Q_3 \alpha$$

$$\bar{Q}_3 = Q_3$$

The Q_i are discussed in some detail and given graphically as well as for zero angle of attack in Ref. 43, showing that a significant increase in complexity results when a nonsymmetric section or nonzero initial angle of attack is considered. For the symmetric section at zero angle of attack, $\delta_{uR} = -\delta_{lR}$, so $Q_0 = Q_2 = 0$ and Q_3 is small and can be discarded, so the aerodynamic formulation reduces to a linear one.

In what has been said up to now, no distinction has been made between dynamic (unsteady) and static behavior. All inviscid pressures are known in terms of the local slope and the distinction between the two lies in a different interpretation of "slope". For static flow, the chordwise slope ξ_f is simply that due to static structural flexibility.

$$\delta_f = \frac{\partial w}{\partial x} \quad (24)$$

where w represents lateral displacement and the x the distance along the chord. Lateral motion introduces an additional component equal to the lateral velocity divided by the freestream velocity, so the total slope becomes

$$\delta_f = \frac{\partial w}{\partial x} + \frac{1}{U_\infty} \frac{\partial w}{\partial t} \quad (25)$$

Vol. 3

Aerodynamic forces for the quasistatic analysis are obtained directly from the above formulation. Generalized aerodynamic forces for the flutter analysis are computed by use of procedures discussed for example in Ref. 42.

A computer program ICAM has been derived in which aerodynamic influence coefficients and generalized aerodynamic forces are determined for use in the STAGS and MOFA programs. The programs include the chord-wise thickness variation of wedge, diamond and parabolic sections, and it is very easy to modify a subroutine PROFIL to account for any other thickness distribution. Each number is assumed to be sufficiently high so the correction for sweepback (Ref. 42) is small enough to be neglected.

Numerical Results

Linear Static Aeroelasticity

Some results from a classical divergence analysis were obtained by use of STAGS and MODIV in combination. With the prestress from a linear analysis STAGS computes vibration modes for use in MODIV.

The dynamic pressure as a function of the distance from the root chord was determined by use of the method discussed in Ref. 43. The pressure distributions for two wing configurations, 42.0 inches behind the nose of the missile body, are shown in Fig. 10. The distributions correspond to missile bodies with a spherical nose. Results are shown for one body with a 2.0 inch and one with a 6.0 inch diameter. In all cases the effect of the body reduces considerably the dynamic pressure over a large portion of the wing. The presence of the missile body, then should result in an increase of the free stream dynamic pressure of which aeroelastic instability occurs.

The results presented in Table 1 apply to a rectangular wing with a 10.0 in chord and 8.0 in span. The cross-section of the wing is "diamond shaped" as shown in Fig. 4. In Table 1a are shown the results for a wing that has only partial support along the root chord, i.e. all displacements are constrained at nodes 7, 8, 9 but the other nodes are free (See Fig. 4). It is seen that the critical velocity increases, as expected, when the effect of the missile body is taken into account. The slight decrease in critical velocity with the angle of attack is due to the change in the generalized aerodynamic forces.

If the same wing is clamped along the entire root chord the critical free stream pressure increases dramatically, as can be seen from Table 1b. Again the presence of the missile body results in an increase of the critical pressure. Most of the results presented in Table 1b include the effect of aerodynamic heating. They correspond to a parabolic temperature distribution with 450° F at the leading and trailing edges and 0° F at mid chord.

TABLE 1
LINEAR DIVERGENCE RESULTS

RECTANGULAR PLANFORM WING 10. IN. CHORD, 8. IN. SPAN. 4.5% T/C DIAMOND SECTION

A) 3 NODE ROOT SUPPORT. ROOM TEMPERATURE.

BODY	ANGLE OF ATTACH (DEG)	DIVERGENCE DYNAMIC PRESSURE (LBS/IN ²)
NONE ↓ 6 IN. DIA. ↓	0.	410.
	2.	404.
	4.	391.
	6.	370.
	0.	566.
	2.	553.
	4.	510.
	6.	447.

B) SAME WING BUT CLAMPED ALONG THE ROOT.

BODY	ANGLE OF ATTACH (DEG)	L.E.&T.E. TEMP. (DEG. F.)	DIVERGENCE DYNAMIC PRESSURE (LBS/IN ²)
NONE	0.	0.	2400.
6 IN. DIA.	0.	0.	3550.
NONE ↓ 6 IN. DIA. ↓	0.	450.	2200.
	2.		2180.
	4.		2150.
	6.		2110.
	0.		2670.
	2.		2620.
↓ 6 IN. DIA. ↓	4.		2490.
	6.		2260.

Nonlinear Static Aeroelasticity

It was indicated above that the linear static aeroelastic analysis presents a rigorous solution only if no component of the divergence mode (eigenfunction) is contained in the precritical deformation pattern. This generally is the case only if the precritical mode is free from lateral displacement, that is, if the wing profile is symmetric and the angle of attack is zero. If a component of the divergence mode is present at subcritical velocity, then this component will grow nonlinearly from the outset. Rigorously correct deformations and stresses in the structure can only be determined from the nonlinear quasistatic solution. The traditional linear solution is adequate for small dynamic pressures but becomes progressively less credible as dynamic pressure increases.

The shortcomings of the linear static aeroelastic analysis was first noted by Padlog, Donato, and Batt (Ref. 13). With a simple but still representative model of a wing susceptible to divergence, it is shown that the classical linear analysis may give nonconservative results. The reason for this is that the nonlinear contribution to the aerodynamic forces is such that the twisting moment grows with the angle of twist at a rate that exceeds the linear rate. Consequently, the curve representing the secondary equilibrium form bends back from the maximum at the critical dynamic pressure. The equilibrium on this secondary path is unstable so the situation is analogous to the well known and much discussed problem with imperfection sensitivity in elastic stability analysis. Of course, the nonlinear structural terms should also be accounted for. If the structure were stiffening under

increasing deformation, the situation could be reversed, resulting in a stable secondary equilibrium path. However, at moderate deformation structural nonlinearities are insignificant for the cantilever plate.

The results of Ref. 13 for nonlinear aerodynamics, but linear structural behavior are indicated in Fig. 11. The lateral displacement at the tip of the leading edge is shown as a function of aerodynamic pressure. If some disturbance is present that will cause a lateral displacement, this displacement will grow at an accelerated rate, until at some point the slope of the curve is infinite. At that point the equilibrium becomes unstable and the existence of a vertical slope may be considered to be a nonlinear divergence condition. The aerodynamic pressure corresponding to aeroelastic instability is below that determined by the linear theory and decreases with the size of the disturbance.

It should be noted that the point of vertical tangent may correspond to very large deformations. Excessive stresses may confine flight to a narrower range. Therefore, it seems that in the majority of applications it is necessary to carry out a nonlinear analysis. In addition to the need to assess structural integrity, there is a need to consider the effects of wing deformation on flight mechanics. In particular the aerodynamic stability derivatives are affected by such deformations. This subject was also studied in Ref. 14 where it is demonstrated that relatively small aerodynamic nonlinearities can sometimes produce dramatic changes in the stability derivatives at high values of the dynamic pressure.

For code verification as well as illustration of the relationship between linear and nonlinear static aeroelastic analysis, STAGS was applied in a study of a wing with rectangular planform and diamond shaped profile as shown in Fig. 4. The same finite difference grid was used and the wing was attached only at the grid points 7, 8, and 9. No thermal or missile body aerodynamic effects were included.

The linear divergence velocity was determined by use of MODIV, and the critical dynamic pressure so computed is shown in Fig. 12.

STAGS was used in the nonlinear analysis. The perturbation causing lateral displacements was introduced in the form of a small lateral force at the tip of the leading edge or by flight with a nonzero angle of attack. Three values of this force imperfections were considered as shown in the figure. For these three cases the angle of attack was zero. In a fourth case no imperfections were introduced, but the initial angle of attack was 2.0 degrees.

The stiffness properties of aluminum was used in the analysis. Even for a high performance alloy, the stresses will be well into the inelastic range when the wing tip displacement reaches a value of 0.5 in. Consequently, at flight with an initial angle of attack of 2.0 degrees the critical dynamic pressure is no more than one-third of that computed from the linear theory.

It may be observed here that the effect of the missile body is to reduce the dynamic pressure on a large part of the wing. For a given maneuver this may have to be compensated for by an increase in the angle of attack. In view

of the reduction of critical free stream velocity with increasing angle of attack the presence of the missile body may on the balance have an unfavorable effect on the static aeroelastic stability.

Dynamic Aeroelasticity

The flutter speed was computed for a number of cases by use of the STAGS-MOFA combination. The flutter analysis in MOFA was based on the three lowest frequencies and corresponding modes, as computed by use of STAGS. As a first example the rectangular wing with a 10.0 in chord and 8.0 in. span (See Fig. 4) was considered. The wing was clamped along the entire root chord. It was assumed to have its leading edge 42.0 aft of the missile body nose tip. The flight was assumed to be at 10000 ft. altitude and at a Mach Number of 5.0. Results are shown in Table 2. As in the static case critical velocities are seen to increase significantly due to the missile body effect and to decrease slowly with increasing angle of attack. To assess the importance of thickness on the aerodynamic forces and the resulting flutter condition it was computed using the "Mach Box" Theory of Ref. 33 and yielded a flutter dynamic pressure of 1600 lbs/in^2 , markedly unconservative relative to the destabilizing influence of thickness is consistent with the vast majority of available literature, such as Refs. 24, 25, 26 and 27.

Table 3 shows some results for a clipped delta wing. Plan form and cross-section of the wing are shown in Fig. 7. The results shown in Table 3a do not include effects of aerodynamic heating. The effects of the missile body and of angle of attack are the same similar to those for the rectangular wing. The slight decrease in flutter speed with angle of attack agrees with Refs. 17, 22, 28 and 29.

Table 3b shows results corresponding to a parabolic temperature distribution with 600°F at leading and trailing edges and with 0°F at midchord.

The body effect is greater for the thermally stressed clipped delta wing than it is in isothermal conditions. This is due to the fact that at high temperatures the structural stiffnesses are being reduced, tending to amplify the relative importance of the aerodynamic terms which are temperature invariant. Thus we have reason to believe that in general, the hotter the structure the more important do the aerodynamic terms become. As was discussed above, solution of the nonlinear equation of motion including displacement dependent aerodynamic loads would yield a complete solution to the aeroelastic problem. While the flutter analysis only indicates the velocity at which a small vibration will grow with time, the integration of Eq. 1 will also show the rate of growth of the oscillation. It may show, for example, that a maneuver that includes a short time at a speed slightly above the flutter velocity still is safe.

Therefore, data may be saved from a quasistatic analysis and STAGS can be restarted at some points along the trajectory with dynamic terms included and with excitation of a small amplitude vibration. To demonstrate such a solution the rectangular wing (Fig. 4) was selected. At room temperature, no body effect and a zero angle of attack the aerodynamic pressure corresponding to flutter computed by the MOFA program is 900. psi. (V_f of 155000. in./sec.). The STAGS analysis was restarted with a vibration excited by a load of 0.1 lbs. instantaneously applied at the tip of the leading edge. Restart was initiated at flight velocities corresponding to .77, .90 and 1.03 times the eigen-solution flutter speed. Fig. 13

shows for these three cases how the lateral displacement at the tip of the leading edge varies with time when structural damping is neglected. There is clear evidence of instability as the flight velocity changes from 0.90 to 1.03 times V_f , suggesting good correlation between the frequency and time domain methods of computing flutter speed. At 0.90 V_f the oscillation is virtually neutrally damped, but at 0.77 V_f a slight dynamic instability is evident over the first three cycles. This anomaly remains to be resolved by further use of the program.

Table 2

BINARY FLUTTER RESULTS-RECTANGULAR PLANFORM WING

10. IN. CHORD, 8. IN SPAN, 4.5% T/C DIAMOND SECTION. ROOM TEMPERATURE.

CLAMPED ROOT, MACH NO.=5.0 AT 10,000 FT ALTITUDE
WING L.E. AT 42.0 IN. AFT OF BODY NOSE

BODY	ANGLE OF ATTACK(DEG.)	FLUTTER DYNAMIC PRESSURE(LBS/IN ²)
NONE	0.	900.
	2.	850.
	4.	800.
v	6.	750.
6. IN. DIA.	0.	1200.
	2.	1100.
	4.	950.
v	6.	850.

Table 3.

BINARY FLUTTER RESULTS-CLIPPED DELTA PLANFORM WING

10. IN. ROOT CHORD, 2.5 IN. TIP CHORD, 8.0 IN. SPAN, 4.5% T/C DIAMOND SECTION
 MACH NO. 5.0 AT 10,000 FT ALTITUDE,
 WING L.E. AT ROOT CHORD AT 42.0 IN. AFT OF BODY NOSE

a) ROOM TEMPERATURE

BODY	ANGLE OF ATTACK(DEG)	FLUTTER DYNAMIC PRESSURE(LBS/IN ²)
NONE	0.	1900.
↓	2.	1880.
↓	4.	1840.
∇	6.	1810.
6. IN. DIA.	0.	2840.
↓	2.	2730.
↓	4.	2530.
∇	6.	2340.

b) LEADING AND TRAILING EDGES AT 600. DEGREES FAHRENHEIT

BODY	ANGLE OF ATTACK(DEG)	FLUTTER DYNAMIC PRESSURE(LBS/IN ²)
NONE	0.	1020.
↓	2.	980.
↓	4.	930.
∇	6.	850.
6. IN. DIA.	0.	1720.
↓	2.	1620.
↓	4.	1500.
∇	6.	1300.

RECOMMENDED PROCEDURE

It is not claimed that the work presented in the preceding sections provides a completely satisfactory solution of the problem of aeroelastic stability of lifting surfaces in hypersonic flight. However, it is believed to advance the state of the art in such analysis. The computer program developed, although somewhat limited, is useful for practical analysis. The code contains many options with respect to the choice of strategy in the aeroelastic analysis. These are all left open to the user, but an effort is made in this section to make recommendation for the choice of strategy. The recommendations are based on the experience acquired during limited application of the code.

It has long been realized that for thin lifting surfaces, a rigorous definition of stresses and deformations can be obtained only if such nonlinear effects are included as deformation dependent loads. It has been shown also that nonlinearities in the aerodynamic formulation are important within a practical range of flight parameters. In a linear analysis, the term $Q(u)$ (Eq. 8) degenerates into $\{Q_0; h\}$.

It is sometimes assumed that an analysis based on such a linearization gives a good estimate of deformations and stresses as long as the flight velocity is somewhat below the classical divergence velocity. For the lifting surfaces and flight conditions typical for hypersonic tactical missiles this does not appear to be the case.

Therefore, unless special circumstances dictate differently, it is necessary to obtain the nonlinear quasistatic solution (Eq. 8). In that case there is no need to obtain a solution to the linear static elasticity problem. Divergence will be indicated by rapidly increasing wing tip deflection.

The nonlinear transient analysis is somewhat more accurate than the linearized flutter analysis since it retains a much larger number of degrees of freedom. In addition, it provides some additional information, such as the rate of growth of the vibration modes in the post critical condition. For a structure that stiffens with increasing deformation the linearized analysis may be unduly conservative. However, these objections appear to be slight in comparison to the computational advantages that are offered by the linearized flutter analysis.

The linearized dynamic aeroelasticity analysis is executed by MOFA and based on frequencies and virtual masses computed by STAGS and generalized aerodynamic forces computed by FLAM. It is clear, that within the range of flight parameters of interest, thermal effects are important. It is not clear whether or not the computed flutter speed is sensitive to the changes in the aerodynamic forces caused by structural deformation or to aerodynamic and geometric nonlinearities. However, in general, it is necessary to obtain the nonlinear quasistatic solution (nonlinear divergence). In that case vibration modes are, of course, obtained for use in the flutter analysis at the time when this solution is established. In fact then the whole aeroelastic problem can be solved in one computer run.

Whether or not geometrically nonlinear terms in the prestress analysis need be retained is not clear at this point. Such terms can easily be suppressed by use of the standard input cards in STAGS. Suppression of these terms may lead to better convergence with little sacrifice in accuracy. The most important effect of structural nonlinearity is presumably in the coupling between inplane stress (thermal) and torsional stiffness of the plate.

The capability to evaluate the linear divergence speed may be useful as a first estimate. Some idea of when divergence is going to occur is needed for selection of the time steps at which vibration analysis is to be carried out. The nonlinear flutter option can be used after a preliminary linear flutter analysis. A restart with excitation of small vibrations can be executed at a time step just below that indicated as the flutter speed.

The problem of leading or trailing edge buckling deserves some consideration. Presently it seems that the best recommendation is that it be treated with benign neglect. Buckling caused by controlled displacement, as is the case if stresses are thermally induced, is generally a stable phenomenon. The gradually increasing amplitude of the buckle relieves the compressive stress. It was observed above that the development of leading edge buckling had little effect on the basic stiffness of the plate. It seems likely that this behavior is typical and that the observation can be extended to similar configurations.

Two different procedures for assessing thermal buckling effects are possible. One is to introduce a small perturbation. In that case the

quasistatic solution corresponds to stable equilibrium for all levels of the temperature. In some temperature range the lowest vibration modes will include the very localized modes corresponding to leading edge buckling. In view of the results discussed above, it is not likely that the presence of these modes will significantly affect the flutter velocity.

If no perturbation is introduced to trigger thermal buckling, convergence will be considerably easier. In that case the quasistatic solution obtained beyond the point of thermal buckling will represent unstable equilibrium. The coefficient matrix used in the vibration analysis has at least one negative root and corresponding eigenvalue is negative. Such solutions to the vibration analysis are ignored in the aeroelastic analysis. If, as expected, leading edge buckling has little effect on the flutter characteristics, the two approaches should lead to approximately the same results.

CONCLUSIONS

A study of the aero-thermo-elastic characteristics of a tactical missile operating at near zero angle of attack in the mach number range $3 \leq M \leq 6$ has produced the following results.

- o An integrated digital program has been developed for the static and dynamic linear and non-linear aeroelastic response of sharp edged aerodynamically heated, cantilevered lifting surfaces representative of a wide range of tactical missile wings and fins. The program utilizes a one-dimensional "through the thickness" flat plate solution for computation of the structural temperature effects, third order piston theory aerodynamics modified to account for the nonuniform flow generated by a hemispherically blunted missile body, and the STAGS nonlinear finite difference program for the structural (response) calculations.

- o In general it is found to be desirable to run a full non-linear quasi-static analysis for each trajectory till its completion or the onset of divergence. Flutter analyses, linear or non-linear, should be performed only at discrete times within each trajectory selected by the analyst using the appropriate prestress conditions from the quasi-static solution. The non-linear flutter solution provides a direct numerical

solution of the coupled nonlinear equations but is in its present form markedly less efficient than the eigenvalue solution obtained through standard type linear flutter analyses.

The following results from the analyses on which the integrated computer program is based may be worth mentioning.

- o Missile nose bluntness generates large spanwise dynamic pressure gradients over the fins, with the value at the root chord being almost half the freestream value in the cases studied. This results in the missile body exercising a powerful influence over the free stream dynamic pressures at which aeroelastic instabilities occur.
- o Thermal-structural analyses conducted to compare with existing (closed form) solutions show excellent agreement where such could be expected and the numerical results follow well known established trends where the problems become too complex for closed form solutions.

Typical results illustrate the thermally induced stiffness changes in wings and demonstrate the importance of boundary conditions, temperature sensitive elastic moduli, initial imperfections, planform and thickness variations, as well as the aerodynamic influence of the missile body.

REFERENCES

- (1) Collar A. R., "The Expanding Domain of Aeroelasticity" J. R. Aero. Soc. Vol. L, August 1946, pp 613-636.
- (2) Rogers M., "Aerothermoelasticity", Aero/Space Engineering Vol. 17, No. 10, October 1958, pp 34-43.
- (3) Zisfein, M. B., Donato V. W., and Farrell R. F. "Supersonic Aeroelastic Effects on Static Stability and Control, Part I Aerodynamics" WADC TR-58-95. December 1958.
- (4) Rattinger, I and Gallagher, R. H. "Supersonic Aeroelastic Effects on Static Stability and Control, Part II, Structures", WADC TR-58-95, April 1960.
- (5) Donato V. "Supersonic Aeroelastic Effects on Stability and Control. Part III Aeroelastic Interaction " WADC TR-58-95. July 1960.
- (6) Blessing A. H., and Honawalt A. J. "Thermal Effects on Static Aeroelastic Stability and Control. Part I Methods of Predicting Structural Temperatures due to Aerodynamic Heating", WADC TR 58-378 Pt 7 June 1959.
- (7) Batt, J. R. and Farrell R. F., "Thermal Effects on Static Aeroelastic Stability and Control. Part II Aerodynamics". WADC TR-58-378 Pt 2 December 1959.
- (8) Bisplinghoff R. L. "Some Structural and Aeroelastic Considerations of High Speed Flight" J. Aero Sci., Vol. 23, No. 4, April 1956, pp 289-329.
- (9) Bisplinghoff, R. L., and Dungundji, J., "Influence of Aerodynamic Heating on Aeroelastic Phenomena" in High Temperature Effects in Aircraft Structures. Edited by N. J. Hoff. Pergamon Press. 1958 pg 288-312.
- (10) Mills, W. R., Schmit, L. A., Balmer H. A., Cener D. and Foss K. A. "Procedures for Including Temperature Effects in Structural Analysis of Elastic Wings. WADC TR-57-754 Parts I, II, III and IV January 1958 to March 1960.
- (11) Batt, J. R., Gallagher, R. H., et al, "Thermal Effects on Static Aeroelastic Stability and Control," WADC-TR-58-378, Numerous Volumes published in 1959.
- (12) Padlog, J., Donato, W. W., and Batt, J. R., "Thermoelastic Effects on Hypersonic Stability and Control," ASD-TR-61-287, Numerous Parts and Volumes published 1961-1963.

- (13) Batt, J. R. and Gallagher, R. H., "Nonlinear Thermoelastic Effects on Hypersonic Stability and Control," Various Parts and Volumes of RDL-TDR-64-16, 1964 and 1965.
- (14) Garrick, I. E. and Rubinow, S. I. "Flutter and Oscillating Force Calculations for an Airfoil in a Two Dimensional Supersonic Flow", NACA TR 846 May 1946.
- (15) Ashley, H. and Zartarian, E. "Piston Theory - A New Aerodynamic Tool for the Aeroelastician", J. Aero. Sci. Vol. 23, No. 12, December 1956. pp 1109-1110.
- (16) Ashley, H. and Zartarian, G. "Supersonic Flutter Trends as Revealed by Piston Theory Calculations", WADC TR-58-74. May 1958.
- (17) Chawla, J. P. "Aeroelastic Instability at High Mach Number" J. Aero. Sci., Vol. 25, No. 4, April 1958 pp 246-258.
- (18) Broadbent, E. G. "Flutter of an Untapered Wing Allowing for Thermal Effects", R.A.F. Report Structures 249 April 1959.
- (19) Mansfield, E. H., "The Influence of Aerodynamic Heating on the Flexural Rigidity of Thin Wing". R & M 3115 September 1957.
- (20) Harder, R. L. et al "Supersonic Flutter Analyses Including Aerodynamic Heating Effects" WADC TR 59-559. February 1960.
- (21) Zartarian, G. and Hsu, P. T. "Theoretical and Experiment Studies on Airloads Related to Hypersonic Aeroelastic Problems of General Slender Pointed Configurations", ASD TR 61-7 April 1961.
- (22) Runyan, H. L. and Morgan H. G. "Flutter at Very High Speeds" NASATND-942 August 1961.
- (23) Green, J. M. and Rosecrans, R. "Effect of Aerodynamic Heating on the Flutter of Thin Flat-Plate Arrow Wings" NASA TN D-1788 May 1963.
- (24) Bennett, R. M. and Yates, E. C. "A Study of Several Factors Affecting the Flutter Characteristics Calculated for Two Swept Wings by Piston Theory and by Quasi Steady Second-Order Theory and Comparison with Experiment" NASA TN D-1794 May 1963.
- (25) Yates, E. C. and Bennett, R. M. "Use of Aerodynamic Parameter from Nonlinear Theory in Modified-Strip-Analysis Flutter Calculations for Finite Span Wings at Supersonic Speeds NASA TN D-1824 July 1963.
- (26) Hanson, P. W. and Levy, G. M. "Experimental and Calculator Results of a Flutter Investigation of Some Very Low Aspect Ratio Flat Plate Surface at Mach Numbers from 0.62 to 3.00", NASA TN D-2038 October 1963.

- (27) Hurley, S. R. "Hypersonic Flutter Model Tests of Advanced Wing Configurations at Initial Angles of Attack" RTD TDR-63-4219 October 1964.
- (28) Goetz, R. C. "Hypersonic Flutter Analysis Using Measured Static Aerodynamic Derivatives and Comparison with Experiment", NASA TN-D-5233, May 1969.
- (29) Yates, E. C. and Bennet, R. M., "Analysis of Supersonic-Hypersonic Flutter of Lifting Surfaces at Angle of Attack." J. Aircraft, Vol. 9, No. 7, July 1972, pp. 481-489.
- (30) Almroth, B. O., Brogan, F. A., STAGS User Manual, LPARL Report No. 1975
- (31) Compton, W. R. and Schultz, L. D., "A FORTRAN IV Program for the Solution of One-Dimensional Heat Conduction Problem in Multilayer Plate Cylinders and Spheres Subject to Arbitrary Aerodynamic Heat Transfer" TN 4061-124, N. W. C. China Lake, July 1965.
- (32) Van Driest, E. G., "The Problem of Aerodynamic Heating", Aeronautical Engineering Review, Vol. 15, No. 10, October 1956.
- (33) Hughes Aircraft Company "Modal Flutter Analysis Study", Report No. SD 15204, April 1971
- (34) Heldenfels, R. R. and Vosteen, L. F., "Approximate Analysis of Effects of Large Deflections and Initial Twist on Torsional Stiffness of a Cantilever Plate Subjected to Thermal Stress", NACA TR 1361, 1958.
- (35) Budiansky, B. and Mayers, J., "Influence of Aerodynamic Heating on the Effective Torsional Stiffness of Thin Wings", J. Aero. Sci., Vol. 23, No. 12, P. 1081, 1956.
- (36) Biot, M. A., "Influence of Thermal Stress on the Aeroelastic Stability of Supersonic Wings", J. Aero. Sci., Vol. 24, No. 6, p 418-241, June 1957.
- (37) Kochanski, S. L. and Argyris, J. H., "Some Effects of Kinetic Heating on the Stiffness of Thin Wings", Aircraft Engineering, Oct. 1957, Feb. 1958, March 1958 and April 1958
- (38) Mansfield, E. H., "Combined Flexure and Torsion of a Class of Heated Thin Wings - A Large Deflection Analysis", R & M 3195, March 1958.
- (39) Van der Neut, A., "Buckling Caused by Thermal Stresses", Chapt. 11 of High Temperature Effects in Aircraft Structures, edited by N. J. Hoff, Pergamon Press, 1958
- (40) Singer, J., "Thermal Buckling of Solid Wings of Arbitrary Aspect Ratio", J. Aero/Space Sci., Vol. 25, No. 9, Sept. 1958 pp. 573-580

- (41) Mansfield, E. H., "Leading Edge Buckling due to Aerodynamic Heating", R & M 3197, May 1959.
- (42) Ericsson, L. E. et al., "Hypersonic Aeroelastic Analysis". LMSC-D056746. September 1975.
- (43) Batt, J. R. "Thermoelastic Effects on Hypersonic Stability and Control Part 1: Hypersonic Aerodynamics" ASD TR-61-287, May 1963.

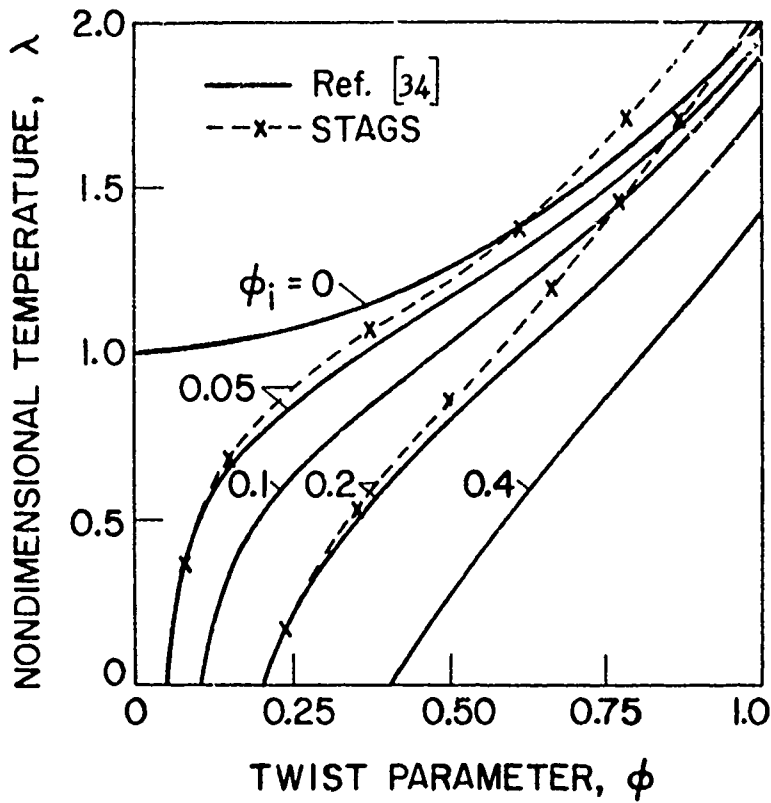


Figure 1: Tip Twist as a Function of Temperature Ratio and Initial Imperfection Amplitude.

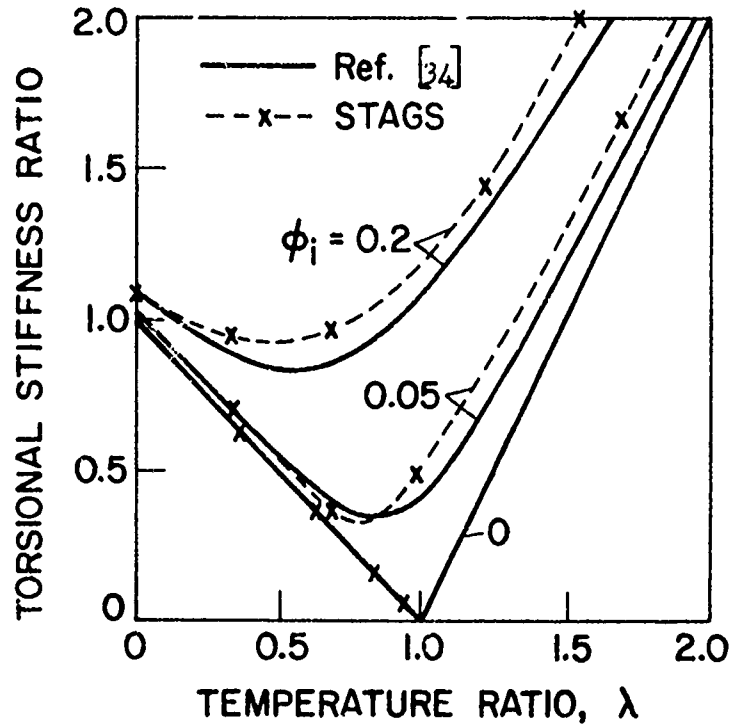


Figure 2: Torsional Stiffness as a Function of Temperature Ratio, for the Square Uniform thickness Plate.

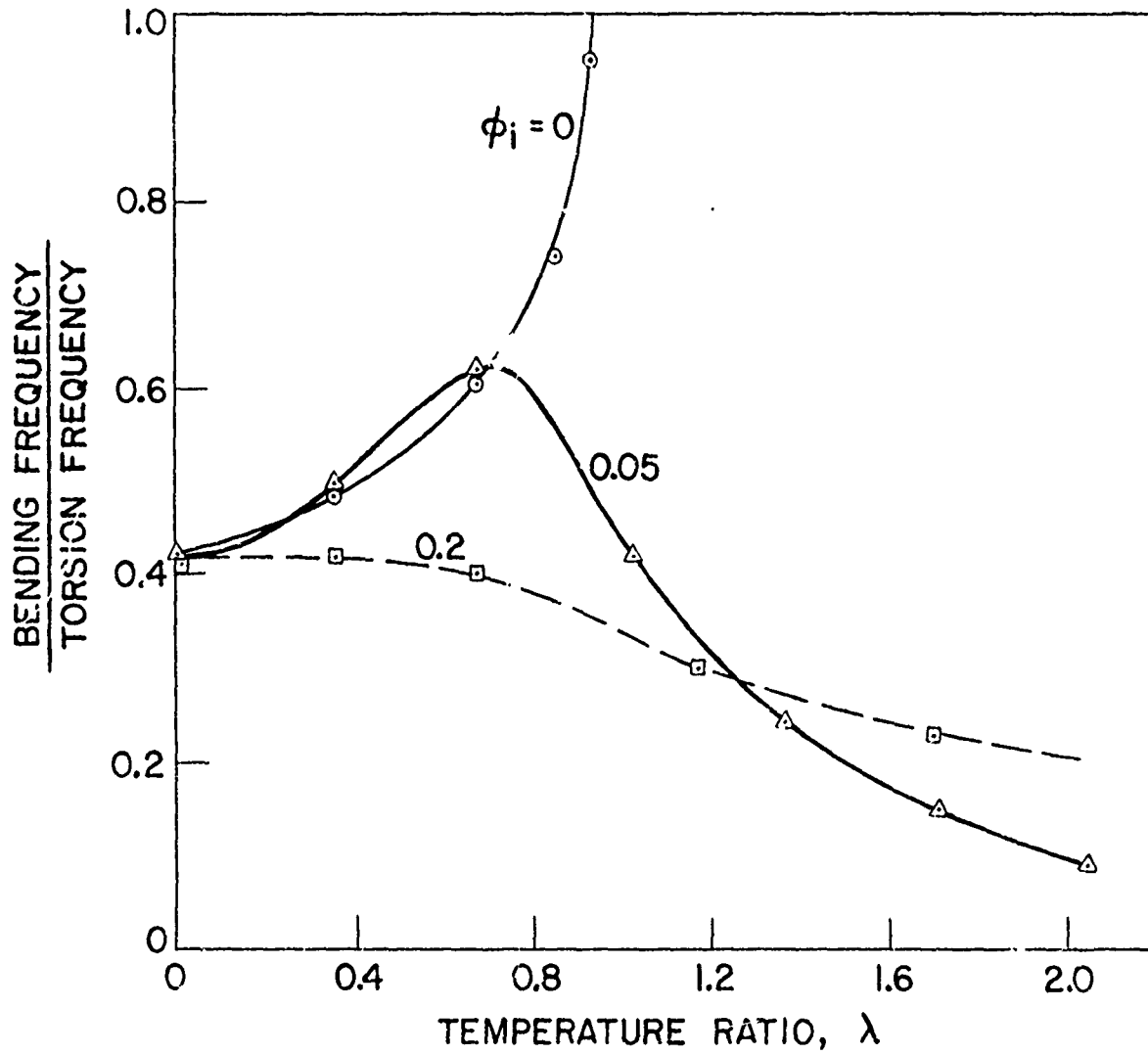


Figure 3 Bending to Torsion Frequency Ratio, STAGS Results.

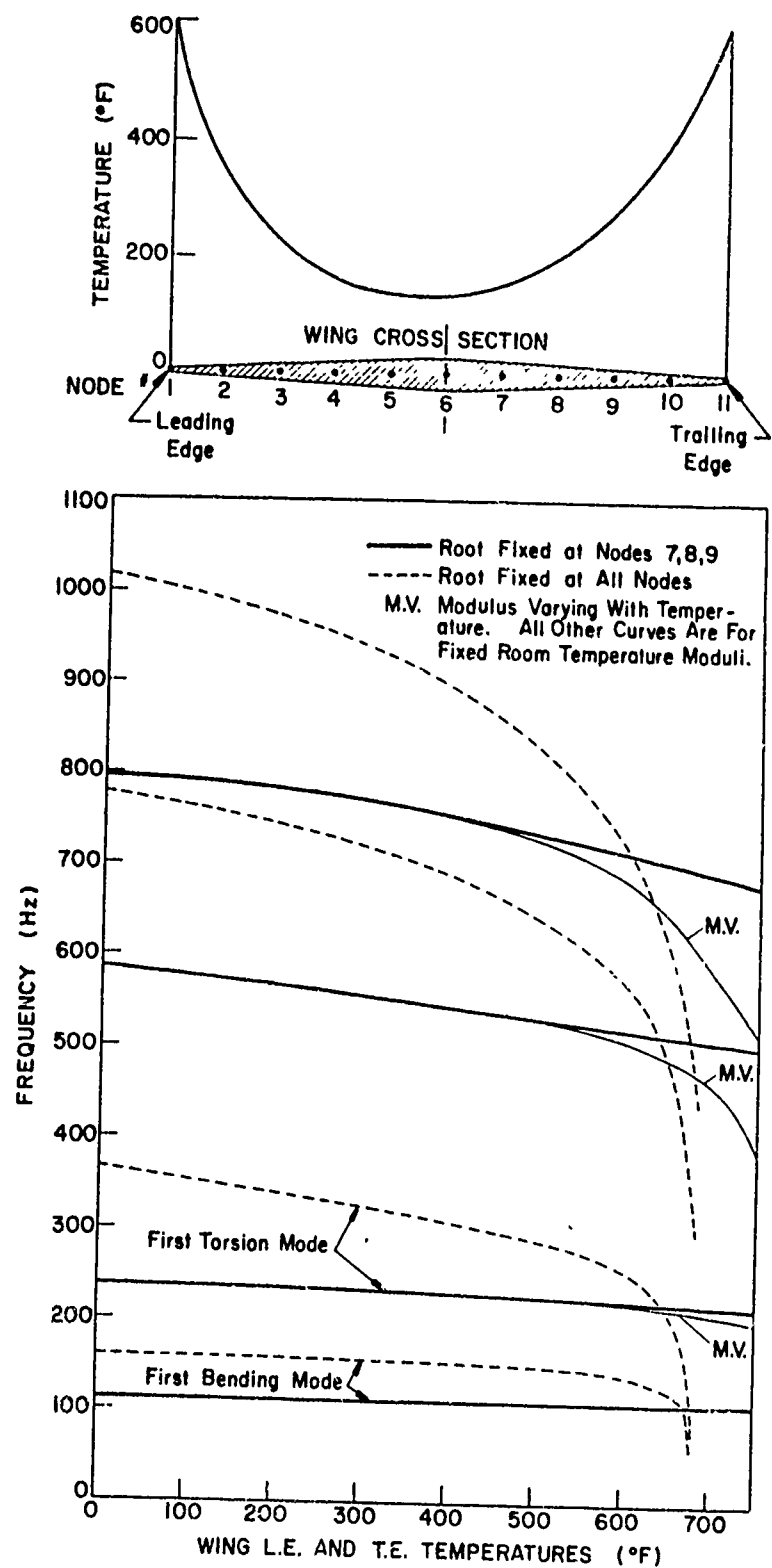
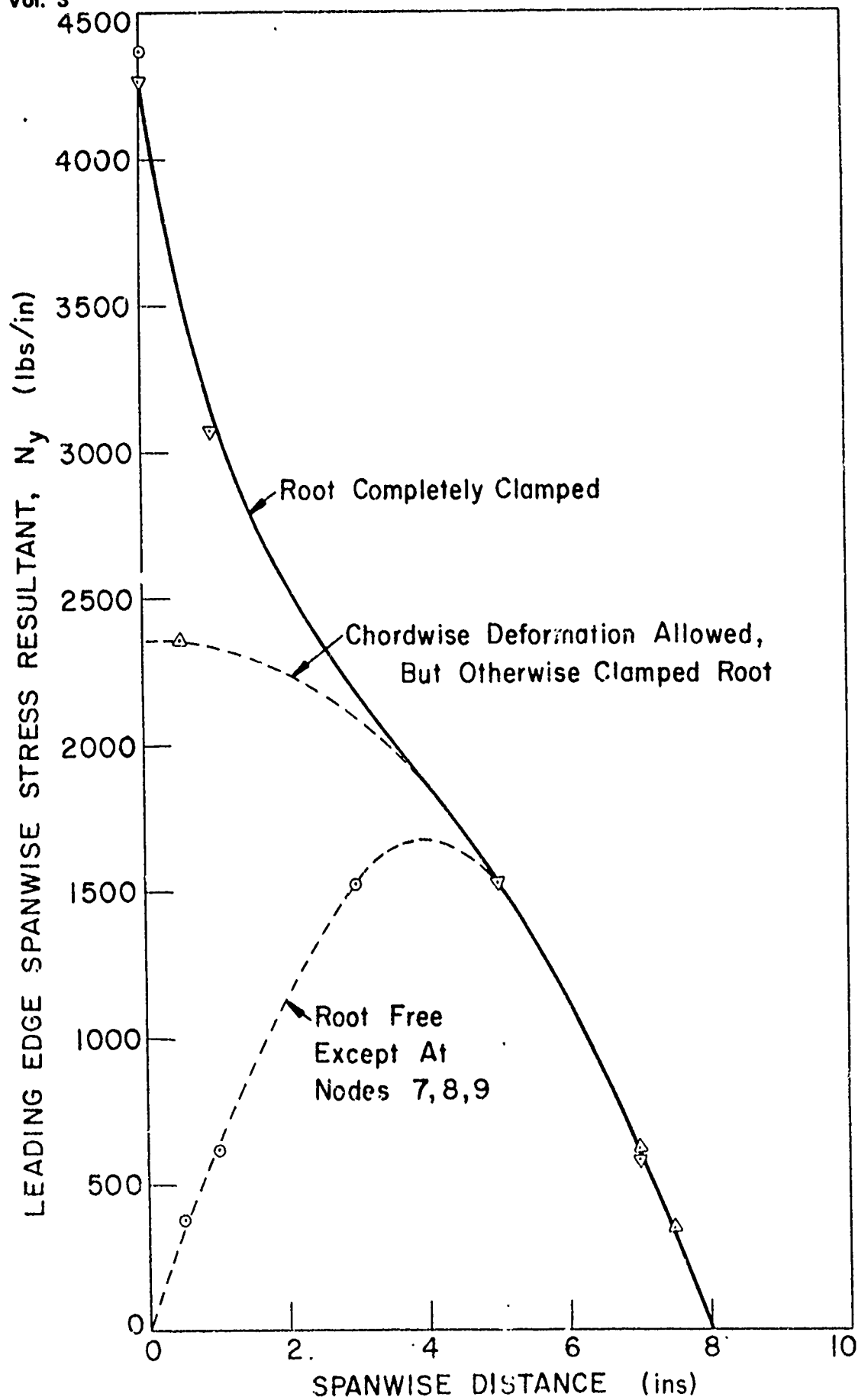


Figure 4: Frequency as a function of Temperature for a Rectangular Diamond cross-section Wing.



398 Fig. 5 Stress Resultants in Rectangular Planform Diamond Profile
Leading Edge Temperature - 100°F

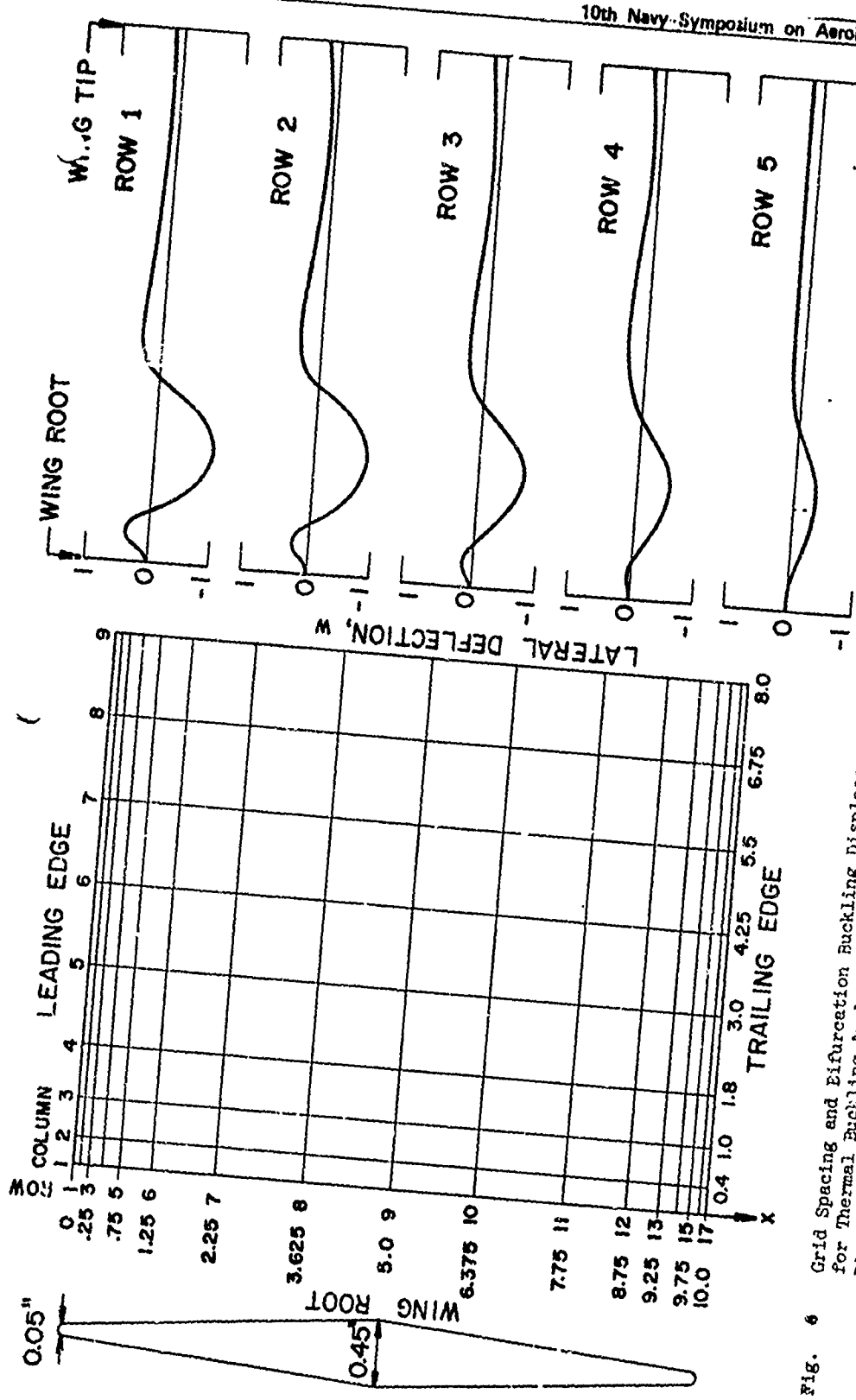


Fig. 6 Grid Spacing and Bifurcation Buckling Displacements for Thermal Buckling Analysis of Rectangular Planform Diamond Section Wing with Clamped Root

Thermal Bifurcation Buckling Eigenfunction
Lateral Displacement

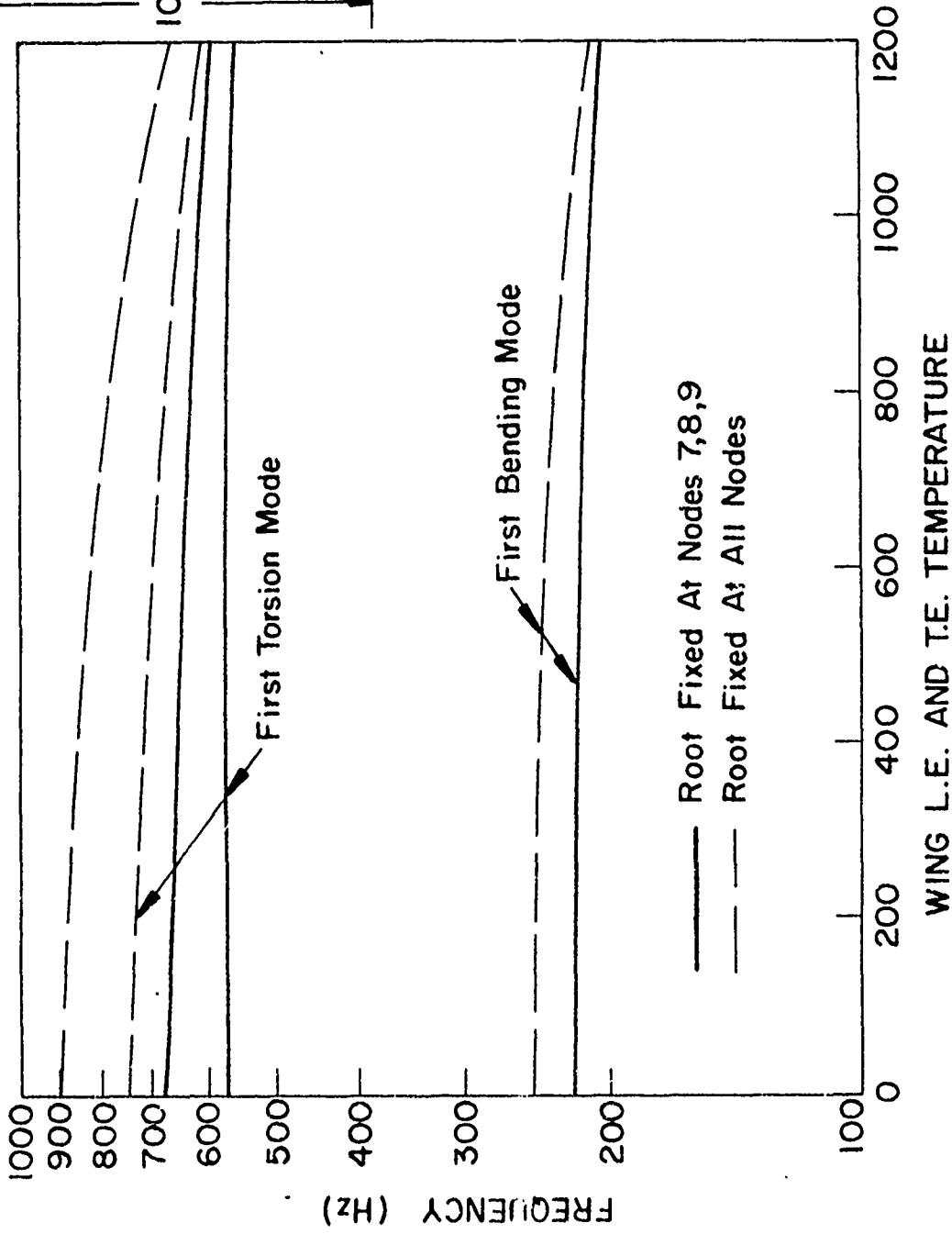
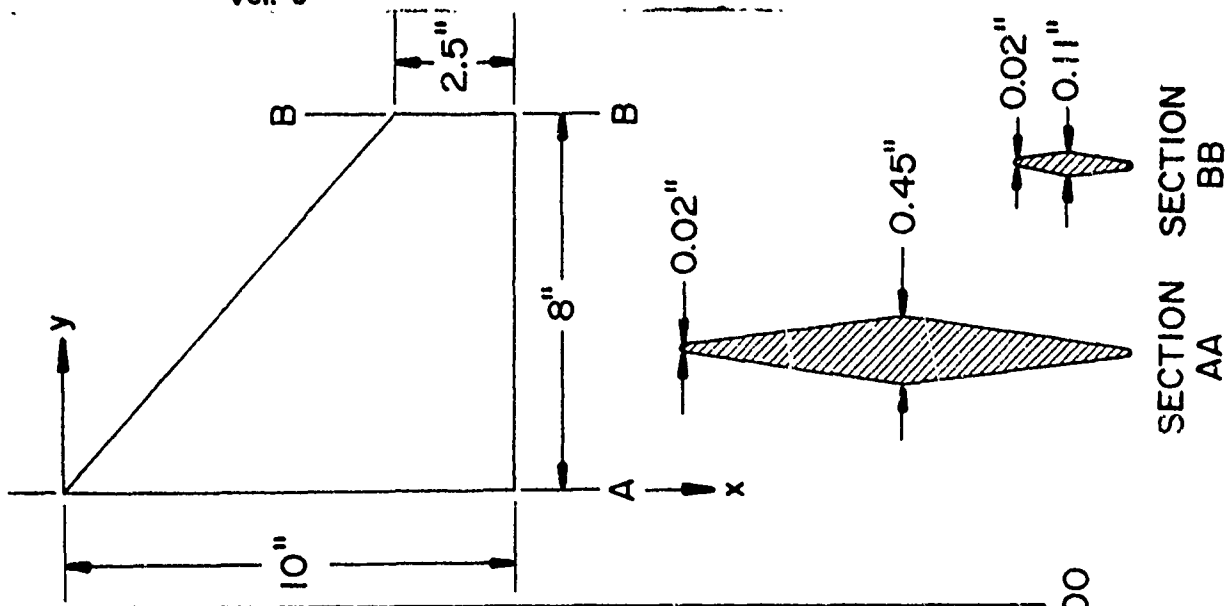


Figure 7: Temperature Dependence of the Frequencies of a Clipped Delta Wing for Quadratic Chordwise Temperature Distribution.

NOTATION

— Rigid Airfoil

- - - Flexible Airfoil

α is the rigid airfoil angle of attack (Positive Clockwise)

δ_f is the slope induced by structural flexibility (Positive Clockwise)

δ_{uR} and $\delta_{\ell R}$ are the rigid body surface slopes measured relative to the x axis

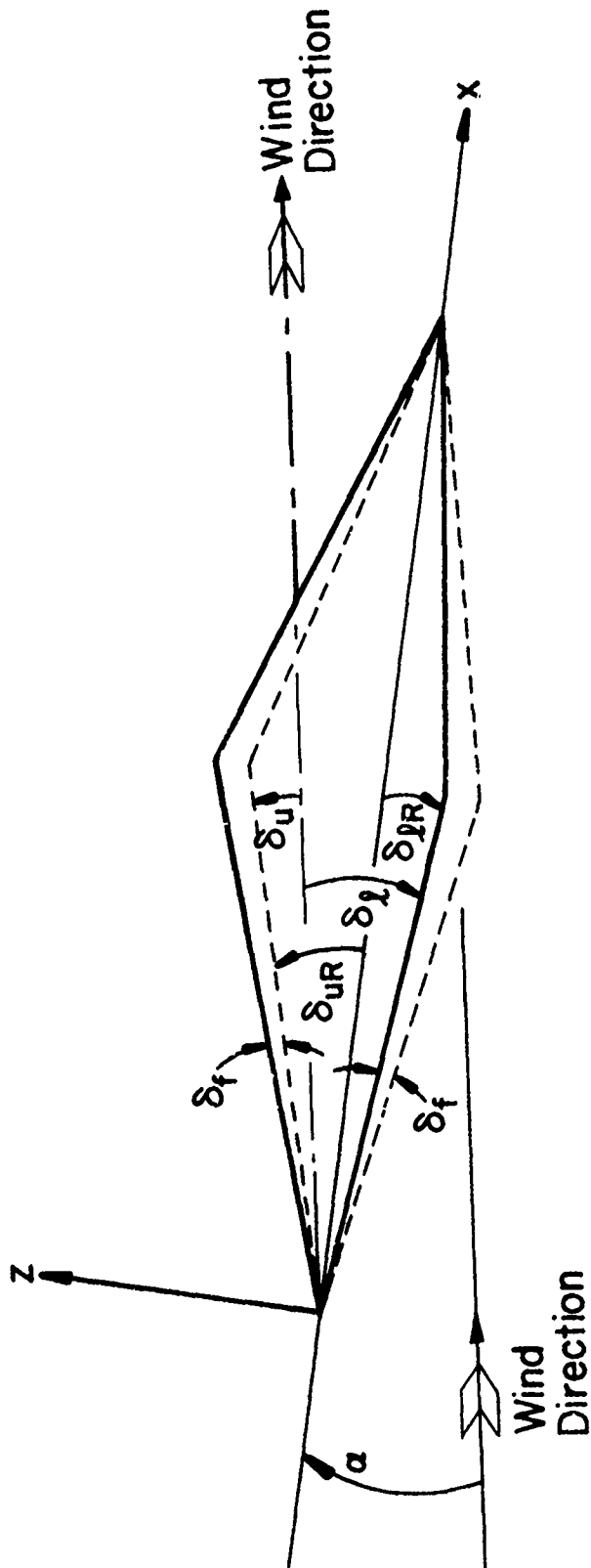
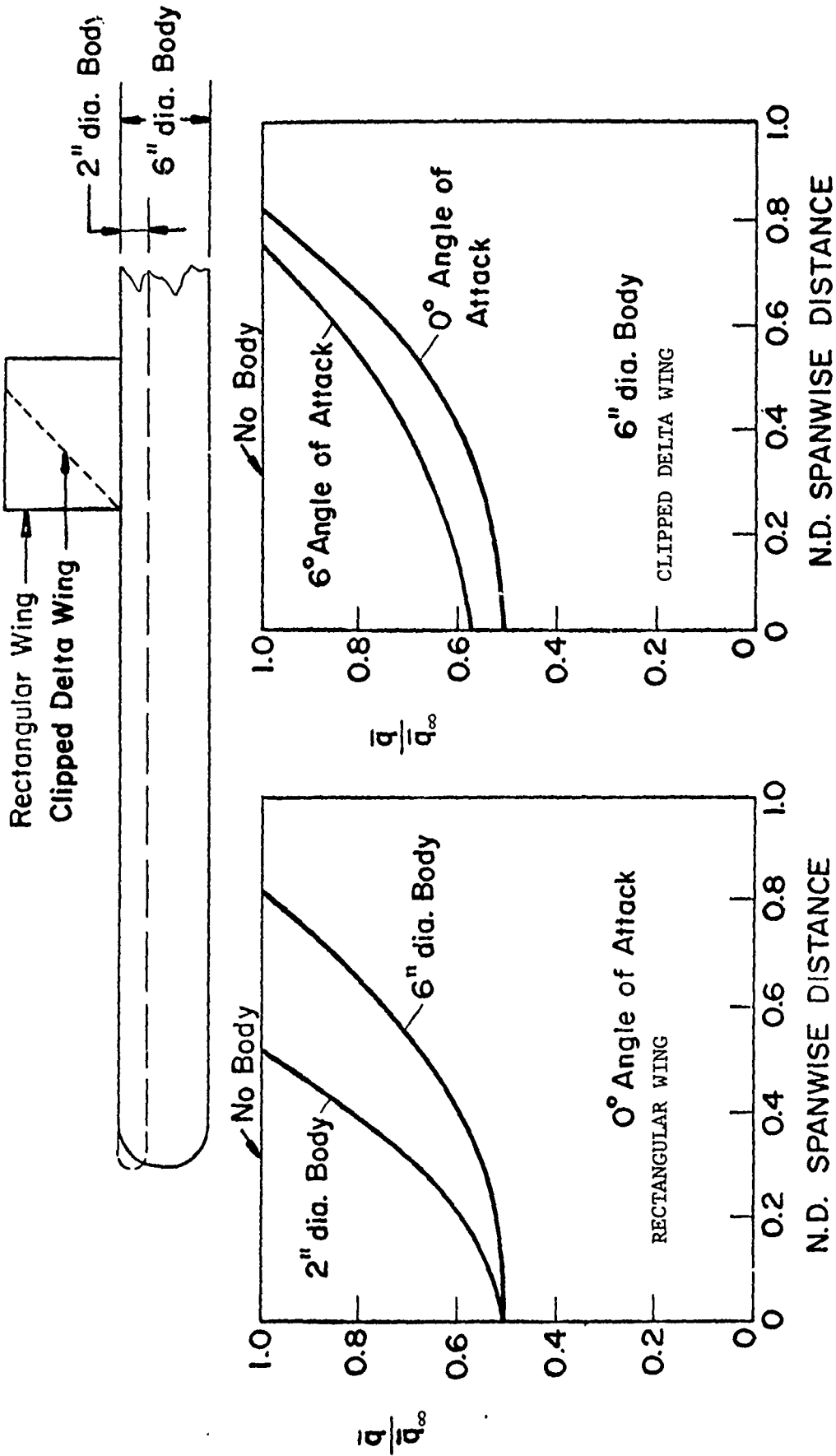


Figure 9 Definition of Slope Components for Rigid and Flexible Airfoils



10. IN. CHORD (ROOT 2.5 IN. TIP CHORD FOR THE CLIPPED DELTA WING. 8. IN. SPAN. WING ROOT LEADING EDGE AT 2.5 IN. BEHIND MISSILE BODY NOSE. MACH NUMBER IS 5.0.

Figure 10: Typical Examples of Dynamic Pressure Defect to Illustrate Importance of Body Diameter Angle of Attack and Wing Planform

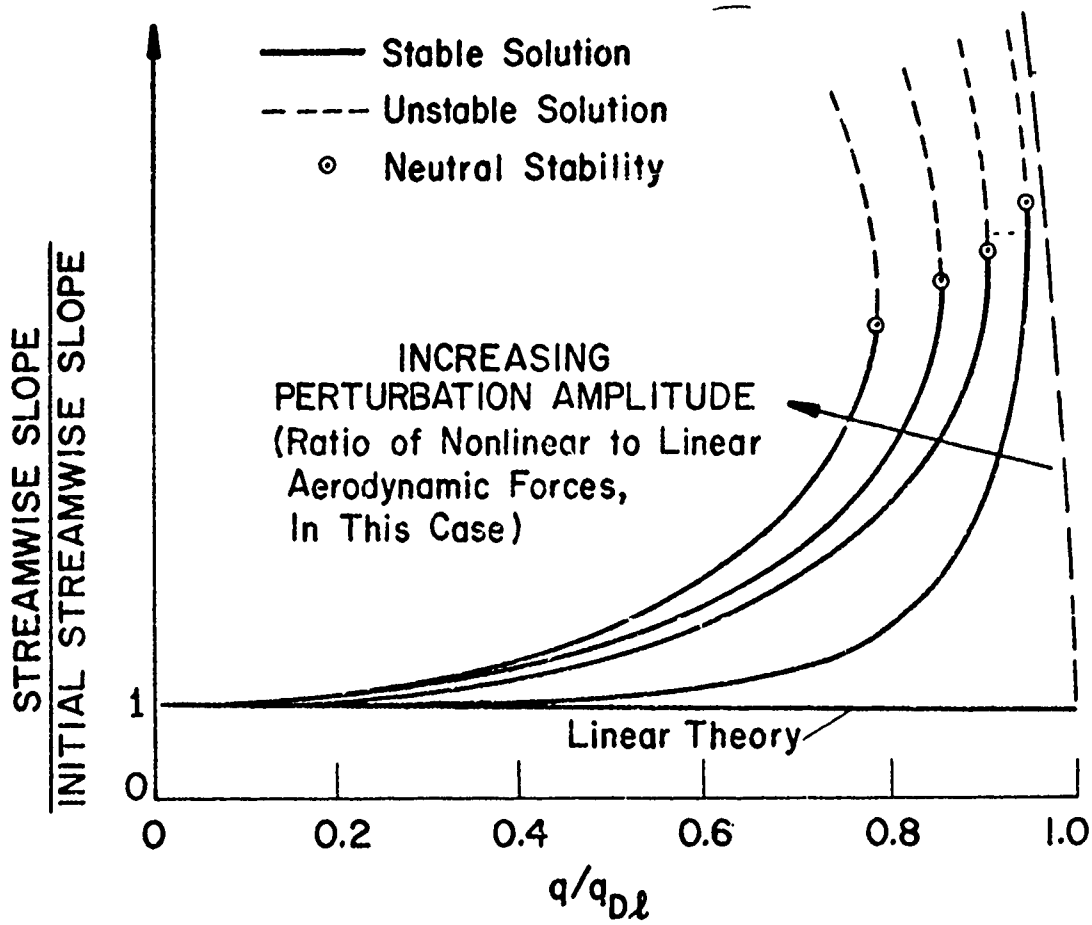


Fig. 14 Static Aeroelastic Stability of a Lifting Surface (from [12]. q_{DL} Denotes Linear Divergence Dynamic Pressure

PAPER NO. 43

A REVIEW OF THE INTEGRAL THEORY OF IMPACT*

Thomas B. McDonough

Aeronautical Research Associates of Princeton, Inc.

50 Washington Road

Princeton, NJ 08540

*This research is supported by the Naval Surface Weapons
Center under Contract N60921-74-C-0313 (ART Program)

NOMENCLATURE

A	surface area of particle
b	particle width
C_D	drag coefficient
E	internal energy of particle
K	kinetic energy of particle
l	particle height
l_0	initial particle height, width, or length
m_p	particle mass
m_t	target mass removed by the impact
p	pressure
R	radius of curvature of the flowing shocked layer
S	axial component of stress
t	time
V_f	speed of particle front
V_L	lateral velocity of particle edge
V_{cm}	speed of the particle's mass center
V^*	characteristic velocity of the target
y	penetration depth
$\dot{\epsilon}$	axial component of stretching tensor
ρ_p	density of particle
ρ_t	density of target
σ_1	strength of target normal to surface
σ_2	strength of target parallel to surface
σ_y	yield strength
ϕ	incidence angle along surface of shocked layer

ξ, η rectangular coordinates originating at particle's mass center

μ_p viscosity of liquid droplet

γ surface tension

Dimensionless Parameters

$$\bar{b} \equiv \frac{b}{\ell_0}$$

$$\bar{v}_1 \equiv \frac{v_1}{v^*}$$

$$\bar{E} \equiv \frac{E}{1/2 m_p v^{*2}}$$

$$\bar{y} \equiv \frac{y}{\ell_0}$$

$$\bar{\ell} \equiv \frac{\ell}{\ell_0}$$

$$\bar{\rho} \equiv \frac{\rho_t}{\rho_p}$$

$$\bar{m} \equiv \frac{m_t}{m_p}$$

$$\bar{\sigma} \equiv \frac{\sigma_2}{\sigma_1}$$

$$\bar{R} \equiv \frac{R}{\ell_0}$$

$$\tau \equiv \frac{v^*}{\ell_0} t$$

A REVIEW OF THE INTEGRAL THEORY OF IMPACT

by

Thomas B. McDonough

An approximate theory for impact cratering by high speed particles is presented with a comparison of observed and predicted trends. The goal of the theory is to provide a simple, economical, and rational approach with which observed experimental trends can be understood. Although the theory is quite simple, it provides considerable insight into the impact phenomenon. The theory retains easy visibility to the primary causes of impact response in terms of materials properties or impact conditions. It is based on global conservation laws and heuristic arguments. Starting from the simplest form, the formulation has been modified step by step, adding further complexities only as required to bring the predictions into better agreement with experimental observations.

Some interesting applications of the theory are presented. For example, the theory accounts for the "state" of the impacting particle during the cratering process. A comparison of predictions with experimental data illustrates the importance of this effect. Furthermore, hard particles are predicted to bound the penetration depth for all normal impacts; the test data show this same behavior when plotted in terms of the appropriate dimensionless parameter. There-

fore, the simple hard particle theory may be useful for design purposes. Another interesting consequence of the theory is that the impact strength of the target can be determined directly from hard particle impact data. Such values correlate linearly with Brinell Hardness for lead, copper, and steel targets. The results of recent applications of the theory to a study of normal impact of ice and water particles are presented. Experimental and flight environments and the effect of a shock layer are included in the study.

1. INTRODUCTION

Recently there has been developed at A.R.A.P. a new analytical approach to the calculation of particle impact.^[1] This new approach was developed to provide a simple rational approach to the problem of terminal ballistics - one which is capable of giving insight into the impact process. Hopefully, this simple approach will complement the use of experiments and multielement computational codes.

The simplified theory is still under development at A.R.A.P. Its realization has followed a step-by-step procedure and has followed heuristic arguments. The theory bears a relationship to an exact solution similar to that borne by momentum integral methods for calculating shear layers to a complete solution.

In the following the present state of the theory is summarized and two applications are presented.

2. BRIEF REVIEW OF THEORY

The new analytic approach is a simple integral method that brings out the physics of the phenomena being studied. Several trends, which have been observed experimentally, have been explained by this approach. An impacting particle is characterized by a single cell representation, but straining of the particle is permitted consistent with an assumed internal velocity field. Using this approximate mode for deformation, the global conservation equations are derived exactly and studied numerically. The theory is a simple one and further complexities are added only as deemed necessary by the particular phenomena under study at the time.

To begin, we characterize the particle as a rectangular parallelepiped of square planform. For normal impact, we assume the particle deforms but that it remains a rectangular parallelepiped. Target penetration by "our particle" is idealized by Figure 1; the height and width of the particle are denoted by l and b , the mass-center velocity by V_{cm} , and the penetration depth by y . It is convenient to draw a "free-body" diagram of the particle - illustrated by Figure 2. The only external forces acting on the body are the contact stresses acting at the contact surface between the particle and the target. In Figure 2, the contact stresses are represented by the total force acting

Deforming particle model

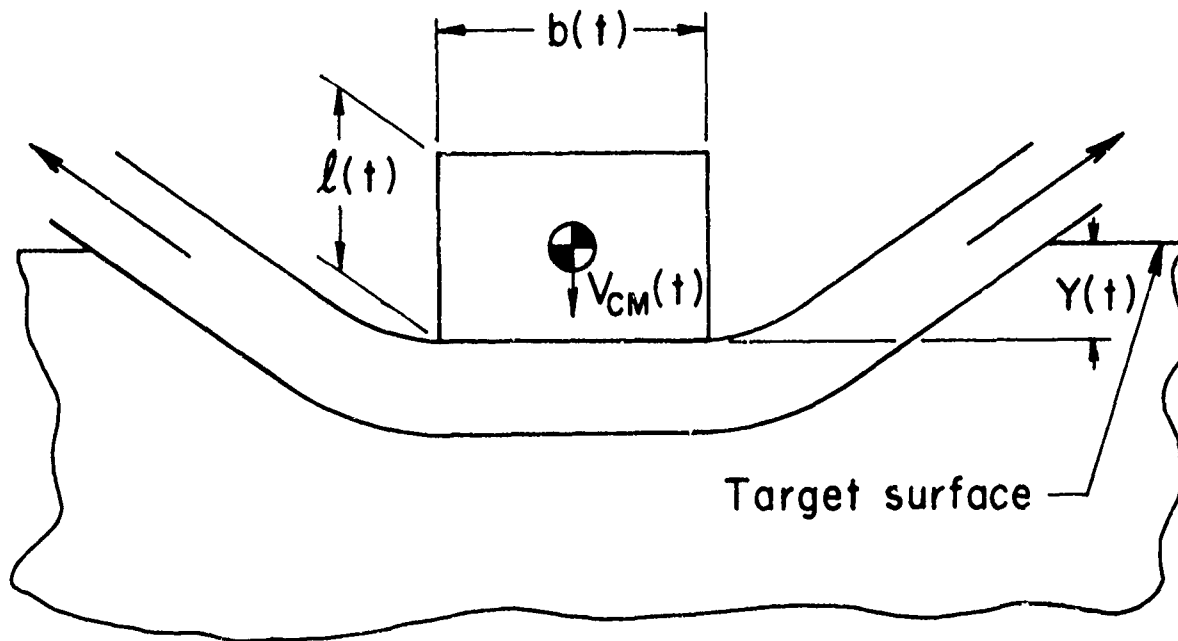


Figure 1

Free-body diagram of particle

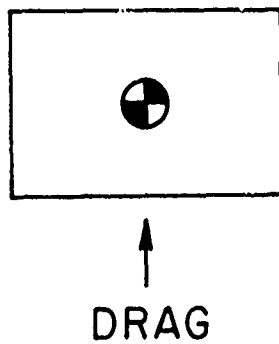


Figure 2

on the particle - denoted "Drag."

We make one more assumption before representing conservation laws; we neglect the compressibility of the particle. The global form of the conservation laws for the particle is given exactly by the following equations (for mass, linear momentum, and energy):

$$\rho b^2 = \text{constant}$$

$$m_p \frac{dV_{cm}}{dt} = - \text{Drag}$$

$$\frac{dK}{dt} + \frac{dE}{dt} = - \text{Drag} \times V_{\perp} \quad (1)$$

where m_p is the particle mass, K and E are the kinetic and internal energy of the particle, and V_{\perp} is the penetration velocity - i.e.,

$$V_{\perp} = \frac{dy}{dt} \quad (2)$$

To complete the system of equations, we must relate K and E to kinematic variables and specify the drag force. For the former, we specify more about the mode of deformation of the particle. The simplest assumption we can make is to assume the material velocity varies linearly with position in the particle. If we define a coordinate system ξ, η centered instantaneously at the mass center and denote the material velocity by V_x, V_y , then the deformation mode may be represented as follows:

$$V_x = \frac{\xi}{b/2} \frac{1}{2} \frac{db}{dt}$$

$$V_y = V_{cm} + \left(\frac{\eta}{\ell/2}\right) (V_{\perp} - V_{cm}) \quad (3)$$

with a similar distribution (similar to V_x) for the third direction. This situation is illustrated by Figure 3. If we substitute the above into the definition of kinetic energy, i.e.,

$$K = \int_{vol.} \frac{\rho_p}{2} (v_x^2 + v_y^2 + v_z^2) dv \quad (4)$$

and integrate over the particle volume, the following expression is derived:

$$K = \frac{1}{2} m_p V_{cm}^2 + \frac{m_p}{6} \left[\frac{1}{2} \left(\frac{db}{dt} \right)^2 + (V_{\perp} - V_{cm})^2 \right] \quad (5)$$

These two terms represent the kinetic energy associated with the mass center motion and the relative kinetic energy, respectively. This expression can be recast into a more convenient form. Since our particle is homogeneous, the mass center coincides with the geometric center at all times. Therefore, we have

$$V_{\perp} - V_{cm} = \frac{1}{2} \frac{d\ell}{dt} \quad (6)$$

From (1)¹ we derive the following:

$$\frac{db}{dt} = - \left(\frac{b}{2\ell} \right) \frac{d\ell}{dt} \quad (7)$$

Substituting (6) and (7) into (5), we derive the recast form for K :

$$K = \frac{1}{2} m_p V_m^2 + \frac{1}{2} m_p \left[\frac{1}{2} \left(\frac{b}{\ell} \right)^2 + 1 \right] \frac{\left(\frac{1}{2} \frac{d\ell}{dt} \right)^2}{3} \quad (8)$$

Deformation field within particle

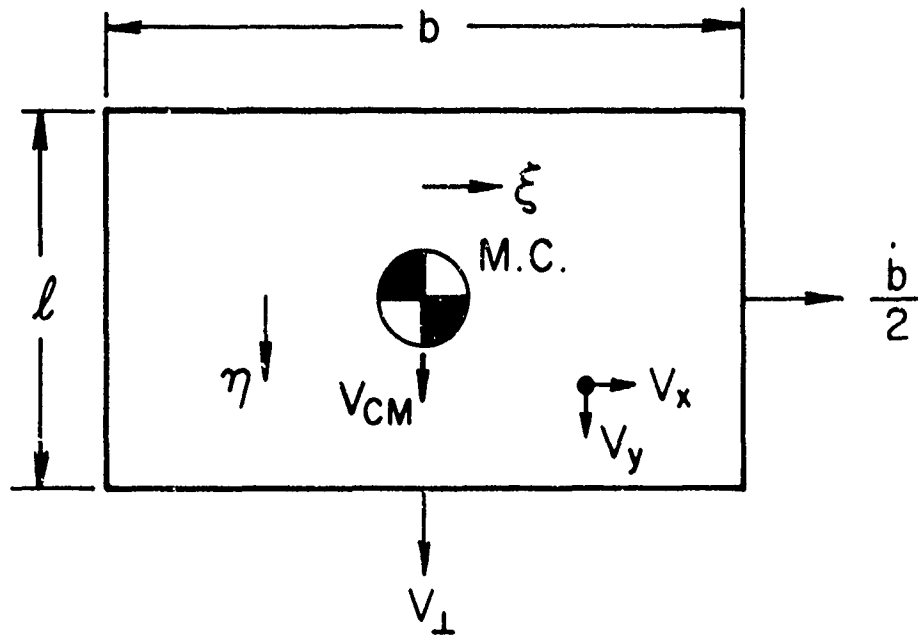


Figure 3

Now consider the internal energy. We assume two modes of storage. The first is a density proportional to the mass of material and the other, which is the surface energy, is proportional to the surface area. Also, since we do not allow energy transfer by heat in our model, the only source of internal energy is the stress power. Consistent with our kinematic model, the stretching is isochoric; therefore, the dissipation is independent of pressure. Because the shear stress depends only on the stretching at any point within the particle and the stretching is uniform within the particle, the shear stress is uniform within the particle. If we replace the density term by the stress power consistent with our model, the internal energy can be written as follows:

$$\frac{dE}{dt} = \frac{3}{2} S \dot{\epsilon} \times \text{Vol.} + \gamma \times \frac{d\text{Area}}{dt} \quad (9)$$

where S and $\dot{\epsilon}$ are the axial components of the stress and stretching tensors and γ is the surface energy. After expanding the geometry terms in terms of dimensions of the cube, (9) becomes

$$\frac{dE}{dt} = \frac{3}{2} S \frac{d\ell}{dt} b^2 + 4\gamma \left[(b + \ell) \frac{db}{dt} + b \frac{d\ell}{dt} \right] \quad (10)$$

where the axial component of the stretching tensor was computed from (3) and (6); i.e.,

$$\dot{\epsilon} = \frac{V_{\perp} - V_{cm}}{\ell/2} = \frac{\dot{\ell}}{2} \quad (11)$$

Finally, we address the constitutive relations, which are specified by defining the relations between S and ϵ . Any model of behavior can be treated, but, because of their general usefulness, four models have been used:

Hydrodynamic Model

$$S = 0 \quad (12)$$

Newtonian Fluid Model

$$S = 2\mu\dot{\epsilon} \quad (13)$$

Rigid Plastic Model

$$S = -\frac{2}{3}\sigma_y \text{ for } \dot{\epsilon} < 0 \quad (14)$$

Rigid Model

$$\dot{\epsilon} = 0 \quad (15)$$

The resistive force is taken proportional to the momentum change in the target material:

$$\text{Drag} = \left(\frac{C_D}{2}\right) \rho_t v_{\perp}^2 b^2 \quad (16)$$

As long as the (Newtonian) pressure is greater than the target material strength, i.e., $(\rho_t v_{\perp}^2 > \sigma_1)$, the particle penetration will continue. Eventually, as the particle slows down, the strength will not be exceeded and penetration ceases. A characteristic velocity is defined for the target material (V^*), which is equivalent to its impact strength (σ_1):

$$V^* = \sqrt{\frac{\sigma_1}{\rho_t}} \quad (17)$$

In the model, particle penetration is permitted until the velocity (V_{\perp}) reduces to the characteristic velocity. At this point, the penetration ceases.

The next step is to predict the volume or mass removed from the target. For this we visualize the flow of target material around the particle as illustrated by Figure 4. The layer thickness ($b/4$) follows from mass conservation.

The two layers (particle and disturbed target) flowing outward carry significant momentum. This flow is turned upward by the pressure difference across the double layer. The pressure from below is taken equal to the Newtonian pressure while that from above is zero. We evaluate the curvature (R) from the following equation of motion:

$$\Delta p = \rho_t V_{\perp}^2 \cos^2 \phi = \int_{R - \frac{b}{4} - \ell}^R \frac{\rho V^2}{z} dz \quad (18)$$

If we assume the lateral velocity is constant through the thickness of each layer independently, the integral has the following approximate solution:

$$\int_{R - \frac{b}{4} - \ell}^R \frac{\rho V^2}{z} dz = \rho_p (V_p)^2 \ln \left(\frac{\frac{4R}{b} - 1}{\frac{4R}{b} - 1 - \frac{4\ell}{b}} \right) + \rho_t V_t^2 \ln \left(\frac{\frac{4R}{b}}{\frac{4R}{b} - 1} \right) \quad (19)$$

Cavity formation

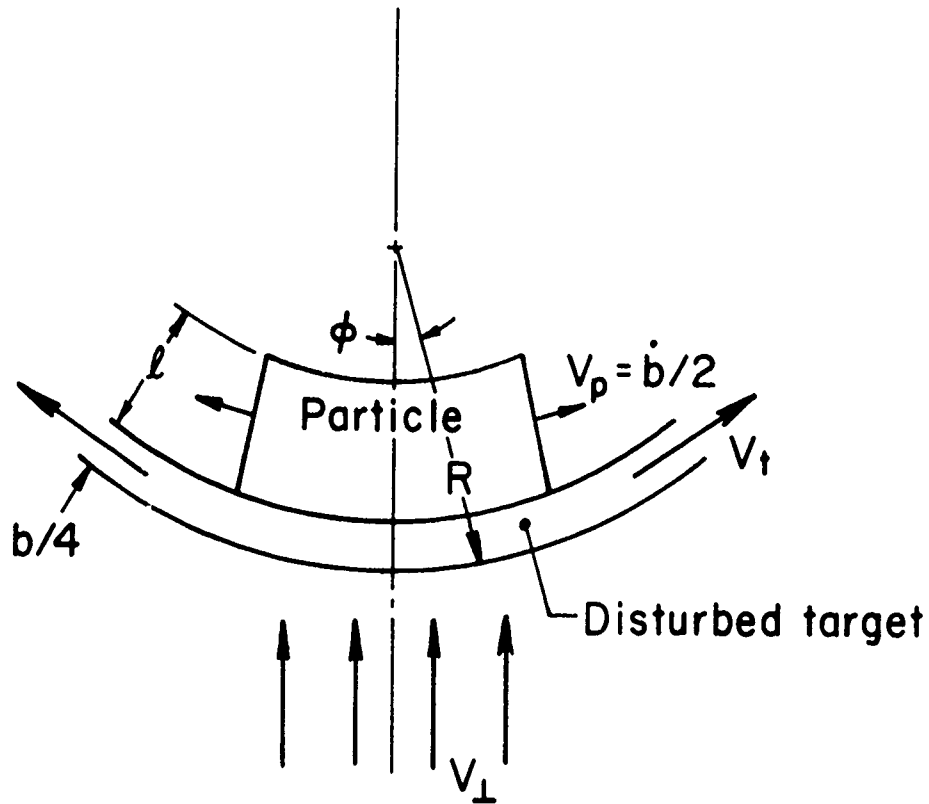


Figure 4

This is substituted into Equation (18) and the result is rearranged and nondimensionalized:

$$\cos^2 \phi = \frac{1}{\rho} \frac{\frac{1}{2} \left(\frac{d\bar{b}}{d\tau} \right)^2}{V_{\perp}^2} \ln \left(\frac{\frac{4\bar{R}}{\bar{b}} - 1}{\frac{4\bar{R}}{\bar{b}} - 1 - \frac{4\bar{\ell}}{\bar{b}}} \right) + \ln \left(\frac{\frac{4\bar{R}}{\bar{b}}}{\frac{4\bar{R}}{\bar{b}} - 1} \right) \quad (20)$$

where the following was used:

$$\frac{\rho_p V_p^2}{\rho_t V_t^2} = \frac{1}{\rho} \left(\frac{\dot{b}/2}{V_{\perp}} \right)^2 \quad (21)$$

This is the case because both V_p and V_t vary linearly with distance from the center. In the above expression the values at the edge of the particle are used. Equation (20) is the final form of the equation which must be solved for the curvature \bar{R} . The shape of the cavity that is created by the flow at a typical instant during the penetration is illustrated by Figure 5a. The final shape of the cavity is illustrated by Figure 5b; as suggested by the figure, it is determined by superposing all of the shapes computed at many time steps during the penetration.

Figure 5a shows a cavity with vertically straight sides. This is caused by the transverse strength of the target material. To analyze this we assume the flow will be turned up at an angle θ by a rigid wall and illustrate the situation by Figure 6. The Newtonian pressure in the flowing layer (produced by the momentum flux from the undisturbed region)

Cavity shape

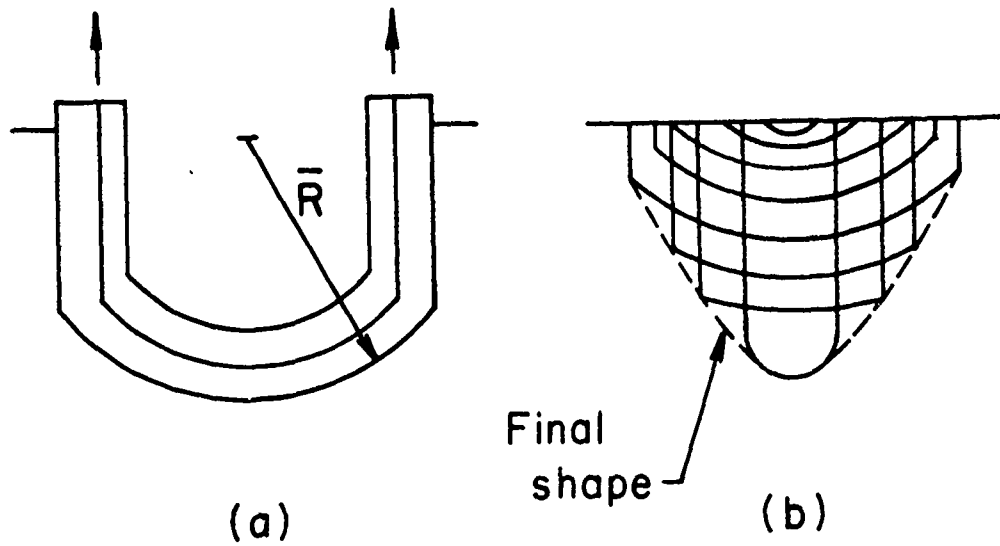


Figure 5

Flow interaction with rigid wall

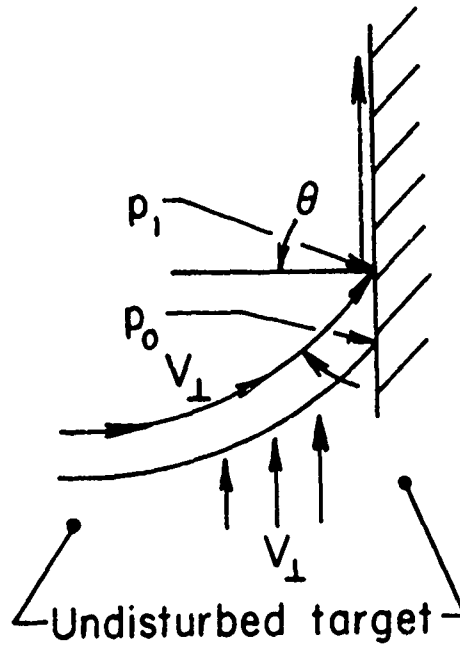


Figure 6

at the angle θ is

$$P_o = \rho_t V_{\perp}^2 \cos^2 \theta \quad (22)$$

To turn the flow vertical requires a pressure increase equal to the horizontal momentum flux of both layers:

$$\Delta P = \frac{\ell \rho_p \left(\frac{\dot{b}}{2}\right)^2 + \left(\frac{b}{4}\right) \rho_t V_{\perp}^2}{\left(\ell + \frac{b}{4}\right)} \cos^2 \theta \quad (23)$$

Therefore, the wall must sustain a pressure of

$$P_1 = P_o + \Delta P = \left[\left(1 + \frac{1}{\frac{4\ell}{b} + 1}\right) \rho_t V_{\perp}^2 + \frac{\frac{4\ell}{b}}{\left(1 + \frac{4\ell}{b}\right)} \rho_p \left(\frac{\dot{b}}{2}\right)^2 \right] \cos^2 \theta \quad (24)$$

or it cannot turn the flow. If we equate this pressure to the transverse strength of the target (σ_2), we can solve for θ_1 - the angle at which the flow will be turned:

$$\theta_1 = \cos^{-1} \left[\frac{\sigma_2}{f \rho_t V_{\perp}^2} \right]^{1/2} = \cos^{-1} \left[\frac{\bar{\sigma}}{f \bar{V}_{\perp}^2} \right]^{1/2} \quad (25)$$

where

$$f = \left(1 + \frac{1}{\frac{4\bar{\ell}}{b} + 1}\right) + \frac{\left(\frac{4\bar{\ell}}{b}\right) \left(\frac{1}{2} \frac{d\bar{b}}{d\tau}\right)^2}{\left(1 + \frac{4\bar{\ell}}{b}\right) \bar{\rho} \bar{V}_{\perp}^2} \quad (26)$$

This discussion completes the summary of the theory. During its development it was found informative and convenient to work in terms of dimensionless parameters. Those

that are pertinent to the reported results are defined by the nomenclature given at the beginning of this paper.

3. ILLUSTRATIVE PREDICTIONS AND CORRELATIONS
WITH EXPERIMENTS

The solution for the penetration of a strong (non-deforming) particle lends itself conveniently to the evaluation of the characteristic properties. For this case

$$l = b = l_0 \quad (27)$$

(6) gives

$$V_{\perp} = V_{cm} \quad (28)$$

and (1)² reduces to

$$\rho_p l_0 \frac{dV_{\perp}}{dt} = \left(\frac{C_D}{2}\right) \rho_t V_{\perp}^2 \quad (29)$$

Using (2) this equation may be arranged as follows

$$\frac{dV_{\perp}}{V_{\perp}} = \frac{C_D}{2} \frac{\rho_t}{\rho_p} \frac{1}{l_0} dy \quad (30)$$

which in turn yields the following solution:

$$\bar{\rho} \bar{y}_{max.} = \frac{1}{\left(\frac{\bar{C}_D}{2}\right)} (\ln V_{\perp 0} - \ln V^*) \quad (31)$$

In this equation the barred terms are dimensionless parameters defined in the Nomenclature, $V_{\perp 0}$ is the initial particle velocity (i.e., when $y = 0$), and V^* is the characteristic velocity of the target below which the particle cannot penetrate. If the dimensionless penetration for hard particle test data is plotted on semilogarithmic graph paper versus the dimensional velocity, both the drag

coefficient and the characteristic velocity are easily evaluated. A straight line should fit the data whose slope determines the drag coefficient and whose intercept determines the characteristic velocity. How well the straight line fits the test data, for the velocity range where the particle remains intact, is a measure of the accuracy of this theory.

Published impact data, which include both hard and deforming particles and a range of impact velocity for a fixed target, are scarce. Fortunately, some data were summarized by Hermann and Jones^[2] for steel, copper, and lead targets impacted by several different particles. Tungsten Carbide (WC) particles provide the hard particle data required for the present theory. The WC penetration for each of the targets is plotted, as discussed above, on Figures 7, 8, and 9. The straight lines were drawn by eye through the data, and the target properties were deduced. The range of impact velocity over which the brittle WC particles survive intact is clearly defined by a drastic change in penetration. The straight line fits are surprisingly good.

Armed with the characteristic properties of the three targets, we can predict the penetrations (\bar{z}) for strengthless particles and compare with the test data. These comparisons are shown for three particles for each target by Figures 10, 11, and 12. The WC particle test data should

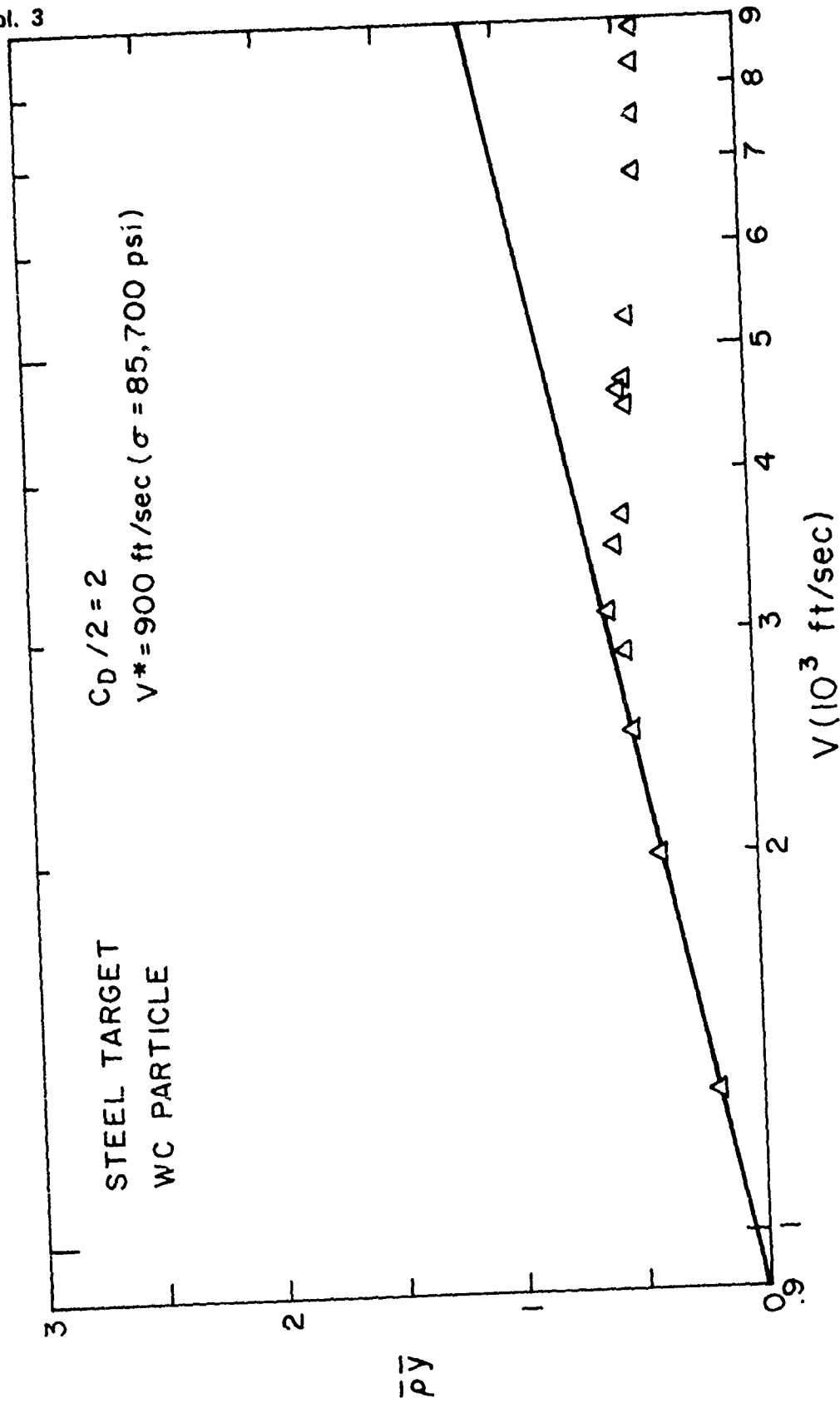


Figure 7

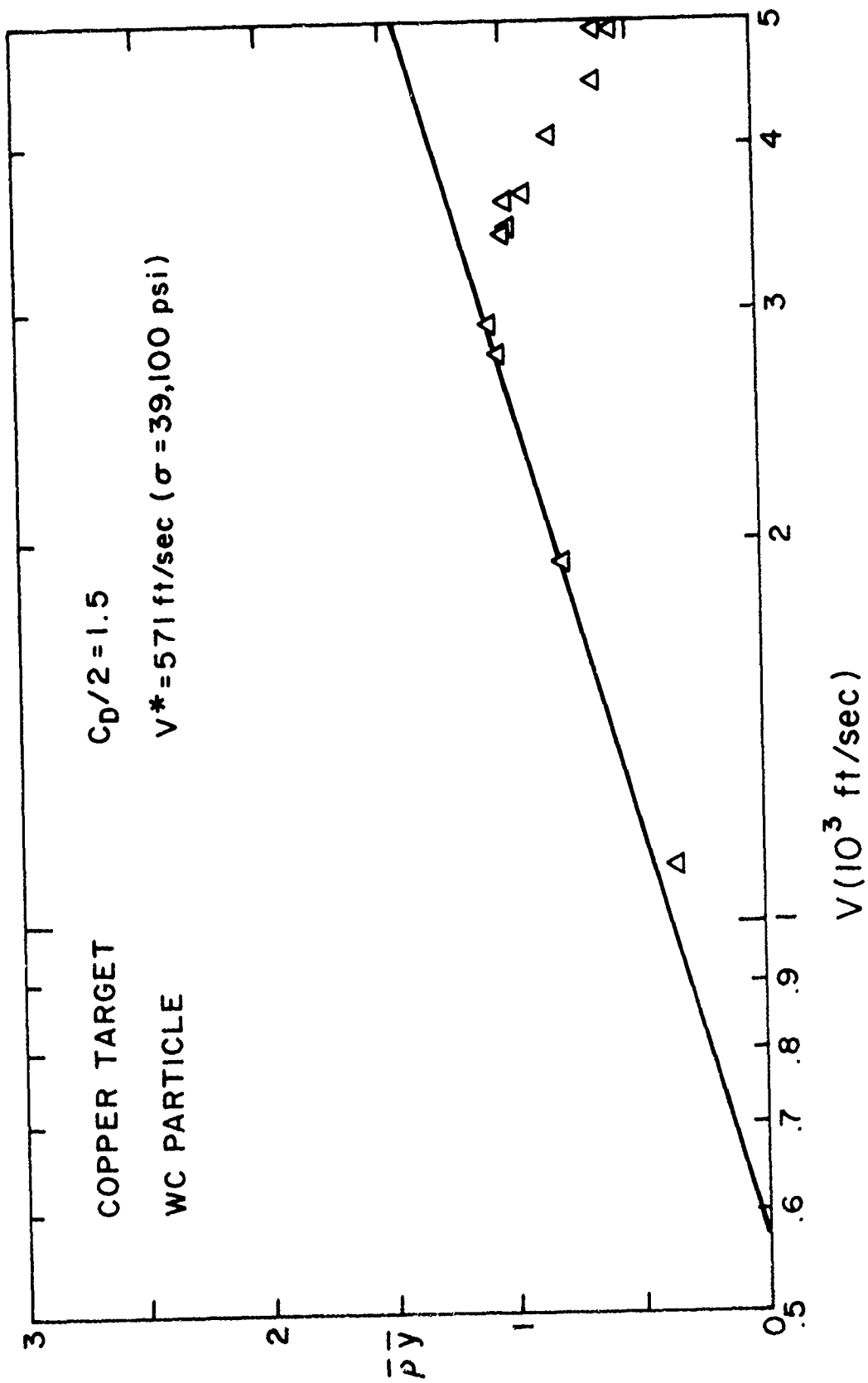


Figure 8

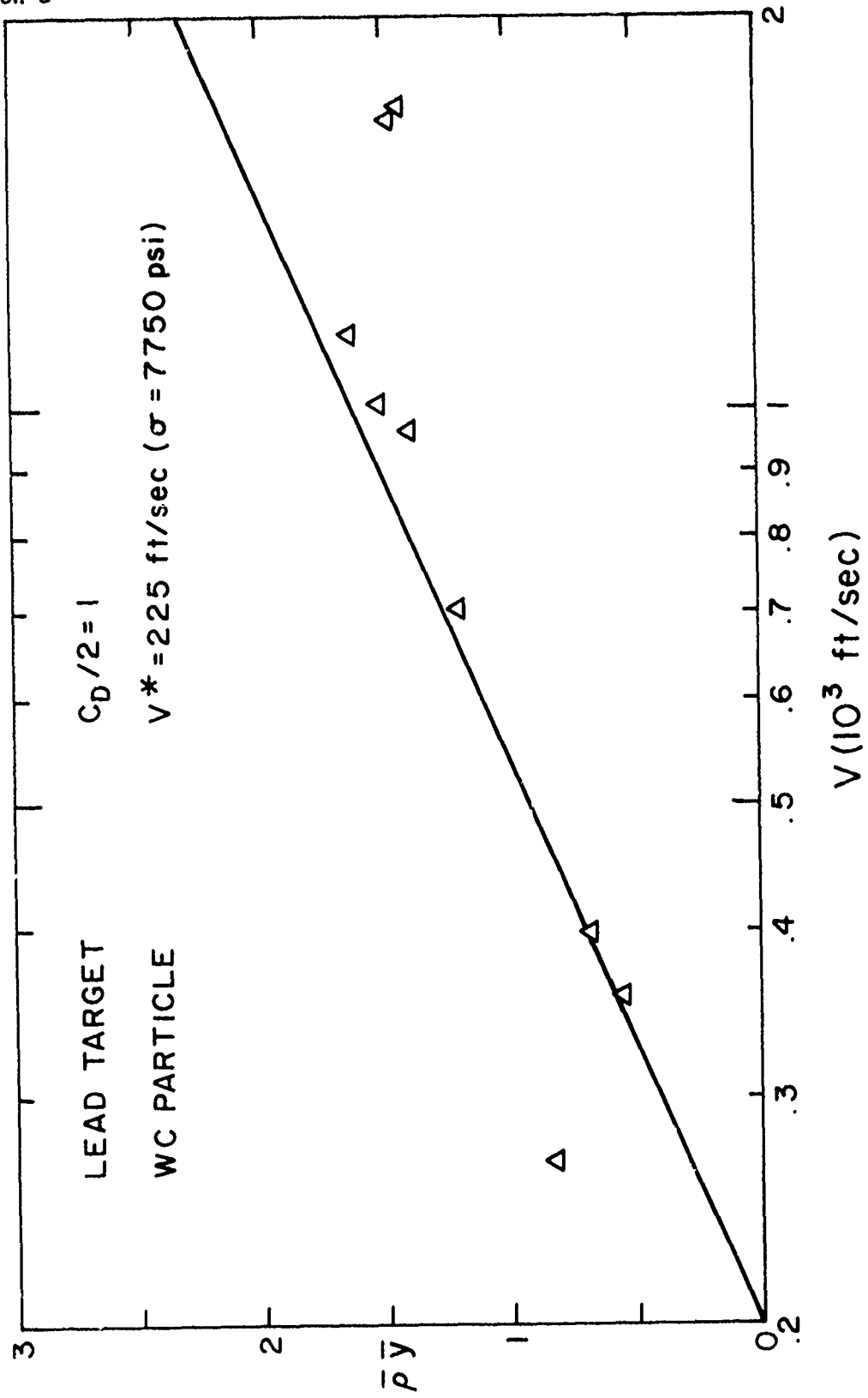


Figure 9

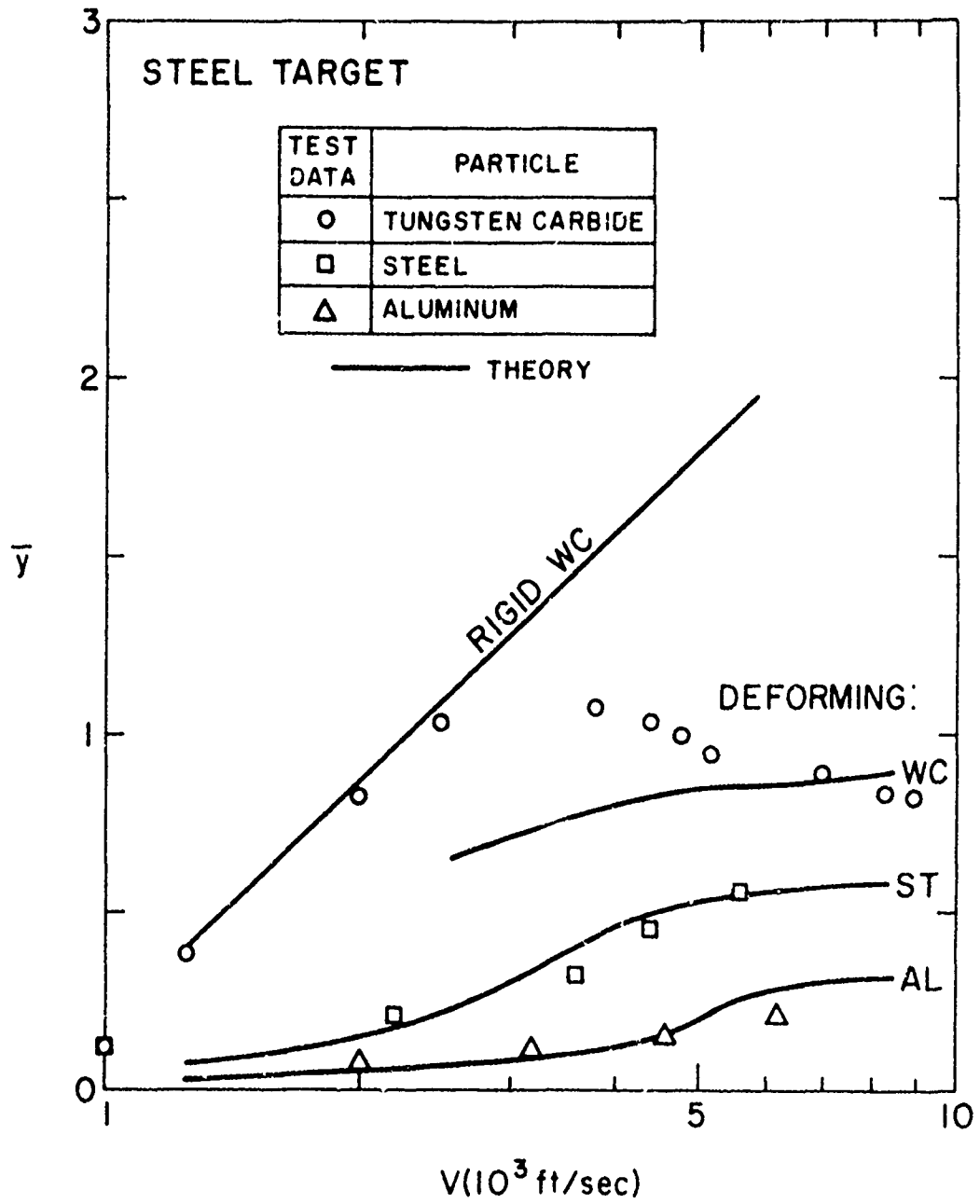


Figure 10

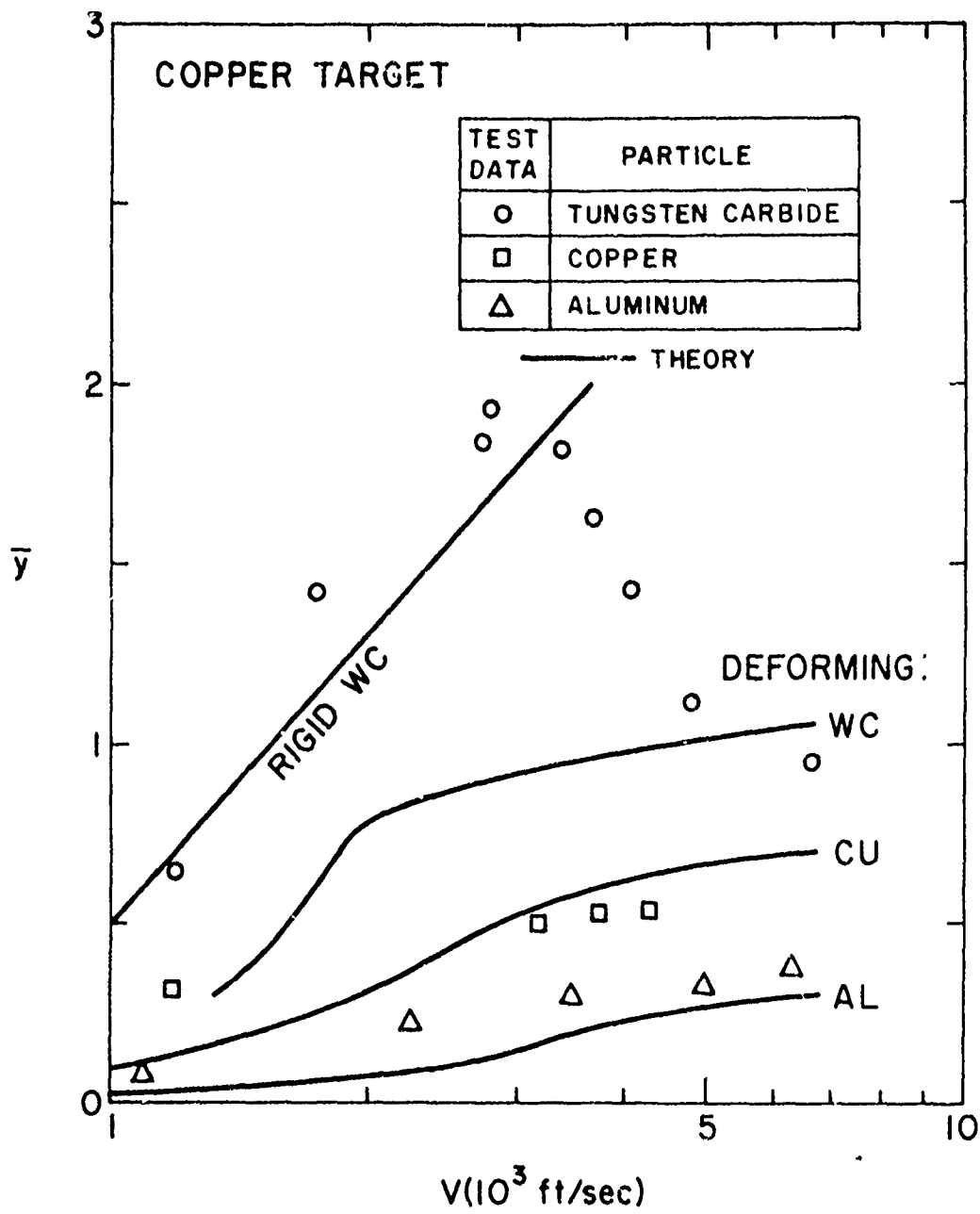


Figure 11

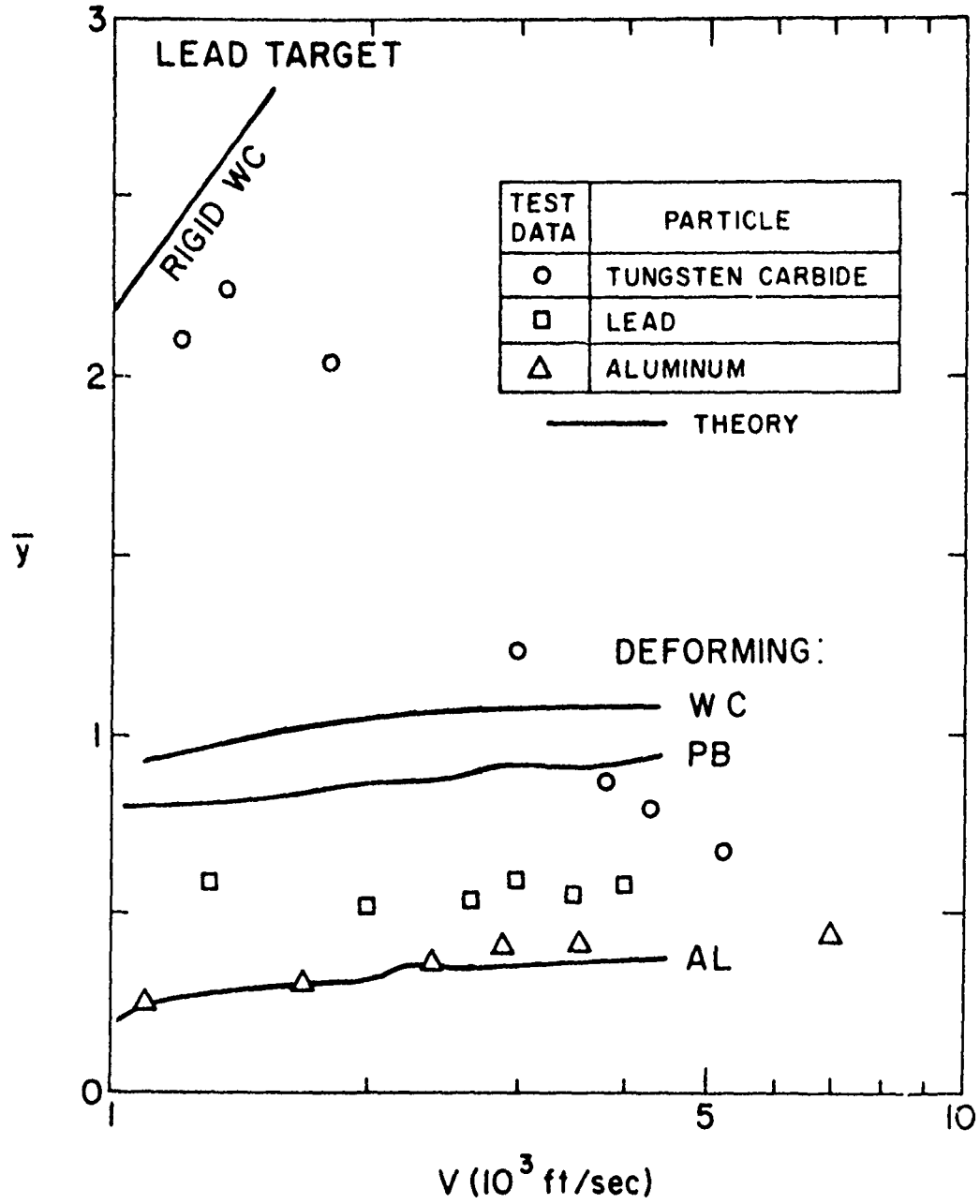


Figure 12

Vol. 3

be compared to the hard particle theory at small impact velocities and to the strengthless theory only at large impact velocities. The excellent correlation of this simple theory with test data suggests that the theory contains the physical parameters which are essential to this phenomenon.

The correlations with the lead data are obviously the worst. Apparently, there are forms of energy dissipation which are important for lead. The next step in the development of this simple integral theory is to study mechanical energy dissipation. The basis for introducing these effects is in the term dE/dt .

4. THE EFFECT OF FILM ENCAPSULATION ON THE IMPACT PROPERTIES OF WATER DROPLETS

Another example of the utility of this theory is borrowed from work performed for the NOL-NSWC.^[3] There is interest in heat shield erosion due to the impact of suspended water droplets in the atmosphere during flight of reentry vehicles. It's important to know the conditions when a droplet impacts the surface of the heat shield - both for understanding flight performance and for developing ground test simulation. The aerodynamic shock layer surrounding a vehicle accelerates and deforms a water droplet which are both important to the impact. Ground test facilities don't reproduce all aspects of flight through a natural rain field; those parameters which are different are always suspect.

To test particles in the NOL Ballistic Range, they are encapsulated in a parylene film. The film is very thin so that its strength is very small; but, compared to the viscosity and surface tension of water, the stiffness of the film may not be negligible. An ice particle is different. Because it has strength, even an unencapsulated particle will not deform (but it will accelerate) while traversing the air shock layer.

At impact the parylene strength is negligible because the pressure generated by the impact of the particle and target is large. With the above rationale in mind, the

behavior of particles traversing the air shock layer is studied. The test simulation is measured by how well the state of an encapsulated particle simulates that of an unencapsulated particle at the time of impact with the target.

Computations were made both with and without the parylene film for the entire range of test conditions. A summary of these conditions is given in Table 1. The computations were based on a target with a nose radius of 0.375 inches. The water and ice particles were spherical and the particle diameter varied from 0.2 to 1.0 mm. The parylene film had a thickness of 2.2μ . All combinations of the two initial velocities (10 and 15 Kft/sec) and two range pressures (0.1 and 1.0 atm) were investigated for each particle. The ambient temperature was assumed to be 70°F . These combinations of range pressure and temperature yield an air density which corresponds to sea level for the high pressure tests and approximately 60 Kft for the low pressure tests.

In addition to the existing data, new test conditions selected to extend the data base to more blunt targets were considered. In order to assist the planning for these tests, a second series of computations was performed. The environmental parameters defining the proposed tests are also summarized in Table 1. For these tests, the target nose radius (2.0 inches) was larger and the particles (0.05 to 0.2 mm)

Table 1.

TEST CONDITIONS FOR WATER & ICE IMPACTS INTO GRAPHITE		
Parameter	Value of parameter	
	Existing NOL Data Base	Extension to NOL Data Base
Nose radius (inches)	0.375	2.0
Particle diameter (mm)	0.2, 0.5, 1.0	0.05, 0.1, 0.2
Parylene C film thickness (microns)	2.2	0.5, 2.2
Particle velocity (K ft/sec)	10, 15	15
Range pressure (atm)	0.1, 1.0	0.1, 1.0

were smaller than for the existing data base. In addition to the nominal parylene thickness of 2.2μ , a second film thickness of 0.5μ was investigated. In this series, only one particle velocity (15 Kft/sec) was considered for each of the two values of range pressure.

Because of the high strain rates associated with the impact process, the parylene film will break immediately upon impacting the target. Hence, the film can only influence the impact process by altering either the shape or velocity of the particle prior to impact, i.e., in the shock layer ahead of the target.

In effect, the encapsulated particle impacts a layer of high pressure air prior to reaching the target. This shock layer imposes a drag force on the particle. The magnitude of the force depends on the density of the air in the shock layer, as well as the velocity and shape of the particle. The total deceleration depends on the time integral of the drag force which clearly depends on the thickness of the shock layer (i.e., the shock standoff distance).

The particle is also deformed while traversing the shock layer. Usually, the axial dimension is decreased while the lateral dimensions are increased. Particle deformation not only depends on shock density and standoff distance, but also on the ability of the particle to resist

deformation (i.e., the particle inertia, viscosity and surface tension).

The shock standoff distance was computed using data supplied by the NOL. Figure 13 shows shock standoff distance normalized by target diameter as a function of velocity and pressure. Data are included from many low pressure tests. Note that the highest pressure for which data are shown corresponds to 0.026 atm (20 mm Hg), well below the lowest pressure (0.1 atm) considered in this study. It should also be noted that for a given velocity, the standoff distance clearly tends toward the equilibrium chemistry limit as the pressure increases. As a result of these observations, it was assumed that the shock standoff distance for a given velocity and pressure is given by the equilibrium chemistry curves.

Table 2 summarizes the shock standoff distance for each combination of pressure and particle velocity. The stand-off distance decreases with increasing velocity and with decreasing pressure. The most extreme cases differ by approximately 30%.

Table 3 summarizes the density ratio across the normal shock at the nose tip. Data are given for both the ideal gas assumption and real gas data correlations. For this ideal gas, the density ratio is independent of pressure and a weak function of velocity for the hypersonic velocities

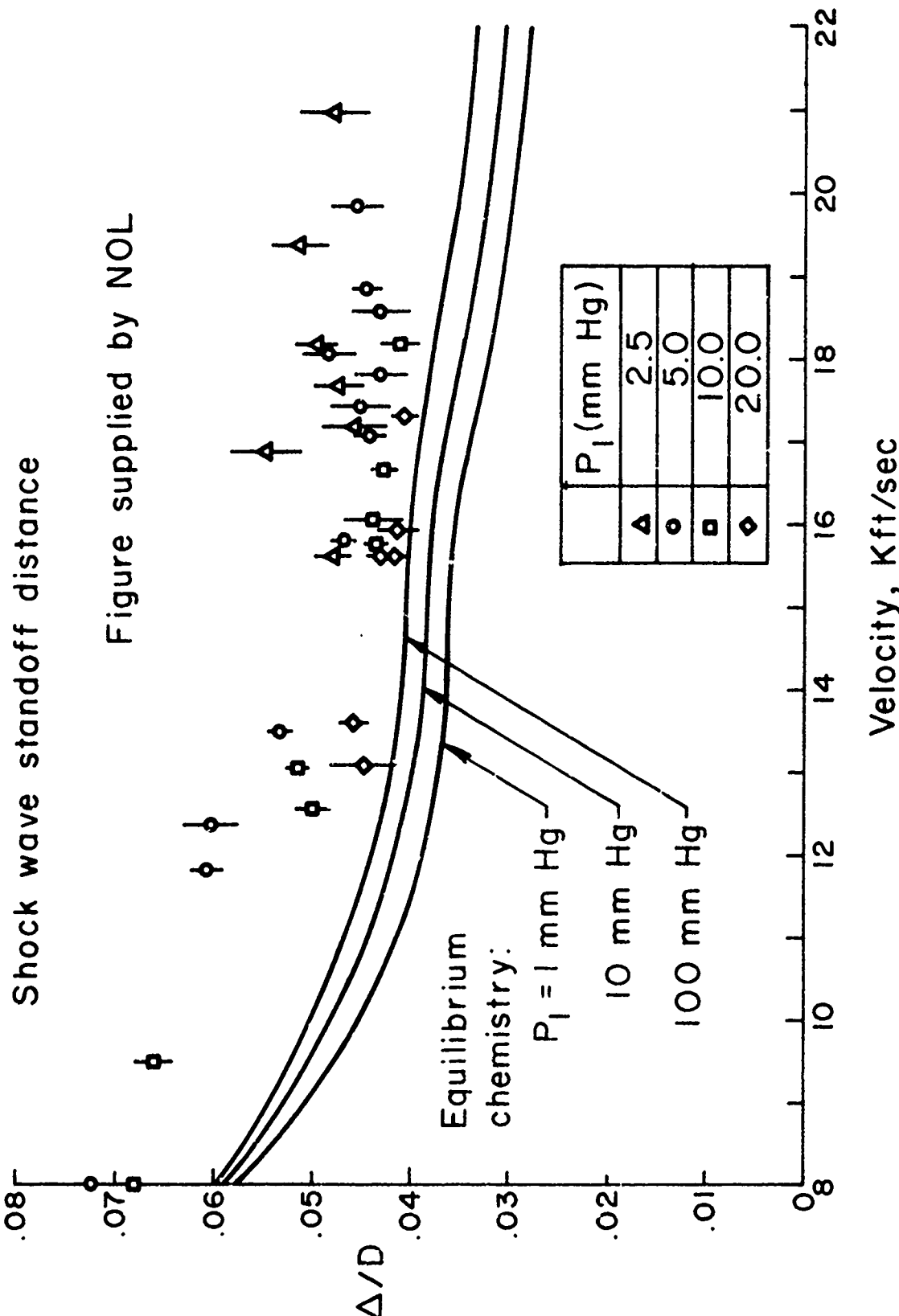


Figure 13

Table 2.

SHOCK WAVE STANDOFF DISTANCE NORMALIZED BY TARGET DIAMETER (Δ/D)		
Pressure (Atm)	Velocity (Kft/sec)	Δ/D
1.0	10	0.052
1.0	15	0.042
0.1	10	0.050
0.1	15	0.040

Table 3.

DENSITY RATIO ACROSS NORMAL SHOCK (FOR AIR)			
Pressure (Atm)	Velocity (Kft/sec)	Density ratio	
		Ideal gas	Real gas
1.0	15	5.84	9.40
0.1	15	5.84	10.0
1.0	10	5.64	7.7
0.1	10	5.64	8.1

being considered. Based on "real gas" correlations, the density ratio is a stronger function of the velocity and, in addition, a small pressure or "altitude" dependence is indicated. In all cases, the density ratio for the real gas is larger than for the ideal gas.

Particle Properties - Water and Ice

Table 4 lists the pertinent physical properties for the water and ice particles. The constitutive equations for the water particle are based on the viscous model which was described earlier. Each of the properties for water is for standard conditions of temperature and pressure. For purposes of this analysis, the temperature dependence of each property was ignored and the value was held constant for each computation.

The ice particle was assumed to be rigid prior to impact. Thus, the only effect of the shock layer on the ice particle which was considered was particle deceleration due to drag.

TABLE 4 WATER AND ICE PROPERTIES		
PROPERTY	Value for	
	ICE	WATER
Density (lbm/ft ³)	56.0	62.4
Specific Heat (btu/lbm-deg)	0.49	1.0
Viscosity (lbf-sec/ft ²)	Rigid	2×10^{-5}
Surface Tension (lbf/ft)	Rigid	5×10^{-3}

Particle Properties - Parylene Theoretical Model

A thin encapsulating coating of parylene tends to constrain the deformation of a particle. In the integral theory we represent this effect as a surface effect. The only modification to the governing equations is an additional contribution to the internal energy production ($\dot{\epsilon}$). Therefore, only equations (9) and (10) are changed - by adding the effect formulated here.

It is assumed that the stress and straining of the parylene is two-dimensional (in the plane of the membrane) and is uniform over the surface of the particle. Also, it is assumed the membrane deformation can adjust quickly so that the stress is isotropic in the plane. Two "ideal models" of stress-strain behavior are formulated to represent the behavior of parylene. Parylene behavior and properties used in this analysis are based on verbal and written communications with Dr. W.F. Beach and Mr. W. Jayne of the Union Carbide Corporation.

Rigid-Plastic Model

Uniaxial test data indicate a yield strength of approximately 7,000 psi, ultimate strain of approximately 300% and an initial Young's modulus of approximately 400,000 psi. For such behavior most of the deformation and energy absorption is associated with the plastic flow; we will represent it as rigid-plastic behavior.

Assuming the material obeys the Mises yield criterion, first we compute the critical value of the second invariant of the stress tensor J_2 . For uniaxial tension

$$J_2 = \frac{\sigma^2}{3} \quad (32)$$

therefore, using a yield strength of 7,000 psi gives

$$J_{CR} = 1.63 \times 10^7 \text{ (psi)}^2$$

Now compute J_2 for the parylene in terms of the isotropic stress σ in the plane of the membrane - assuming the stress in the thickness direction is zero.

$$\begin{aligned} J_2 &= \frac{1}{6}[(\sigma - \sigma)^2 + (\sigma - 0)^2 + (0 - \sigma)^2] \\ &= \frac{\sigma^2}{3} \end{aligned} \quad (33)$$

Therefore, the yield strength in biaxial tension is equal numerically to the uniaxial yield strength.

The rate at which energy is dissipated by plastic flow is

$$\dot{W}_P = \sigma_{11}\dot{\epsilon}_{11} + \sigma_{22}\dot{\epsilon}_{22} > 0 \quad (34)$$

where "1" and "2" are perpendicular directions in the membrane. For our model

$$\sigma \equiv \sigma_{11} = \sigma_{22} \quad (35)$$

$$\dot{\epsilon} \equiv \dot{\epsilon}_{11} = \dot{\epsilon}_{22} \quad (36)$$

Therefore,

$$\dot{W}_P = 2\sigma\dot{\epsilon} \quad (37)$$

and

$$\begin{aligned} S &> 0 \quad \text{if } \dot{\epsilon} > 0 \\ S &< 0 \quad \text{if } \dot{\epsilon} < 0 \end{aligned} \quad (38)$$

The volume of the membrane is hA , where h is the membrane thickness and A is the surface area of the particle. Multiplying the plastic working by the volume gives the total contribution to the internal energy production.

$$\Delta \dot{E} = 2h\sigma A \dot{\epsilon} \quad (39)$$

From the kinematics of isotropic straining of an area

$$\dot{\epsilon} = \frac{1}{2} \frac{\dot{A}}{A} \quad (40)$$

Therefore, the internal energy production may be written

$$\Delta \dot{E} = (h\sigma) \dot{A} \quad (41)$$

This looks much like "free surface energy" with an effective surface tension of $h\sigma$. An important difference though is that for plastic behavior the energy is dissipated irreversibly.

$$(h\sigma) \dot{A} \geq 0 \quad (42)$$

Based on the data, a value of 7000 psi has been used for σ in the studies.

Elastic Model

At high strain rates, measurements indicate brittle behavior of parylene. Apparently, brittle fracture precedes plastic flow at high strain rate. To represent this behavior, the parylene is characterized as purely elastic using the measured value of Young's modulus. The formulation is based on representations developed for rubbery materials (see Frederickson [4] for more details).

In general, the formulation is written as follows:

$$\underline{\underline{S}} = - p \underline{\underline{\delta}} + 2 \frac{\partial W}{\partial I_1} \underline{\underline{B}} - 2 \frac{\partial W}{\partial I_2} \underline{\underline{B}}^{-1} \quad (43)$$

where $\underline{\underline{S}}$ is the stress tensor

p is the pressure

$\underline{\underline{\delta}}$ is the unit tensor

W is the strain energy function

I_1, I_2, I_3 are the invariants of $\underline{\underline{B}}$

$\underline{\underline{B}}^{-1}$ is the Cauchy-Green deformation tensor.

This formulation is more general than the available test data can specify. A simple and special version of the above is the following neo-Hookean theory [5]:

$$\underline{\underline{S}} = - p \underline{\underline{\delta}} + \mu \underline{\underline{B}} \quad (44)$$

$$\text{subject to } \text{tr } \underline{\underline{B}} = 0 \quad (45)$$

which can be evaluated on the basis of a single modulus. The strain energy function is

$$W = \frac{1}{2} \mu (I_1 - 3) \quad (46)$$

To match the small strain measurements μ is taken equal to the initial shear modulus. For rubbery material,

$$\mu \approx \frac{E}{3} \quad (47)$$

Therefore, for parylene

$$\mu = .133 \times 10^6 \text{ psi}$$

Now apply this theory - particularly the strain energy function - to our particle model. Consider the stretch (λ) as isotropic in the plane of the membrane and evaluate $\underline{\underline{B}}$ in terms of it:

$$B_{11} = B_{22} = \lambda^2, \quad B_{33} = \frac{1}{\lambda^4} \quad (48)$$

Therefore,

$$I_1 = 2\lambda^2 + \frac{1}{\lambda^4} \quad (49)$$

and the strain energy function becomes

$$W = \frac{1}{2} \mu \left(2\lambda^2 + \frac{1}{\lambda^4} - 3 \right) \quad (50)$$

If we denote the "stress-free" state of the membrane as having area A_0 and thickness h_0 then

$$\lambda^2 = \frac{A}{A_0} \quad (51)$$

$$\text{Volume} = h_0 A_0 \quad (52)$$

Using these expressions we derive the following equation for the total strain energy in the membrane.

$$h_0 A_0 W = \frac{\mu}{2} h_0 A_0 \left[2 \left(\frac{A}{A_0} \right) + \frac{1}{\left(\frac{A}{A_0} \right)^2} - 3 \right] \quad (53)$$

If we differentiate (53) with respect to time, we obtain the term we are seeking - the internal energy production:

$$\Delta \dot{E} = \frac{\mu}{2} h_0 A_0 \left[2 \left(\frac{\dot{A}}{A_0} \right) \left(1 - \frac{1}{\left(\frac{A}{A_0} \right)^3} \right) \right] \quad (54)$$

Of course, elastic behavior is totally reversible which is very different from plastic behavior. The elastic model causes the particle shape to oscillate in many of the cases studied. The difference between the two models is illustrated by Figure 14, which presents predictions for water encapsulated particles. The particle width (\bar{b}) is plotted against the

Particle deformation for two parylene models

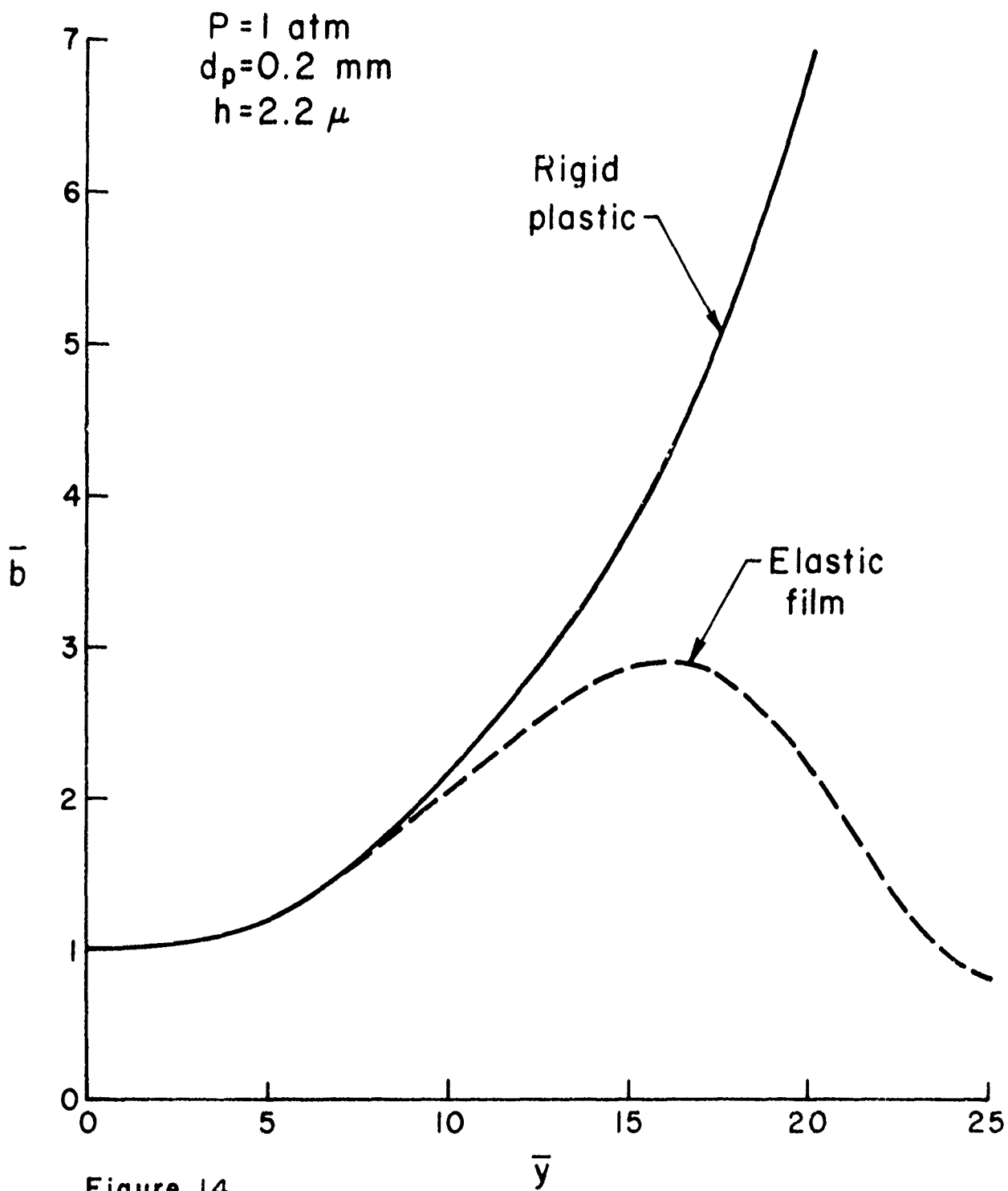


Figure 14

penetration depth (\bar{y}) during a penetration. The parylene film was not permitted to rupture during this penetration. The elastic rebound is obvious and occurred similarly in the other calculations.

Under the conditions of high strain rate the ultimate elongation of the material is not well known; therefore, it is convenient to consider a reasonable range - say, 0 to 80%. In our calculations the strain is not predicted, so it is convenient to convert from ultimate strain to a critical value for one of the geometric parameters. Consistent with our particle model, Figure 15 represents a critical value for the particle width.

Small Nose Radius Target - Predictions

In this section, the effect of the parylene film on the existing NOL data base for the small nose radius target is described. It was previously noted that the parylene influences the impact process only while the particle is in the shock layer. Therefore, it is important to examine the effect of each of the test parameters on the particle conditions at impact. In addition to particle encapsulation, the effects of particle size, initial velocity and range pressure are also presented.

Although the particle experiences both deformation and deceleration while traversing the shock layer, the results indicate that the former effect is considerably larger than

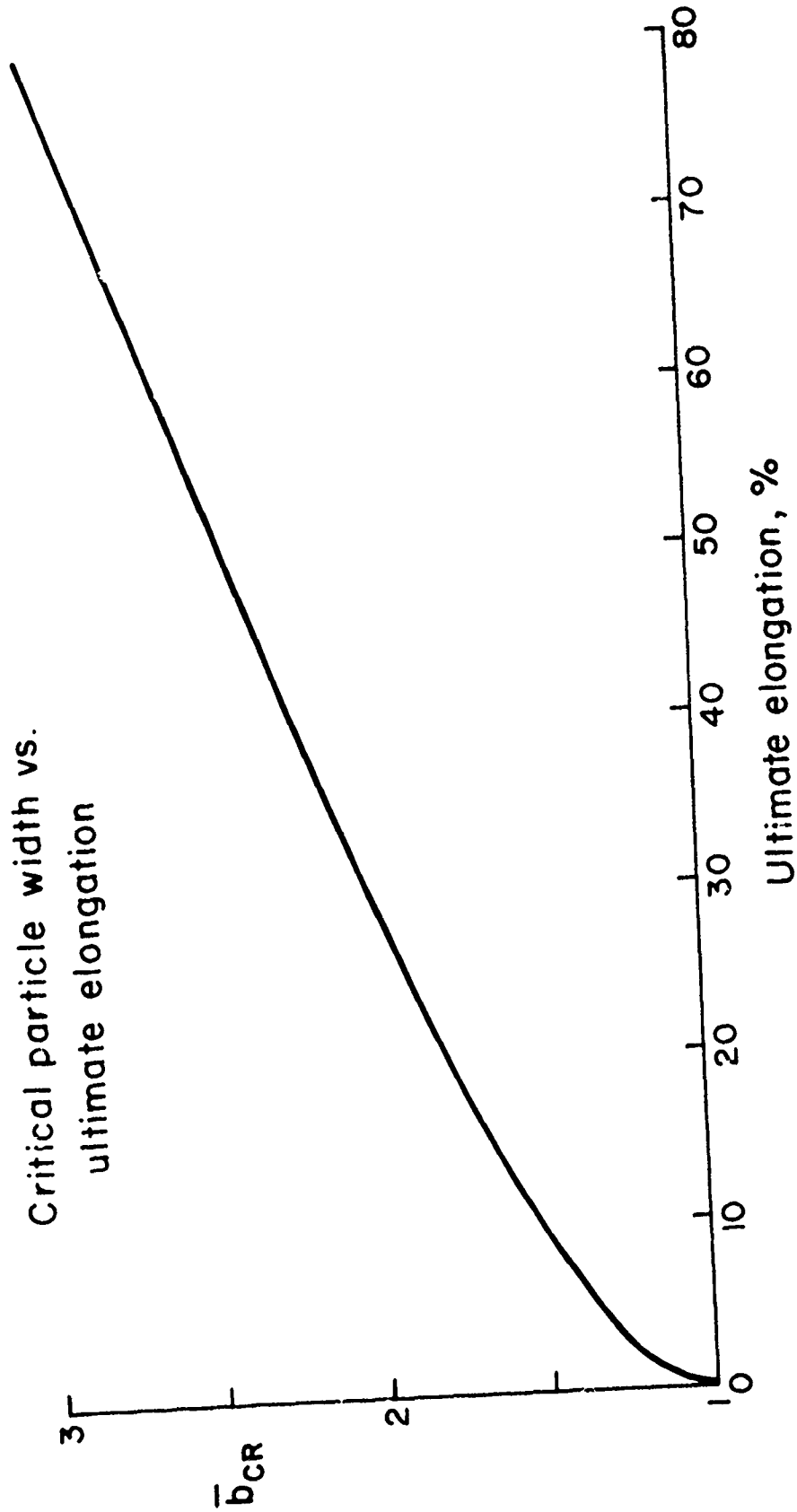


Figure 15

the latter effect for the relatively thin shock layers associated with this target. Hence, emphasis will be placed on particle deformation (i.e., the lateral elongation of the particle) and only brief mention will be made of particle deceleration through the shock layer.

Figure 16 shows the deformation history of two different diameter particles. The ordinate of the figure represents the lateral dimension of the particle and the abscissa is the depth of penetration through the shock layer (with the zero value at the shock front). The bars over each symbol denote nondimensional quantities. In this case, lengths were normalized by the initial width of the particle.*

Both curves are drawn for an initial particle diameter of 0.2 mm. The solid curve is based on real gas shock layer properties; the dashed curve is based on the ideal gas approximation. It is evident that the larger particle deformation occurs for the real gas model. This is a result of the larger density in the shock layer for the real gas (see Table 3).

Superimposed on each curve are circular data symbols. These symbols portray the deformation history of a larger

*Because the A.R.A.P. model is two-dimensional, the spherical particle was initially transformed to a cubic particle of equivalent volume. The initial width of the particle (l_0) was therefore related to the particle diameter (d_p) by

$$l_0 = 3.22d_p.$$

Effect of particle size on particle width
in shock layer

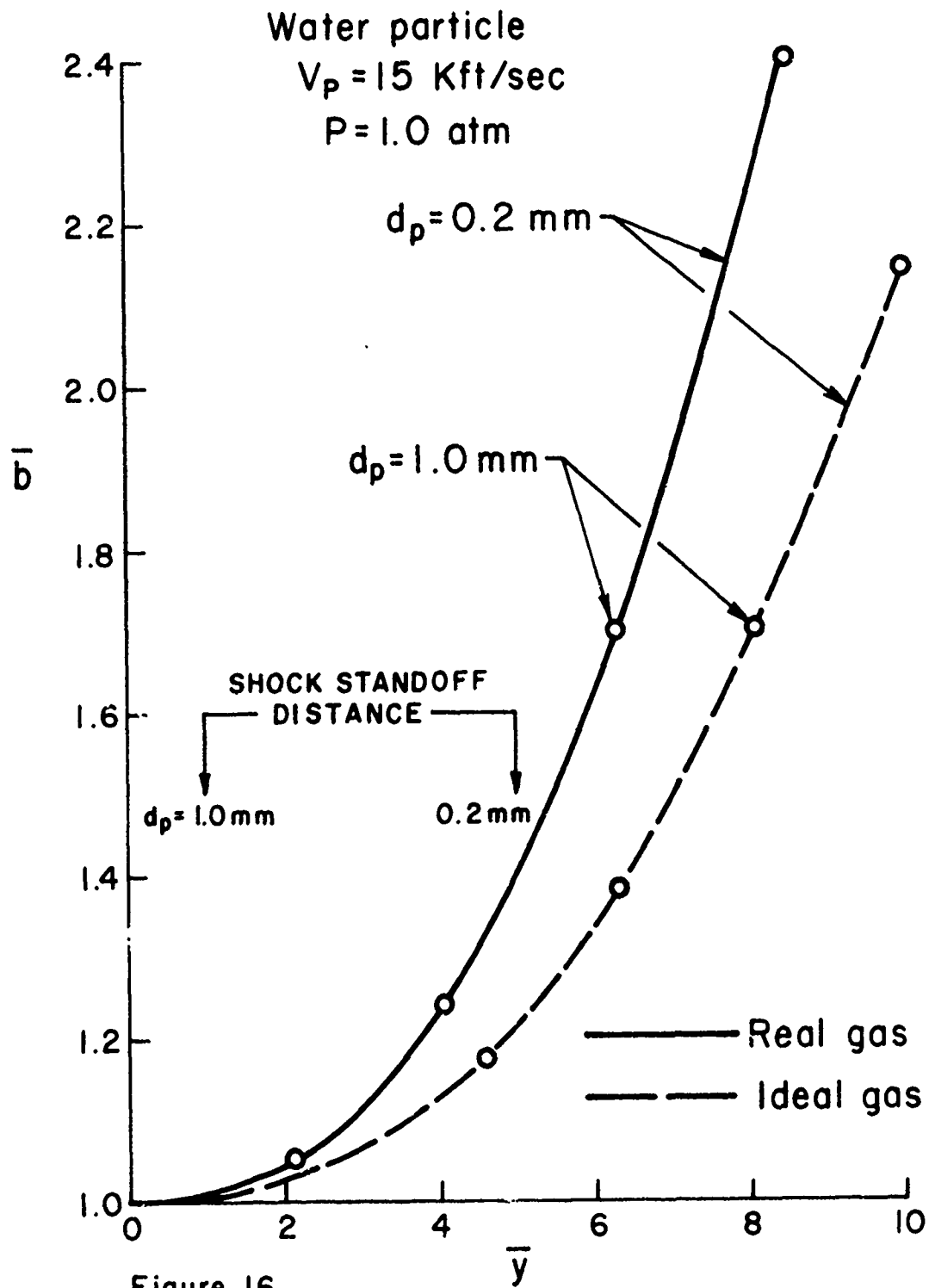


Figure 16

water particle ($d_p = 1.0$ mm). The conclusion is evident: the rate of deformation of the particle through the shock layer is independent of the initial size of the particle. The size independence shows that viscosity and surface tension have only negligible effects for these cases.

The deformation rates shown in the figure are applicable to a shock layer of infinite thickness. In actuality, a sharp discontinuity must occur at the point of impact with the target. The location of this point (i.e., the normalized shock standoff distance) is denoted for each particle diameter on the figure. It varies from $\bar{y} = 0.99$ for the large particle to $\bar{y} = 4.96$ for the small particle. The values of \bar{b} at these \bar{y} locations represent, therefore, the relative deformation of each particle at impact. For the large particle, the deformation at impact is less than 2%. The large particle simply did not travel enough particle diameters to be very much affected. In contrast, the small particle, which travels a much larger distance in terms of particle diameters, grows by 40% prior to impact. Since the area varies as the linear dimension squared, the frontal area increases by approximately 100%.

Figure 17 shows the effect of range pressure on particle deformation. Both the real gas and ideal gas results are shown for each value of pressure. Much larger deformations occur for the higher pressure because of the order-of-magnitude increase of the air density in the shock layer. The

Effect of range pressure on particle width in shock layer

Water particle

$V_p = 15$ Kft/sec

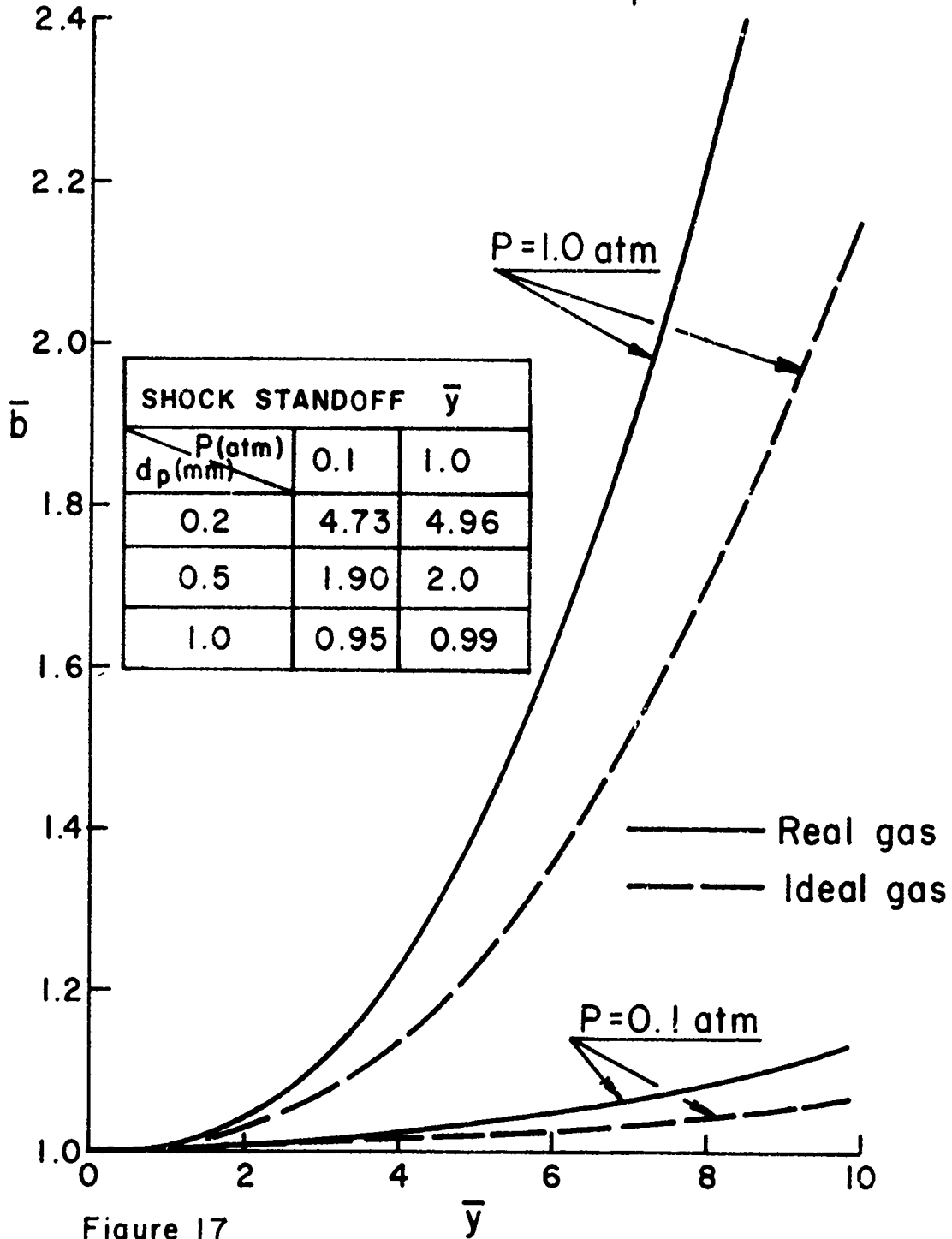


Figure 17

values of \bar{y} corresponding to the shock standoff distance are summarized in the table included in the figure.

The value of \bar{b} at impact as a function of particle diameter is shown in Figure 18. The relative deformation clearly increases as the particle diameter is decreased. But the effect is less than 3% for the low pressure, compared to 40% for the high pressure. Note also that the effect of pressure on \bar{b} is less than 1% for particle diameters in excess of 1 mm.

Figure 19 shows the corresponding curves for the ratio of impact velocity to initial velocity. The shock layer decreases the velocity by at most 2% for the low pressure case and 13% for the high pressure case.

Figure 20 shows the effect of initial particle velocity on particle deformation. Two particle velocities are shown for both the real gas and ideal gas models. Two opposing trends should be noted. First, particle deformation clearly increases with increasing particle velocity for a given depth of penetration. However, the shock standoff distance decreases with increasing particle velocity (i.e., decreases with Mach no.); and, in fact, the latter effect is larger than the former for these test conditions.

The net result of these two factors is illustrated in Figure 21, which shows particle width at impact. It is clear that for a given particle diameter, the deformation is

Particle width at impact

Effect of range pressure

Water particle

$V_p = 15$ Kft/sec

Real gas shock layer properties

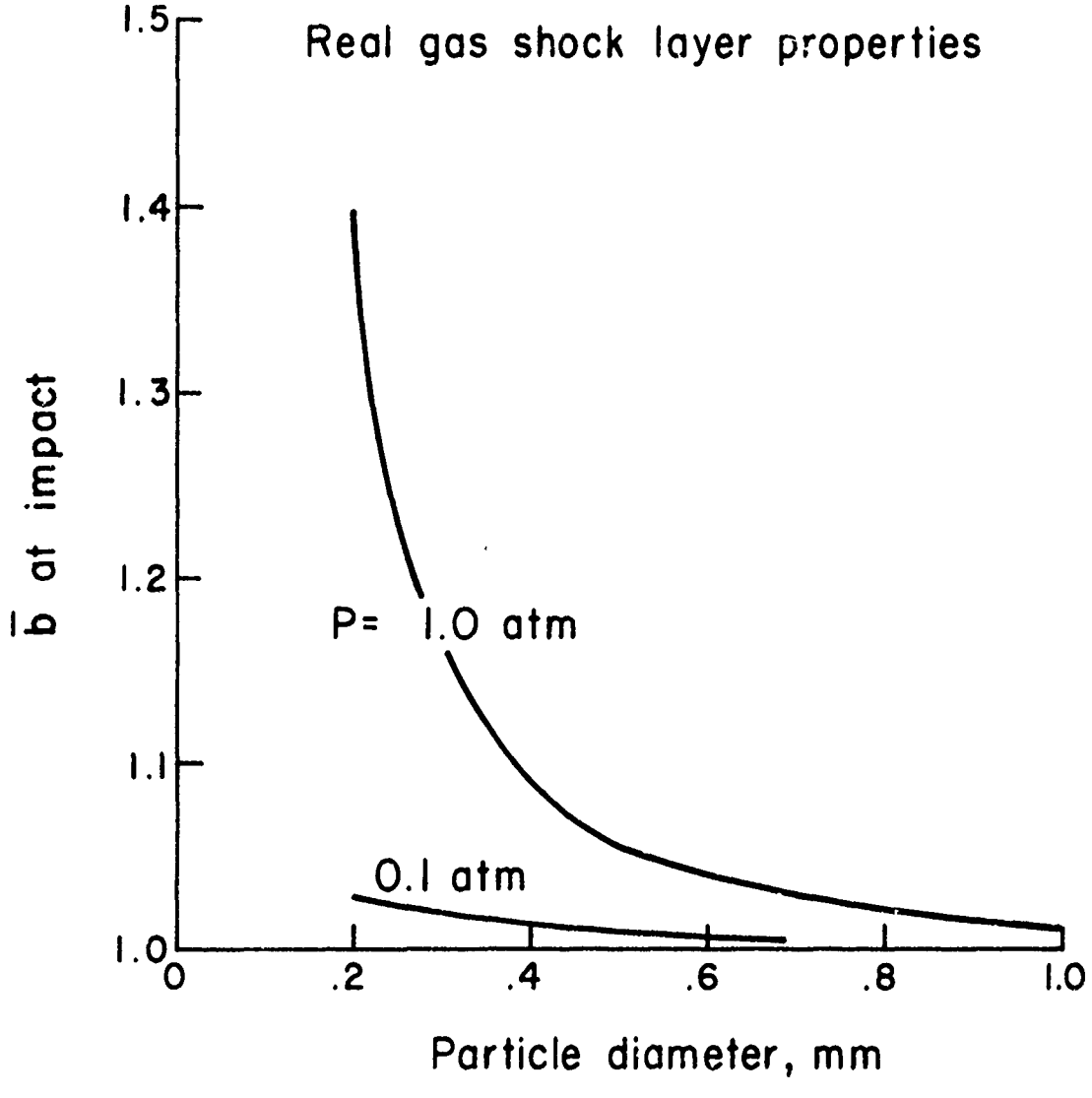


Figure 18

Particle velocity at impact
 Effect of range pressure

Water particle $V_p = 15$ K ft/sec

Real gas shock layer properties

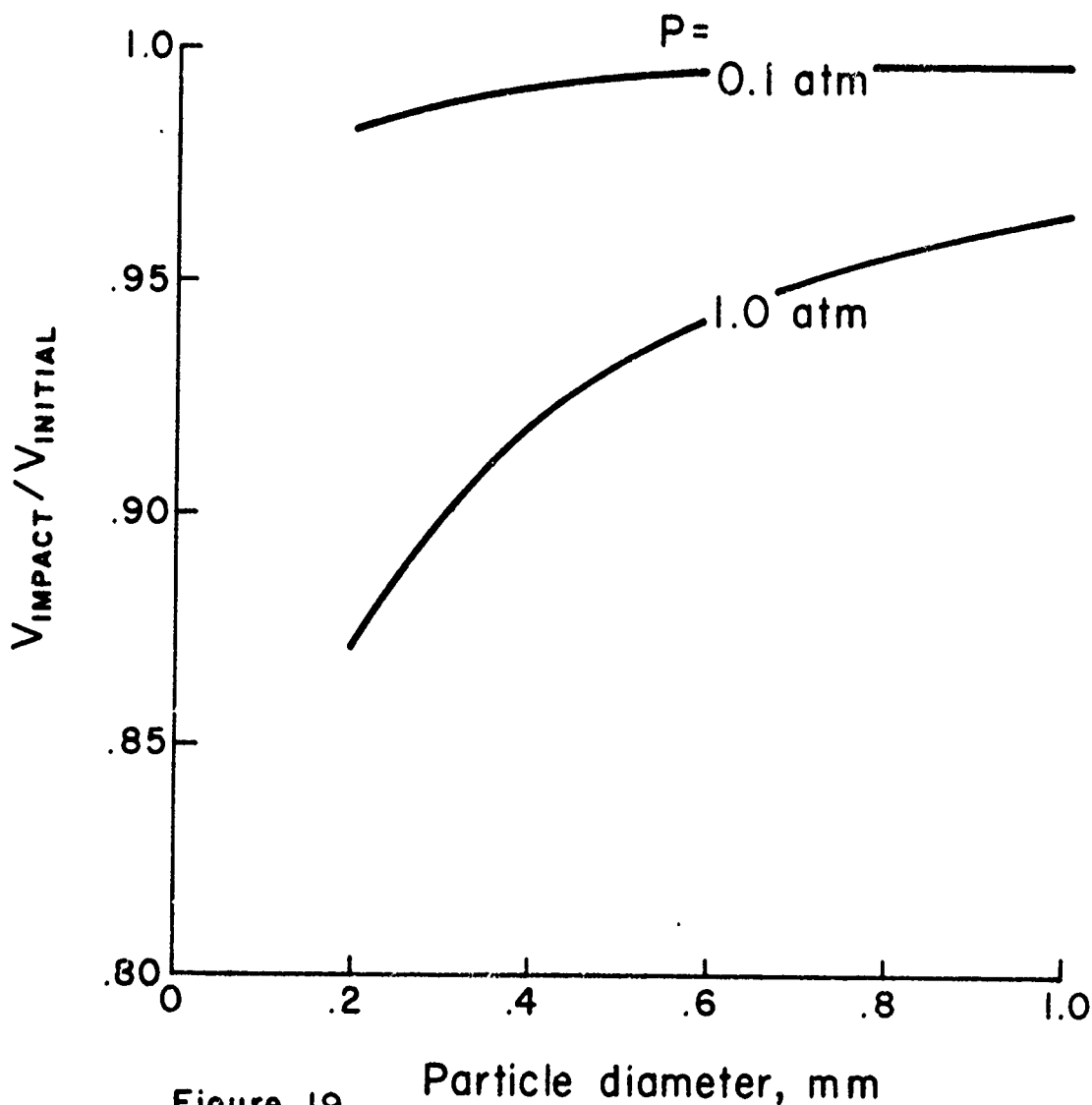


Figure 19

Particle diameter, mm

Effect of particle velocity on particle width in shock layer

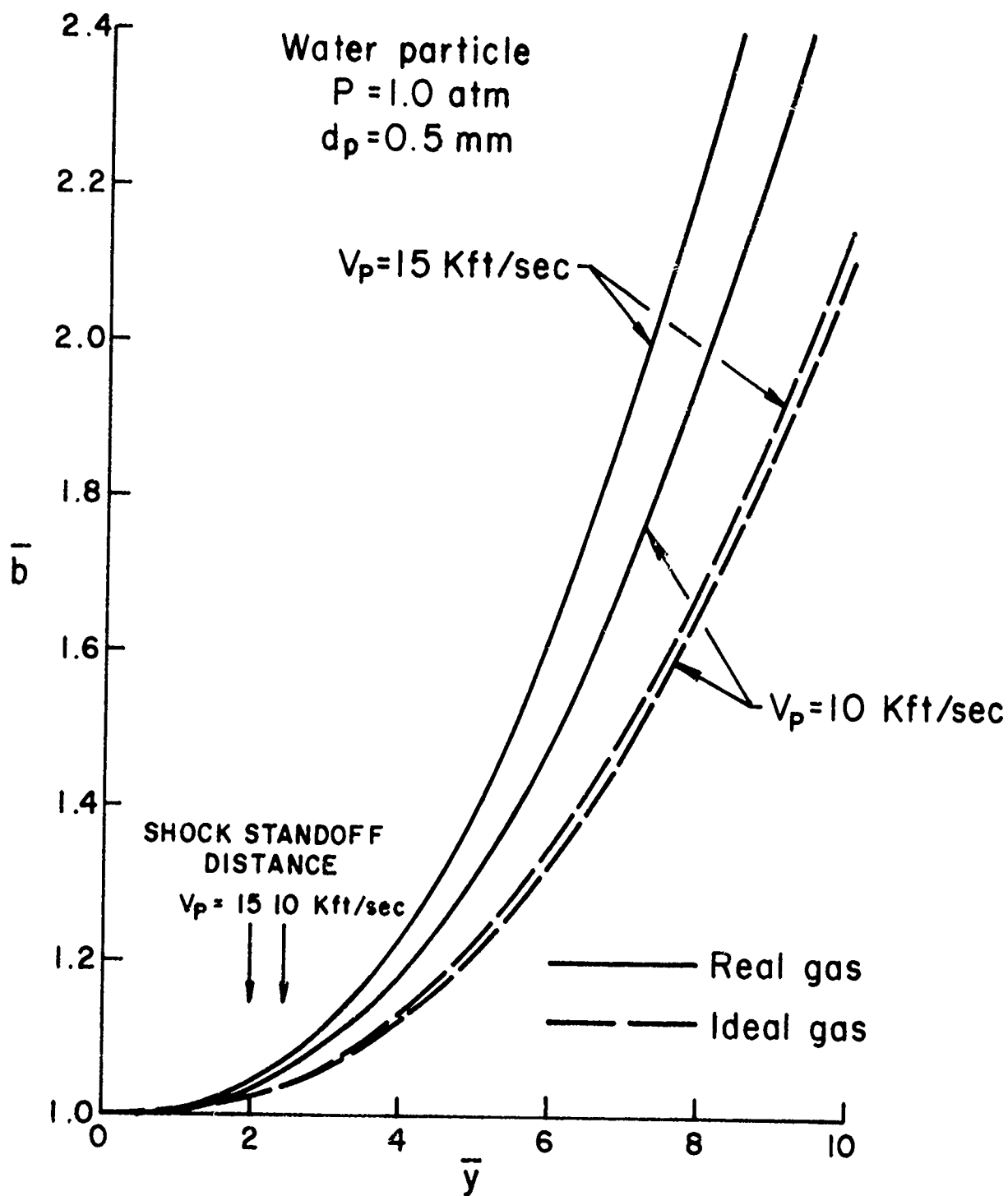


Figure 20

Particle width at impact
Effect of particle velocity

Water particle

P=1.0 atm

Real gas shock layer properties

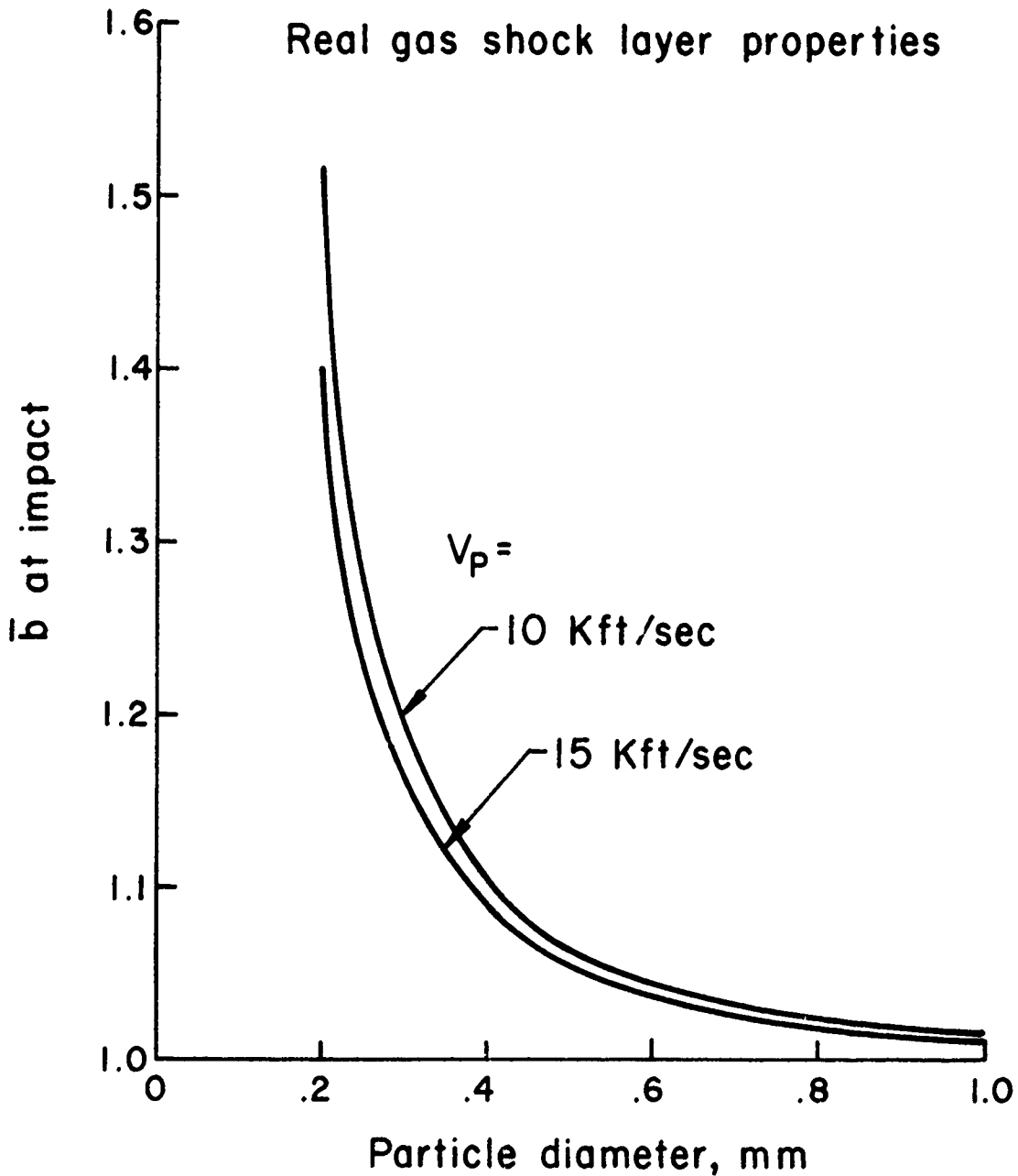


Figure 21

larger for the lower initial velocity. The effect is small for the large particle but is approximately 10% for the smallest particle diameter.

The impact velocity curve analogous to Figure 21 has not been included because the effects are insignificant. For either velocity, the data are within 1% of the high pressure data shown in Figure 19.

Figure 22 shows the effect of the parylene film on particle deformation. It is evident that for $\bar{y} < 5$, the parylene film has very little effect on the shape of the particle at impact. Although this figure refers to a specific set of test conditions, the same result was obtained for every combination of test conditions for this target. The shock layer is too thin for the parylene to appreciably influence the properties of the particle prior to impact. Hence, using the argument put forth at the beginning of this section, if the parylene does not change the particle properties prior to impact, then it has no effect on the impact process. Therefore, the erosion data can be considered as representative of unencapsulated water particles.

Large Nose Radius Target - Predictions

In this section, the effects of the parylene film for future test planning are considered. The conditions for these tests were summarized in Table 1. Compared to the

Effect of parylene film on particle width in shock layer

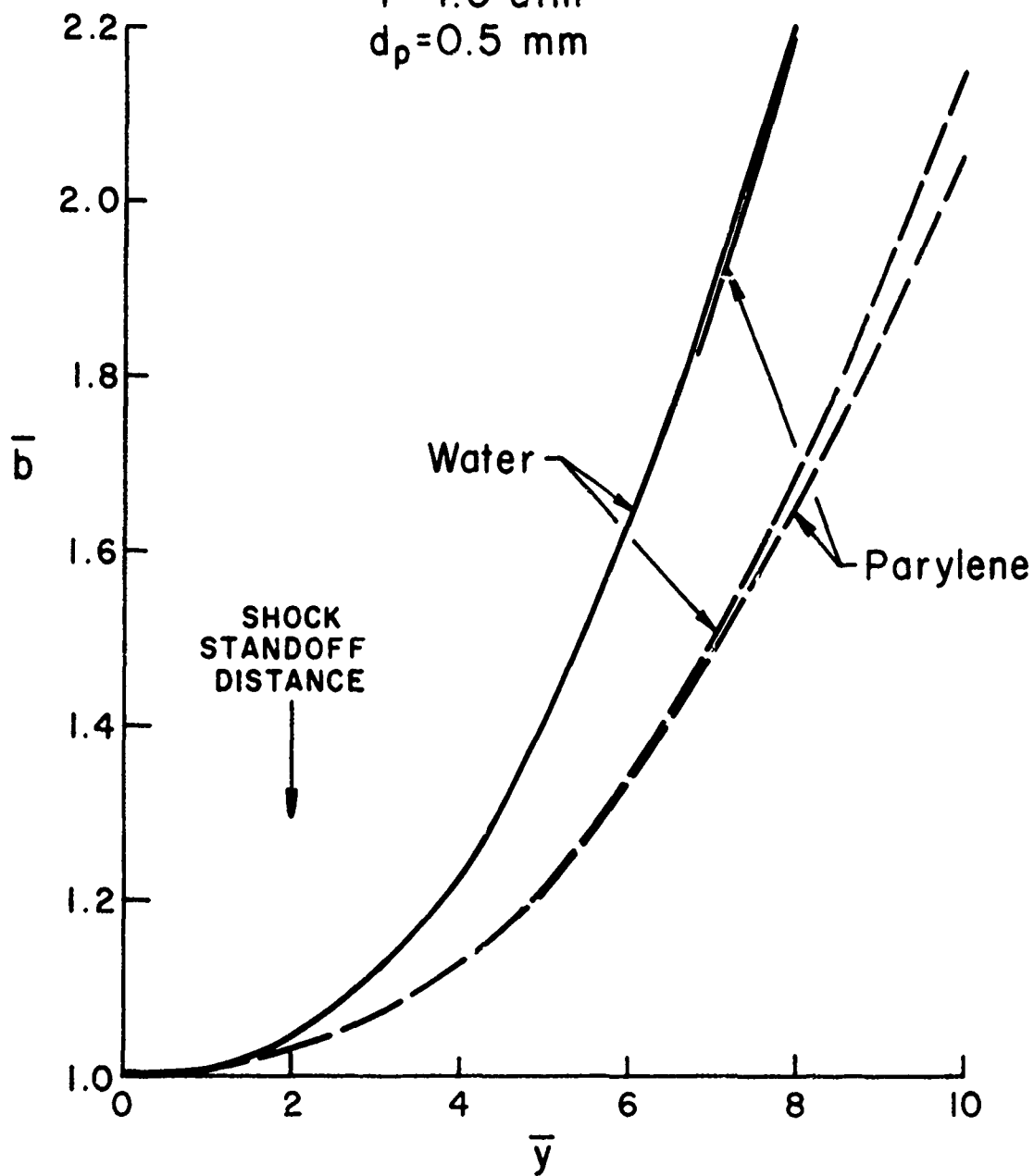
 $V_p = 15 \text{ Kft/sec}$ $P = 1.0 \text{ atm}$ $d_p = 0.5 \text{ mm}$ 

Figure 22

conditions used in the previous section, these tests are for (1) smaller particles and (2) much thicker shock layers. Both of these conditions tend to make the presence of the parylene film more significant.

The magnitude of the effect will be bounded by considering the four test conditions which represent the extreme values of test pressure and particle diameter. The computations were made for both real gas and ideal gas shock layer properties.

For each test condition, the particle deformation - represented by the width of the particle (b) - and the particle velocity - represented by the front-face velocity (V_{\perp}) - are presented as a function of the depth of penetration (y) through the shock layer. The lengths are again normalized by the initial length of the particle. The velocity is normalized by V^* , a velocity which is related to the strength of the target. For this analysis, a value of $V^* = 1,730$ ft/sec was used.

Figures 23 and 24 show \bar{b} and \bar{V}_{\perp} time histories for $P = 1.0$ atm and $d_p = 0.2$ mm. Four curves are contained in each figure; one each for water and ice and two for encapsulated water. Figure 23 shows a very steep deformation rate for the water particle. Assume for the moment that the ultimate elongation of the parylene film is infinity, then the elasticity of the parylene retards the steep deformation

Particle width in shock layer

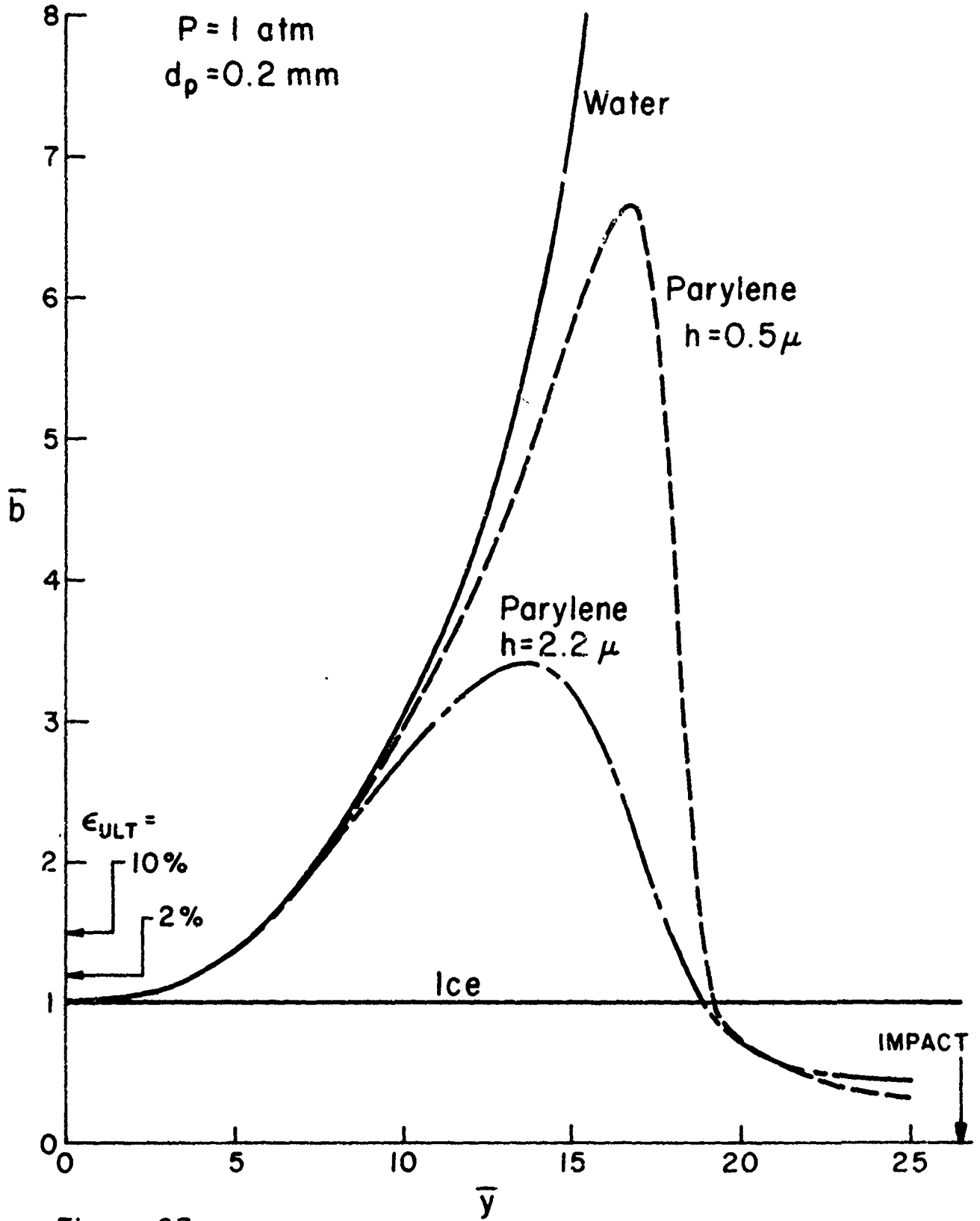


Figure 23

Particle velocity in shock layer

$P = 1 \text{ atm}$
 $d_p = 0.2 \text{ mm}$

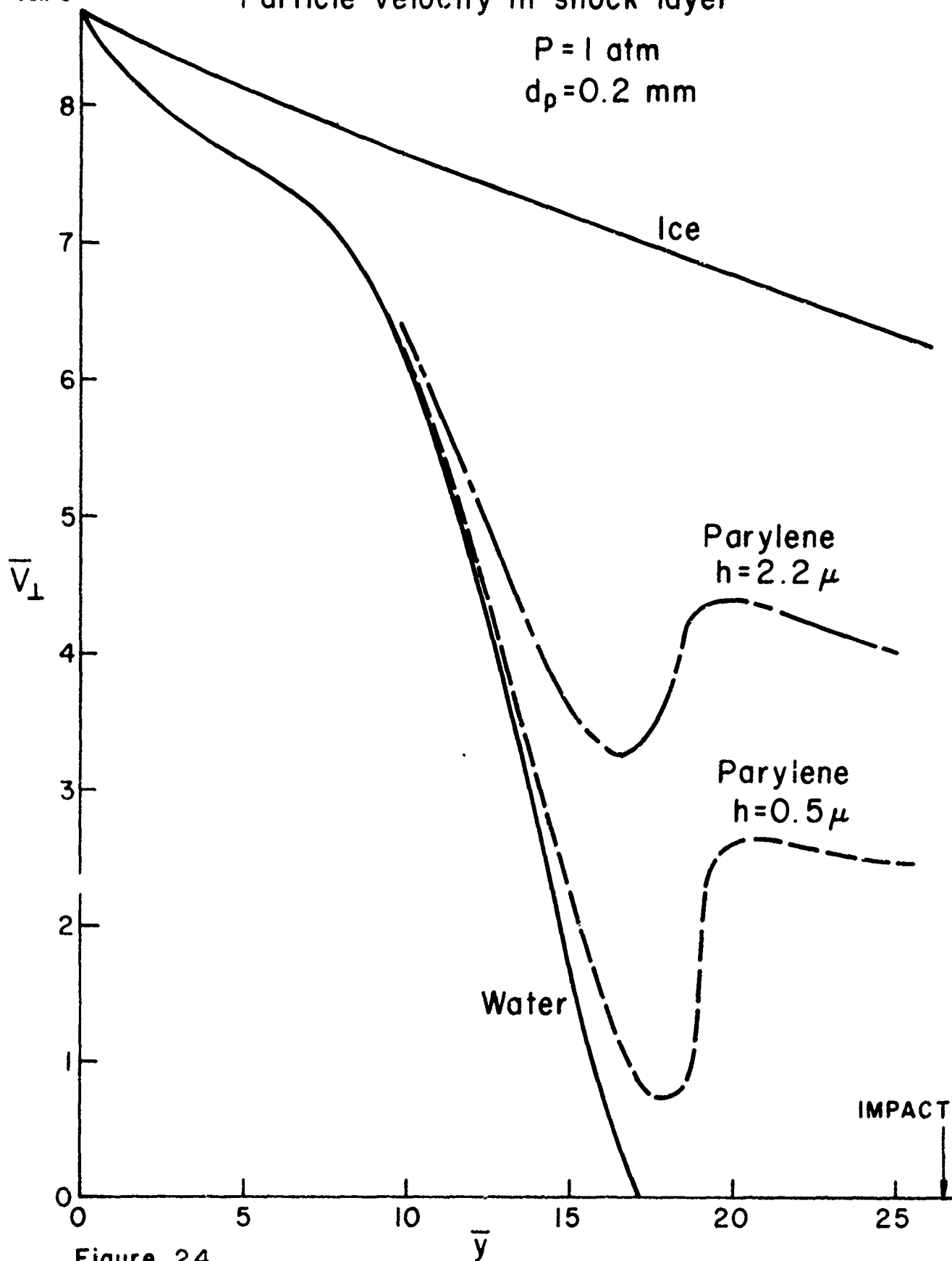


Figure 24

rate of the water particle and eventually causes the particle to return to its original size. Parylene, of course, has a finite ultimate elongation which varies somewhere between 2% and 10%. These elongations correspond to \bar{b} values of 1.2 and 1.5, respectively. When these deformations are exceeded, the parylene film breaks and the particle behaves as an ordinary water particle. It is evident from Figure 23 that the parylene film will break before it has had a noticeable effect on the shape of the particle.

Figure 23 shows the corresponding time history of the particle front-face velocity. Note the extremely rapid deceleration of the water particle corresponding to the rapid deformation rate. In particular, note that $\bar{V} < 1$ at $\bar{y} = 16$. A value of 1 is the point below which the particle has insufficient energy to damage the target. Because the impact point corresponds to $\bar{y} = 26.5$, it is apparent that the water particle will not damage the target. In contrast, the ice particle which is rigid through the shock layer, impacts with almost 75% of its initial velocity.

If the parylene had remained intact, then it would have impacted within a wide range of velocity depending upon the film thickness. Although the front-face velocity shows a large bump due to the elasticity of the parylene, the velocity

at the center of the mass of the particle is a monotonically decreasing function of \bar{y} - consistent with momentum conservation principles.

Figures 25 and 26 show similar results for a smaller particle diameter ($d_p = 0.05$ mm). The cases with parylene show oscillations which are due to the elastic behavior of the film. On the one hand, the drag force tends to deform the particle but the elastic membrane tends to restore its shape. For this case, the impact value of \bar{y} is 106. It is evident that the water particle will be destroyed well before it reaches the target. Also, the parylene film will fracture before its elasticity can restrain the deformation.

The results shown in Figures 23-26 are for a range pressure of one atmosphere. Figures 27 and 28 show the results for a lower pressure ($P = 0.1$ atm) and for a particle diameter of 0.2 mm. For this case, the changes in \bar{b} and \bar{V}_1 through the shock layer are considerably smaller than for the high pressure condition. The water particle will impact the target with 93% of its initial velocity and with a width about two times its original width. The parylene film will break (assuming an ultimate elongation of 10%) before it has had a noticeable effect on either the deformation or deceleration of the particle.

The results are somewhat different for the smallest particle ($d_p = 0.05$ mm) for the low pressure condition.

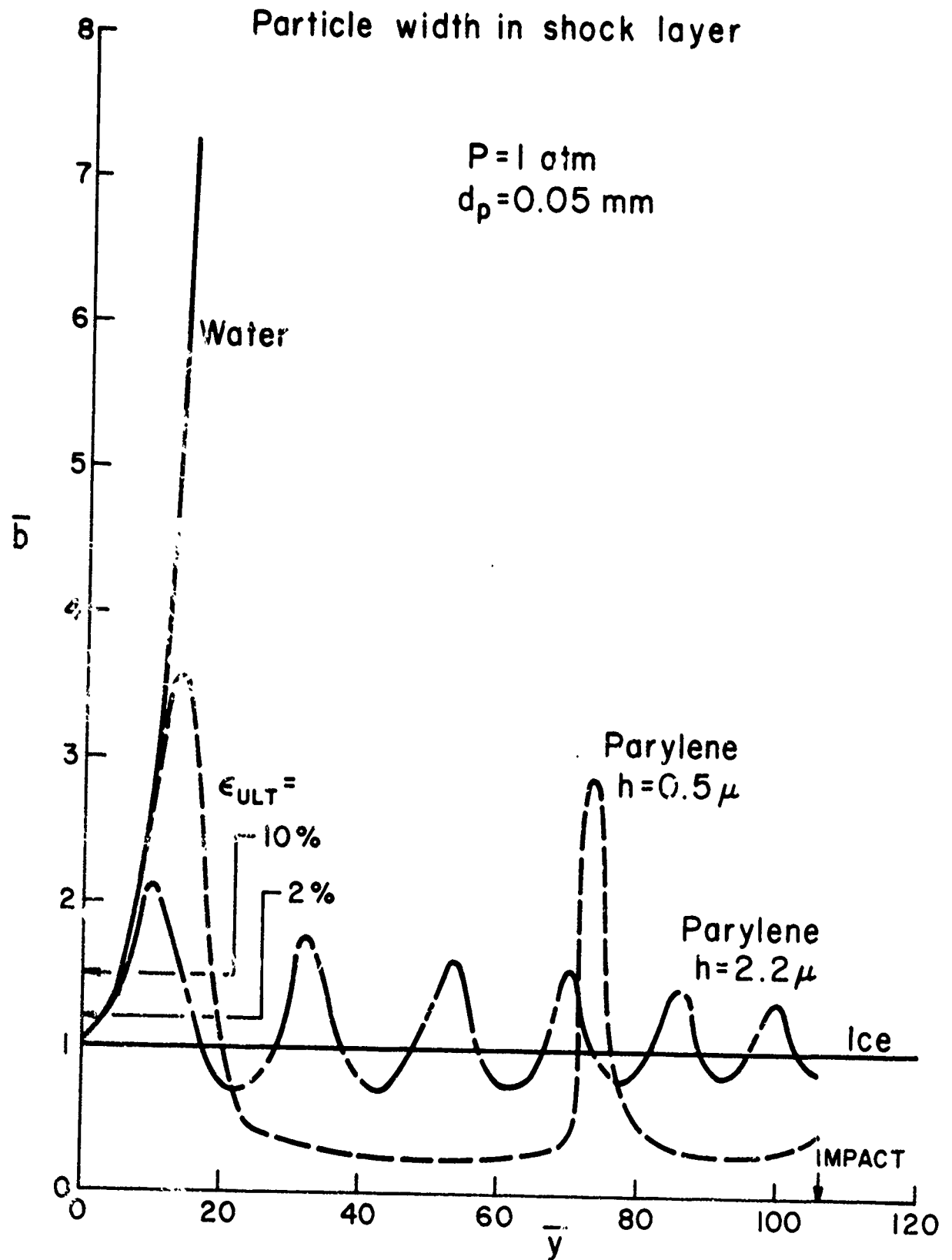


Figure 25

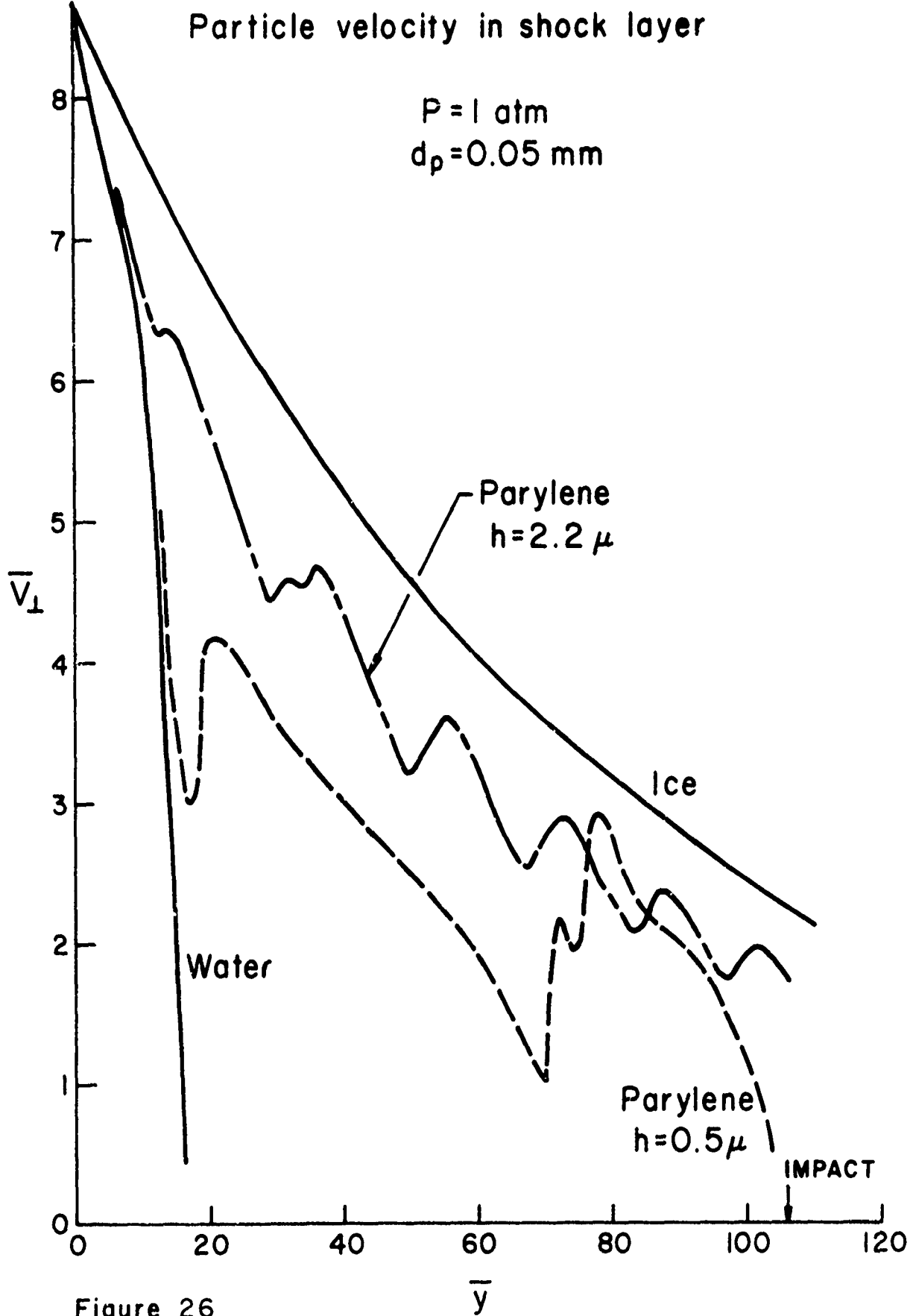


Figure 26

Particle width in shock layer

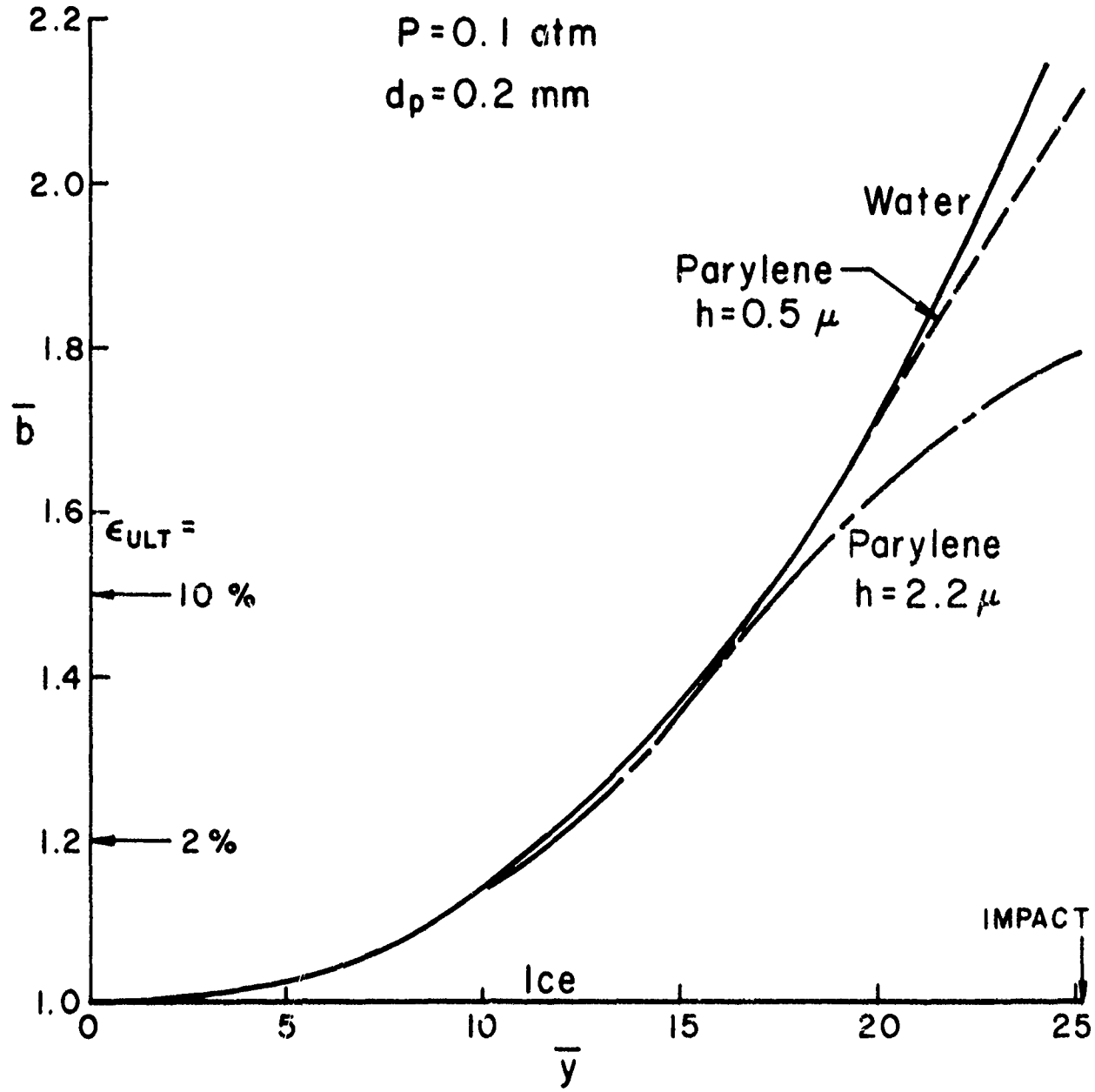


Figure 27

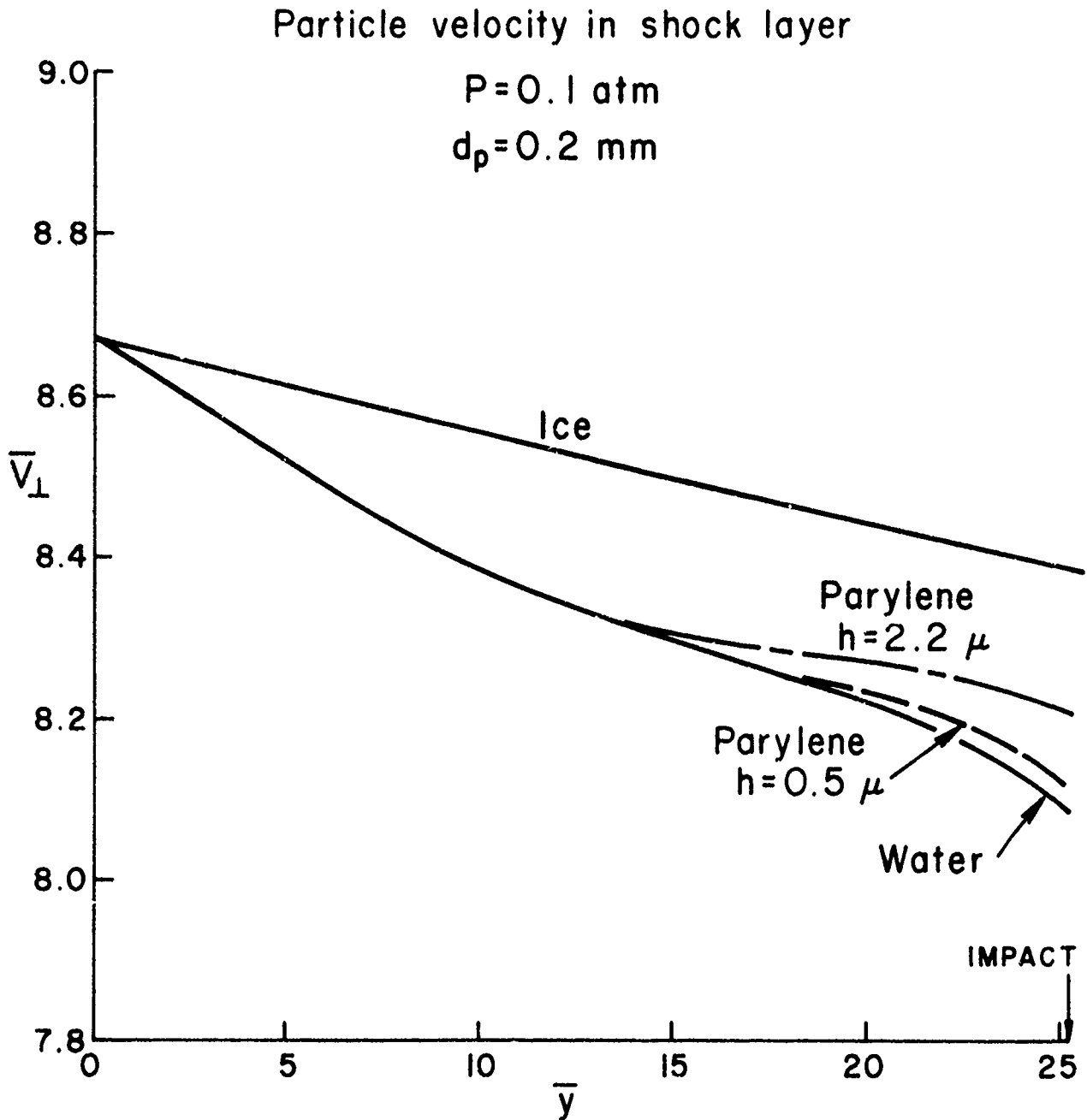


Figure. 28

Figures 29 and 30 show that the water particle will be destroyed prior to impacting the target. However, if the particle is encapsulated with a 2.2μ film of parylene, then the maximum elongation of the particle will be between 2% and 10%. As a result, it is possible that the film will not break in the shock layer. If this is indeed the case, then Figures 29 and 30 indicate that the properties of the particle at impact will more closely approximate those of ice than those of water. To avoid this, a thinner parylene film can be used. For example, if the film is only 0.5μ thick, then the predicted particle elongation is in excess of 10% and the particle will not reach the target. Thus, one should be careful when interpreting erosion data for these test conditions.

The parylene curves shown in Figures 23-30 used an infinite value for the ultimate elongation of the film. It was assumed that if the state of the particle (indicated by \bar{b} and \bar{V}_1) was near that of the water drop when the parylene fractured, then the further penetration of the two would be similar. Some calculations were performed to verify this assumption.

The next series of figures shows the results of these computations. Because the results are so similar to the corresponding data in Figures 23-30, only the deformation data are shown. It should be noted that these computations

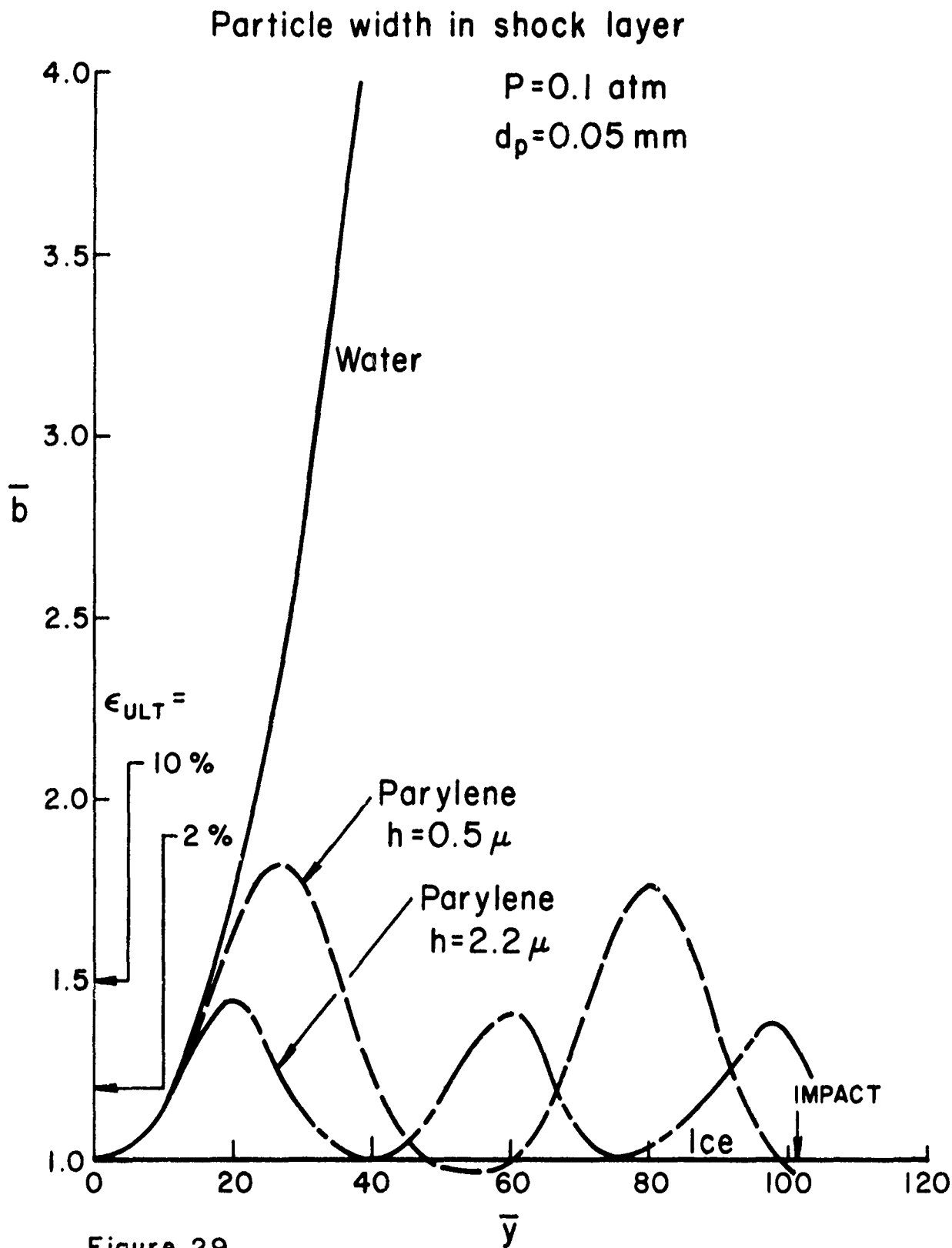


Figure 29

Particle velocity in shock layer

$P = 0.1 \text{ atm}$
 $d_p = 0.05 \text{ mm}$

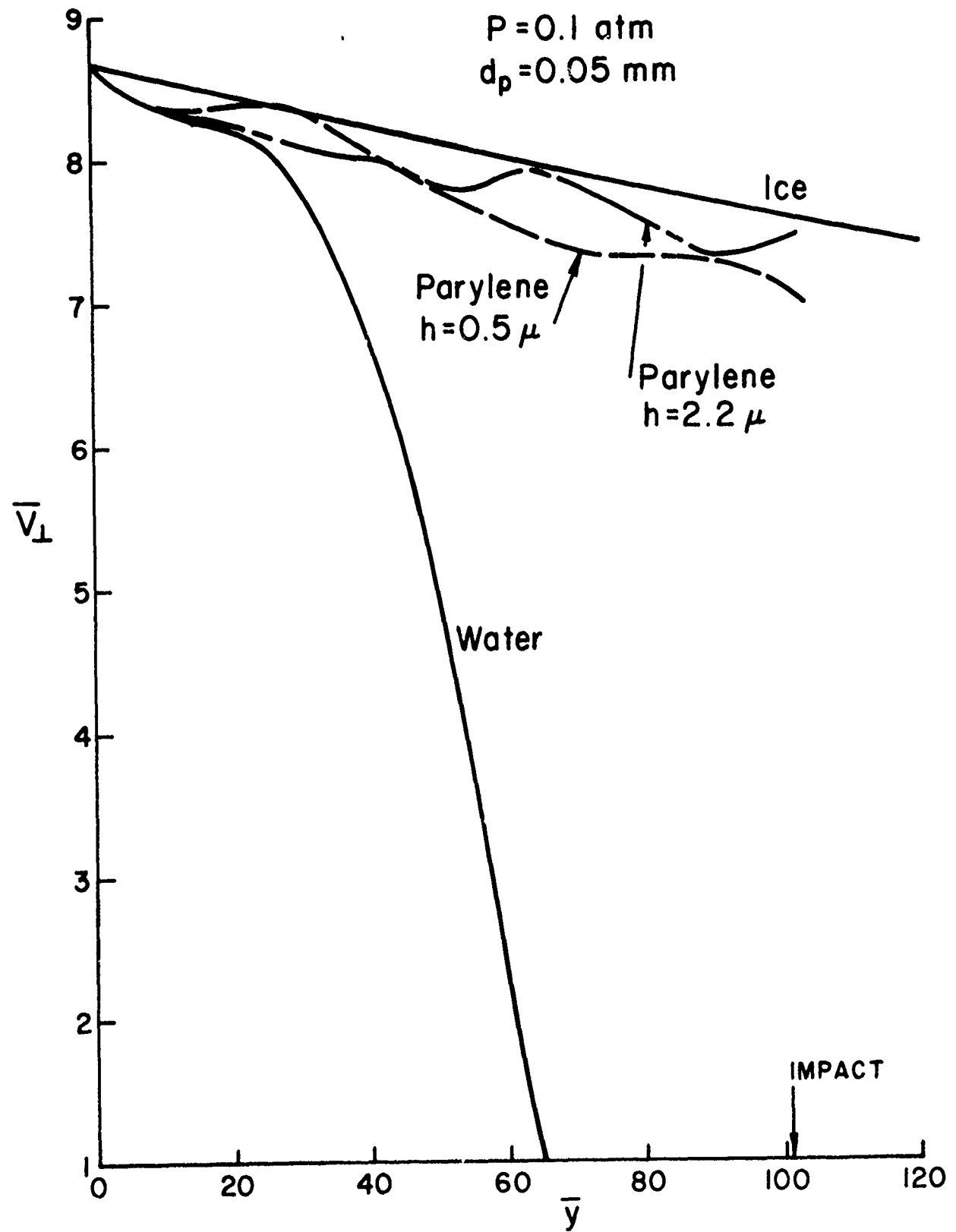


Figure 30

Vol. 3

are based on the ideal gas shock layer properties. Hence, the curves differ from their counterparts in previous figures. However, it will be shown that the results are the same for either model and, therefore, the results are not dependent on the model used to compute the shock layer properties.

The test conditions for Figure 31 are $P = 1.0$ atm and $d_p = 0.2$ mm. The parylene breaking point for 10% elongation is noted and the ensuing deformation is seen to closely parallel the water curve. Note that an ultimate elongation in excess of 80% is required before the parylene can survive the shock layer. Also, if the parylene fractures, then the particle, as for the water droplet, will reach the target surface with negligible velocity.

Figure 32 is for a smaller particle ($d_p = .05$ mm), but it shows the same result. In this case, an elongation in excess of 25% is required for the parylene encapsulated particle to survive the shock layer and impact the target.

The test conditions for Figure 33 are $P = 0.1$ atm and $d_p = 0.2$ mm. For this case, the uncertainty in the ultimate elongation of the parylene results in a spread of about 5% in the width of the particle at impact.

The only test condition for which the parylene may significantly influence the impact data is for $P = 0.1$ atm and $d_p = 0.05$ mm. This case is shown in Figure 34. An ultimate elongation of less than 5% results in particle

Particle width in shock layer

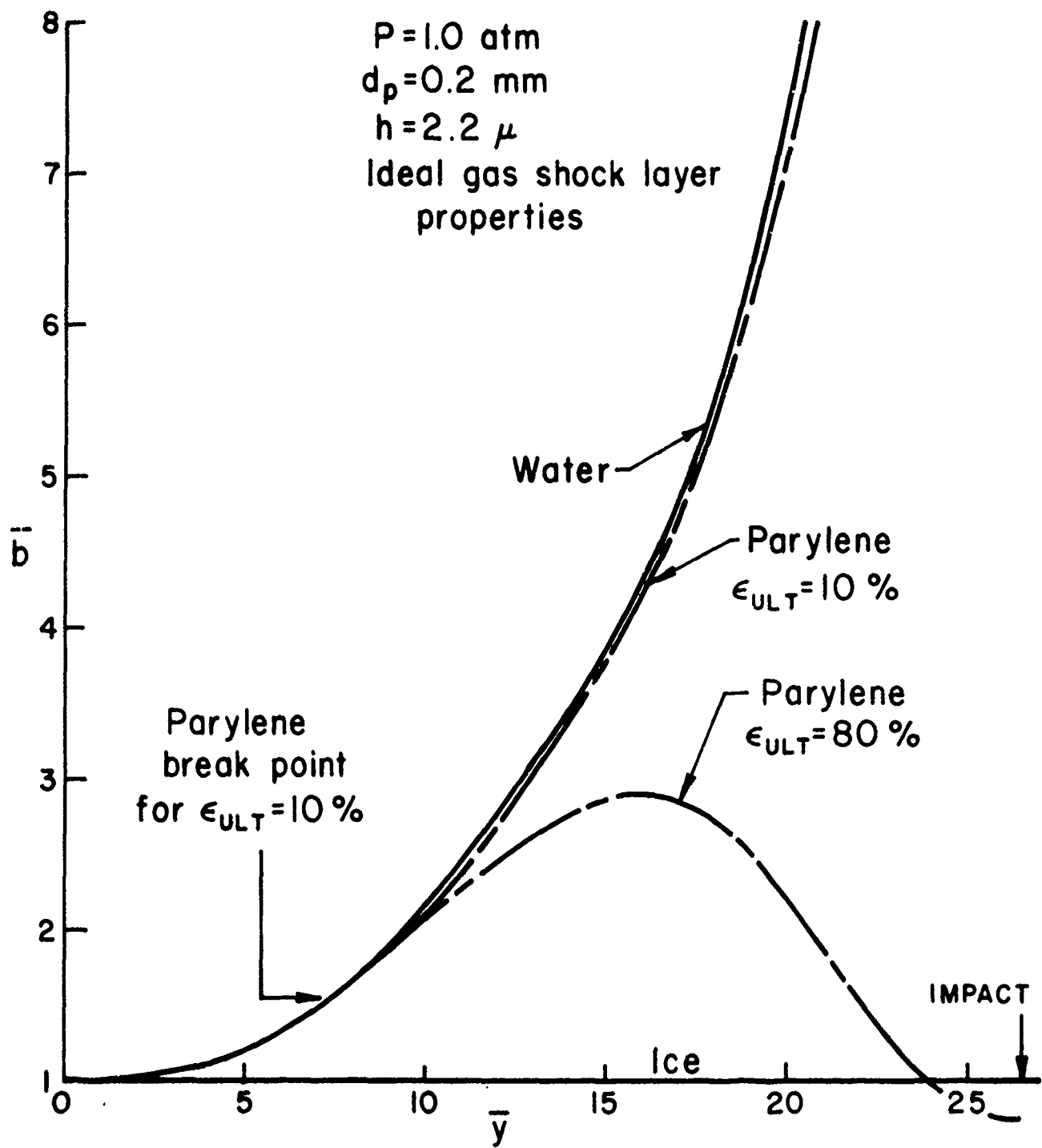


Figure 31

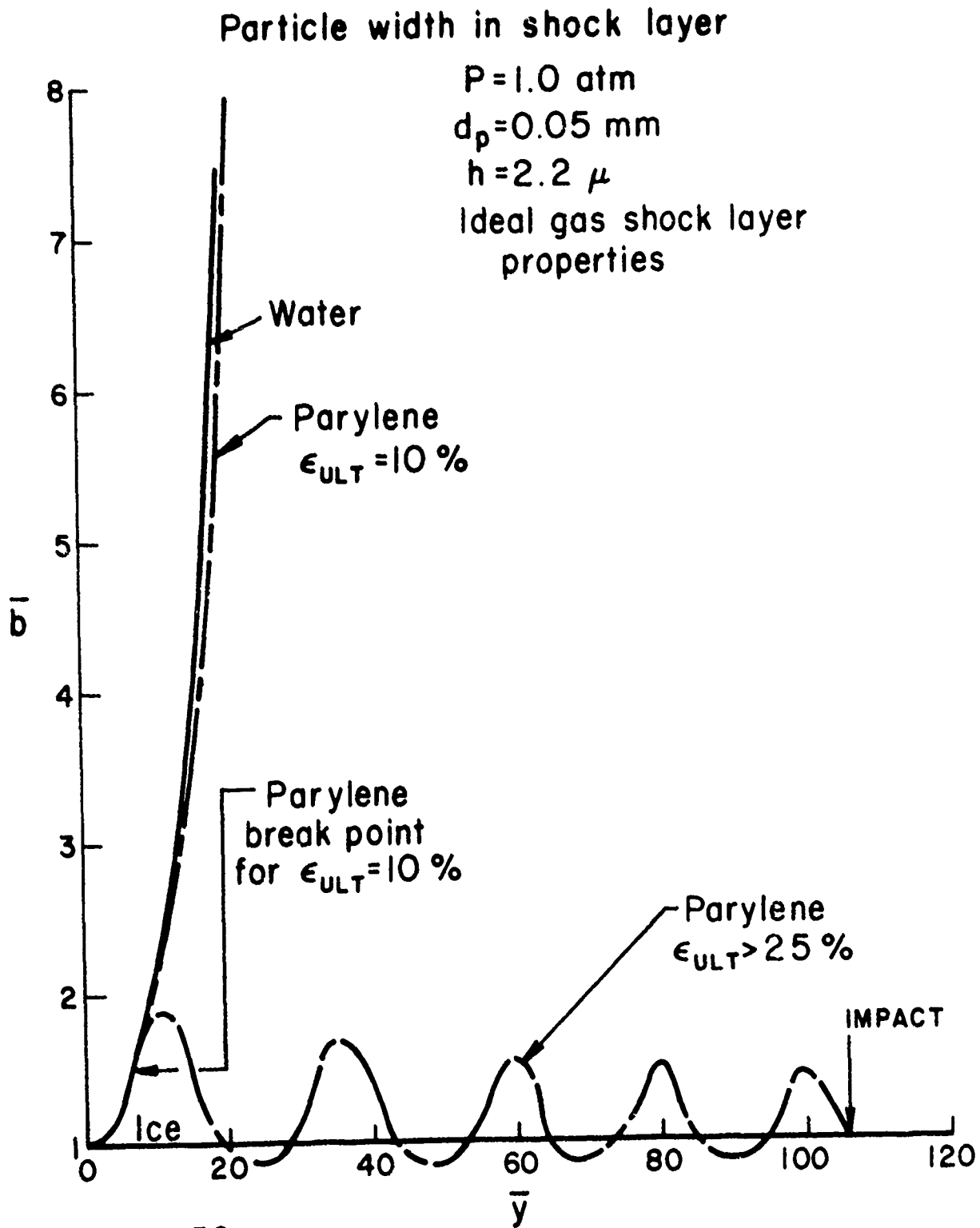


Figure 32

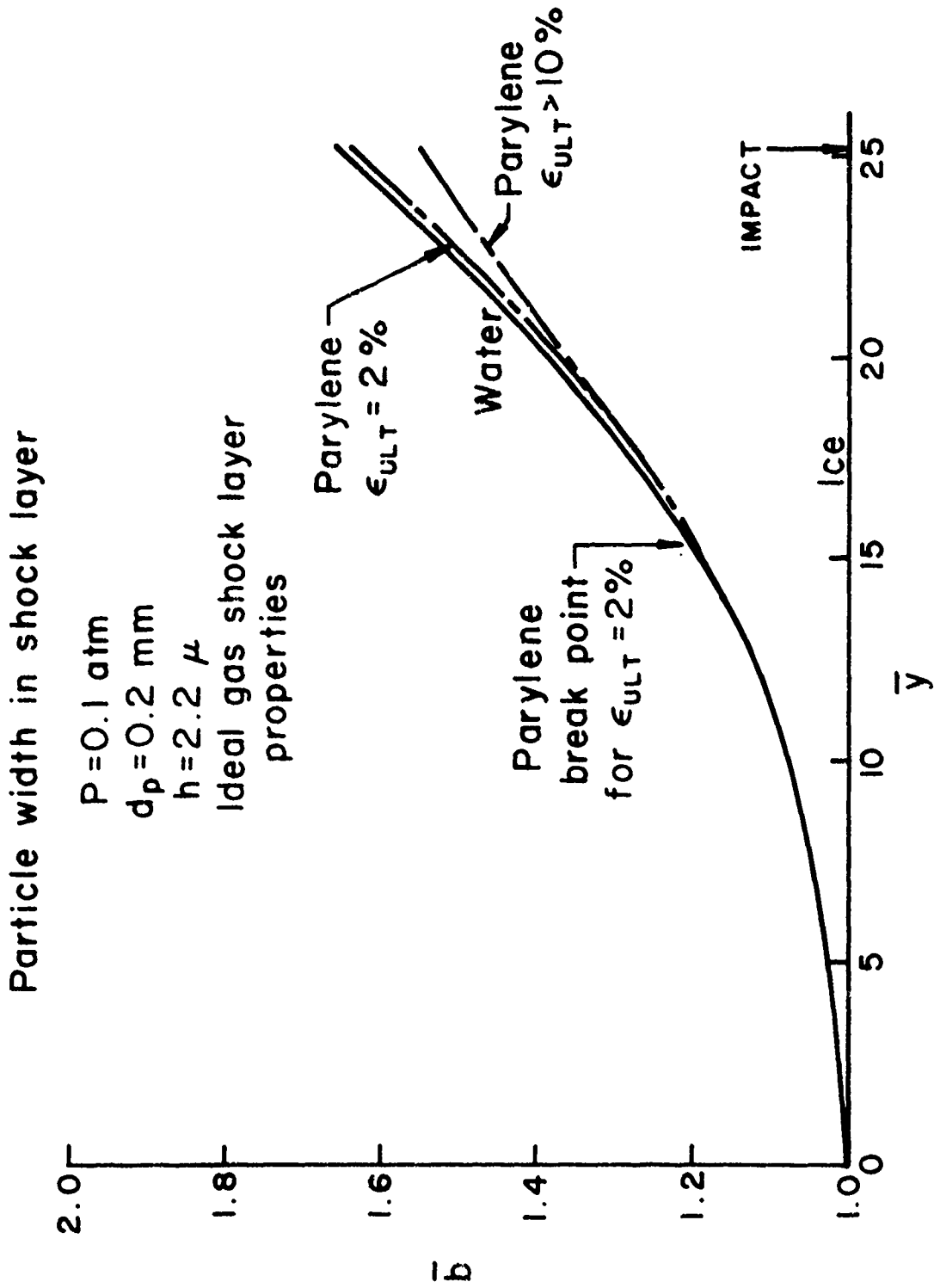


Figure 33

Particle width in shock layer

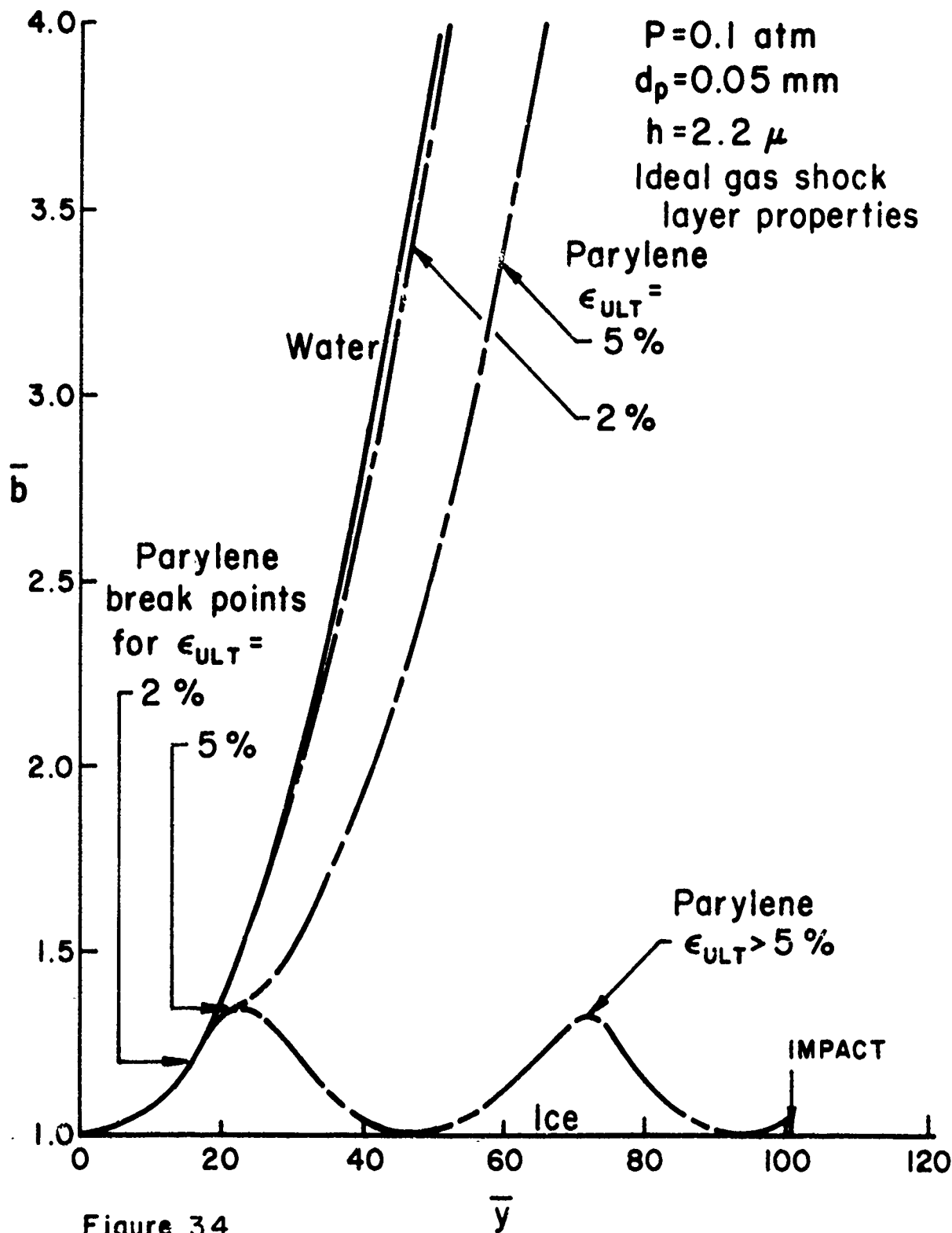


Figure 34

destruction prior to impact as is the case for water. However, an elongation between 5% and 10% may be enough to permit the particle to penetrate the shock layer. For these conditions, the particle would be more like ice than water.

Figure 35 suggests one method of improving the experimental simulation. A reduction of the parylene thickness to 0.5μ would require the film to survive an elongation in excess of 15% before the encapsulated particle would be different from the water droplet.

Figure 36 shows a summary curve of the impact velocity for each of the low pressure test conditions. For particle diameters in excess of 0.1 mm, the parylene encapsulated particle differs only slightly from the water droplet. However, for particle diameters less than 0.1 mm, the particle impact velocity is strongly dependent on the ultimate elongation of the parylene. It is in this region that one must be careful when analyzing test data, especially when trying to simulate environmental conditions.

Particle width in shock layer

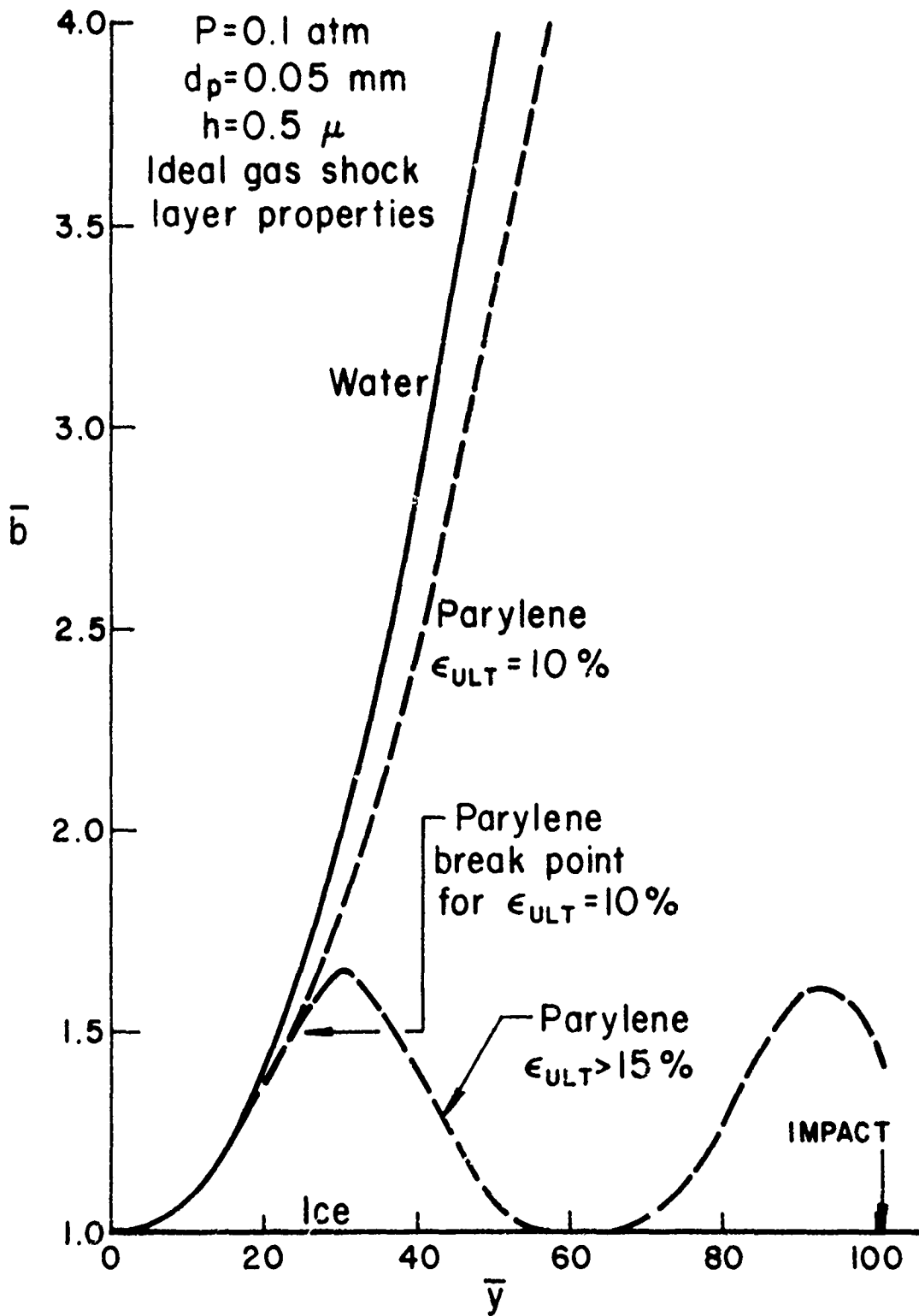


Figure 35

Impact velocity for low pressure tests

$P = 0.1 \text{ atm.}$ $V_p = 15 \text{ Kft/sec}$

$R_n = 2 \text{ in}$ $h = 2.2 \mu$

Ideal gas shock layer properties

Initial velocity

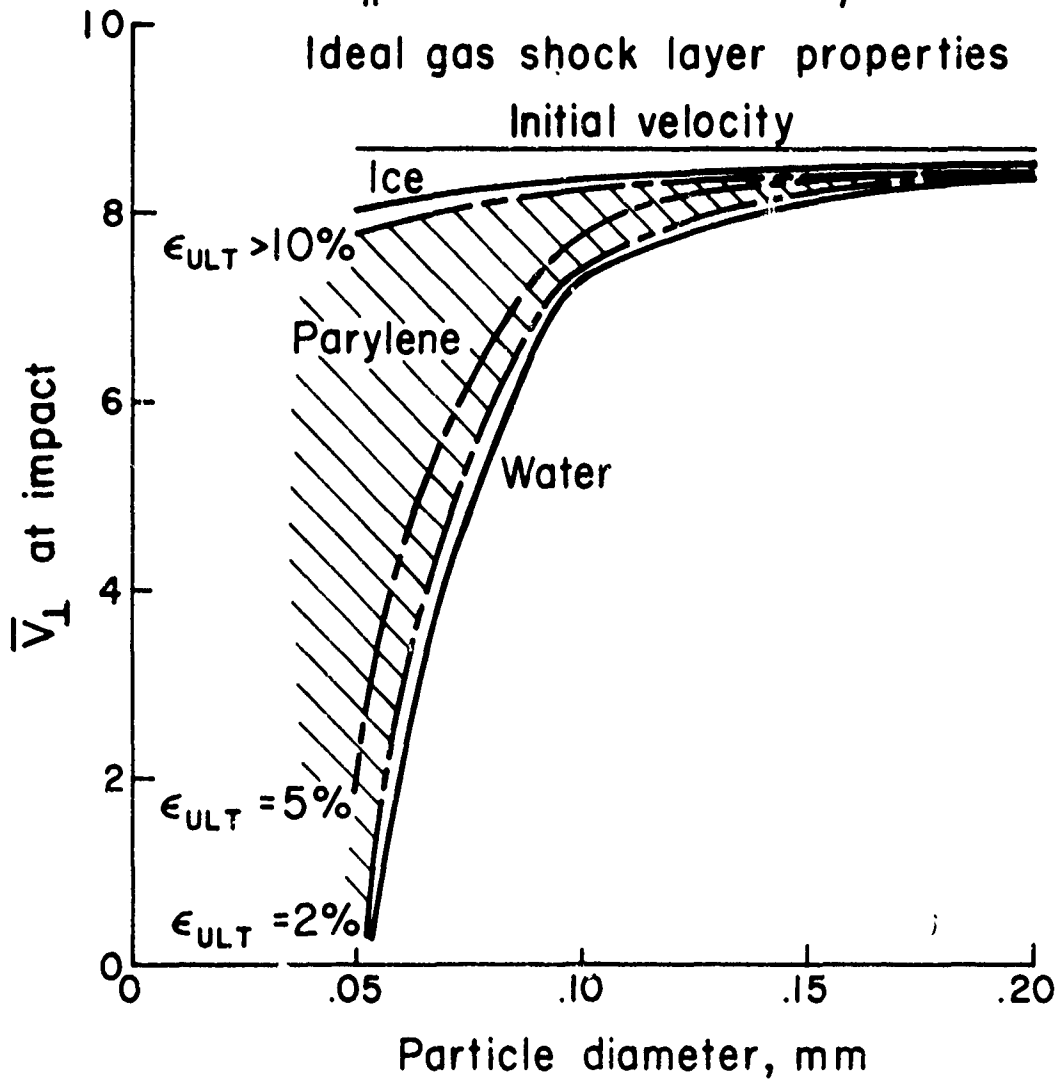


Figure 36

6. REFERENCES

1. Donaldson, Coleman duP. and McDonough, Thomas B.: A Simple Integral Theory for Impact Cratering by High Speed Particles. DNA 3234F, December 1973.
2. Hermann, W. and Jones, A.H.: Survey of Hypervelocity Impact Information. MIT Aero. & Structures Res. Lab., Report No. 99-1, September 1961.
3. McDonough, Thomas B. and Contiliano, Ross M.: Studies of the Simulation of Graphite Erosion Testing. A.R.A.P. Report No. 239, March 1975.
4. Frederickson, A.G.: Principles and Applications of Rheology. Prentice-Hall, Englewood Cliffs, NJ, 1964, pp. 98-117.
5. Truesdell, C. and Noll, W.: Nonlinear Field Theories of Mechanics. Encyclopedia of Physics (S. Flügge, ed.), Vol. III/3, Springer-Verlag, 1965, pp. 349-355.

PAPER NO. 44

THERMOSTRUCTURAL ANALYSIS OF IR SEEKER DOMES

by

W. R. COMPTON, C. F. MARKARIAN and B. M. RYAN

NAVAL WEAPONS CENTER
CHINA LAKE, CALIFORNIA

INTRODUCTION

Thermal stresses induced in seeker domes of air-launched, infrared (IR) missiles by aerodynamic heating during high-speed flight can be of sufficient magnitude to cause thermostructural failures. Because the design of such domes is constrained by the limited number of suitable materials, optical requirements, and economic considerations, the thermostructural limitations often lead to launch restrictions. Since the launch restrictions limit the operational effectiveness of the system, it is mandatory that such restrictions are based on the best possible estimate of the thermostructural capabilities of the dome. Efforts are currently being conducted at the Naval Weapons Center to develop improved capability for predicting the thermostructural failure or survival of IR seeker domes. While this paper specifically addresses IR domes, the same problems exist with electro-optical (EO) domes and radomes.

Figure 1 shows the steps required in the thermostructural design of a dome. While the tools necessary to conduct a thermal stress analysis of a dome are available in the form of computer codes, there are several technological deficiencies which limit the ability to accurately predict the ultimate thermostructural survival of the dome. The major deficiencies, as described below, are in the areas of material properties, boundary layer transition and failure criteria.

Material Properties. Insufficient data on the mechanical and thermal properties of dome materials, especially at elevated temperatures, interferes with accurate prediction and interpretation of dome thermal stresses.

Boundary Layer Transition. Accurate prediction of the aerodynamic heating to the dome requires knowledge of the location and extent of transition from a laminar to turbulent boundary layer. While reliable predictions of this sort are not yet possible and probably will not be in the immediate future, criteria which are based on the best available data are required for dome analyses.

Failure Criteria. Even if dome thermal stresses are accurately predicted, it is not possible to directly relate these stresses to the probability of dome survival because of the lack of verified failure criteria for full-scale domes.

Work is currently underway at NWC on the development of improved boundary layer prediction techniques and development of failure criteria. Programs to develop improved properties for IR dome materials are scheduled for the coming year. This paper presents descriptions of techniques currently being used at NWC to predict thermal stresses in domes and describes the efforts which are being conducted in the areas of boundary layer transition and failure criteria.

PREDICTION OF THERMAL STRESS

The thermal response of the IR domes considered in this investigation is derived from the finite-difference techniques available in the general thermal analyzer computer code, SINDA (Ref. 1). Special-purpose subroutines have been combined with the SINDA code to determine the thermal response of IR domes to aerodynamic heat transfer (Ref. 2). These subroutines utilize the method of Andrews (Ref. 3) to compute the pressure distribution on the dome, the method of Fay and Riddell (Ref. 4) to compute the stagnation point aerodynamic heat transfer, the method of Lees (Ref. 5) to compute the laminar boundary layer aerodynamic heat transfer to spherical portions of the dome, and integral techniques described by Kays (Ref. 6) to compute the laminar boundary layer aerodynamic heat transfer to non-spherical dome segments and the turbulent boundary layer aerodynamic heat transfer to the dome. Boundary layer transition is initiated at a user-specified momentum thickness Reynolds number. This modified version of the SINDA computer code is capable of calculating the thermal response of spherically-tipped cones, cylinders, and ogives at zero angle of attack. While the analytical techniques used are basically engineering approximations, their applicability to the configurations of interest has been verified with sophisticated boundary-layer computer codes (e.g. Spalding-Patankar and Smith-Clutter).

The SINDA code is used in conjunction with an automated network

generator which divides the dome into a specified number of nodes and computes node volumes, areas and path lengths. Node capacitances and conductances are computed within the SINDA code using temperature-dependent thermal properties. An axisymmetric thermal model is generated which includes heat transfer in the radial and streamwise directions. Input data include trajectory information (velocity and altitude versus time) and atmospheric conditions (temperature and pressure versus altitude). The program output consists of the node coordinates and the temperature-time history of each node.

Thermal stresses in IR domes are obtained from the finite-element techniques available in the computer code, SAAS-III (Ref. 7). Temperature distributions within the IR dome which are obtained directly from the modified version of SINDA in the form required by SAAS-III are used as input information to obtain the thermal stress field in the dome as a function of time. Aerodynamic loading may also be included by inputting the surface pressure distribution; however, the resulting stresses are generally small, compared to the thermal stresses.

As part of the effort to improve the accuracy of the predictive techniques, studies were made of the effect of thermal and structural model grid size and internal thermal radiation.

A parametric analysis of the effect of grid size on the

truncation errors observed in the solutions obtained from the combined thermal stress model was performed. Numerical errors were estimated by increasing the number of nodes or elements in a particular model until successive solutions converged. Convergence of thermal stress solutions was not obtained until the node thickness (radial) in the dome thermal model was less than 15% of the dome thickness, and the element thickness (radial) in the dome structural model was less than 10% of the dome thickness. It was also determined that the node-fineness ratio (radial thickness to streamwise length) in the thermal model had to be less than three, and element-fineness ratio had to be less than two in the structural model in order to obtain convergence of solutions.

Internal thermal radiation in an IR dome was simulated by the differential approximation (Ref. 8) to radiant energy transfer through an absorbing, emitting, and scattering non-gray medium. Results obtained for free-flight conditions encountered in current IR missiles indicate that internal thermal radiation does not significantly affect either the temperature or stress distributions in an IR dome.

The thermal/structural predictive techniques described above were compared with the data from two different tests of IR domes in order to evaluate their accuracy. Both tests were conducted at NWC. In the first test, the temperatures along the inner wall of a magnesium fluoride dome were measured during free-flight of a

boost-glide missile following a Mach 1.8 launch at an altitude of 42,000 feet. A comparison between the predicted and measured dome inner surface temperature response during the flight is shown in Figure 2 for two locations on the dome: the stagnation point and fifty degrees from the stagnation point. While there is excellent agreement between the measured and predicted temperature response, it was necessary to assume that the boundary layer over the dome was completely laminar. The results of this test are discussed further in the following section on boundary layer transition.

The second test involved a similar magnesium fluoride dome which was subjected to a constant radiant heat flux of 2.5 Btu/ft²-sec. This dome was instrumented with both temperature sensors and strain gages. A comparison between the predicted and measured dome inner surface temperature response is shown in Figure 3. Again, excellent agreement was obtained. A comparison between predicted and measured thermal strains in the hoopwise and streamwise directions is shown in Figure 4. While good agreement was obtained with the hoop strains, there is some disagreement between the measured and predicted meridional strains. It is felt that most of the disagreement is due to the lack of adequate material properties.

BOUNDARY LAYER TRANSITION

Sudden changes in aerodynamic heating can occur when the boundary layer flow over an IR dome goes through a transition from laminar to turbulent conditions. The predicted effect of boundary layer transition on the temperature and stress distribution in a typical IR dome following a supersonic launch is shown in Figure 5. The increase in aerodynamic heating rates and resulting thermal stresses caused by transition can be sufficient to cause thermostructural failure of the dome. Because of this, the design of such a dome requires the capability to accurately predict the location and extent of the boundary layer transition region. Efforts at the Naval Weapons Center in boundary layer transition are oriented specifically at developing criteria for application to domes. This is being done by evaluating existing criteria and data which are applicable to the dome configurations of interest, identifying data deficiencies, and, when possible, conducting experiments.

The problem of transition has been studied for over seventy years, and the literature is replete with correlation techniques and data (see Ref. 9). Much of the data, however, is incomplete, inconsistent, or inadequately described. Many of the correlation techniques apply only to the restricted set of data analyzed. In addition, in recent years it has been learned that ground facilities are not supplying results immediately applicable to flight conditions. Flight data is

difficult and expensive to obtain, and conditions cannot always be controlled or even determined adequately. Theoretical attempts have been mostly (not completely) confined to the linear case (such as stability theory), and transition is a highly non-linear phenomenon.

Nevertheless, while it is obvious transition is a difficult problem, progress is being made. The advent of high-speed digital computers has greatly increased the possibilities for the analyses that can guide and/or verify experiment. The recognition of the effects of flow turbulence and the acoustic environment, as well as other problems, on the results of tests in ground facilities will eventually lead to meaningful application to the flight regime. The accurate prediction of transition location is still in the future, but interim, practical engineering criteria are needed now for application to current design problems.

The transition criteria presently in use at the Naval Weapons Center utilizes the comparatively simple and direct local boundary layer parameter, momentum thickness Reynolds number (Re_θ). The momentum thickness (θ) is a measure of the decrement of momentum flux caused by the boundary layer and is defined as

$$\theta = \int_0^{\infty} \frac{\rho u}{\rho_{\infty} u_{\infty}} \left(1 - \frac{u}{u_{\infty}}\right) dy$$

Where y = direction normal to surface

u = velocity along surface

ρ = density

(the subscript ∞ denotes free stream conditions)

Correlations utilizing Re_θ have been very popular in the literature, but Re_θ alone does not necessarily show good correlation. This is demonstrated in Fig. 6 which summarizes momentum thickness Reynolds numbers at transition obtained from flight tests of vehicles with nose configurations similar to IR domes. At the present time, Re_θ for transition is largely determined by intuition and past experience. At the Naval Weapons Center, a value of Re_θ ranging from 600 to 750 is chosen for free-flight predictions.

The selection of the boundary layer computation technique is important and can lead to differences in the effect of transition on the heat transfer coefficient distribution as shown in Figure 7. The use of Re_θ in the Spalding and Patankar technique (Ref. 10) is to indicate the start of the turbulence leading to transition. In the Kays technique, which is used in the thermal response predictions described in the previous section, Re_θ determines the initiation of the divergence of the heat transfer coefficient from the laminar value. The transitional and turbulent Stanton number, St , is determined from an equation of the form,

$$St = f(Re_\theta) - \frac{A}{Re_\theta^2}$$

where Re_θ is computed from turbulent boundary layer relations. The value of A is chosen so that the laminar and turbulent Stanton numbers are equal at the start of boundary layer transition (i.e., where Re_θ computed from laminar boundary layer relations is equal to the chosen transition momentum thickness Reynolds number).

It is generally accepted that roughness has a significant effect on transition location. At the present time, roughness is not considered in the NWC transition predictions although attempts will be made to include this effect. IR domes are polished to an optical finish with a typical surface roughness of less than one microinch (RMS). While this is smoother than most of the metal noses on which free flight transition measurements have been made, the surface of IR domes is degraded with time through handling and rain and dust erosion. The resulting surfaces are usually acceptable optically but can have significant effect on promoting early transition. Unfortunately, the extent of roughness is unknown in much of the available flight test data. While nominal nose surface roughness values are given for the data shown in Fig. 6, their accuracy and completeness is unknown. In many cases, the flight vehicles were exposed to conditions before launch which could have considerably changed the nose surface.

The free flight temperature measurements on the inner wall of a magnesium fluoride IR dome described in the previous section provided valuable information on the occurrence of transition on domes in a typical air-launched missile environment. Four temperature sensors were mounted on the inner wall of the 2.84 inch diameter, 0.16 inch-thick dome. The sensors were located at the stagnation point and at 25, 50 and 68 degrees from the stagnation point, with the latter sensor near the dome shoulder. While the temperature of the

outer surface of the dome gives a more definite indication of transition, the many problems associated with such a measurement made it impractical. Thermal response calculations for the expected flight conditions had shown that transition could be detected by the inner wall temperature distribution if its effect were significant. As mentioned previously, the measured dome temperature response data from this flight correlated best with laminar predictions. Another indication of an all-laminar boundary layer on the dome is shown in Fig. 8 which plots the measured streamwise temperature along the dome and the predicted temperature distributions for both laminar and transitional boundary layers. The data follows the predicted laminar distribution and does not show the inflection in the temperature distribution which would occur if transition were present to a noticeable extent. The maximum momentum thickness Reynolds number on the dome during this flight was 440.

FAILURE CRITERIA

A common method of estimating dome failure in a given stress field utilizes the modulus of rupture (MOR) - an ultimate tensile strength that is derived from four-point loading of beams made from small coupons of the material used to fabricate the dome. This method usually relies on a statistical mean value of the MOR and, even though the MOR data is derived from uniaxial stresses, it is applied in triaxial stress fields. Variation of MOR values that inevitably

result when testing brittle materials can be statistically described, but the extrapolation from uniaxial test data to triaxial stress fields remains highly questionable. Fig. 9 shows MOR versus temperature data obtained from flexural testing of magnesium fluoride specimens. These results typify the spread in such data. Also shown in Fig. 9 are the maximum stresses and corresponding temperatures from three tests of magnesium fluoride domes, two of which resulted in dome failure due to breakage. Note that all three tests resulted in stresses near the lower boundary of the MOR data band.

The most promising methods of estimating dome failure, from the designer's viewpoint, rely on statistical methods such as those used in the Weibull (Ref. 11) and Batdorf (Ref. 12) volume flaw failure criteria and the Batdorf (Ref. 13) surface flaw failure criterion. The volume flaw theories derive a function that specifies the probability that a flaw exists in a given volume that will fail at some known stress state. The function used in these theories is derived from uniaxial tensile tests of the material in question. Of the two volume flaw failure criteria, Weibull's method is more empirical in application.

Fracture mechanics analyses, performed by the Naval Research Laboratory, indicate that failure of magnesium fluoride initiates from surface microcracks. This information resulted in the selection of Batdorf's surface flaw failure criterion for this

investigation. The surface flaw failure criterion is based on a function that specifies the probability that a surface flaw (micro-crack) exists in a given surface that will fail at some known stress state. The surface flaw function is determined from the ultimate tensile stresses measured in an equibiaxial stress field on small discs of the dome material. The probability of IR dome failure is then determined by summing the probabilities of failure of individual finite elements at the dome surface in the SAAS-III model. The stress state at each surface finite element is determined from the SINDA/SAAS-III model of the dome.

Batdorf's surface flaw failure criterion was applied to the thermal stress field predicted for the aforementioned free flight of a magnesium fluoride dome. The surface flaw failure criterion predicted a maximum probability of failure for the flight of 30% at a time-of-flight corresponding to maximum dome temperature. The predicted probability of failure at the time of flight corresponding to maximum temperature gradient in the dome was less than 10%. The IR dome did not fail during this free flight. The surface flaw failure criterion was also applied to data obtained on an IR dome that was tested to failure in the McDonnell-Douglas hot core wind tunnel. The predicted probability of dome failure at the time of observed dome failure in this test was 90%.

Additional testing of full-scale domes is to be continued next fiscal year in an attempt to further verify the transfer function

between destructive testing of small laboratory specimens and full-scale failures. Several magnesium fluoride domes similar to that used in the free flight test will be tested to destruction in the NWC T-Range hot core free jet facility. The nominal flow conditions in the free jet tests will be a Mach number of 2.5, a total temperature of 1000⁰ F and a total pressure of 250 psi. Predicted temperatures and stresses on the inner surface of the dome after three seconds' exposure to the free jet conditions are shown in Fig. 10 and 11, respectively. The resulting dome probability of failure as determined from the Batdorf surface flaw technique is shown in Fig. 12. The analysis indicates a 99.4% probability of failure for the dome under these conditions. As many domes as possible will be tested in order to develop a useful, full-scale dome failure data base.

In addition to providing a data base for the evaluation of failure criteria, the free jet tests will be used in evaluating non-destructive testing techniques. Such techniques would be valuable in screening domes in the lower percentile of structural capability. Non-destructive tests under consideration include optical scattering, acoustic emission and laser interferometry. Each dome will be subjected to the non-destructive tests prior to testing in the free jet facility so that attempts can later be made to correlate the dome failures with the results of the non-destructive tests.

SUMMARY

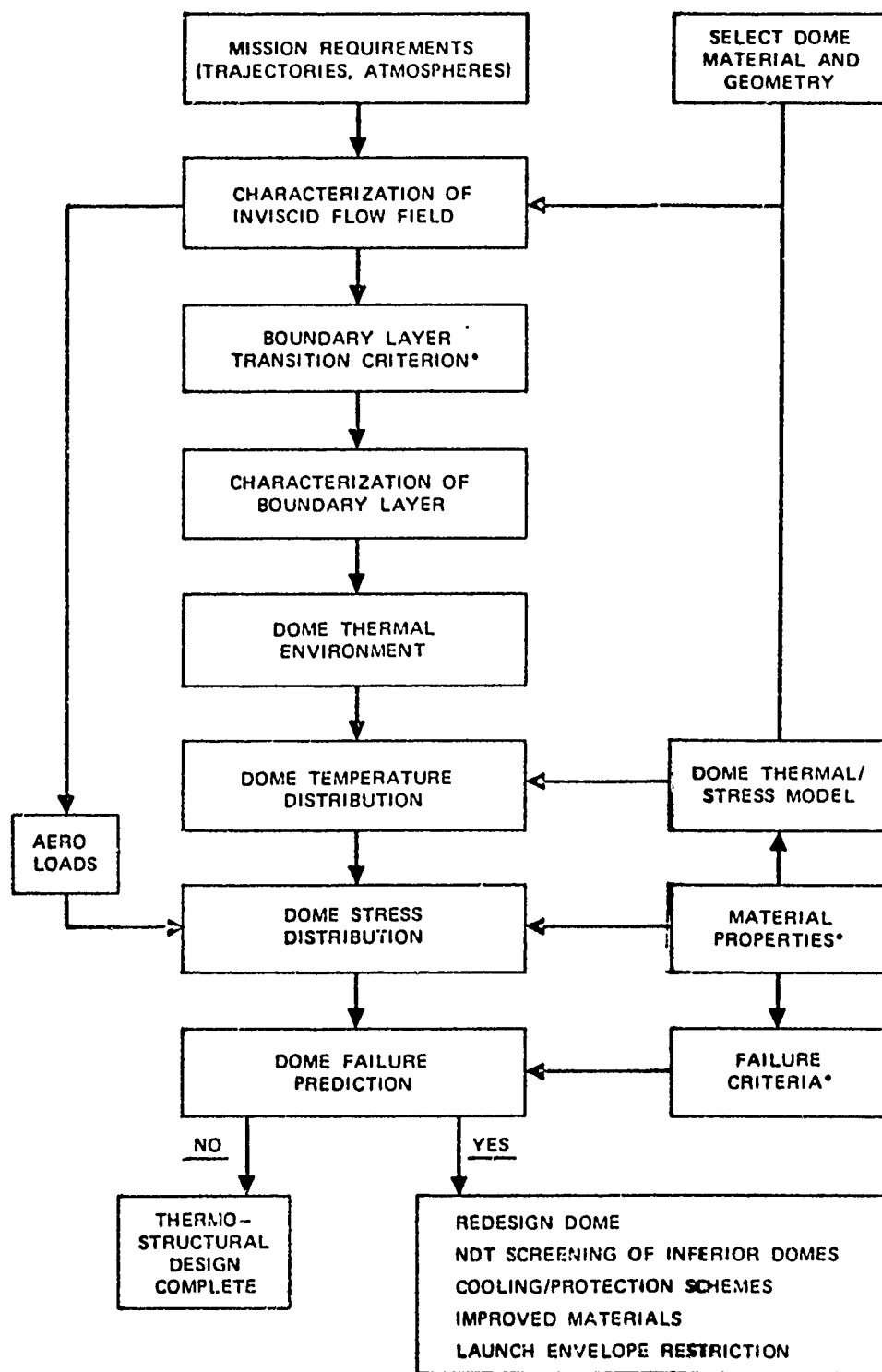
Efforts are being conducted at the Naval Weapons Center to improve capabilities for predicting thermostructural survivability of IR missile domes. Thermal stress prediction techniques currently in use are described in this paper, and correlations are shown with experimental temperature and strain data. Parametric analyses have been made to determine thermal and stress model grid size requirements and the effect of internal radiation on dome thermal stress.

Work is being performed to improve deficiencies in the prediction of boundary layer transition on domes. The transition criteria currently in use is a momentum thickness Reynolds number ranging from 600 to 750, depending on specific conditions. Additional correlations are being performed with the objective of developing recommended criteria specifically for application to domes which are based on the best available experimental data.

Statistical failure criteria have been evaluated, and a surface flaw technique has been determined to be the most applicable for predicting the failure of magnesium fluoride domes. Tests to destruction of full-scale IR domes in a hot gas test facility are planned to develop a data base for further evaluation of the failure criteria.

REFERENCES

1. Gaski, J. D., Fink, L. C., and Ishimoto, T., "Systems Improved Numerical Differencing Analyzer Users Manual", TRW Report 11027-6003-R0-00, Sept. 1970.
2. Compton, W. R., "Aerodynamic Heating of Spherically Tipped Cylinders, Cones, and Ogives Using the General Thermal Analyzer, SINDA", NWC TN 4061-172, June 1974.
3. Andrews, J. S., "Steady State Airload Distribution on Hammerhead Shaped Payload of a Multistaged Vehicle at Transonic Speeds", Boeing Company Report #D2-22947-1; AD-465-140, January 1964.
4. Fay, J. A. and Riddell, F. R., "Theory of Stagnation Point Heat Transfer in Disassociated Air", Journal of Aerospace Sciences, Volume 26, Number 2, February 1958.
5. Lees, L., "Laminar Heat Transfer Over Blunt-Nosed Bodies at Hypersonic Flight Speeds", Jet Propulsion, Volume 26, Number 4, April 1956.
6. Kays, W. M., "Convective Heat and Mass Transfer", McGraw-Hill Book Company, 1966.
7. Crose, J. G., and Jones, R. M., "SAAS-III Finite Element Stress Analysis of Axisymmetric and Plane Solids with Different Orthotropic, Temperature Dependent Material Properties in Tension and Compression", Aerospace Corporation Report TR-0059 (S6816-53) -1, June 1971.
8. Vincenti, W. G. and Kruger, C. H., "Introduction to Physical Gas Dynamics", John Wiley & Sons, 1965.
9. Ryan, B. M., "Survey of Boundary Layer Transition Data with Emphasis on Application to Missile Seeker Domes", NWC TN 4061-178 (in process).
10. Patankar, W. V. and Spalding, D. B., "Heat and Mass Transfer in Boundary Layers", 2nd edition, Intertext Books, London, 1970.
11. W. Weibull, "A Statistical Theory of the Strength of Materials", Ingeniors Vetenskaps Akademiens Handlingar Nr. 151 (1939).
12. Batdorf, S. B., "A Statistical Theory for Failure of Brittle Materials Under Combined Stresses", AIAA Paper Number 73-381. Presented at AIAA/ASME/SAE 14th Structures, Structural Dynamics, and Materials Conference, Williamsburg, Virginia, 20 March 1973.
13. Batdorf, S. B., "Fracture Statistics of Isotropic Brittle Materials with Surface Flaws", Aerospace Corporation Report TR-0074 (4450-76) -2, December 1973.



*TECHNOLOGY DEFICIENCY AREAS

FIG. 1. THERMOSTRUCTURAL DESIGN OF IR DOMES

MACH 1.8 LAUNCH AT 42,000 FEET

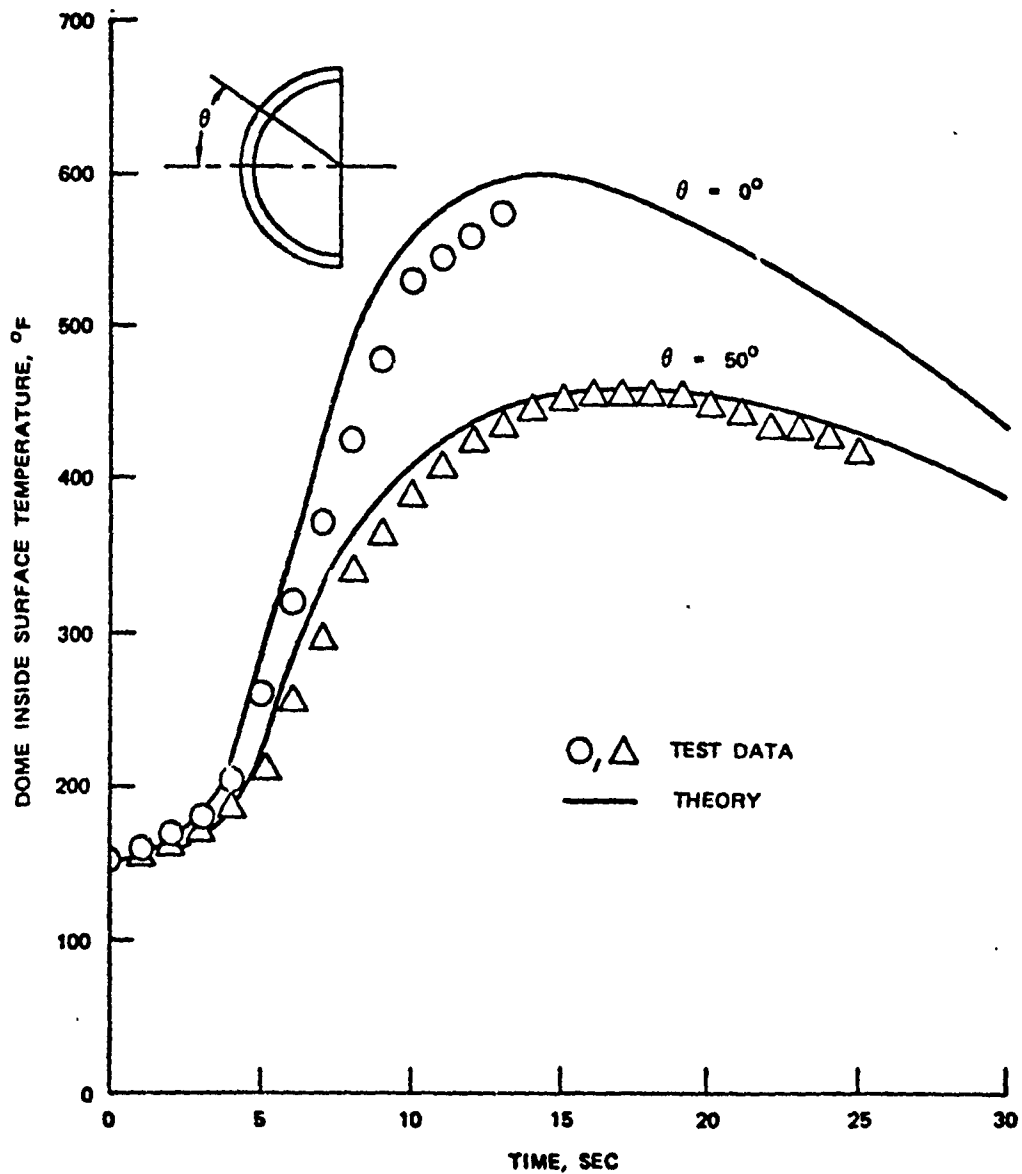


FIG. 2. IR DOME FREE FLIGHT TEMPERATURE RESPONSE

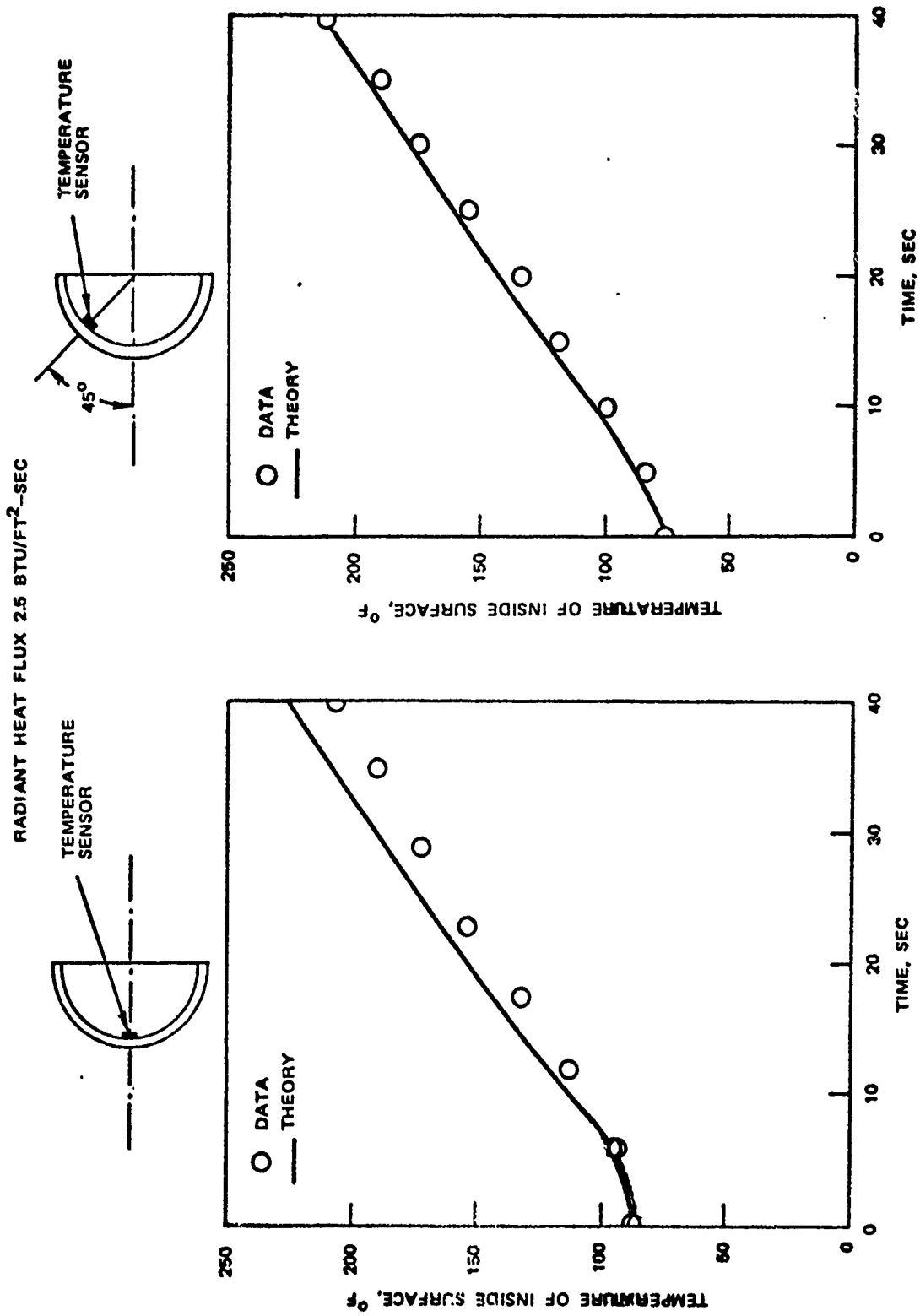


FIG. 3. IR DOME RADIANT HEATING TEMPERATURE RESPONSE

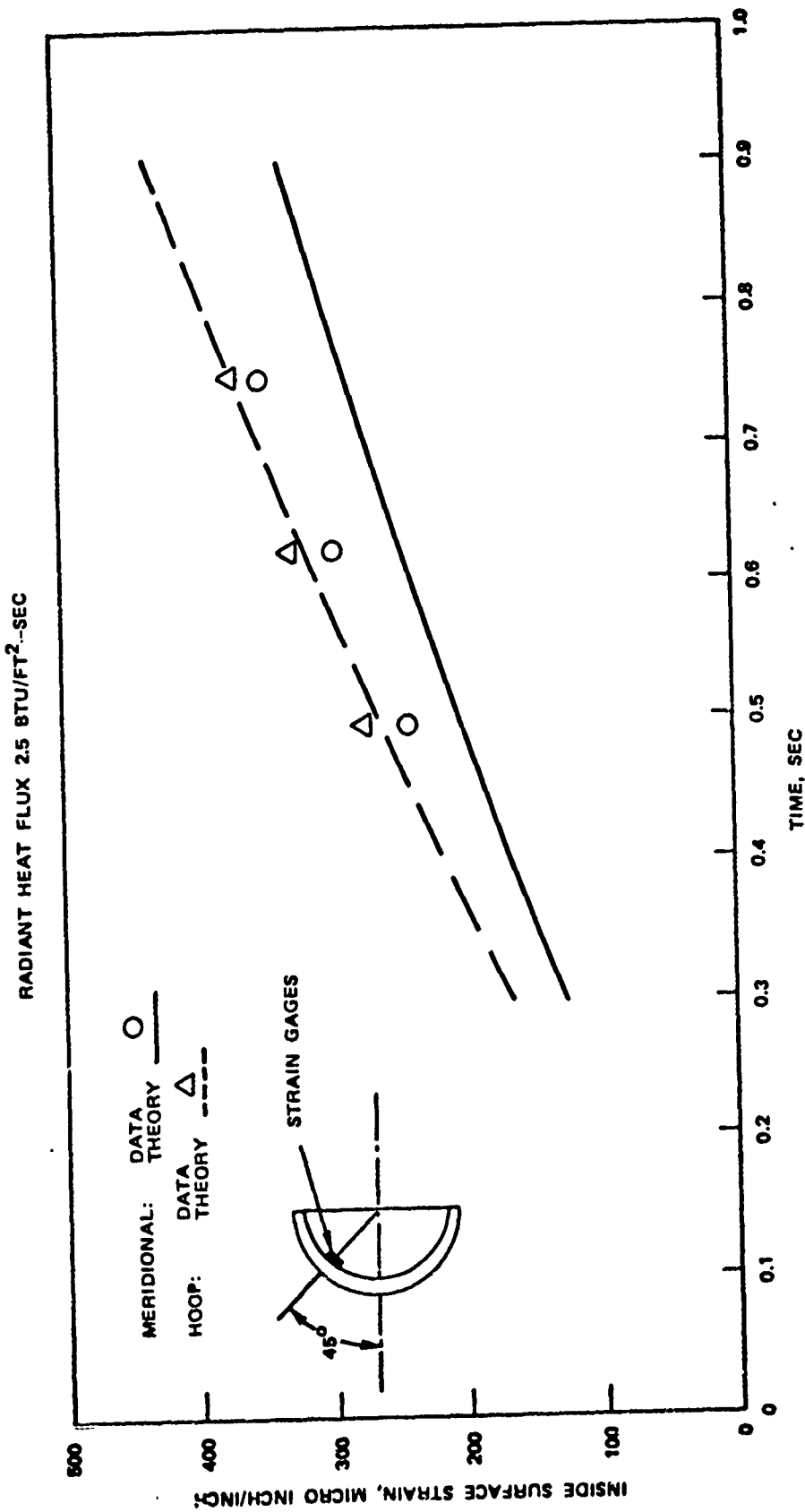


FIG. 4. IR DOME RADIANT HEATING STRAINS

MAGNESIUM FLUORIDE DOME
MACH 1.6 LAUNCH AT 30K

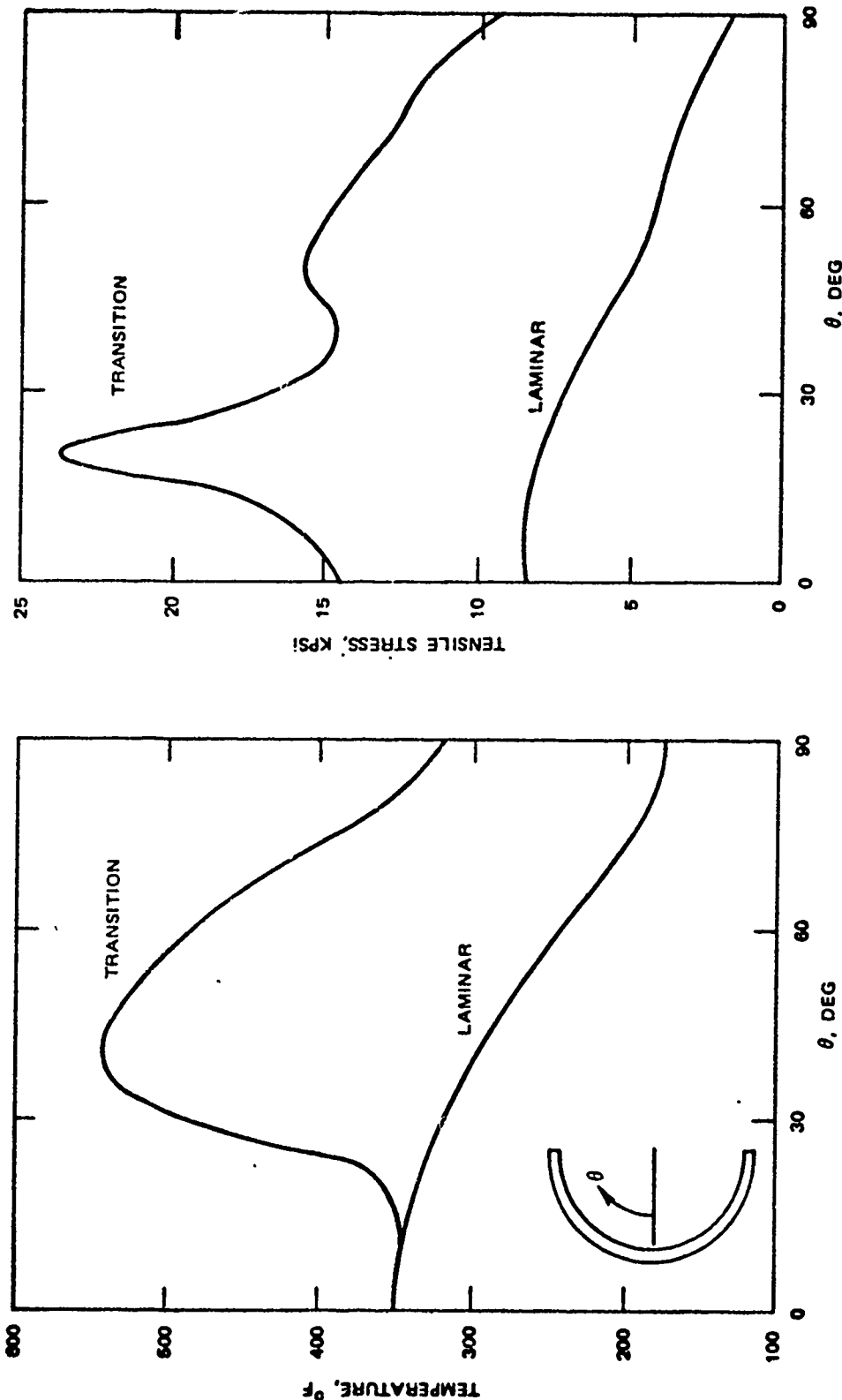


FIG. 5. EFFECT OF BOUNDARY LAYER TRANSITION ON IR DOME INNER WALL TEMPERATURE AND STRESS

SYMBOL	INVESTIGATORS	CONFIGURATION	RMS ROUGHNESS, MICROINCHES
○	HALL, SPEEGLE, PILAND	HEMISP-CYLINDER (8 IN. DIAMETER)	1-5
□	KRASNICAN, WISNIEWSKI	HEMISP-CYLINDER (9 IN. DIAMETER)	3-5
◇	GARLAND, SWANSON, SPEEGLE	1/10 POWER NOSE	6-8 (MAX 15)
△	BUGLIA	HEMISPHERE-CONE (HEMISP DIAM 12.582 IN.)	2-4
▽	GARLAND, CHAUVIN	HEMISP-CYLINDER (8 IN. DIAMETER)	26

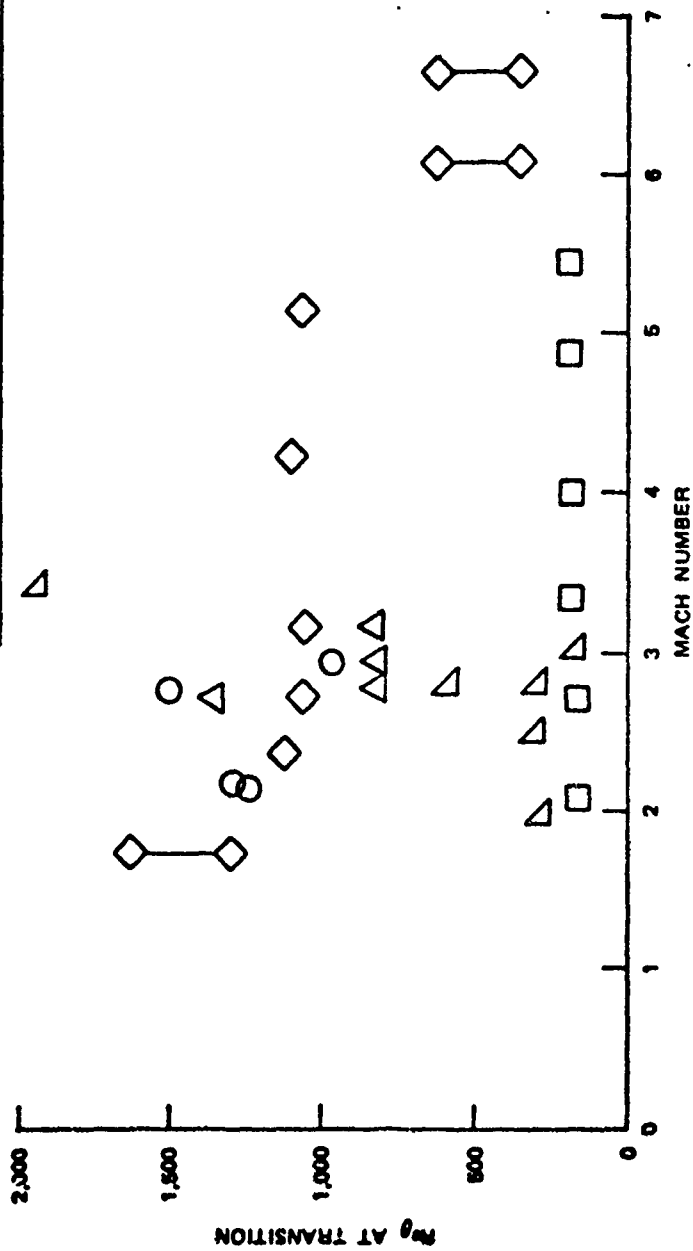


FIG. 6. FLIGHT TEST TRANSITION REYNOLDS NUMBER DATA

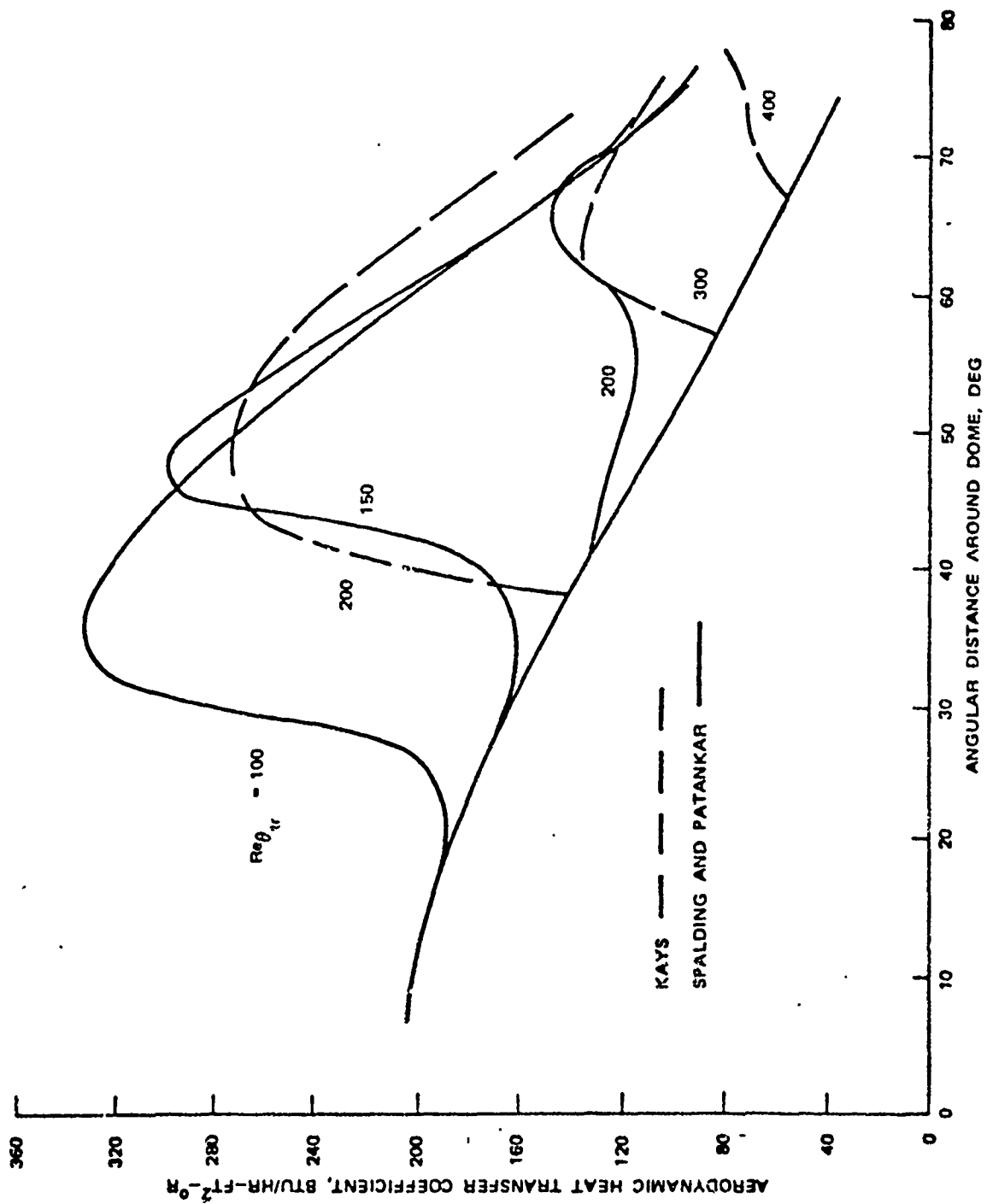


FIG. 7. EFFECT OF TRANSITION REYNOLDS NUMBER ON DOME HEAT TRANSFER COEFFICIENT DISTRIBUTION

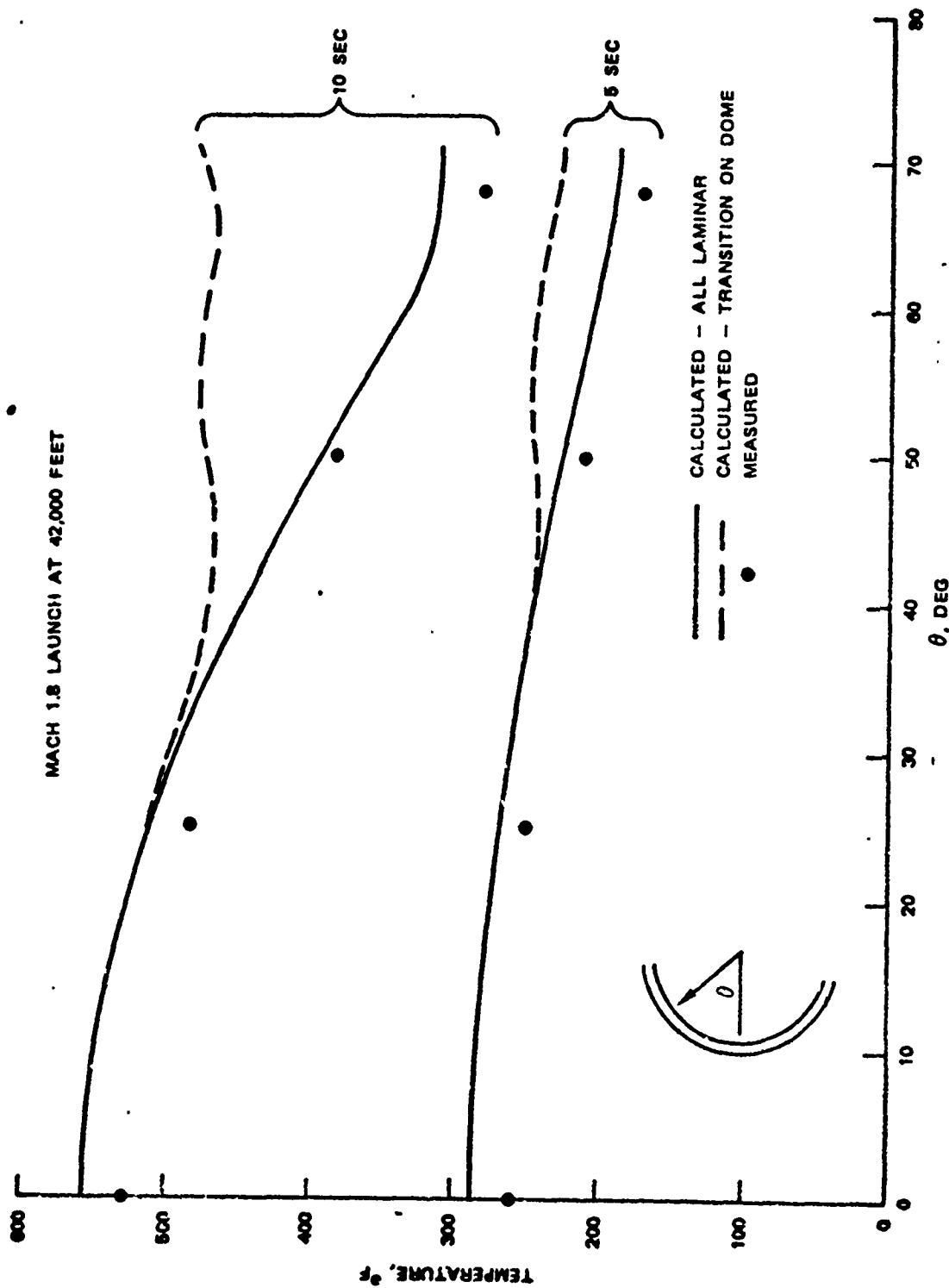


FIG. 8. IR DOME INNER WALL TEMPERATURE DISTRIBUTION

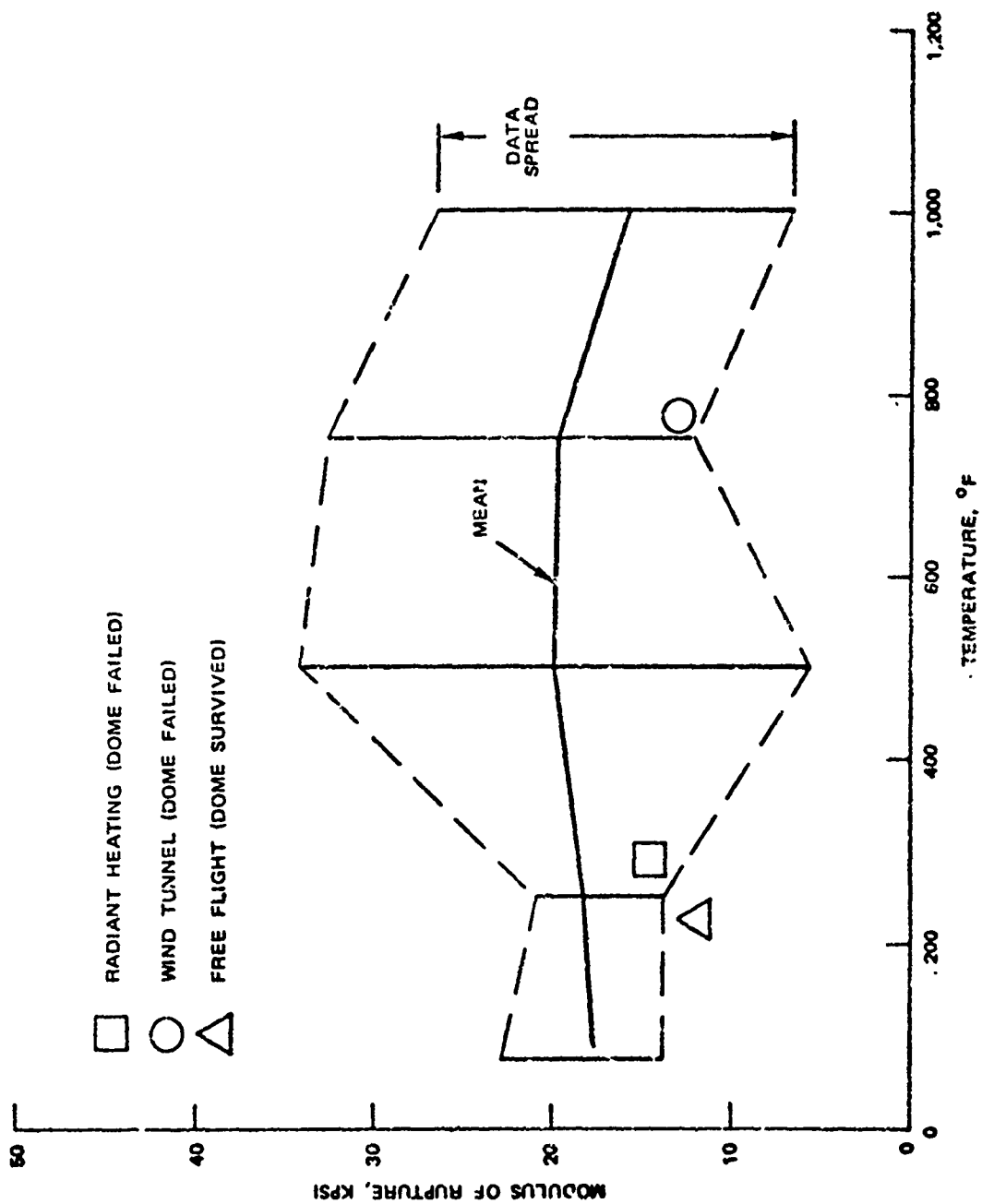


FIG. 9. COMPARISON OF MgF₂ FLEXURAL STRENGTH DATA AND PREDICTED STRESS LEVELS

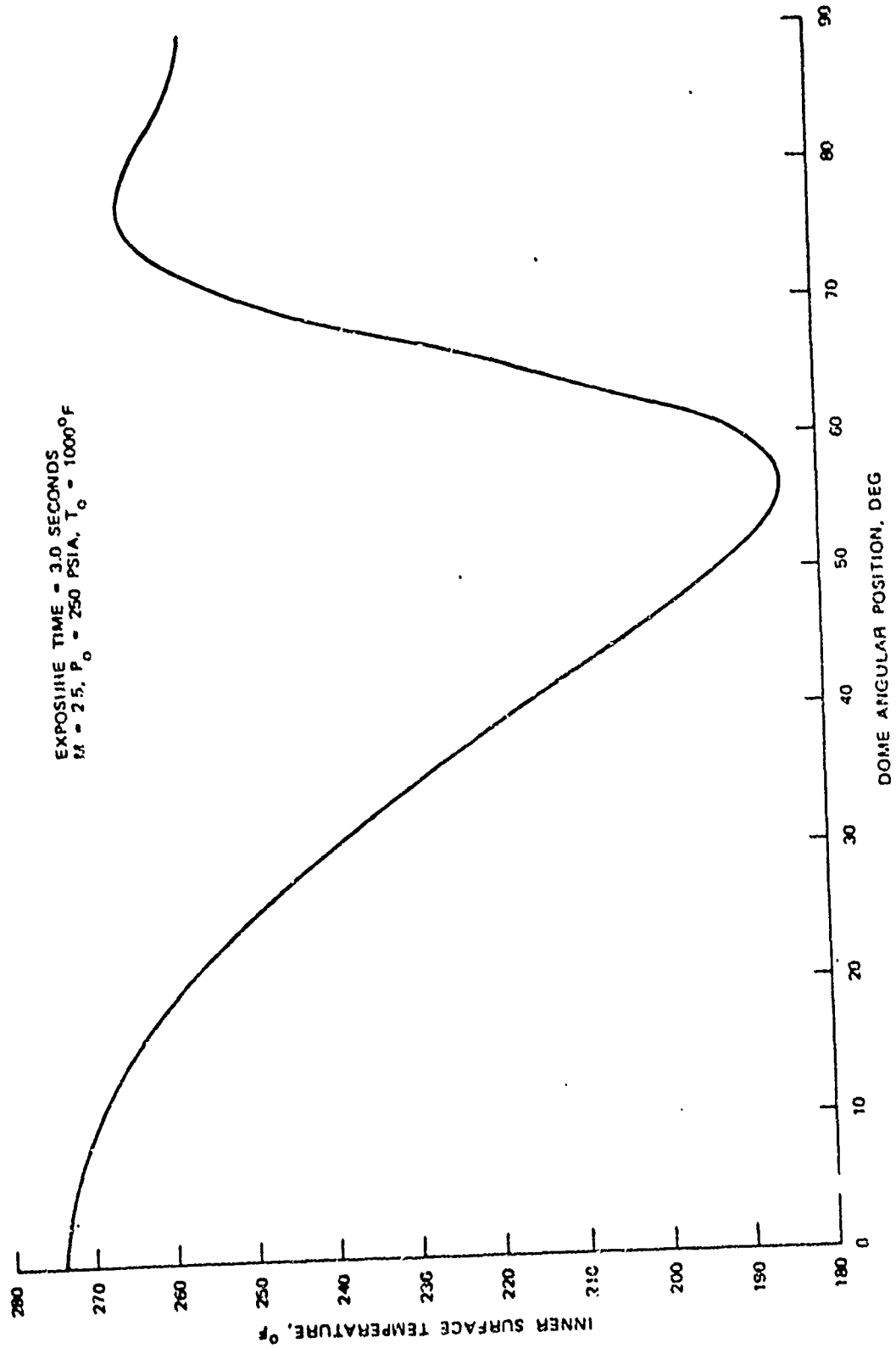


FIG. 10. PREDICTED IR DOME INNER WALL TEMPERATURE DISTRIBUTION — MNC T-RANGE FREE-JET SIMULATION

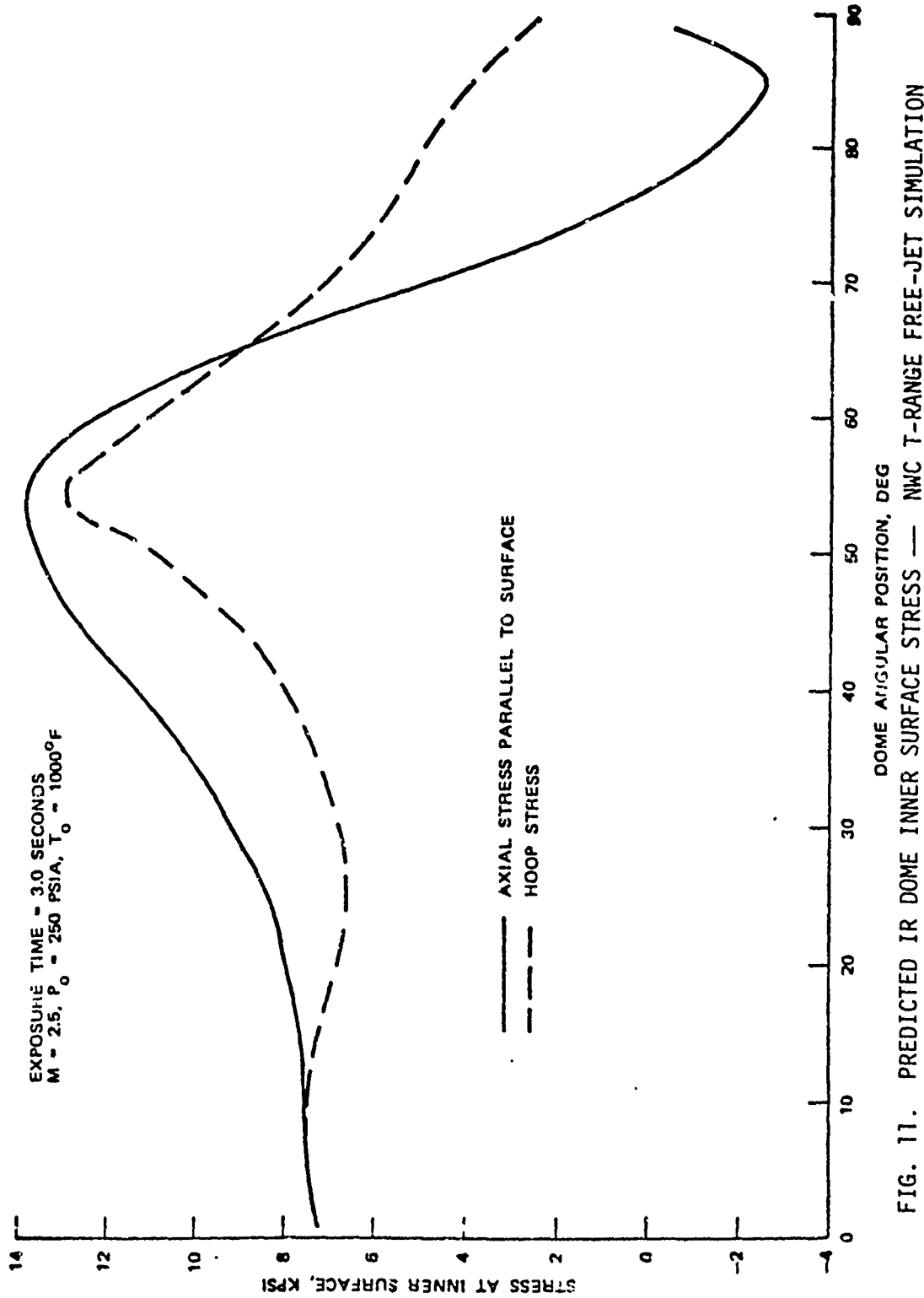


FIG. 11. PREDICTED IR DOME INNER SURFACE STRESS — NWC T-RANGE FREE-JET SIMULATION

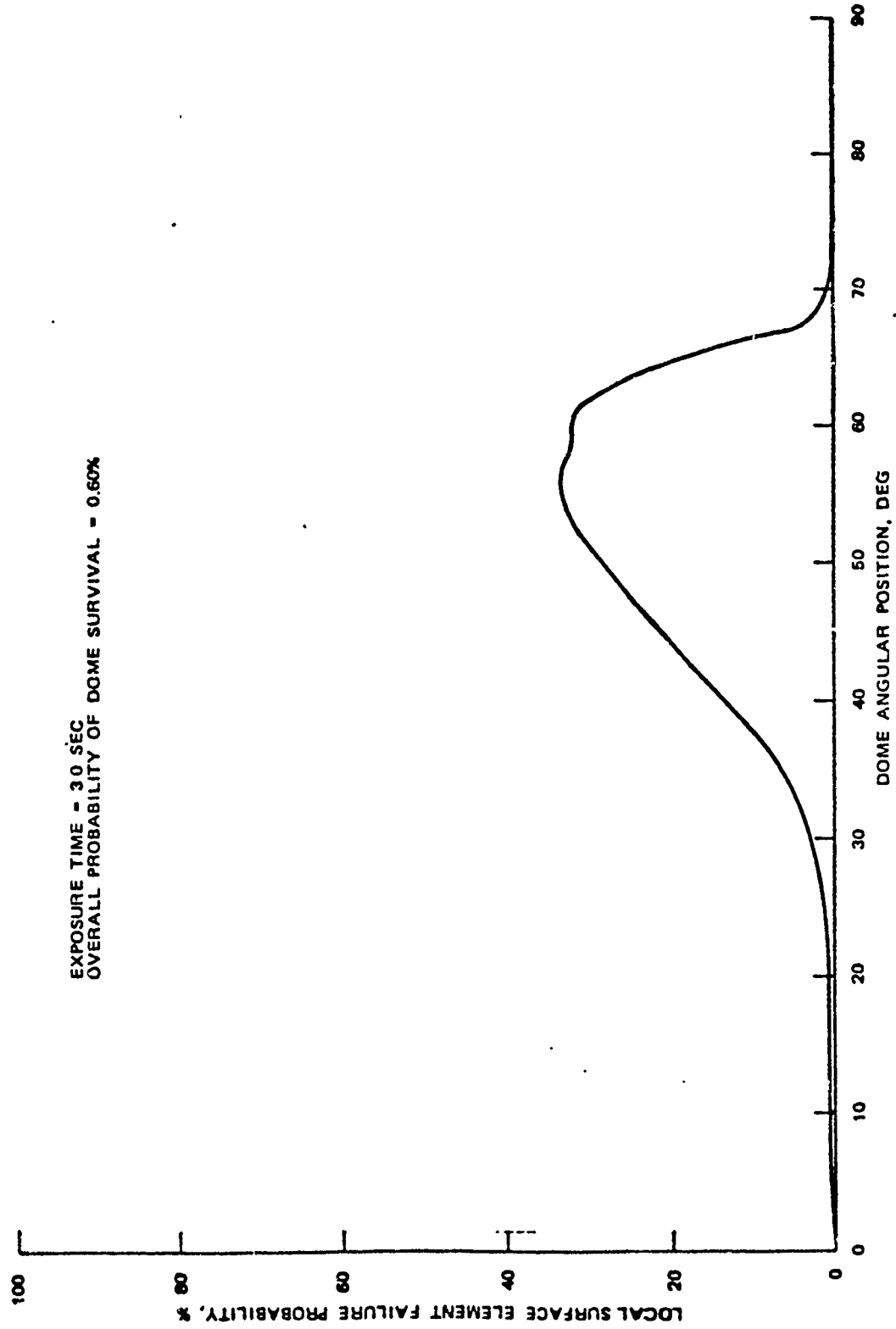


FIG. 12 PREDICTED IR DOME PROBABILITY OF SURVIVAL — NWC T-RANGE FREE-JET SIMULATION

PAPER NO. 45

Effect of Multiple Impacts on Erosion
Characteristics of Nose-tip Materials (U)

Norman W. Sheetz, Jr.

Naval Surface Weapons Center
White Oak Laboratory
Silver Spring, Maryland

ABSTRACT

(U) This paper summarizes the results of studies conducted in the Missile Dynamics Division of the Naval Surface Weapons Center, White Oak Laboratory, to determine the effects of multiple impacts on the erosion characteristics of R/V nose tips. It includes both experimental data obtained in a number of ballistics range tests and supporting analytical studies. The experimental data were obtained in the White Oak Laboratory Hyperballistics Range and Aerophysics Range. Test specimens were launched through precision simulated rain fields and the erosion rates determined from high resolution in-flight photographs and recovered specimens.

(U) Data are shown from single impact tests into virgin targets. They are compared with multiple impact tests where the number of impacts are increased until the target material is fully damaged. Details of single particle impacts are used to predict the increased erosion rates associated with multiple impacts. The number of impacts required to "fully damage" a material at various velocities is determined. These results are used to analyze typical re-entry flights through weather erosion environments to determine where single impact and where multiple impact data are appropriate to predict erosion response of nose tips. Also, calculated impact craters are compared with measured crater geometries obtained from recovered samples of impacted materials.

INTRODUCTION

(U) Performance requirements for current re-entry vehicles have led to the selection of ablative heat shields and nose tips. The erosion characterization of these materials, typically, is a time-consuming and expensive process. The initial step usually consists of relatively inexpensive "screening type" tests of a family of materials in a single impact facility to select the most promising members. The most promising candidates are then tested in ground based multiple impact facilities. These include ballistics ranges, wind tunnels, whirling arms, sled tracks, etc. From these multiple impact tests, modeling codes can be developed to predict the erosion performance during a re-entry flight through a hostile environment. Flight tests are then conducted on material samples to test the validity of the modeling predictions. Once confidence is obtained in the performance of the various exterior materials, full-scale flight tests are performed on the entire re-entry vehicle.

(U) This lengthy development process is required due to the complicated nature of hypervelocity erosion. That is, the erosion of re-entry materials is dependent not only on the mass impacted but upon many other aspects of the encounter. Parameters that apparently affect the process to some degree include: impact velocity, particle state, particle size, cloud density, ambient pressure, cloud material, target material, target size, target geometry, and target state. It is the

Vol. 3

objective of this study to investigate the significance of many of these parameters upon the erosion performance of a typical nose-tip material.

(U) For most nose-tip and heat-shield materials, the study of erosion can be divided into two regimes, the discrete impact regime and the multiple impact regime. This is illustrated in Figure 1.

(U) The "discrete impact regime" represents the first portion of the flight in which the vehicle encounters an erosion environment. It is characterized by relatively large spacing between impacts with no interaction between impacts. The recession rates in this regime are low because the material is still relatively strong, being weakened only by ablation during the earlier phase of re-entry. If the erosion cloud is relatively thin, the entire surface may not be altered by erosion. In this case, the most significant effect of the cloud may be to induce a roughness which could seriously alter the ablation rate for the remainder of the flight or to degrade the accuracy of the vehicle.

(U) If the cloud is sufficiently thick so that impacts begin to overlap, the vehicle gets into the "multiple impact regime" at later flight times. This regime is characterized by interacting or overlapping of impacts and usually higher recession rates because of weakening of the material by previous impacts.

(U) The degree to which a surface has been altered is often defined in terms of the "obscuration." The definition of

obscuration is shown in Figure 2. It is a measure of how completely the impacting particles cover or shade the target surface. Specifically, it is the ratio of the summation of the cross sectional area of all the particles that have hit the surface and normalized by the cross sectional area of the target. For a uniform size of particles, the obscuration increases directly with the number of impacts.

(U) Figure 3 shows the relation of impact regimes to obscuration. The discrete impact regime occurs at lower obscuration rates where impacts are far enough apart so that neither crater or the damaged areas around the craters overlap. As the obscuration increases with additional impacts, the damaged regions start to overlap, and the process moves into the multiple impact regime. As illustrated in Figure 3, the erosion rate for typical re-entry vehicle material is generally much lower in the discrete impact regime as compared to the multiple impact regime. This difference may be a factor of four or more. Another concept of significance illustrated in Figure 3 is the "critical obscuration." It is a description of the number of impacts required to effectively damage the material and truly move it into the multiple impact state.

(U) Since the erosion rates can be drastically different in the various impact regimes, it is necessary to provide the missile designer information regarding both when a vehicle would be expected to be in each regime and what the corresponding erosion rates are. The specific objectives of this study are directed towards these goals. They include:

- a. Defining parameters that affect obscuration.
- b. Obtaining discrete particle and multiple particle data and relating the two.
- c. Describing typical re-entry missions in terms of obscuration regimes.
- d. Incorporating these effects into a prediction code if necessary.

Many of these objectives have been met and will be discussed in this paper.

RANGE TESTS

(U) To obtain experimental erosion and obscuration data, a series of tests were conducted in the Naval Surface Weapons Center, White Oak Laboratory, Hyperballistics Range (HBR). Samples of a typical carbon-carbon nose-tip material were mounted on the forward section of the range models. The models were accelerated to the required test velocity by the launcher. The sabot or launch support material was separated in the forward section of the range which was isolated from the test section by a baffle. The test section contained both a simulated rain environment and optical station to monitor the erosion rate. The rain environment was simulated by placing water drops encapsulated in thin films and placed in a precise array on the flight path. The delicate support films were only 2,000 Å thick. By varying the spacing of the drops on the film and the distance between the films, the density of the erosion field could be controlled. The erosion rate was

determined from high resolution laser photographs taken of the model in flight before it entered the rain field and as it progressed through the field. Figure 4 shows a typical pair of photographs taken before and after encountering a rain field.

(U) Figure 5a shows the test results obtained on a carbon-carbon impacting 400 μ diameter rain at a nominal velocity of 11,000 fps. The plot shows the variation in mass loss ratio, that is the mass eroded normalized by the mass impacted, as a function of obscuration or number of impacts. In addition to the White Oak Laboratory HBR points shown by the circles, there is also shown a single impact mass loss ratio (plotted at an obscuration value of zero) obtained on similar material at the Science Applications, Inc., (SAI) impact facility. A number of observations can be made from this figure. First of all, it seems clear that data obtained at the higher obscurations are well within the "multiple impact regime" described earlier. This is characterized by the eventual obscuration. Secondly, the multiple impact mass loss ratio of about 50 was twice that measured for the single impact or discrete impact tests. Figure 5b shows a similar series of tests through larger rain particles, 600 μ in diameter. In this case, the multiple impact rate was more like a factor of three greater than the single impact data also obtained at SAI.

COMPARISON OF SINGLE AND MULTIPLE IMPACTS

(U) In addition to measuring the critical obscuration in the multiple impact tests in the White Oak Laboratory HBR,

Vol. 3

an attempt was made to predict these values based on single impact test results. The measured crater diameter to particle diameter ratio for the SAI single impact test was approximately five. Using this information, a computer program was run simulating multiple impacts into a carbon-carbon target at 11,000 fps, i.e., identical to the range test results shown in Figure 5. The results of the computer simulation are shown in Figure 6. In the simulation, impacts were allowed to occur at random spacing on the target surface. The impact formed a crater five times larger than the particle diameter. Two hundred simulated cases were run with 1,000 impacts occurring for each case. As the obscuration or number of impacts was increased, the percentage of the new impacts that were occurring on previously cratered or "damaged" materials was tabulated. Obviously, the more times the surface was impacted, the greater the percentage of times a previously impacted site was hit. Using Figure 6 as a guide, it would be predicted that the surface would be "effectively" cratered at an obscuration of 0.08 to 0.1. However, the range data showed a critical obscuration of nearly twice that value. This implies that for carbon carbon, an area may have to be hit two or more times to "fully" damage the material.

(U) Using the range data generated under this study and other carbon-carbon range data obtained at the White Oak Laboratory a definition of impact regimes as a function of obscuration and impact velocity was made. The results are shown in Figure 7. For a given velocity, the mass loss ratios obtained at

obscurations below the transition zone were near those measured in discrete impact facilities. At obscuration above the transition zone, true multiple impact "plateaus" appeared to exist. In the transition zone, values would fluctuate from one extreme to the other. This curve, plus the mass loss ratios for the regimes, is the real design data the engineer needs to predict the erosion performance of a re-entry vehicle. Equipped with these, he can calculate the change in obscuration as the vehicle flies through a design cloud of interest and apply the correct mass loss ratio to the different regimes.

APPLICATION TO FLIGHT

(U) For many trajectory/cloud combinations, the regime of prime importance is the multiple impact regime, and, for practical purposes, the discrete impact regime only has a second order effect on the total erosion recession. Figure 8 shows the distance a re-entry vehicle would have to fly through clouds of various densities before reaching critical obscuration at a velocity of approximately 1,500 fps. Calculations are shown for clouds with nominal particle diameters of 100μ and 500μ .

(U) The width of the band represents a factor of two uncertainties in the critical obscuration. The upper edge is an assumed value of .1 and the lower edge is .05. The significant point here is that very short flight distances are required to "fully damage" the surface. For example, for a cloud density of $.5 \text{ gm/M}^3$, a carbon-carbon nose tip would be "fully damaged" within 25 to 85 meters at a velocity of 15,000 fps.

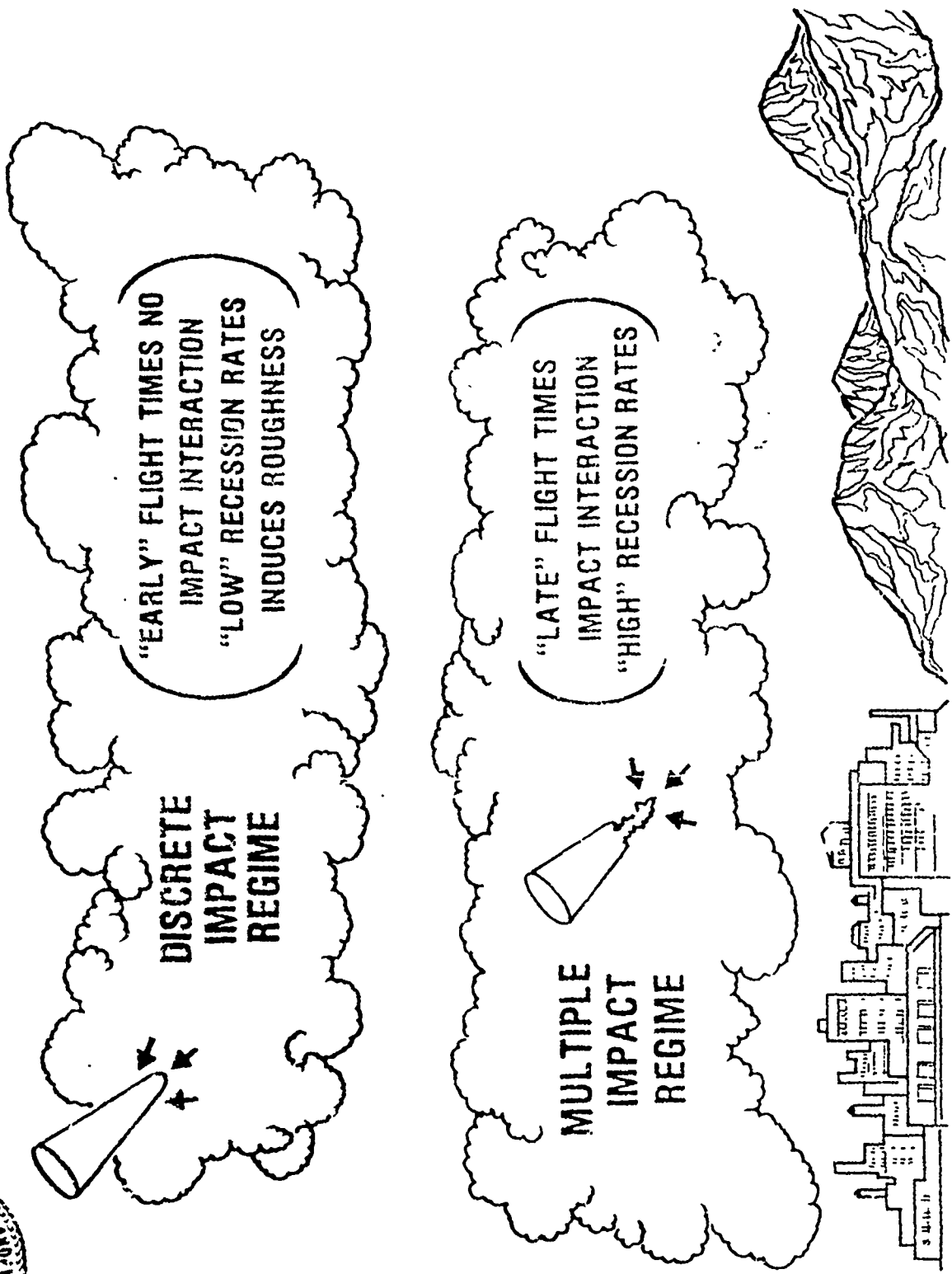
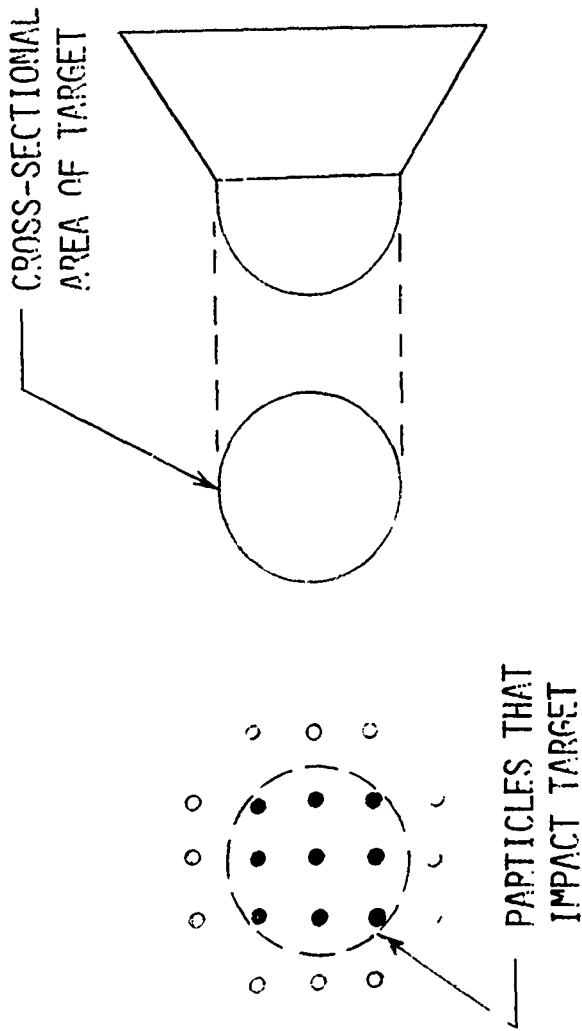


FIGURE 1 ILLUSTRATION OF IMPACT REGIMES





Σ c-s area of particles
c-s area of target

Obscuration =

FIGURE 2 DEFINITION OF OBSCURATION

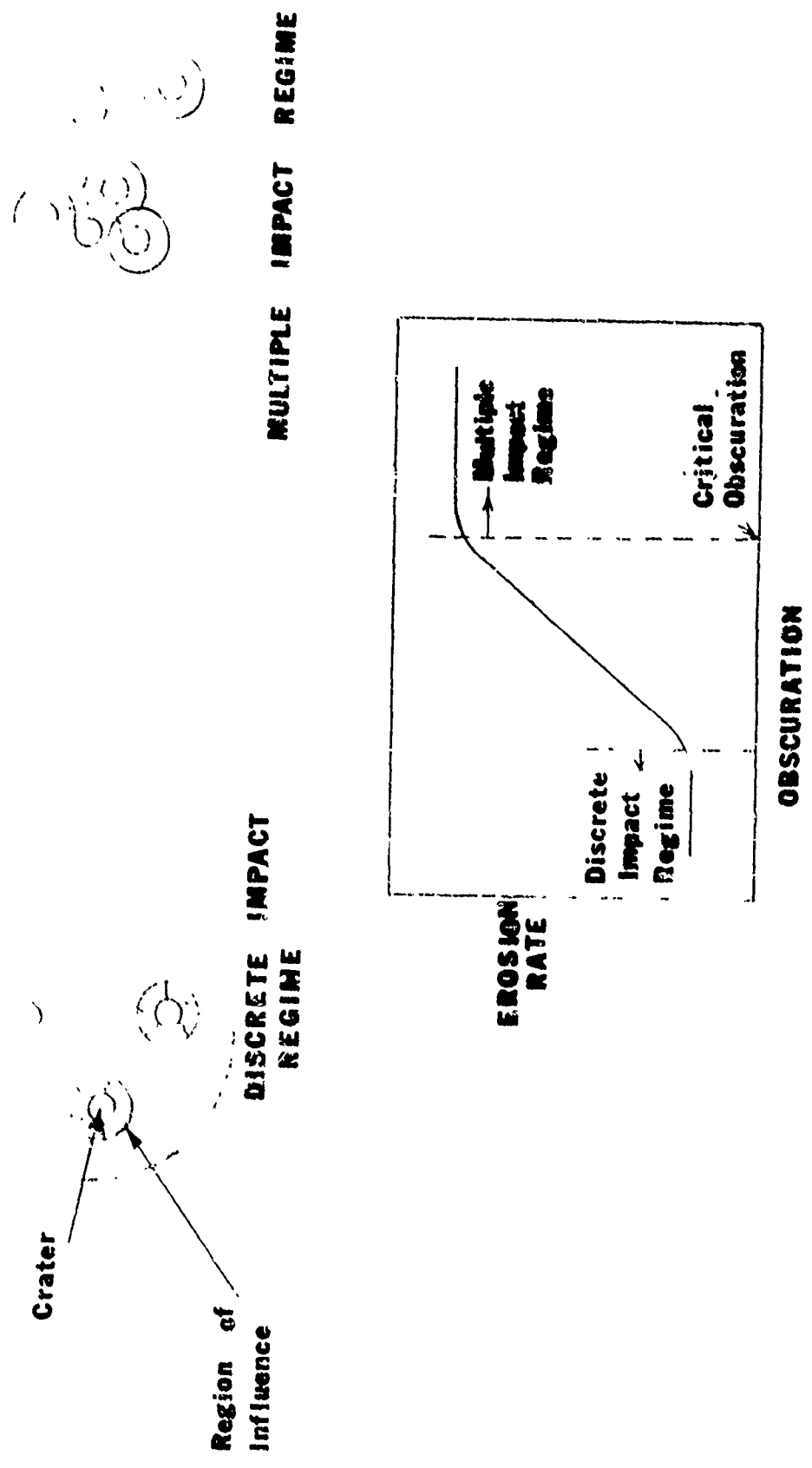


FIGURE 3 OBSCURATION REGIMES



FIGURE 4 EFFECT OF RAIN FIELD ON CARBON/CARBON

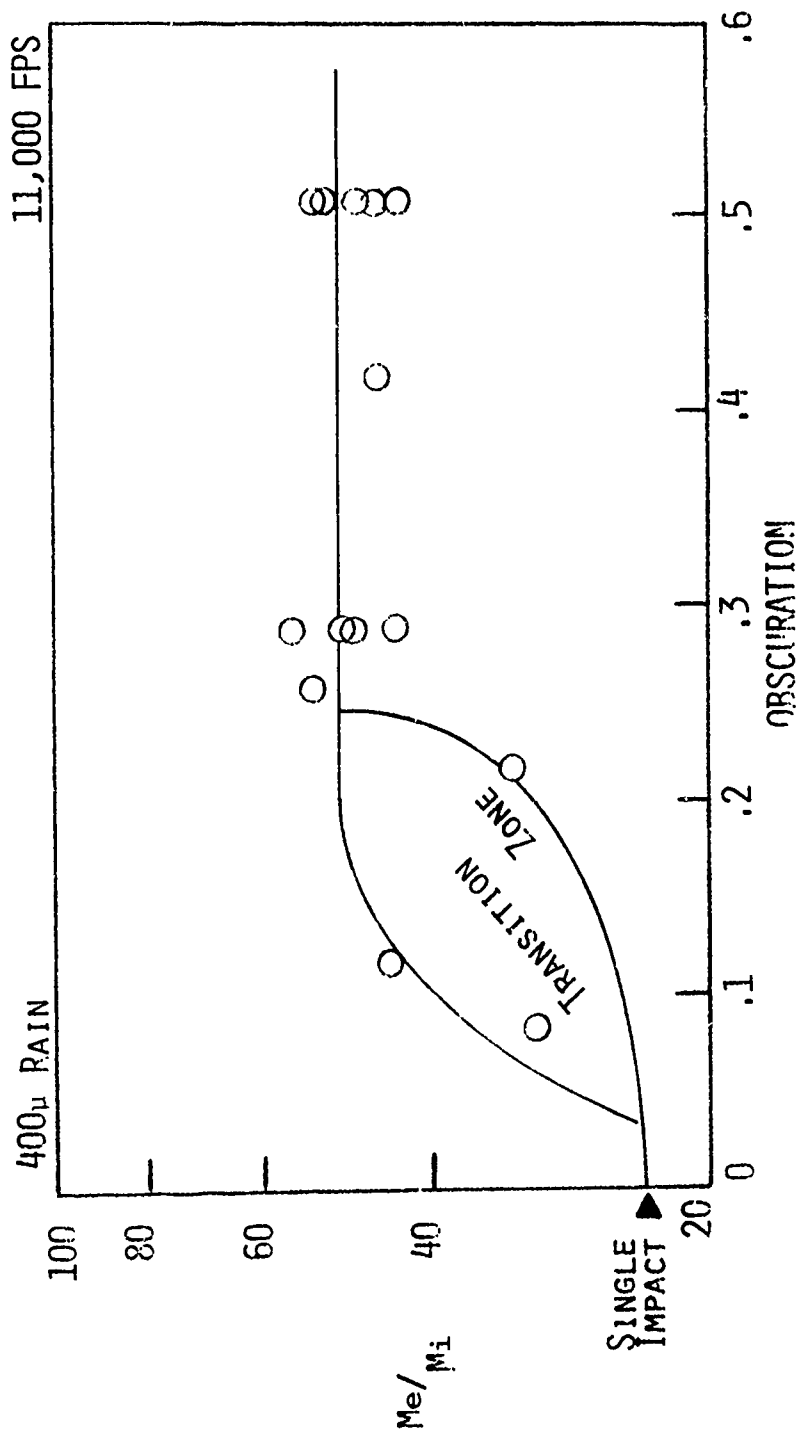
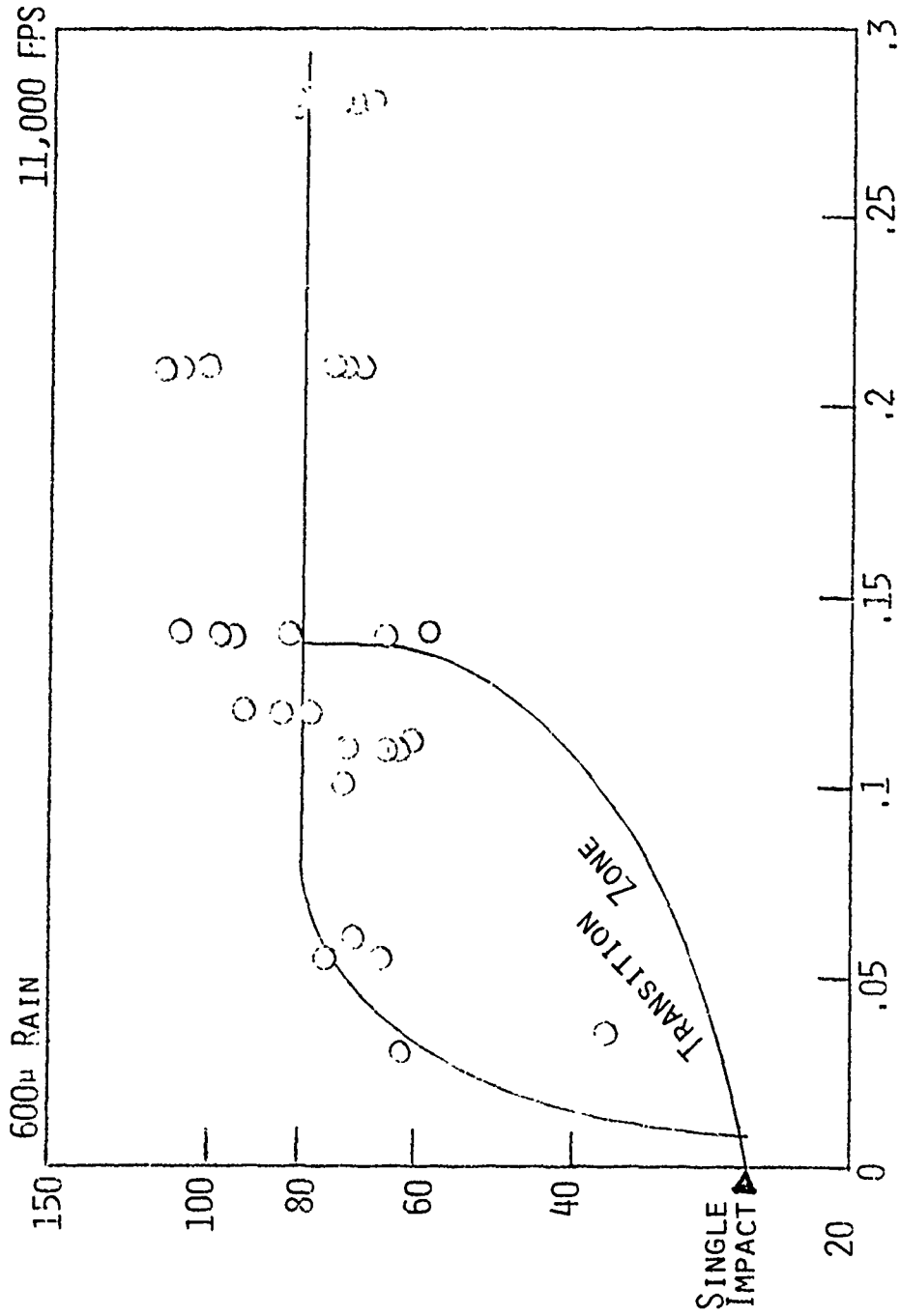


FIGURE 5A EROSION OF CARBON/CARBON SPECIMEN



OBSCURATION
FIGURE 5b EROSION OF CARBON/CARBON SPECIMEN

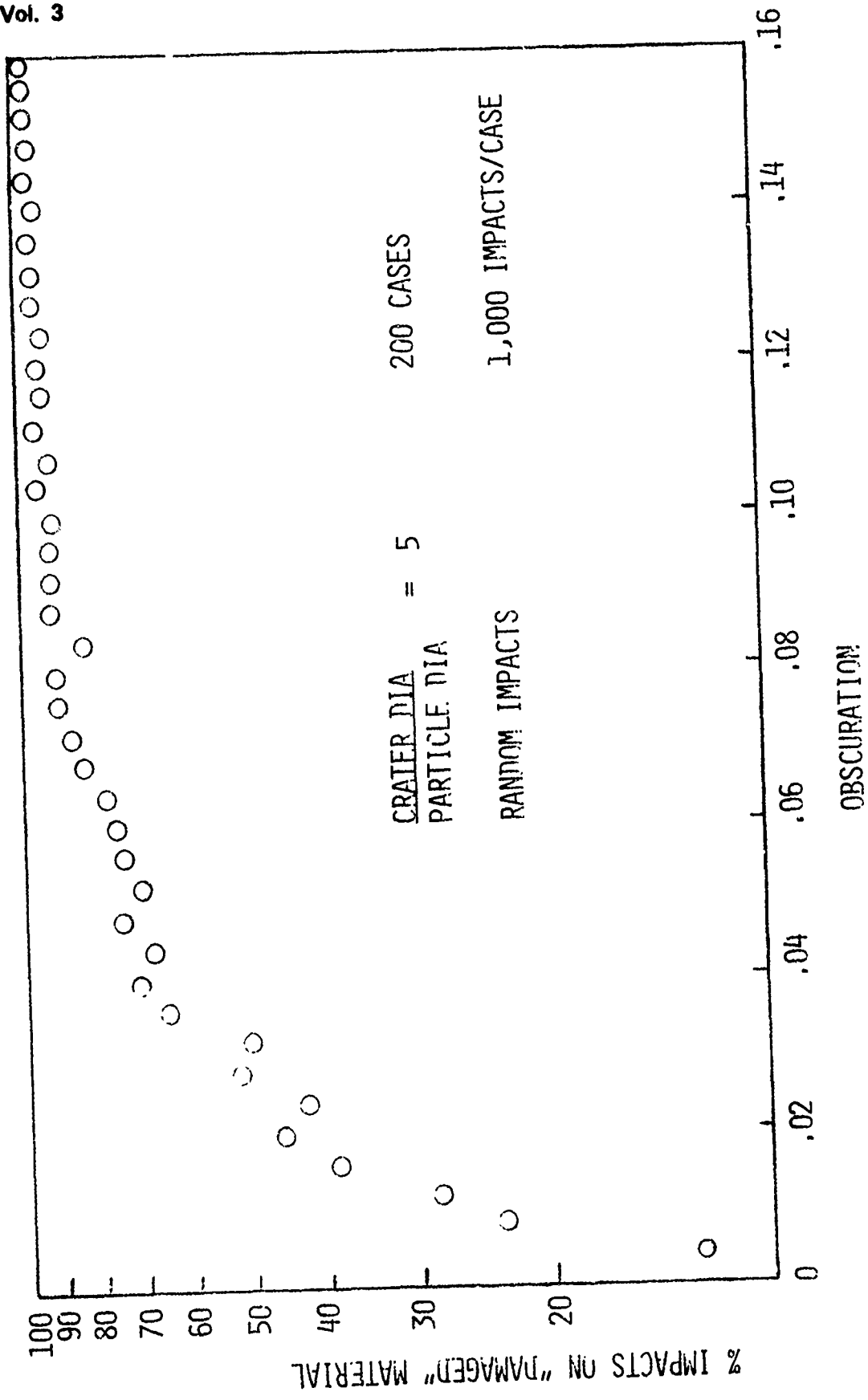


FIGURE 6 COMPUTER SIMULATION OF MULTIPLE IMPACTS

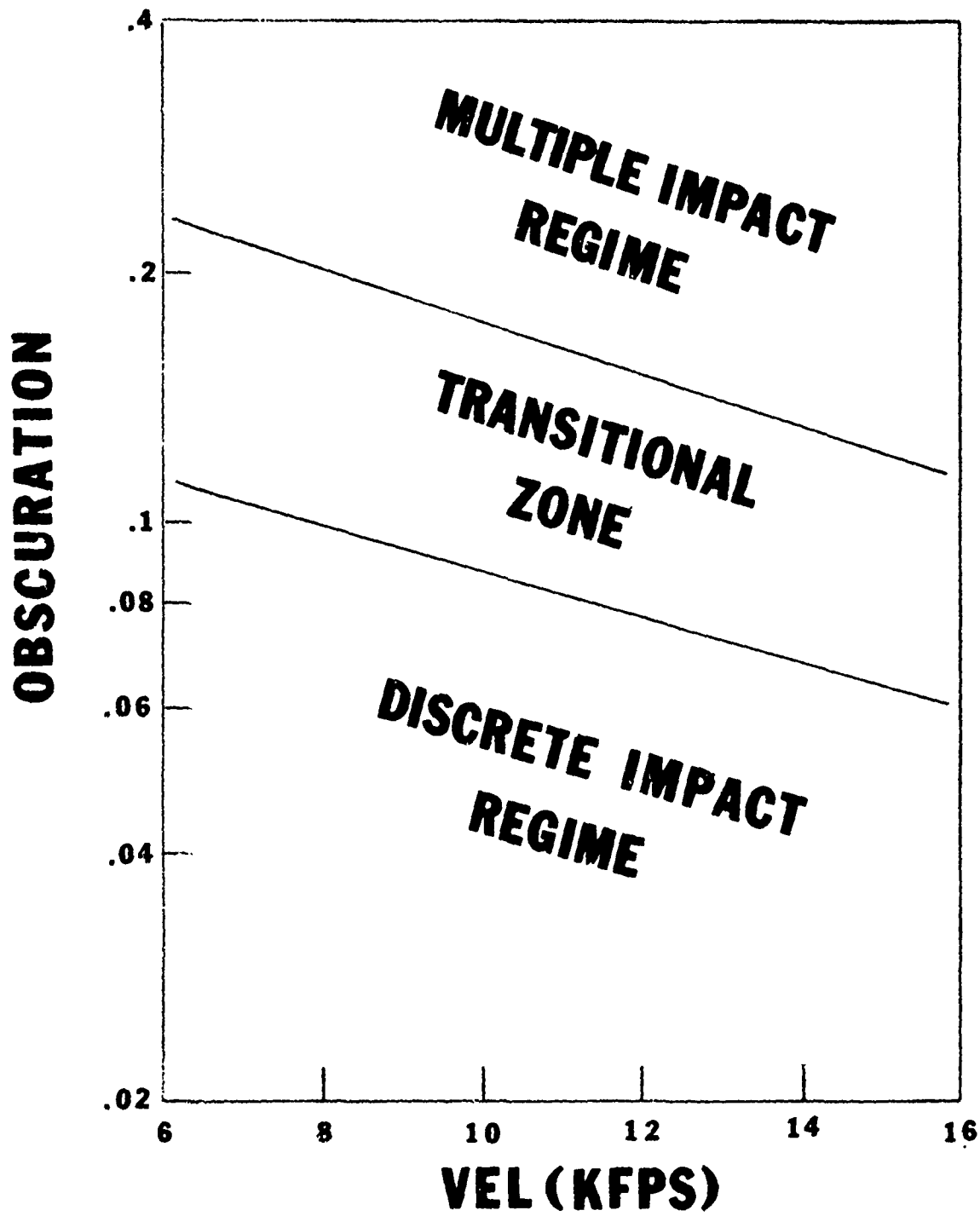


FIGURE 7 CARBON/CARBON IMPACT REGIMES

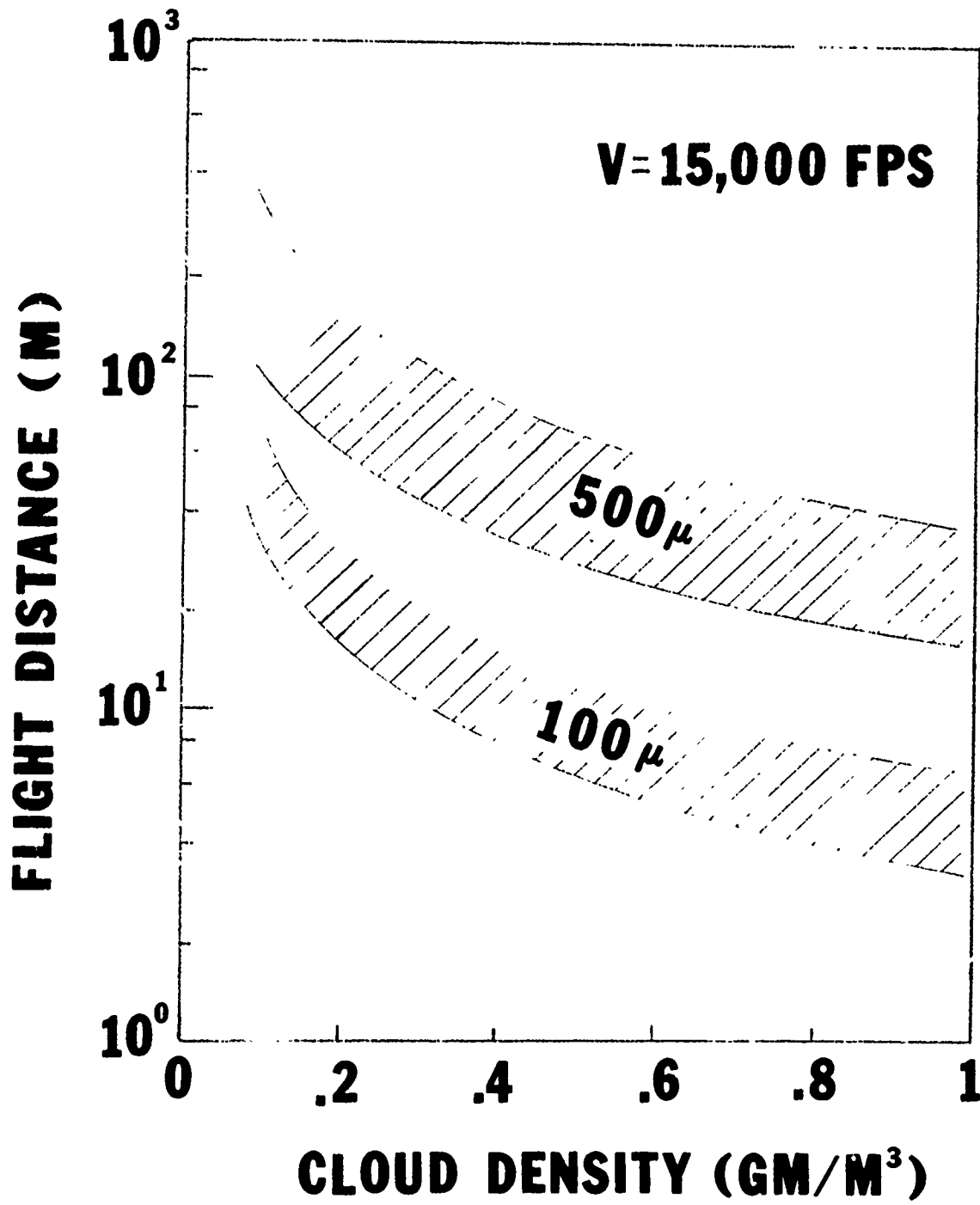


FIGURE 8 FLIGHT DISTANCES REQUIRED TO "FULLY DAMAGE"
CARBON/CARBON